WOODHEAD PUBLISHING SERIES IN ENERGY

Wind energy systems

Optimising design and construction for safe and reliable operation

Edited by John D. Sørensen and Jens N. Sørensen

WP
WOODHEAD PUBLISHING

Wind energy systems

Related titles:

Stand-alone and hybrid wind energy systems: Technology, energy storage and applications
(ISBN 978-1-84569-527-9)
Wind power generation is fast becoming one of the leading renewable energy sources worldwide, with increasing penetration of stand-alone and hybrid wind energy systems, particularly in distributed, isolated and community power networks. Advanced energy storage and grid integration systems are required to provide secure, reliable power supply to the end user. This book provides a comprehensive reference on the development of stand-alone and hybrid wind energy systems, as well as energy storage and building-/grid-integration systems. Chapters cover the design, construction, monitoring, control and optimisation of stand-alone and hybrid wind energy technologies, and the continuing development of these systems.

Fatigue life prediction of composites and composite structures
(ISBN 978-1-84569-525-5)
This important book will address the highly topical subject of fatigue life prediction of composites and composite structures. Fatigue is the progressive and localised structural damage that occurs when a material is subjected to cyclic loading. The use of composites is growing in structural applications and they are replacing traditional materials, primarily metals. Many of the composites being used have only recently been developed and there are uncertainties about the long-term performance of these composites and how they will perform under cyclic fatigue loadings. The book will provide a comprehensive review of fatigue damage and fatigue life modelling.

Details of these and other Woodhead Publishing materials books can be obtained by:

- visiting our web site at www.woodheadpublishing.com
- contacting Customer Services (e-mail: sales@woodheadpublishing.com; fax: +44 (0) 1223 832819; tel.: +44 (0) 1223 499140 ext. 130; address: Woodhead Publishing Limited, 80 High Street, Sawston, Cambridge CB22 3HJ, UK)

If you would like to receive information on forthcoming titles, please send your address details to: Francis Dodds (address, tel. and fax as above; e-mail: francis.dodds@woodheadpublishing.com). Please confirm which subject areas you are interested in.

Woodhead Publishing Series in Energy: Number 10

Wind energy systems

Optimising design and construction for safe and reliable operation

Edited by

John D. Sørensen and Jens N. Sørensen

Oxford Cambridge Philadelphia New Delhi

Published by Woodhead Publishing Limited, 80 High Street, Sawston,
Cambridge CB22 3HJ, UK
www.woodheadpublishing.com

Woodhead Publishing, 1518 Walnut Street, Suite 1100, Philadelphia,
PA 19102-3406, USA

Woodhead Publishing India Private Limited, G-2, Vardaan House 7/28 Ansari Road,
Daryaganj, New Delhi – 110002, India
www.woodheadpublishingindia.com

First published 2011, Woodhead Publishing Limited

British Library Cataloguing in Publication Data
A catalogue record for this book is available from the British Library.

ISBN 978-1-84569-580-4 (print)
ISBN 978-1-85709-063-8 (online)
ISSN 2044-9364 Woodhead Publishing Series in Energy (print)
ISSN 2044-9372 Woodhead Publishing Series in Energy (online)

The publisher's policy is to use permanent paper from mills that operate a sustainable forestry policy, and which has been manufactured from pulp which is processed using acid-free and elemental chlorine-free practices. Furthermore, the publisher ensures that the text paper and cover board used have met acceptable environmental accreditation standards.

Typeset by RefineCatch Limited, Bungay, Suffolk
Printed by TJI Digital, Padstow, Cornwall, UK

Contents

Contributor contact details

(* = main contact)

Editors

Professor John D. Sørensen
Aalborg Universitet
School for Civil Engineering
Denmark
E-mail: jds@civil.aau.dk

Professor Jens N. Sørensen
Technical University of Denmark
Department of Mechanical Engineering
Nils Koppels Alle
Building 403, room 226
2800 Kgs. Lyngby
Denmark
E-mail: jns@mek.dtu.dk

Chapter 1

Professor R. J. Barthelmie* and Professor Sara C. Pryor
Atmospheric Science Program
Multidisciplinary Science Building II
702 N. Walnut Grove
Indiana University, Bloomington
IN 47405
USA
E-mail: rbarthel@indiana.edu

Chapter 2

Professor James M. Tinjum*, PhD, PE
Department of Engineering Professional Development
University of Wisconsin-Madison
432 North Lake Street
Madison
WI 53706
USA
E-mail: tinjum@epd.engr.wisc.edu

Dr Richard W. Christensen
R W Christensen, Inc.
N739 Old 26
Fort Atkinson
WI 53538
USA
E-mail: rchriste@charter.net

Chapter 3

Dr V. A. Riziotis*
School of Mechanical Engineering
National Technical University of Athens
9 Heroon Polytechniou str.
15780 Athens
Greece
E-mail: vasilis@fluid.mech.ntua.gr

Dr H. A. Madsen
Wind Energy Division
Risø National Laboratory for Sustainable Energy
Technical University of Denmark
P.O. Box 49, DK-4000 Roskilde
Denmark
E-mail: hama@risoe.dtu.dk

Chapter 4

Professor Jens N. Sørensen
Technical University of Denmark
Department of Mechanical Engineering
Nils Koppels Alle
Building 403, room 226
2800 Kgs. Lyngby
Denmark
E-mail: jns@mek.dtu.dk

Chapter 5

Dr Paul S. Veers
Distinguished Member of the Technical Staff
Wind and Water Power Technologies
Sandia National Laboratories
Albuquerque
NM 87185
USA
E-mail: psveers@sandia.gov

Chapter 6

Senior Scientist Christian Bak
Risø National Laboratory for Sustainable Energy
Technical University of Denmark
Wind Energy Division
Building 118
P.O. Box 49
DK-4000 Roskilde
Denmark
E-mail: chba@risoe.dtu.dk

Chapter 7

Professor Z. Chen
Institute of Energy Technology
Aalborg University
Pontoppidanstraede 101
DK-9220 Aalborg East
Denmark
E-mail: zch@et.aau.dk

Chapter 8

Ir. T. van Engelen* and Dr S. Kanev
Energy Research Centre of the Netherlands (ECN)
Wind Energy
P.O. Box 1
1755 ZG Petten
The Netherlands
E-mail: vanengelen@ecn.nl; kanev@ecn.nl

Chapter 9

Professor Milan Veljkovic*
Luleå University of Technology
971 87 Luleå
Sweden
E-mail: milan.veljkovic@ltu.se

Professor Markus Feldmann, Dr Johannes Naumes and Daniel Pak
RWTH Aachen University
52074 Aachen
Germany
E-mail: feldmann@stb.rwth-aachen.de; naumes@stb.rwth-aachen.de; pak@stb.rwth-aachen.de

Professor Luis Simões da Silva and Associate Professor Carlos Rebelo
University of Coimbra
3030-788 Coimbra
Portugal
E-mail: luisss@dec.uc.pt; crebelo@dec.uc.pt

Chapter 10

Associate Professor Imad Alsyouf
Department of Mechanical Engineering
School of Engineering
Linnaeus University
Luckligs Plats 1
SE-35195 Växjö
Sweden
E-mail: Imad.Alsyouf@lnu.se

Chapter 11

Jochen Giebhardt
Fraunhofer Institute for Wind Energy and Energy System Technology (IWES)
Königstor 59
D-34119 Kassel
Germany
Email: jochen.giebhardt@iwes.fraunhofer.de

Chapter 12

Professor Takao Maeda*
Division of Mechanical Engineering
Mie University
1577 Kurimamachiya-cho
Tsu
Mie 514-8507
Japan
E-mail: maeda@mach.mie-u.ac.jp

Dr G. Schepers
Energy Research Centre of the Netherlands (ECN)
Wind Energy
P.O. Box 1
1755 ZG Petten
The Netherlands
E-mail: schepers@ecn.nl

Chapter 13

Dr Matthew Clifton-Smith
Garrad Hassan Pacific Pty Ltd
Suite 5A, Level 2
OTP House
10 Bradford Close
Kotara
New South Wales
Australia
E-mail: Matthew.Clifton-Smith@garradhassan.com

Dr David Wood*
Schulich School of Engineering
University of Calgary
Canada
E-mail: dhwood@ucalgary.ca

Dr Andrew Wright
School of Engineering
Faculty of Engineering and Built Environment
ES Building – ES408
University of Newcastle
University Drive
Callaghan
NSW 2308
Australia
and
Hydro Tasmania Consulting
4 Elizabeth St
Hobart
TAS 7000
Australia
E-mail: Andrew.Wright@hydro.com.au

Chapter 14

Professor L. Battisti
Department of Mechanical and Structural Engineering
University of Trento
Via Mesiano 77
38050 Povo
Trento
Italy
E-mail: lorenzo.battisti@ing.unitn.it

Chapter 15

Dr Ir. Jan van der Tempel*,
Ir. N. F. B. Diepeveen,
Ir. W. E. de Vries and
Ir. D. Cerda Salzmann
DUWIND
Delft University of Technology
The Netherlands
E-mail: j.vandertempel@tudelft.nl

Chapter 16

PD Dr-Ing. habil. Kerstin Lesny*
Institute of Geotechnical Engineering
University of Duisburg-Essen
45117 Essen
Germany
E-mail: kerstin.lesny@uni-due.de

Professor Dr-Ing. habil. Werner Richwien
Lichtenbergplatz 5
30449 Hannover
Germany
E-mail: werner.richwien@uni-due.de

Chapter 17

Ir. M. B. Zaaijer
Faculty of Aerospace Engineering
Delft University of Technology
P.O. Box 5058
2600 GB Delft
Kluyverweg 1
2629 HS Delft
The Netherlands
E-mail: M.B.Zaayer@tudelft.nl

Chapter 18

Luc Rademakers*, Henk Braam and Tom Obdam
Energy Research Centre of the Netherlands (ECN)
Wind Energy
P.O. Box 1
1755 ZG Petten
The Netherlands
E-mail: rademakers@ecn.nl

Woodhead Publishing Series in Energy

1 **Generating power at high efficiency: Combined cycle technology for sustainable energy production**
Eric Jeffs

2 **Advanced separation techniques for nuclear fuel reprocessing and radioactive waste treatment**
Edited by Kenneth L. Nash and Gregg J. Lumetta

3 **Bioalcohol production: Biochemical conversion of lignocellulosic biomass**
Edited by K. W. Waldron

4 **Understanding and mitigating ageing in nuclear power plants: Materials and operational aspects of plant life management (PLiM)**
Edited by Philip G. Tipping

5 **Advanced power plant materials, design and technology**
Edited by Dermot Roddy

6 **Stand-alone and hybrid wind energy systems: Technology, energy storage and applications**
Edited by J. K. Kaldellis

7 **Biodiesel science and technology: From soil to oil**
Jan C. J. Bart, Natale Palmeri and Stefano Cavallaro

8 **Developments and innovation in carbon dioxide (CO_2) capture and storage technology Volume 1: Carbon dioxide capture, transport and industrial applications**
Edited by M. Mercedes Maroto-Valer

9 **Geological repository systems for safe disposal of spent nuclear fuels and radioactive waste**
Edited by Joonhong Ahn and Michael J. Apted

10 **Wind energy systems: Optimising design and construction for safe and reliable operation**
Edited by John D. Sørensen and Jens N. Sørensen

11 **Solid oxide fuel cell technology: Principles, performance and operations**
Kevin Huang and John Bannister Goodenough

12 **Handbook of advanced radioactive waste conditioning technologies**
Edited by Michael I. Ojovan

13 **Nuclear reactor safety systems**
Edited by Dan Gabriel Cacuci

14 **Materials for energy efficiency and thermal comfort in buildings**
Edited by Matthew R. Hall

15 **Handbook of biofuels production: Processes and technology**
Edited by Rafael Luque, Juan Campelo and James Clark

16 **Developments and innovation in carbon dioxide (CO_2) capture and storage technology Volume 2: Carbon dioxide storage and utilisation**
Edited by M. Mercedes Maroto-Valer

17 **Oxy-fuel combustion for power generation and carbon dioxide (CO_2) capture**
Edited by Ligang Zheng

18 **Small and micro combined heat and power (CHP) systems: Advanced design, performance, materials and applications**
Edited by Robert Beith

19 **Hydrocarbon fuel conversion technology: Advanced processes for clean fuel production**
Edited by M. Rashid Khan

20 **Modern gas turbine systems: High efficiency, low emission, fuel flexible power generation**
Edited by Peter Jansohn

21 **Concentrating solar power (CSP) technology: Developments and applications**
Edited by Keith Lovegrove and Wes Stein

22 **Nuclear corrosion science and engineering**
Edited by Damien Féron

23 **Power plant life management and performance improvement**
Edited by John Oakey

24 **Direct-drive wind and marine energy systems**
Edited by Markus Mueller

25 **Advanced membrane science and technology for sustainable energy and environmental applications**
Edited by Angelo Basile and Suzana Nunes

26 **Irradiation embrittlement of reactor pressure vessels (RPVs)**
Edited by Naoki Soneda

27 **High temperature superconductors (HTS) for energy applications**
Edited by Ziad Melhem

28 **Infrastructure and methodologies for the justification of nuclear power programmes**
Edited by Agustín Alonso Santos

1

Meteorology and wind resource assessment for wind farm development

R. J. BARTHELMIE and S. C. PRYOR,
Indiana University, USA

Abstract: Assessing wind resources (wind speeds, directional distribution, turbulence intensity, etc.) for wind energy projects demands a level of detail and accuracy regarding the spatial and temporal variations of the wind and turbulence climate, which is beyond that required for other purposes. Hence a wide range of measurements and models have been developed and are employed to provide assessments for initial site identification, quantifying the long-term wind resource based on short-term measurements, extrapolating the vertical wind speed profile, calculating the potential power output from each turbine and for wind farm layout to optimize power output. Here we give an overview of the state of the art in wind resource assessment and look to the near-future in terms of developments in modeling and measurement techniques.

Key words: wind resource, measurements, modeling, wakes, climate.

1.1 Introduction

The process of identifying promising sites for wind energy development depends not only on the magnitude of the wind energy resource,[1] but also on other factors such as the proximity to the electrical grid. Environmental impact assessments and/or planning restraints often result in wind turbines within wind farms or even whole wind farms being modified, moved or even rejected during the planning phase. Nevertheless, herein we shall exclusively focus on the meteorological parameters that dictate the wind resource and review the mechanisms by which a robust wind resource assessment can be made. We will further discuss the meteorological factors that dictate the actual power production at a site and briefly articulate the methods used to make power production forecasts.

1.2 Assessment of the wind climate

The wind climate of a particular location is a function of processes at numerous temporal and spatial scales,[2] and the variability of wind and turbulence on scales from decades to seconds impacts the overall economics/desirability of a site from a wind energy perspective. In order to characterize site specific wind energy resources for wind energy development, a number of steps are usually undertaken that are shown schematically in Fig. 1.1 and are described in the following sections.

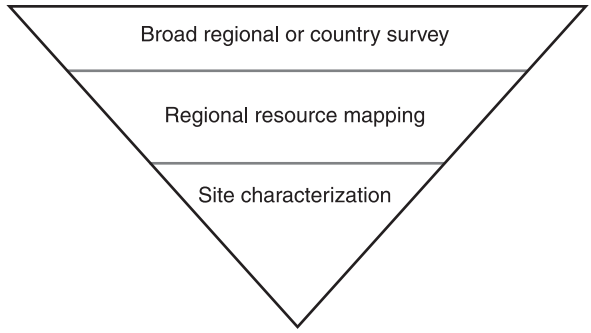

1.1 Steps towards developing site climatology.

1.2.1 National assessments

A regional-scale wind climate assessment can be made using a variety of data sources and methods that are not necessarily of sufficient accuracy to constitute a 'bankable' wind resource, but will likely identify areas worthy of further investigation. The precise wind speed and energy density climate necessary to make a development economic varies according to, among other things, the type of support mechanism in place and whether extension of the electrical grid to the site is necessary and will be installed by the transmission operator or whether this has to be part of the wind energy development. This means that the wind climate is frequently articulated in terms of wind speed classes so that users can make their own judgments about whether the available wind resources designate the area or site as worth pursuing.

Wind climate assessments have been made for some countries/regions by governmental or other agencies (e.g. national meteorological services or departments of energy) using a variety of approaches and data sources, including:

1 Analysis of reanalysis products.[3–5] Reanalysis projects draw data from a range of sources, which are quality controlled and assimilated with a consistent data simulation system (models). These reanalysis products are thus a hybrid of the observations that are assimilated and 'background' information used to provide complete representations of the atmosphere that are derived from a short-range forecast initiated from the most recent previous analysis. The reanalysis products thus comprise four-dimensional, homogenized and systematic datasets. The reanalysis systems were not designed principally for wind climates, and comparisons with independent observations of wind speeds exhibit substantial discrepancies.[6] Nevertheless, they have the advantage of being physically consistent and continuous in time and space, but the disadvantage is that global reanalysis datasets are available only on fairly coarse time and space (horizontal and vertical) scales. However, recently regional reanalyses with relatively high temporal and spatial resolution have

been undertaken (e.g. the North American Regional Reanalysis is available at a resolution of ~ 32 × 32 km for 1979–2006).[7]

2 Pressure gradient data.[8,9] An estimate of the geostrophic wind speed (i.e. the wind speed that would be attained in the absence of frictional effects and curvature of isobars) may be derived from mean-sea-level pressure data. The technique has proved particularly useful in the context of reconstructing long-time series in order to examine climate variability,[10] but naturally does not reflect the actual wind climate at a specific location. Pressure gradients have also been used to estimate extreme wind speeds.[11]
3 Near-surface meteorological or other wind speed measurements from national weather observing networks.[12,13] Observational records of near-surface wind speeds are subject to data inhomogeneities associated with the introduction of new measurement technologies or protocols (e.g. deployment of the Automated Surface Observing System in the USA during the 1990s) or site relocations/modification of site characteristics, hence care has to be taken in interpreting these data.[6]
4 Mesoscale modeling. Numerical and analytical[14] models have been applied to map the wind climate and wind energy resource at a range of spatial resolutions for regional, national and continental domains, e.g. Ref. 15 and Ref. 16. These research activities are described in more detail below.
5 Satellite-borne remote sensors have been used to obtain estimates of offshore wind climates.[17] The satellite data most widely used to date derive from polar orbiting satellites equipped with scatterometers (e.g. QuikSCAT) and/or Synthetic Aperture Radar (SAR).[18–21] The resulting datasets have high spatial coverage;[22] however, they have limitations in terms of the accuracy of the wind speed estimates, data truncation due to the operational range of the methods used to invert the back-scatter to wind speeds, limited data availability in the coastal zone and availability of sufficient images for characterizing wind resources.[23,24]

It is instructive to briefly reflect on the strengths and weaknesses of these data sources. Direct in-situ observational data are essentially free from parameterizations but are subject to inhomogeneities resulting from changes in instrumentation, instrument malfunction, station moves, changes in land-use or obstacles around the station and may be limited by substantial missing data and have comparatively coarse data resolution in the context of computing a robust wind climate (e.g. in the USA wind speeds from the NWS network are reported to the nearest whole knot). Additionally, observational sites may or may not be regionally representative. Conversely, the reanalysis simulation packages ensure that the datasets are homogenous and complete, but near-surface wind speeds are strongly influenced by model physics, resolution and the data that are assimilated. Satellite-borne instrumentation such as SAR and scatterometers provide excellent spatial coverage but often with low temporal resolution, relatively low precision and are limited in their ability to retrieve accurate data in the coastal zone. Numerical models can in principal simulate the dynamical causes of wind variability, but

their accuracy is of course dictated by factors such as the parameterizations used and the accuracy of lateral boundary conditions. As a result of these relative strengths and weaknesses, wind climates are often derived from a combination of one or more of the above.

Plate I (see between pages 286 and 287) shows the well-known wind resource map from the European Wind Atlas[13] that has been updated by Risø DTU (see *www.wasp.dk*). The WAsP model used in this study[14] has been used to map wind resources in many countries and is described in brief below.

1.2.2 Regional wind climate assessments

Once areas have been identified that have suitable wind climates (i.e. moderate or better wind resources), further modeling or mapping can be used to characterize wind speeds at higher resolution in space and time in order that possible development sites can be identified. Although a variety of approaches have been used in the past including, for example, for offshore measurements from ships[25] or surface observations,[26] the most common contemporary method is mesoscale modeling.

Mesoscale meteorological models commonly applied for wind energy resource estimation are essentially numerical weather prediction models that discretize the fluid domain and solve primitive equations (i.e. fundamental equations of atmospheric dynamics).[27] These models describe the time evolution of the atmosphere in three dimensions in terms of temperature, pressure, humidity, etc.[28] Mesoscale modeling has the advantage in terms of wind resource estimation that it does not require local on-site meteorological data; it can be applied even in moderately complex terrain[29,30] and for offshore[31–33] and can be run (assuming sufficient computational resources are available) at a resolution down to approximately 1 km. As with all modeling, the quality of the output is determined by the quality of the input data used to provide lateral, boundary and initial conditions, and the parameterizations employed for unresolved processes. For wind energy, key input data include orographic and surface roughness fields that can be derived in detail from remote sensing data. Mesoscale models can be initialized using a variety of data sources (e.g. temperature profiles obtained from reanalysis data or radiosonde measurements). In terms of generating a wind climate, mesoscale models are usually run for specific climatologically representative cases with subsequent compositing to generate a comprehensive wind climate[29] rather than being used to simulate a full climatology of multiple years. Although initially limited computing resources meant that mesoscale models were used to simulate particular situations or phenomena (e.g. Ref. 34), they are increasingly used to generate wind energy atlases. Examples include:

- the Canadian Wind Energy Atlas *http://www.windatlas.ca/*, which is based on the MC2 mesoscale model[35]
- wind mapping over Sweden using the MIUU mesoscale model.[36]

1.2.3 Site assessments

Once a prospective development site has been identified, most projects depending on their location and/or financing require an on-site resource assessment to be conducted. Such a project would typically have two parts: a short period during which meteorological measurements were conducted in situ, followed by an analysis designed to relate these measurements to the longer-term climate conditions that the wind turbines, once installed, will be expected to experience. There may be exceptions to the necessity of on-site measurement if, for example, good quality measurements are available from one or more close and similar site(s) in homogeneous conditions and the project does not need to obtain external funding.

1.3 From wind climates to wind resources

The instantaneous energy density in the wind, E, is proportional to the cube of the wind speed, U:

$$E = \frac{1}{2}\rho U^3. \qquad [1.1]$$

Hence uncertainties in the measured wind speed are magnified as uncertainties in energy density and is one of the reasons that specific on-site measurements are required.[37] As described above, wind measurements made for other purposes may exist but these will rarely be of sufficient quality to make an accurate wind energy assessment. Accurately determining the mean wind speed at hub height is by no means sufficient. Because power output is strongly dependent on the wind speed via the turbine power curve, and the energy density is dominated by the upper percentiles of the wind speed probability distribution, the whole wind speed distribution must be characterized. An illustration of the relationship between the wind speed regime – energy density and potential electricity production – is given here for a coastal site in Denmark. The probability distribution of wind speeds as observed at 50 m for 1997–2003 is shown in Fig. 1.2, along with the fit to the data from a two-parameter Weibull distribution, where the frequency of occurrence $f(u)$ of a wind speed u is given by:

$$f(u) = \frac{k}{A}\left(\frac{u}{A}\right)^{k-1} \exp\left(-\left(\frac{u}{A}\right)^{k}\right). \qquad [1.2]$$

The mean wind speed at the site is 8.1 ms^{-1}, the Weibull scale factor A (which is related to the central tendency) is 9.1 ms^{-1} and the shape factor k (which is related to the variability) is 2.25. As shown in Fig. 1.2, the data are well represented by the two-parameter Weibull distribution as is common in sites in simple topography in northern Europe that do not have channeled flows or a high number of calms.[38]

A sample power curve for a Bonus 1 MW turbine with a hub height of 50 m is also given in Fig. 1.2. The total potential power output (P) can be calculated by combining the wind speed distribution with the power curve ($P(u)$):[39]

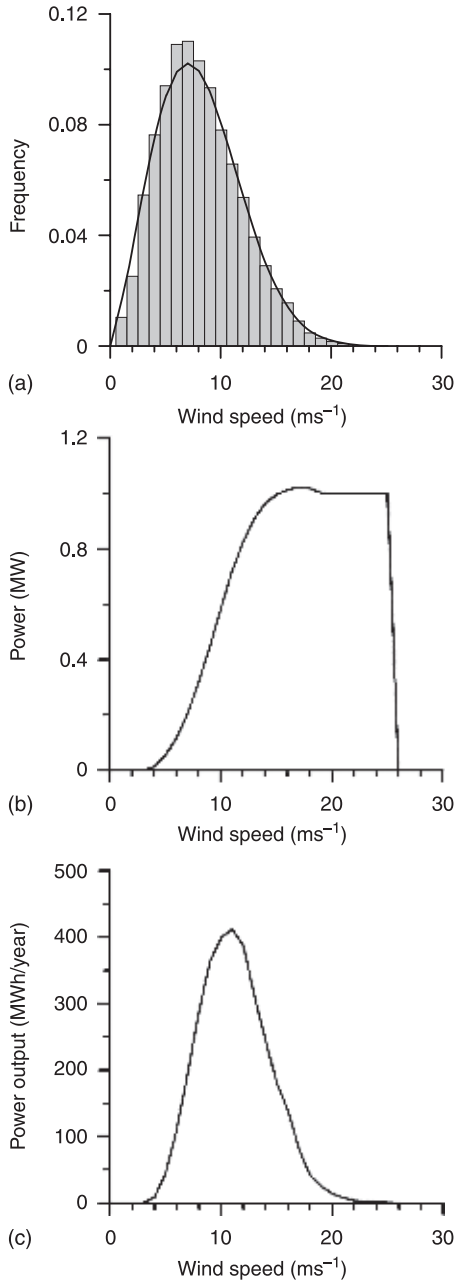

1.2 (a) Example wind speed distribution from observations (bars) and a Weibull fit (line). (b) A sample power curve for a Bonus 1 MW turbine. (c) Power output (in MW hours per year) for this site for the Bonus 1 MW turbine shown by wind speed.

$$P = \int_0^\infty \left(\frac{k}{A}\right)\left(\frac{u}{A}\right)^{k-1} \exp\left(-\left(\frac{u}{A}\right)^k\right) P(u)du. \quad [1.3]$$

As shown in Fig. 1.2, wind speeds above 11 ms^{-1} are observed less than 20% of the time but responsible for about half the total power output. Although not a focus of this chapter it is worthy of note that the wind climate also plays a key role in dictating extreme and fatigue turbine loads.[40] High wind speeds close to 25 ms^{-1} (the wind speed at which most turbines shut down for safety reasons) may be important in a power integration context but, in most areas, wind speeds above 20 ms^{-1} contribute relatively little to the total power output because they are too infrequently observed (Fig. 1.2).

Making accurate on-site resource measurements for wind energy is a skilled task. Measurements to wind turbine hub height are always recommended because this will reduce the overall uncertainty in the energy prediction. However, for small projects and particularly for offshore developments, the expense of measuring beyond 50 m may be prohibitive. In this case, some method of extrapolating the vertical wind speed profile will be necessary and these are discussed below. It will also be necessary to consider the longer-term wind speed variations due to natural climate variability and these are also considered below.

1.3.1 *In situ* measurements

In situ measurements on traditional meteorological masts have largely been limited to heights lower than 100 m,[41] although some facilities such as the FINO research platforms in the North Sea have provided a platform for extending the top measurement height up to or above 100 m.[42,43] It should be recognized that the accuracy required for wind speed measurements for wind resource assessment far exceeds requirements for general meteorological purposes and that great care must be taken in the measurement campaign to ensure data quality and representativeness,[37,44] particularly if the measurements are to be 'bankable'. Key aspects in making good quality in-situ measurements include: careful site selection, use of a suitable meteorological mast and high quality calibrated instrumentation, use of sufficiently long and slender booms, mounts and clamps, considering the impact of tower shadow on the wind speed measurement, and robust and reliable data acquisition, storage and transmission.

Recently, ground-based remote sensing tools, such as SODAR (sound detection and ranging)[45–47] and LIDAR (light detection and ranging)[48–51] systems, have been deployed to characterize wind speed and turbulence profiles. SODARs and LIDARs operate by emitting pulses of radiation a small fraction of which is scattered back to the receivers. The Doppler shift in the return signal is related to the relative movement of the particles that reflected the radiation. These systems can in principle retrieve vertical discretized profiles of wind speed to several hundreds of meters above the ground.[52] The quality of SODAR-retrieved wind

speeds is very much dependent on ambient noise, while LIDARs exhibit sensitivity to signal contamination from cloud and fog. Nevertheless when careful data processing methods are applied, wind speeds derived from LIDAR systems exhibit relatively good closure with in-situ measurements from sonic and cup-anemometers,[53–55] and may provide bankable measurements and as such become an alternative to a tall meteorological mast.[48,49]

1.3.2 Extrapolating in space and time

In situ measurements are typically only undertaken at a limited number (frequently only one) of locations within the proposed area of the wind farm, for a short time period (frequently only one year), and extrapolating beyond those data often requires use of wind farm models. These models can be used to extrapolate in time – i.e. from the short measured time series to a climatologically representative period, and to assess the degree of variability across the wind farm site.

Wind farm models tend to be highly parameterized or linearized in order to increase their speed (or decrease the amount of computing resource required). It is common to use such models to simulate the wind resource over areas of about 25 km^2 and to predict annual power output of about 100 turbines. For this kind of task, a typical computing time for such models would be 10 minutes or less. Herein we use the WAsP[14] as an exemplar of wind farm models, and will discuss it below in the context of micro-siting. WAsP works on the similarity principle – that is, it takes observations from one site within a region and, along with information regarding surface characteristics, uses it to develop an estimate of the wind climate at other locations within the region. The model thus requires as input a time series of wind speed and wind direction measurements and information about the orography, roughness and presence of obstacles within the region. WAsP first runs a series of models to 'clean' the dataset of these local influences and presents the resulting wind resource as a regional wind climate. Then assuming that the site for which the wind climate is to be predicted lies within the same wind regime, the process is run in reverse supplying orography, roughness and obstacles for the site to be predicted. WAsP does not model flow separation so should not be applied for flow in complex terrain. However, there are tools for improving predictions in moderately complex terrain.[56] WAsP also assumes that the wind speed data fit a two-parameter Weibull distribution as described above. Clearly the quality of the wind resource assessments produced by wind farm models such as WAsP are dependent on the quality of the data used as input. For example, if only a short-time series is used as input, corrections to extrapolate to the long-term wind climate would need to be applied to WAsP results. WAsP extrapolates from different measurement heights to turbine hub heights using a modified form of the logarithmic wind speed profile that is slightly stable (see below). Different parameters are used for on- and off-shore and the parameters can be modified if more information is available such as the surface heat flux. WAsP also modifies the

wind speed profile according to roughness changes in each directional sector. However, it does not account for time-varying stability changes such as, for example, the diurnal cycle.[57] Wind farm models may also include modules for visualization and grid layouts and other tools useful in wind farm design.

An alternative to the use of wind farm models is to apply a mesoscale model[32,33,58] at high resolution. Because mesoscale models are less parameterized than wind farm models and represent (broadly) the physics of the atmosphere, they are much more demanding in terms of computing resources and are still rarely applied in time-series mode. It is more common to simulate a number of representative cases and then combine these according to the site climatology to make a resource assessment.[59] Mesoscale models have many advantages over linearized models in that, if applied correctly, they can model thermal flows such as sea breezes and have time-varying atmospheric stability. However, results from the model, even at 1 km resolution, still have to be downscaled to a specific site typically using statistical techniques[29] or wind farm models.[60] A mesoscale model applied in a sufficiently large domain to capture the dominant thermo-topographic flows and then downscaled with a wind farm model can be a very useful combination.

The accessibility of large computing resources means that computational fluid dynamics (CFD) models are starting to be applied in a wind resource context. An example of this is the Norwegian Wind Atlas (*http://www.windsim.com/wind_energy/wind_atlas/index.html*), which is based on the WindSim model. To date CFD has mainly been applied for modeling specific cases[61,62] but CFD could also be a powerful tool as part of a wind resource assessment particularly in complex terrain. CFD can also be combined with other types of model such that it could, for example, be used as a downscaling tool.[63] Other types of non-linear modeling including large eddy simulations are also beginning to be applied for examining flow in specific cases.[64]

On-site wind speed measurements are usually only available for short periods of one or two years, whereas energy output assessment has to be made for the lifetime of the wind farm. Even in the absence of climate non-stationarity, variations in wind energy density over seasonal and inter-annual time scales can be significant.[65] The inter- (and intra-)annual variability of wind speeds, wind indices and energy density are naturally a function of the regional climate, and frequency and intensity of transient storm systems, and of the spatial scale of aggregation. At the short time scales this variability leads to intermittency of electricity production and the need for short-term prediction of power output (see below), and at longer time scales it has relevance for project economics.[66] Variability in wind speeds and energy density is often quantified using wind indices (WI):[67]

$$\mathrm{WI} = \sum_{j=1}^{n} \frac{U_j^3}{U_{i\ldots k}^3} \times 100, \qquad [1.4]$$

where $j = 1, n$ indicates the time series from the period of interest, and $i\ldots k$ indicates the normalization period. For example, in the wind index used in Ref. 67 $i\ldots k$ represent four-times-daily observations over the normalization period 1990–2001

and $j = 1$, n are four-times-daily observations from the year of interest. Thus WI gives an annual index of energy density. If WI is 100% the year of interest has an energy density equal to the long-term mean experienced in the normalization period.

Historical inter-annual variability across much of Europe, measured as the standard deviation of annual wind indices, is approximately ±10–15% (Ref. 2 and Ref. 67) and inter-decadal variability is approximately ±30% (Ref. 2). An example of a WI computed using output from a reanalysis model is shown in Fig. 1.3 for a site in Northern Europe, where a normalization period of 1948–2006 was used. As shown, the inter-annual variability is up to ±40%. Even assuming that a 30-year record is available, there is still variability of the order of ±8% compared to the mean over the whole period (1948–2006).

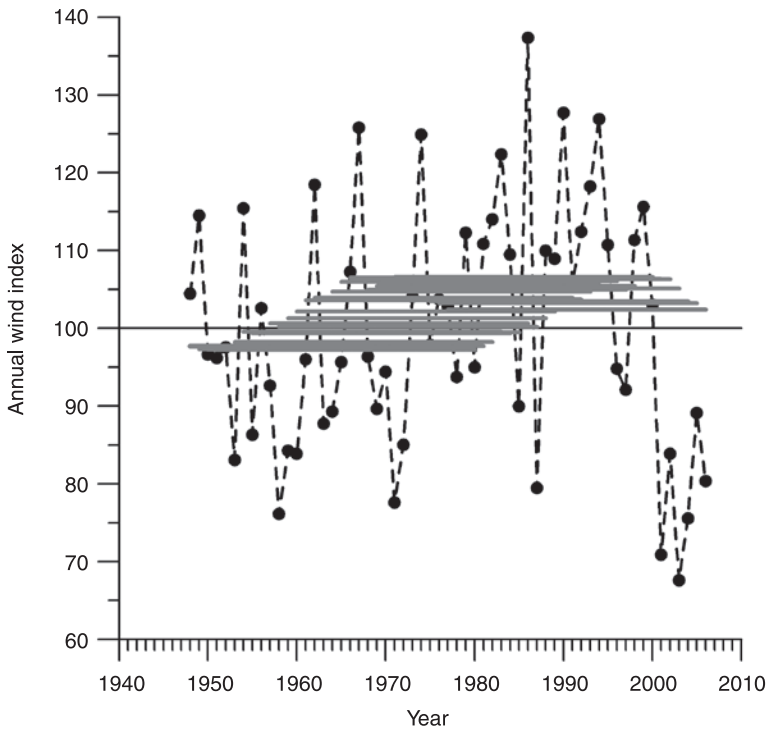

1.3 Annual wind index from the NCEP/NCAR reanalysis dataset for a grid cell near Edinburgh, Scotland, computed using a normalization period of 1948–2006. The dots and black dashed lines show the wind index for individual years. The grey lines show 30-year averages of the wind index moving year-by-year through the record.

This emphasizes the need to consider short-term records in a longer-term context. There are several methods of making this correction such as:

- Measure–correlate–predict – a standard method of relating two time series usually using linear correlation (e.g. Ref. 68). This method is shown schematically in Fig. 1.4. The relationship between the short-term site wind speed measurements and the overlap period with the long-term reference dataset is established (usually by directional sector), typically with a linear regression equation. The equation(s) is (are) then applied to the long-term reference dataset to produce a wind climate for the site, which is representative for the long-term period. An alternative is to use the ratios of the two parameters of the Weibull distribution for the two periods but this may not correctly reproduce the energy density.
- Assume that the ratio of energy density at the long-term reference site for the short overlap period (R_S) to the long-term (R_L) is the same as the ratio of energy density for the two periods at the measurement site (M_S (short-term) and M_L (long-term)), that is:

$$\frac{M_s}{M_L} = \frac{R_s}{R_L}. \qquad [1.5]$$

  Energy density predictions for the measurement site can be calculated from data from the reference site, for example in WAsP for the short overlap period (R_S) and for the long-term (R_L). The 'long-term corrected' energy density (M_L) can then be approximated from equation [1.5] using the energy density from short-term measurements (M_S).
- Compare energy predictions from the overlap period with a wind energy index.[67]

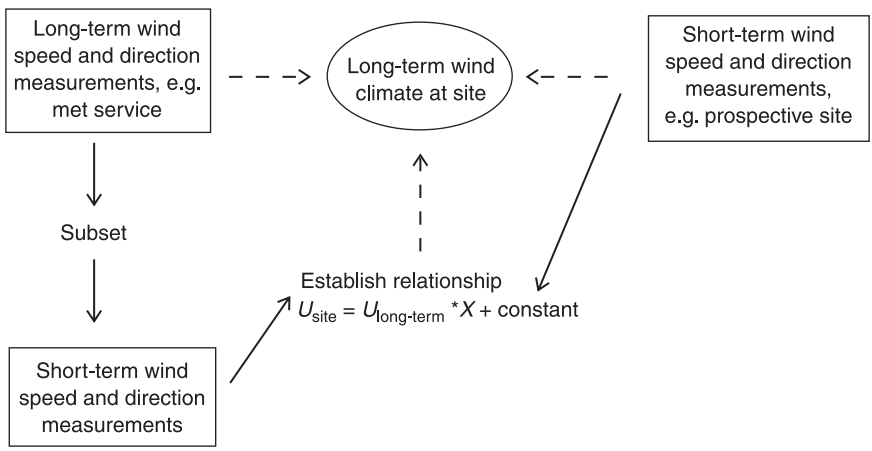

1.4 Schematic of measure–correlate–predict method for extrapolating from short-term measurements to a long-term site wind climate.

These methods should be considered approximate since it is apparent that the short-term site data have to be assumed to be broadly representative of the longer-term climate in terms of representing the directional distribution of wind speeds and of capturing the range of wind speed, turbulence and wind shear conditions at the site. For this reason it is imperative that a full year of data is used for the short-term measurements, particularly for offshore where stability variations are seasonal rather than diurnal.[57]

1.3.3 Extrapolating vertically

Wind speed varies strongly with height within the first few tens of meters in the atmosphere. Several models have been developed to describe this variation. The simplest is the power law where the wind speed (U_z) at height z is related to the wind speed (U_r) at reference height z_r via a wind shear exponent α:

$$U_z = U_r \left(\frac{z}{z_r}\right)^{\alpha}. \qquad [1.6]$$

The wind shear exponent carries all the site information so that no assumptions about roughness changes or stability are used, although the site data could be broken down into directional sectors or specific time periods and the shear exponent evaluated for each of these.

An alternative is to use the logarithmic profile where the wind shear depends on the logarithm of the height, the roughness length z_0 and the friction velocity u_*:

$$U_z = \frac{u^*}{\kappa} \ln\left(\frac{z}{z_0}\right). \qquad [1.7]$$

However, to avoid the need to calculate the friction velocity, the equation is more commonly used to calculate the wind at height z from the wind speed at a reference height:

$$U_z = U_r \ln\left(\frac{z}{z_0}\right) / \ln\left(\frac{z_r}{z_0}\right), \qquad [1.8]$$

where κ is the von-Karman constant (0.4). There are a number of methods for estimating z_0, the simplest being to use the surface type (e.g. Ref. 13 and Ref. 69). Equation [1.7] implicitly assumes the atmosphere is near-neutral (i.e. that all turbulence derives from mechanical sources and is unmodified by thermal effects). The stability corrected or diabatic wind speed profile is defined by:[70]

$$U_z = \frac{u^*}{\kappa}\left[\ln\frac{z}{z_0} + \Psi_m\left(\frac{z}{L}\right)\right], \qquad [1.9]$$

where $\Psi_m(z/L)$ is the stability function for momentum and L is the Monin–Obukhov length which is a metric of atmospheric stability:[70]

$$L = \frac{-u_*^3}{(\kappa(g/\overline{\theta}_v)(\overline{w'\theta'}_v))}, \qquad [1.10]$$

where the over-bar indicates a time average, g is acceleration due to gravity, $w'\theta_v'$ is the virtual kinematic heat flux and θ_v is the virtual potential temperature.

The stability function $\psi_m(z/L)$ in stable conditions, where L is positive, is given as:[70]

$$\Psi_m = 4.7\,\frac{z}{L}. \qquad [1.11]$$

For unstable conditions, L is negative, and the correction is:

$$\Psi_m = -2\ln\left(\frac{1+x}{2}\right) - \ln\left(\frac{1+x^2}{2}\right) + 2\tan^{-1}(x) - \frac{\pi}{2}, \qquad [1.12]$$

$$\text{where } x = \left(1 - 15\frac{z}{L}\right)^{1/4}.$$

Figure 1.5 provides examples of the wind speed profile that would be derived using equation [1.6] or [1.7] to extrapolate to 100 m from a measurement height of 10 m expressed as a vertical extrapolation factor (i.e. the ratio U_r/U_{10}). As shown, there is a difference of about 10% between a wind speed extrapolated to 100 m using the logarithmic profile with a roughness suitable for water surface, $z_0 = 0.0002$ m and a power law with shear (or power law) coefficient/exponent of 0.14. Historically this value of the shear exponent was widely applied for wind speed profile extrapolation, but recent measurements indicate that in many onshore contexts this value is too low,[71] though this value is specified as appropriate for offshore in the IEC 61400-3 Design Requirements for Offshore Turbines. As shown in Ref. 72 this exponent provides a good description of the observed vertical wind speed profile at the FINO1 offshore research platform 45 km offshore in the German Bight provided conditions are not strongly stable.

As shown in Fig. 1.5, discrepancies between vertical wind speed profiles derived using the logarithmic wind speed and the power law can be much larger for a moderate surface roughness (0.1 m) especially if a relatively high shear exponent is applied. One of the major differences between the two latter cases is that the logarithmic profile shown is derived for near-neutral stability, while the power law with higher shear exponent may be better suited to stable cases.

The average turbine size currently being installed on land is close to 1.8 MW with a hub height close to 70 m and a rotor diameter of 70–80 m.[73] As hub heights increase, the errors associated with extrapolating from 10 m or even 50 m to hub height also increase. Figure 1.5 also shows the vertical extrapolation factor for different height pairs and roughnesses using the logarithmic profile (equation [1.7]). The smaller the factor the lower the uncertainty will typically be. Using measurements from 50 m rather than 10 m to extrapolate upwards will give smaller errors, while conversely extrapolating from measurements at 2 m (such as typify measurement heights on buoys) will give a very large degree of uncertainty. A further issue is that for larger wind turbines where the rotor diameter is significant, it is no longer adequate to use solely the hub-height wind speed to predict power output, as wind shear across the rotor plane of large machines can be large and can impact the power output.[74,75]

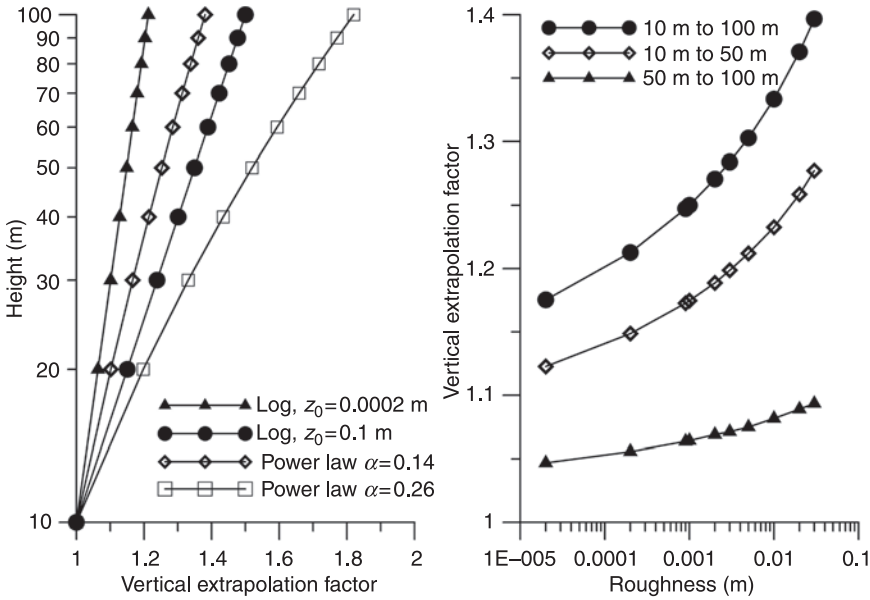

1.5 Vertical wind speed extrapolation using both the logarithmic profile (equation [1.7]) and the power law (equation [1.6]). The vertical extrapolation factor is the ratio between wind speeds at different heights for different roughness lengths using equation [1.7]. As an example, if the roughness length is 0.01 m to extrapolate wind speeds from 10 to 100 m, the wind speed at 10 m is multiplied by the vertical extrapolation factor of 1.33.

The above discussion of vertical wind speed profiles is based upon meteorological theories that assume that there is a surface constant flux layer. Broadly speaking this means that there is one uniform surface layer in which the logarithmic or power-law profile can be used. As turbine hub heights increase, wind turbines are no longer confined to the surface layer, and this assumption may no longer be valid, especially offshore where the boundary-layer height is typically much lower than over land. Two adaptations of the approaches to describing the vertical wind profile have been proposed. The first assumes that the Ekman layers of the atmosphere and ocean are coupled by an atmospheric surface layer which is a shallow wave boundary layer.[76–78] An alternative approach adapts equation [1.9] to include the height of the atmospheric boundary layer, and thus incorporate non-local effects.[52]

1.4 Wind farm layout

Most new wind energy developments are in relatively large wind farms. For example, the average size of wind farm in Scotland increased from 15 MW in the 1990s to 40 MW in 2006.[79] The average capacity of wind farms installed in California and

Texas in 2008 exceeded 80 MW. This tendency towards increasingly large developments is particularly true offshore.[80] Although wind farm layouts are not solely a function of wind resource with grid and road access, noise and visual impact being key factors, optimal power output can be obtained by micrositing (i.e. siting individual turbines so as to optimize total array power output). Micrositing usually focuses on two aspects: to optimize turbine locations in complex terrain to take advantage of any topographic channeling, and to optimize turbine locations in all contexts to reduce power losses from wind turbine wakes. This latter concern has become a big issue as wind farms on land expand and for offshore where large developments are more economic. Many of the existing wind farm models use traditional wake models that were developed for small wind farms on land (e.g. Ref. 81, Ref. 82 and Ref. 83). Therefore it is not surprising that in small to medium size wind farms (say 3–4 rows), standard wind farm models and parameters appear to capture wake losses adequately, even offshore.[46,84] Initial assessment of large wind farms offshore[85,86] suggested that wake losses offshore are larger than for equivalent wind farms on land and wind farm models underestimated wake losses.[87] Recent work indicates power losses due to wakes can be modeled with standard parameters[88] or with modification.[89–91] Wake losses in large wind farms on land still have to be evaluated.

Micrositing is typically done using a wind farm model such as WAsP[14] (*http://www.wasp.dk*), Windfarmer (*http://www.garradhassan.com*) or WindPro (*http://www.emd.dk*), although SODAR and LIDAR are ideal for checking micrositing when planning large wind farms where their mobility means that they can be calibrated at the on-site meteorological mast then placed at prospective wind turbine locations even for relatively short periods. Short-term measurements from the microsite will not be representative of the longer-term wind climate and will need to be corrected using the long-term meteorological mast measurements and compared with model predictions to assess potential power output at individual turbine sites.

1.5 Special considerations for offshore wind farms

Offshore areas are typically characterized by greater persistence of wind speeds in the power producing classes and the lower frequency of calms.[92] For these and other reasons,[93] of the total 180 GW of wind energy capacity to be installed in the European Union by 2020, 20–40 GW is expected to be located offshore.[80] Most of the issues described in this chapter are relevant for both on- and offshore developments. However, there are some major differences between on- and offshore wind resource assessment,[94] including:

- The difficulty and expense of making accurate measurements for wind resource estimation in offshore environments.[41] While this may be partly offset by the availability of remotely sensed data, the offshore environment presents a significant challenge in terms of installation and operation of in-situ measurement platforms.

- Most offshore wind energy developments are still within 50 km of the coast, and thus are influenced by the presence of land areas via the effects of coastal topography, or changes in temperature, humidity or surface roughness as air moves across the coastline.[31] Differences in the thermal properties of land and sea (e.g. the lack of diurnal cycle in sea surface temperature,[57] and the seasonal cycle in the temperature difference between land and sea, in coastal areas)[95] can be associated with generation of complex mesoscale phenomena such as sea breezes,[96] roll vortices[97] and low level jets.[98]
- In contrast to land areas, water surfaces exhibit a lower surface roughness, and although it varies with wind speed, in general wind shear and turbulence are considerably lower offshore.[99] This has significant implications for propagation of wind turbine wakes.[100]

1.6 Short-term forecasting

Wind energy is not an unpredictable resource. It is a variable resource and as such it places special demands on the whole electricity system that is designed around generating systems with fixed output. For a variable resource like wind energy, short-term forecasting is very valuable in assisting in integration into the electrical grid and for load managers.

Short-term forecasting of wind farm power production[101–106] is a topic of great and growing importance as wind energy capacity and contribution to the energy portfolio of many countries increases.[107,108] Information on short-term wind power generation from a few hours to a few days ahead (i.e. short-term forecasting) may become even more crucial as wind energy developments increasingly focus on large offshore wind farms,[109] since they concentrate a large capacity at a single location, and where limited accessibility increases the value of maintenance planning.

Increasing the accuracy of short-term forecasting of wind speeds for wind energy projects has become a major part of the wind energy industry because predicting energy output increases the value of electricity when traded, for example in Nordpool in Scandinavia[110] or in the UK.[79] Depending on the electricity price and conditions, estimates of the value of short-term forecasts are up to €10/MWh.[111] Short-term forecasting is usually defined in a window of 30 minutes to 48 hours ahead. Predictions are made based on the large-scale output of numerical weather prediction (NWP) models such as HIRLAM or ECMWF and downscaled to wind farm scale using either statistical approaches (relating onsite data, usually power output to wind fields from the NWP model using a transfer function)[109] or dynamical tools (using a mesoscale or linearized model or both).[112] There has been considerable progress in the accuracy of short-term forecasts over the last decade due in part to projects such as ANEMOS[113] and to the recognition by meteorological services of the demand for more accuracy in wind forecasts than had previously been necessary. In general, errors in the forecast are still mainly due to errors from the NWP models[114] associated with the

timing and exact location of events (e.g. frontal passages) that are very difficult to predict accurately. However, it is also much more difficult to give accurate predictions in complex terrain than in flat terrain or offshore where higher wind speeds are generally more persistent and this is reflected in the associated errors.[115]

1.7 Future trends

Expansion of the wind energy industry in terms of the scales of development, size of the turbines being deployed and the locations being considered presents new challenges in the context of meteorological components of site selection:

- As wind turbines extend higher into regions of the atmosphere that have not been routinely and accurately measured for wind and turbulence new measurement techniques and modeling tools and parameterizations are required.
- As wind farms are developed in more heterogeneous areas, close to forests and in complex terrain more advanced modeling tools are required that also provide more detail of wind speeds and turbulence in both time and space.
- As wind farms expand in size, better micrositing and wake models are required to ensure optimal wind farm layouts and maximized power production.
- Accurately quantifying site wind resources to make an energy assessment that will be valid over the lifetime of the wind farm is a challenging task. Further understanding of long-term variability of wind resources is needed, together with an assessment of the impacts of climate change on wind resources.[116]

Many of these issues are already being tackled. In the context of in-situ measurements, new remote sensing tools (both ground-based and satellite-borne) are evolving that are both more accurate and precise, and in the context of ground-based LIDARs and can be used to characterize the vertical wind profile over increasing heights with decreasing vertical resolution. While more comprehensive measurement campaigns are needed to evaluate these technologies, they show real promise for both evaluating existing models and evolving new parameterizations suitable for use in wind farm models.

Increased computing resources mean that mesoscale meteorological models can be run on finer grids and computational fluid dynamics models are being evaluated for resource assessment. Neither can currently replace the traditional wind farm model but should be seen as important additions to an ever more demanding task. New extensive multinational measurement campaigns are being planned to develop and evaluate the simulation of the wind climate including turbulence conditions. Additionally, new datasets from large wind farms are being analyzed and modeled to improve wind farm assessment tools. These aspects of model evaluation and the insights gained therefrom are critical to improving these tools and should be given the highest priority.

Evaluation of past climates and projections of future climates are being used to assess the uncertainty in wind resources in a climatological context. Global

climate change may change the geographic distribution and/or the inter- and intra-annual variability of the wind resource, or alter other aspects of the external conditions for wind developments. Only very limited research has been conducted in this field, and to determine possible changes in variability across a range of temporal scales, more research is certainly warranted. Tools are being developed that allow assessment of the likely changes in wind resources and extremes in the context of differing climate forcing,[117–119] and while this field is in its infancy, those tools are increasingly skillful and can be used to bound likely future climate change impacts on the wind energy industry.

All of these efforts should ensure that even as demands on wind resource assessment become more stringent, accuracy of wind resource predictions will continue to improve.

1.8 Acknowledgements

The authors acknowledge financial support from the National Science Foundation (grant nos. 0618364 and 0828655) and the EU UPWind project (SES6 019945).

1.9 References

1 AWEA, *AWEA Siting Handbook*. 2008, American Wind Energy Association, Washington, D.C., p. 183. Available from: *http://www.awea.org/sitinghandbook/*.
2 Petersen E, L Mortensen, L Landberg, J Højstrup and H Frank, Wind power meteorology. Part I: climate and turbulence. *Wind Energy*, 1998. 1, 2–22.
3 Kalnay E, M Kanamitsu, R Kistler, W Collins, D Deaven, L Gandin *et al*., The NCEP/NCAR 40-year reanalysis project. *Bulletin of the American Meteorological Society*, 1996. 77, 437–77.
4 Halpern D, A Hollingsworth and F Wentz, ECMWF and SSM/I global surface wind speeds. *Journal of Atmospheric and Oceanic Technology*, 1994. 11(3), 779–88.
5 Uppala S M, P W Kållberg, A J Simmons, U Andrae, V da Costa Bechtold, M Fiorino *et al*., The ERA-40 re-analysis. *Quarterly Journal of the Royal Meteorological Society*, 2005. 131, 2961–3012.
6 Pryor S C, R J Barthelmie, D T Young, E S Takle, R W Arritt, D Flory, W J Gutowski Jr, A Nunes and J Road, Wind speed trends over the contiguous USA. *Journal of Geophysical Research – Atmospheres*, 2009. 114, D14105, doi: 10.1029/2008JD011416.
7 Mesinger F, G DiMego, E Kalnay, K Mitchell, P C Shafran, W Ebisuzaki *et al*., North American regional reanalysis. *Bulletin of the American Meteorological Society*, 2006. 87(3), 343–60.
8 Benjamin S G and P A Miller, An alternative sea level pressure reduction and a statistical comparison of geostrophic wind estimated with observed surface winds. *Monthly Weather Review*, 1990. 118(10), 2099–116.
9 Halliday J, G Watson, J Palutikof, T Holt, R J Barthelmie, J Coelingh, L Folkerts, E van Zuylen and J Cleijne. *POWER – A methodology for predicting offshore wind energy resources. 2001 European Wind Energy Conference and Exhibition*. 2001. Copenhagen, July 2001.
10 Barring L and K Fortuniak, Multi-indices analysis of southern Scandinavian storminess

1780–2005 and links to interdecadal variations in the NW Europe–North Sea region. *International Journal of Climatology*, 2009. 29, 373–84.
11 Miller C, A once in 50-year wind speed map for Europe derived from mean sea level pressure measurements. *Journal of Wind Engineering and Industrial Aerodynamics*, 2004. 91, 1813–26.
12 Elliott D L, C G Holladay, W R Barchet, H P Foote and W F Sandusky, *Wind Energy Resource Atlas of the United States*. 1986, Solar Technical Information Program. US Department of Energy Washington, D.C., 210pp.
13 Troen I and E L Petersen, *European Wind Atlas*. 1989, Roskilde, Denmark: Risø National Laboratory, p. 656.
14 Mortensen N G, D Heathfield, L Landberg, O Rathmann, I Troen and E Petersen (2000), *Getting started with WAsP 7.0*. 60 Risø-I-1532(EN). Available from: *http://www.wasp.dk/Download/DownloadFiles/WAsP/WAsP7/Getting%20Started%20with%20WAsP%207.pdf*.
15 Vector A S. *Norwegian Wind Atlas*. 2003, Revision: 2.0.0. Available from: *http://www.nve.no/vindatlas/* (accessed 01 September 2003).
16 Canada E. *Canadian Wind Energy Atlas*. 2009, Available from: *http://www.windatlas.ca/en/index.php* (accessed 22 April 2009).
17 Hasager C B, A Pena, M B Christiansen, P Astrup, M Nielsen, F Monaldo, D Thompson and P Nielsen, Remote sensing observation used in offshore wind energy. *IEEE Journal of Selected Topics in Applied Earth Observations and Remote Sensing*, 2008. 1(1), 67–79.
18 Monaldo F, D Thomson, W Pichel and P Clemente-Colon, A systematic comparison of QuikSCAT and SAR ocean surface wind speeds. *IEEE Transactions on Geoscience and Remote Sensing*, 2004. 42, 283–91.
19 Sempreviva A M, B Furevik, R J Barthelmie, F Cheruy, B Jimenes and C Transerici, Offshore wind energy potential in the Mediterranean Basin. *Proceedings of the Conference, Offshore Wind Energy in Mediterranean and Other European Seas, OWEMES, Civitavecchia, Italy 19–21 April 2006*. Available on CDROM.
20 Hasager C B, R Barthelmie, M Christiansen, M Nielsen and S Pryor, Quantifying offshore wind resources from satellite maps: study area the North Sea. *Wind Energy*, 2006. 9(1–2), 63–74.
21 Lehner S, J Horstmann, W Koch and W Rosenthal, Mesoscale wind measurements using recalibrated ERS SAR images. *Journal of Geophysical Research: Oceans*, 1998. 103, 7847–56.
22 Hasager C B, E Dellwik, M Nielsen and B R Furevik, Validation of ERS-2 SAR offshore wind-speed maps in the North Sea. *International Journal of Remote Sensing*, 2004. 25, 3817–41.
23 Barthelmie R J and S C Pryor, Can satellite sampling of offshore wind speeds realistically represent wind speed distributions? *Journal of Applied Meteorology*, 2003. 42, 83–94.
24 Pryor S C, M Nielsen, R J Barthelmie and J Mann, Can satellite sampling of offshore wind speeds realistically represent wind speed distributions? Part II: Quantifying uncertainties associated with sampling strategy and distribution fitting methods. *Journal of Applied Meteorology*, 2004. 43, 739–50.
25 Matthies H G, A Garrad, N Scherweit, C Nath, M A Wastling, T Siebers, T Schellin and D C Quarton, *Study of Offshore Wind Energy in the EC*. 1995, Brekendorf: Verlag Natürliche Energie.

26 Børreson J A, *Wind Atlas for the North Sea and the Norwegian Sea*. 1987, Oslo: Norwegian University Press, p. 346.
27 Lions J L, R Temamt and S Wang, New formulations of the primitive equations of atmosphere and applications. *Nonlinearity*, 1992. 5, 237–88.
28 Storm B, J Dudhia, S Basu, A Swift and I Giammanco, Evaluation of the weather research and forecasting model on forecasting low-level jets: implications for wind energy. *Wind Energy*, 2009. 12(1), 81–90.
29 Pinard J P, R Benoit and J D Wilson, Mesoscale wind climate modelling in steep mountains. *Atmosphere-Ocean*, 2009. 47(1), 63–78.
30 Bergstrom H and N Juuso, A study of valley winds using the MIUU meso-scale model. *Wind Energy*, 2006. 9(1–2), 109–29.
31 Barthelmie R J, J Badger, S C Pryor, C B Hasager, M B Christiansen and B H Jørgensen, Wind speed gradients in the coastal offshore environment: Issues pertaining to design and development of large offshore wind farms. *Wind Engineering*, 2007. 31(6), 369–82.
32 Bailey B H and J M Freedman, A regional assessment of the US offshore wind energy resource through the use of mesoscale modeling. *Marine Technology Society Journal*, 2008. 42(2), 8–18.
33 Badger J, R Barthelmie, S Frandsen and M Christiansen. *Mesoscale modelling for an offshore wind farm. European Wind Energy Association Conference*. 2006, Athens, Greece, February 2006.
34 Kallstrand B, H Bergstrom, J Højstrup and A S Smedman, Mesoscale wind field modifications over the Baltic Sea. *Boundary-Layer Meteorology*, 2000. 95, 161–88.
35 Benoit R, M Desgagne, P Pellerin, S Pellerin, Y Chartier and S Desjardins, The Canadian MC2: A semi-Lagrangian, semi-implicit wide band atmospheric model suited for fine scale process studies and simulation. *Monthly Weather Review*, 1997. 125, 2382–415.
36 Bergström H, *Wind resource mapping of Sweden using the MIUU Model*. 2007, Air, Water and Landscape Sciences, Department of Earth Sciences: Wind Energy Report WE2007:1. The Bergstrom reference is now at: *http://www.energimyndigheten.se/Global/Om%20oss/Vindkraft/Wind%20resource%20mapping%20of%20Sweden%20using%20the%20MIUU%20model%20ver%20070330.pdf*.
37 Bailey B, S McDonald, D Bernadett, M Markus and K Elsholz, *Wind Resource Assessment Handbook*. 1997, National Renewable Energy Laboratory. p. 79. Available from: *http://www.nrel.gov/wind/pdfs/22223.pdf*.
38 Tuller S E and A C Brett, The characteristics of wind velocity that favor the fitting of a Weibull distribution in wind speed analysis. *Journal of Climate and Applied Meteorology*, 1984. 23, 124–34.
39 Mortensen N G, L Landberg, I Troen and E L Petersen, *Wind Analysis and Application Program (WASP)*. 1993, Risø National Laboratory: Risø-I-666 (EN). Roskilde, Denmark.
40 DNV/Risø, *Guidelines for the Design of Wind Turbines*. 2nd ed. 2002. Copenhagen, Denmark: Jydsk cetraltrykkeri, p. 286.
41 Barthelmie R, O Hansen, K Enevoldsen, J Højstrup, S Larsen, S Frandsen, S Pryor, M Motta and P Sanderhoff, Ten years of meteorological measurements for offshore wind farms. *Journal of Solar Energy Engineering*, 2005. 127(2), 170–6.
42 Argyriadis K, G Fischer, P Frohböse, D Kindler and F Reher, Research platform FINO 1 – some measurement results. *European Wind Energy Conference*. 2006. Athens.

43 Emeis S and M Türk, Offshore wind and turbulence characteristics – new insights from the FINO1 data. *DEWEK 2008*. 2008.
44 Mortensen N G, Wind measurements for wind energy applications – a review. *BWEA* 1994, p. 16.
45 Barthelmie R J, L Folkerts, F Ormel, P Sanderhoff, P Eecen, O Stobbe and N M Nielsen, Offshore wind turbine wakes measured by SODAR. *Journal of Atmospheric and Oceanic Technology*, 2003. 30, 466–77.
46 Barthelmie R J, L Folkerts, K Rados, G C Larsen, S C Pryor, S Frandsen, B Lange and G Schepers, Comparison of wake model simulations with offshore wind turbine wake profiles measured by sodar. *Journal of Atmospheric and Oceanic Technology*, 2006. 23(7), 888–901.
47 Emeis S, M Harris and R M Banta, Boundary-layer anemometry by optical remote sensing for wind energy applications. *Meteorologische Zeitschrift*, 2007. 16(4), 337–47.
48 Antoniou I, H E Jørgensen, T Mikkelsen, T F Pedersen, G Warmbier and D Smith, *Comparison of wind speed and power curve measurements using a cup anemometer, a LIDAR and a SODAR*. in *2004 European Wind Energy Conference and Exhibition, 22–25 Nov 2004*. 2004. London (GB): European Wind Energy Association.
49 Clive P J M, Lidar and resource assessment for wind power applications: the state of the art. *Proceedings of the SPIE – The International Society for Optical Engineering*, 2008. 7111, 711107 (10 pp.).
50 Clive P J M, Compensation of bias in Lidar wind resource assessment. *Wind Engineering*, 2008. 32(5), 415–32.
51 Clive P J M. *Recent advances in Lidar wind measurement*. *American Wind Energy Association*. 2008. Houston, Texas.
52 Peña A, S E Gryning and C B Hasager, *Measurements and modelling of the wind speed profile in the marine atmospheric boundary layer*. Boundary-Layer Meteorology 2008. 129, 479–95, doi: 10.1007/s10546-008-9323-9.
53 Davies F, C G Collier, K E Bozier and G N Pearson, On the accuracy of retrieved wind information from Doppler lidar observations. *Quarterly Journal of the Royal Meteorological Society*, 2003. 129(587), 321–34.
54 Wachter M, A Rettenmeier, M Kuhn and J Peinke, *Wind velocity measurements using a pulsed LIDAR system: first results*. *14th International Symposium for the Advancement of Boundary Layer Remote Sensing*. 2008, IOP Conf. Series: Earth and Environmental Science 1, (2008) 012066.
55 Peña A, C B Hasager, S E Gryning, M Courtney, I Antoniou and T Mikkelsen, Offshore wind profiling using light detection and ranging measurements. *Wind Energy*, 2009. 12(2), 105–24.
56 Mortensen N G, A J Bowen and I Antoniou, *Improving WAsP predictions in (too) complex terrain*. *2006 European Wind Energy Conference and Exhibition*. 2006. Athens 27 February–2 March 2006, European Wind Energy Association, Brussels.
57 Barthelmie R J, B Grisogono and S C Pryor, *Observations and simulations of diurnal cycles of near-surface wind speeds over land and sea*. Journal of Geophysical Research (Atmospheres), 1996. 101(D16), 21, 327–37.
58 Bergström H, Boundary-layer modelling for wind climate estimates. *Wind Engineering*, 2002. 25(5), 289–99.
59 Frank H, O Rathmann, N Mortensen and L Landberg, *The numerical wind atlas – the KAMM/WasP method*. 2001, Risø National Laboratory, ISBN 87-550-2909-4. Risø-R-1252(EN) Roskilde, Denmark. The Frank references can be found at: *http://130.226.56.153/rispubl/VEA/veapdf/ris-r-1252.pdf*.

60 Frank H P, O Rathmann, N G Mortensen and L Landberg, *The numerical wind atlas – the KAMM/WAsP method*. 2001. Risoe-R-1252(EN) Roskilde, DK, 60pp.
61 Politis E S, K Rados, J M Prospathopoulos, P K Chaviaropoulos and A Zervos, *CFD modeling issues of wind turbine wakes under stable atmospheric conditions*. *European Wind Energy Conference*, 2009. Marseilles, March 2009.
62 Troldborg N, J N Sørensen and R Mikkelsen. *Numerical simulation of wakes of wind turbines in wind farms*. *European Wind Energy Conference and Exhibition*, February 2006, Athens.
63 Berge E, Ø Byrkjedal, Y Ydersbond and D Kindler, *Modelling of offshore wind resources*. *Comparison of a mesoscale model and measurements from FINO 1 and North Sea oil rigs*. *European Wind Energy Conference*. 2006, Marseilles.
64 Ayotte K, Computational modelling for wind energy assessment, *Journal of Wind Engineering and Industrial Aerodynamics*, 2008. 96, 1571–90.
65 Pryor S C, R J Barthelmie and J T Schoof, The impact of non-stationarities in the climate system on the definition of 'a normal wind year': a case study from the Baltic. *International Journal of Climatology*, 2005. 25, 735–52.
66 Frandsen S and E L Petersen, *The importance of a good wind year to start on when building a wind farm*. *European Wind Energy Conference 1993*. 1993, Travemunde.
67 Pryor S C, R J Barthelmie and J T Schoof, Inter-annual variability of wind indices across Europe. *Wind Energy*, 2006. 9, 27–38.
68 Rogers A, J Rogers and J F Manwell, Comparison of the performance of four measure-correlate-predict algorithms. *Journal of Wind Engineering and Industrial Aerodynamics*, 2005. 93, 243–64.
69 Wieringa J, *Representative roughness parameters for homogeneous terrain*. Boundary Layer Meteorology, 1993. 63(4), 323–63.
70 Stull R B, *An introduction to boundary layer meteorology*. ISBN 90-277-2768-6 ed. 1988. Dordrecht: Kluwer, p. 666.
71 Schwartz M and D Elliott, *Wind shear characteristics at central plains tall towers*. 2006, Battelle: National Renewable Energy Laboratory, p. 10.
72 Neumann T, S Emeis and C Illig, *Report on the research project OWID – offshore wind design parameter*. DEWI Magazine Nr. 2006. 28: 51–3.
73 IEA, *IEA Wind Energy Annual Report 2007*. 2008, ISBN 0-9786383-2-8. p. 286. Available from: *http://www.ieawind.org/AnnualReports_PDF/2007/2007%20IEA%20Wind%20AR.pdf*.
74 Antoniou I and S M Pedersen. *Influence of turbulence, wind shear and low-level jets on the power curve and the AEP of a wind turbine*. *European Wind Energy Conference and Exhibition*. 2009, Marseilles, March 2009.
75 Wagner R, I Antoniou, S M Pedersen, M S Courtney and H E Jørgensen, The influence of the wind speed profile on wind turbine performance measurements. *Wind Energy*, 2009. 12(4), 348–62.
76 Bye J, Inertially coupled Ekman layers, *Dynamics of Atmospheres and Oceans*, 2002. 35, 27–39.
77 Tambke J, M Lange, U Focken, J Wolff and J Bye, Forecasting offshore wind speeds above the North Sea. *Wind Energy*, 2005. 8, 3–16.
78 Tambke J, K Suselj and O J Wolff, Micro- & meso-scale models for offshore wind speed profiles. *European Wind Energy Conference* 2009, Marseilles, March 2009.
79 Barthelmie R J, F Murray and S C Pryor, The economic benefit of short-term forecasting for wind energy in the UK electricity market. *Energy Policy*, 2008. 36(5), 1687–96.

80 Barthelmie R J and M Kuhn, Editoral: Preface to special issue on Offshore Wind Energy. *Wind Energy*, 2009. 12, 103.
81 Jensen N O, *A note on wind turbine interaction*. 1983, Roskilde, Denmark: Risø National Laboratory, p. 61. Risø-M-2411.
82 Ainslie J F, Calculating the flow field in the wake of wind turbines. *Journal of Wind Engineering and Industrial Aerodynamics*, 1988. 27, 213–24.
83 Katic I, J Højstrup and N O Jensen. *A simple model for cluster efficiency. European Wind Energy Association*. 1986. Rome.
84 Barthelmie R J, S T Frandsen, N M Nielsen, S C Pryor, P E Rethore and H E Jørgensen, *Modelling and measurements of power losses and turbulence intensity in wind turbine wakes at Middelgrunden offshore wind farm*. Wind Energy, 2007. 10, 217–28, doi: 10.1002/we.238.
85 Jensen L, *Wake measurements from the Horns Rev wind farm. European Wind Energy Conference*. 2004: EWEA. Available on CD.
86 Mechali M, L Jensen, R Barthelmie, S Frandsen and P E Rethore, Wake effects at Horns Rev and their influence on energy production. *European Wind Energy Conference and Exhibition*. 2006. Athens, Greece.
87 Barthelmie R J, S T Frandsen, O Rathmann, K Hansen, E Politis, J Prospathopoulos, D Cabezón, K Rados, S van der Pijl, G Schepers, W Schlez, J Phillips and A Neubert, Flow and wakes in large wind farms in complex terrain and offshore. *European Wind Energy Conference*. 2008. Brussels.
88 Sørensen T, P Nielsen and M L Thøgersen, Recalibrating wind turbine wake model parameters – validating the wake model performance for large offshore wind farms. *European Wind Energy Conference and Exhibition*. 2006.
89 Cleve J, M Grenier, P Enevoldsen, B Birkemose and L Jensen, Model-based analysis of wake-flow data in the Nysted offshore wind farm. *Wind Energy*, 2009, doi: 10.1002/we.314.
90 Schlez W, A Neubert and G Smith, New developments in precision wind farm modelling. *Deutsche Windenergie Konferenz*. 2006. Bremen.
91 Barthelmie R J, S T Frandsen, K Hansen, J G Schepers, K Rados, W Schlez, A Neubert, L E Jensen and S Neckelmann, Modelling the impact of wakes on power output at Nysted and Horns Rev. *European Wind Energy Conference and Exhibition* 2009. Marseille, March 2009.
92 Pryor S C and R J Barthelmie, Persistence of offshore winds: Implications for power quality. *Proceedings of the European Wind Energy Conference*. 2001. Copenhagen, Denmark.
93 Jacob Ladenburg, Stated public preferences for on-land and offshore wind power generation – a review. *Wind Energy*, 2009. 12(2), 171–81.
94 Barthelmie R J, S C Pryor and S T Frandsen, Climatological and meteorological aspects of predicting offshore wind energy. in *Offshore Wind Energy*, J. Twidell and G. Gaudiosi, Editors. 2009, Multi-Science Publishing Co. Ltd., p. 425.
95 Motta M, R J Barthelmie and P Vølund, The influence of non-logarithmic wind speed profiles on potential power output at Danish offshore sites. *Wind Energy*, 2005. 8, 219–36.
96 Simpson J E, *Sea Breeze and Local Winds*. 1994, Cambridge: Cambridge University Press, p. 234.
97 Smedman A S, Occurrence of roll circulations in a shallow boundary layer. *Boundary-Layer Meteorology*, 1991. 57(4), 343–58.

98 Smedman A S, U Hogstrom and H Bergstrom, Low level jets – a decisive factor for off-shore wind energy siting in the Baltic Sea. *Wind Engineering*, 1996. 20(3), 137–47.
99 Barthelmie R J, Evaluating the impact of wind induced roughness change and tidal range on extrapolation of offshore vertical wind speed profiles. *Wind Energy*, 2001. 4, 99–105.
100 Barthelmie R J, K Hansen, S T Frandsen, O Rathmann, J G Schepers, W Schlez, J Philips, K Rados, A Zervos, E S Politis and P K Chaviaropoulos, Modelling and measuring flow and wind turbine wakes in large wind farms offshore. *Wind Energy*, 2009. 12(5), 431–444, doi: 10.1002/we.348.
101 Giebel G, R Brownsword and G Kariniotakis, *The State-of-the-Art in Short-Term Prediction of Wind Power. A Literature Overview*, p. 36. Available from: *http://anemos.cma.fr/download/ANEMOS_D1.1_StateOfTheArt_v1.1.pdf*.
102 Voisin N, A F Hamlet, L P Graham, D W Pierce, T P Barnett and D P Lettenmaier, The role of climate forecasts in Western US power planning. *Journal of Applied Meteorology and Climatology*, 2006. 45(5), 653–73.
103 Parkes J, J Wasey, A Tindal and L Munoz, Wind energy trading benefits through short-term forecasting. *European Wind Energy Conference*. 2006. Athens.
104 Lange B, K Rohrig, B Ernst, F Schlogl, U Cali, R Jursa and J Moradi, Wind power forecasting in Germany – recent advances and future challenges. *Zeitschrift fur Energiewirtschaft*, 2006. 30, 115–20.
105 Gibescu M, A J Brand and W L Kling, Estimation of variability and predictability of large-scale wind energy in The Netherlands. *Wind Energy*, 2009. 12(3), 241–60.
106 Pinson P, H Madsen, H Nielsen, G Papaefthymiou and B Klöckl, From probabilistic forecasts to statistical scenarios of short-term wind power production. *Wind Energy*, 2009. 12(1), 51–62.
107 IEA, *Renewable Energy Essentials: Wind*. 2008. Paris, France: International Energy Agency, OECD. Available from: *http://www.iea.org*.
108 de Vries E, The DEWI report: wind energy study 2008. *Renewable Energy World*, 2008. 11(6), 93–101.
109 Pinson P and H Madsen, Ensemble-based probabilistic forecasting at Horns Rev. *Wind Energy*, 2009. 12(2), 137–55.
110 Holttinen H, Optimal electricity market for wind power. *Energy Policy*, 2005. 33, 2052–63.
111 Parkes J and A Tindal, Forecasting short-term wind farm production in complex terrain. *European Wind Energy Conference*. 2006. Athens.
112 Lange M and U Focken, *Physical Approach to Short-Term Wind Power Prediction* 2006, The Netherlands: Springer-Verlag, p. 208.
113 Kariniotakis G, J Halliday, R Brownsword, I Marti, A Palomares, I Cruz *et al*., Next generation short-term forecasting of wind power – overview of the ANEMOS project. *European Wind Energy Conference* 2006. Athens, February 2006.
114 Kusiak A, H Zheng and Z Song, Wind farm power prediction: a data-mining approach. *Wind Energy*, 2009. 12(3), 275–93.
115 Martí I, G Kariniotakis, P Pinson, I Sanchez, T Nielsen, H Madsen *et al*., Evaluation of advanced wind power forecasting models – results of the Anemos project. *European Wind Energy Conference and Exhibition*. 2006. Athens, February 2006.
116 Pryor S C and R J Barthelmie, Climate change impacts on wind energy: a review. *Renewable and Sustainable Energy Reviews* 2009, doi: 10.1016/j.rser.2009.07.028.

117 Pryor S C, R J Barthelmie and E Kjellström, Analyses of the potential climate change impact on wind energy resources in northern Europe using output from a regional climate model. *Climate Dynamics*, 2005. 25, 815–35.

118 Pryor S C, J T Schoof and R J Barthelmie, Winds of change? Projections of near-surface winds under climate change scenarios. *Geophysical Research Letters*, 2006. 33(L11702), doi: 10.1029/2006GL026000.

119 Pryor S C, R J Barthelmie, N E Claussen, N M Nielsen, E Kjellstrom and M Drews, Climate change impacts on extreme wind speeds. *Regional Climate Models 2009*. Lund, Sweden. International BALTEX Secretariat Publication Series. ISSN 1681–6471. Available from: *http://www.baltex-research.eu/RCM2009/Material/RCM2009_Proceedings_low.pdf*

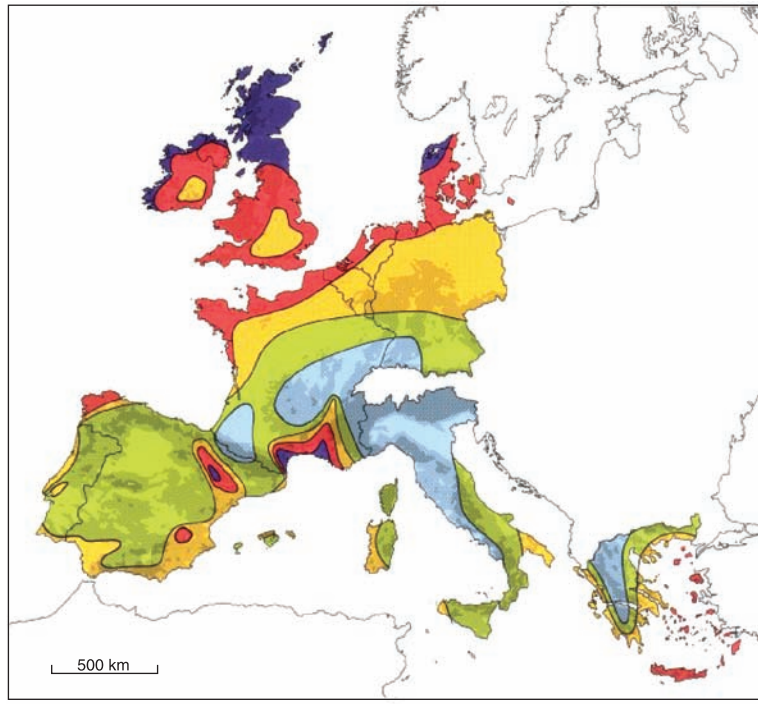

Wind resources at 50 metres above ground level for five different topographic conditions										
	Sheltered terrain		Open plain		At a sea coast		Open sea		Hills and ridges	
	ms^{-1}	Wm^{-2}	ms^{-1}	Wm^{-2}	ms^{-1}	Wm^{-2}	ms^{-1}	Wm^{-2}	ms^{-1}	Wm^{-2}
	> 6.0	> 250	> 7.5	> 500	> 8.5	> 700	> 9.0	> 800	> 11.5	> 1800
	5.0-6.0	150-250	6.5-7.5	300-500	7.0-8.5	400-700	8.0-9.0	600-800	10.0-11.5	1200-1800
	4.5-5.0	100-150	5.5-6.5	200-300	6.0-7.0	250-400	7.0-8.0	400-600	8.5-10.0	700-1200
	3.5-4.5	50-100	4.5-5.5	100-200	5.0-6.0	150-250	5.5-7.0	200-400	7.0-8.5	400-700
	< 3.5	< 50	< 4.5	< 100	< 5.0	< 150	< 5.5	< 200	< 7.0	< 400

Plate I Map of wind resources for Europe based on near-surface wind speed measurements and application of the WAsP model (from http://www.wasp.dk based on Ref. 13. Copyright: Risø DTU).

2

Site investigation, characterization and assessment for wind turbine design and construction

J. M. TINJUM, University of Wisconsin-Madison, USA and
R. W. CHRISTENSEN, R W Christensen, Inc., USA

Abstract: To have a successful wind power plant buildout, you must carefully address many issues, including site layout and control, geotechnical and foundation assessment, site civil design and substation and collector system design. With the recent proliferation of wind energy projects around the world, the details inherent in wind site environmental/geotechnical assessments and turbine foundation and civil design have become important issues in this multi-disciplinary business. Because of the somewhat unusual loading conditions and because wind farms may contain from a few to thousands of turbines, the investigations and design analyses are rather different from those that many engineers are accustomed to.

Key words: turbine foundation design, access roads and crane pads, wind geotechnical investigation, turbine erection and lift calculations, wind collector system design.

2.1 Introduction to wind energy civil design

With the recent proliferation of wind energy projects, the subject of wind turbine foundations and wind energy civil design has become an important consideration for geotechnical and civil engineers alike. Because of the somewhat unusual loading conditions and the fact that wind energy sites may contain from a few to thousands of turbines, the geotechnical investigation and analysis requirements are rather different from those to which most geotechnical engineers are accustomed. The sites occupy large areas with tens to thousands of individual tower locations. As an example, a recent project in the USA near Lafayette, Indiana (Fowler Ridge Wind Farm), encompasses an area approximately 16 km × 23 km and contains 222 (182 Vestas, 40 Clipper) turbines, with more to come. The loading conditions are different – relatively light vertical loads combined with large overturning moments. Also, every turbine requires a temporary access road for delivery of the turbine components, some of which become permanent for maintenance purposes. In this chapter, we will focus on geotechnical investigations, foundation evaluation and design, and civil design including access roads, crane pads and collector trenches.

2.2 Wind energy geotechnical investigation

2.2.1 Geotechnical design parameters

The site investigation and geotechnical report for a wind energy site must provide site-specific soil parameters for the design of turbine foundations, access roads and crane pads, collector trenches and ancillary structures. These parameters are typically collected by a combination of intrusive borings into the soil and bedrock at the site, soil sampling from grab samples (e.g. from test trenches) and devices such as thin-walled tubes (e.g. Shelby tubes) and standard penetration tests (SPTs), direct push techniques such as cone penetrometer testing (CPT) and geophysical testing including resistivity arrays and seismic surveys. A laboratory testing program includes typical engineering properties of soil (strength and consolidation parameters), thermal properties and chemical compatibility testing. Following are groups of soil parameters that are typically scoped for the geotechnical investigation at a wind energy site.

Parameters for the solution of allowable bearing pressure equation

Sampling to address bearing capacity and settlement usually involves SPTs and thin-walled tube sampling, similar to what would be done for any large foundation. Laboratory strength testing will depend on the soil types encountered in the profile, such as unconfined compression or unconsolidated–undrained test for cohesive soils. Rarely, triaxial and/or direct shear tests may also be conducted. Additionally, CPT probes are frequently used to assess undrained shear strength of clays. Typically, in the case of granular soils, strength or bearing capacity is based on correlations with the SPT blow counts and/or CPT cone resistance. To perform a standard allowable bearing pressure analysis, the following soil parameters are required:

- internal angle of friction (ϕ', drained strength),
- undrained strength (c or S_u),
- unit weight of soil, γ.

Shear wave and compression wave velocities

Shear wave (V_s) velocities are required for the generation of soil moduli. Soil moduli are used to calculate foundation stiffness, which is typically provided by turbine manufacturers. Because measurements of modulus are extremely sensitive to sample disturbance, V_s is typically determined in the field and then related directly to elastic modulus. Compression wave (V_p) velocity is generally not reliably measured in the field, especially in saturated soil. The relevant elastic equations, with units (F = force, L = length) in brackets, are as follows:

$$\text{Shear modulus, } G = \rho \cdot V_s^2 = \frac{E}{2(1+\upsilon)} \Rightarrow \left[\frac{F}{L^2}\right] \quad [2.1]$$

$$\text{Poisson's ratio, } \upsilon = \frac{0.5\left(\left.V_p\right/V_s\right)^2 - 1}{\left(\left.V_p\right/V_s\right)^2 - 1} \Rightarrow [-] \quad [2.2]$$

$$\text{Young's modulus, } E = 2 \cdot (1 + \upsilon) \cdot \rho \cdot V_s^2 \Rightarrow \left[\frac{F}{L^2}\right] \quad [2.3]$$

where ρ is soil density. Because equation [2.2] is only reliable for unsaturated soil, υ is usually estimated. The seismic wave velocities may be determined by traditional surface geophysical methods (preferably with shear force input), Refraction Microtremor (ReMi), CPT seismic probe or seismic dilatometer. The CPT method has several advantages, including the ability to measure V_s at several depths within the soil profile and that the instrument can be used for in-situ determination of strength parameters. Typical values of V_s and V_p in common soil and rock are shown in Table 2.1.

Consolidation parameters

To evaluate settlement, compressibility testing usually includes one-dimensional compression tests for clays (and sometimes for sand as well). The parameters obtained from laboratory testing include:

- compression index, C_c;
- recompression index, C_r;
- time rate of consolidation, C_v.

Settlement analyses may include both total and differential settlement. However, because the sustained vertical loads are relatively light, settlement is usually not a major concern for wind turbine foundations. Settlement in sand is usually based on SPT blow counts and/or CPT tip resistance.

Ground water conditions

Foundation design for more than one wind farm has been complicated by a shallow and/or uncertain water table. Since the shallow spread foundations are typically embedded 2–2.5 m below grade, a water table shallower than that will reduce the effective weight of the submerged portion of the foundation to the buoyant value. This reduces the overall vertical load and, in turn, increases the eccentricity, requiring an increase in the size of the foundation or compensation for the weight loss by placing additional fill over the top of the foundation.

Table 2.1 Typical shear- and compression-wave velocities of common foundation soil and rock

Material	V_p (m/s)	V_s (m/s)	Useful relationships
Granite	5000–6000	2500–3300	P-wave velocity: $V_p = \sqrt{\frac{M}{\rho}} = \sqrt{\frac{E}{\rho}\frac{1-v}{(1-2v)(1+v)}}$
Basalt	5400–6400	2700–3500	
Limestone	3600–6000	2000–3100	S-wave velocity: $V_s = \sqrt{\frac{G}{\rho}} = \sqrt{\frac{E}{\rho}\frac{1}{2(1+v)}}$
Sandstone	1450–1650	900–1200	
Shale	2200–4000	1400–3000	Velocity ratio: $\frac{V_s}{V_p} = \sqrt{\frac{1}{2}\frac{1-2v}{1-v}}$
Till	1500–2200	800–1400	
Gravel*	740–900	375–495	
Dry loose sand*	250–450	100–300	
Dry dense sand*	400–600	200–500	
Sat. loose sand*	1450–1900	100–300	
Sat. dense sand*	1450–1900	200–500	
Sat. clays*	100–2200	75–40	
Distilled water	1480	N/A	
Seawater	1530	N/A	
Concrete	3500–4500	1850–2400	

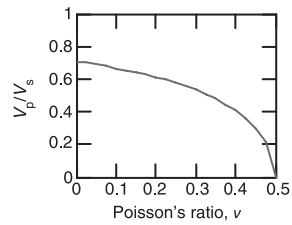

S-wave velocity and effective stresses

$$V_s = \alpha\left(\frac{\sigma'_{mean}}{p_r}\right)^{\beta}$$

where p_r = 1 kPa and σ'_{mean} is the mean effective stress in the S-wave propagation plane.

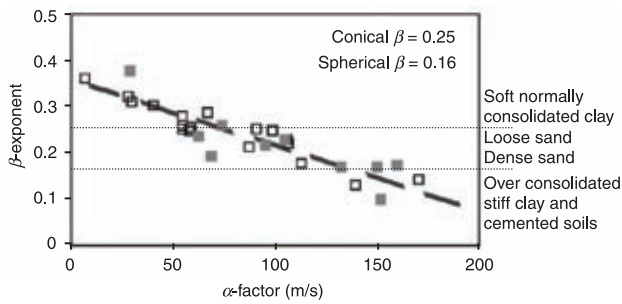

* Wave velocities in surface soils are controlled by effective stresses in soils. Poisson's ratios in wave propagation in soils vary between 0.1 and 0.2.
Notation: Young's modulus E, shear modulus G, constraint modulus M, Poisson's ratio v, S-wave velocity-effective stress parameters α and β, normalizing stress p_r, and mean effective stress in the propagation plane σ'_{mean}.
Sources: Dobrin and Savit (1988), Fernandez (2000), Fratta *et al.* (2005), Jamiolkowski *et al.* (1994), Kim (2009), Knight and Enders (2005), Mavko *et al.* (1998), Santamarina *et al.* (2001), Santamarina *et al.* (2005), Telford *et al.* (1990).

Thermal resistivity

One of the most important properties to be evaluated is the thermal resistivity of the near surface soils in which electrical cables of the collector system will be buried. Usual practice for this testing involves compacting soils from shallow (1–2 m) bulk samples at various relative compaction levels, representing compaction conditions typical of a backfilled utility trench. The samples are then subjected to tests consisting of collecting a series of thermal resistivity readings as the soil sample dries to develop a thermal dry-out curve of thermal resistivity versus moisture content. An example of thermal resistivity test results is shown in Fig. 2.1.

Rock properties

Analysis of rock properties is more field oriented as the presence of fissures, joints or other discontinuities will control the overall strength of the rock mass. Rock properties are mainly of interest with respect to excavation and/or rock anchor

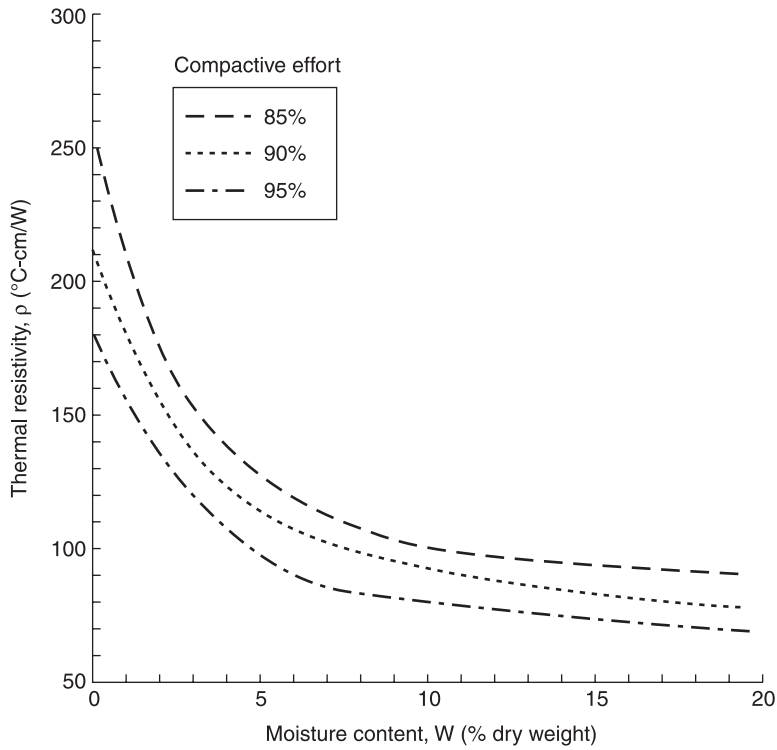

2.1 Example of a thermal resistivity dry-out curve for a site soil compacted to three different levels of compaction.

capacity. Determination of rock properties is based on information from both laboratory and field testing, including:

- rock classification (ASTM C294)
- depth of overburden
- rock quality designation (RQD)
- joint spacing and orientation
- stratification.

Miscellaneous parameters

Soil parameters for the design of access roads, crane pad and walk paths, and slabs-on-grade typically require one or more of the following properties be evaluated in the geotechnical investigation:

- California bearing ratio (CBR)
- R-value
- modulus of subgrade reaction, k_v.

2.2.2 Geotechnical investigation and reporting

In current wind energy geotechnical investigation practice, a minimum of one boring or CPT at each turbine location is specified, as well as several borings along access road alignments and substation locations. Bulk samples are collected to test for thermal properties. Electrical resistivity measurements are also required and may be obtained with traditional surface methods or in conjunction with the CPT probes. The turbine manufacturers typically specify the performance criteria for the foundations, primarily (rotational) stiffness.

2.3 Turbine foundations

2.3.1 Foundation types

Shallow foundations

Many foundation types can and have been used to support wind turbines. Shallow turbine foundations are typically reinforced concrete (140–460 m^3), octagonal (12–18 m diameter, about 0.7 m thick at the edges, and 2.5–3.5 m thick at the center, with a 1.5-m. pedestal in the center), contain 125–360 kN of rebar, and cost US $100 000 to $250 000. For this type of foundation, the minimum width is usually dictated by either the foundation stiffness or the maximum allowable edge pressure. An example of this type of foundation under construction is shown in Fig. 2.2.

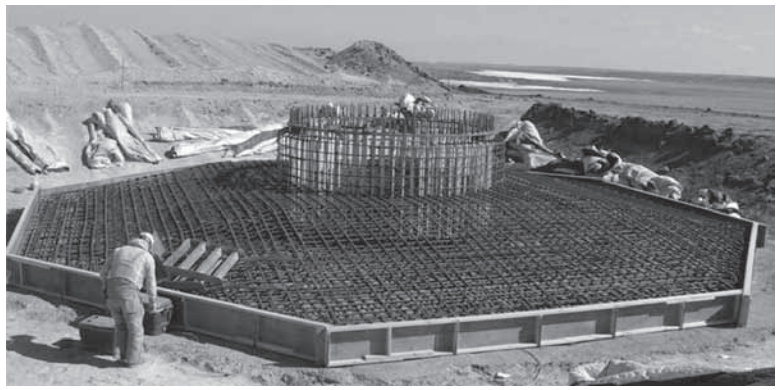

(a)

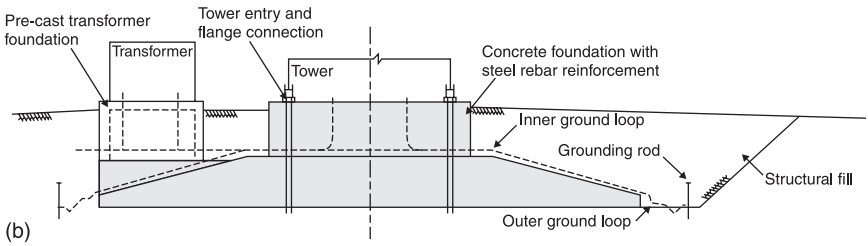

(b)

2.2 Octagonal wind turbine foundation: (a) under construction and (b) as a schematic.

Deep foundations

Many types of deep foundations have been used to support wind turbines. These include typical pile or drilled pier foundations, rammed aggregate piers, as well as patented systems. Pile or pier foundations would be designed in the same way as, for example, a tall stack foundation. The main differences would be that the wind turbine would be subjected to greater eccentricity and less vertical load.

One of the patented foundation types that has been used extensively in the United States for wind turbines is Patrick and Henderson's Tensionless Pier®. This pier consists of a post-tensioned concrete annulus, typically 4.5–5.5 m in diameter and 8–12 m deep. The annulus is constructed by placing two corrugated metal cylinders in an excavated or drilled hole, and filling the annular space with concrete. The interior space is backfilled with a three-foot-thick concrete plug, followed by uncompacted excavation spoil. The pier is capped with a structural slab. The exterior space between the outer corrugated cylinder and the natural soil is backfilled with sand–cement slurry or grout. The principal advantage claimed for this foundation type is cost savings. However, there are aspects to the construction of these piers that can negate the apparent savings, principally, caving soils and large grout takes.

Ground improvement

Various types of ground improvement have been proposed and/or used to create subgrade conditions suitable for shallow foundations. Among these are over excavation and replacement, dynamic compaction, rammed aggregate piers and stone columns. Over excavation and replacement can be economical to a depth of 3 m or so below the base of the foundation. Limitations include caving soils, which increases the volume of excavation, and shallow groundwater. Dynamic compaction can be effective to depths of 7 to, perhaps, 10 m. The use of this method is limited to coarse-grained soil.

Rammed aggregate piers are increasingly used in conjunction with conventional spread footings. This technique is appropriate where the soil profile contains a soft/loose upper layer underlain by more competent material. Pier lengths up to about 7 m can be installed with auger rigs; greater lengths may be achieved with casing and mandrel systems (impact piers).

2.3.2 Foundation analysis and design

Large octagonal spread footings are the most commonly used non-proprietary foundation type for land-based wind turbines. Factors of design include design life, material strength, serviceability and fatigue analysis. Design loads are provided by the turbine manufacturer and consist of combinations of wind, ice, operations, fatigue, seismic and wave action (for off shore installations). This discussion will thus be confined to the geotechnical issues of shallow octagonal spread footings: bearing capacity, settlement sliding, and foundation stiffness. Structural design and liquefaction potential will not be covered.

Bearing capacity

The general form of the ultimate bearing capacity of a foundation is expressed as:

$$q_{ult} = c'N_c + \sigma'_D N_q + 0.5\gamma' BN\gamma \qquad [2.4]$$

where,

c' = effective cohesion of supporting soil

N_c, N_q, N_γ = bearing capacity factors, which depend on the soil effective friction angle

σ'_D = effective vertical stress at base of footing

γ' = effective unit weight of the supporting soil

B = footing width

The three terms on the right-hand side of equation [2.4] represent the contributions due to cohesion, overburden pressure and soil weight. The bearing capacity factors may be found in charts or tables in textbooks or manuals or may be

computed by a variety of equations or charts in foundation engineering textbooks or manuals. In practice, equation [2.4] is rarely applied in its complete form. The more commonly used forms are:

$$q_{ult} = \sigma'_D N_q + 0.5\gamma' BN\gamma \ \{\text{granular soil}\} \quad [2.5]$$

and

$$q_{ult} = c' N_c + \sigma_D \ \{\text{cohesive soil}\} \quad [2.6]$$

Equations [2.4]–[2.6] were derived for plane-strain conditions and thus must be modified with correction factors for circular (octagonal) shapes. There are many other possible modifications to the bearing capacity equations (e.g. depth, load, inclination base inclination and ground inclination), which are beyond the scope of this discussion.

Bearing capacity is rarely the controlling factor in the design of shallow wind turbine foundations, except in regard to the high edge pressures due to the large moments applied to the foundation (see Fig. 2.3). Corrections for eccentricity based on the concept of effective foundation area can be applied as follows (Det Norske Veritas, 2002):

$$A_{eff} = 2\left[R^2 \arccos\left(\frac{e}{R}\right) - e\sqrt{R^2 - e^2} \right] \ \{\text{circular foundation}\} \quad [2.7]$$

with major axes

$$b_e = 2(R - e) \quad [2.8]$$

and

$$l_e = 2R\sqrt{1 - \left(1 - \frac{b}{2R}\right)^2} \quad [2.9]$$

with the dimensions and terms shown in Fig. 2.3.

Settlement

In the case of wind turbine foundations, settlement can occur as a result of compression of the underlying soil. Given the magnitude of the vertical loads from the wind turbines and the typical size of the spread footings, the contact pressure from vertical loads is quite low, typically in the range of 50–75 kPa. Most soil profiles that have adequate bearing capacity and stiffness (see next section) will settle less than 2.5 cm. In cohesive soils, undisturbed samples are usually taken and tested for consolidation settlement. In granular soils, settlement analysis could be done using the Schmertmann *et al*. (1978) procedure or some other form of 'elastic' analysis. Other than the elastic half-space analysis, the methods are

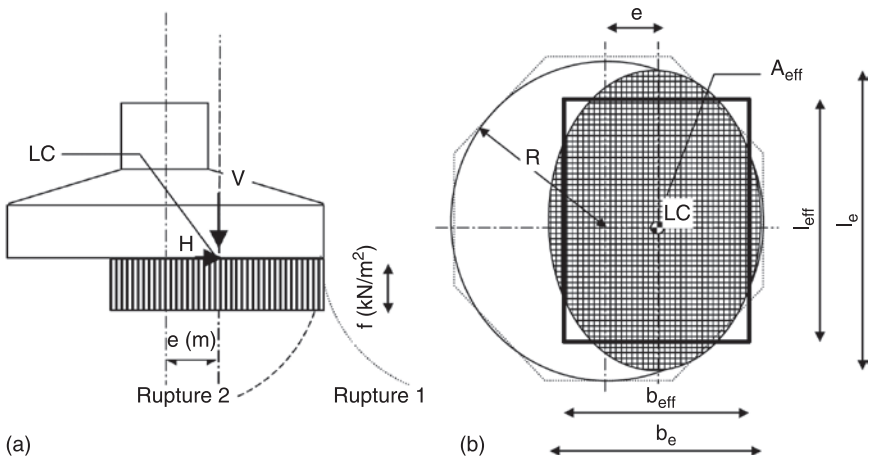

2.3 Representation of how the (a) eccentric loading to a turbine foundation (b) translates to a reduction in the effective area, A_{eff} (Det Norske Veritas, 2002).

incremental, allowing the compressibility of the soil layers within the zone of influence of the foundation to be incorporated into the analysis. The downside, in conventional settlement analysis, is that the size of the foundation influences the soil profile to considerable depth, and even small strains summed over large depth can result in what may appear to be unacceptable settlements. Cutting off the computations at depths where the stress increase is 10–20% of the overburden pressure generally solves the problem.

On most wind energy projects, the elastic properties of the soil are measured at small strain, by either CPT or surface methods. By properly reducing the small strain values obtained by the field measurements, settlements can be computed using elastic methods. A reduction of the small strain values on the order of 65% is recommended for use in settlement calculations.

Sliding resistance

Design lateral loads are specified by the turbine manufacturers. In the case of the typical octagonal shallow foundation, resistance to sliding is obtained from the sliding friction between the base and the soil upon which it rests and the passive resistance of the backfill soil. Due to the large contact area of the base, the passive resistance of the backfill soil is usually ignored. The sliding friction resistance is computed by the following equations:

For granular soil:

$$SR = W \cdot \tan\delta$$

where, SR = sliding resistance
W = dead weight of tower and foundation
$\tan\delta$ = coefficient of sliding friction between foundation and supporting soil

For cohesive soil:

$$SR = C_a \cdot A$$

where, C_a = adhesion between foundation and supporting soil
A = contact area of foundation

Values of the coefficient of sliding friction or the adhesion are typically estimated from published values. A good source for friction and adhesion values for various foundation subgrade materials is NAVFAC DM-7.2 (1982). Incidentally, it is also appropriate to evaluate the sliding resistance for cohesive soils based on a long-term 'effective angle of sliding friction', which may be taken as some fraction (typically about 2/3) of the long-term effective stress friction angle of the soil. A safety factor of at least 1.5 is recommended for sliding resistance.

Sliding resistance of deep foundations is specific to the type of foundation selected, but would typically be based on the passive resistance of the foundation elements. In most cases, the sliding resistance at the base of a pile or pier cap is not relied upon due to the likelihood that separation between the cap and underlying soil will develop over time.

Foundation stiffness

Foundation stiffness refers to the rotational stiffness of the turbine foundation. The minimum value is often specified by the turbine manufacturer. The definition of rotational stiffness (which is the rotational analog of the spring constant in vertical loading) is the ratio of the applied moment to the angular rotation. For a rigid circular foundation resting on an elastic half-space and subjected to rocking motion, Richart *et al*. (1970) provide the following equation for rotational stiffness, k_ψ:

$$k_\psi = \frac{8Gr^3}{3(1-\upsilon)} = \frac{M}{\theta} \qquad [2.10]$$

where M = applied moment, θ = rotation (in radians), and r = radius of foundation.

Det Norske Veritas (2002) extends the equations for rotational stiffness for the cases of soil over bedrock, a two-layer infinite half-space and embedment in soil over bedrock, as follows:

$$\text{Soil over bedrock: } k_\psi = k_{\psi,RHW}\left(1 + \frac{r}{6h}\right) \qquad [2.11]$$

where $k_{\psi,RHW}$ = Richart *et al*. (1970) value
h = thickness of soil layer

Two layer infinite half-space:

$$k_\psi = k_{\psi,RHW} \frac{1 + \dfrac{r}{6h}}{1 + \dfrac{r}{6h}\dfrac{G_1}{G_2}};\ 0.75 \le {}^{h}\!/_{r} \le 2 \qquad [2.12]$$

where h = thickness of upper layer

G_1, G_2 = shear modulus of upper and lower layers

Foundation embedded in soil over bedrock:

$$k_\psi = k_{\psi,RHW}\left(1 + \frac{r}{6h}\right)\left(1 + 2\frac{d}{r}\right)\left(1 + 0.7\frac{d}{h}\right) \qquad [2.13]$$

where d = depth of embedment.

Det Norske Veritas (2002) also provides stiffness equations for vertical, horizontal (sliding), and torsional motions, which are not routinely considered.

The key soil parameter in the stiffness equations is the shear modulus. Det Norske Veritas (2002) provides for estimating G from empirical correlations with void ratio and overconsolidation ratio, undrained shear strength or relative density. However, in current US-based practice, G is typically obtained from CPT seismic or surface geophysical methods. These methods measure the shear modulus at very small strain, and this value is designated as G_o. The strain associated with typical foundation loads (with safety factor of ~2.5–3.0) is significantly larger than that produced in the CPT seismic or surface geophysical measurements. Det Norske Veritas (2002) recommends a value of $G = 0.35G_o$ for use in computing foundation stiffness. A graph of shear modulus reduction values for normally consolidated soil is provided in Fig. 2.4. Multiple references exist for the G_o reduction values for a variety of soil types (Mayne *et al*., 2009).

Other design considerations for turbine foundation design include liquefaction and foundation sliding. However, liquefaction analysis is beyond the scope of this discussion. In addition, the safety factor for sliding is unlikely to be a problem for large, octagonal-shaped spread footings.

2.4 Civil design and micro-siting

The primary civil-engineering-related items of wind power plant siting, design and construction include, but are not limited to, the geotechnical investigation (see Section 2.2), site grading, access roads and crane pads, turbine foundations (see Section 2.3) including grounding, civil design of the transmission lines and the interconnection, and the collector system. The civil design package likely includes many of the following components:

- title/site location sheet;
- transportation plan;

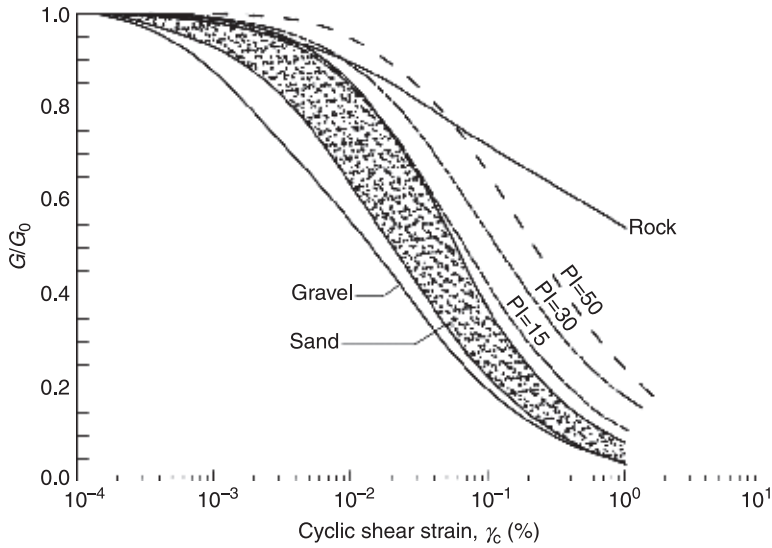

2.4 Variation of the normalized shear modulus for normally consolidated soil based on plasticity index, PI, and granular soil as a function of cyclic shear strain, γ_c (after Sykora *et al.*, 1992 and Vucetic and Dobry, 1991).

- turbine coordinate tables;
- site plan;
- plan or plan/profile sheets (can be 100+);
- public road improvement detail sheets;
- road and crane details sheets;
- foundation detail sheets;
- collector trench layout and detail sheets.

The site plan must include specific detail on setbacks from property lines, wetlands, homes, roads and drains, in addition to any special zones that may include historic and/or archaeological areas, sensitive habitats (vegetation, nesting areas), endangered or threatened species, etc. A micro-siting/constructability review is an essential component of civil design, where a detail review of turbine locations post-modeling is optimized with respect to constructability and actual field conditions. Following is a discussion of just a few components of the overall site civil design.

2.4.1 Access roads and crane pads

The primary purposes of access roads are to convey and support the heavy loading and traffic volumes during the relatively short duration of the construction phase and to act as a permanent access for lower traffic volume and loads for the long-term

wind site operation and maintenance activities. The design must consider the extreme loads of the transporters (e.g., a nacelle may weigh 700 kN and transmit 90+ kN per axle). In addition, the access roads are heavily used during construction by concrete trucks, road cranes and trailers with long wheelbases and low profiles (e.g., for tower sections). A typical design approach is the method described in Giroud and Han (2004a, 2004b). The relevant variables are subgrade and aggregate CBR, tire pressure, axial load and number of axle passes. Geogrid reinforcement may be considered to reduce the aggregate thickness requirement. A typical 5-m-wide access road is generally built to turbine delivery specifications, which varies depending on the manufacturer. Design and construction issues might include:

- stripping of organic material and topsoil;
- compacted subgrade (e.g., minimum. 95% relative compaction);
- 0.2–0.3 m of compacted aggregate road base;
- geotextile or geogrid reinforcing layer based on recommendations from geotechnical report;
- no more than 10% grade;
- no dips or bumps greater than 0.5 m over a 20-m distance;
- proper turning radius (maximum ~ 35 m);
- area at turbine to turn delivery trucks exiting site.

The primary purpose of crane pads is to provide an area for crane stability during the offloading of turbine components and erection lifts. The crane pads are usually designed to the main lift crane requirements, and may be used for permanent parking areas after construction. The typical design requirements of a crane pad consist of a level area with positive drainage, maximum 1% grade, a designed thickness of aggregate over a compacted subgrade and potential use of crane mats. A crane pad is typically 17 m × 25 m. Aggregate thickness requirements are typically based on bearing capacity considerations. A crane path is typically 10 m wide, with positive drainage to an edge, grades to not exceed 10%, and proof-rolled prior to the crane walk. Finally, a construction assembly area is also required, typically 90 m × 90 m, which is used for the staging and assembly of turbine and tower components.

2.4.2 Collection system

After wind resource assessment and turbine siting, the next most important aspect of project site selection is the electrical interconnection. Getting the distributed power to the interconnection with minimal electrical losses (in other words, lost revenues) is very important. A properly designed and constructed collection system safely, effectively and efficiently collects and transmits distributed power generated from separate turbine locations, often separated by multiple km, to a central interconnection location. In the United States, collection is commonly an underground system. In this context, losses are a function of:

- distance of cabling from turbines to interconnection point;
- voltage of cabling from turbines to interconnection point;
- size of cabling;
- soil thermal resistivity (rho or ρ);
- transformer efficiency.

Line losses are directly related to:

$$I^2 \cdot R \qquad [2.14]$$

where I = the electrical current in the cables and R is the resistance of the cabling, itself a function of cable size, cable length, and soil rho. From the perspective of the site civil/geotechnical design, high soil rho limits the cable's ability to dissipate heat from losses and increases the cable temperature, which in turn increases resistance. For example, the bedrock surface is very important to define and map accurately because most rock types increase thermal resistivity and also increase installation costs. The collection system should be optimized to minimize these line losses and optimize installed cost by minimizing line length.

Collection systems are normally installed adjacent to site roads to allow access for construction and maintenance. Proper compaction of backfill in collection trenches is a major issue. Because trenches normally follow and/or cross access roads, improperly compacted backfill in trenches can lead to ground subsidence and ruts/dips in these roads. Industry standard is to compact trench backfill to 95% relative compaction, minimum. Backfill placed in trenches must be suitable and not damage cables. For example, crushed rock with angular edges can damage cables. Cables are often placed in a layer of sand or other suitable material.

As discussed in Section 2.4.2, thermal resistivity is the ability of soil to dissipate heat. If the soil cannot properly dissipate the heat generated from current flowing in underground cables, cables can overheat, which in turn leads to drying of the electrical insulation and potential high voltage cable failures. In addition, thermal dry-out increases soil rho as moisture is driven from the backfill surrounding the cables. Most cables are rated to be installed in soil of 90°C-cm/W. If soil rho is higher, cable capacities must be de-rated, which may mean cables cannot carry the required amount of power or may have high line losses. Corrective or engineered backfill can be placed in the collection trenches to mitigate this effect. Typical values of soil rho are provided in Table 2.2.

In routing underground collection networks, the trenches should be roadside wherever possible and be designed to minimize road crossings. Furthermore, turbine crane pads, which have substantial short-term loads, should not be located on top of collection trenches. Routing should attempt to minimize potential interferences between turbine transport vehicles, erection cranes and trenching equipment due to the difficult logistical problems that may ensue. Finally, all trenches should be installed so that they are accessible for repairs in the event of a cable failure.

Table 2.2 Typical soil rho values

Soil type	Thermal resistivity (°C-cm/W)
Sandy soil (dry)	200
Sandy soil (moist)	83
Sandy soil (saturated)	40
Sandy-gravelly soil	71
Sandy silty-clay	55
Sandy clay loam	32
Silt loam	33
Clayey sand	79
Clayey soil	67
Lean clay	90
Fat clay	100
Volcanic soil	100

Note: rho values based on saturated soil, except where noted. Adapted from Buonanno *et al.* (1995), Lu *et al.* (2009), and various geotechnical investigation reports for wind turbine sites in the United States.

2.4.3 Turbine interface to collection system and turbine grounding

All turbines require a transformer to connect to the collection system. Some transformers are located in the nacelle and others are located adjacent to the turbine base. Conduits are required to route cables for the connection of the turbine and must be carefully coordinated with the reinforcing steel placed within the turbine foundation.

Each turbine must be connected to a valid ground reference to ensure that the turbine will safely perform and remain undamaged through anomalies on the collection system (i.e., short circuits). Turbine manufacturers typically specify that required resistance to ground be less than 5 ohms, for each individual turbine. Meeting this requirement can be very difficult in rocky areas with very high soil resistivity. Common turbine grounding systems consist of rings of copper cable installed concentrically around the turbine foundation (Fig. 2.5). Connected to these rings are copper rods driven into the earth (typically 2.5–6.0 m long). Resistance to ground is a function of soil electrical resistivity, area of the grounding system, diameter of copper wire installed in the grounding system, and length and diameter of ground rods installed.

If the specified resistance to ground is difficult to attain, the following measures can be taken.

1. Add additional rings of copper wire and additional copper ground rods (subject to the law of diminishing returns).

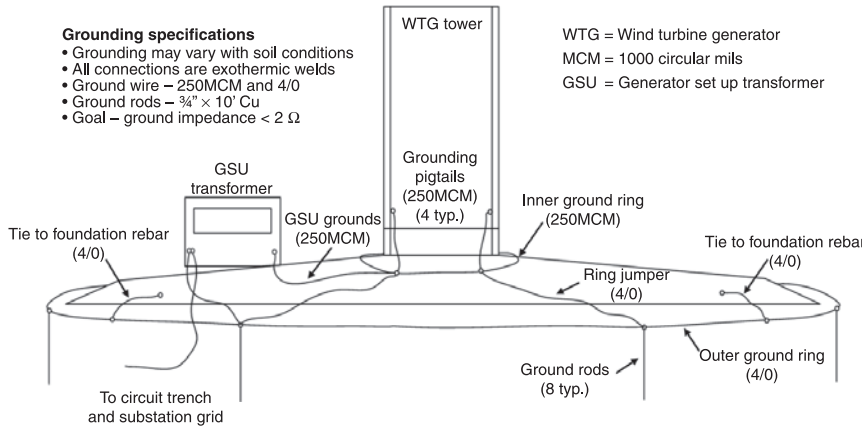

2.5 Example schematic of grounding specifications at the wind turbine foundation/tower interface.

2. Grounding rods and cables can be installed in enhanced grounding material. Essentially, holes larger than the rods are drilled and backfilled with this material (subject to high cost).
3. Connect grounding system to the turbine foundation reinforcing in several locations. This effectively uses the turbine foundation as a huge ground rod (subject to applying proper cathodic protection).
4. Special chemical grounding rods are available, which release chemicals into the surrounding soil to reduce soil electrical resistivity (subject to high cost and maintenance for refilling of the chemicals).

2.5 Sources of further information and advice

Burland, J B (1989), 'Small is beautiful – the stiffness of soils at small strains', Ninth Lauritz Bjerrum Memorial Lecture, *Can. Geotech. J.*, 26, 499–516.

Das, B M (2004), *Principles of Foundation Engineering*, Brooks/Cole-Thomson Learning, Pacific Grove, CA.

2.6 References

Buonanno, G, Carotenuto, A, Dell'Isola, M and Villacci, D (1995), 'Effect of radiative and convective heat transfer on thermal transients in power cables', *IEE Proceedings – Generation Transmission & Distribution*, 142(4), 436–44.

Department of the Navy (1982), Foundations and earth structures, NAVFAC DM-7.2.

Det Norske Veritas (2002), *Guidelines for Design of Wind Turbines*, Risø National Laboratory, Copenhagen.

Dobrin, M B and Savit, C H (1988), *Introduction to Geophysical Prospecting*, McGraw-Hill, New York.

Fernandez, A L (2000), Tomographic imaging the state of stress, PhD dissertation, Georgia Institute of Technology, Atlanta, GA.

Fratta, D, Alshibli, K A, Tanner, W M and Roussel, L (2005), 'Combined TDR and P-wave velocity measurements for the determination of in-situ soil density', *ASTM Geotechnical Testing Journal*, 28(6), 553–63.

Giroud, J P and Han, H J (2004a), 'Design method for geogrid-reinforced unpaved roads I. Development of design method', *Journal of Geotechnical and Geoenvironmental Engineering*, 130(8), 775–86.

Giroud, J P and Han, H J (2004b), 'Design method for geogrid-reinforced unpaved roads II. Calibration and applications', *Journal of Geotechnical and Geoenvironmental Engineering*, 130(8), 787–97.

Jamiolkowski, M, Lancellotta, R, Lo Presti, D C F and Pallara, O (1994), Stiffness of Toyura sand at small and intermediate strain, *Proceedings of the 13th International Conference on Soil Mechanics and Foundations Engineering*, New Delhi, India, 5–10 January, pp. 169–72.

Kim, K-S (2009), *Wave-based imaging and sensing technologies for characterization of structural and geotechnical engineering systems*, PhD dissertation, University of Wisconsin-Madison, Madison, WI.

Knight, R J and Enders, A L (2005), 'An introduction to rock physics principles for near-surface geophysics', in Buttler, D. (ed.), *Near Surface Geophysics*, Society of Exploration Geophysics, Tulsa, UK, pp. 31–70.

Lu, X, Rin, T and Gong, Y (2009), 'Experimental investigation of thermal dispersion in saturated solid with one-dimensional water flow', *Soil Science Society America Journal*, 73(6), 1912–20.

Mavko, G, Mukerji, T and Dvorkin, J (1998), *The Rock Physics Handbook – Tools for Seismic Analysis in Porous Media*, Cambridge University Press, Cambridge.

Mayne, P W, Coop, M R, Springman, S M, Huang, A-B and Zornberg, J G (2009), 'Geomaterial behavior and testing', in M. Hamza *et al*. (eds), *Proceedings of the 17th International Conference on Soil Mechanics Geotechnical and Engineering*, Alexandria, Egypt, 5–9 October, pp. 2777–872.

Richart, F E, Hall, J and Woods, R (1970), *Vibrations of Soils and Foundations*, Prentice-Hall, Englewood Cliffs, NJ.

Santamarina, J C, Klein, K and Fam, M (2001), *Soils and Waves – Particulate Materials Behavior, Characterization and Process Monitoring*, John Wiley and Sons, Chichester, UK.

Santamarina, J C, Rinaldi, V A, Fratta, D, Klein, K A, Wang, Y-H, Cho, G-C, *et al*. (2005), 'A survey of elastic and electromagnetic properties of near-surface soils in near-surface geophysics', in Buttler, D. (ed.), *Near Surface Geophysics*, Society of Exploration Geophysics., Tulsa, OK, pp. 71–87.

Schmertmann, J H, Hartman, J P and Brown, P R (1978), 'Improved strain influence factor diagrams', *Journal of the Geotechnical Engineering Division*, 104(GT8), 1131–35.

Sykora, D W, Wahl, R E and Wallace, D C (1992), '*USACE geotechnical earthquake engineering software*', Instruction Report GL-92-4, US Army Corps of Engineers, Washington, DC.

Telford, W M, Geldart, L P and Sheriff, R E (1990), *Applied Geophysics*, Cambridge University Press, Cambridge, UK.

Vucetic, M and Dobry, R (1991), 'Effect of soil plasticity on cyclic response', *Journal of the Geotechnical Engineering Division*, 117(1), 89–107.

3

Aeroelasticity and structural dynamics of wind turbines

V. A. RIZIOTIS, National Technical University of Athens, Greece and H. A. MADSEN, Risø DTU, The National Laboratory for Sustainable Energy at the Technical University of Denmark, Denmark

Abstract: In the present chapter, the aeroelastic modeling and optimized design of modern megawatt-scale wind turbines are addressed. In the first part of the chapter, the aeroelastic equations of motion for the flexible wind turbine components and the dynamics of the full wind turbine system are presented in the context of beam theory, multi-body dynamic analysis and finite element method. In the second part, the main aspects relating to an improved aeroelastic design are discussed. First, the nature of the external loads on a wind turbine is described. Then, aeroelastic instability problems encountered in the past or expected in future designs, methods for improving the aeroelastic behavior of wind turbines and some future trends concerning aeroelastic design are discussed.

Key words: aeroelasticity, damping, instability, loads, design.

3.1 Introduction

The wind turbine is a flexible structure that operates mainly under the action of the aerodynamic loads on the rotor. The airflow passing through the rotor, besides rotating the blades, also deforms the whole structure. As the wind turbine deforms, the elastic motion of the various components affects the aerodynamic loading, which in turn differentiates the deformation field. In this way, the coupled aerodynamic–structural dynamic problem is formed.

Aeroelastic analysis of a wind turbine lies in determining the elastic deflections and internal loads along the various components, arising from its interaction with the incoming wind. It is understood that this is a very important task in the design process since it provides the design limits for the dimensioning of the individual components. However, given the stochastic nature of the wind, the unsteadiness of the flow over the rotor blades, the complex structure of the blades and the different degrees of freedom (DOFs) of motion undergone by the various components (rotor rotation, blades pitching, nacelle yaw, etc.), it is also understood that it is by no means an easy task.

The present chapter consists of two parts. In the first part, the modeling of the wind turbine structural dynamics and aeroelastics is described in the context of the beam theory and finite element analysis, as applied in most current design and analysis tools. In the second part, the main aspects toward improved aeroelastic design are discussed. This part begins with describing the nature of the external

loads on a wind turbine. Then, aeroelastic instability problems encountered in the past or expected in the future designs, methods for improving aeroelastic behavior of wind turbines and some future trends concerning aeroelastic design are discussed.

3.2 Structural dynamics of wind turbines

3.2.1 Finite element method (FEM) modeling of the wind turbine components using beam theory

One-dimensional approximation of solid structures (beam theory) is probably the most widely used modeling approach for wind turbine applications. Most existing structural dynamics and aeroelastic design tools (Schepers *et al*., 2002) are based on this approach for the structural modeling of the flexible components of the wind turbine (i.e., blades, tower, shaft). The basic limitation is that the structure must be slender in shape or else that one of the dimensions must be significantly larger than the other two. Regular asymptotic analysis justifies elimination of the dependence on the two shortest dimensions, and thus, formulation of the problem can be performed only with respect to the remaining third. In the direction of this dominant dimension of the structure, the elastic axis of the beam is defined that is usually assumed to be rectilinear [curved beam axis has also been dealt with by Hodges (2003)]. In the near past, first-order, non-linear beam models, or even linearized modal-based methods, were employed in most state-of-the-art design tools for wind turbines, suggesting small or moderate deflections. With the increasing size and flexibility of modern turbines, the necessity for higher order models that account for large deflections has emerged and models of this type have been very recently implemented in aeroelastic codes (Riziotis and Voutsinas, 2006; Kallesøe, 2007; Riziotis *et al*., 2008). The main aspects of the non-linear beam theory, including analysis of highly flexible beams undergoing large deflections, are discussed in the present section.

Also, the finite element method (FEM) for the numerical discretization of the beam differential equations is presented.

Kinematics of the beam

Let Oxyz be the global coordinate system of the beam (see Fig. 3.1). The y axis of the system is aligned to the axis of the beam (shear center axis) while x and z axes lie in the cross-section plane of the undeformed beam, defining the two bending directions of the beam. The $O'\xi_0\eta_0\zeta_0$ is the local coordinate system of the undeformed cross-section (Fig. 3.1), where the ξ_0 and ζ_0 are rotated with respect to the global x and z axes only for the section pre-twist. Finally, $O_1\ \xi\eta\zeta$ is the local coordinate system of the deformed cross-section (Fig. 3.1). The analysis presented in the sequel is based on the assumptions of the Euler–Bernoulli beam theory (Hodges and

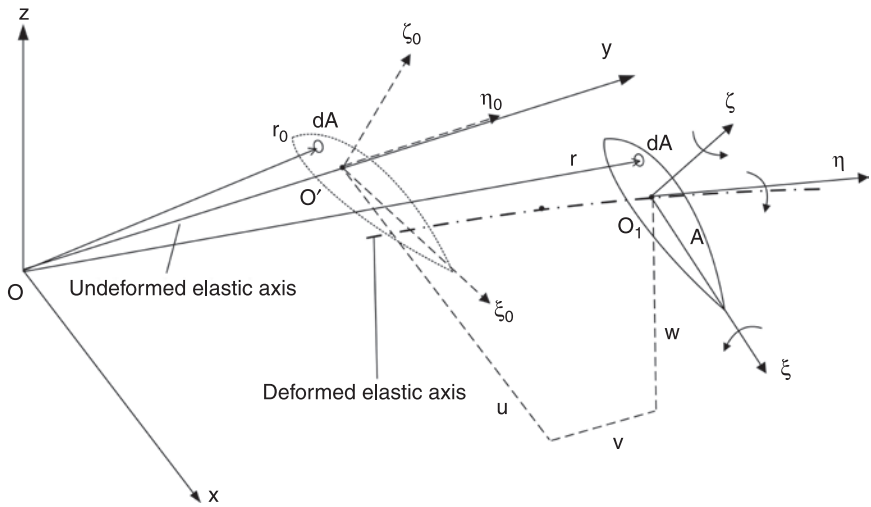

3.1 Kinematics of a beam structure.

Dowell, 1974). According to Euler–Bernoulli hypotheses, every cross-section along the beam can only translate and rotate uniformly under the action of external bending, axial and torsion loads. However, it always remains planar and its shape remains undistorted. This is a reasonable assumption, taking into account that for beam structures, the cross-section dimensions are relatively small compared to the beam-wise dimension. Moreover, cross-sections of the beam rotate in such a way that they always remain perpendicular to the deformed elastic axis. This means that rotation of the sections results only from the bending of the structure, and therefore, deformations due to traverse shear are neglected. In such a way, a direct relation between bending displacements and rotations can be derived.

The position vector **r** of any arbitrary point along the beam at the deformed state is given by the following general expression:

$$\mathbf{r} = \begin{Bmatrix} 0 \\ y \\ 0 \end{Bmatrix} + \begin{Bmatrix} u \\ v \\ w \end{Bmatrix} + \mathbf{E} \cdot \begin{Bmatrix} \xi \\ 0 \\ \zeta \end{Bmatrix} \qquad [3.1]$$

where u and w are the two bending displacements in the direction of the global x and z axes, respectively, while v is the axial displacement of the cross-sections initially located at the y axial position. The **E** matrix is the transformation matrix from the local coordinates of the deformed section (ξ, η, ζ) to the global coordinates of the beam (x, y, z).

In terms of the Euler angles φ, ψ and ω shown in Fig. 3.2, matrix **E** is written in the following form:

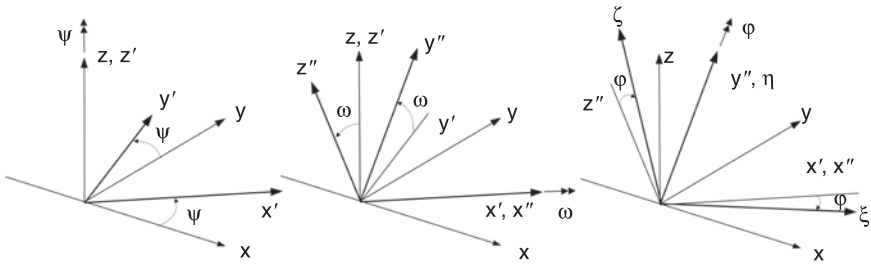

3.2 Transformation from local system of the cross-section to global system of the beam.

$$\mathbf{E} = \begin{pmatrix} \cos\psi & -\sin\psi & 0 \\ \sin\psi & \cos\psi & 0 \\ 0 & 0 & 1 \end{pmatrix} . \begin{pmatrix} 1 & 0 & 0 \\ 0 & \cos\omega & -\sin\omega \\ 0 & \sin\omega & \cos\omega \end{pmatrix} . \begin{pmatrix} \cos\varphi & 0 & \sin\varphi \\ 0 & 1 & 0 \\ -\sin\varphi & 0 & \cos\varphi \end{pmatrix} \qquad [3.2]$$

where ψ and ω are directly related to u and w (the two bending displacements), while φ represents the torsion deformation plus the cross-section pre-twist.

Following an ordering scheme in which terms up to second-order accuracy are retained (Hodges and Dowell, 1974) in expressing Euler angles in terms of the bending displacement fields u and w, matrix $\mathbf{E}$ can be written in the following form:

$$\mathbf{E} = \begin{bmatrix} \cos(\theta_t + \hat{\theta} - u'w') \cdot \left(1 - \frac{u'^2}{2}\right) & u' & \sin(\theta_t + \hat{\theta} - u'w') \cdot \left(1 - \frac{u'^2}{2}\right) \\ -u'\cos(\theta_t + \hat{\theta}) + w'\sin(\theta_t + \hat{\theta}) & 1 - \frac{u'^2}{2} - \frac{w'^2}{2} & -u'\sin(\theta_t + \hat{\theta}) - w'\cos(\theta_t + \hat{\theta}) \\ -\sin(\theta_t + \hat{\theta}) \cdot \left(1 - \frac{w'^2}{2}\right) & w' & \cos(\theta_t + \hat{\theta}) \cdot \left(1 - \frac{w'^2}{2}\right) \end{bmatrix}$$

[3.2a]

In equation [3.2a], $(\quad)'$ denotes the spatial derivative with respect to the beam-wise coordinate y. Moreover, θ_t is the blade local pre-twist, θ is the twisting deformation with respect to the global beam axis y and $\hat{\theta} = \theta + \int_0^y u''w'\,dy$ is the local torsion deformation with respect to the local deformed beam axis η (Hodges and Dowell, 1974), such that $\varphi = \hat{\theta} + \theta_t$.

If second-order terms are dropped, then equation [3.2a] is significantly simplified and takes the form (first-order accurate):

$$\mathbf{E} = \begin{bmatrix} \cos\theta_t - \sin\theta_t \cdot \theta & u' & \sin\theta_t + \cos\theta_t \cdot \theta) \\ -u'\cos\theta_t + w'\sin\theta_t & 1 & -u'\sin\theta_t - w'\cos\theta_t \\ -\sin\theta_t - \cos\theta_t \cdot \theta & w' & -\cos\theta_t - \sin\theta_t \cdot \theta \end{bmatrix} \qquad [3.2b]$$

Equations of structural equilibrium beam equations

On the basis of the above kinematic considerations, the equations of dynamic equilibrium for the beam structure can be derived. Let us consider a differential element of the beam, with cross-section A, and width dy, as shown in Fig. 3.3. The incremental mass of the infinitesimal element dA is dm = ρdA, where ρ is the local mass density of the material of the cross-section (see Fig. 3.3). Let also $\delta\mathbf{P} = \{\delta P_x, \delta P_y, \delta P_z\}^T$ be the external forces per unit length exerted on the element, $d\mathbf{F} = \{dF_x, dF_y, dF_z\}^T$ be the net elastic internal (reaction) forces, $\mathbf{g} = \{g_x, g_y, g_z\}^T$ be the acceleration of gravity, and $\mathbf{p}^i = \{p_x^i, p_y^i, p_z^i\}^T$ and $\mathbf{p}^e = \{p_x^e, p_y^e, p_z^e\}^T$ be the total inertial and external forces, respectively. Then, the balance of forces with respect to the blade local coordinate system Oxyz is written as follows:

$$\underbrace{\left(\int_A \rho \cdot dA \cdot \ddot{\mathbf{r}}\right) dy}_{p^i \cdot dy} = d\mathbf{F} + \underbrace{\left(\int_A \rho \cdot dA \cdot \mathbf{g}\right) dy + \delta\mathbf{P}\, dy}_{p^e \cdot dy} \qquad [3.3]$$

Similarly, the balance of the moments with reference to the origin (1) of the incremental element dy (see Fig. 3.3) is written as:

$$\underbrace{\left(\int_A \rho \cdot dA \cdot \mathbf{r}_p \times \ddot{\mathbf{r}}\right) dy}_{q^i dy} = d\mathbf{M} + d\mathbf{r}_e \times (\mathbf{F} + d\mathbf{F}) + \underbrace{\left(\int_A \rho \cdot dA \cdot \mathbf{r}_p \times \mathbf{g}\right) dy + \mathbf{r}_a \times \delta\mathbf{P}\, dy}_{q^e dy} \qquad [3.4]$$

In equation [3.4], $\mathbf{F} + d\mathbf{F}$ is the vector of the resultant elastic force at the end point (2), $d\mathbf{M} = \{dM_x, dM_y, dM_z\}^T$ is the net elastic moments of the element, $\mathbf{q}^i = \{q_x^i, q_y^i, q_z^i\}^T$ and $\mathbf{q}^e = \{q_x^e, q_y^e, q_z^e\}^T$ are the inertial and external moments acting on the element, respectively, and $\mathbf{r_a}$ is the local position of the external forces,

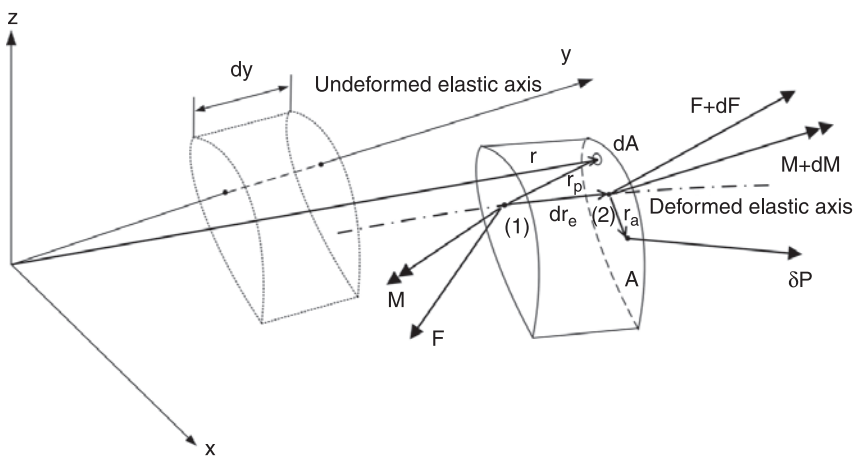

3.3 Dynamics of a beam structure.

centre with respect to the elastic axis of the beam. Moreover, $\mathbf{r_p} = \mathbf{r} - \mathbf{r_e^{(1)}}$ and $d\mathbf{r_e} = \mathbf{r_e^{(2)}} - \mathbf{r_e^{(1)}}$ where $\mathbf{r_e}$ is the position vector of a point on the deformed elastic axis, while indices (1) and (2) indicate the beginning and end of the differential element dy, respectively. The position vector $\mathbf{r_e}$ is given by:

$$\mathbf{r}_e = \begin{Bmatrix} 0 \\ y \\ 0 \end{Bmatrix} + \begin{Bmatrix} u \\ v \\ w \end{Bmatrix} \quad [3.5]$$

The vector equation [3.3] and equation [3.4] of equilibrium are analyzed in components relative to the undeformed axes x, y and z. The force equations are written as:

$$p_x^i = F_x' + p_x^e \quad [3.6a]$$

$$p_y^i = F_y' + p_y^e \quad [3.6b]$$

$$p_z^i = F_z' + p_z^e \quad [3.6c]$$

Similarly, the moment equations are written as:

$$q_x^i = M_x' + F_z - F_y w' + q_x^e \quad [3.7a]$$

$$q_y^i = M_y' - F_z u' + F_x w' + q_y^e \quad [3.7b]$$

$$q_z^i = M_z' - F_x + F_y u' + q_z^e \quad [3.7c]$$

As already stated, traverse shear is neglected in the present analysis. Under the assumption of very high shear rigidity (negligible shear deformations), the cross-sections of the beam remain perpendicular to the deformed elastic axis, and therefore bending rotations (angles ψ and ω) are not independent variables of the problem. Therefore, the two bending moment equation [3.7a] and [3.7c] are used for eliminating spatial derivatives of the internal shear forces F_x' and F_z' from equation [3.6c] and [3.6a], respectively. Thereby, the six equilibrium equations can be reduced to four equations for the four independent deflections u, v, w and θ defined with reference to the undeformed system:

$$p_x^i (q_z^i)' = M_z'' + (F_y u')' + p_x^e + (q_z^e)' \quad \text{(force } x\text{)} \quad [3.8a]$$

$$p_y^i = F_y' + p_y^e \quad \text{(force } y\text{)} \quad [3.8b]$$

$$p_z^i - (q_x^i)' = -M_x'' + (F_y w')' + p_z^e - (q_x^e)' \quad \text{(force } z\text{)} \quad [3.8c]$$

$$q_y^i + q_x^i u' + q_z^i w' = M_y' + M_x u' + M_z w' + q_y^e + q_x^e u' + q_z^e w' \quad \text{(moment } y\text{)} \quad [3.8d]$$

To close the system [3.8], expressions for the resultant internal loads, as functions of the unknown deflections field, must be defined. The internal loads are obtained by integrating stresses over the cross-section surface. Stresses, in turn, are related to strains and thereby to elastic deflections through Hooke's law.

The strain tensor ε based on Green's (Crisfield, 1998) definition is determined by:

$$d\mathbf{r}^{T}\cdot d\mathbf{r} - d\mathbf{r}_{0}^{T}\cdot d\mathbf{r}_{0} = 2\cdot\{d\xi \quad d\eta \quad d\zeta\}\cdot\begin{bmatrix}\varepsilon_{\xi\xi} & \varepsilon_{\xi\eta} & \varepsilon_{\xi\zeta}\\ \varepsilon_{\eta\xi} & \varepsilon_{\eta\eta} & \varepsilon_{\eta\zeta}\\ \varepsilon_{\zeta\xi} & \varepsilon_{\zeta\eta} & \varepsilon_{\zeta\zeta}\end{bmatrix}\cdot\begin{Bmatrix}d\xi\\ d\eta\\ d\zeta\end{Bmatrix} \qquad [3.9]$$

Furthermore, under the assumption of a homogeneous and isotropic material, Hooke's law takes the form:

$$\begin{Bmatrix}\sigma_{\eta\eta}\\ \sigma_{\eta\xi}\\ \sigma_{\eta\zeta}\end{Bmatrix} = \begin{bmatrix}E & 0 & 0\\ 0 & G & 0\\ 0 & 0 & G\end{bmatrix}\cdot\begin{Bmatrix}\varepsilon_{\eta\eta}\\ \varepsilon_{\eta\xi}\\ \varepsilon_{\eta\zeta}\end{Bmatrix} \qquad [3.10]$$

Equation [3.9] yields the strain displacement expressions. By retaining terms up to second order, the following relationships are obtained:

$$\varepsilon_{\eta\eta} = v' + \underline{\frac{u'^{2}}{2} + \frac{w'^{2}}{2}} + \underline{(\xi^{2}+\zeta^{2})\cdot\left(\theta_{t}'\theta'\frac{\theta'^{2}}{2}\right)}$$
$$-u''\cdot\left(\xi\cdot\cos(\theta_{t}+\underline{\hat{\theta}}) + \zeta\cdot\sin(\theta_{t}+\underline{\hat{\theta}})\right) + w''\cdot\left(\xi\cdot\sin(\theta_{t}+\underline{\hat{\theta}}) - \zeta\cdot\cos(\theta_{t}+\underline{\hat{\theta}})\right) \qquad [3.11a]$$

$$\varepsilon_{\eta\xi} = \frac{1}{2}\zeta\cdot\theta' \qquad [3.11b]$$

$$\varepsilon_{\eta\zeta} = \frac{1}{2}\xi\cdot\theta' \qquad [3.11c]$$

Accordingly, equation [3.10] and equation [3.11] provide stress deflection relationships.

By integrating normal and shear stresses over the cross-section surface, the resultant loads with respect to the local deformed coordinate system are determined (second-order accurate as well):

Axial force F

$$F_{\eta} = \int_{A}\sigma_{\eta\eta}\,dA = EA\left(v' + \underline{\frac{u'^{2}}{2} + \frac{w'^{2}}{2}}\right) + \underline{EI_{t}\cdot\left(\theta_{t}'\theta' + \frac{\theta'^{2}}{2}\right)}$$
$$-u''\cdot\left(EA_{\zeta}\cdot\cos(\theta_{t}+\underline{\hat{\theta}}) + EA_{\xi}\cdot\sin(\theta_{t}+\underline{\hat{\theta}})\right) + w''\cdot\left(EA_{\zeta}\cdot\sin(\theta_{t}+\underline{\hat{\theta}}) + EA_{\xi}\cdot\cos(\theta_{t}+\underline{\hat{\theta}})\right) \qquad [3.12a]$$

Bending moment ξ

$$M_{\xi} = -\int_{A}\zeta\cdot\sigma_{\eta\eta}\,dA = EI_{\xi\xi}\cdot\left(\sin(\theta_{t}+\underline{\hat{\theta}})\cdot u'' + \cos(\theta_{t}+\underline{\hat{\theta}})\cdot w''\right)$$
$$- EA_{\xi}\left(v' + \underline{\frac{u'^{2}}{2} + \frac{w'^{2}}{2}}\right) + \underline{EI_{t\xi}\cdot\left(\theta_{t}'\theta' + \frac{\theta'^{2}}{2}\right)} \qquad [3.12b]$$

Bending moment ζ

$$M_\xi = \int_A \xi \cdot \sigma_{\eta\eta}\, dA = -EI_{\zeta\zeta} \cdot \left(\cos(\theta_t + \hat{\underline{\theta}}) \cdot u'' + \sin(\theta_t + \hat{\underline{\theta}}) \cdot w''\right) + EA_\zeta \left(v' + \underline{\frac{u'^2}{2} + \frac{w'^2}{2}}\right) + \underline{EI_{t\zeta} \cdot \left(\theta_t' \theta' + \frac{\theta'^2}{2}\right)} \quad [3.12c]$$

Torsion moment η

$$\begin{aligned} M_\eta &= \int_A \left(\zeta \cdot \sigma_{\eta\xi} - \xi \cdot \sigma_{\eta\zeta}\right) dA + (\theta_t' + \theta') \cdot \int_A \left(\zeta^2 + \xi^2\right) \sigma_{\eta\eta} \cdot dA \\ &= GI_t \cdot \theta' + \underline{EI_t \cdot (\theta_t' + \theta') \cdot \left(v' + \frac{u'^2}{2} + \frac{w'^2}{2}\right)} + \underline{EI_{t2} \cdot \theta_t'^2 \cdot \theta'} \\ &\quad - \underline{\left(\left(EI_{t\xi} \cdot \cos(\theta_t + \hat{\theta}) + EI_{t\xi} \cdot \sin(\theta_t + \hat{\theta})\right) \cdot u''\right.} \\ &\quad + \underline{\left.\left(EI_{t\xi} \cdot \cos(\theta_t + \hat{\theta}) - EI_{t\zeta} \cdot \sin(\theta_t + \hat{\theta})\right) \cdot w''\right) \cdot (\theta_t' + \theta')} \end{aligned} \quad [3.12d]$$

In deriving equation [3.12], the assumption that the local axes ξ and ζ coincide with the principal axes of the cross-section is made. The structural properties of the beam involved in equation [3.12] are defined as follows:

$$EA = \int_A E \cdot dA,\ EA_\xi = \int_A E \cdot \zeta\, dA,\ EA_\zeta = \int_A E \cdot \xi\, dA,\ EI_{\xi\xi} = \int_A E \cdot \zeta^2\, dA,\ EI_{\zeta\zeta} = \int_A E \cdot \xi^2\, dA,$$

$$GI_t = \int_A G \cdot (\xi^2 + \zeta^2)\, dA,\ EI_t = \int_A E \cdot (\xi^2 + \zeta^2)\, dA,\ EI_{t2} = \int_A E \cdot (\xi^2 + \zeta^2)^2\, dA,$$

$$EI_{t\xi} = \int_A E \cdot \zeta \cdot (\xi^2 + \zeta^2)\, dA,\ \ EI_{t\zeta} = \int_A E \cdot \xi \cdot (\xi^2 + \zeta^2)\, dA$$

In equation [3.11] and equation [3.12], the underlined terms are the non-linear second-order ones. By omitting those terms, standard first-order linear expressions are obtained.

The reaction loads (forces and moments) of equation [3.12] are expressed in the local deformed system $O_1\xi\eta\zeta$. Therefore, before being substituted in equation [3.8], they have to be transformed in Oxyz. This is done through the rotation matrix **E** given by the equation [3.2]. In this way, the final system of the second-order beam equations is derived:

Force x

$$\begin{aligned} &p_x^i + \left(q_z^i\right)' - p_x^e - \left(q_z^e\right)' = \left(M_\zeta \cdot \cos(\theta_t + \hat{\theta}) - M_\xi \sin(\theta_t + \hat{\theta})\right)'' + \left(F_\eta u'\right)' \\ &= \left(\left(EA_\zeta \cdot \cos(\theta_t + \hat{\underline{\theta}}) + EA_\xi \cdot \sin(\theta_t + \hat{\underline{\theta}})\right) \cdot \left(v' + \underline{\frac{u'^2}{2} + \frac{w'^2}{2}}\right)\right. \\ &\quad - \left(EI_{\zeta\zeta} \cdot \cos^2(\theta_t + \hat{\underline{\theta}}) + EI_{\xi\xi} \cdot \sin^2(\theta_t + \hat{\underline{\theta}})\right) \cdot u'' - \frac{1}{2}\left(EI_{\xi\xi} - EI_{\zeta\zeta}\right) \cdot \sin(2 \cdot (\theta_t + \hat{\underline{\theta}})) \cdot w'' \\ &\quad + \underline{\left.\left(EI_{t\zeta} \cdot \cos(\theta_t + \hat{\underline{\theta}}) + EI_{t\xi} \cdot \sin(\theta_t + \hat{\underline{\theta}})\right) \cdot \theta_t \theta'\right)''} + \left(F_\eta u'\right)' \end{aligned} \quad [3.13a]$$

Force y

$$p_y^i - p_y^e = F_\eta'$$

$$= \left(EA\left(v' + \underline{\underline{\frac{u'^2}{2} + \frac{w'^2}{2}}} \right) + \underline{\underline{EI_t \cdot \left(\theta_t' \theta' + \frac{\theta'^2}{2} \right)}} \right.$$

$$- u'' \cdot \left(EA_\zeta \cdot \cos(\theta_t + \underline{\hat{\theta}}) + EA_\xi \cdot \sin(\theta_t + \underline{\hat{\theta}}) \right)$$

$$\left. + w'' \cdot \left(EA_\zeta \cdot \sin(\theta_t + \underline{\hat{\theta}}) - EA_\xi \cdot \cos(\theta_t + \underline{\hat{\theta}}) \right)' \right) \qquad [3.13b]$$

Force z

$$p_z^i - \left(q_x^i\right)' - p_z^e + \left(q_z^e\right)' = -\left(M_\xi \cdot \cos(\theta_t + \hat{\theta}) + M_\zeta \sin(\theta_t + \hat{\theta})\right)'' + \left(F_\eta w'\right)'$$

$$= \left(\left(EA_\xi \cdot \cos(\theta_t + \underline{\hat{\theta}}) + EA_\zeta \cdot \sin(\theta_t + \underline{\hat{\theta}}) \right) \cdot \left(v' + \underline{\frac{u'^2}{2} + \frac{w'^2}{2}} \right) \right.$$

$$- \frac{1}{2}\left(EI_{\xi\xi} - EI_{\zeta\zeta}\right) \cdot \sin(2 \cdot (\theta_t + \underline{\hat{\theta}})) \cdot u'' - \left(EI_{\xi\xi} \cdot \cos^2(\theta_t + \underline{\hat{\theta}}) + EI_{\zeta\zeta} \cdot \sin^2(\theta_t + \underline{\hat{\theta}})\right) \cdot w''$$

$$\left. + \underline{\left(EI_{t\xi} \cdot \cos(\theta_t + \hat{\theta}) + EI_{t\zeta} \cdot \sin(\theta_t + \hat{\theta})\right) \cdot \theta_t \theta'} \right)'' + \left(F_\eta w'\right)' \qquad [3.13c]$$

Moment y

$$q_y^i + q_x^i u' + q_z^i w' - q_y^e + q_x^e u' + q_z^e w' =$$

$$M_\eta' - M_\xi \left(\cos(\theta_t + \hat{\theta}) \cdot u'' - \sin(\theta_t + \hat{\theta}) \cdot w''\right) - M_\zeta \left(\sin(\theta_t + \hat{\theta}) \cdot u'' + \cos(\theta_t + \hat{\theta}) \cdot w''\right)$$

$$= \left(GI_t \theta' + \underline{\underline{EI_t \cdot (\theta_t' + \theta') \cdot \left(v' + \frac{u'^2}{2} + \frac{w'^2}{2} \right)}} + \underline{EI_{t2} \cdot \theta_t'^2 \cdot \theta'} \right.$$

$$- \underline{\left(\left(EI_{t\zeta} \cdot \cos(\theta_t + \hat{\theta}) + EI_{t\xi} \cdot \sin(\theta_t + \hat{\theta}) \right) \cdot u'' \right.}$$

$$\left. \left. + \underline{\left(EI_{t\xi} \cdot \cos(\theta_t + \hat{\theta}) - EI_{t\zeta} \cdot \sin(\theta_t + \hat{\theta}) \right) \cdot w'' \right) \cdot (\theta_t' + \theta')} \right)'$$

$$+ \underline{\left(EA_\xi \cdot \cos(\theta_t + \hat{\theta}) - EA_\xi \cdot \sin(\theta_t + \hat{\theta}) \right) \cdot \left(v' + \frac{u'^2}{2} + \frac{w'^2}{2} \right) \cdot u''}$$

$$- \underline{\left(EA_\zeta \cdot \cos(\theta_t + \hat{\theta}) + EA_\xi \cdot \sin(\theta_t + \hat{\theta}) \right) \cdot \left(v' + \frac{u'^2}{2} + \frac{w'^2}{2} \right) \cdot w''}$$

$$- \underline{\underline{\frac{1}{2}\left(EI_{\xi\xi} - EI_{\zeta\zeta}\right) \cdot \sin(2 \cdot (\theta_t + \hat{\theta})) \cdot \left(u''^2 - w''^2\right)}}$$

$$- \underline{\underline{\left(EI_{\xi\xi} - EI_{\zeta\zeta}\right) \cdot \cos(2 \cdot (\theta_t + \hat{\theta})) \cdot u'' \cdot w''}} \qquad [3.13d]$$

The left-hand side of equation [3.13] represents inertia and external loads, whereas the right-hand side describes structural internal loads, and it is therefore

associated with the stiffness of the beam. As in the case of strain displacements and internal loads displacements expressions, higher-order non-linear terms are underlined. Terms $(F_\eta \cdot u')'$ and $(F_\eta \cdot w')'$ in force *x* and force *z* equations, though non-linear, are considered as first-order ones. This is because they are expected to contribute significantly, especially in the case of rotating beams where axial loads increase due to the centrifugal effect. The two terms give rise to virtual stiffening of the beam as the rotational speed increases. Among the different second-order structural terms, those appearing in the equation [3.13] are the ones that by experience are expected to be of greater importance as the beam becomes more and more flexible and are also doubly underlined. The second doubly underlined term in equation [3.13b] and the first doubly underlined term in equation [3.13d] correspond to the coupling of the beam torsion with the beam tension. As indicated in equation [3.11a], the torsion of the beam generates axial strains $\varepsilon_{\eta\eta}$ and stresses $\sigma_{\eta\eta}$ and vice versa (see equation [3.12d]), and the axial stresses contribute to the twisting moment M_η. The last four terms in equation [3.13d] are related to bending–torsion coupling. As the bending displacements of the blade increase, the local bending moments, M_ξ and M_ζ, generate torsion moment about the undeformed blade axis *y*, as illustrated in Fig. 3.4. The magnitude of this twisting moment depends primarily on the bending curvatures u'' and w''. It also depends on the offset of the cross-section tension axis from the elastic axis.

The above-mentioned non-linear structural coupling terms are only important when the beam undergoes large deflections. For conventional wind turbine blades, in the megawatt (MW) scale, classical first-order, linear beam theory provides sufficiently good predictions. This is because current wind turbine designs are relatively stiff, so that non-linear beam modeling is not expected to drastically

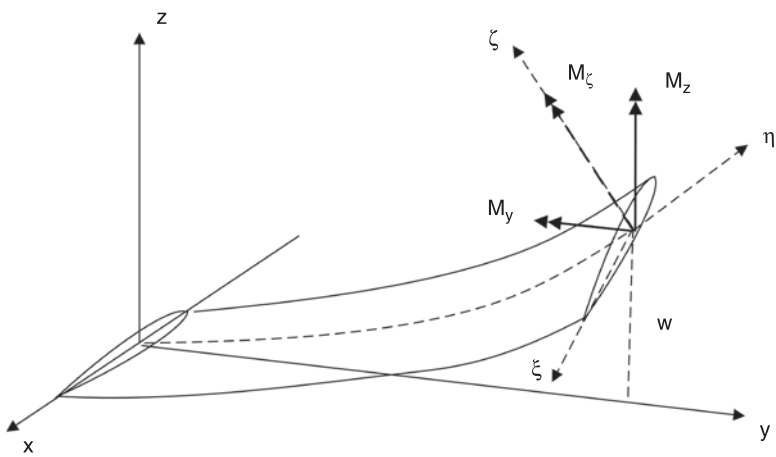

3.4 Explanation of the bending–torsion coupling effect in the case of large flapping deflection.

change the quality of the predictions. However, as the size of the wind turbines increases and the blades become more flexible, adoption of this kind of structural modeling becomes a necessity (Riziotis *et al*., 2008).

The derivation presented in Section 3.2 is based on the application of Newton's second law (Newtonian approach). In view of a more systematic and general framework for formulating dynamic equations, Hamilton's principle has also been used (Hodges, 1990). Nevertheless, the former is selected for the reason that it is much more illustrative and comprehensible for readers who are unfamiliar with the basic concepts of structural dynamics. The above-mentioned non-linear beam model is a specific example amongst several models of varying complexity that have been developed. For example, it is possible to include traverse shear effect by applying Timoshenko theory (Crisfield, 1998) or introduce anisotropy of the cross-sections by upgrading Hooke's law (equation [3.10]) to incorporate off-diagonal elements (Hodges and Yu, 2007). Even the present model can be easily upgraded to model possible distortion of the plane shape of the cross-sections due to torsional deformation (warping effect) (Hodges and Dowell, 1974).

Finite element discretization

The beam equations are fourth order in space with respect to bending and second order with respect to tension and torsion. So, for a finite element (FE) approximation of the equations, C^1 shape functions are used for u and w and C^0 for v and θ. At the element level, u and w are approximated with third-order polynomials and the discrete DOFs are the values and spatial derivatives at the end nodes, while v and θ are approximated with first-order polynomials and the DOFs are again considered at the end nodes of the FE. In the use of second-order beam theory, higher-order polynomials can be used for v and θ, and then additional intermediate nodes are required. So, within an FE 'e',

$$\mathbf{u}_e(y;t) = \mathbf{N}^e(y)\cdot\hat{\mathbf{u}}_e(t) \qquad [3.14]$$

where $\mathbf{u_e}(y;t) = \{u, v, w, \theta\}^T$ is the vector of the independent deflections along the element, $\mathbf{N^e}(y)$ is the shape functions matrix and $\hat{\mathbf{u}}_\mathbf{e}(t)$ is the vector of the DOFs at the nodes of the elements (Bathe, 1996; Crisfield, 1998). By using Galerkin formulation, the discrete form of the equation [3.13] is generated. The set of the four differential equations [3.13] is symbolically represented as $f(\mathbf{u}, \dot{\mathbf{u}}, \ddot{\mathbf{u}}) = 0$. For any admissible virtual displacement field $\delta\mathbf{u} = \{\delta u, \delta v, \delta w, \delta\theta\}^T$, we require that:

$$\int_0^L \delta\mathbf{u}^T\cdot f(\mathbf{u},\dot{\mathbf{u}},\ddot{\mathbf{u}})\cdot dy = \sum_e \int_0^{L_e} \delta\mathbf{u}_e^T\cdot f(\mathbf{u}_e,\dot{\mathbf{u}}_e,\ddot{\mathbf{u}}_e)\cdot dy = 0 \qquad [3.15]$$

Given that $\delta\mathbf{u_e}(y;t) = \delta\hat{\mathbf{u}}_e^T(t)\cdot\mathbf{N^e}(y)$, it follows that:

$$\sum_e \int_0^{L_e} N^{e\,T}\cdot f(\mathbf{N}^e\hat{\mathbf{u}}_e, \mathbf{N}^e\dot{\hat{\mathbf{u}}}_e, \mathbf{N}^e\ddot{\hat{\mathbf{u}}}_e)\cdot dy = 0 \qquad [3.16]$$

which is a set of second-order ordinary differential equations in time with respect to the discrete DOFs $\hat{\mathbf{u}}_e(t)$. Although $f(\mathbf{u}, \dot{\mathbf{u}}, \ddot{\mathbf{u}}) = 0$ contains non-linear terms, it can always be put in the common form:

$$\mathrm{M}(\tilde{\hat{\mathbf{u}}}) \cdot \ddot{\hat{\mathbf{u}}} + \mathrm{C}(\tilde{\hat{\mathbf{u}}}) \cdot \dot{\hat{\mathbf{u}}} + \mathrm{K}(\tilde{\hat{\mathbf{u}}}) \cdot \hat{\mathbf{u}} = \mathrm{Q}(\tilde{\hat{\mathbf{u}}}) \qquad [3.17]$$

where the mass, damping and stiffness matrices as well as the generalized loads in the right-hand side, in general, will depend on the displacement field and its time derivatives (noted by the tilde).

3.2.2 Dynamics of the wind turbine

In the previous section, the equations of the beam structure were derived for the case where the coordinate system Oxyz, attached to the beam, is not moving. In this connection, the beam only deflects with respect to the fixed Oxyz system. Of course, in the case of the wind turbine, the various components (i.e., blades, shaft, tower) not only are deflecting but also undergo rigid body motion of their own (e.g. blades azimuthally rotate and pitch). Also, as a result of being connected to other bodies, they follow the motion (rigid body and elastic) of the bodies attached to them.

The involvement of different body motions for each component, in combination with the fact that certain component-to-component connection points exist, whereby loads and displacements are communicated from one body to another, calls for a global treatment of the dynamic problem. To this end, most works adopt the so-called 'multi-body' approach (Riziotis and Voutsinas, 1997; Larsen, Hansen *et al*., 2004a), which consists of considering each component separately from the others but is subjected to specific free-body boundary kinematic and/or loading conditions that fit the different components into the complete configuration. In the multi-body context, each component *k* is assigned a local coordinate system Oxyz, as defined in Section 3.2.1. The elastic motion of the component with respect to each own system is the one determined through equation [3.1]. All other motions are communicated through appropriate kinematic conditions. Having this in mind, the position vector $\mathbf{r}_{Gk}$ of a point on the *k* component with respect to an inertial reference frame $O_G x_G y_G z_G$ is given by (see Fig. 3.5):

$$\mathbf{r}_{GK} = \rho_k + \mathbf{A}_k \cdot \mathbf{r}_k \qquad [3.18]$$

where ρ_k is the position vector of the origin of Oxyz with respect to the fixed system and $\mathbf{A}_k$ is the local-to-global rotation matrix. The exact form of ρ_k and $\mathbf{A}_k$ not only depends on the kinematic conditions introduced when connecting the body to the complete configuration (e.g. blades to hub or shaft to tower top) but also on the type of its own motion (e.g. pitch of the blades, rotation of the shaft). For each body, a number of kinematic DOFs (consisting of translations and rotations) are introduced that determine ρ_k and $\mathbf{A}_k$. This set of kinematic DOFs is denoted as $\mathbf{q}_k$ and so, $\rho_k = \rho_k(\mathbf{q}_k; t)$ and $\mathbf{A}_k = \mathbf{A}_k(\mathbf{q}_k, t)$. In particular, the vector $\mathbf{q}_k$

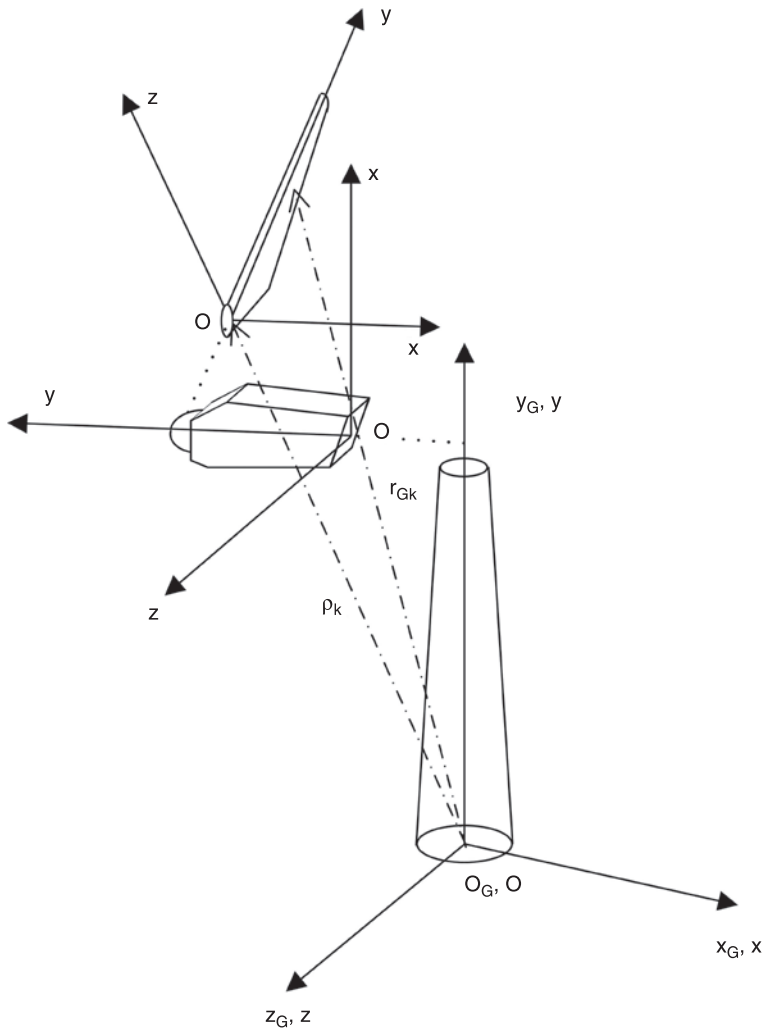

3.5 Wind turbine inertial system and local components systems.

can not only include both large rigid body rotations and translations (controlled or free) but also structural deflections (displacements and rotations) of the bodies attached to the body *k*. For example, the blades follow the structural motion of the tower, and so for the blades, vector **q** will include the tower-top deflections, as illustrated in Fig. 3.6(a). Also, for the blades, **q** will include yaw of the nacelle, rotation of the shaft and pitch rotation, which are all not only DOFs of controlled motion, but also foundation movements (for floating wind turbines) and teeter rotation (for two-blade machines), which are both DOFs of free motion (see Fig. 3.6(b)). From the above discussion, it is obvious that ρ_k is defined as a series

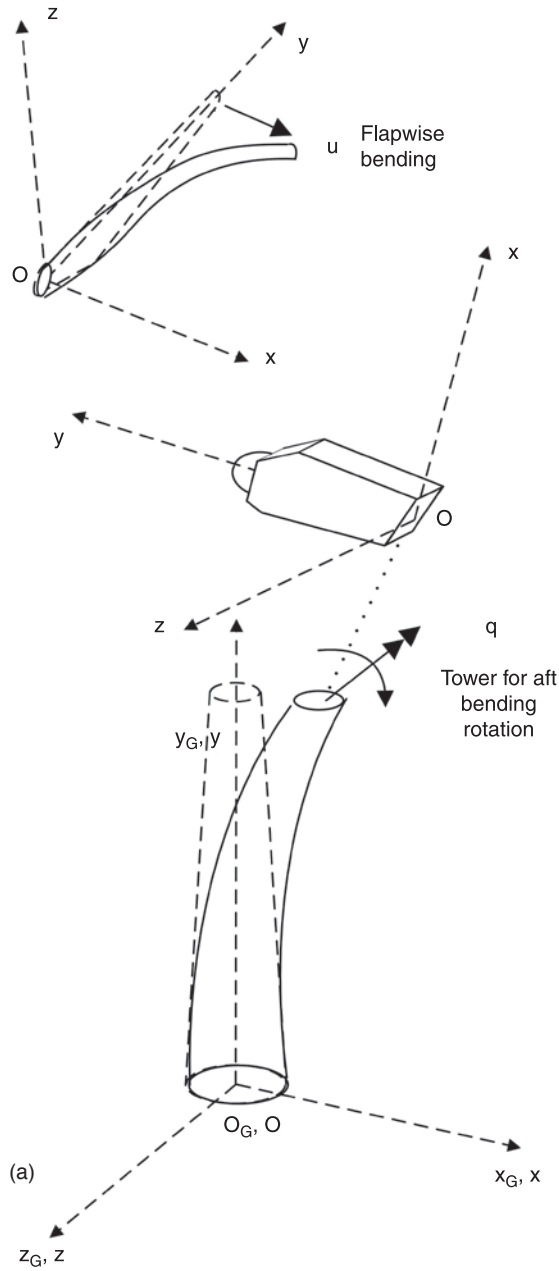

3.6 Realization of multi-body kinematics. (a) DOFs corresponding to elastic deflections.

(*Continued*)

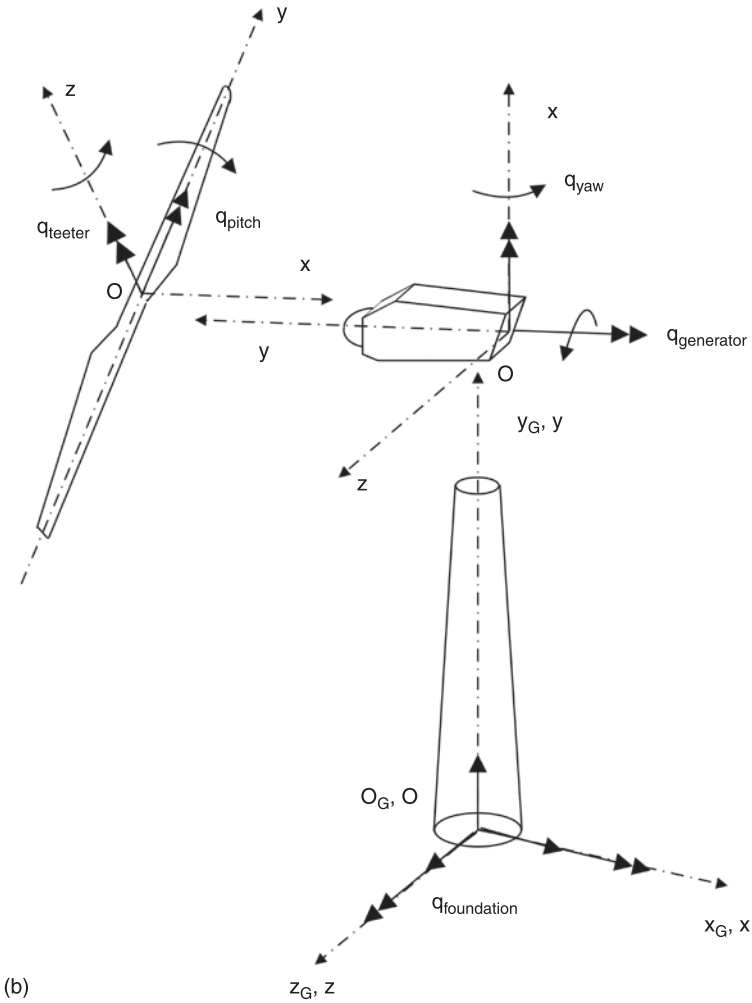

3.6 (b) DOFs corresponding to rigid body free or controlled motion.

of elementary translations and rotations, whereas $\mathbf{A}_k$ is solely defined as a series of elementary rotations. It is also noted that in order to establish a connection between the bodies, besides kinematic conditions, loading conditions should be satisfied. So, it is clear that the bodies contributing the kinematics will in response receive internal (reaction) loads. So, in the previous example, the tower will be subjected to the loads of the nacelle.

The global acceleration of the *k*-th body, expressed with respect to its local system, is then given by:

$$\mathbf{A}_k^T \cdot \ddot{\mathbf{r}}_{GK} = \underbrace{\mathbf{A}_k^T \cdot \ddot{\rho}_k}_{\text{acceleration of the origin}} + \underbrace{\mathbf{A}_k^T \cdot \ddot{\mathbf{A}}_k \cdot \mathbf{r}_k}_{\text{centrifugal acceleration}} + \underbrace{2 \cdot \mathbf{A}_k^T \cdot \dot{\mathbf{A}}_k \cdot \dot{\mathbf{r}}_k}_{\text{Coriolis acceleration}} + \ddot{\mathbf{r}}_k \quad [3.19]$$

By introducing equation [3.19] into equation [3.3] and [3.4], the centrifugal and Coriolis terms of the inertia loads will appear as a result of the time derivatives of $\mathbf{A}_k$. By combining the equations of all components, the complete system of dynamic equations is obtained in the form of equation [3.17] with respect to an extended vector of DOFs that also includes **q** DOFs.

Modal analysis of the structural wind turbine system

The structural characterization of the wind turbine system is provided through identification of the main system natural frequencies. By performing eigenvalue analysis to the dynamic system [3.17], for the full wind turbine configuration, the natural frequencies ω_i and the vibration shapes (mode shapes) Φ_i are obtained. This is done by solving the following eigenvalue problem:

$$\left(\mathrm{K} - \omega_i^2 \mathrm{M}\right) \cdot \Phi_i = 0 \qquad [3.20]$$

It is clear that the natural frequencies of the individual components (considered separately) differ from those obtained when the components are joined together into the full configuration. This is a result of the dynamic coupling taking place between inter connected components. It is noted that identification of the system's natural frequencies is usually performed at standstill because these are the conditions for which measured data usually exist. Nevertheless, given that the rotational speed is rather low, it is not expected to change substantially the distribution of the eigenvalues.

In the sequel description of the first, standstill system modes (eight lowest) are provided for the typical three-bladed wind turbine. Plots of the modes are given in Figs 3.7–3.14. The shapes of the modes are expected to be similar for almost every wind turbine of the same type and design philosophy. Also, in Fig. 3.15, the frequencies of those modes are given as multiples of the rotational frequency *P*, for four wind turbines of increasing size. It is noted that the bigger the size of the wind turbine, the more current is the design, implying that Fig. 3.15 also provides information concerning design trends and evolution of modern turbines. As already mentioned, the modes obtained from the eigenvalue analysis of system [3.17] are coupled and therefore concern the full wind turbine and not any individual component. However, in order to distinguish them, they are named after the component and the deflection direction, which each time is more excited.

Modes M1 and M2 are the first two modes of the tower in the two bending directions lateral and fore–aft, respectively (Fig. 3.7 and Fig. 3.8). Those two modes are close in frequency due to the symmetry of the tower in the two bending directions. The small difference originates from the asymmetric placement of the rotor at the top of the tower. The frequency of those modes is usually found between 1*P* and 2*P*. Mode M3 is the first symmetric edgewise mode of the rotor (Fig. 3.9). This mode is highly coupled to the torsion of the shaft that results in a significant reduction of the mode frequency with respect to the frequency of the

3.7 M1 first tower lateral bending mode (rear, side, top view).

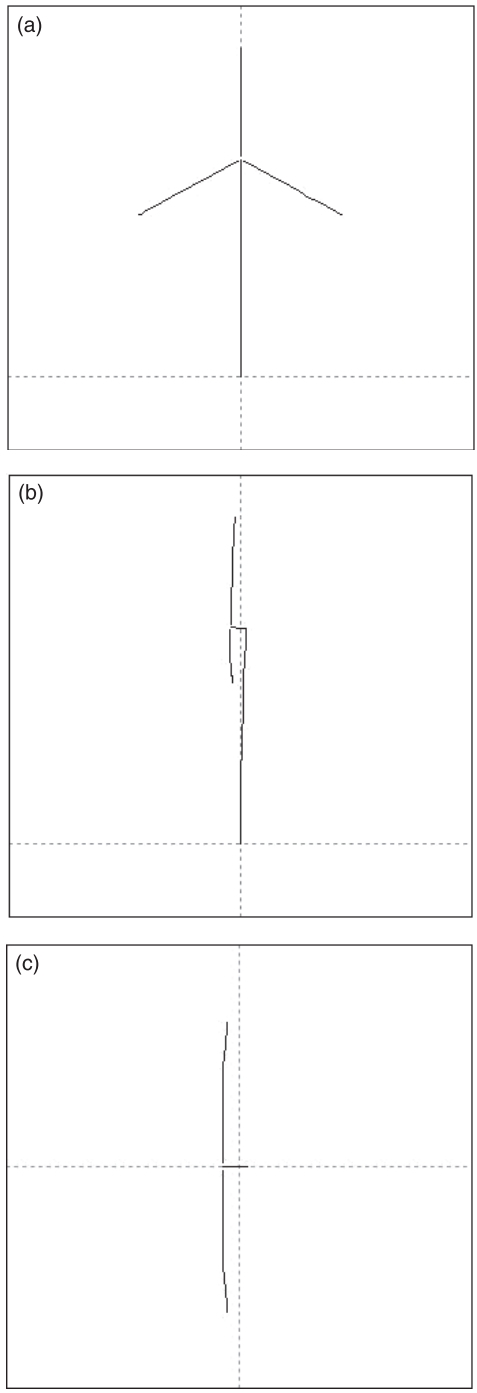

3.8 M2 first tower front-back bending mode (rear, side, top view).

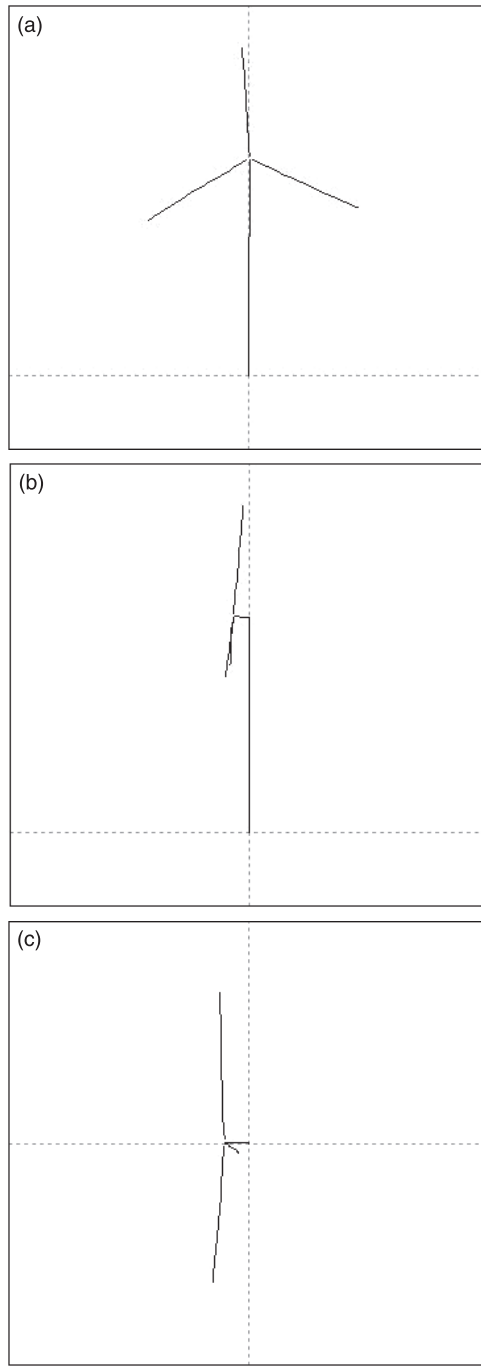

3.9 M3 first symmetric (collective) edgewise mode/shaft torsion (rear, side, top view).

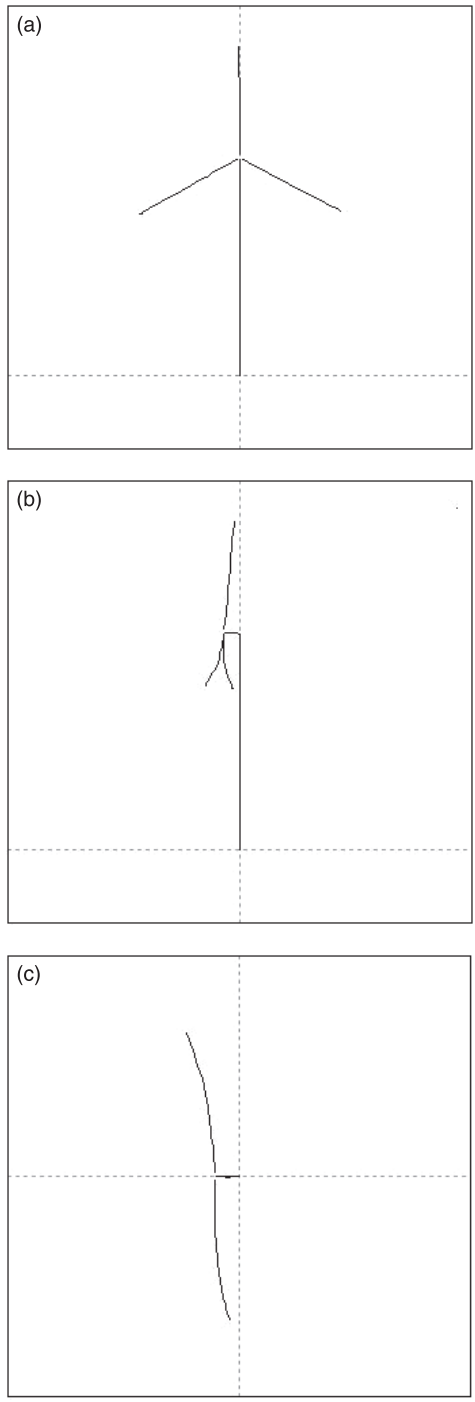

3.10 M4 first asymmetric flapwise mode (yaw) (rear, side, top view).

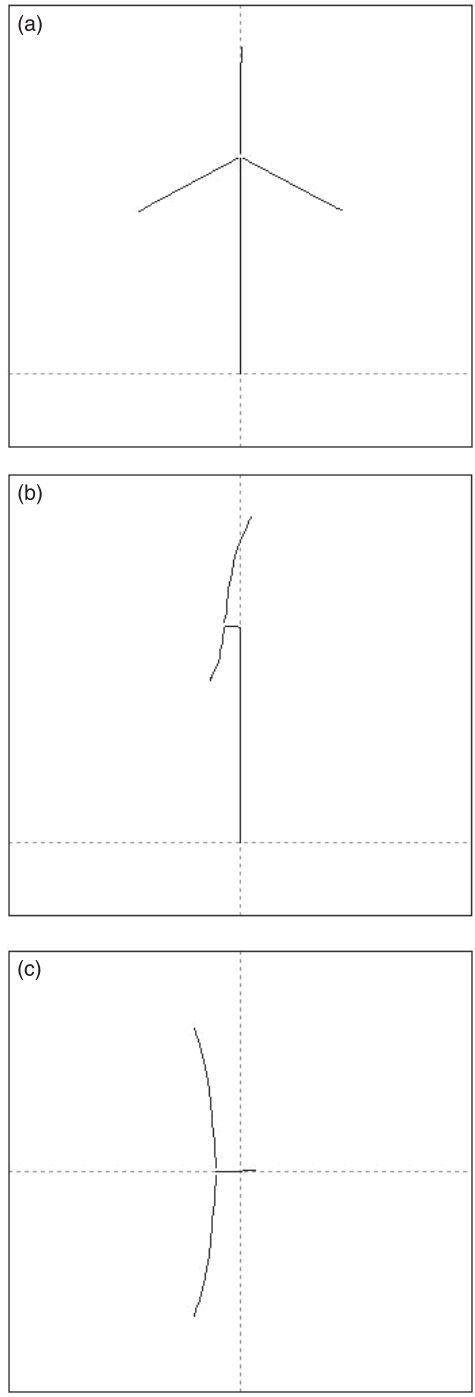

3.11 M5 first asymmetric flapwise mode (tilt) (rear, side, top view).

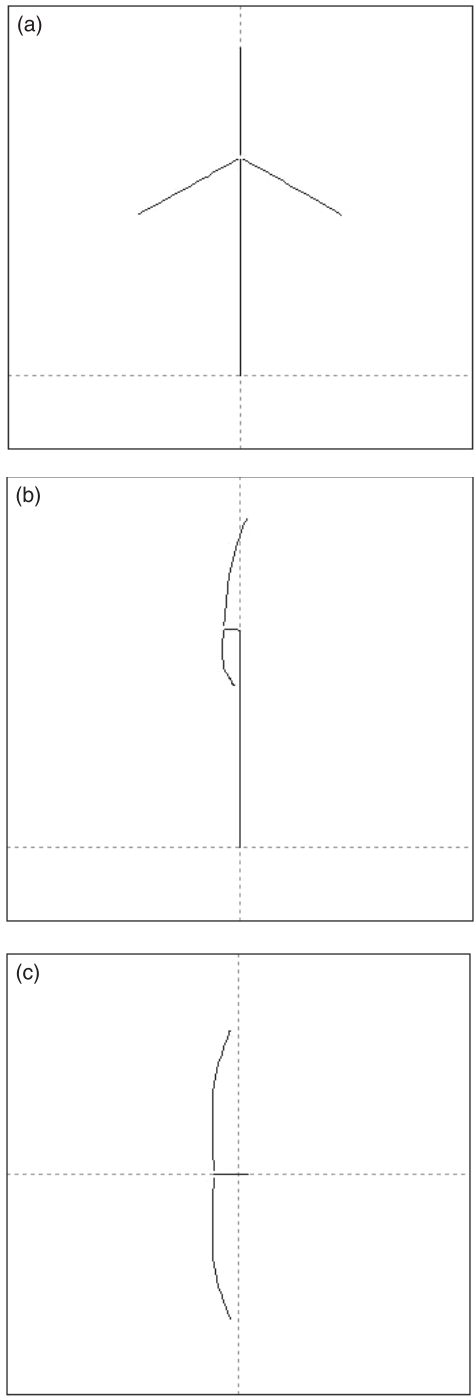

3.12 M6 first symmetric (collective) flapwise mode (rear, side, top view).

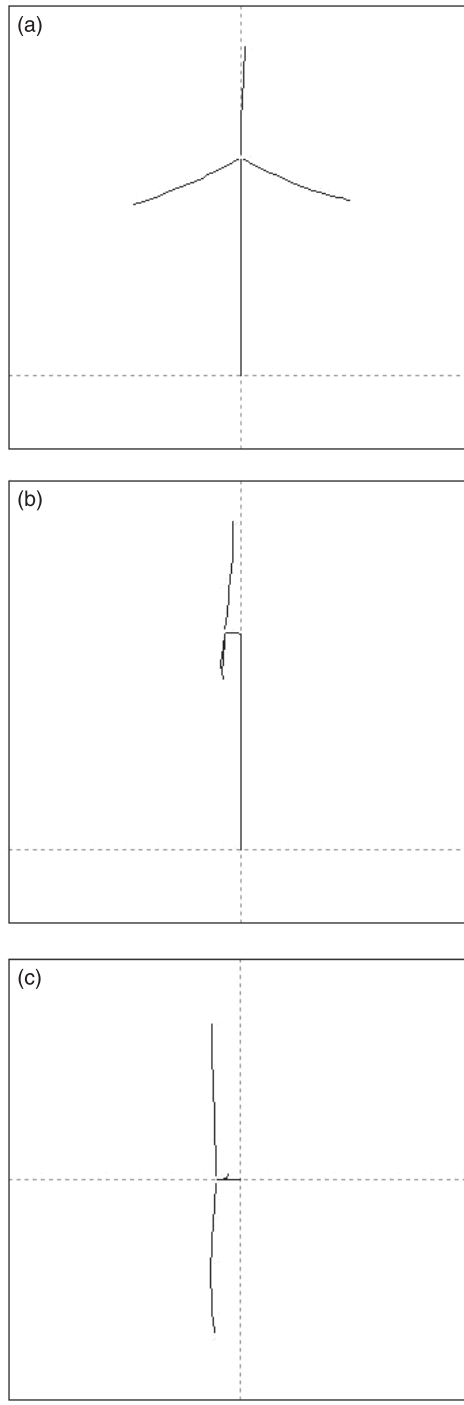

3.13 M7 first asymmetric edgewise mode (vertical) (rear, side, top view).

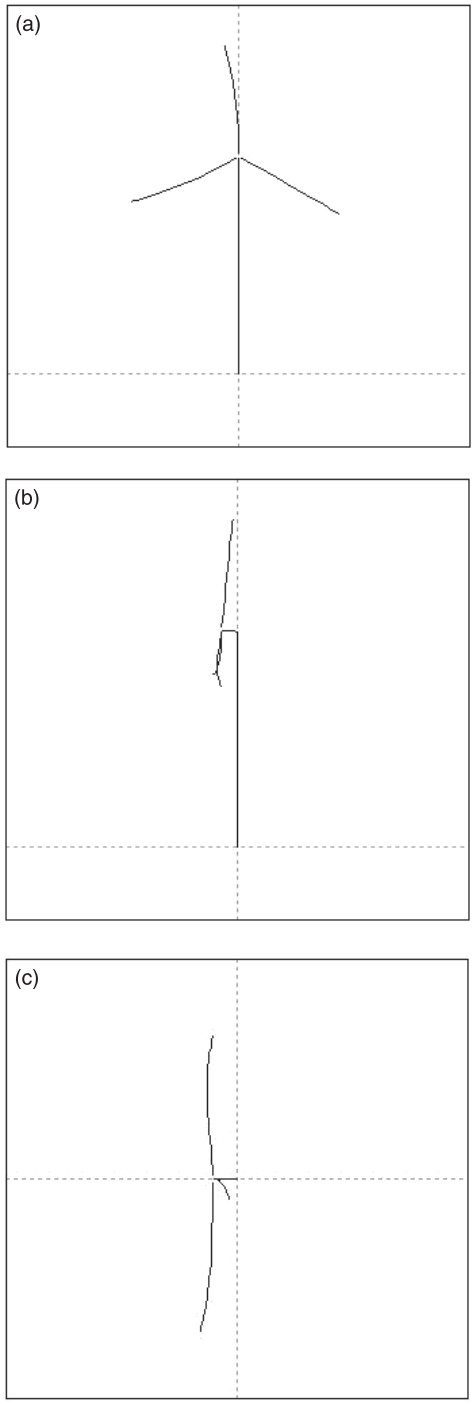

3.14 M8 first asymmetric edgewise mode (horizontal) (rear, side, top view).

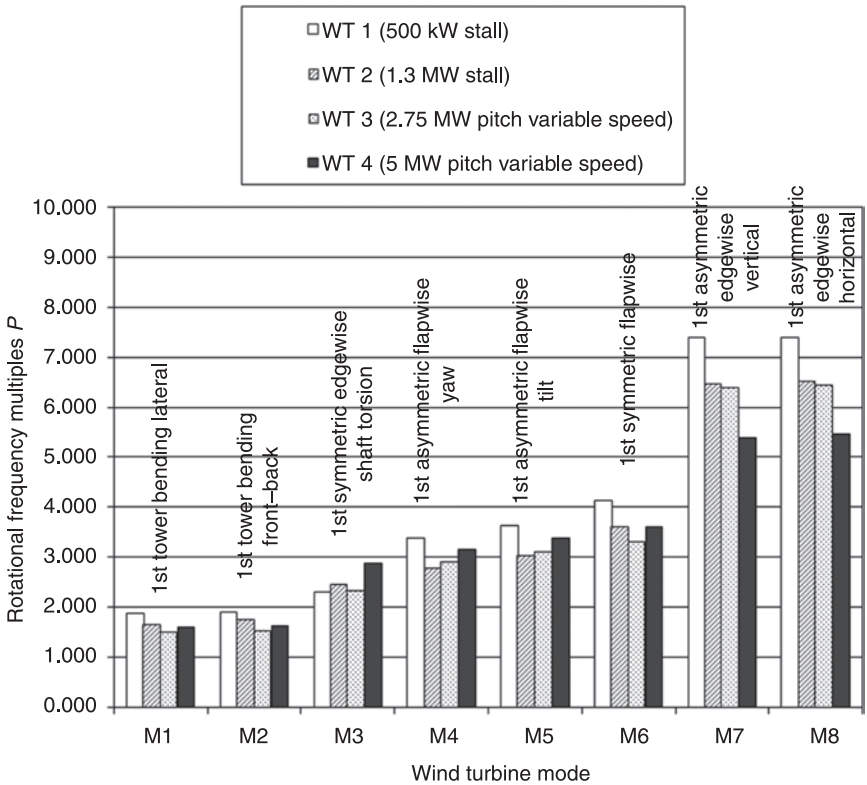

3.15 Comparison of various wind turbines in terms of standstill natural frequencies.

isolated blade edgewise mode. The frequency of this mode is usually placed between 2*P* and 3*P*, although in some wind turbines, it can be lower than the frequency of M1 and M2. Modes M4 and M5, and M6 are the two asymmetric and the symmetric flapwise rotor modes, respectively. In the two asymmetric modes, the blades deflect in opposite directions, whereas in the symmetric mode, the rotor moves collectively (Figs 3.10–3.12). In the two asymmetric modes, a coupling takes place with the yawing and the tilting flexibility of the tower, respectively (see Figs 3.10 and 3.11). This coupling gives rise to a reduction of their frequency as compared to that of the isolated blade. By contrast, the frequency of the symmetric mode is close to the frequency of the isolated blade. Usually, modes M4–M6 are placed in the frequency range of 3*P*–4*P*. Finally, modes M7 and M8 are the two edgewise rotor asymmetric modes that are coupled with the vertical and horizontal flexibility of the tower (see Figs 3.13 and 3.14). The frequencies of those two modes are usually slightly different depending on the tower flexibilities, and they slightly deviate from the edgewise frequency of the isolated blade. M7 and M8 are usually found between 5*P* and 7*P*. As noted from Fig. 3.15,

the two edgewise modes are those that are affected the most by the increase in size. It is clear that the design evolution brings flapwise and edgewise modes closer to each other.

3.3 Aeroelastics of wind turbines under operational conditions

The level of deformation of a wind turbine structure depends on the design characteristics (flexibility of the components) and the loading action. Besides gravitational loads, explicitly addressed in Section 3.2.1, wind turbines are mainly subjected to aerodynamic loads as a result of their operation. In offshore applications, wave loads (hydrodynamic loading) are also added. As the airflow passes over the wind turbine, aerodynamic loads develop as a result of the flow–solid interaction that rotates the blades and deforms the whole structure. The flow seen by the rotor is unsteady, not only because of the turbulent nature of the wind but also due to other reasons that cause incoming-to-the-rotor flow to deviate from axisymmetric conditions (shear, yaw misalignment, etc.). Moreover, under certain operating conditions, flow is highly non-linear. Especially, not only for stall-regulated (SR) wind turbines but also for pitch machines under rated operating conditions, the onset of stall is always a difficulty we have to deal with. Besides introducing significant vibrations due to hysteresis phenomena, it can also degrade stability as a result of negative aerodynamic damping. As regards hydrodynamic loading, it consists of mainly four sub-components: a radiation component related to the loads on the wind turbine support structure originating from the waves that the body radiates away from itself (it includes contribution of added mass and wave radiation damping), a scattering component related to loading due to incident waves, a hydrostatic component related to the support structure buoyancy and finally a viscous drag component (Jonkman and Buhl, 2007). The main characteristic of the above-described external aerodynamic and hydrodynamic loads is that they both depend on the level and rate of deformations (deflection velocities) of the wind turbine. It is therefore clear that a non-linear coupling (called aero/hydro elastic) establishes between external acting loads and structural response when aerodynamic and hydrodynamic loads are considered in dynamic equation [3.13].

3.3.1 Aeroelastic coupling and non-linear time domain analysis

In the application of a beam approach for the structural modeling of the blades, external aerodynamic loads $\delta\mathbf{P}$ in equation [3.3] and equation [3.4] represent aerodynamic loads per unit length of the blade. So they are sectional loads that can be given in terms of sectional dimensionless aerodynamic properties, namely the lift C_L, drag C_D and moment C_M coefficients. If the blade section of Fig. 3.16

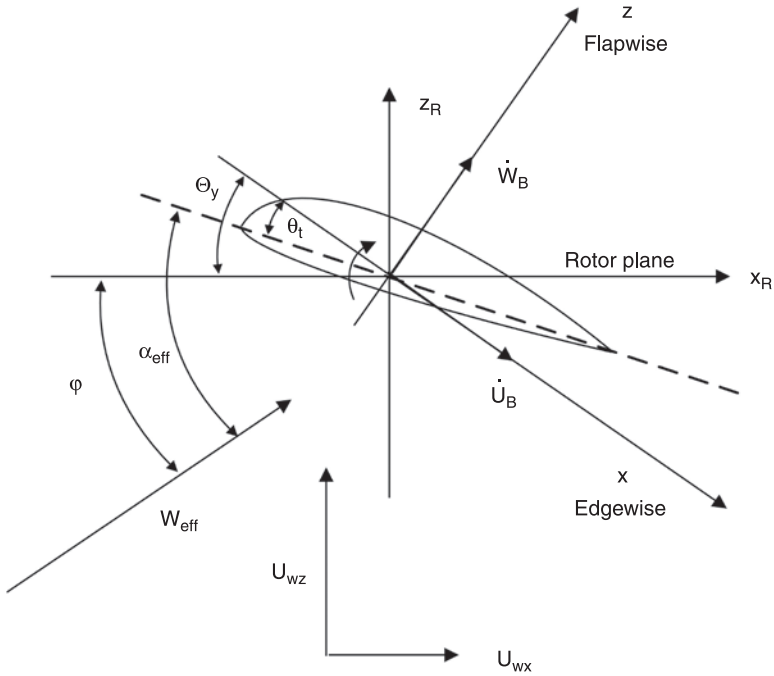

3.16 Basic notation on the blade section.

is considered, the local aerodynamic loads on this section are given by the following expressions:

$$\delta P_x = -\delta L \sin(\varphi + \Theta_y) + \delta D \cos(\varphi + \Theta_y) = \left(-C_L \sin(\varphi + \Theta_y) + C_D \cos(\varphi + \Theta_y)\right) \cdot \frac{\rho}{2} W_{eff}^2 \, c \, \delta y$$

$$\delta P_z = \delta L \cos(\varphi + \Theta_y) + \delta D \sin(\varphi + \Theta_y) = \left(C_L \cos(\varphi + \Theta_y) + C_D \sin(\varphi + \Theta_y)\right) \cdot \frac{\rho}{2} W_{eff}^2 \, c \, \delta y$$

$$\delta M_y = \delta M_p = C_M \cdot \frac{\rho}{2} W_{eff}^2 \, c \, \delta y$$

[3.21]

where δL, δD are the local lift and drag forces, δM is the pitching moment, φ is the local flow angle with respect to the rotor plane, Θ_y is the local pitch of the blade including torsion deformation, W_{eff} is the local velocity and c is the local blade chord. Given that wake-induced velocities are known, local flow characteristics (angle and velocity) are derived using the following expressions:

$$\tan\varphi = \frac{U_{wz} - \dot{W}_B \cos\Theta_y + \dot{U}_B \sin\Theta_y}{U_{wx} - \dot{W}_B \sin\Theta_y - \dot{U}_B \cos\Theta_y} = \frac{U_{effz}}{U_{effx}},$$

$$W_{eff} = \sqrt{U_{effx}^2 + U_{effz}^2},$$

$$\alpha_{eff} = \varphi - \theta_t + \Theta_y \qquad [3.22]$$

where α_{eff} is the local angle of attack, θ_t is the local twist of the blade, U_{wx} and U_{wz} are the components of the wind velocity including wake-induced effects, and $\dot{U}_B$ and $\dot{W}_B$ are the local blade velocities in the flapwise and edgewise directions, respectively (including rigid body motion and elastic deformation). According to equation [3.1], $\dot{U}_B$ and $\dot{W}_B$ are given by the following expression:

$$\begin{Bmatrix} \dot{U}_B \\ \dot{V}_B \\ \dot{W}_B \end{Bmatrix} = \mathbf{A}^T \cdot \dot{\mathbf{r}}_G = \mathbf{A}^T \cdot \left(\dot{\rho} + \dot{\mathbf{A}} \cdot \mathbf{r} + \mathbf{A} \cdot \dot{\mathbf{r}} \right) \qquad [3.23]$$

Remembering that the aerodynamic loads are unsteady, and therefore, in the context of a blade element approach, unsteady, C_L, C_D and C_M can be calculated by application of any unsteady dynamic stall aerodynamic model (Leishman and Crouse, 1989; Petot, 1989). It is clear that the aerodynamic loads in equation [3.21] are implicitly related to the dynamics of the system and the structural responses. So, besides the structural dynamic equations being non-linear, additional non-linearity is introduced to system [3.13] through the aerodynamic loads equation [3.21].

Solution of the non-linear system of the aeroelastic equations requires an iterative procedure, where at every time step of the computation, we are matching aerodynamic loads to structural deformations. The system of the coupled aeroelastic equations can be put in the form:

$$\mathbf{M}(\underset{\sim}{\mathbf{u}}) \cdot \ddot{\mathbf{u}} + \mathbf{C}(\underset{\sim}{\mathbf{u}}) \cdot \dot{\mathbf{u}} + \mathbf{K}(\underset{\sim}{\mathbf{u}}) \cdot \mathbf{u} = \mathbf{Q}(\underset{\sim}{\mathbf{u}})$$

where $\underset{\sim}{\mathbf{u}} = \{\mathbf{u}, \dot{\mathbf{u}}, \ddot{\mathbf{u}}\}$. This, for example, can be done by applying Taylor expansion to all DOFs and eliminating second-order terms. In such a case, the system is written in a perturbed form:

$$\mathbf{M}(\underset{\sim}{\mathbf{u}}^{n-1}) \cdot \delta\ddot{\mathbf{u}} + \mathbf{C}(\underset{\sim}{\mathbf{u}}^{n-1}) \cdot \delta\dot{\mathbf{u}} + \mathbf{K}(\underset{\sim}{\mathbf{u}}^{n-1}) \cdot \delta\mathbf{u} = \mathbf{Q}(\underset{\sim}{\mathbf{u}}^{n-1})$$

where $\underset{\sim}{\mathbf{u}}^{n-1} = \{\mathbf{u}^{n-1}, \dot{\mathbf{u}}^{n-1}, \ddot{\mathbf{u}}^{n-1}\}$ stands for the solution at n – 1 iteration while $\delta\underset{\sim}{\mathbf{u}} = \{\delta\mathbf{u}, \delta\dot{\mathbf{u}}, \delta\ddot{\mathbf{u}}\}$ is such that $\underset{\sim}{\mathbf{u}}^n = \underset{\sim}{\mathbf{u}}^{n-1} + \delta\underset{\sim}{\mathbf{u}}$. Obviously, the solution of the non-linear system is obtained when perturbations reach zero. Other methods for solving the non-linear problem can be found in Crisfield (1998). Time marching can be performed by using any first or higher order integration scheme. Well suited for the systems, like the one described herein, is the second-order implicit Newmark method.

3.3.2 Eigenvalue stability analysis

Where aerodynamics is modeled using blade element momentum theory, loads are provided in a closed form (see equation [3.21]), and so linearization of the system of aeroelastic equations can be performed. Linearization is carried out with

reference to a steady or periodic equilibrium (reference) state. For its definition, the non-linear set of equations is integrated in time until a periodic response (with respect to the rotor speed) is reached. In the case of unstable conditions, where periodicity is never reached, the time domain calculations provide a response that contains significant components in all basic system frequencies. In such a case, by means of Fourier transformation, only the parts corresponding to the rotational frequency (1*P*) and its basic multiple N*P* (where N is the number of blades) are retained. This provides an approximation of the periodic conditions.

The linearized system of equations is formulated into a first-order system:

$$\dot{\mathbf{x}} = \mathbf{A}(\mathbf{x}_0, \dot{\mathbf{x}}_0) \cdot \mathbf{x} + \mathbf{B} \qquad [3.24]$$

where $\mathbf{x}_0$ denotes the reference state and $\mathbf{x}$ are the perturbations of the state variables about this reference state. The eigenvalues of matrix $\mathbf{A}$ provide the natural frequencies and damping characteristics of the linearized system of equations, given that $\mathbf{A}$ is a constant coefficient matrix (Johnson, 1980).

The equations of motion of the rotating blades, being expressed in the rotating frame, involve periodic coefficients. It is possible to eliminate these periodic coefficients and treat the full wind turbine configuration in a linear eigenvalue context with reference to the non-rotating frame, by introducing a multi-blade transformation of all the rotating DOFs. This transformation of coordinates capitalizes on the polar symmetry of rotors with identical blades, and in the case of a three-bladed rotor is given by (Coleman and Feingold, 1957; Johnson, 1980):

$$x_m = x_0 + x_c \cdot \cos\psi_m + x_s \cdot \sin\psi_m \qquad [3.25]$$

where x_m is any rotating DOF of the *m*-th blade being at an azimuth position $\Psi_m = \Omega \cdot t + (2\pi/N) \cdot (m - 1)$, $m = 1, 2, 3$, $N = 3$ and x_0, x_c and x_s are the transformed coordinates (designated as symmetric/collective, cyclic cosine and cyclic sine, respectively) expressed in the non-rotating frame. Of course, besides transforming the rotating DOFs into the non-rotating frame, the same should be done to the equations of the blades, which express the blade dynamics in the rotating frame. To this end, the following operators are applied to the blade aeroelastic equations:

$$\begin{aligned}
(\text{non-rotating equation})_1 &= \frac{1}{N}\sum_{m=1}^{N}(\text{rotating equation})_m \\
(\text{non-rotating equation})_2 &= \frac{2}{N}\sum_{m=1}^{N}(\text{rotating equation})_m \cdot \cos\psi_m \\
(\text{non-rotating equation})_3 &= \frac{1}{N}\sum_{m=1}^{N}(\text{rotating equation})_m \cdot \sin\psi_m
\end{aligned} \qquad [3.26]$$

The eigenvalue analysis of the transformed matrix $\mathbf{A}$ will provide the natural frequencies of the rotor system with reference to the non-rotating frame. The 'non-rotating' frequencies are now associated with the corresponding non-rotating DOFs (i.e. symmetric and cyclic). For an isolated three-bladed rotor, it can be

shown (Hansen, 2007) that the collective frequencies will be identical with the natural frequencies of the m-th blade, while the two sets of cyclic frequencies, designated as backward whirling (or regressive) and forward whirling (or progressive), will differ by $-\Omega$ and $+\Omega$, respectively. As regards the shape of the modes in the symmetric mode, all blades deflect collectively, while in the cyclic modes, they undergo whirling motion with a phase difference of $\pm 2\pi/3$.

3.4 Application toward improved aeroelastic design and construction

3.4.1 General introduction

By the general term 'improved aeroelastic design', it is meant that the response of the turbine is changed in such a way that the load level on the turbine components is reduced and that any unstable response is avoided that could lead to a major failure of the whole turbine or parts of it.

As a basis for the discussion of ways and procedures for an improved aeroelastic response of wind turbines, it is valuable to learn from experimental observations. A discussion of such observations is included first in the present section.

The aeroelastic response depends on the load input to the system, and it is therefore important to know the characteristics of the different types of external loads on the wind turbine, such as loads from turbulent inflow, loads from operation in wakes and loads from waves if it is an offshore installation. Load input is an extensive topic, and it will therefore only be presented in a little detail.

Then follows the section in which design procedures or methods to obtain an improved aeroelastic response are discussed. This comprises ways for reduction of the load input to the system as well as design of the turbine dynamics so that the response is reduced.

3.4.2 Natural aeroelastic frequencies and damping of wind turbines in normal operation – common aeroelastic instabilities

Identification of the natural aeroelastic frequencies of the various modes of vibration of a wind turbine and the aeroelastic damping characteristics associated with those modes of vibration is a very important step in the design process. Negative aerodynamic damping of a mode may lead to amplifying vibrations and failure, depending on the external excitation and the structural damping of the system. By the term 'aeroelastic', it is meant that frequencies and damping refer to the coupled system that includes the effect of the aerodynamics. In the current section, typical examples of wind turbine aeroelastic frequencies and damping characteristics are presented. Also, the various instabilities that have been

observed in modern wind turbines or could be experienced by future designs are discussed, thus providing guidelines for an improved aeroelastic design.

The two example wind turbines, for which aeroelastic modal frequencies and damping characteristics are presented, are typical of the two representative concepts, SR and pitch-regulated variable speed (PRVS). The SR machine has a rated power of 500 kW, while the PRVS is a 2.75-MW machine. The natural frequencies and damping characteristics of the two wind turbines have been obtained through eigenvalue stability analysis, as formulated in the previous Section 3.3 (Riziotis *et al*., 2004).

Figure 3.17 presents the variation of the eight lowest aeroelastic frequencies with the wind speed for the SR wind turbine. For this SR machine, rotational

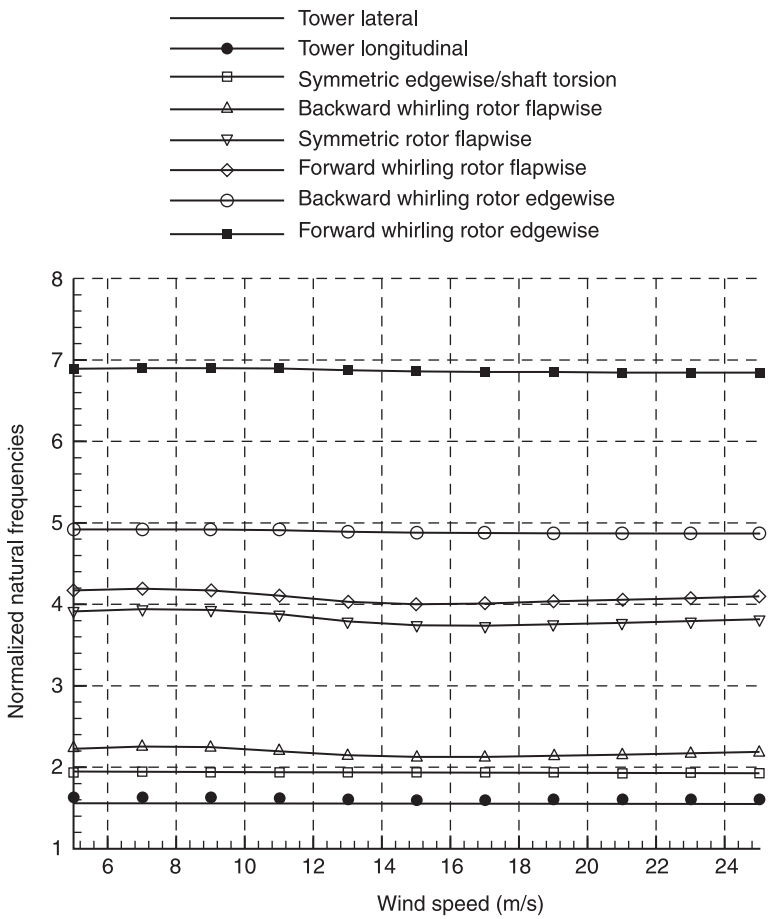

3.17 Aeroelastic frequencies of a 500 kW stall-regulated wind turbine in multiples of the nominal rotational frequency.

speed and blade pitch remain fixed for all wind speeds. However, it is noted that the frequencies exhibit a small variation with the wind speed. This is because, as already mentioned, the effect of the aerodynamics has been taken into account in obtaining those frequencies. Since aerodynamic loads depend on the wind speed, the same happens with the natural 'aeroelastic' frequencies. Typically, the eight lowest modes of the full wind turbine system are the two tower bending modes, the three rotor flapwise modes–collective and two cyclic (forward and backward whirling) – and the three rotor edgewise modes–collective and two cyclic. In Fig. 3.18(a), the damping of the two tower modes is shown. Of the two, the tower lateral bending mode is usually poorly damped. The tower fore-aft bending mode exhibits higher damping values driven by the high aerodynamic damping of the rotor thrust force. In the same figure, the effect of generator dynamics is presented. It is clear that the dynamics of the generator improve the stability characteristics of the tower lateral bending mode. In Fig. 3.18(b), the damping of the rotor edgewise modes is shown and is compared to the damping of the isolated blade. It is noted that all modes are negatively damped (structural damping has not been included in the computations); however, the damping of the collective mode is considerably augmented by the inclusion of the generator dynamics (as shown in

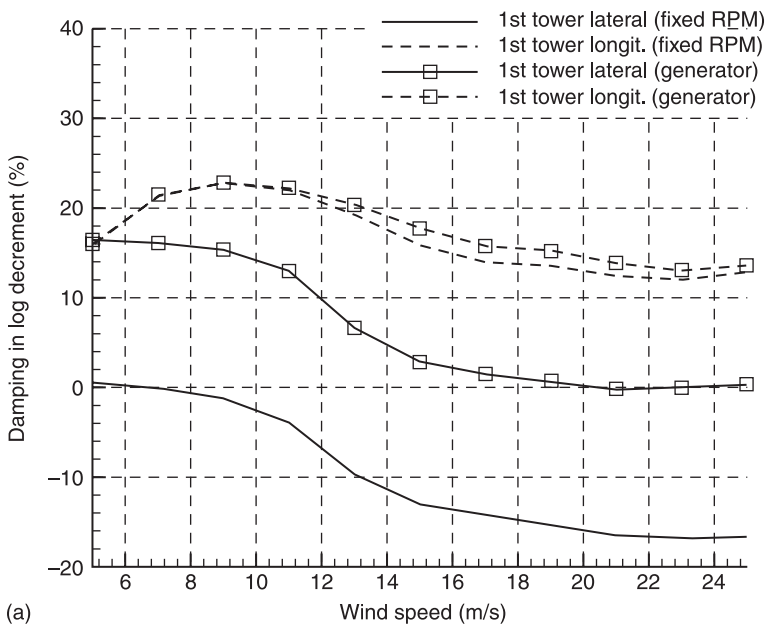

3.18 (a)–(d) Aeroelastic damping of a 500 kW stall-regulated wind turbine mode. (a) Tower modes (with and without generator dynamics). (*Continued*)

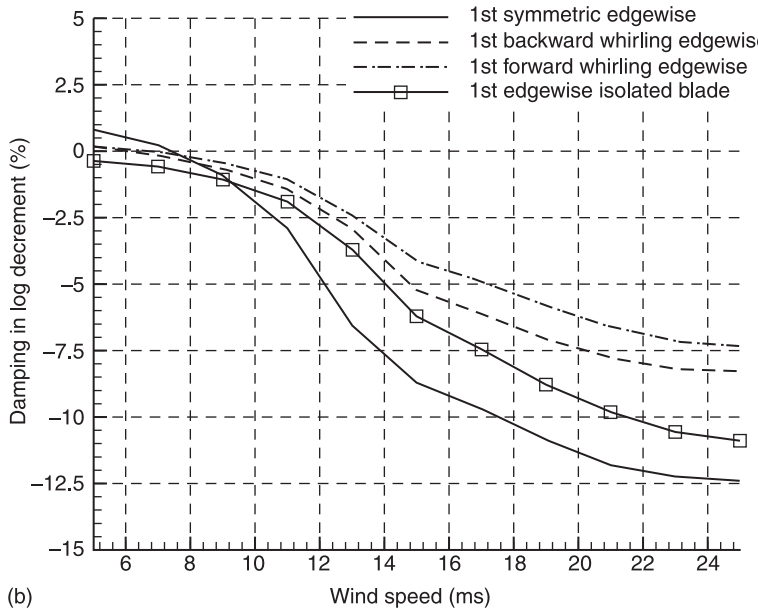

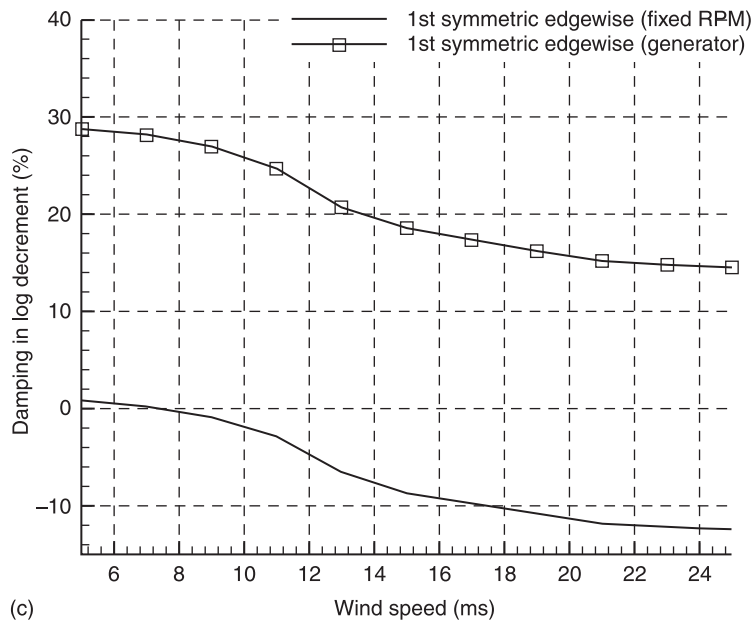

3.18 (b) Rotor edgewise; (c) symmetric rotor edgewise (with and without generator dynamics).

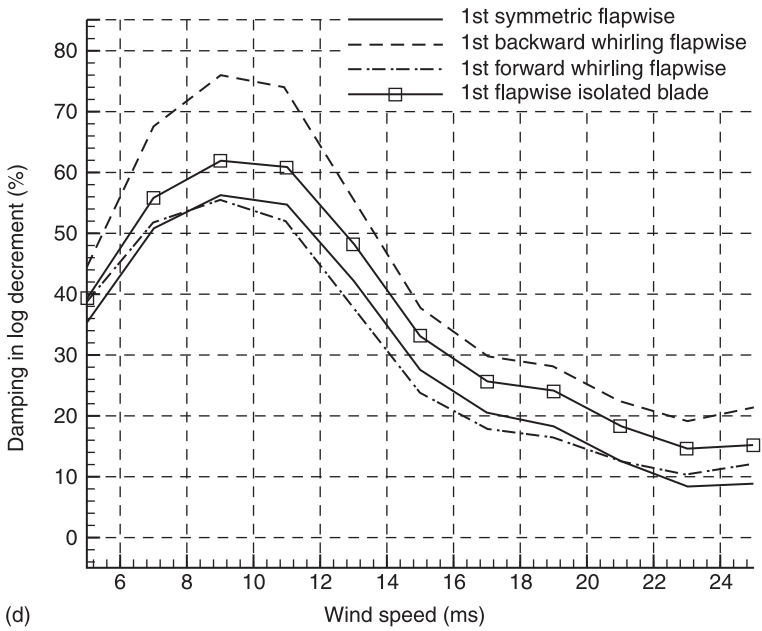

3.18 (d) Rotor flapwise.

Fig. 3.18(c)). Finally, the three flapwise modes are highly damped, as seen in Fig. 3.18(d). As a general conclusion, significant reduction of the damping of all modes is noted as the wind speed increases. This is linked to stalled operation and, as will be discussed in the following section in the case of the edgewise modes, often results in high negative aerodynamic damping values (called stall-induced edgewise vibrations). It is also noted that there is a clear deviation between the damping characteristics of the isolated blade compared to those of the blade being mounted on the wind turbine. This indicates that the structural interaction of the various components affects the damping characteristics of the wind turbine modes. Finally, the modes that appear to be the lowest damped are the two cyclic edgewise modes and this is typical for most wind turbines.

Figure 3.19 presents the frequency variation of the PRVS wind turbine modes. In this case, the variation of the frequencies is higher as a result of the varying rotational speed (up to 9 m/s) and the varying pitch (beyond 13 m/s). Comparing the damping characteristics of the various modes (see Fig. 3.20(a)–(c)) with those of the SR machine, it is observed that (1) the tower lateral bending mode and the rotor edgewise modes are still the lowest damped modes of the wind turbine, and (2) considerable increase of the damping is obtained at high wind speeds as a result of the blades' pitching, indicating that when the stall is avoided, edgewise vibrations are suppressed.

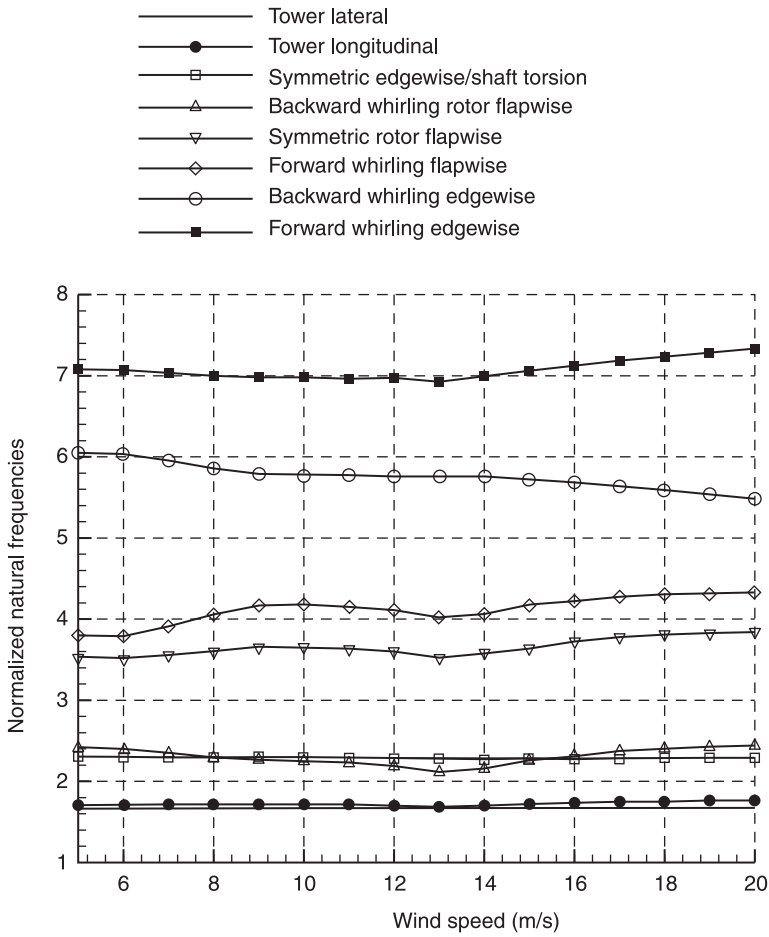

3.19 Aeroelastic frequencies of a 2.75 MW pitch-regulated variable speed wind turbine in multiples of the nominal rotational frequency.

In the following, various wind turbine instabilities are discussed and explained through application examples.

Stall-induced edgewise vibrations

When the blades operate in stall, negative aerodynamic damping is introduced by the aerodynamic loads acting, which give rise to reduced damping of both the flapwise and the edgewise modes. In particular, the edgewise modes become negatively damped, and so, amplifying vibrations in the edgewise frequency are obtained.

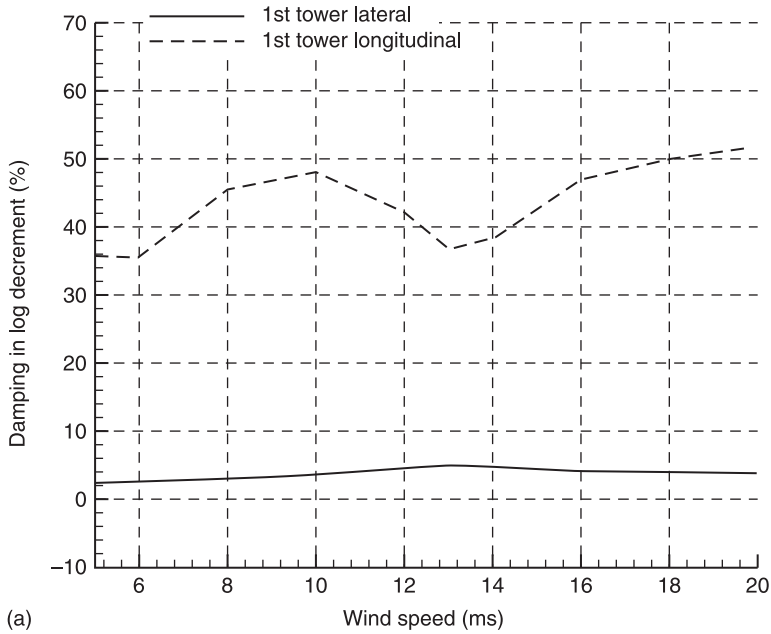

(a)

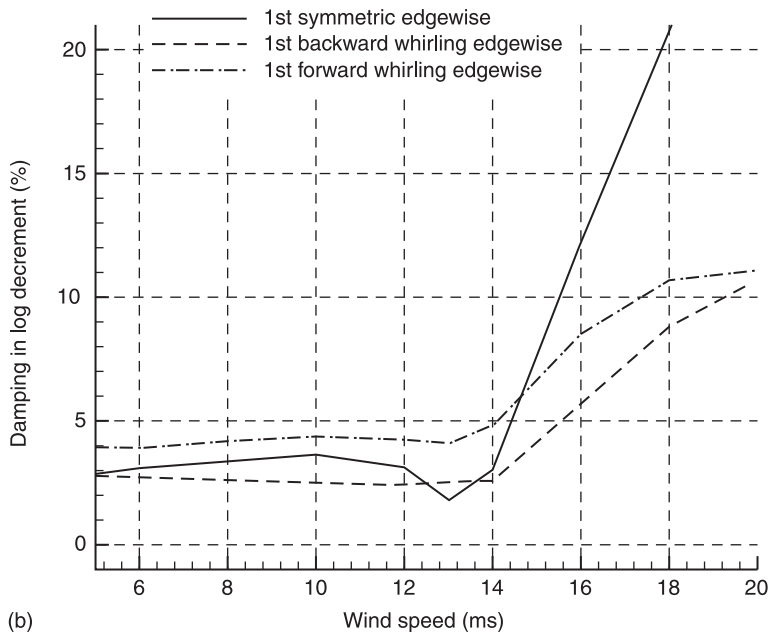

(b)

3.20 (a)–(c) Aeroelastic damping of 2.75 MW pitch-regulated variable speed wind turbine modes. (a) Tower modes; (b) rotor edgewise modes.

(*Continued*)

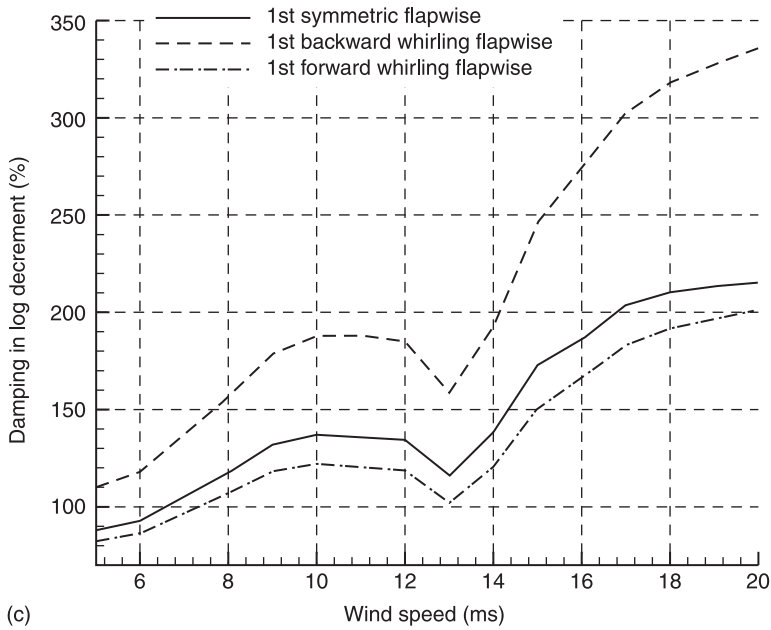

3.20 (c) Rotor flapwise modes.

The first experimental evidence of this instability was seen in the mid 1990s on stall-regulated rotors with a diameter of 35–40 m. An example of a 500-kW turbine is presented in Fig. 3.21, and it is seen that the amplitude of the edgewise blade root moment (which at steady conditions varies with 1*P* due to the gravity) increases two to three times due to the instability during operation in stall. Also, computed with HAWCstab, damping characteristics of the two edgewise modes (forward whirling and backward whirling) are shown in Fig. 3.22 (Hansen, 2003) and compared with the damping characteristics measured by Thomsen *et al*. (2000) on a 600-kW turbine. Both predictions and measurements indicate the decrease in damping for increasing wind speed and the difference in damping between the two cyclic modes. The higher damping of the forward whirling mode is due to a higher content of out-of-plane motion in this mode as compared to the backward whirling mode (Hansen, 2003). The experimental evidence of the edgewise instability led to considerable research on this subject, and a major European project 'Prediction of Dynamic Loads and Induced Vibrations in Stall' funded by the European Union (EU) was carried out in the period from 1995 to 1998 (Petersen *et al*., 1998).

The origin of the instability was found in the basic aerodynamic damping characteristics of a rotating, vibrating airfoil section. Linearization of equation [3.21] with respect to the two principle vibration directions (flapwise and edgewise) provides the following damping coefficients (Petersen *et al*., 1998):

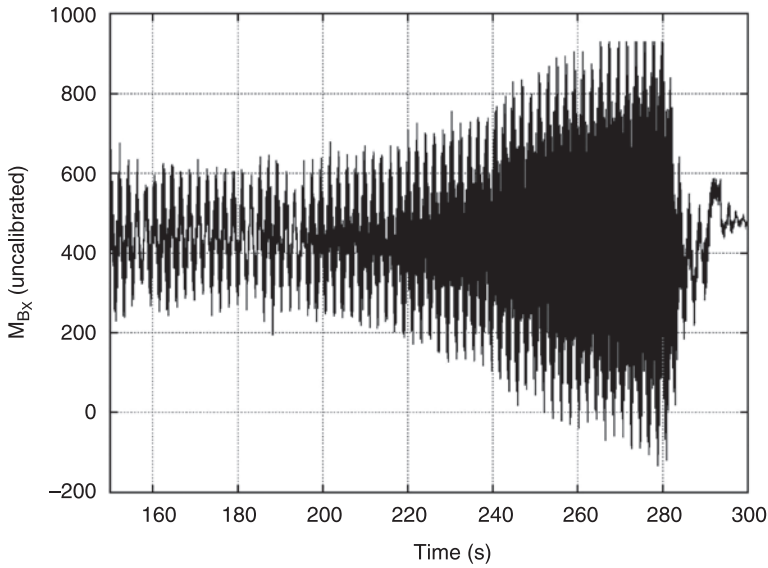

3.21 Measured edgewise blade root moment on a stall-regulated rotor at high wind showing an edgewise vibration instability development in the time interval from 220 seconds to 280 seconds.

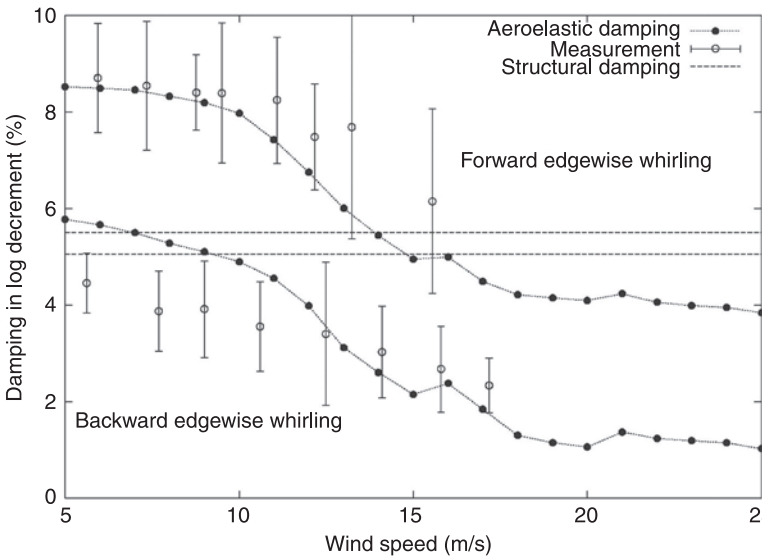

3.22 Predicted and measured aeroelastic damping of the forward and backward edgewise whirling modes of a 600 kW turbine, together with the structural damping to show the change in damping due to the interaction with aerodynamic forces (Hansen, 2004).

$$c_{xx}^{R}(r,V)=\frac{1}{2}c\varrho\frac{r\Omega}{W}\left[\left(\frac{2r^2\Omega^2+V^2}{r\Omega}\right)C_D-V\frac{\partial C_D}{\partial\alpha}-VC_L+\frac{V^2}{r\Omega}\frac{\partial C_L}{\partial\alpha}\right]$$

$$c_{xy}^{R}(r,V)=\frac{1}{2}c\varrho\frac{r\Omega}{W}\left[-VC_D+r\Omega\frac{\partial C_D}{\partial\alpha}+\left(\frac{2V^2+r^2\Omega^2}{r\Omega}\right)C_L+V\frac{\partial C_L}{\partial\alpha}\right]$$

$$c_{yx}^{R}(r,V)=\frac{1}{2}c\varrho\frac{r\Omega}{W}\left[-VC_D+\frac{V^2}{r\Omega}\frac{\partial C_D}{\partial\alpha}-\left(\frac{2r^2\Omega^2+V^2}{r\Omega}\right)C_L+V\frac{\partial C_L}{\partial\alpha}\right]$$

$$c_{yy}^{R}(r,V)=\frac{1}{2}c\varrho\frac{r\Omega}{W}\left[\left(\frac{2V^2+r^2\Omega^2}{r\Omega}\right)C_D+V\frac{\partial C_D}{\partial\alpha}-VC_L+r\Omega\frac{\partial C_L}{\partial\alpha}\right]$$

[3.27]

where Ω is the angular velocity of the blade section, r is the local radius, W is the relative velocity and V is the free wind speed (see Fig. 3.23 for the definitions). c_{xx}^{R} and c_{xy}^{R} are the damping coefficients in the in-plane or edgewise direction, due to the flapwise and edgewise motions, respectively. Similarly, c_{yy}^{R} and c_{yx}^{R} are the damping coefficients in the out-of-plane or flapwise motion. From the above equations, it is seen that the lift or drag coefficient is present in all the terms for determination of the damping coefficients, and the aerodynamic characteristics of the blade section are thus of great importance for damping identification. However, for a more specific analysis, suitable airfoil data have to be inserted.

The damping coefficient c_{xx}^{R} is now derived for the airfoil section vibrating in a direction determined by the angle θ_{RB} relative to the rotor plane (see Fig. 3.24)

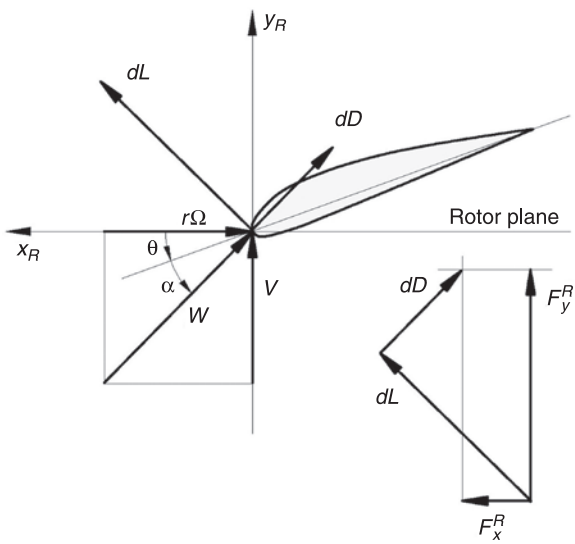

3.23 Flow forces and velocities at a blade section (Petersen *et al.,* 1998).

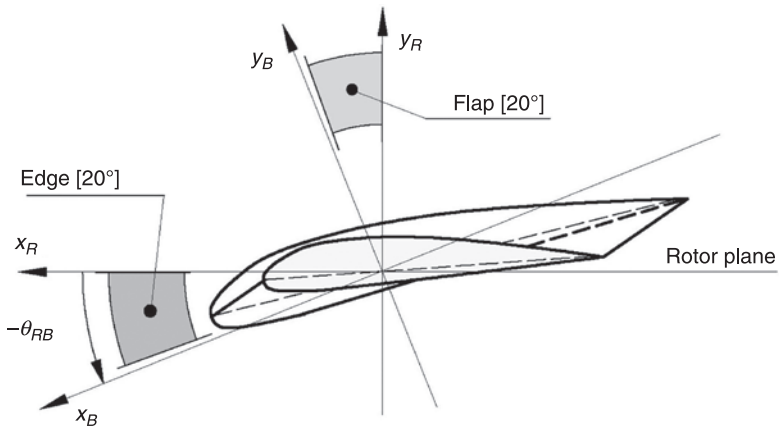

3.24 Typical ranges for the edgewise and flapwise vibration (Petersen *et al.,* 1998).

and shown for three different wind speeds in Fig. 3.25. Typical vibration direction intervals for the edgewise and flapwise modes are included in Fig. 3.25. The damping coefficient for the edgewise mode is generally low and even negative in part of the operational interval. However, the flapwise mode is highly damped except at a wind speed of 20 m/s. This simple example illustrates the fundamental

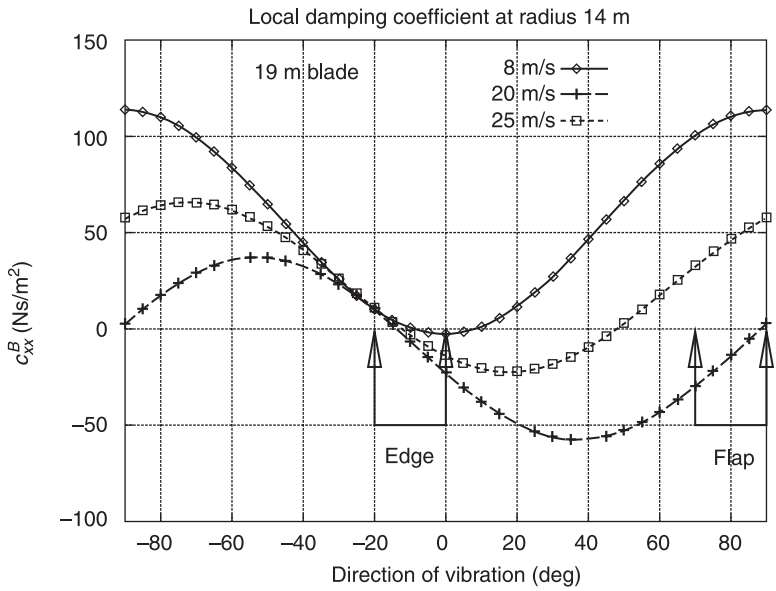

3.25 Damping coefficient c^B_{xx} as a function of the vibration direction θ_{RB} (Petersen *et al.,* 1998).

mechanism of unstable aeroelastic response, but the complexity of the full aeroelastic instability problem should not be neglected, as a much more detailed modeling is necessary to understand the aeroelastic response of a complete turbine. It is worth noting that when the first observations of the edgewise instability occurred on some turbines, there could be other turbines using the same blades where no severe edgewise vibrations were seen. So, although the aerodynamic characteristics of the blades are very important for the edgewise instability, there are also a number of other important parameters that affect the stability behavior of the system. As an example, it was shown in the study by Petersen *et al*. (1998, p. 131–132 (Hansen 2003)) that an increase in the main shaft stiffness could remove the edgewise blade instability. The overall result of the study was guidelines designed for avoiding stall-induced vibrations related to the aerodynamic characteristics of the blade, structural characteristics of the blade, material and structural properties related to structural damping, and properties of the supporting structure. The referenced EU-funded project was followed by a number of research studies on the edgewise blade instability and later, more generally, on the stability of the complete wind turbine (Chaviaropoulos, 2001; Chaviaropoulos *et al*., 2003; Hansen and Buhl, 2006; Markou *et al*., 2007).

Vibrations at standstill

Wind turbines are designed to operate up to a maximum wind speed of, for example, 25 m/s and are shut down for higher wind speeds. They have thus to withstand the wind loads at extreme wind speeds, with the wind coming from any direction to the rotor. This can result in quite extreme inflow conditions on the blade, with inflow angles covering the whole interval. It seems that this load condition is of major importance, although direct documentation by measurements is not seen in the open literature. However, even at lower wind speeds (10–20 m/s), the parked rotor condition can lead to high edgewise blade vibrations in some special inflow cases. This is a situation that is quite common during erection of turbines in wind farms where there can be a time span of several weeks from the turbine installation until it can be connected to the grid. During this period, the rotor is locked and this can be a more dangerous situation than an idling rotor that requires that the turbine is connected to the grid. A combination of low aerodynamic damping at specific inflow direction, and vortex shedding from the blade might be the mechanism behind the severe blade vibrations at relative low wind speeds from 10 to 20 m/s.

Owing to the lack of measured vibrations at standstill, an example of a simulated edgewise blade response in turbulent wind with a mean wind speed of 50 m/s is shown in Fig. 3.26. The wind direction has an angle of 60° to the rotor axis and the blades are at zero pitch. Oscillations are clearly seen in the edgewise blade root moment, although the amplitude does not increase continuously. For comparison, the edgewise moment during normal operation at 8 m/s is also shown.

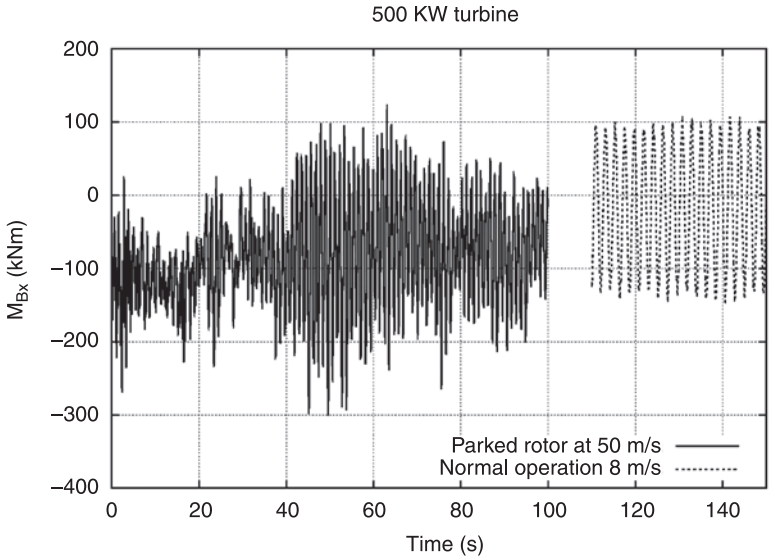

3.26 Simulated edgewise blade root moment on a 500 kW turbine at normal operation at an average wind speed of 8 m/s and with parked rotor at an average wind speed of 50 m/s with an inflow wind direction of 60° relative to the rotor axis.

Figure 3.27 and Fig. 3.28 present the aeroelastic damping characteristics of the first flapwise and edgewise modes of a parked blade (90° pitched at feathering position) at various angles of the local flow (Politis *et al*., 2009). For a blade at feathering position, 0° local flow angle corresponds to 0° yaw error with respect to the rotor plane. As seen in the plots, both flapwise and edgewise modes become low or even negatively damped for flow angles around ±20°. This is in line with the results presented earlier for a normal operation, where low or even negative damping values of the flapwise and edgewise modes are obtained when the local flow angles of attack, beyond the maximum C_L angle in the post-stall regime, are experienced by the blade sections. Moreover, negative damping values of the edgewise mode are also obtained for very high flow angles in the vicinity of ±90°. The difference between this and the previous case is that the flapwise mode is now highly damped. At ±90° angle of attack, the drag coefficient is expected to be maximum while the lift coefficient will be zero and the slope of the lift curve will be negative. High values of the drag give rise to an enhanced aerodynamic damping of the blade. On the other hand, negative slope of the lift curve degrades damping. In cases where the edgewise motion is highly coupled to the flapwise motion, edgewise vibrations are likely to occur. This is illustrated in Fig. 3.29, where the trace of the blade-coupled flapwise/edgewise motion is shown. In the same figure, the velocity triangles and lift force acting on the blade are plotted for the parts of the blade motion such that the flapping velocity becomes maximum.

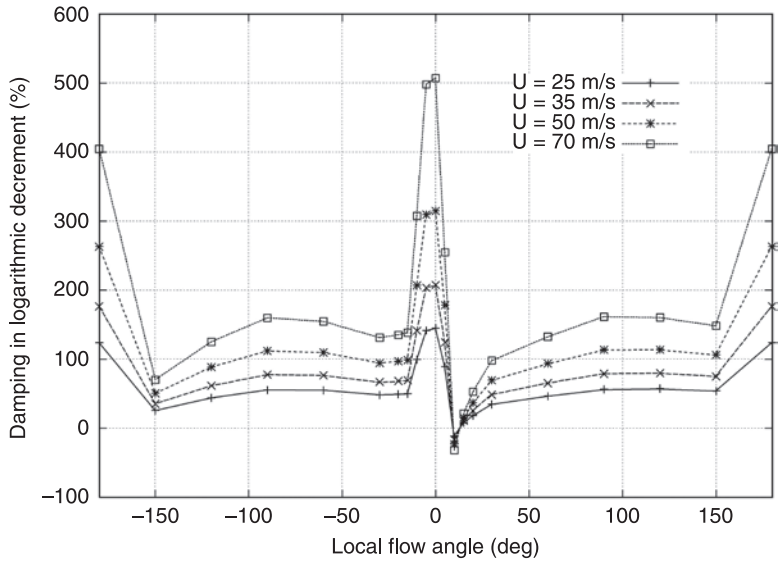

3.27 Aeroelastic damping of the first flapwise mode for different wind speed values using quasi-steady modeling.

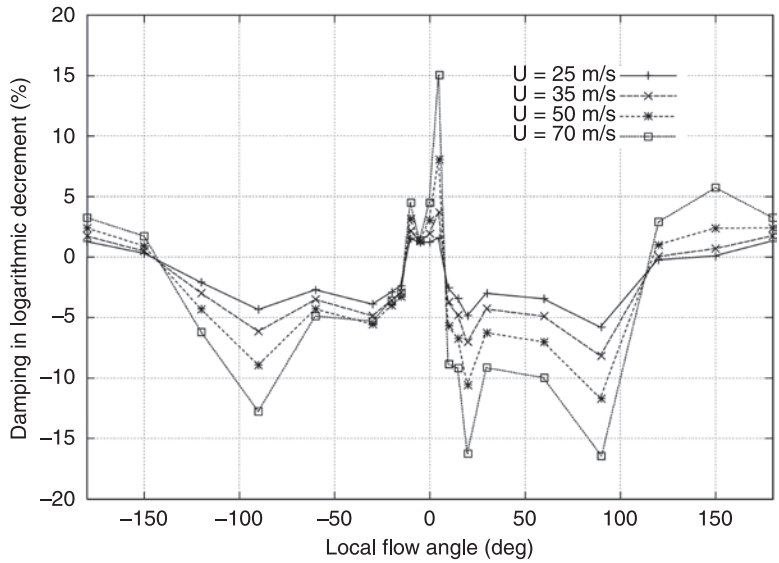

3.28 Aeroelastic damping of the first edgewise mode for different wind speed values using quasi-steady modeling.

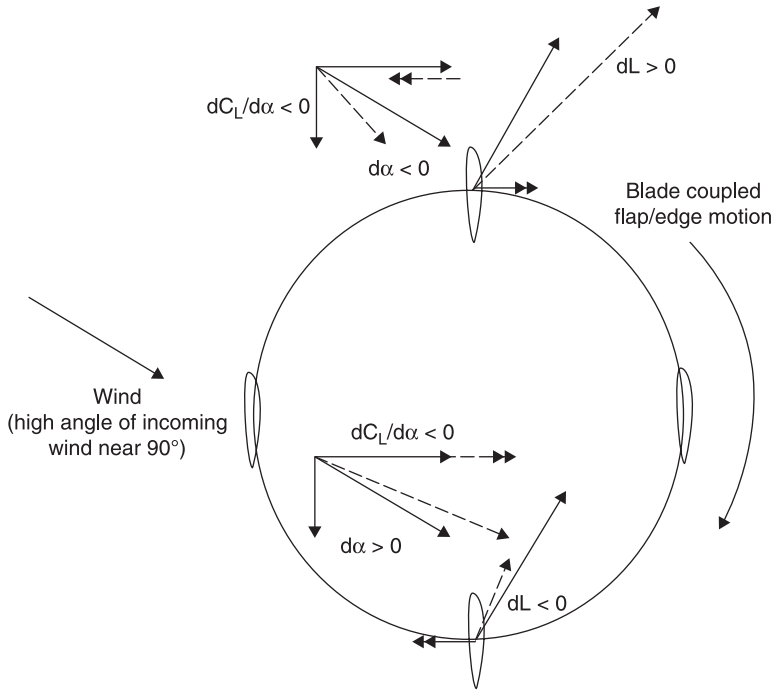

3.29 Qualitative explanation of the damping decrease at high angles of attack.

The solid lines present the incoming wind and the lift force acting on a blade element due to this wind. Dashed lines present the change in the effective velocity seen by the blade, and the lift force when flapping motion is taken into account (double-arrowed lines). Given the negative slope of the lift curve, when the blade is lagging, the lift force becomes smaller as a result of the higher angles of attack, and so lower restoring force (opposing to the blade motion) is generated. When the blade is leading, the opposite behavior is observed. The lift force of the blade increases as a result of the reduction of the local flow incidence, and so a higher diversion force develops.

Tower lateral bending instability

This type of instability or low damped vibrational mode has been experienced on many types of turbines from the stall-regulated 500 kW range turbines in the mid 1990s to the newest pitch-regulated MW turbines. Hansen (2007) has investigated this type of vibrations in more detail and found that a typical direction for the lateral vibrations of a stall-regulated turbine is around 45° relative to the rotor axis, whereas for the pitch-regulated turbine, the direction is closer to being perpendicular to the rotor shaft axis. This can be explained by the different

operational range of the airfoils along the blade influenced by the pitch of the blade. Using the stability tool HAWCStab (Hansen 2004), the damping of the longitudinal and lateral tower mode was computed for a stall-regulated MW turbine (Hansen 2007). The damping curves, as a function of the wind speed, are shown in Fig. 3.30, and it is clear that the lateral mode is considerably less damped than the longitudinal mode and even becomes negative at high winds.

For offshore installed turbines, the wave loading can exaggerate the problem of low lateral damping as the wave direction for some periods can be quite different from the wind direction and gives considerable load input on the low damped lateral tower mode. Kallesøe and Hansen (2010) investigated this problem by simulations on a conceptual 5 MW reference wind turbine (RWT) using the HAWC2 code (Larsen, 2009; Larsen, Hansen *et al*., 2004; and Larsen, Madsen *et al*., 2005). Operational conditions were a wind speed of 6 m/s with 20.2% turbulence, and irregular waves with an average height of 1.63 m and an angle of 90° to the wind direction. The simulated lateral and longitudinal tower bottom moment and the wave height are shown in Fig. 3.31, and it can be seen that the variations of lateral moment are considerably higher than the variations of the longitudinal moment. One method to damp the lateral tower moment is to use a suitable control on the generator torque, and Kallsøe and Hansen (2010) demonstrated 40% reduction in the fatigue of this load component. Another very common way to damp lateral tower vibrations, widely used by the industry, is by installing a suitable damper in the tower top.

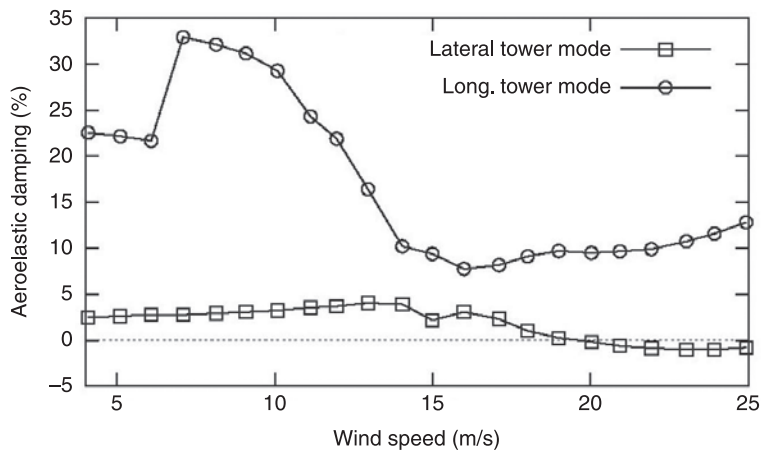

3.30 Aeroelastic damping of the first lateral and longitudinal (Long.) tower bending modes as a function of wind speed computed for a stall-regulated MW turbine by the aeroelastic stability tool HAWCStab. Graph from Hansen (2007).

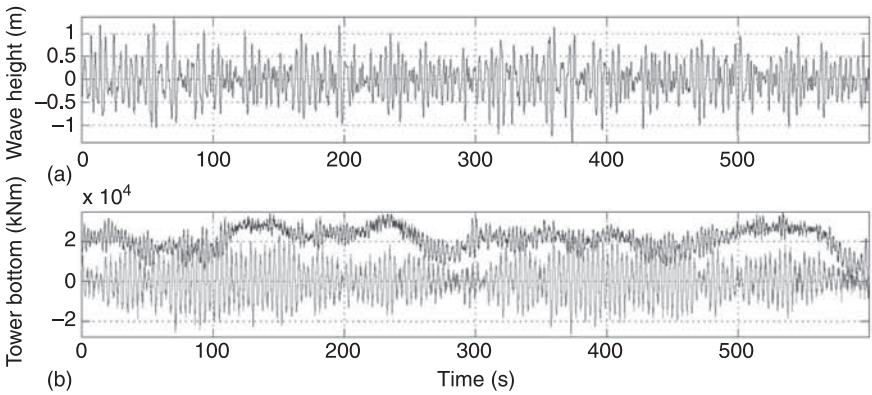

3.31 Results ((a) wave height; (b) lateral tower bottom bending (lower trace) and axial tower bottom bending (upper trace)) from aeroelastic simulations with the code HAWC2 on the 5 MW RWT with combined wave loading and turbulence (Reproduced from Kallesøe and Hansen (2010)).

Classical flutter

Classical flutter is a well-known instability from aircraft wing applications. It originates from the aeroelastic coupling of the flapwise modes with the first torsion mode at high flight speeds. In particular, the change in the angles of attack resulting from the torsion deformation of the wing sections generates aerodynamic lift forces that are in phase with the flapwise bending motion. This gives rise to violently amplifying flapwise vibrations that cannot be compensated by structural damping. Although classical flutter instability has not been reported in wind turbines, it has been given special attention by many researchers (Lobitz, 2005; Hansen *et al*., 2006; Hansen, 2007) for the reason that as wind turbine blades become more flexible, the frequency of the first torsion mode drops and comes closer to the lowest flapwise eigen frequencies.

In the study by Hansen (2007), the classical flutter instability has been investigated in detail and it has been identified that the main driving mechanisms that increase the risk of such instability are:

- operation at low angles of attack (in the attached flow regime), so the increase in the angle of attack (nose-up torsion) is associated with higher lift values;
- high tip speeds to ensure sufficient energy in the aerodynamic forces;
- low torsion stiffness or better, lower values of the torsion to flapwise frequencies ratio;
- placement of the center of gravity of the blade sections aft of the aerodynamic centre to ensure the correct phasing of the flapwise and torsional components in the flutter mode.

In wind turbine blades, the risk of experiencing flutter instability is usually measured by the ratio of the rotor speed at which such instability first takes place

to the nominal speed of the rotor at normal operation. For modern large-scale wind turbines, such ratio lies in the vicinity of two (Lobitz, 2005). This means that the risk of flutter instability is not far from the design limits of modern wind turbines. This is especially true if we take into account that up to a certain limit, rotor over-speeds are allowed by the controller in extreme wind events. It has further been shown by Hansen *et al*. (2006) that the high peaks in relative velocity for a blade on a rotor in yaw is enough to trigger flutter. A reduction of 13% in flutter speed was reported for a rotor in 50° yaw and operating at 8 m/s (Hansen *et al*., 2006).

In wind turbine blades, the mode that usually becomes a flutter one is the second flapwise (Lobitz, 2005; Hansen, 2004; Hansen *et al*., 2006) mode. This can be observed in Figs 3.32 and 3.33 where computations of the aeroelastic frequencies and damping of the isolated blade (performed with GAST, Riziotis and Voutsinas, 1997) are shown as function of the rotor speed. It is noted that the frequency of both the first and the second flap modes increases with the rotor speed toward the frequency of the first torsion mode. At the rotor speed of 2 rad/s (nominal 1.267 rad/s), a coupling of the second flap with the torsion mode takes place (indicated with the arrows) that leads to a sudden reduction of the second flap mode damping (see Fig. 3.33). At the rotor speed of 2.4 rad/s, the damping of the second flap mode becomes negative. Other examples of even more violent flutter instabilities can be found in Hansen (2007).

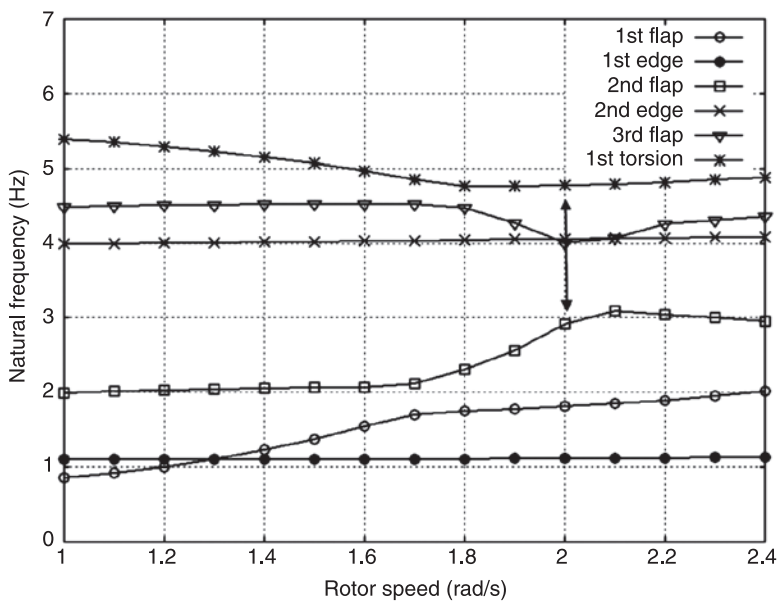

3.32 Aeroelastic frequencies of the isolated blade modes as a function of the rotor speed.

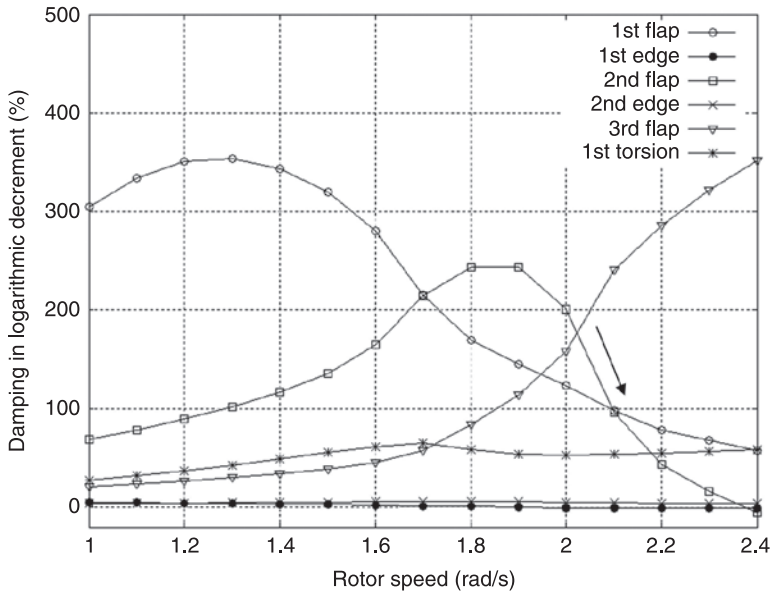

3.33 Aeroelastic damping of the isolated blade modes as a function of the rotor speed.

3.4.3 Characteristics of load input and load cases

Wind loads

Atmospheric turbulence in the inflow to the turbine is the main load driver, and turbines are certified to specific wind turbine classes (1, 2 or 3) with an associated reference wind speed and a turbulence intensity. The dominant international standard for the design of wind turbines is the IEC61400-1 (2005) standard for onshore wind turbines and the IEC61400-3 (2005) standard for offshore wind turbines. The latter is often used in combination with the DNV-OS-J101 (2004) offshore standard. In the IEC standard, two turbulence models are proposed: the Mann uniform shear model (Mann, 1994, 1998), and the Kaimal spectral and exponential coherence model (Kaimal *et al*., 1972). However, the standard recommends use of the Mann turbulence model, and this model will be used for the turbulence in the simulations presented below.

When the turbulence eddies pass through the rotor, the blades cut through the eddies that have sizes ranging from several times the rotor diameter D to smaller than D. This causes the so-called rotational sampling of the turbulence, which is known to move energy from the lower frequencies to multiples (1p, 2p, 3p, etc.) of higher frequencies of the rotor speed (Kristensen and Frandsen, 1982). As an example, a time trace of the axial velocity component at hub height is compared with the corresponding component on the rotating blade at a radius of 63 m in Fig. 3.34(a).

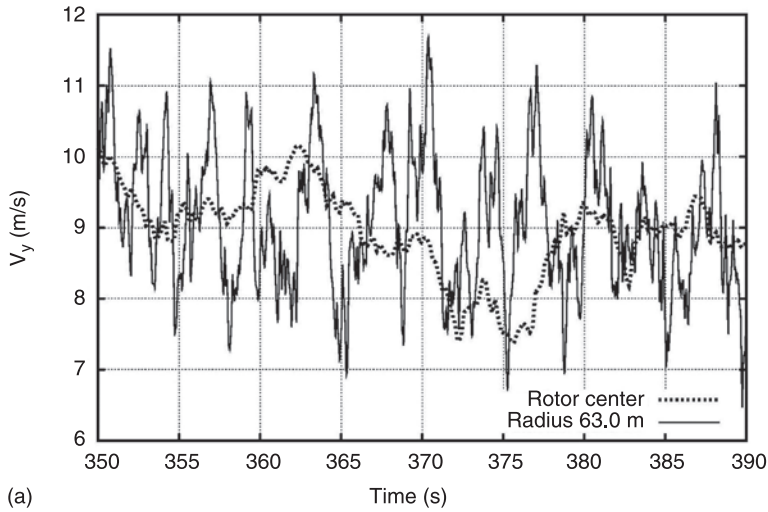

(a)

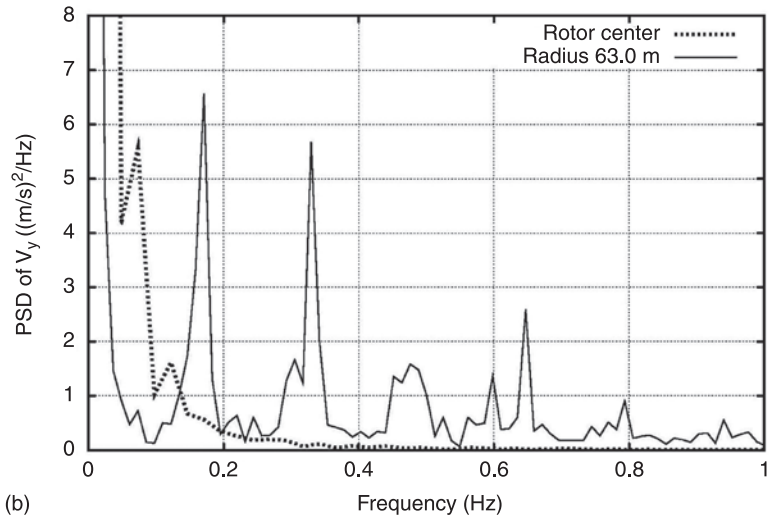

(b)

3.34 (a) Comparison of inflow velocity in turbulent wind at the rotor center and at a point on the rotating blade with a radius of 63 m. Simulations with HAWC2 on the RWT at 8 m/s and a turbulence intensity of 8 m/s. (b) Comparison of power spectral density (PSD) of the inflow velocity in turbulent wind at the rotor center and at a point on the rotating blade with a radius of 63 m. Simulations with HAWC2 on the RWT at 8 m/s and a turbulence intensity of 15%.

The difference between the two traces is considerable with a characteristic 1p variation in the trace of the wind speed seen from the point on the blade. The power spectral density (PSD) of the same two wind speeds is shown in Fig. 3.34(b), and the above-mentioned movement of energy from the low frequencies in the spectrum of the wind speed in the fixed frame of reference to higher frequencies (1p, 2p, etc.) for the rotating point is made clear.

The mechanism of rotational sampling of the turbulence is of fundamental importance for the loading on turbines and for optimizing the aeroelastic response because the wind load input to the system will be concentrated on specific frequencies. To illustrate this, a simulation has been performed on a stiff structural model of a conceptual 5-MW RWT (Jonkman, 2005) using the HAWC2 code and for the same turbulence input, as used in the example above. Spectra of the moment in the turbine components, which are most important for the turbine design and dimensioning, are shown in Fig. 3.35(a) and (b), and they are found to have the following different characteristics.

Flapwise blade root moment M_{Bl_x}

It is observed from Fig. 3.35(a) that this moment has peaks at multiples of the rotational frequency, which means at 1p (0.16 Hz), 2p (0.32 Hz), 3p (0.48 Hz), etc., although the peaks at the higher multiples are small. The spectrum correlates well with the spectrum of the turbulent wind seen from the rotating blade, as shown in Fig. 3.34(b). This is due to the close connection between the inflow angle along the blade and the wind speed.

Tower bottom moments M_{TB_x} (longitudinal) and M_{TB_y} (lateral)

For the longitudinal tower moment, it appears that almost all the energy is concentrated on 3p, with much smaller peaks at 1p and 6p. In the case of small differences in, for example, blade pitch angles combined with shear in the inflow, there could be some energy on the 1p. Regarding the lateral tower moment, the load input is almost zero.

Tower top moments M_{TT_x} (tilt moment) and M_{TT_z} (yaw moment)

The peaks of these two moments (see Fig. 3.35b) are almost similar with decreasing peaks at 1p, 3p, 6p, etc. The higher values for the yaw moment are probably due to a slow change in the wind direction caused by a trend in the horizontal turbulence component.

Besides the influence from the turbulence in the wind to the peaks in the load spectrum, wind shear will also contribute, however, with quite different amount for the different load components. Finally, the mean wind speed will determine the mean loads.

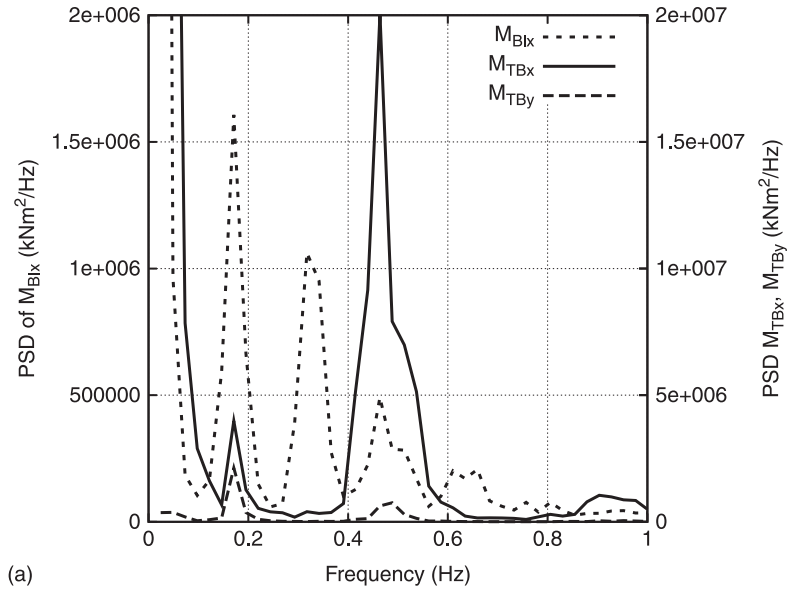

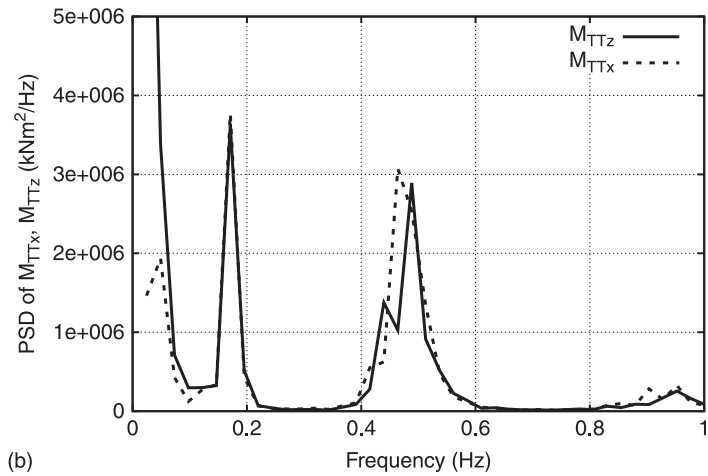

3.35 Turbulent load input. (a) Spectra of tower base moments in longitudinal and lateral directions and of the blade root flapwise moment based on time simulations with the HAWC2 code on the RWT turbine at 8 m/s, 15% turbulence and using a stiff structural dynamic model. (b) Spectra of tower top moments, the yaw moment M_{TT_z} and the tilt moment M_{TT_x} based on time simulations with the HAWC2 code on the RWT at 8 m/s, 15% turbulence and using a stiff structural dynamic model.

Wake loads

The standard IEC61400-3 (2005) specifies how to take operation in wind farms into account when certifying turbines for such sites. Basically, the concept works with an increase of the ambient turbulence to what is called an 'effective turbulence I_e', as formulated by Frandsen (2003). The effective turbulence is determined, for example, by the spacing of the neighboring wind turbines and their thrust coefficient, but also with a factor taking into account which component of the turbine is considered. An example of the variation of I_e in the wake of a single turbine and as a function of the distance from the wake generating turbine is shown in Fig. 3.36 (Frandsen, 2003).

However, it has turned out that there is a need in the industry to supplement the above procedure for more detailed simulations of the loading in wake operation. This led to the development of the dynamic wake meandering (DWM) model (Thomsen and Madsen, 2004; Larsen *et al*., 2008; Madsen *et al*., 2008), where the basic elements are the velocity deficit in the wake and the movement of this deficit determined by the big lateral turbulence components in the atmospheric flow. This modeling approach enables the computation of the mean turbine loads as well as the turbulence loads in wake operation and provides, in general, detailed information of the loading. An example is shown in Fig. 3.37 from Thomsen and Madsen (2004). Measured and simulated variation of average and standard deviation of electrical power, flapwise blade root moment and of yaw moment as a function of direction to an upstream 2 MW turbine aligned at 205° and at a distance of 3.5D are observed. In general, there is a good correlation between measured and simulated data, and one of the advantages of the DWM model compared with the model using an effective turbulence is that both the mean and

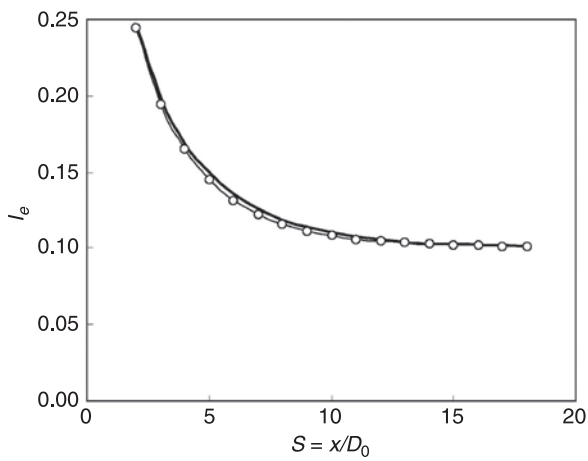

3.36 Variation of the effective turbulence I_e as a function of distance to the wake generating turbine for an ambient turbulence intensity of 10% (Frandsen, 2003).

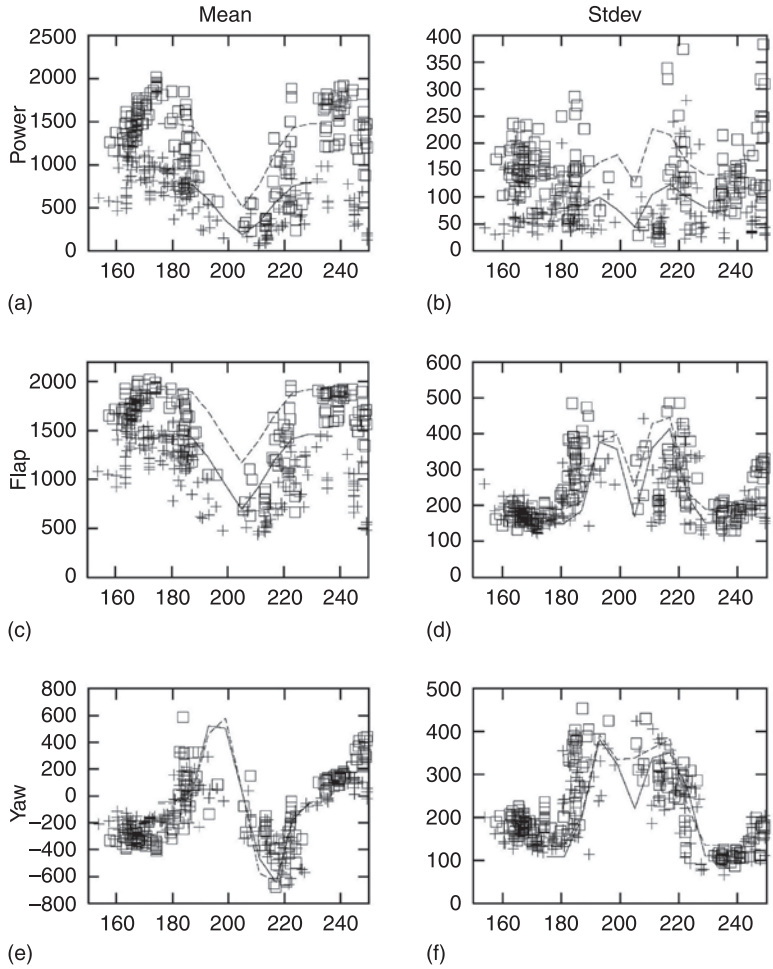

3.37 Measured and simulated variation of average (left panels) and standard deviation (right panels) of electrical power ((a) and (b)), flapwise blade root moment ((c) and (d)) and of yaw moment ((e) and (f)) as a function of direction to an upstream 2 MW turbine aligned at 205° and at a distance of 3.5D. Simulations with the dynamic wake meandering (DWM) model at two different wind speeds shown by dashed lines (Thomsen and Madsen, 2004).

the standard deviation can be computed which, for example, for the yaw loading, is important for providing more accurate design loads.

Extreme loads

Besides the load cases during normal operation with input from turbulence, waves or wakes, the standard IEC61400-3 (2005) also describes a number of extreme

external conditions that must be considered. Some of these extreme external conditions as, for example, cases 'extreme operating gust' (EOG), 'extreme direction change' (EDC) and 'extreme coherent gust with direction change' (ECD), have to be investigated for the turbine in normal operation or combined, for example with an emergency shutdown situation of the turbine. Another important extreme load case is the extreme wind speed for a 50-year recurrence period that has to be computed for the parked turbine, either with the rotor standing still or with the rotor idling.

Many of these extreme load cases are quite challenging in the wind turbine design process and will define the design loads for some components, while fatigue loads will be most important for other components or for part of a component. For a blade, it can often be a combination of fatigue and extreme loads that defines the design loads.

In the discussion below on optimized aeroelastic design, the focus will be on the normal operation cases leading to fatigue loading because this can be discussed in a more general sense, whereas the extreme load conditions are often closely linked to the specific design.

3.4.4 Methods for improved aeroelastic response

The methods for improved aeroelastic response can be divided into two major groups and then into a number of subgroups.

1 Reduction of load input/excitation:
   (a) active methods
      (i) pitch regulation (collective, cyclic or individual pitch)
      (ii) trailing edge flaps
   (b) passive methods
      (i) stall control
      (ii) stall strips
      (iii) flap/pitch coupling
      (iv) flexibility
      (v) hinges
2 Optimized wind turbine dynamics:
   (c) passive methods
      (i) separate excitation from frequency of aeroelastic modes
      (ii) increase coupling of modes with low damping to the higher damped modes
      (iii) increase structural damping
      (iv) passive dampers
   (d) active methods
      (i) powered dampers in tower, nacelle or blades
      (ii) pitch regulation (collective, cyclic or individual)
      (iii) generator torque regulation

However, there can be many designs in which methods from different groups are used on the same turbine.

Reduction of load input/excitation

It is obvious that reduction of the load input is a direct method to control or reduce the response and this can be done actively or passively. The best illustration of this is the difference between a stall-controlled and a pitch-controlled rotor. Basically, the two concepts make use of different operational points on the airfoil characteristics of the profile sections along the blade. For the power control, the stall-controlled rotor depends very much on the rise in airfoil drag when the power output will be limited around rated power. The lift forces do not necessarily decrease for increasing wind speed, so the thrust will increase as a function of wind speed, but the dynamic load input from the turbulence is reduced due to the small slope or even negative slope of the lift versus the angle of attack. The dynamic load and torque input on the pitch-regulated rotor is high, and it is therefore necessary to use variable speed in combination with pitch control.

The collective pitch of the blades is used for the power control, whereas the cyclic pitch can be used to reduce typically the 1p variation in flapwise blade and rotor moments (tilt and yaw moment). The individual pitch control has a higher load reduction potential as loads within a wider frequency range can be controlled and trailing edge flaps open for a distributed load control along the blade.

Regarding passive methods, hinges between the blades and the hub can reduce the load input, as well as the transmission of loads to the nacelle and the tower quite effectively. The two-bladed teetering rotor, eventually with a delta3 hinge, is a good example. Tilt and yaw moments can be reduced almost down to zero depending on the stiffness in the teetering system. On the other hand, the challenge is the considerable flapwise movement of the blade tips, and therefore the teetering rotor is mostly used in downwind turbines in order to keep clearance to the tower. However, it is possible to limit the teeter angle excursions considerably by use of pitch control of the blades using the teeter velocity (Larsen *et al*., 2007). Another major problem is to control the rotor during startup and shut down. During startup, the blades can easily be in a deep stalled mode, and if it is a rotor with low teeter stiffness, some additional mechanical system has to be used to limit the teeter excursions. Advanced pitch or flap control may be developed in the future to better control the aerodynamics of the blades during these conditions.

By increasing the teeter stiffness, there is a soft transition to rotors without a teeter hinge but with highly flexible blades and a flexible hub. Such designs could considerably benefit individual pitch or flap control.

Optimized wind turbine dynamics

It has been shown that the loads from turbulence are concentrated on peaks in the load spectra. One of the important objectives in the aeroelastic design of a turbine

is therefore to separate, as far as possible, the frequency of the aeroelastic modes from the peaks in the load input. On the other hand, this is quite challenging, as turbines – because of noise limitations and aerodynamic optimization – are operated at a variable speed, and then it is not only a number of load peaks that should be avoided but also a number of frequency bands. As an example, the aeroelastic response of the tower of the 5 MW RWT is shown in Fig. 3.38. For the same wind turbine, the load input for some components was presented previously in Fig. 3.35(a) and (b). Besides the response for the standard turbine, the response for three other tower configurations is shown, where the first longitudinal bending tower frequency has been changed from 0.34 to 0.30, 0.26 and 0.22 Hz. It is observed that lowering the tower eigen frequency reduces the tower response around the load input at 3p, and for the lowest tower frequency, the response around 3p is lower than the input (depicted in the spectrum of the stiff wind turbine). However, for this configuration, the response rises at 1p where there is some load input.

The results are shown in a different way in Fig. 3.39 where the amplification of the tower fatigue response (material factor $m = 3$) measured relative to the fatigue of the input is shown as a function of the ratio between the frequency of excitation (3p) relative to the first longitudinal bending tower frequency. When this ratio increases, the amplification decreases which is a well-known result from the basic vibration theory. In Fig. 3.39, the operational range of the RWT is also shown, and it is observed that the ratio of frequency of load input to tower eigen frequency

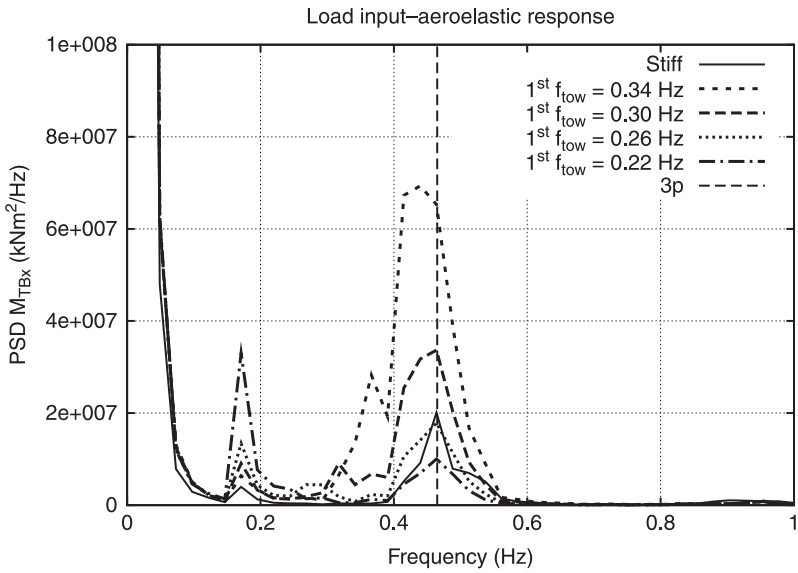

3.38 Power spectrum of the tower bottom bending moment M_{TBx} for different values of tower stiffness, based on simulations with the HAWC2 code on the 5 MW RWT turbine at 8 m/s and 15% turbulence.

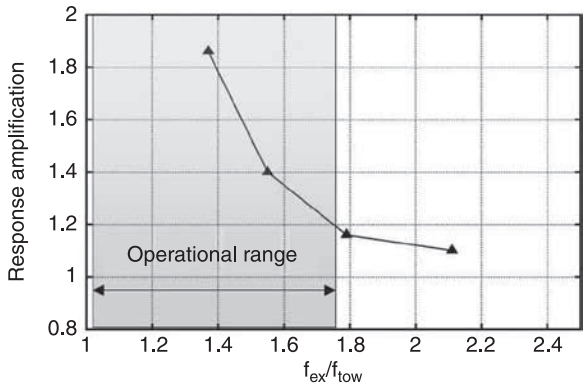

3.39 Aeroelastic tower response amplification as a function of the ratio between excitation frequency (3p) and first tower bending eigen frequency.

in the lower end is close to 1. However, this corresponds to the lowest wind speeds where the load input is low.

Moreover, in Fig. 3.40, the power spectrum of the blade root flapwise bending moment is presented for the same 5 MW RWT being infinitely stiff and flexible. Comparison of the two spectrums indicates that for the stiff design, the maximum energy is obtained at 1*P* which is reasonable, taking into account that the maximum energy from the wind is at the same frequency (see Fig. 3.34(b)). For the flexible wind turbine, the maximum peak in the spectrum is obtained at 2*P*, and this is because many of the wind turbine natural frequencies are close to this frequency.

The presented examples illustrate that it is important in the design process to keep track of a number of frequencies of aeroelastic modes relative to the load input bands. Considerable reduction in fatigue loads can be obtained by a suitable positioning of the eigen frequency of the different aeroelastic turbine modes.

Another important design procedure from the toolbox is to increase the coupling between a low damped aeroelastic mode and a mode with higher damping. Solutions for the edgewise vibration problem described previously are a good example. The task here is to increase the coupling of the edgewise modes with the flapwise modes as the latter often have a higher damping. Even in cases where the flapwise mode is negatively damped, non-linear aerodynamic effects, such as stall hysteresis, will typically limit the amplitudes of such vibrations to acceptable limits. The potential of design for optimal couplings seems big because this, for example, can be done with suitable orientation of the fibers in the blades. However, it requires advanced computational tools to model such couplings in detail.

Increased structural damping is also an important tool for optimized aeroelastic response, and this method has been studied intensively in the past, for example, to solve the problems of edgewise vibrations.

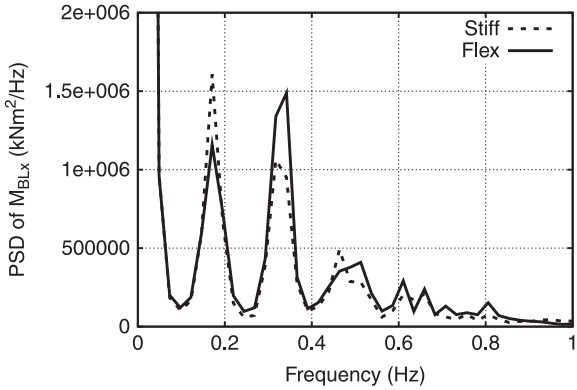

3.40 Power spectrum of flapwise blade root response for the 5 MW RWT based on time simulations with the HAWC2 code at 8 m/s, 15% turbulence and using a stiff structural and flexible structural dynamic model.

Passive and active dampers in different turbine components have been used widely in the past. Again, edgewise vibrations have not only been controlled with suitable dampers in the blades but also with suitable tuned damper systems in, for example, the rear of the nacelle. The last method is a very good illustration of how coupled the blade modes can be with the dynamics of the other part of the turbine. Also, tower vibrations are often controlled with damper systems.

Finally, the pitch system can be used to damp tower loads as well as rotor loads. The difference in the load reduction systems, which also make use of pitch control, is that the input to the control now is, for example, accelerations in the tower top. Lateral tower vibrations can effectively be controlled by the generator torque, as already discussed above.

3.5 Future trends

The future trends in wind turbine design and concepts are influenced by a variety of parameters and conditions and certainly not only determined by potential technology achievements. The ratio between the onshore and offshore market is, for example, an important parameter as the turbines for offshore application might take another development path, perhaps with bigger machines and higher tip speeds than onshore turbines.

3.5.1 Load reduction by control surfaces or boundary-layer control

During the last five to seven years, there has been an increasing research on control of the aerodynamic loads on the blades by control surfaces such as flexible

trailing edge flaps (Buhl *et al*., 2005) or by controlling the boundary layer with, for example, jets. The background for this development is that the biggest blades now have a length of around 63 m, and within a short time, it might increase to 70–80 m. For such blades, there is a need to have a distributed control along the blade as the turbulent inflow conditions can be quite different at different radial positions. Also, in order to be able to damp the individual aeroelastic modes, it is necessary to apply such distributed control techniques. Flexible trailing edge flaps could cover the whole trailing edge of a blade, as illustrated by Andersen *et al*. (2009) in Fig. 3.41, but only with a few sections being active. Andersen *et al*. (2009) report computed reduction in flapwise fatigue blade moments of 25%, 34% and 37% for one flap, two flaps and three flaps covering 10%, 20% and 30% of total blade span, respectively.

The challenge in increasing the load reduction more than 20–25%, which can be achieved with cyclic or individual pitch control as reported by Larsen, Madsen *et al*. (2004), is that it requires more and more accurate control signals. Sensors that can be used are those monitoring the strain in the blade and/or acceleration of the blade or those monitoring the flow over the blade (pressure sensors) or those measuring the inflow to the blade such as five-hole pitot tubes. Also, time delay and noise in sensor signals is critical for increasing the load alleviation by flaps as shown by Andersen *et al*. (2009). The main barrier at the moment in order to implement trailing edge flaps on MW turbines is that robust and reliable flap concepts have not yet been developed.

3.5.2 Flexible blades with bend/pitch coupling

Coupling the flapwise bending of the blade with pitch is an efficient way of changing the aeroelastic response of the blade. This is because a change in pitch directly couples to a change in effective angle of attack of the blade section and thus also to the aerodynamic load of the airfoil section. Recent results from Sandia Laboratories presented by Ashwill *et al*. (2010) show an increase in annual energy capture by 10–12% for the same loads as a baseline rotor on a Zond 750 test turbine. The new

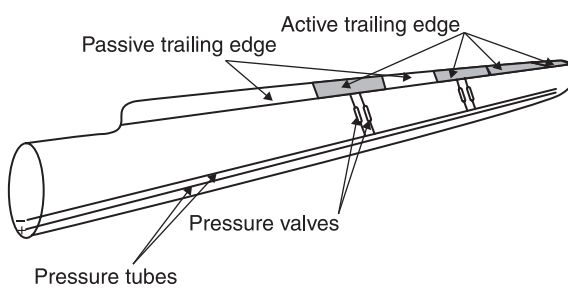

3.41 An illustration of a wind turbine blade with flaps for load alleviation (Andersen *et al.,* 2010).

blade had a flap twist coupling due to a sweep of the blade in the rotor plane and the lower loads were incorporated in the design by increasing the rotor diameter.

Bend/torsion coupling can also result from large blade deflections. Up-scaling of modern wind turbines to multi-MW sizes calls for lighter blade designs in order to reduce weight-induced loads (mass increases with the cube of the scaling factor) and increase cost efficiency. Reduction of weight can be achieved either by reducing the thickness of the blade walls while at the same time reinforcing the blade by using more advanced material or by slendering the blade (reducing the blade chords). Following current design trends, reduction in weight, for a certain blade planform, is followed by a loss in stiffness, and so the blades become more flexible.

It has been identified (Riziotis *et al*., 2008) that large flexible blades of MW wind turbines can undergo flapwise deflections, in normal operation, that exceed 10% of their radius. As indicated in Section 3.2.1, such high deflections can give rise to structural non-linear couplings not met in smaller and stiffer blades. One of the couplings that was found to have a significant contribution to blade torsion loads is the bending–torsion coupling, already addressed in Section 3.2.1. As illustrated in Fig. 3.4, when the blade exhibits very large flapwise deflections and blade curvature is high, the local edgewise bending moment comprises a twisting component with respect to the undeformed coordinate system. In Fig. 3.42, the time series of the

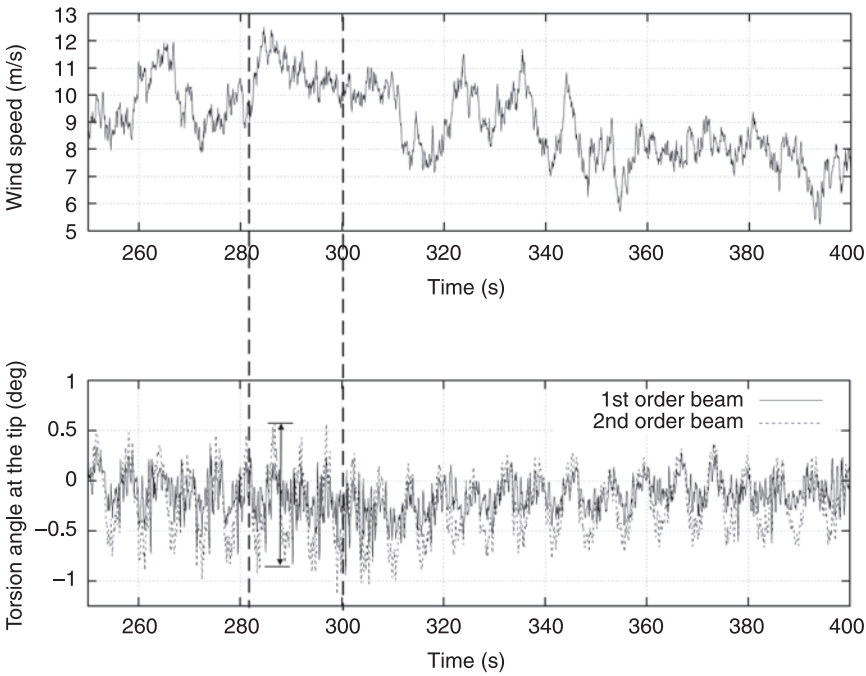

3.42 Time-series of wind speed and torsion angle at blade tip of a 5-MW wind turbine (mean wind speed 8 m/s).

torsion angle at the blade tip is shown for the RWT 5 MW wind turbine operating near the rated speed (around 11 m/s). Comparison of the torsion deformations predicted with a first- and a second-order model indicates that the amplitudes of the torsion angle variations obtained with the higher order model are much higher. It is also noted that they become higher when the wind turbine operates closer to the rated conditions where thrust and, therefore, flapwise deformations become maximum. Predictions of the equivalent blade root torsion moment presented in Fig. 3.43 indicate that pitch bearing loads can be more than twice as those predicted by a conventional first-order model near rated wind conditions.

3.5.3 Integrated design

Future turbine designs will probably have a number of subsystems, for example, for load alleviation, for vibration control or for noise reduction. The turbines will be optimized for low weight and flexibility in order to reduce load input and the transmission of loads between components. The design of such turbines must take place in an integrated environment, and this requires that the design tools and design procedures are developed such that the optimization of aerodynamic, aeroelastic and control properties can be carried out in a fully coupled system.

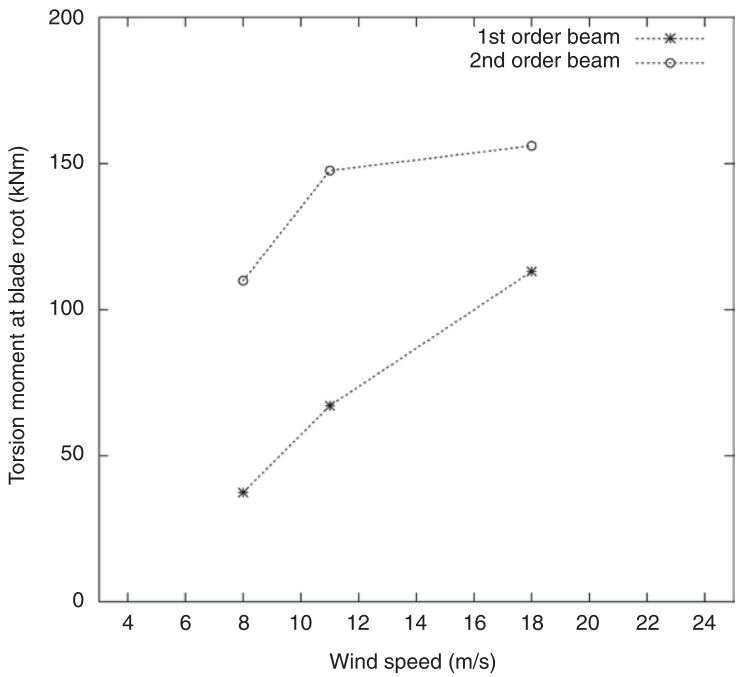

3.43 Equivalent fatigue loads of torsion moment at blade root (1 Hz, $m = 12$).

3.5.4 Pitch or stall control

The stall control concept, in combination with a fixed rotational speed and the use of an induction generator had, due to its robustness, a big success in the beginning of the modern wind turbine development in the 1980s and the 1990s. Later, active stall control was introduced in bigger machines in order to better regulate peak power and for the shutdown of the machines. Also, in recent wind farm installations, the concept has been used as an example for the Danish Rødsand 165 MW wind farm with 72 wind turbines from Bonus Energy, commissioned in 2003. Akhmatov and Nielsen (2005) describe the use of the active stall control in this wind farm temporarily to reduce the mechanical power and contribute to voltage re-establishment in the grid in the case of a short-circuit fault, as required by the Danish transmission system operator (TSO). This shows that a turbine without pitch control and variable speed can fulfill the grid requirements.

The active stall concept solved major problems of the fixed pitch stall machines, but on the other hand, it also became a more complicated system with a full pitch system of the blades and thus in a way comparable in complexity with the pitch-regulated turbines, but with much lower pitch activity than on a pitch-regulated turbine.

A rotor concept in which stall regulation fits well is the two-bladed turbine without a teetering hub. The advantage of the stall-controlled rotor is that the dynamic flapwise moments and also the tilt and yaw moments are smaller than on a pitch-regulated rotor. Therefore, acceptable levels of loading on shaft bending and on the yaw system can be obtained with this design.

3.5.5 Floating wind turbines

Most of the today's offshore wind energy capacity has been installed around the North and Baltic seas, at water depths not exceeding 20 m. For such shallow water applications, fixed-bottom wind turbines are installed using either monopiles driven into the seabed or concrete gravity bases. Recently, there has been a growing interest in exploiting the available wind resource potential at much higher depths (exceeding 30 m), where technologies already used in shallow water environments are no longer economical. For such deep water applications, the use of floating support platforms seems economically more feasible.

Designing of such floating wind turbines calls for integrated computational environments that are capable of simulating the aerodynamics of the rotor, the structural dynamics of the full wind turbine, the wave loads and the dynamics of the support platform, the loads from the mooring lines as well as their interaction (Jonkman and Sclavounos, 2006; Jonkman and Buhl, 2007).

3.6 Sources of further information and advice

Besides citations provided in the previous sections, the reader can get more information about the basic principles of aeroelasticity in the following general

textbooks (Bisplinghoff *et al*., 1955; Dowell, 1995; Fung, 1955). Specifically, for rotorcraft applications, the two textbooks by Johnson (1980) and Bielawa (2006) are excellent, although they focus on aeronautical applications (helicopter rotors and aircraft propellers). With respect to wind turbines, the literature for aeroelasticity is rather limited. Some information can be found in Hansen (2008). There are, nevertheless, many journal publications that deal with all the issues discussed in the chapter. Among those, special references should be made to some review papers providing information on the recent advances in the field of wind turbines aeroelasticity (Rasmussen *et al*., 2003; Hansen *et al*., 2006; Hansen, 2007). Finally, for the reader who would be interested in going deeper into FE analysis and beam modeling, some classic textbooks are those by Bathe (1996), Zienkiewicz and Taylor (1994) and Crisfield (1998).

3.7 References

Akhmatov, V and Nielsen, A H (2005), 'Fixed-speed active-stall wind turbines in offshore applications', *Euro Trans Electr Power*, 15, 1–12.

Andersen, P B, Henriksen, L, Gaunaa, M, Bak, C and Buhl, T (2009), 'Deformable trailing edge flaps for modern megawatt wind turbine controllers using strain gauge sensors', *Wind Energy*, 13(2–3), 193–206.

Ashwill, T D, Kanaby, G, Jackson, K and Zuteck, M (2010), 'Development of the swept twist adaptive rotor (STAR) blade', *Paper AIAA 2010–1582, 48th AIAA Aerospace Sciences Meeting Including the New Horizons Forum and Aerospace Exposition*, 4–7 January, Orlando, FL

Bathe, K J (1996), *Finite Element Procedures*, Prentice Hall, Upper Saddle River, NJ.

Bielawa, R L (2006), *Rotary Wing Structural Dynamics And Aeroelasticity*, AIAA education series, Reston, VA.

Bisplinghoff, R L, Ashley, H and Halfman, R L (1955), *Aeroelasticity*, Addison-Wesley, Cambridge, MA.

Buhl, T, Gaunaa, M and Bak, C (2005), 'Potential load reduction using airfoils with variable trailing edge geometry', *Journal of Solar Energy Engineering*, 127, 503–16.

Chaviaropoulos, P K (2001), 'Flap/lead-lag aeroelastic stability of wind turbine blades', *Wind Energy*, 4, 183–200.

Chaviaropoulos, P, Politis, E S, Sørensen, N N, Hansen, M, Bulder, B H, Winkelaar, D, *et al*. (2003), 'Recent advances on damped wind turbine rotor blades, the DAMPBLADE project', *Proceedings of the 2003 European Wind Energy Conference and Exhibition*, 16–19 June, Madrid, Spain.

Coleman, R P and Feingold, A M (1957), *Theory of Self-excited Mechanical Oscillations of Helicopter Rotors with Hinged Blades*, NASA TN 3844.

Crisfield, M A (1998), *Non-linear Finite Element Analysis of Solids and Structures, Essentials*, John Wiley and Sons, New York.

DNV-OS-J101 (2004), *Design of Offshore Wind Turbine Structures*, Det Norske Veritas, Offshore standard.

Dowell, E H (Ed.) (1995), *A Modern Course in Aeroelasticity*, Kluwer Academic, London.

Frandsen, S (2003), *Turbulence and Turbulence Generated Fatigue in Wind Turbine Clusters*, Risø report R-1188.

Fung, Y C (1955), *An Introduction to the Theory of Aeroelasticity*, John Wiley and Sons, New York.

Hansen, M H (2003), 'Improved modal dynamics of wind turbines to avoid stall-induced vibrations', *Wind Energy*, 6, 179–95.

Hansen, M H (2004), 'Aeroelastic stability analysis of wind turbines using an eigenvalue approach', *Wind Energy*, 7, 133–43.

Hansen, M H (2007), 'Aeroelastic instability problems for wind turbines', *Wind Energy*, 10(6), 551–77.

Hansen, M H and Buhl, T (2006), *Design Guidelines for Passive Instability Suppression – Task 11 Report*, Technical report of STABCON project (NNK5-CT 2002–00627 contract), Risoe-R-1575(EN), RISOE National Laboratory.

Hansen, M O L (2008), *Aerodynamics of Wind Turbines*, Earthscan, London.

Hansen, M O L, Soerensen, J N, Voutsinas, S, Sorensen, N and Madsen, H Aa (2006), 'State of the art in wind turbine aerodynamics and aeroelasticity', *Progress in Aerospace Sciences*, 42, 285–330.

Hodges, D H (1990), 'A mixed variational formulation based on exact intrinsic equations for dynamics of moving beams', *International Journal of Solids and Structures*, 26(11), 1253–73.

Hodges, D H (2003), 'Geometrically exact, intrinsic theory for dynamics of curved and twisted anisotropic beams', *AIAA Journal*, 41(6), 1131–37.

Hodges, D H and Dowell, E H (1974), *Nonlinear Equations of Motion for the Elastic Bending and Torsion of Twisted Non-Uniform Rotor Blades*, NASA TN D-7818.

Hodges, D H and Yu, W (2007), 'A rigorous, engineer-friendly approach for modelling realistic composite rotor blades', *Wind Energy*, 10, 179–93.

IEC61400-1 (2005), *Wind Turbines – Part 1: Design Requirements*, International Electrotechnical Commission, Geneva, Switzerland.

IEC61400-3 (2005), *Wind Turbines – Part 3: Design Requirements for Offshore Wind Turbines, IEC TC88 WG3*, International Electrotechnical Commission, Geneva, Switzerland.

Johnson, W (1980), *Helicopter Theory*, Princeton University Press, Princeton, NJ.

Jonkman, J M (2005), *NREL 5 MW Baseline Wind Turbine*, Technical report, NREL/NWTC.

Jonkman, J M and Buhl, M L Jr. (2007), 'Development and verification of a fully coupled simulator for offshore wind turbines', *AIAA Paper 2007–0212, 45th AIAA Aerospace Sciences Meeting and Exhibition, Wind Energy Symposium*, Reno, Nevada, 8–11 January.

Jonkman, J M and Sclavounos, P D (2006), 'Development of fully coupled aeroelastic and hydrodynamic models for offshore wind turbines', *AIAA Paper 2006–0995, 44th AIAA Aerospace Sciences Meeting and Exhibition, Wind Energy Symposium*, Reno, Nevada, 10–12 January.

Kaimal, J C, Wyngaard, J C, Izumi, Y and Cote, O R (1972), 'Spectral characteristics of surface-layer turbulence', *Quarterly Journal of the Royal Meteorological Society*, 98, 563–98.

Kallesøe, B S (2007), 'Equations of motion for a rotor blade, including gravity pitch action and rotor speed variations', *Wind Energy*, 10, 207–30.

Kallesøe, B S and Hansen, M H (2010), 'Lateral tower load mitigation by generator torque control', *Paper AIAA 2010–1001 presented at 48th AIAA Aerospace Sciences Meeting Including the New Horizons Forum and Aerospace Exposition*, 4–7 January, Orlando, FL.

Kristensen, L and Frandsen, S (1982), 'Model for power spectra of the blade of a wind turbine measured from the moving frame of reference', *Journal of Wind Engineering and Industrial Aerodynamics*, 10(2), 249–62.

Larsen, G C, Madsen, H Aa, Thomsen, K and Larsen, T J (2008), 'Wake meandering: a pragmatic approach', *Wind Energy*, 11, 377–95.

Larsen, T J (Ed.) (2009), *How 2 Hawc2, the User's Manual*. Risø-r-1597 (ver.3–7)(en), Risø National Laboratory, Roskilde, Denmark.

Larsen, T J, Hansen, A and Buhl, T (2004), 'Aeroelastic effects of large blade deflections for wind turbines', *Proceedings of the special topic conference: The science of making torque from wind*, Roskilde, Denmark, pp. 238–46.

Larsen, T J, Madsen, H Aa, Hansen, A M and Thomsen, K (2005), 'Investigation of stability effects of an offshore wind turbine using the new aeroelastic code HAWC2', *Proceedings (CD-ROM), Copenhagen Offshore Wind Conference 2005*, 25–28 September, Copenhagen, p. 6.

Larsen, T J, Madsen, H Aa and Thomsen, K (2004), 'Active load reduction using individual pitch, based on local blade flow measurements, *Wind Energy*, 8, 67–80.

Larsen, T J, Madsen, H Aa, Thomsen, K and Rasmussen, F (2007), 'Reduction of teeter angle excursions for a two-bladed downwind rotor using cyclic pitch control', *Proceedings of the 2007 European Wind Energy Conference and Exhibition, Milan (IT)*, EWEA, Brussels, 7–10 May, p. 9.

Leishman, J G and Crouse, G L (1989), *State-Space Model for Unsteady Airfoil Behavior and Dynamic Stall*, AIAA Paper 89–1319 CP.

Lobitz, D W (2005), 'Parameter sensitivities affecting the flutter speed of a MW-sized blade', *Journal of Solar Energy Engineering, Transaction of the ASME 2005*, 127, 538–43.

Madsen, H Aa, Larsen, G C, Mikkelsen, R and Troldborg, N (2008), 'Wake deficit and turbulence simulated with two models compared with inflow measurements on a 2 MW wind turbine in wake conditions', *Proceedings from EWEC2008*, 31 March – 3 April 2008, Scientific Track, Brussels, Belgium.

Mann, J (1994), 'The spatial structure of neutral atmospheric surface-layer turbulence', *Journal of Fluid Mechanics*, 273, 141–68.

Mann, J (1998), 'Wind field simulation', *Probabilistic Engineering Mechanics*, 13(4), 269–82.

Markou, H, Hansen, M H, Buhl, T, Engelen, T van, Politis, E S, Riziotis, V A, *et al*. (2007), 'Aeroelastic stability and control of large wind turbines – main results', *Proceedings of the 2007 European wind energy conference and exhibition*, 7–10 May 2007, Milan, Italy.

Petersen, J T, Madsen, H Aa, Björck, A, Enevoldsen, P, Øye, S, Ganander, H, *et al*. (1998), *Prediction of Dynamic Loads and Induced Vibrations in Stall. Risø-R-1045(EN)*, Risø National Laboratory, Roskilde, Denmark.

Petot, D (1989), 'Differential equation modelling of dynamic stall', *Recherché Aerospatiale*, 5, 59–72.

Politis, E S, Chaviaropoulos, P K, Riziotis, V A, Voutsinas, S G and Romero-Sanz, I (2009), 'Stability analysis of parked wind turbine blades', *Proceedings of the EWEC 2009*, 16–19 March, Scientific Track, Marseille, France.

Rasmussen, F, Hansen, M H, Thomsen, K, Larsen, T J, Bertagnolio, F, Johansen, J, *et al*. (2003), 'Present status of aeroelastcity of wind turbines', *Wind Energy*, 6, 213–28.

Riziotis, V A and Voutsinas, S G (1997), 'Gast: a general aerodynamic and structural prediction tool for wind turbines', *Proceedings of the EWEC 1997*, October 1997, Dublin, Ireland, pp. 448–52.

Riziotis, V A and Voutsinas, S G (2006), 'Advanced aeroelastic modeling of complete wind turbine configurations in view of assessing stability characteristics', *Proceedings of the EWEC*, 27 February–2 March, Scientific Track, Athens, Greece.

Riziotis, V A, Voutsinas, S G, Politis, E S and Chaviaropoulos, P K (2004), 'Aeroelastic stability of wind turbines: the problem the methods and the issue', *Wind Energy*, 7, 373–92.

Riziotis, V A, Voutsinas, S G, Politis, E S, Chaviaropoulos, P K, Hansen, A M, Madsen, H A, *et al*. (2008), 'Identification of structural non-linearities due to large deflections on a 5 MW wind turbine blade', *Proceedings of the EWEC*, 31 March–3 April, Scientific Track, Brussels, Belgium.

Schepers(editor), J G, Heijdra, J J, Foussekis, D, Øye, S, Rawlinson Smith, R, Belessis, M, *et al*. (2002), *Verification of European Wind Turbine Design Codes, VEWTDC: Final Report*. Technical report ECN-C-01-055, Netherlands Energy Research Foundation ECN. Available from: http://www.ecn.nl/publicaties/default.aspx?nr=ECN-C-01-055 [Accessed 7 Feb 2010].

Thomsen, K and Madsen, H Aa (2004), 'A new simulation method for turbines in wake – applied to extreme response during operation', *Wind Energy*, 8, 35–47.

Thomsen, K, Petersen, J T, Nim, E, Øye, S and Petersen B A (2000), 'A method for determination of damping for edgewise blade vibrations', *Wind Energy*, 3, 233–46.

Zienkiewicz, O C and Taylor, R L (1994), *The Finite Element Method Volume 1 and 2*, McGraw-Hill, London.

3

Aeroelasticity and structural dynamics of wind turbines

V. A. RIZIOTIS, National Technical University of Athens, Greece and H. A. MADSEN, Risø DTU, The National Laboratory for Sustainable Energy at the Technical University of Denmark, Denmark

Abstract: In the present chapter, the aeroelastic modeling and optimized design of modern megawatt-scale wind turbines are addressed. In the first part of the chapter, the aeroelastic equations of motion for the flexible wind turbine components and the dynamics of the full wind turbine system are presented in the context of beam theory, multi-body dynamic analysis and finite element method. In the second part, the main aspects relating to an improved aeroelastic design are discussed. First, the nature of the external loads on a wind turbine is described. Then, aeroelastic instability problems encountered in the past or expected in future designs, methods for improving the aeroelastic behavior of wind turbines and some future trends concerning aeroelastic design are discussed.

Key words: aeroelasticity, damping, instability, loads, design.

3.1 Introduction

The wind turbine is a flexible structure that operates mainly under the action of the aerodynamic loads on the rotor. The airflow passing through the rotor, besides rotating the blades, also deforms the whole structure. As the wind turbine deforms, the elastic motion of the various components affects the aerodynamic loading, which in turn differentiates the deformation field. In this way, the coupled aerodynamic–structural dynamic problem is formed.

Aeroelastic analysis of a wind turbine lies in determining the elastic deflections and internal loads along the various components, arising from its interaction with the incoming wind. It is understood that this is a very important task in the design process since it provides the design limits for the dimensioning of the individual components. However, given the stochastic nature of the wind, the unsteadiness of the flow over the rotor blades, the complex structure of the blades and the different degrees of freedom (DOFs) of motion undergone by the various components (rotor rotation, blades pitching, nacelle yaw, etc.), it is also understood that it is by no means an easy task.

The present chapter consists of two parts. In the first part, the modeling of the wind turbine structural dynamics and aeroelastics is described in the context of the beam theory and finite element analysis, as applied in most current design and analysis tools. In the second part, the main aspects toward improved aeroelastic design are discussed. This part begins with describing the nature of the external

loads on a wind turbine. Then, aeroelastic instability problems encountered in the past or expected in the future designs, methods for improving aeroelastic behavior of wind turbines and some future trends concerning aeroelastic design are discussed.

3.2 Structural dynamics of wind turbines

3.2.1 Finite element method (FEM) modeling of the wind turbine components using beam theory

One-dimensional approximation of solid structures (beam theory) is probably the most widely used modeling approach for wind turbine applications. Most existing structural dynamics and aeroelastic design tools (Schepers *et al*., 2002) are based on this approach for the structural modeling of the flexible components of the wind turbine (i.e., blades, tower, shaft). The basic limitation is that the structure must be slender in shape or else that one of the dimensions must be significantly larger than the other two. Regular asymptotic analysis justifies elimination of the dependence on the two shortest dimensions, and thus, formulation of the problem can be performed only with respect to the remaining third. In the direction of this dominant dimension of the structure, the elastic axis of the beam is defined that is usually assumed to be rectilinear [curved beam axis has also been dealt with by Hodges (2003)]. In the near past, first-order, non-linear beam models, or even linearized modal-based methods, were employed in most state-of-the-art design tools for wind turbines, suggesting small or moderate deflections. With the increasing size and flexibility of modern turbines, the necessity for higher order models that account for large deflections has emerged and models of this type have been very recently implemented in aeroelastic codes (Riziotis and Voutsinas, 2006; Kallesøe, 2007; Riziotis *et al*., 2008). The main aspects of the non-linear beam theory, including analysis of highly flexible beams undergoing large deflections, are discussed in the present section.

Also, the finite element method (FEM) for the numerical discretization of the beam differential equations is presented.

Kinematics of the beam

Let Oxyz be the global coordinate system of the beam (see Fig. 3.1). The y axis of the system is aligned to the axis of the beam (shear center axis) while x and z axes lie in the cross-section plane of the undeformed beam, defining the two bending directions of the beam. The $O'\xi_0\eta_0\zeta_0$ is the local coordinate system of the undeformed cross-section (Fig. 3.1), where the ξ_0 and ζ_0 are rotated with respect to the global x and z axes only for the section pre-twist. Finally, $O_1\ \xi\eta\zeta$ is the local coordinate system of the deformed cross-section (Fig. 3.1). The analysis presented in the sequel is based on the assumptions of the Euler–Bernoulli beam theory (Hodges and

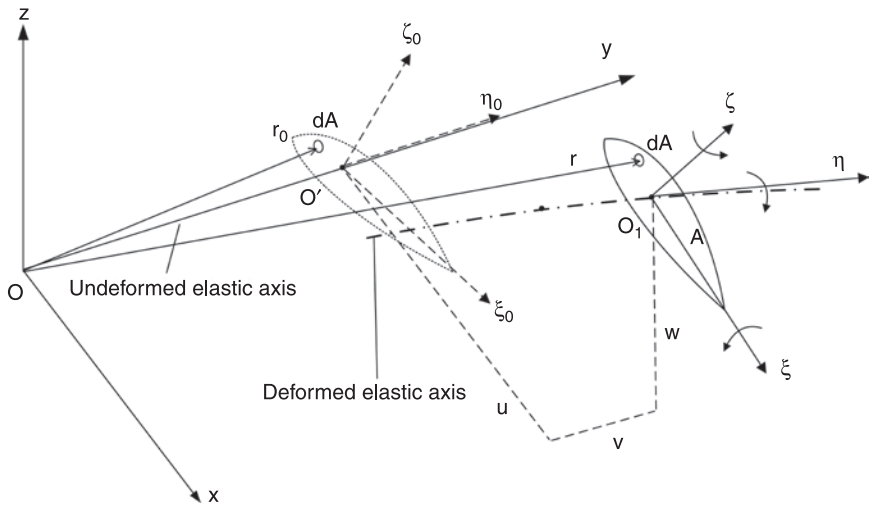

3.1 Kinematics of a beam structure.

Dowell, 1974). According to Euler–Bernoulli hypotheses, every cross-section along the beam can only translate and rotate uniformly under the action of external bending, axial and torsion loads. However, it always remains planar and its shape remains undistorted. This is a reasonable assumption, taking into account that for beam structures, the cross-section dimensions are relatively small compared to the beam-wise dimension. Moreover, cross-sections of the beam rotate in such a way that they always remain perpendicular to the deformed elastic axis. This means that rotation of the sections results only from the bending of the structure, and therefore, deformations due to traverse shear are neglected. In such a way, a direct relation between bending displacements and rotations can be derived.

The position vector **r** of any arbitrary point along the beam at the deformed state is given by the following general expression:

$$\mathbf{r} = \begin{Bmatrix} 0 \\ y \\ 0 \end{Bmatrix} + \begin{Bmatrix} u \\ v \\ w \end{Bmatrix} + \mathbf{E} \cdot \begin{Bmatrix} \xi \\ 0 \\ \zeta \end{Bmatrix} \qquad [3.1]$$

where u and w are the two bending displacements in the direction of the global x and z axes, respectively, while v is the axial displacement of the cross-sections initially located at the y axial position. The **E** matrix is the transformation matrix from the local coordinates of the deformed section (ξ, η, ζ) to the global coordinates of the beam (x, y, z).

In terms of the Euler angles φ, ψ and ω shown in Fig. 3.2, matrix **E** is written in the following form:

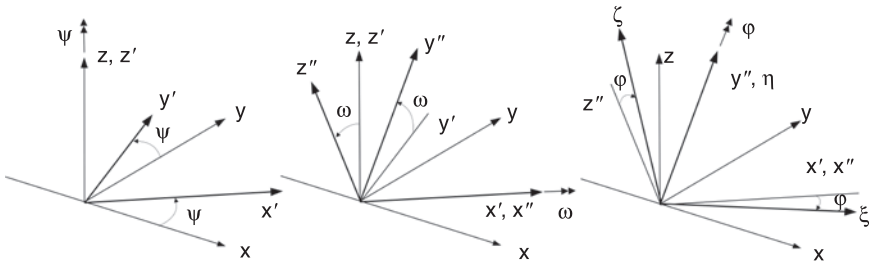

3.2 Transformation from local system of the cross-section to global system of the beam.

$$\mathbf{E} = \begin{pmatrix} \cos\psi & -\sin\psi & 0 \\ \sin\psi & \cos\psi & 0 \\ 0 & 0 & 1 \end{pmatrix} . \begin{pmatrix} 1 & 0 & 0 \\ 0 & \cos\omega & -\sin\omega \\ 0 & \sin\omega & \cos\omega \end{pmatrix} . \begin{pmatrix} \cos\varphi & 0 & \sin\varphi \\ 0 & 1 & 0 \\ -\sin\varphi & 0 & \cos\varphi \end{pmatrix} \qquad [3.2]$$

where ψ and ω are directly related to u and w (the two bending displacements), while φ represents the torsion deformation plus the cross-section pre-twist.

Following an ordering scheme in which terms up to second-order accuracy are retained (Hodges and Dowell, 1974) in expressing Euler angles in terms of the bending displacement fields u and w, matrix $\mathbf{E}$ can be written in the following form:

$$\mathbf{E} = \begin{bmatrix} \cos(\theta_t + \hat{\theta} - u'w') \cdot \left(1 - \frac{u'^2}{2}\right) & u' & \sin(\theta_t + \hat{\theta} - u'w') \cdot \left(1 - \frac{u'^2}{2}\right) \\ -u'\cos(\theta_t + \hat{\theta}) + w'\sin(\theta_t + \hat{\theta}) & 1 - \frac{u'^2}{2} - \frac{w'^2}{2} & -u'\sin(\theta_t + \hat{\theta}) - w'\cos(\theta_t + \hat{\theta}) \\ -\sin(\theta_t + \hat{\theta}) \cdot \left(1 - \frac{w'^2}{2}\right) & w' & \cos(\theta_t + \hat{\theta}) \cdot \left(1 - \frac{w'^2}{2}\right) \end{bmatrix}$$

[3.2a]

In equation [3.2a], $(\quad)'$ denotes the spatial derivative with respect to the beam-wise coordinate y. Moreover, θ_t is the blade local pre-twist, θ is the twisting deformation with respect to the global beam axis y and $\hat{\theta} = \theta + \int_0^y u''w'\,dy$ is the local torsion deformation with respect to the local deformed beam axis η (Hodges and Dowell, 1974), such that $\varphi = \hat{\theta} + \theta_t$.

If second-order terms are dropped, then equation [3.2a] is significantly simplified and takes the form (first-order accurate):

$$\mathbf{E} = \begin{bmatrix} \cos\theta_t - \sin\theta_t \cdot \theta & u' & \sin\theta_t + \cos\theta_t \cdot \theta) \\ -u'\cos\theta_t + w'\sin\theta_t & 1 & -u'\sin\theta_t - w'\cos\theta_t \\ -\sin\theta_t - \cos\theta_t \cdot \theta & w' & -\cos\theta_t - \sin\theta_t \cdot \theta \end{bmatrix} \qquad [3.2b]$$

Equations of structural equilibrium beam equations

On the basis of the above kinematic considerations, the equations of dynamic equilibrium for the beam structure can be derived. Let us consider a differential element of the beam, with cross-section A, and width dy, as shown in Fig. 3.3. The incremental mass of the infinitesimal element dA is dm = ρdA, where ρ is the local mass density of the material of the cross-section (see Fig. 3.3). Let also $\delta\mathbf{P} = \{\delta P_x, \delta P_y, \delta P_z\}^T$ be the external forces per unit length exerted on the element, $d\mathbf{F} = \{dF_x, dF_y, dF_z\}^T$ be the net elastic internal (reaction) forces, $\mathbf{g} = \{g_x, g_y, g_z\}^T$ be the acceleration of gravity, and $\mathbf{p}^i = \{p_x^i, p_y^i, p_z^i\}^T$ and $\mathbf{p}^e = \{p_x^e, p_y^e, p_z^e\}^T$ be the total inertial and external forces, respectively. Then, the balance of forces with respect to the blade local coordinate system Oxyz is written as follows:

$$\underbrace{\left(\int_A \rho \cdot dA \cdot \ddot{\mathbf{r}}\right) dy}_{p^i \cdot dy} = d\mathbf{F} + \underbrace{\left(\int_A \rho \cdot dA \cdot \mathbf{g}\right) dy + \delta\mathbf{P}\, dy}_{p^e \cdot dy} \qquad [3.3]$$

Similarly, the balance of the moments with reference to the origin (1) of the incremental element dy (see Fig. 3.3) is written as:

$$\underbrace{\left(\int_A \rho \cdot dA \cdot \mathbf{r}_p \times \ddot{\mathbf{r}}\right) dy}_{q^i dy} = d\mathbf{M} + d\mathbf{r}_e \times (\mathbf{F} + d\mathbf{F}) + \underbrace{\left(\int_A \rho \cdot dA \cdot \mathbf{r}_p \times \mathbf{g}\right) dy + \mathbf{r}_a \times \delta\mathbf{P}\, dy}_{q^e dy} \qquad [3.4]$$

In equation [3.4], $\mathbf{F} + d\mathbf{F}$ is the vector of the resultant elastic force at the end point (2), $d\mathbf{M} = \{dM_x, dM_y, dM_z\}^T$ is the net elastic moments of the element, $\mathbf{q}^i = \{q_x^i, q_y^i, q_z^i\}^T$ and $\mathbf{q}^e = \{q_x^e, q_y^e, q_z^e\}^T$ are the inertial and external moments acting on the element, respectively, and $\mathbf{r_a}$ is the local position of the external forces,

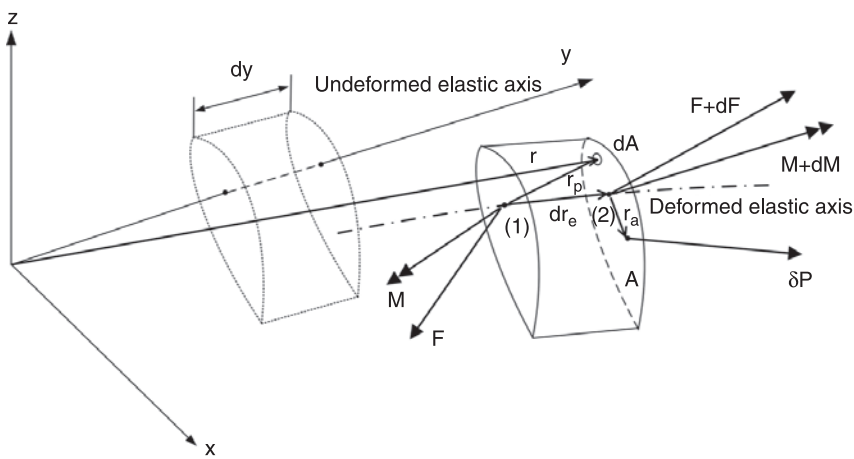

3.3 Dynamics of a beam structure.

centre with respect to the elastic axis of the beam. Moreover, $\mathbf{r_p} = \mathbf{r} - \mathbf{r_e^{(1)}}$ and $d\mathbf{r_e} = \mathbf{r_e^{(2)}} - \mathbf{r_e^{(1)}}$ where $\mathbf{r_e}$ is the position vector of a point on the deformed elastic axis, while indices (1) and (2) indicate the beginning and end of the differential element dy, respectively. The position vector $\mathbf{r_e}$ is given by:

$$\mathbf{r}_e = \begin{Bmatrix} 0 \\ y \\ 0 \end{Bmatrix} + \begin{Bmatrix} u \\ v \\ w \end{Bmatrix} \quad [3.5]$$

The vector equation [3.3] and equation [3.4] of equilibrium are analyzed in components relative to the undeformed axes x, y and z. The force equations are written as:

$$p_x^i = F_x' + p_x^e \quad [3.6a]$$

$$p_y^i = F_y' + p_y^e \quad [3.6b]$$

$$p_z^i = F_z' + p_z^e \quad [3.6c]$$

Similarly, the moment equations are written as:

$$q_x^i = M_x' + F_z - F_y w' + q_x^e \quad [3.7a]$$

$$q_y^i = M_y' - F_z u' + F_x w' + q_y^e \quad [3.7b]$$

$$q_z^i = M_z' - F_x + F_y u' + q_z^e \quad [3.7c]$$

As already stated, traverse shear is neglected in the present analysis. Under the assumption of very high shear rigidity (negligible shear deformations), the cross-sections of the beam remain perpendicular to the deformed elastic axis, and therefore bending rotations (angles ψ and ω) are not independent variables of the problem. Therefore, the two bending moment equation [3.7a] and [3.7c] are used for eliminating spatial derivatives of the internal shear forces F_x' and F_z' from equation [3.6c] and [3.6a], respectively. Thereby, the six equilibrium equations can be reduced to four equations for the four independent deflections u, v, w and θ defined with reference to the undeformed system:

$$p_x^i (q_z^i)' = M_z'' + (F_y u')' + p_x^e + (q_z^e)' \quad \text{(force } x\text{)} \quad [3.8a]$$

$$p_y^i = F_y' + p_y^e \quad \text{(force } y\text{)} \quad [3.8b]$$

$$p_z^i - (q_x^i)' = -M_x'' + (F_y w')' + p_z^e - (q_x^e)' \quad \text{(force } z\text{)} \quad [3.8c]$$

$$q_y^i + q_x^i u' + q_z^i w' = M_y' + M_x u' + M_z w' + q_y^e + q_x^e u' + q_z^e w' \quad \text{(moment } y\text{)} \quad [3.8d]$$

To close the system [3.8], expressions for the resultant internal loads, as functions of the unknown deflections field, must be defined. The internal loads are obtained by integrating stresses over the cross-section surface. Stresses, in turn, are related to strains and thereby to elastic deflections through Hooke's law.

The strain tensor ε based on Green's (Crisfield, 1998) definition is determined by:

$$d\mathbf{r}^{T}\cdot d\mathbf{r} - d\mathbf{r}_{0}^{T}\cdot d\mathbf{r}_{0} = 2\cdot\{d\xi \quad d\eta \quad d\zeta\}\cdot\begin{bmatrix}\varepsilon_{\xi\xi} & \varepsilon_{\xi\eta} & \varepsilon_{\xi\zeta}\\ \varepsilon_{\eta\xi} & \varepsilon_{\eta\eta} & \varepsilon_{\eta\zeta}\\ \varepsilon_{\zeta\xi} & \varepsilon_{\zeta\eta} & \varepsilon_{\zeta\zeta}\end{bmatrix}\cdot\begin{Bmatrix}d\xi\\ d\eta\\ d\zeta\end{Bmatrix} \qquad [3.9]$$

Furthermore, under the assumption of a homogeneous and isotropic material, Hooke's law takes the form:

$$\begin{Bmatrix}\sigma_{\eta\eta}\\ \sigma_{\eta\xi}\\ \sigma_{\eta\zeta}\end{Bmatrix} = \begin{bmatrix}E & 0 & 0\\ 0 & G & 0\\ 0 & 0 & G\end{bmatrix}\cdot\begin{Bmatrix}\varepsilon_{\eta\eta}\\ \varepsilon_{\eta\xi}\\ \varepsilon_{\eta\zeta}\end{Bmatrix} \qquad [3.10]$$

Equation [3.9] yields the strain displacement expressions. By retaining terms up to second order, the following relationships are obtained:

$$\varepsilon_{\eta\eta} = v' + \underline{\frac{u'^{2}}{2} + \frac{w'^{2}}{2}} + \underline{(\xi^{2}+\zeta^{2})\cdot\left(\theta_{t}'\theta'\frac{\theta'^{2}}{2}\right)}$$
$$-u''\cdot\left(\xi\cdot\cos(\theta_{t}+\underline{\hat{\theta}}) + \zeta\cdot\sin(\theta_{t}+\underline{\hat{\theta}})\right) + w''\cdot\left(\xi\cdot\sin(\theta_{t}+\underline{\hat{\theta}}) - \zeta\cdot\cos(\theta_{t}+\underline{\hat{\theta}})\right) \qquad [3.11a]$$

$$\varepsilon_{\eta\xi} = \frac{1}{2}\zeta\cdot\theta' \qquad [3.11b]$$

$$\varepsilon_{\eta\zeta} = \frac{1}{2}\xi\cdot\theta' \qquad [3.11c]$$

Accordingly, equation [3.10] and equation [3.11] provide stress deflection relationships.

By integrating normal and shear stresses over the cross-section surface, the resultant loads with respect to the local deformed coordinate system are determined (second-order accurate as well):

Axial force F

$$F_{\eta} = \int_{A}\sigma_{\eta\eta}\,dA = EA\left(v' + \underline{\frac{u'^{2}}{2} + \frac{w'^{2}}{2}}\right) + \underline{EI_{t}\cdot\left(\theta_{t}'\theta' + \frac{\theta'^{2}}{2}\right)}$$
$$-u''\cdot\left(EA_{\zeta}\cdot\cos(\theta_{t}+\underline{\hat{\theta}}) + EA_{\xi}\cdot\sin(\theta_{t}+\underline{\hat{\theta}})\right) + w''\cdot\left(EA_{\zeta}\cdot\sin(\theta_{t}+\underline{\hat{\theta}}) + EA_{\xi}\cdot\cos(\theta_{t}+\underline{\hat{\theta}})\right) \qquad [3.12a]$$

Bending moment ξ

$$M_{\xi} = -\int_{A}\zeta\cdot\sigma_{\eta\eta}\,dA = EI_{\xi\xi}\cdot\left(\sin(\theta_{t}+\underline{\hat{\theta}})\cdot u'' + \cos(\theta_{t}+\underline{\hat{\theta}})\cdot w''\right)$$
$$- EA_{\xi}\left(v' + \underline{\frac{u'^{2}}{2} + \frac{w'^{2}}{2}}\right) + \underline{EI_{t\xi}\cdot\left(\theta_{t}'\theta' + \frac{\theta'^{2}}{2}\right)} \qquad [3.12b]$$

Bending moment ζ

$$M_\xi = \int_A \xi \cdot \sigma_{\eta\eta}\, dA = -EI_{\zeta\zeta} \cdot \left(\cos(\theta_t + \hat{\underline{\theta}}) \cdot u'' + \sin(\theta_t + \hat{\underline{\theta}}) \cdot w''\right) + EA_\zeta \left(v' + \underline{\frac{u'^2}{2} + \frac{w'^2}{2}}\right) + \underline{EI_{t\zeta} \cdot \left(\theta_t' \theta' + \frac{\theta'^2}{2}\right)} \quad [3.12c]$$

Torsion moment η

$$\begin{aligned} M_\eta &= \int_A \left(\zeta \cdot \sigma_{\eta\xi} - \xi \cdot \sigma_{\eta\zeta}\right) dA + (\theta_t' + \theta') \cdot \int_A \left(\zeta^2 + \xi^2\right) \sigma_{\eta\eta} \cdot dA \\ &= GI_t \cdot \theta' + \underline{EI_t \cdot (\theta_t' + \theta') \cdot \left(v' + \frac{u'^2}{2} + \frac{w'^2}{2}\right)} + \underline{EI_{t2} \cdot \theta_t'^2 \cdot \theta'} \\ &\quad - \underline{\left(\left(EI_{t\xi} \cdot \cos(\theta_t + \hat{\theta}) + EI_{t\xi} \cdot \sin(\theta_t + \hat{\theta})\right) \cdot u''\right.} \\ &\quad + \underline{\left.\left(EI_{t\xi} \cdot \cos(\theta_t + \hat{\theta}) - EI_{t\zeta} \cdot \sin(\theta_t + \hat{\theta})\right) \cdot w''\right) \cdot (\theta_t' + \theta')} \end{aligned} \quad [3.12d]$$

In deriving equation [3.12], the assumption that the local axes ξ and ζ coincide with the principal axes of the cross-section is made. The structural properties of the beam involved in equation [3.12] are defined as follows:

$$EA = \int_A E \cdot dA,\ EA_\xi = \int_A E \cdot \zeta\, dA,\ EA_\zeta = \int_A E \cdot \xi\, dA,\ EI_{\xi\xi} = \int_A E \cdot \zeta^2\, dA,\ EI_{\zeta\zeta} = \int_A E \cdot \xi^2\, dA,$$

$$GI_t = \int_A G \cdot (\xi^2 + \zeta^2)\, dA,\ EI_t = \int_A E \cdot (\xi^2 + \zeta^2)\, dA,\ EI_{t2} = \int_A E \cdot (\xi^2 + \zeta^2)^2\, dA,$$

$$EI_{t\xi} = \int_A E \cdot \zeta \cdot (\xi^2 + \zeta^2)\, dA,\ \ EI_{t\zeta} = \int_A E \cdot \xi \cdot (\xi^2 + \zeta^2)\, dA$$

In equation [3.11] and equation [3.12], the underlined terms are the non-linear second-order ones. By omitting those terms, standard first-order linear expressions are obtained.

The reaction loads (forces and moments) of equation [3.12] are expressed in the local deformed system $O_1\xi\eta\zeta$. Therefore, before being substituted in equation [3.8], they have to be transformed in Oxyz. This is done through the rotation matrix **E** given by the equation [3.2]. In this way, the final system of the second-order beam equations is derived:

Force x

$$\begin{aligned} &p_x^i + \left(q_z^i\right)' - p_x^e - \left(q_z^e\right)' = \left(M_\zeta \cdot \cos(\theta_t + \hat{\theta}) - M_\xi \sin(\theta_t + \hat{\theta})\right)'' + \left(F_\eta u'\right)' \\ &= \left(\left(EA_\zeta \cdot \cos(\theta_t + \hat{\underline{\theta}}) + EA_\xi \cdot \sin(\theta_t + \hat{\underline{\theta}})\right) \cdot \left(v' + \underline{\frac{u'^2}{2} + \frac{w'^2}{2}}\right)\right. \\ &\quad - \left(EI_{\zeta\zeta} \cdot \cos^2(\theta_t + \hat{\underline{\theta}}) + EI_{\xi\xi} \cdot \sin^2(\theta_t + \hat{\underline{\theta}})\right) \cdot u'' - \frac{1}{2}\left(EI_{\xi\xi} - EI_{\zeta\zeta}\right) \cdot \sin(2 \cdot (\theta_t + \hat{\underline{\theta}})) \cdot w'' \\ &\quad + \underline{\left.\left(EI_{t\zeta} \cdot \cos(\theta_t + \hat{\underline{\theta}}) + EI_{t\xi} \cdot \sin(\theta_t + \hat{\underline{\theta}})\right) \cdot \theta_t \theta'\right)''} + \left(F_\eta u'\right)' \end{aligned} \quad [3.13a]$$

Force y

$$p_y^i - p_y^e = F_\eta'$$

$$= \left(EA\left(v' + \underline{\underline{\frac{u'^2}{2} + \frac{w'^2}{2}}} \right) + \underline{\underline{EI_t \cdot \left(\theta_t' \theta' + \frac{\theta'^2}{2} \right)}} \right.$$

$$- u'' \cdot \left(EA_\zeta \cdot \cos(\theta_t + \underline{\hat{\theta}}) + EA_\xi \cdot \sin(\theta_t + \underline{\hat{\theta}}) \right)$$

$$\left. + w'' \cdot \left(EA_\zeta \cdot \sin(\theta_t + \underline{\hat{\theta}}) - EA_\xi \cdot \cos(\theta_t + \underline{\hat{\theta}}) \right)' \right) \qquad [3.13b]$$

Force z

$$p_z^i - \left(q_x^i\right)' - p_z^e + \left(q_z^e\right)' = -\left(M_\xi \cdot \cos(\theta_t + \hat{\theta}) + M_\zeta \sin(\theta_t + \hat{\theta})\right)'' + \left(F_\eta w'\right)'$$

$$= \left(\left(EA_\xi \cdot \cos(\theta_t + \underline{\hat{\theta}}) + EA_\zeta \cdot \sin(\theta_t + \underline{\hat{\theta}}) \right) \cdot \left(v' + \underline{\frac{u'^2}{2} + \frac{w'^2}{2}} \right) \right.$$

$$- \frac{1}{2}\left(EI_{\xi\xi} - EI_{\zeta\zeta}\right) \cdot \sin(2 \cdot (\theta_t + \underline{\hat{\theta}})) \cdot u'' - \left(EI_{\xi\xi} \cdot \cos^2(\theta_t + \underline{\hat{\theta}}) + EI_{\zeta\zeta} \cdot \sin^2(\theta_t + \underline{\hat{\theta}})\right) \cdot w''$$

$$\left. + \underline{\left(EI_{t\xi} \cdot \cos(\theta_t + \hat{\theta}) + EI_{t\zeta} \cdot \sin(\theta_t + \hat{\theta})\right) \cdot \theta_t \theta'} \right)'' + \left(F_\eta w'\right)' \qquad [3.13c]$$

Moment y

$$q_y^i + q_x^i u' + q_z^i w' - q_y^e + q_x^e u' + q_z^e w' =$$

$$M_\eta' - M_\xi \left(\cos(\theta_t + \hat{\theta}) \cdot u'' - \sin(\theta_t + \hat{\theta}) \cdot w''\right) - M_\zeta \left(\sin(\theta_t + \hat{\theta}) \cdot u'' + \cos(\theta_t + \hat{\theta}) \cdot w''\right)$$

$$= \left(GI_t \theta' + \underline{\underline{EI_t \cdot (\theta_t' + \theta') \cdot \left(v' + \frac{u'^2}{2} + \frac{w'^2}{2} \right)}} + \underline{EI_{t2} \cdot \theta_t'^2 \cdot \theta'} \right.$$

$$- \underline{\left(\left(EI_{t\zeta} \cdot \cos(\theta_t + \hat{\theta}) + EI_{t\xi} \cdot \sin(\theta_t + \hat{\theta}) \right) \cdot u'' \right.}$$

$$\left. \left. + \underline{\left(EI_{t\xi} \cdot \cos(\theta_t + \hat{\theta}) - EI_{t\zeta} \cdot \sin(\theta_t + \hat{\theta}) \right) \cdot w'' \right) \cdot (\theta_t' + \theta')} \right)'$$

$$+ \underline{\left(EA_\xi \cdot \cos(\theta_t + \hat{\theta}) - EA_\xi \cdot \sin(\theta_t + \hat{\theta}) \right) \cdot \left(v' + \frac{u'^2}{2} + \frac{w'^2}{2} \right) \cdot u''}$$

$$- \underline{\left(EA_\zeta \cdot \cos(\theta_t + \hat{\theta}) + EA_\xi \cdot \sin(\theta_t + \hat{\theta}) \right) \cdot \left(v' + \frac{u'^2}{2} + \frac{w'^2}{2} \right) \cdot w''}$$

$$- \underline{\underline{\frac{1}{2}\left(EI_{\xi\xi} - EI_{\zeta\zeta}\right) \cdot \sin(2 \cdot (\theta_t + \hat{\theta})) \cdot \left(u''^2 - w''^2\right)}}$$

$$- \underline{\underline{\left(EI_{\xi\xi} - EI_{\zeta\zeta}\right) \cdot \cos(2 \cdot (\theta_t + \hat{\theta})) \cdot u'' \cdot w''}} \qquad [3.13d]$$

The left-hand side of equation [3.13] represents inertia and external loads, whereas the right-hand side describes structural internal loads, and it is therefore

associated with the stiffness of the beam. As in the case of strain displacements and internal loads displacements expressions, higher-order non-linear terms are underlined. Terms $(F_\eta \cdot u')'$ and $(F_\eta \cdot w')'$ in force *x* and force *z* equations, though non-linear, are considered as first-order ones. This is because they are expected to contribute significantly, especially in the case of rotating beams where axial loads increase due to the centrifugal effect. The two terms give rise to virtual stiffening of the beam as the rotational speed increases. Among the different second-order structural terms, those appearing in the equation [3.13] are the ones that by experience are expected to be of greater importance as the beam becomes more and more flexible and are also doubly underlined. The second doubly underlined term in equation [3.13b] and the first doubly underlined term in equation [3.13d] correspond to the coupling of the beam torsion with the beam tension. As indicated in equation [3.11a], the torsion of the beam generates axial strains $\varepsilon_{\eta\eta}$ and stresses $\sigma_{\eta\eta}$ and vice versa (see equation [3.12d]), and the axial stresses contribute to the twisting moment M_η. The last four terms in equation [3.13d] are related to bending–torsion coupling. As the bending displacements of the blade increase, the local bending moments, M_ξ and M_ζ, generate torsion moment about the undeformed blade axis *y*, as illustrated in Fig. 3.4. The magnitude of this twisting moment depends primarily on the bending curvatures u'' and w''. It also depends on the offset of the cross-section tension axis from the elastic axis.

The above-mentioned non-linear structural coupling terms are only important when the beam undergoes large deflections. For conventional wind turbine blades, in the megawatt (MW) scale, classical first-order, linear beam theory provides sufficiently good predictions. This is because current wind turbine designs are relatively stiff, so that non-linear beam modeling is not expected to drastically

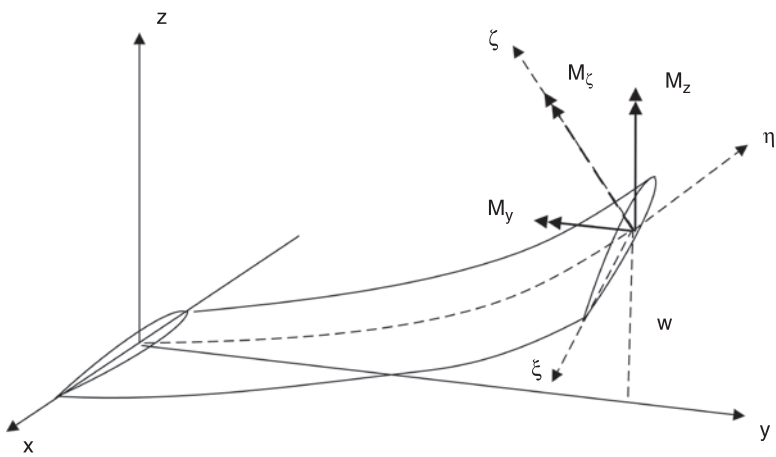

3.4 Explanation of the bending–torsion coupling effect in the case of large flapping deflection.

change the quality of the predictions. However, as the size of the wind turbines increases and the blades become more flexible, adoption of this kind of structural modeling becomes a necessity (Riziotis *et al*., 2008).

The derivation presented in Section 3.2 is based on the application of Newton's second law (Newtonian approach). In view of a more systematic and general framework for formulating dynamic equations, Hamilton's principle has also been used (Hodges, 1990). Nevertheless, the former is selected for the reason that it is much more illustrative and comprehensible for readers who are unfamiliar with the basic concepts of structural dynamics. The above-mentioned non-linear beam model is a specific example amongst several models of varying complexity that have been developed. For example, it is possible to include traverse shear effect by applying Timoshenko theory (Crisfield, 1998) or introduce anisotropy of the cross-sections by upgrading Hooke's law (equation [3.10]) to incorporate off-diagonal elements (Hodges and Yu, 2007). Even the present model can be easily upgraded to model possible distortion of the plane shape of the cross-sections due to torsional deformation (warping effect) (Hodges and Dowell, 1974).

Finite element discretization

The beam equations are fourth order in space with respect to bending and second order with respect to tension and torsion. So, for a finite element (FE) approximation of the equations, C^1 shape functions are used for u and w and C^0 for v and θ. At the element level, u and w are approximated with third-order polynomials and the discrete DOFs are the values and spatial derivatives at the end nodes, while v and θ are approximated with first-order polynomials and the DOFs are again considered at the end nodes of the FE. In the use of second-order beam theory, higher-order polynomials can be used for v and θ, and then additional intermediate nodes are required. So, within an FE 'e',

$$\mathbf{u}_e(y;t) = \mathbf{N}^e(y)\cdot\hat{\mathbf{u}}_e(t) \qquad [3.14]$$

where $\mathbf{u_e}(y;t) = \{u, v, w, \theta\}^T$ is the vector of the independent deflections along the element, $\mathbf{N^e}(y)$ is the shape functions matrix and $\hat{\mathbf{u}}_\mathbf{e}(t)$ is the vector of the DOFs at the nodes of the elements (Bathe, 1996; Crisfield, 1998). By using Galerkin formulation, the discrete form of the equation [3.13] is generated. The set of the four differential equations [3.13] is symbolically represented as $f(\mathbf{u}, \dot{\mathbf{u}}, \ddot{\mathbf{u}}) = 0$. For any admissible virtual displacement field $\delta\mathbf{u} = \{\delta u, \delta v, \delta w, \delta\theta\}^T$, we require that:

$$\int_0^L \delta\mathbf{u}^T\cdot f(\mathbf{u},\dot{\mathbf{u}},\ddot{\mathbf{u}})\cdot dy = \sum_e \int_0^{L_e} \delta\mathbf{u}_e^T\cdot f(\mathbf{u}_e,\dot{\mathbf{u}}_e,\ddot{\mathbf{u}}_e)\cdot dy = 0 \qquad [3.15]$$

Given that $\delta\mathbf{u_e}(y;t) = \delta\hat{\mathbf{u}}_e^T(t)\cdot\mathbf{N^e}(y)$, it follows that:

$$\sum_e \int_0^{L_e} N^{e\,T}\cdot f(\mathbf{N}^e\hat{\mathbf{u}}_e, \mathbf{N}^e\dot{\hat{\mathbf{u}}}_e, \mathbf{N}^e\ddot{\hat{\mathbf{u}}}_e)\cdot dy = 0 \qquad [3.16]$$

which is a set of second-order ordinary differential equations in time with respect to the discrete DOFs $\hat{\mathbf{u}}_e(t)$. Although $f(\mathbf{u}, \dot{\mathbf{u}}, \ddot{\mathbf{u}}) = 0$ contains non-linear terms, it can always be put in the common form:

$$\mathrm{M}(\tilde{\hat{\mathbf{u}}}) \cdot \ddot{\hat{\mathbf{u}}} + \mathrm{C}(\tilde{\hat{\mathbf{u}}}) \cdot \dot{\hat{\mathbf{u}}} + \mathrm{K}(\tilde{\hat{\mathbf{u}}}) \cdot \hat{\mathbf{u}} = \mathrm{Q}(\tilde{\hat{\mathbf{u}}}) \qquad [3.17]$$

where the mass, damping and stiffness matrices as well as the generalized loads in the right-hand side, in general, will depend on the displacement field and its time derivatives (noted by the tilde).

3.2.2 Dynamics of the wind turbine

In the previous section, the equations of the beam structure were derived for the case where the coordinate system Oxyz, attached to the beam, is not moving. In this connection, the beam only deflects with respect to the fixed Oxyz system. Of course, in the case of the wind turbine, the various components (i.e., blades, shaft, tower) not only are deflecting but also undergo rigid body motion of their own (e.g. blades azimuthally rotate and pitch). Also, as a result of being connected to other bodies, they follow the motion (rigid body and elastic) of the bodies attached to them.

The involvement of different body motions for each component, in combination with the fact that certain component-to-component connection points exist, whereby loads and displacements are communicated from one body to another, calls for a global treatment of the dynamic problem. To this end, most works adopt the so-called 'multi-body' approach (Riziotis and Voutsinas, 1997; Larsen, Hansen *et al*., 2004a), which consists of considering each component separately from the others but is subjected to specific free-body boundary kinematic and/or loading conditions that fit the different components into the complete configuration. In the multi-body context, each component *k* is assigned a local coordinate system Oxyz, as defined in Section 3.2.1. The elastic motion of the component with respect to each own system is the one determined through equation [3.1]. All other motions are communicated through appropriate kinematic conditions. Having this in mind, the position vector $\mathbf{r}_{Gk}$ of a point on the *k* component with respect to an inertial reference frame $O_G x_G y_G z_G$ is given by (see Fig. 3.5):

$$\mathbf{r}_{GK} = \rho_k + \mathbf{A}_k \cdot \mathbf{r}_k \qquad [3.18]$$

where ρ_k is the position vector of the origin of Oxyz with respect to the fixed system and $\mathbf{A}_k$ is the local-to-global rotation matrix. The exact form of ρ_k and $\mathbf{A}_k$ not only depends on the kinematic conditions introduced when connecting the body to the complete configuration (e.g. blades to hub or shaft to tower top) but also on the type of its own motion (e.g. pitch of the blades, rotation of the shaft). For each body, a number of kinematic DOFs (consisting of translations and rotations) are introduced that determine ρ_k and $\mathbf{A}_k$. This set of kinematic DOFs is denoted as $\mathbf{q}_k$ and so, $\rho_k = \rho_k(\mathbf{q}_k; t)$ and $\mathbf{A}_k = \mathbf{A}_k(\mathbf{q}_k, t)$. In particular, the vector $\mathbf{q}_k$

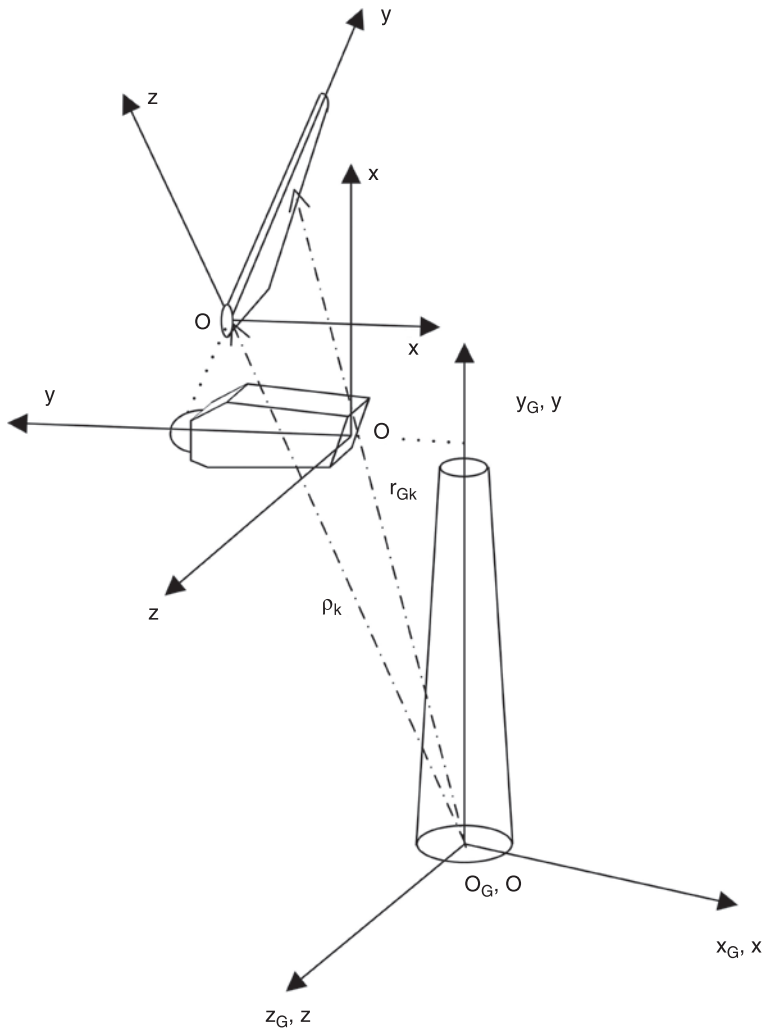

3.5 Wind turbine inertial system and local components systems.

can not only include both large rigid body rotations and translations (controlled or free) but also structural deflections (displacements and rotations) of the bodies attached to the body *k*. For example, the blades follow the structural motion of the tower, and so for the blades, vector **q** will include the tower-top deflections, as illustrated in Fig. 3.6(a). Also, for the blades, **q** will include yaw of the nacelle, rotation of the shaft and pitch rotation, which are all not only DOFs of controlled motion, but also foundation movements (for floating wind turbines) and teeter rotation (for two-blade machines), which are both DOFs of free motion (see Fig. 3.6(b)). From the above discussion, it is obvious that ρ_k is defined as a series

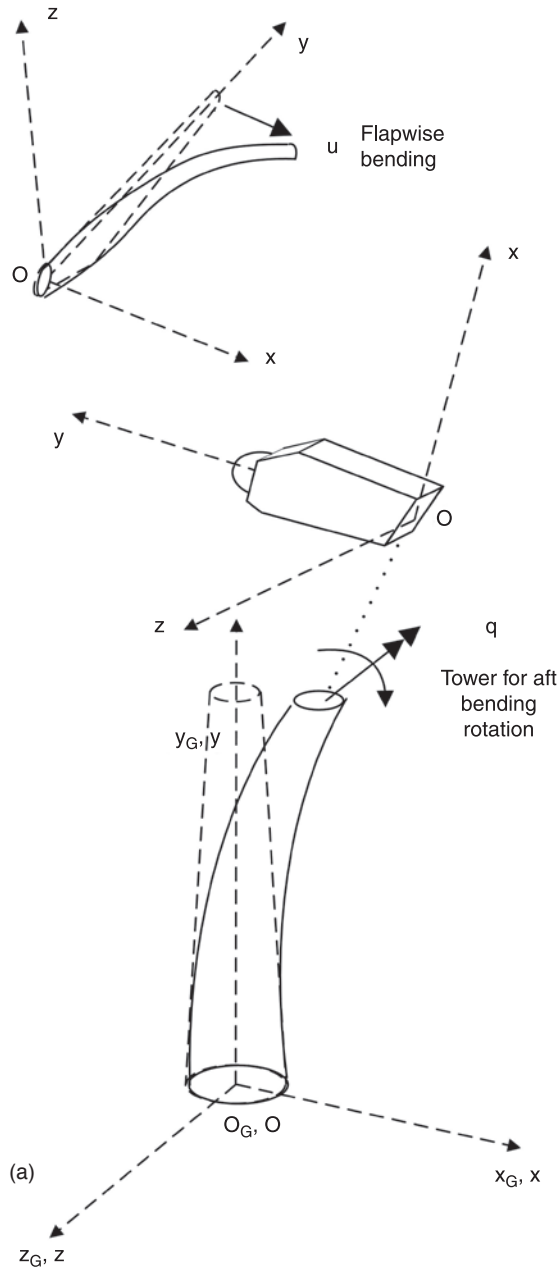

3.6 Realization of multi-body kinematics. (a) DOFs corresponding to elastic deflections.

(*Continued*)

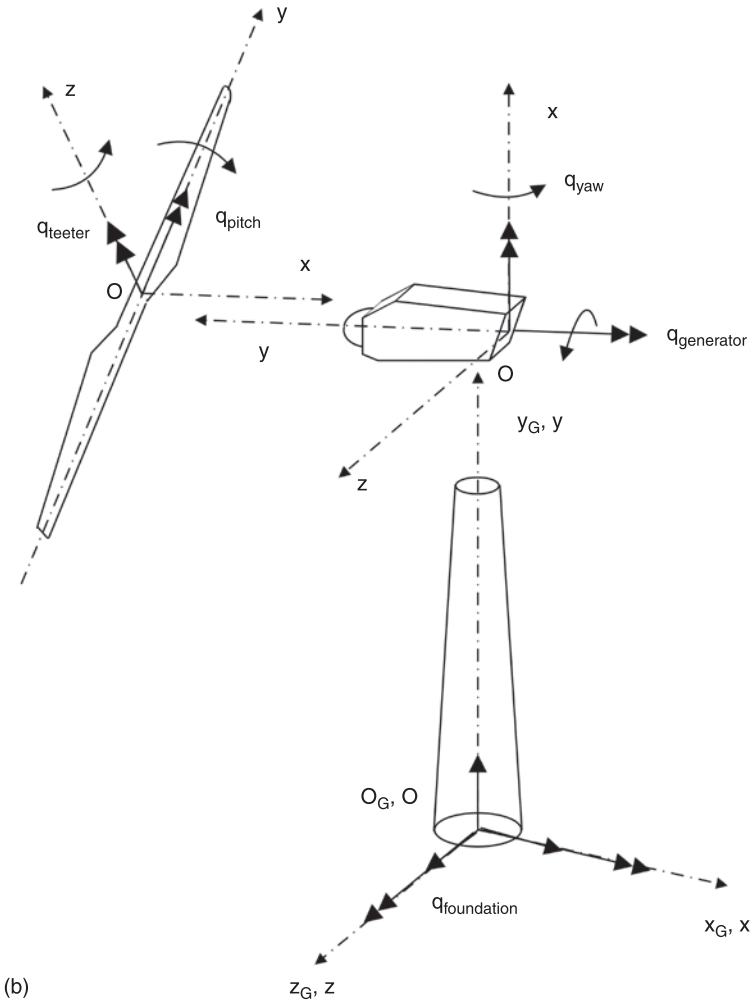

3.6 (b) DOFs corresponding to rigid body free or controlled motion.

of elementary translations and rotations, whereas $\mathbf{A}_k$ is solely defined as a series of elementary rotations. It is also noted that in order to establish a connection between the bodies, besides kinematic conditions, loading conditions should be satisfied. So, it is clear that the bodies contributing the kinematics will in response receive internal (reaction) loads. So, in the previous example, the tower will be subjected to the loads of the nacelle.

The global acceleration of the *k*-th body, expressed with respect to its local system, is then given by:

$$\mathbf{A}_k^T \cdot \ddot{\mathbf{r}}_{GK} = \underbrace{\mathbf{A}_k^T \cdot \ddot{\rho}_k}_{\text{acceleration of the origin}} + \underbrace{\mathbf{A}_k^T \cdot \ddot{\mathbf{A}}_k \cdot \mathbf{r}_k}_{\text{centrifugal acceleration}} + \underbrace{2 \cdot \mathbf{A}_k^T \cdot \dot{\mathbf{A}}_k \cdot \dot{\mathbf{r}}_k}_{\text{Coriolis acceleration}} + \ddot{\mathbf{r}}_k \quad [3.19]$$

By introducing equation [3.19] into equation [3.3] and [3.4], the centrifugal and Coriolis terms of the inertia loads will appear as a result of the time derivatives of $\mathbf{A}_k$. By combining the equations of all components, the complete system of dynamic equations is obtained in the form of equation [3.17] with respect to an extended vector of DOFs that also includes **q** DOFs.

Modal analysis of the structural wind turbine system

The structural characterization of the wind turbine system is provided through identification of the main system natural frequencies. By performing eigenvalue analysis to the dynamic system [3.17], for the full wind turbine configuration, the natural frequencies ω_i and the vibration shapes (mode shapes) Φ_i are obtained. This is done by solving the following eigenvalue problem:

$$\left(\mathrm{K} - \omega_i^2 \mathrm{M}\right) \cdot \Phi_i = 0 \qquad [3.20]$$

It is clear that the natural frequencies of the individual components (considered separately) differ from those obtained when the components are joined together into the full configuration. This is a result of the dynamic coupling taking place between inter connected components. It is noted that identification of the system's natural frequencies is usually performed at standstill because these are the conditions for which measured data usually exist. Nevertheless, given that the rotational speed is rather low, it is not expected to change substantially the distribution of the eigenvalues.

In the sequel description of the first, standstill system modes (eight lowest) are provided for the typical three-bladed wind turbine. Plots of the modes are given in Figs 3.7–3.14. The shapes of the modes are expected to be similar for almost every wind turbine of the same type and design philosophy. Also, in Fig. 3.15, the frequencies of those modes are given as multiples of the rotational frequency *P*, for four wind turbines of increasing size. It is noted that the bigger the size of the wind turbine, the more current is the design, implying that Fig. 3.15 also provides information concerning design trends and evolution of modern turbines. As already mentioned, the modes obtained from the eigenvalue analysis of system [3.17] are coupled and therefore concern the full wind turbine and not any individual component. However, in order to distinguish them, they are named after the component and the deflection direction, which each time is more excited.

Modes M1 and M2 are the first two modes of the tower in the two bending directions lateral and fore–aft, respectively (Fig. 3.7 and Fig. 3.8). Those two modes are close in frequency due to the symmetry of the tower in the two bending directions. The small difference originates from the asymmetric placement of the rotor at the top of the tower. The frequency of those modes is usually found between 1*P* and 2*P*. Mode M3 is the first symmetric edgewise mode of the rotor (Fig. 3.9). This mode is highly coupled to the torsion of the shaft that results in a significant reduction of the mode frequency with respect to the frequency of the

3.7 M1 first tower lateral bending mode (rear, side, top view).

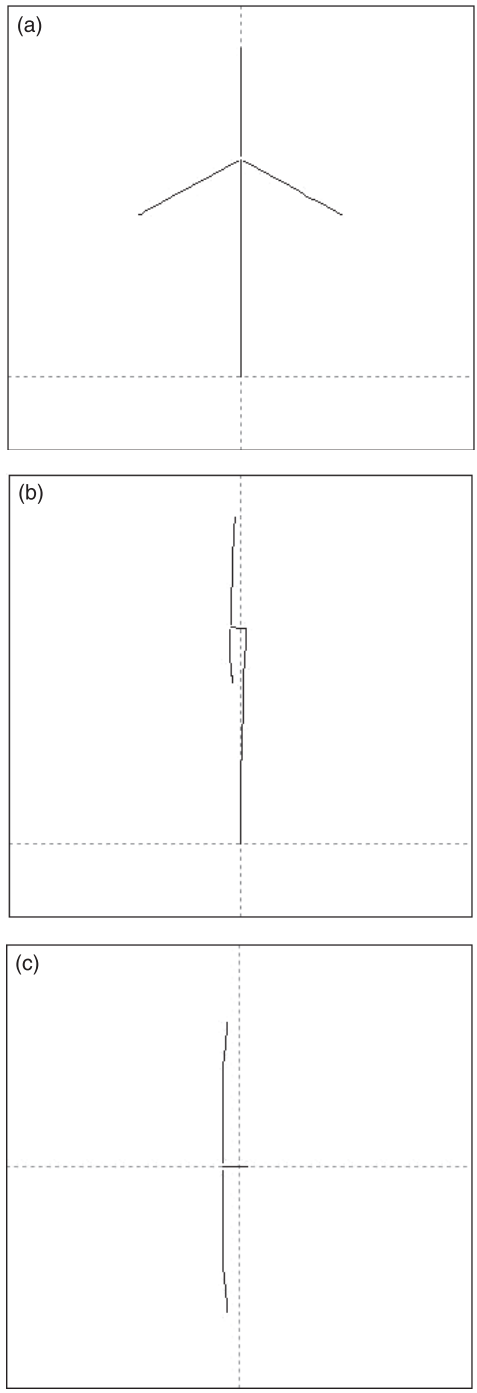

3.8 M2 first tower front-back bending mode (rear, side, top view).

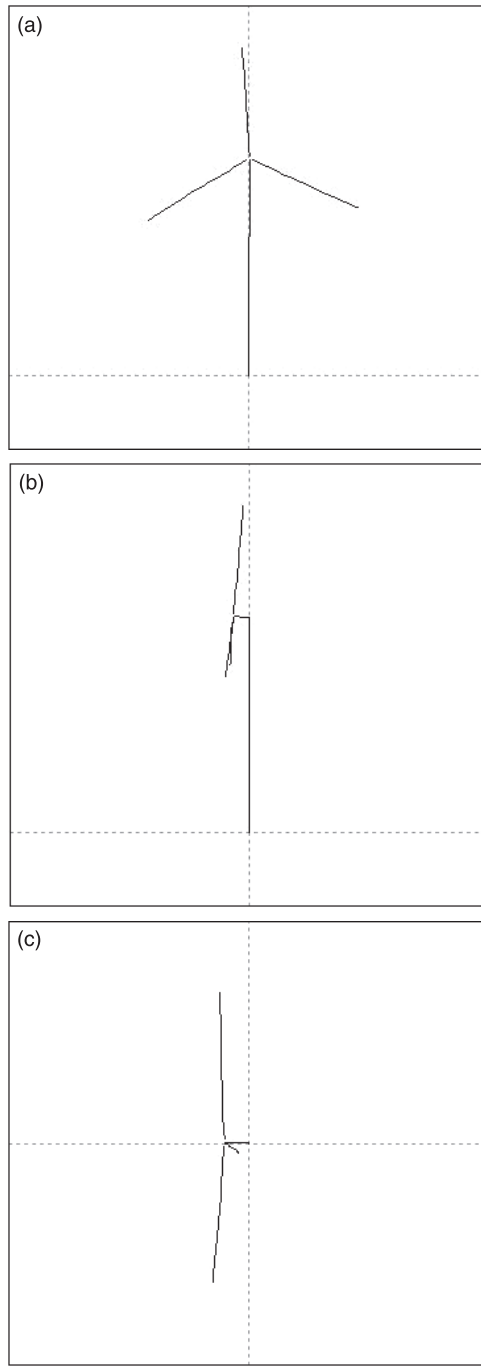

3.9 M3 first symmetric (collective) edgewise mode/shaft torsion (rear, side, top view).

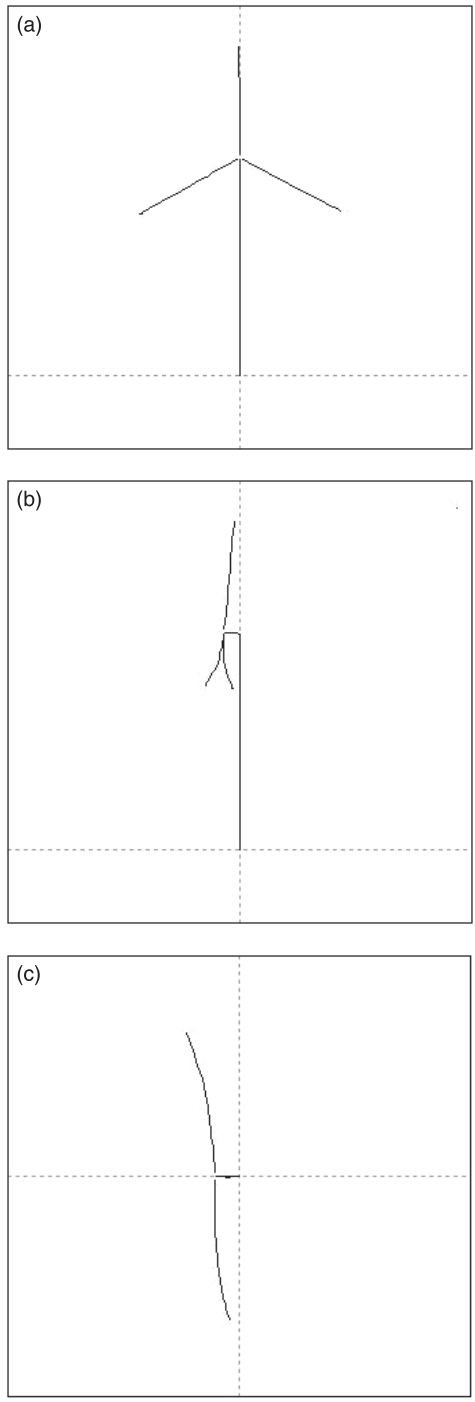

3.10 M4 first asymmetric flapwise mode (yaw) (rear, side, top view).

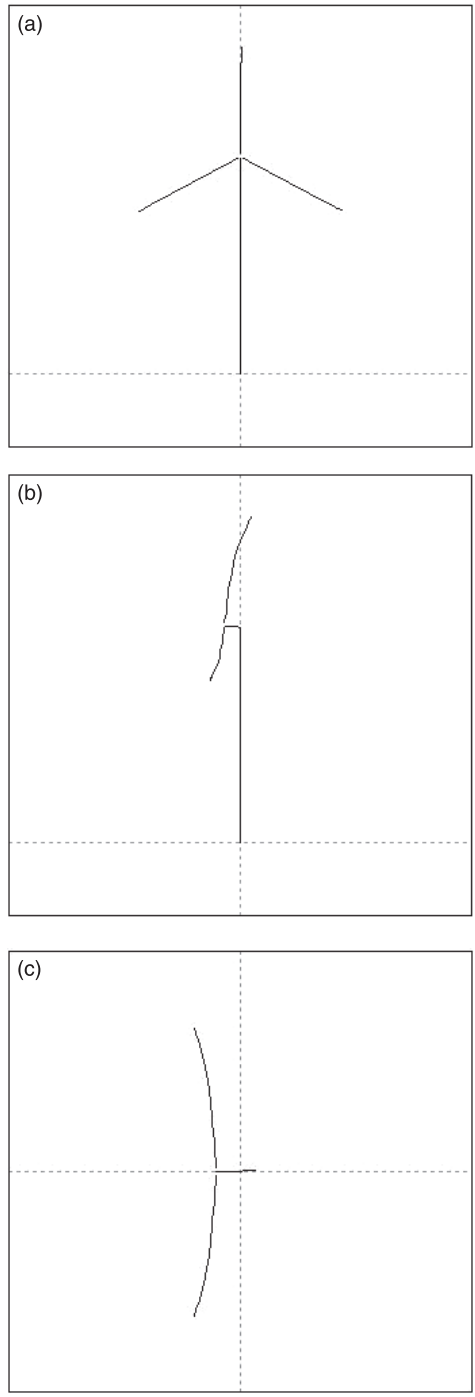

3.11 M5 first asymmetric flapwise mode (tilt) (rear, side, top view).

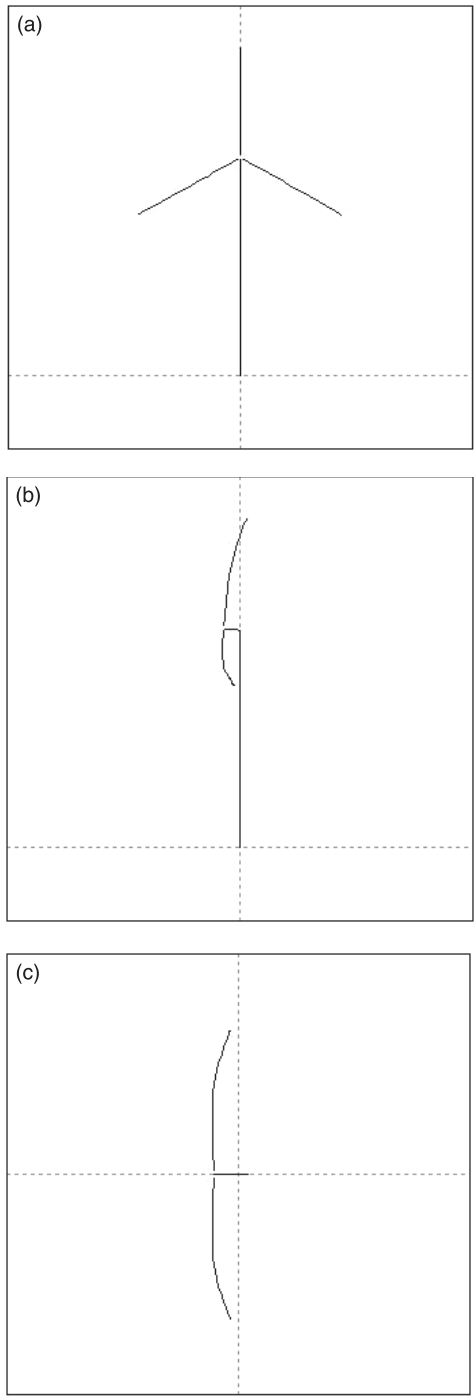

3.12 M6 first symmetric (collective) flapwise mode (rear, side, top view).

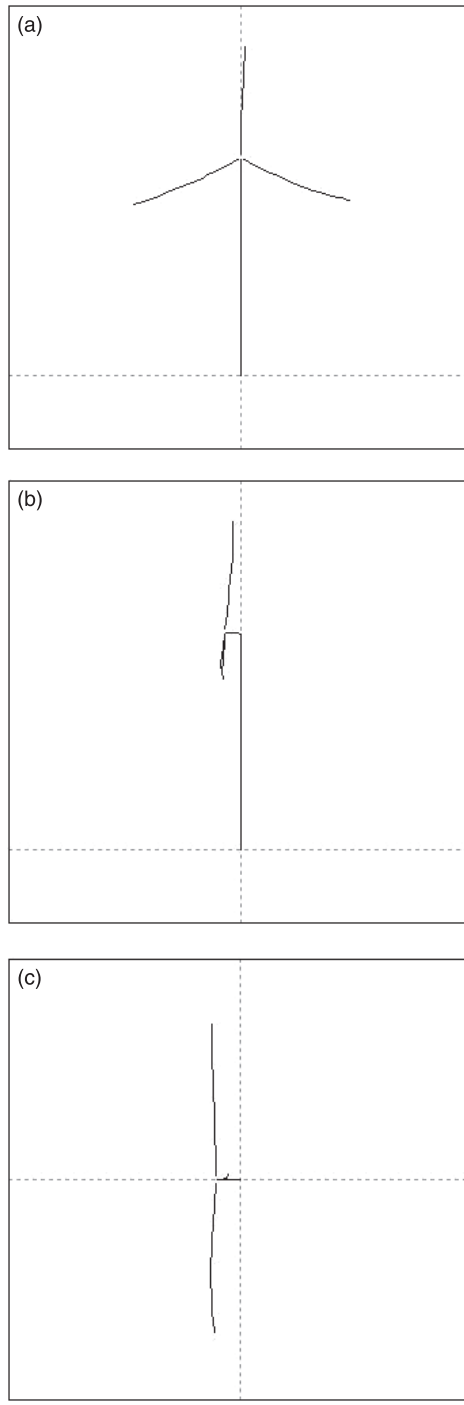

3.13 M7 first asymmetric edgewise mode (vertical) (rear, side, top view).

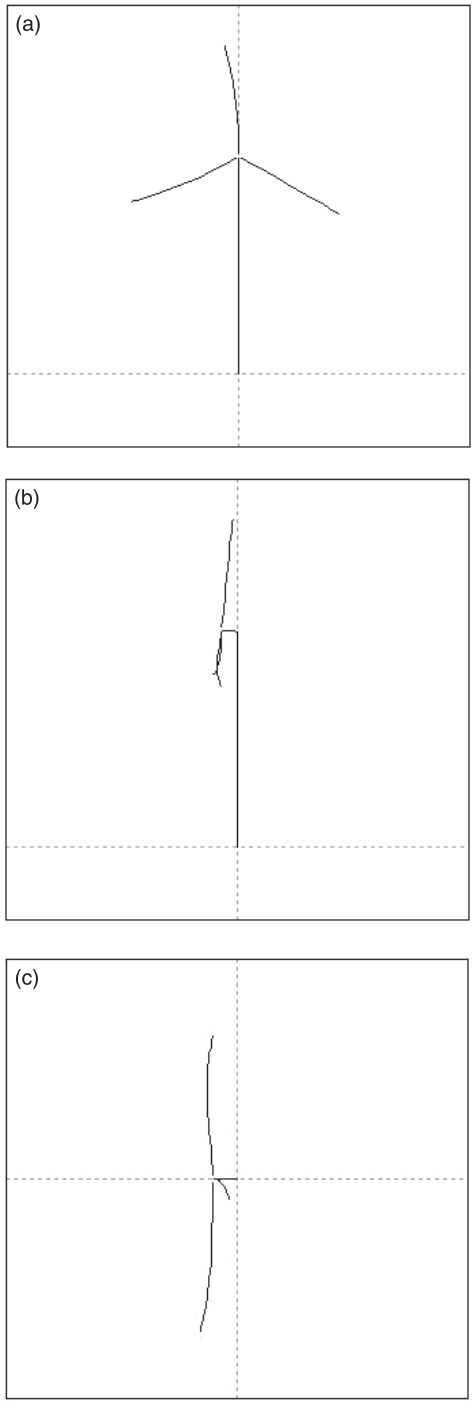

3.14 M8 first asymmetric edgewise mode (horizontal) (rear, side, top view).

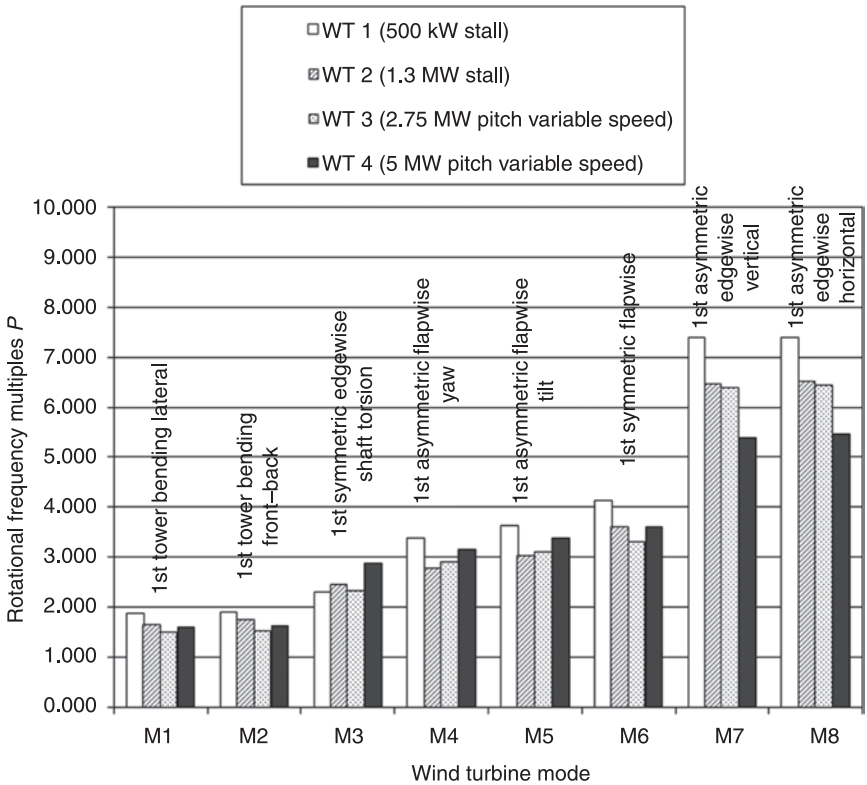

3.15 Comparison of various wind turbines in terms of standstill natural frequencies.

isolated blade edgewise mode. The frequency of this mode is usually placed between 2*P* and 3*P*, although in some wind turbines, it can be lower than the frequency of M1 and M2. Modes M4 and M5, and M6 are the two asymmetric and the symmetric flapwise rotor modes, respectively. In the two asymmetric modes, the blades deflect in opposite directions, whereas in the symmetric mode, the rotor moves collectively (Figs 3.10–3.12). In the two asymmetric modes, a coupling takes place with the yawing and the tilting flexibility of the tower, respectively (see Figs 3.10 and 3.11). This coupling gives rise to a reduction of their frequency as compared to that of the isolated blade. By contrast, the frequency of the symmetric mode is close to the frequency of the isolated blade. Usually, modes M4–M6 are placed in the frequency range of 3*P*–4*P*. Finally, modes M7 and M8 are the two edgewise rotor asymmetric modes that are coupled with the vertical and horizontal flexibility of the tower (see Figs 3.13 and 3.14). The frequencies of those two modes are usually slightly different depending on the tower flexibilities, and they slightly deviate from the edgewise frequency of the isolated blade. M7 and M8 are usually found between 5*P* and 7*P*. As noted from Fig. 3.15,

the two edgewise modes are those that are affected the most by the increase in size. It is clear that the design evolution brings flapwise and edgewise modes closer to each other.

3.3 Aeroelastics of wind turbines under operational conditions

The level of deformation of a wind turbine structure depends on the design characteristics (flexibility of the components) and the loading action. Besides gravitational loads, explicitly addressed in Section 3.2.1, wind turbines are mainly subjected to aerodynamic loads as a result of their operation. In offshore applications, wave loads (hydrodynamic loading) are also added. As the airflow passes over the wind turbine, aerodynamic loads develop as a result of the flow–solid interaction that rotates the blades and deforms the whole structure. The flow seen by the rotor is unsteady, not only because of the turbulent nature of the wind but also due to other reasons that cause incoming-to-the-rotor flow to deviate from axisymmetric conditions (shear, yaw misalignment, etc.). Moreover, under certain operating conditions, flow is highly non-linear. Especially, not only for stall-regulated (SR) wind turbines but also for pitch machines under rated operating conditions, the onset of stall is always a difficulty we have to deal with. Besides introducing significant vibrations due to hysteresis phenomena, it can also degrade stability as a result of negative aerodynamic damping. As regards hydrodynamic loading, it consists of mainly four sub-components: a radiation component related to the loads on the wind turbine support structure originating from the waves that the body radiates away from itself (it includes contribution of added mass and wave radiation damping), a scattering component related to loading due to incident waves, a hydrostatic component related to the support structure buoyancy and finally a viscous drag component (Jonkman and Buhl, 2007). The main characteristic of the above-described external aerodynamic and hydrodynamic loads is that they both depend on the level and rate of deformations (deflection velocities) of the wind turbine. It is therefore clear that a non-linear coupling (called aero/hydro elastic) establishes between external acting loads and structural response when aerodynamic and hydrodynamic loads are considered in dynamic equation [3.13].

3.3.1 Aeroelastic coupling and non-linear time domain analysis

In the application of a beam approach for the structural modeling of the blades, external aerodynamic loads $\delta\mathbf{P}$ in equation [3.3] and equation [3.4] represent aerodynamic loads per unit length of the blade. So they are sectional loads that can be given in terms of sectional dimensionless aerodynamic properties, namely the lift C_L, drag C_D and moment C_M coefficients. If the blade section of Fig. 3.16

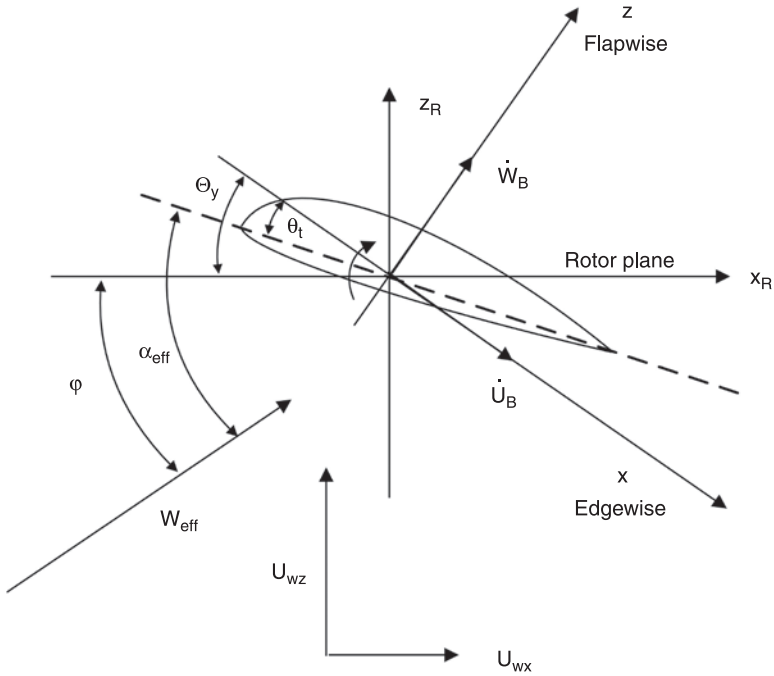

3.16 Basic notation on the blade section.

is considered, the local aerodynamic loads on this section are given by the following expressions:

$$\delta P_x = -\delta L \sin(\varphi + \Theta_y) + \delta D \cos(\varphi + \Theta_y) = \left(-C_L \sin(\varphi + \Theta_y) + C_D \cos(\varphi + \Theta_y)\right) \cdot \frac{\rho}{2} W_{eff}^2 \, c \, \delta y$$

$$\delta P_z = \delta L \cos(\varphi + \Theta_y) + \delta D \sin(\varphi + \Theta_y) = \left(C_L \cos(\varphi + \Theta_y) + C_D \sin(\varphi + \Theta_y)\right) \cdot \frac{\rho}{2} W_{eff}^2 \, c \, \delta y$$

$$\delta M_y = \delta M_p = C_M \cdot \frac{\rho}{2} W_{eff}^2 \, c \, \delta y$$

[3.21]

where δL, δD are the local lift and drag forces, δM is the pitching moment, φ is the local flow angle with respect to the rotor plane, Θ_y is the local pitch of the blade including torsion deformation, W_{eff} is the local velocity and c is the local blade chord. Given that wake-induced velocities are known, local flow characteristics (angle and velocity) are derived using the following expressions:

$$\tan\varphi = \frac{U_{wz} - \dot{W}_B \cos\Theta_y + \dot{U}_B \sin\Theta_y}{U_{wx} - \dot{W}_B \sin\Theta_y - \dot{U}_B \cos\Theta_y} = \frac{U_{effz}}{U_{effx}},$$

$$W_{eff} = \sqrt{U_{effx}^2 + U_{effz}^2},$$

$$\alpha_{eff} = \varphi - \theta_t + \Theta_y \qquad [3.22]$$

where α_{eff} is the local angle of attack, θ_t is the local twist of the blade, U_{wx} and U_{wz} are the components of the wind velocity including wake-induced effects, and $\dot{U}_B$ and $\dot{W}_B$ are the local blade velocities in the flapwise and edgewise directions, respectively (including rigid body motion and elastic deformation). According to equation [3.1], $\dot{U}_B$ and $\dot{W}_B$ are given by the following expression:

$$\begin{Bmatrix} \dot{U}_B \\ \dot{V}_B \\ \dot{W}_B \end{Bmatrix} = \mathbf{A}^T \cdot \dot{\mathbf{r}}_G = \mathbf{A}^T \cdot \left(\dot{\rho} + \dot{\mathbf{A}} \cdot \mathbf{r} + \mathbf{A} \cdot \dot{\mathbf{r}} \right) \qquad [3.23]$$

Remembering that the aerodynamic loads are unsteady, and therefore, in the context of a blade element approach, unsteady, C_L, C_D and C_M can be calculated by application of any unsteady dynamic stall aerodynamic model (Leishman and Crouse, 1989; Petot, 1989). It is clear that the aerodynamic loads in equation [3.21] are implicitly related to the dynamics of the system and the structural responses. So, besides the structural dynamic equations being non-linear, additional non-linearity is introduced to system [3.13] through the aerodynamic loads equation [3.21].

Solution of the non-linear system of the aeroelastic equations requires an iterative procedure, where at every time step of the computation, we are matching aerodynamic loads to structural deformations. The system of the coupled aeroelastic equations can be put in the form:

$$\mathbf{M}(\underset{\sim}{\mathbf{u}}) \cdot \ddot{\mathbf{u}} + \mathbf{C}(\underset{\sim}{\mathbf{u}}) \cdot \dot{\mathbf{u}} + \mathbf{K}(\underset{\sim}{\mathbf{u}}) \cdot \mathbf{u} = \mathbf{Q}(\underset{\sim}{\mathbf{u}})$$

where $\underset{\sim}{\mathbf{u}} = \{\mathbf{u}, \dot{\mathbf{u}}, \ddot{\mathbf{u}}\}$. This, for example, can be done by applying Taylor expansion to all DOFs and eliminating second-order terms. In such a case, the system is written in a perturbed form:

$$\mathbf{M}(\underset{\sim}{\mathbf{u}}^{n-1}) \cdot \delta\ddot{\mathbf{u}} + \mathbf{C}(\underset{\sim}{\mathbf{u}}^{n-1}) \cdot \delta\dot{\mathbf{u}} + \mathbf{K}(\underset{\sim}{\mathbf{u}}^{n-1}) \cdot \delta\mathbf{u} = \mathbf{Q}(\underset{\sim}{\mathbf{u}}^{n-1})$$

where $\underset{\sim}{\mathbf{u}}^{n-1} = \{\mathbf{u}^{n-1}, \dot{\mathbf{u}}^{n-1}, \ddot{\mathbf{u}}^{n-1}\}$ stands for the solution at n – 1 iteration while $\delta\underset{\sim}{\mathbf{u}} = \{\delta\mathbf{u}, \delta\dot{\mathbf{u}}, \delta\ddot{\mathbf{u}}\}$ is such that $\underset{\sim}{\mathbf{u}}^n = \underset{\sim}{\mathbf{u}}^{n-1} + \delta\underset{\sim}{\mathbf{u}}$. Obviously, the solution of the non-linear system is obtained when perturbations reach zero. Other methods for solving the non-linear problem can be found in Crisfield (1998). Time marching can be performed by using any first or higher order integration scheme. Well suited for the systems, like the one described herein, is the second-order implicit Newmark method.

3.3.2 Eigenvalue stability analysis

Where aerodynamics is modeled using blade element momentum theory, loads are provided in a closed form (see equation [3.21]), and so linearization of the system of aeroelastic equations can be performed. Linearization is carried out with

reference to a steady or periodic equilibrium (reference) state. For its definition, the non-linear set of equations is integrated in time until a periodic response (with respect to the rotor speed) is reached. In the case of unstable conditions, where periodicity is never reached, the time domain calculations provide a response that contains significant components in all basic system frequencies. In such a case, by means of Fourier transformation, only the parts corresponding to the rotational frequency (1*P*) and its basic multiple N*P* (where N is the number of blades) are retained. This provides an approximation of the periodic conditions.

The linearized system of equations is formulated into a first-order system:

$$\dot{\mathbf{x}} = \mathbf{A}(\mathbf{x}_0, \dot{\mathbf{x}}_0) \cdot \mathbf{x} + \mathbf{B} \qquad [3.24]$$

where $\mathbf{x}_0$ denotes the reference state and $\mathbf{x}$ are the perturbations of the state variables about this reference state. The eigenvalues of matrix $\mathbf{A}$ provide the natural frequencies and damping characteristics of the linearized system of equations, given that $\mathbf{A}$ is a constant coefficient matrix (Johnson, 1980).

The equations of motion of the rotating blades, being expressed in the rotating frame, involve periodic coefficients. It is possible to eliminate these periodic coefficients and treat the full wind turbine configuration in a linear eigenvalue context with reference to the non-rotating frame, by introducing a multi-blade transformation of all the rotating DOFs. This transformation of coordinates capitalizes on the polar symmetry of rotors with identical blades, and in the case of a three-bladed rotor is given by (Coleman and Feingold, 1957; Johnson, 1980):

$$x_m = x_0 + x_c \cdot \cos\psi_m + x_s \cdot \sin\psi_m \qquad [3.25]$$

where x_m is any rotating DOF of the *m*-th blade being at an azimuth position $\Psi_m = \Omega \cdot t + (2\pi/N) \cdot (m - 1)$, $m = 1, 2, 3$, $N = 3$ and x_0, x_c and x_s are the transformed coordinates (designated as symmetric/collective, cyclic cosine and cyclic sine, respectively) expressed in the non-rotating frame. Of course, besides transforming the rotating DOFs into the non-rotating frame, the same should be done to the equations of the blades, which express the blade dynamics in the rotating frame. To this end, the following operators are applied to the blade aeroelastic equations:

$$\begin{aligned}
(\text{non-rotating equation})_1 &= \frac{1}{N}\sum_{m=1}^{N}(\text{rotating equation})_m \\
(\text{non-rotating equation})_2 &= \frac{2}{N}\sum_{m=1}^{N}(\text{rotating equation})_m \cdot \cos\psi_m \\
(\text{non-rotating equation})_3 &= \frac{1}{N}\sum_{m=1}^{N}(\text{rotating equation})_m \cdot \sin\psi_m
\end{aligned} \qquad [3.26]$$

The eigenvalue analysis of the transformed matrix $\mathbf{A}$ will provide the natural frequencies of the rotor system with reference to the non-rotating frame. The 'non-rotating' frequencies are now associated with the corresponding non-rotating DOFs (i.e. symmetric and cyclic). For an isolated three-bladed rotor, it can be

shown (Hansen, 2007) that the collective frequencies will be identical with the natural frequencies of the m-th blade, while the two sets of cyclic frequencies, designated as backward whirling (or regressive) and forward whirling (or progressive), will differ by $-\Omega$ and $+\Omega$, respectively. As regards the shape of the modes in the symmetric mode, all blades deflect collectively, while in the cyclic modes, they undergo whirling motion with a phase difference of $\pm 2\pi/3$.

3.4 Application toward improved aeroelastic design and construction

3.4.1 General introduction

By the general term 'improved aeroelastic design', it is meant that the response of the turbine is changed in such a way that the load level on the turbine components is reduced and that any unstable response is avoided that could lead to a major failure of the whole turbine or parts of it.

As a basis for the discussion of ways and procedures for an improved aeroelastic response of wind turbines, it is valuable to learn from experimental observations. A discussion of such observations is included first in the present section.

The aeroelastic response depends on the load input to the system, and it is therefore important to know the characteristics of the different types of external loads on the wind turbine, such as loads from turbulent inflow, loads from operation in wakes and loads from waves if it is an offshore installation. Load input is an extensive topic, and it will therefore only be presented in a little detail.

Then follows the section in which design procedures or methods to obtain an improved aeroelastic response are discussed. This comprises ways for reduction of the load input to the system as well as design of the turbine dynamics so that the response is reduced.

3.4.2 Natural aeroelastic frequencies and damping of wind turbines in normal operation – common aeroelastic instabilities

Identification of the natural aeroelastic frequencies of the various modes of vibration of a wind turbine and the aeroelastic damping characteristics associated with those modes of vibration is a very important step in the design process. Negative aerodynamic damping of a mode may lead to amplifying vibrations and failure, depending on the external excitation and the structural damping of the system. By the term 'aeroelastic', it is meant that frequencies and damping refer to the coupled system that includes the effect of the aerodynamics. In the current section, typical examples of wind turbine aeroelastic frequencies and damping characteristics are presented. Also, the various instabilities that have been

observed in modern wind turbines or could be experienced by future designs are discussed, thus providing guidelines for an improved aeroelastic design.

The two example wind turbines, for which aeroelastic modal frequencies and damping characteristics are presented, are typical of the two representative concepts, SR and pitch-regulated variable speed (PRVS). The SR machine has a rated power of 500 kW, while the PRVS is a 2.75-MW machine. The natural frequencies and damping characteristics of the two wind turbines have been obtained through eigenvalue stability analysis, as formulated in the previous Section 3.3 (Riziotis *et al*., 2004).

Figure 3.17 presents the variation of the eight lowest aeroelastic frequencies with the wind speed for the SR wind turbine. For this SR machine, rotational

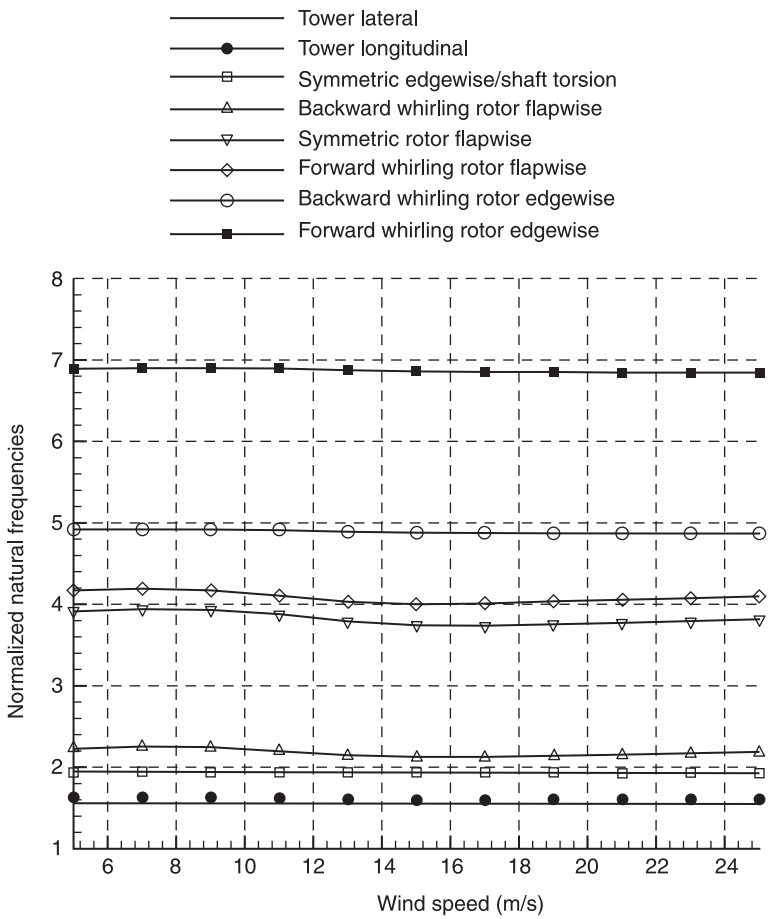

3.17 Aeroelastic frequencies of a 500 kW stall-regulated wind turbine in multiples of the nominal rotational frequency.

speed and blade pitch remain fixed for all wind speeds. However, it is noted that the frequencies exhibit a small variation with the wind speed. This is because, as already mentioned, the effect of the aerodynamics has been taken into account in obtaining those frequencies. Since aerodynamic loads depend on the wind speed, the same happens with the natural 'aeroelastic' frequencies. Typically, the eight lowest modes of the full wind turbine system are the two tower bending modes, the three rotor flapwise modes–collective and two cyclic (forward and backward whirling) – and the three rotor edgewise modes–collective and two cyclic. In Fig. 3.18(a), the damping of the two tower modes is shown. Of the two, the tower lateral bending mode is usually poorly damped. The tower fore-aft bending mode exhibits higher damping values driven by the high aerodynamic damping of the rotor thrust force. In the same figure, the effect of generator dynamics is presented. It is clear that the dynamics of the generator improve the stability characteristics of the tower lateral bending mode. In Fig. 3.18(b), the damping of the rotor edgewise modes is shown and is compared to the damping of the isolated blade. It is noted that all modes are negatively damped (structural damping has not been included in the computations); however, the damping of the collective mode is considerably augmented by the inclusion of the generator dynamics (as shown in

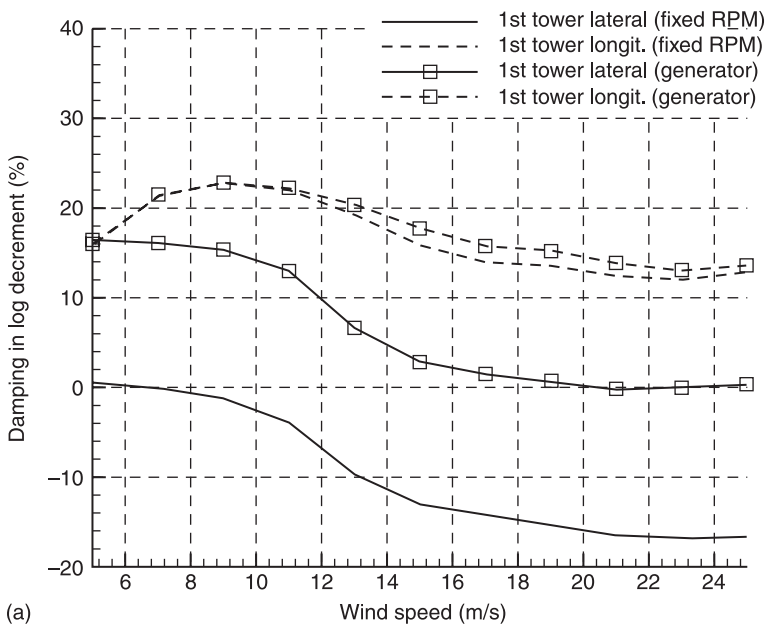

3.18 (a)–(d) Aeroelastic damping of a 500 kW stall-regulated wind turbine mode. (a) Tower modes (with and without generator dynamics). (*Continued*)

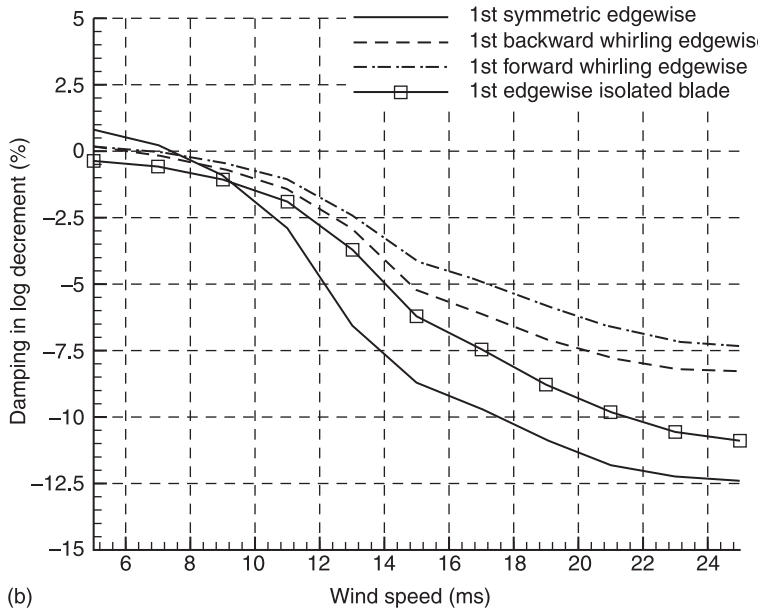

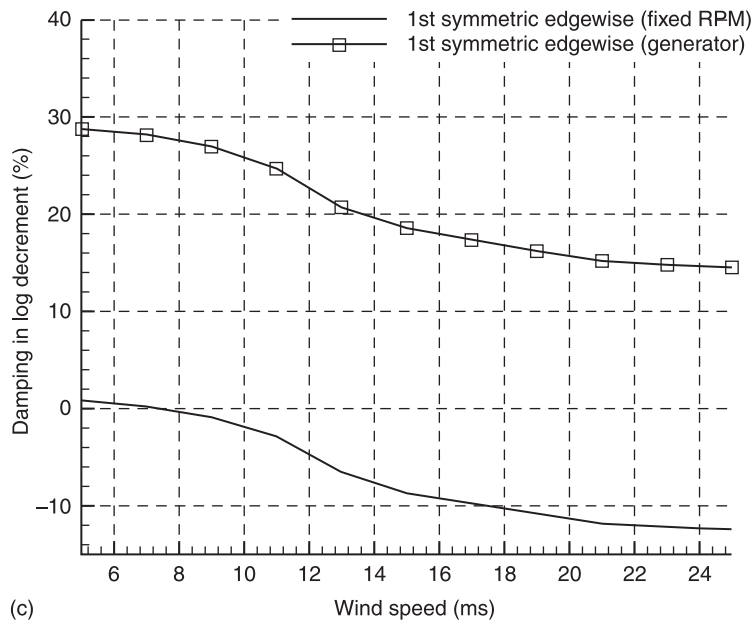

3.18 (b) Rotor edgewise; (c) symmetric rotor edgewise (with and without generator dynamics).

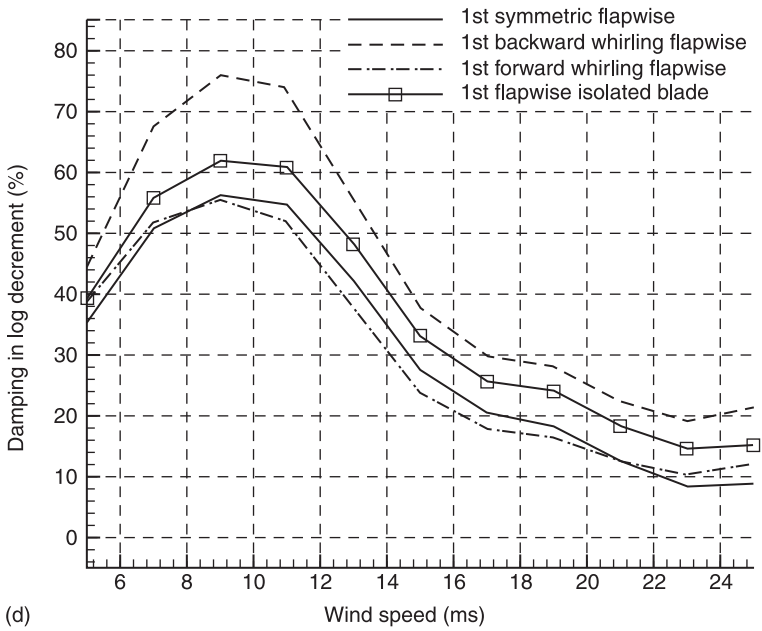

3.18 (d) Rotor flapwise.

Fig. 3.18(c)). Finally, the three flapwise modes are highly damped, as seen in Fig. 3.18(d). As a general conclusion, significant reduction of the damping of all modes is noted as the wind speed increases. This is linked to stalled operation and, as will be discussed in the following section in the case of the edgewise modes, often results in high negative aerodynamic damping values (called stall-induced edgewise vibrations). It is also noted that there is a clear deviation between the damping characteristics of the isolated blade compared to those of the blade being mounted on the wind turbine. This indicates that the structural interaction of the various components affects the damping characteristics of the wind turbine modes. Finally, the modes that appear to be the lowest damped are the two cyclic edgewise modes and this is typical for most wind turbines.

Figure 3.19 presents the frequency variation of the PRVS wind turbine modes. In this case, the variation of the frequencies is higher as a result of the varying rotational speed (up to 9 m/s) and the varying pitch (beyond 13 m/s). Comparing the damping characteristics of the various modes (see Fig. 3.20(a)–(c)) with those of the SR machine, it is observed that (1) the tower lateral bending mode and the rotor edgewise modes are still the lowest damped modes of the wind turbine, and (2) considerable increase of the damping is obtained at high wind speeds as a result of the blades' pitching, indicating that when the stall is avoided, edgewise vibrations are suppressed.

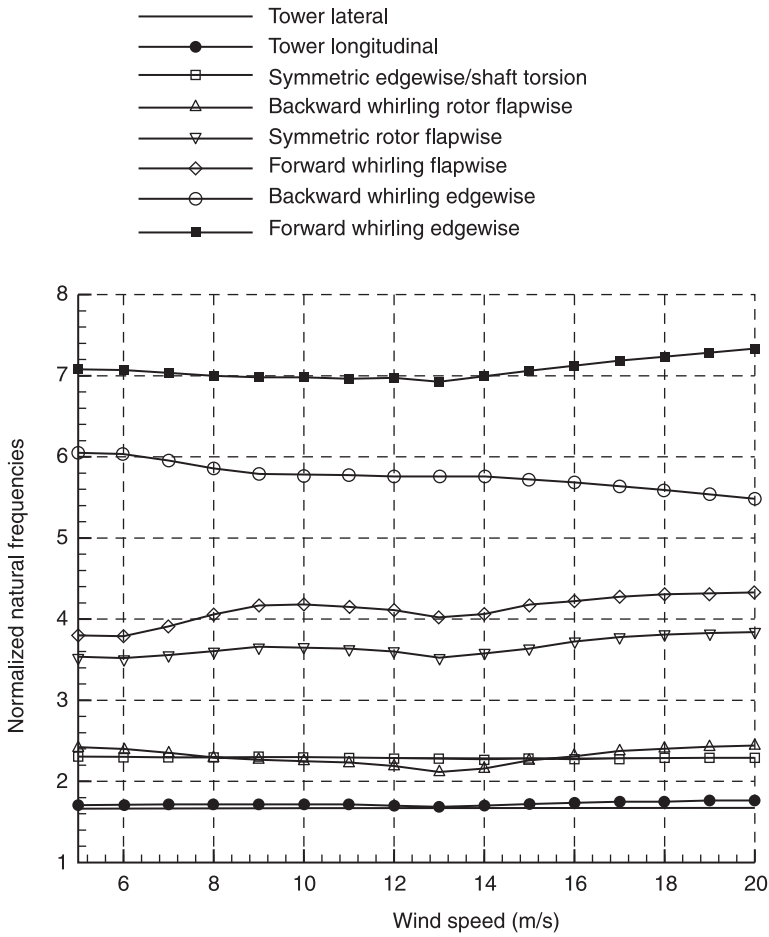

3.19 Aeroelastic frequencies of a 2.75 MW pitch-regulated variable speed wind turbine in multiples of the nominal rotational frequency.

In the following, various wind turbine instabilities are discussed and explained through application examples.

Stall-induced edgewise vibrations

When the blades operate in stall, negative aerodynamic damping is introduced by the aerodynamic loads acting, which give rise to reduced damping of both the flapwise and the edgewise modes. In particular, the edgewise modes become negatively damped, and so, amplifying vibrations in the edgewise frequency are obtained.

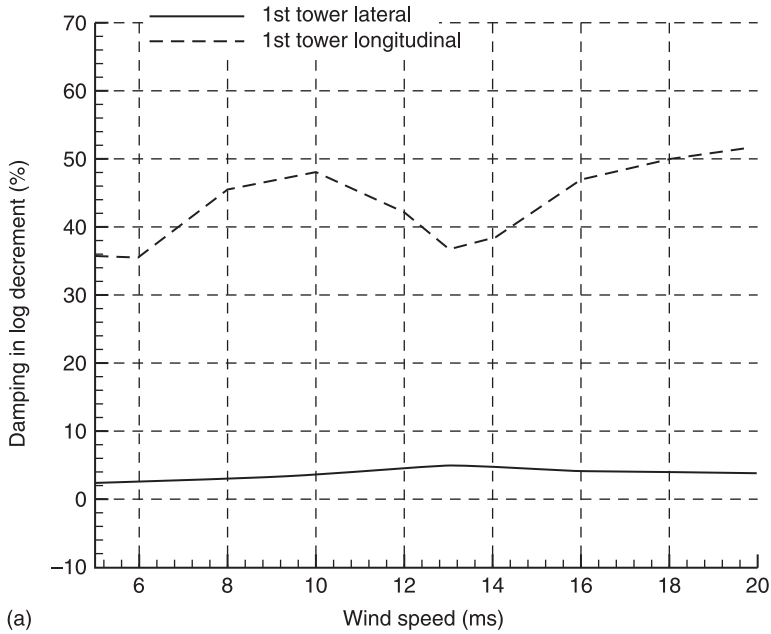

(a)

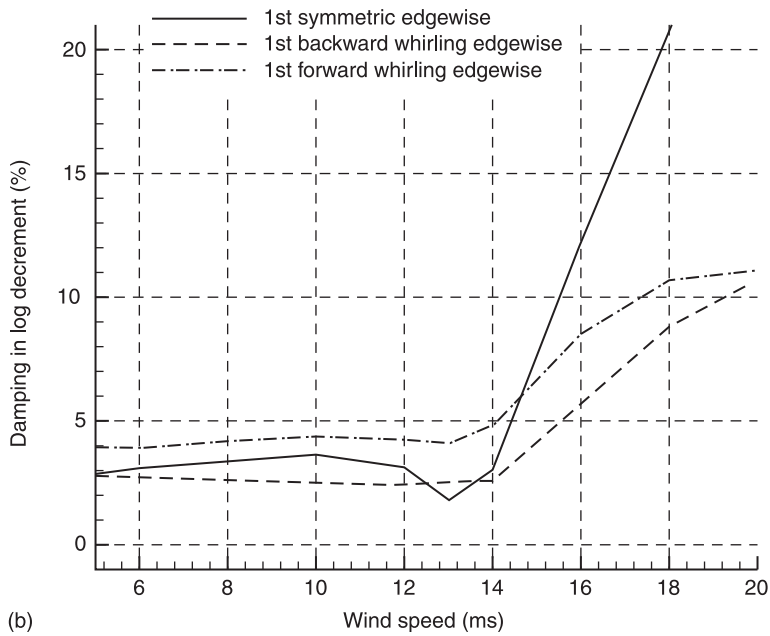

(b)

3.20 (a)–(c) Aeroelastic damping of 2.75 MW pitch-regulated variable speed wind turbine modes. (a) Tower modes; (b) rotor edgewise modes.

(*Continued*)

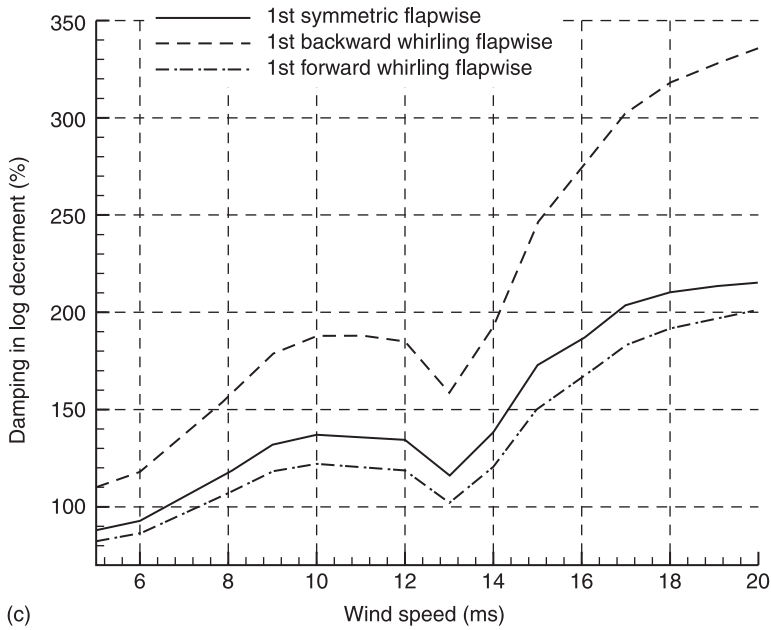

3.20 (c) Rotor flapwise modes.

The first experimental evidence of this instability was seen in the mid 1990s on stall-regulated rotors with a diameter of 35–40 m. An example of a 500-kW turbine is presented in Fig. 3.21, and it is seen that the amplitude of the edgewise blade root moment (which at steady conditions varies with 1*P* due to the gravity) increases two to three times due to the instability during operation in stall. Also, computed with HAWCstab, damping characteristics of the two edgewise modes (forward whirling and backward whirling) are shown in Fig. 3.22 (Hansen, 2003) and compared with the damping characteristics measured by Thomsen *et al*. (2000) on a 600-kW turbine. Both predictions and measurements indicate the decrease in damping for increasing wind speed and the difference in damping between the two cyclic modes. The higher damping of the forward whirling mode is due to a higher content of out-of-plane motion in this mode as compared to the backward whirling mode (Hansen, 2003). The experimental evidence of the edgewise instability led to considerable research on this subject, and a major European project 'Prediction of Dynamic Loads and Induced Vibrations in Stall' funded by the European Union (EU) was carried out in the period from 1995 to 1998 (Petersen *et al*., 1998).

The origin of the instability was found in the basic aerodynamic damping characteristics of a rotating, vibrating airfoil section. Linearization of equation [3.21] with respect to the two principle vibration directions (flapwise and edgewise) provides the following damping coefficients (Petersen *et al*., 1998):

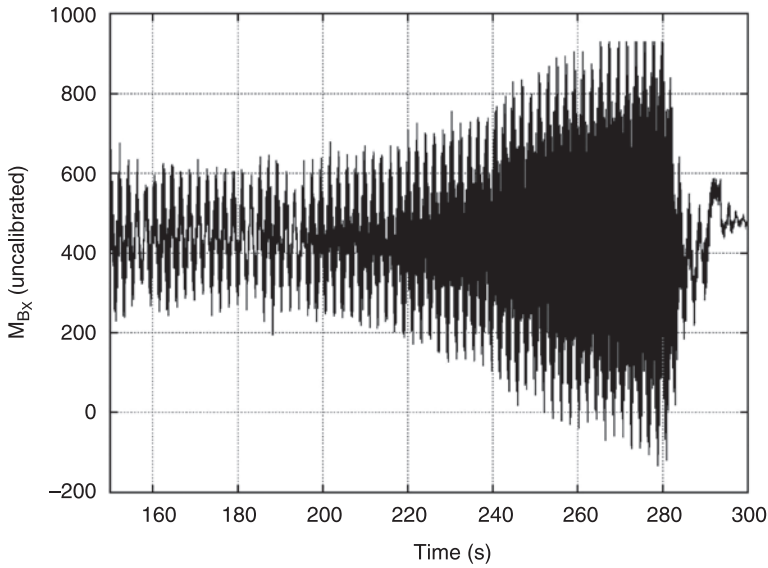

3.21 Measured edgewise blade root moment on a stall-regulated rotor at high wind showing an edgewise vibration instability development in the time interval from 220 seconds to 280 seconds.

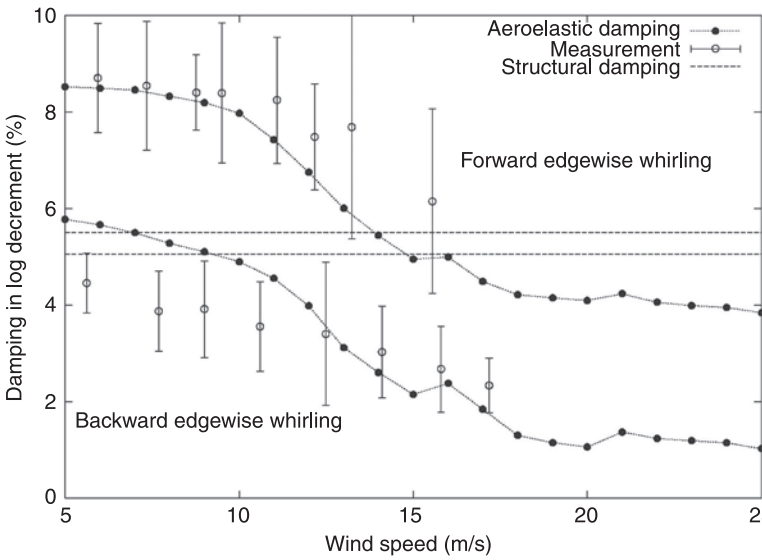

3.22 Predicted and measured aeroelastic damping of the forward and backward edgewise whirling modes of a 600 kW turbine, together with the structural damping to show the change in damping due to the interaction with aerodynamic forces (Hansen, 2004).

$$c_{xx}^{R}(r,V)=\frac{1}{2}c\varrho\frac{r\Omega}{W}\left[\left(\frac{2r^2\Omega^2+V^2}{r\Omega}\right)C_D-V\frac{\partial C_D}{\partial\alpha}-VC_L+\frac{V^2}{r\Omega}\frac{\partial C_L}{\partial\alpha}\right]$$

$$c_{xy}^{R}(r,V)=\frac{1}{2}c\varrho\frac{r\Omega}{W}\left[-VC_D+r\Omega\frac{\partial C_D}{\partial\alpha}+\left(\frac{2V^2+r^2\Omega^2}{r\Omega}\right)C_L+V\frac{\partial C_L}{\partial\alpha}\right]$$

$$c_{yx}^{R}(r,V)=\frac{1}{2}c\varrho\frac{r\Omega}{W}\left[-VC_D+\frac{V^2}{r\Omega}\frac{\partial C_D}{\partial\alpha}-\left(\frac{2r^2\Omega^2+V^2}{r\Omega}\right)C_L+V\frac{\partial C_L}{\partial\alpha}\right]$$

$$c_{yy}^{R}(r,V)=\frac{1}{2}c\varrho\frac{r\Omega}{W}\left[\left(\frac{2V^2+r^2\Omega^2}{r\Omega}\right)C_D+V\frac{\partial C_D}{\partial\alpha}-VC_L+r\Omega\frac{\partial C_L}{\partial\alpha}\right]$$

[3.27]

where Ω is the angular velocity of the blade section, r is the local radius, W is the relative velocity and V is the free wind speed (see Fig. 3.23 for the definitions). c_{xx}^{R} and c_{xy}^{R} are the damping coefficients in the in-plane or edgewise direction, due to the flapwise and edgewise motions, respectively. Similarly, c_{yy}^{R} and c_{yx}^{R} are the damping coefficients in the out-of-plane or flapwise motion. From the above equations, it is seen that the lift or drag coefficient is present in all the terms for determination of the damping coefficients, and the aerodynamic characteristics of the blade section are thus of great importance for damping identification. However, for a more specific analysis, suitable airfoil data have to be inserted.

The damping coefficient c_{xx}^{R} is now derived for the airfoil section vibrating in a direction determined by the angle θ_{RB} relative to the rotor plane (see Fig. 3.24)

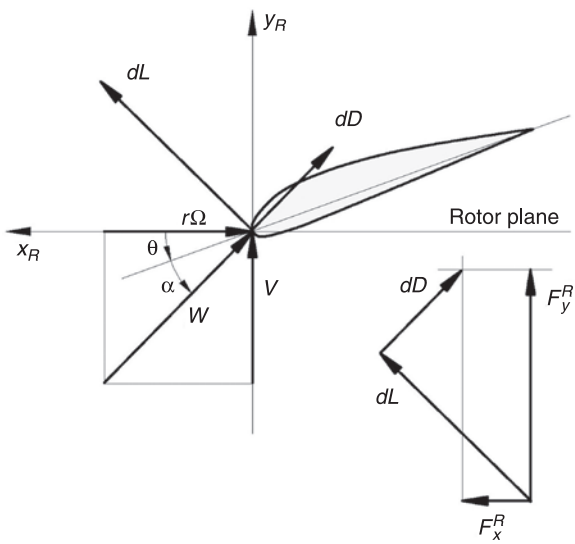

3.23 Flow forces and velocities at a blade section (Petersen *et al.,* 1998).

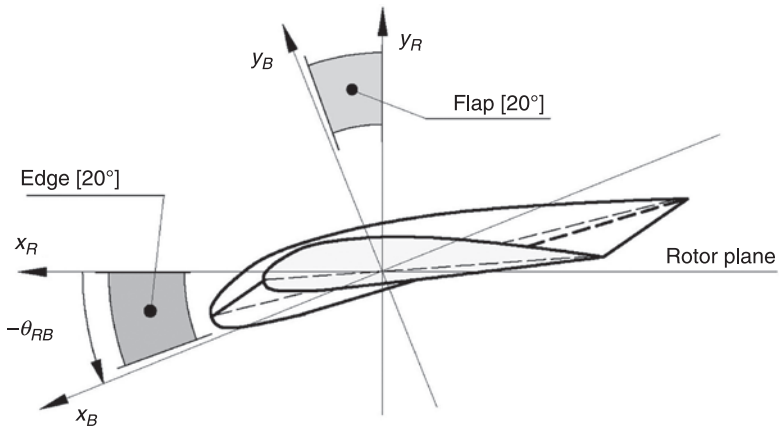

3.24 Typical ranges for the edgewise and flapwise vibration (Petersen *et al.,* 1998).

and shown for three different wind speeds in Fig. 3.25. Typical vibration direction intervals for the edgewise and flapwise modes are included in Fig. 3.25. The damping coefficient for the edgewise mode is generally low and even negative in part of the operational interval. However, the flapwise mode is highly damped except at a wind speed of 20 m/s. This simple example illustrates the fundamental

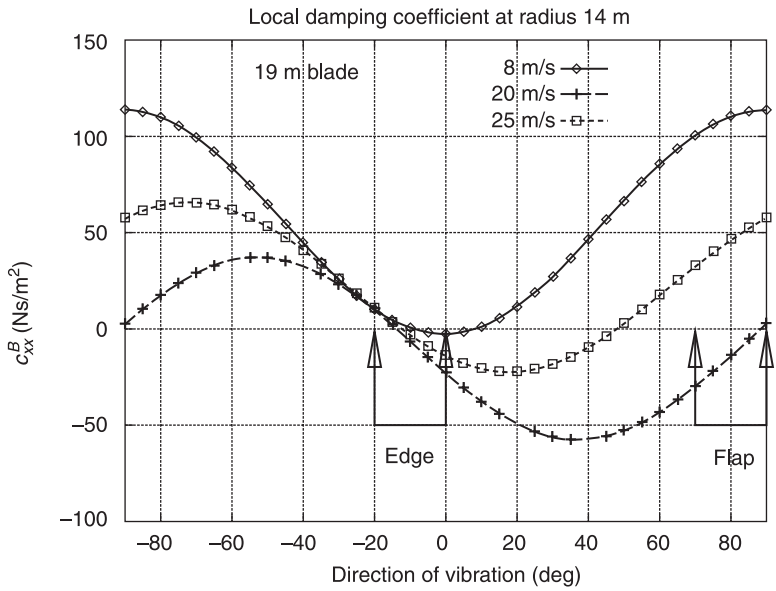

3.25 Damping coefficient c^B_{xx} as a function of the vibration direction θ_{RB} (Petersen *et al.,* 1998).

mechanism of unstable aeroelastic response, but the complexity of the full aeroelastic instability problem should not be neglected, as a much more detailed modeling is necessary to understand the aeroelastic response of a complete turbine. It is worth noting that when the first observations of the edgewise instability occurred on some turbines, there could be other turbines using the same blades where no severe edgewise vibrations were seen. So, although the aerodynamic characteristics of the blades are very important for the edgewise instability, there are also a number of other important parameters that affect the stability behavior of the system. As an example, it was shown in the study by Petersen *et al*. (1998, p. 131–132 (Hansen 2003)) that an increase in the main shaft stiffness could remove the edgewise blade instability. The overall result of the study was guidelines designed for avoiding stall-induced vibrations related to the aerodynamic characteristics of the blade, structural characteristics of the blade, material and structural properties related to structural damping, and properties of the supporting structure. The referenced EU-funded project was followed by a number of research studies on the edgewise blade instability and later, more generally, on the stability of the complete wind turbine (Chaviaropoulos, 2001; Chaviaropoulos *et al*., 2003; Hansen and Buhl, 2006; Markou *et al*., 2007).

Vibrations at standstill

Wind turbines are designed to operate up to a maximum wind speed of, for example, 25 m/s and are shut down for higher wind speeds. They have thus to withstand the wind loads at extreme wind speeds, with the wind coming from any direction to the rotor. This can result in quite extreme inflow conditions on the blade, with inflow angles covering the whole interval. It seems that this load condition is of major importance, although direct documentation by measurements is not seen in the open literature. However, even at lower wind speeds (10–20 m/s), the parked rotor condition can lead to high edgewise blade vibrations in some special inflow cases. This is a situation that is quite common during erection of turbines in wind farms where there can be a time span of several weeks from the turbine installation until it can be connected to the grid. During this period, the rotor is locked and this can be a more dangerous situation than an idling rotor that requires that the turbine is connected to the grid. A combination of low aerodynamic damping at specific inflow direction, and vortex shedding from the blade might be the mechanism behind the severe blade vibrations at relative low wind speeds from 10 to 20 m/s.

Owing to the lack of measured vibrations at standstill, an example of a simulated edgewise blade response in turbulent wind with a mean wind speed of 50 m/s is shown in Fig. 3.26. The wind direction has an angle of 60° to the rotor axis and the blades are at zero pitch. Oscillations are clearly seen in the edgewise blade root moment, although the amplitude does not increase continuously. For comparison, the edgewise moment during normal operation at 8 m/s is also shown.

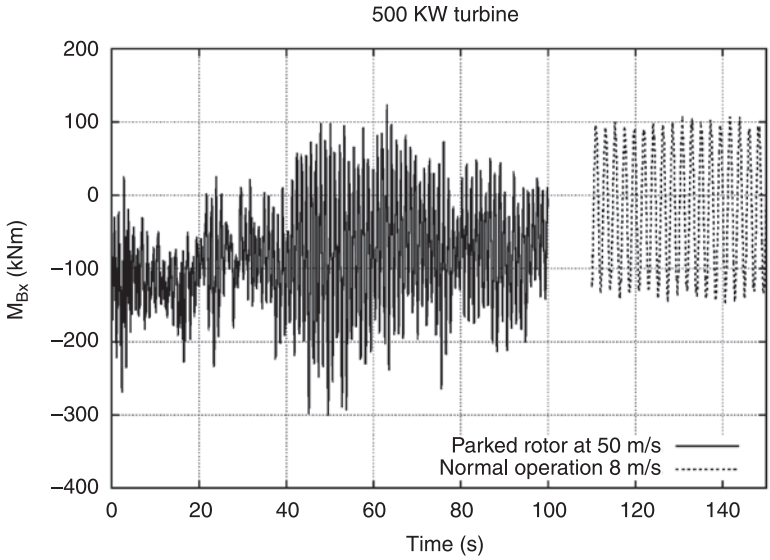

3.26 Simulated edgewise blade root moment on a 500 kW turbine at normal operation at an average wind speed of 8 m/s and with parked rotor at an average wind speed of 50 m/s with an inflow wind direction of 60° relative to the rotor axis.

Figure 3.27 and Fig. 3.28 present the aeroelastic damping characteristics of the first flapwise and edgewise modes of a parked blade (90° pitched at feathering position) at various angles of the local flow (Politis *et al*., 2009). For a blade at feathering position, 0° local flow angle corresponds to 0° yaw error with respect to the rotor plane. As seen in the plots, both flapwise and edgewise modes become low or even negatively damped for flow angles around ±20°. This is in line with the results presented earlier for a normal operation, where low or even negative damping values of the flapwise and edgewise modes are obtained when the local flow angles of attack, beyond the maximum C_L angle in the post-stall regime, are experienced by the blade sections. Moreover, negative damping values of the edgewise mode are also obtained for very high flow angles in the vicinity of ±90°. The difference between this and the previous case is that the flapwise mode is now highly damped. At ±90° angle of attack, the drag coefficient is expected to be maximum while the lift coefficient will be zero and the slope of the lift curve will be negative. High values of the drag give rise to an enhanced aerodynamic damping of the blade. On the other hand, negative slope of the lift curve degrades damping. In cases where the edgewise motion is highly coupled to the flapwise motion, edgewise vibrations are likely to occur. This is illustrated in Fig. 3.29, where the trace of the blade-coupled flapwise/edgewise motion is shown. In the same figure, the velocity triangles and lift force acting on the blade are plotted for the parts of the blade motion such that the flapping velocity becomes maximum.

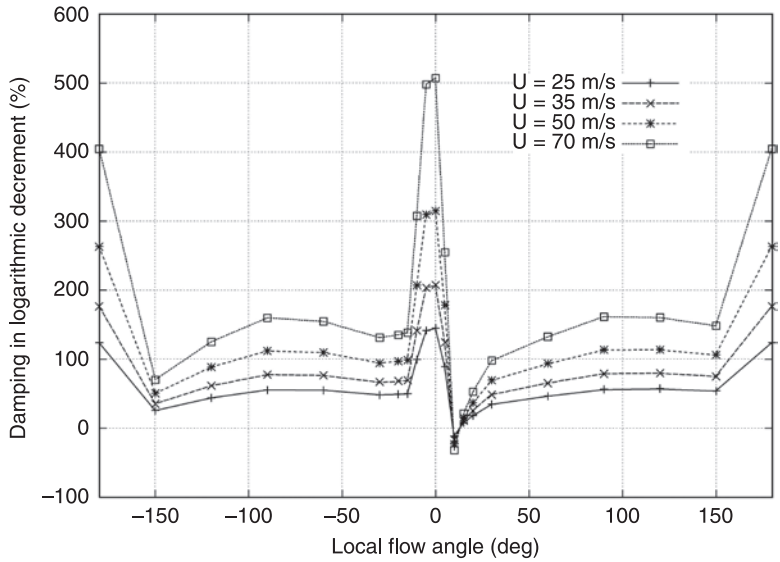

3.27 Aeroelastic damping of the first flapwise mode for different wind speed values using quasi-steady modeling.

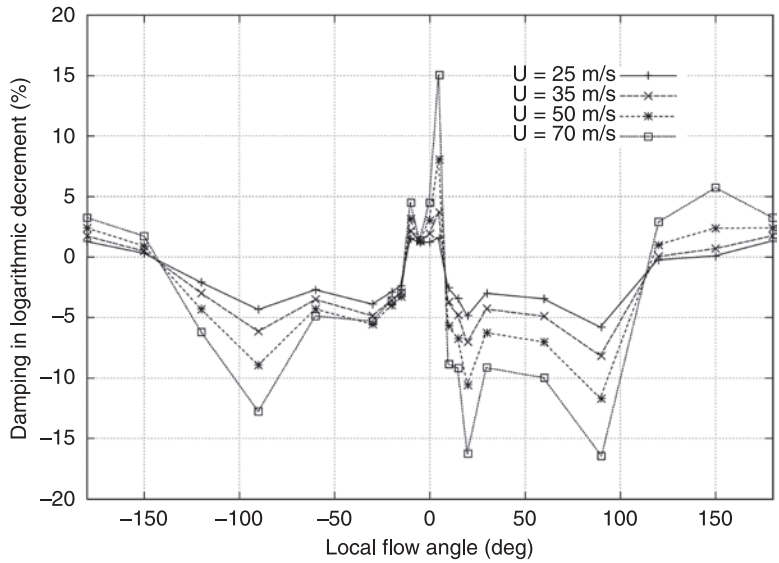

3.28 Aeroelastic damping of the first edgewise mode for different wind speed values using quasi-steady modeling.

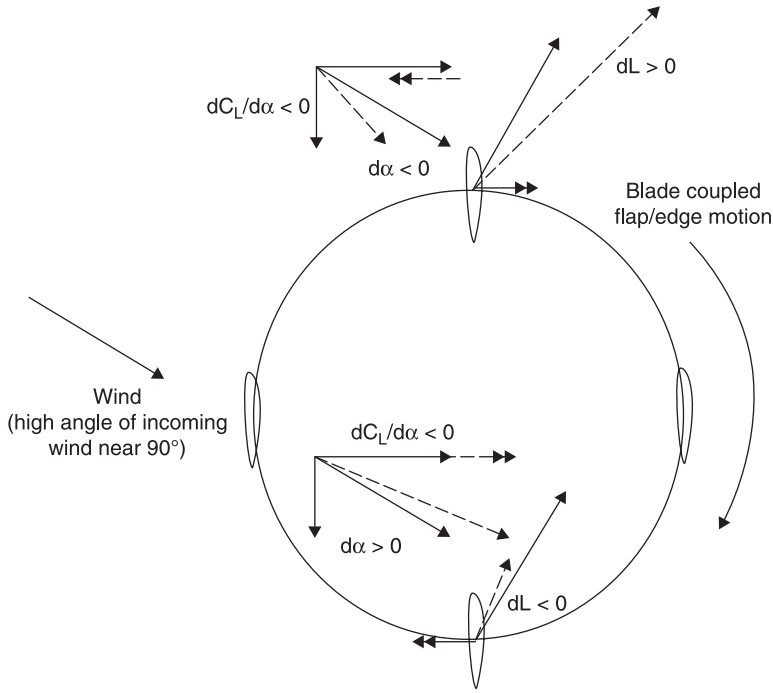

3.29 Qualitative explanation of the damping decrease at high angles of attack.

The solid lines present the incoming wind and the lift force acting on a blade element due to this wind. Dashed lines present the change in the effective velocity seen by the blade, and the lift force when flapping motion is taken into account (double-arrowed lines). Given the negative slope of the lift curve, when the blade is lagging, the lift force becomes smaller as a result of the higher angles of attack, and so lower restoring force (opposing to the blade motion) is generated. When the blade is leading, the opposite behavior is observed. The lift force of the blade increases as a result of the reduction of the local flow incidence, and so a higher diversion force develops.

Tower lateral bending instability

This type of instability or low damped vibrational mode has been experienced on many types of turbines from the stall-regulated 500 kW range turbines in the mid 1990s to the newest pitch-regulated MW turbines. Hansen (2007) has investigated this type of vibrations in more detail and found that a typical direction for the lateral vibrations of a stall-regulated turbine is around 45° relative to the rotor axis, whereas for the pitch-regulated turbine, the direction is closer to being perpendicular to the rotor shaft axis. This can be explained by the different

operational range of the airfoils along the blade influenced by the pitch of the blade. Using the stability tool HAWCStab (Hansen 2004), the damping of the longitudinal and lateral tower mode was computed for a stall-regulated MW turbine (Hansen 2007). The damping curves, as a function of the wind speed, are shown in Fig. 3.30, and it is clear that the lateral mode is considerably less damped than the longitudinal mode and even becomes negative at high winds.

For offshore installed turbines, the wave loading can exaggerate the problem of low lateral damping as the wave direction for some periods can be quite different from the wind direction and gives considerable load input on the low damped lateral tower mode. Kallesøe and Hansen (2010) investigated this problem by simulations on a conceptual 5 MW reference wind turbine (RWT) using the HAWC2 code (Larsen, 2009; Larsen, Hansen *et al*., 2004; and Larsen, Madsen *et al*., 2005). Operational conditions were a wind speed of 6 m/s with 20.2% turbulence, and irregular waves with an average height of 1.63 m and an angle of 90° to the wind direction. The simulated lateral and longitudinal tower bottom moment and the wave height are shown in Fig. 3.31, and it can be seen that the variations of lateral moment are considerably higher than the variations of the longitudinal moment. One method to damp the lateral tower moment is to use a suitable control on the generator torque, and Kallsøe and Hansen (2010) demonstrated 40% reduction in the fatigue of this load component. Another very common way to damp lateral tower vibrations, widely used by the industry, is by installing a suitable damper in the tower top.

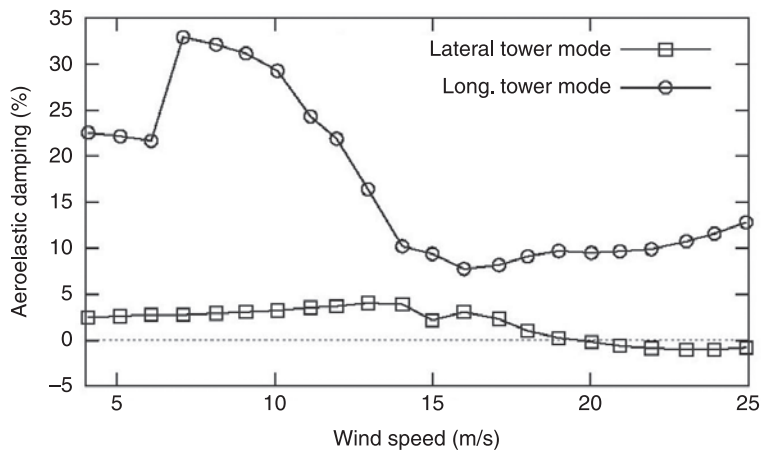

3.30 Aeroelastic damping of the first lateral and longitudinal (Long.) tower bending modes as a function of wind speed computed for a stall-regulated MW turbine by the aeroelastic stability tool HAWCStab. Graph from Hansen (2007).

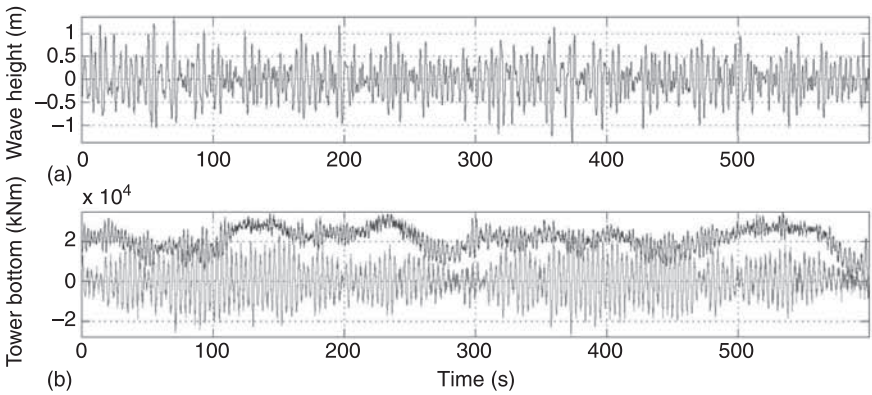

3.31 Results ((a) wave height; (b) lateral tower bottom bending (lower trace) and axial tower bottom bending (upper trace)) from aeroelastic simulations with the code HAWC2 on the 5 MW RWT with combined wave loading and turbulence (Reproduced from Kallesøe and Hansen (2010)).

Classical flutter

Classical flutter is a well-known instability from aircraft wing applications. It originates from the aeroelastic coupling of the flapwise modes with the first torsion mode at high flight speeds. In particular, the change in the angles of attack resulting from the torsion deformation of the wing sections generates aerodynamic lift forces that are in phase with the flapwise bending motion. This gives rise to violently amplifying flapwise vibrations that cannot be compensated by structural damping. Although classical flutter instability has not been reported in wind turbines, it has been given special attention by many researchers (Lobitz, 2005; Hansen *et al*., 2006; Hansen, 2007) for the reason that as wind turbine blades become more flexible, the frequency of the first torsion mode drops and comes closer to the lowest flapwise eigen frequencies.

In the study by Hansen (2007), the classical flutter instability has been investigated in detail and it has been identified that the main driving mechanisms that increase the risk of such instability are:

- operation at low angles of attack (in the attached flow regime), so the increase in the angle of attack (nose-up torsion) is associated with higher lift values;
- high tip speeds to ensure sufficient energy in the aerodynamic forces;
- low torsion stiffness or better, lower values of the torsion to flapwise frequencies ratio;
- placement of the center of gravity of the blade sections aft of the aerodynamic centre to ensure the correct phasing of the flapwise and torsional components in the flutter mode.

In wind turbine blades, the risk of experiencing flutter instability is usually measured by the ratio of the rotor speed at which such instability first takes place

to the nominal speed of the rotor at normal operation. For modern large-scale wind turbines, such ratio lies in the vicinity of two (Lobitz, 2005). This means that the risk of flutter instability is not far from the design limits of modern wind turbines. This is especially true if we take into account that up to a certain limit, rotor over-speeds are allowed by the controller in extreme wind events. It has further been shown by Hansen *et al*. (2006) that the high peaks in relative velocity for a blade on a rotor in yaw is enough to trigger flutter. A reduction of 13% in flutter speed was reported for a rotor in 50° yaw and operating at 8 m/s (Hansen *et al*., 2006).

In wind turbine blades, the mode that usually becomes a flutter one is the second flapwise (Lobitz, 2005; Hansen, 2004; Hansen *et al*., 2006) mode. This can be observed in Figs 3.32 and 3.33 where computations of the aeroelastic frequencies and damping of the isolated blade (performed with GAST, Riziotis and Voutsinas, 1997) are shown as function of the rotor speed. It is noted that the frequency of both the first and the second flap modes increases with the rotor speed toward the frequency of the first torsion mode. At the rotor speed of 2 rad/s (nominal 1.267 rad/s), a coupling of the second flap with the torsion mode takes place (indicated with the arrows) that leads to a sudden reduction of the second flap mode damping (see Fig. 3.33). At the rotor speed of 2.4 rad/s, the damping of the second flap mode becomes negative. Other examples of even more violent flutter instabilities can be found in Hansen (2007).

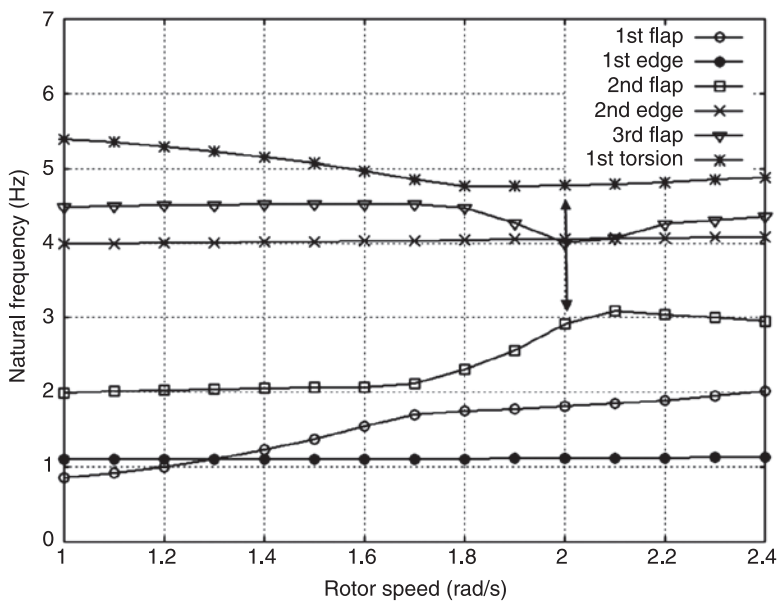

3.32 Aeroelastic frequencies of the isolated blade modes as a function of the rotor speed.

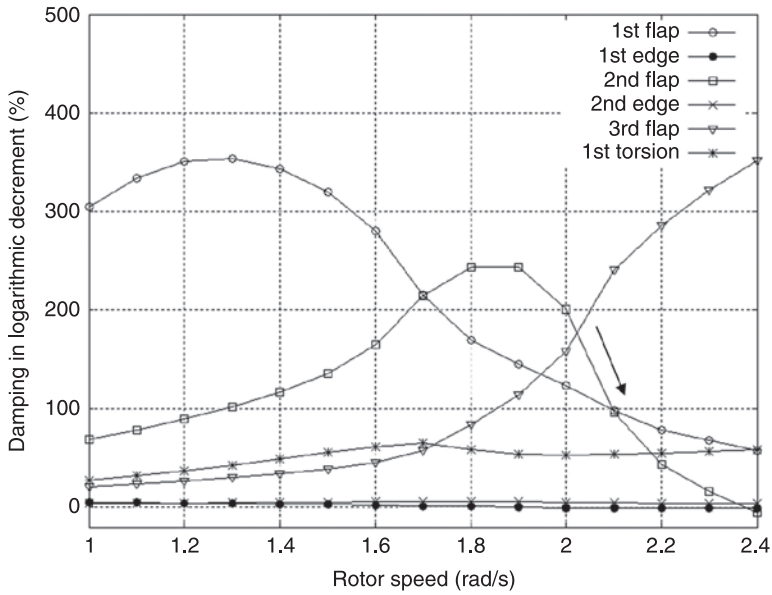

3.33 Aeroelastic damping of the isolated blade modes as a function of the rotor speed.

3.4.3 Characteristics of load input and load cases

Wind loads

Atmospheric turbulence in the inflow to the turbine is the main load driver, and turbines are certified to specific wind turbine classes (1, 2 or 3) with an associated reference wind speed and a turbulence intensity. The dominant international standard for the design of wind turbines is the IEC61400-1 (2005) standard for onshore wind turbines and the IEC61400-3 (2005) standard for offshore wind turbines. The latter is often used in combination with the DNV-OS-J101 (2004) offshore standard. In the IEC standard, two turbulence models are proposed: the Mann uniform shear model (Mann, 1994, 1998), and the Kaimal spectral and exponential coherence model (Kaimal *et al*., 1972). However, the standard recommends use of the Mann turbulence model, and this model will be used for the turbulence in the simulations presented below.

When the turbulence eddies pass through the rotor, the blades cut through the eddies that have sizes ranging from several times the rotor diameter D to smaller than D. This causes the so-called rotational sampling of the turbulence, which is known to move energy from the lower frequencies to multiples (1p, 2p, 3p, etc.) of higher frequencies of the rotor speed (Kristensen and Frandsen, 1982). As an example, a time trace of the axial velocity component at hub height is compared with the corresponding component on the rotating blade at a radius of 63 m in Fig. 3.34(a).

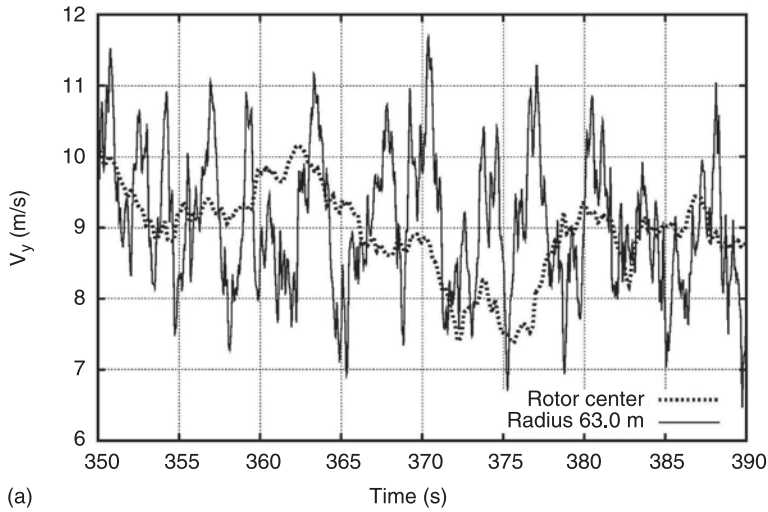

(a)

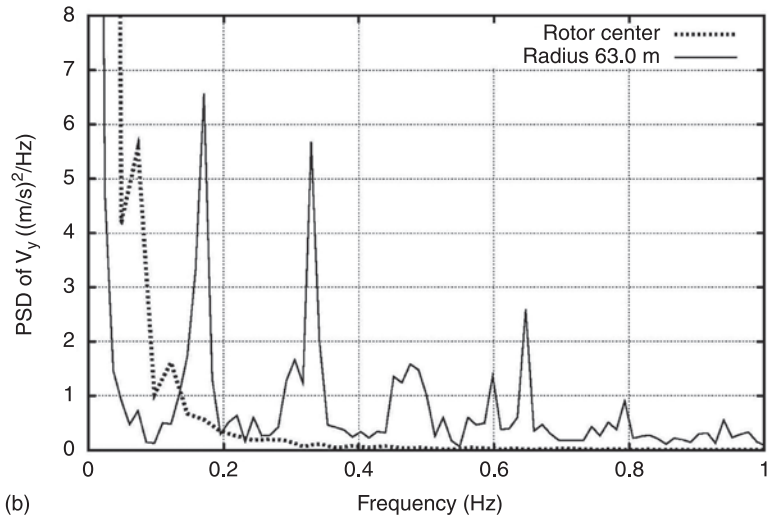

(b)

3.34 (a) Comparison of inflow velocity in turbulent wind at the rotor center and at a point on the rotating blade with a radius of 63 m. Simulations with HAWC2 on the RWT at 8 m/s and a turbulence intensity of 8 m/s. (b) Comparison of power spectral density (PSD) of the inflow velocity in turbulent wind at the rotor center and at a point on the rotating blade with a radius of 63 m. Simulations with HAWC2 on the RWT at 8 m/s and a turbulence intensity of 15%.

The difference between the two traces is considerable with a characteristic 1p variation in the trace of the wind speed seen from the point on the blade. The power spectral density (PSD) of the same two wind speeds is shown in Fig. 3.34(b), and the above-mentioned movement of energy from the low frequencies in the spectrum of the wind speed in the fixed frame of reference to higher frequencies (1p, 2p, etc.) for the rotating point is made clear.

The mechanism of rotational sampling of the turbulence is of fundamental importance for the loading on turbines and for optimizing the aeroelastic response because the wind load input to the system will be concentrated on specific frequencies. To illustrate this, a simulation has been performed on a stiff structural model of a conceptual 5-MW RWT (Jonkman, 2005) using the HAWC2 code and for the same turbulence input, as used in the example above. Spectra of the moment in the turbine components, which are most important for the turbine design and dimensioning, are shown in Fig. 3.35(a) and (b), and they are found to have the following different characteristics.

Flapwise blade root moment M_{Bl_x}

It is observed from Fig. 3.35(a) that this moment has peaks at multiples of the rotational frequency, which means at 1p (0.16 Hz), 2p (0.32 Hz), 3p (0.48 Hz), etc., although the peaks at the higher multiples are small. The spectrum correlates well with the spectrum of the turbulent wind seen from the rotating blade, as shown in Fig. 3.34(b). This is due to the close connection between the inflow angle along the blade and the wind speed.

Tower bottom moments M_{TB_x} (longitudinal) and M_{TB_y} (lateral)

For the longitudinal tower moment, it appears that almost all the energy is concentrated on 3p, with much smaller peaks at 1p and 6p. In the case of small differences in, for example, blade pitch angles combined with shear in the inflow, there could be some energy on the 1p. Regarding the lateral tower moment, the load input is almost zero.

Tower top moments M_{TT_x} (tilt moment) and M_{TT_z} (yaw moment)

The peaks of these two moments (see Fig. 3.35b) are almost similar with decreasing peaks at 1p, 3p, 6p, etc. The higher values for the yaw moment are probably due to a slow change in the wind direction caused by a trend in the horizontal turbulence component.

Besides the influence from the turbulence in the wind to the peaks in the load spectrum, wind shear will also contribute, however, with quite different amount for the different load components. Finally, the mean wind speed will determine the mean loads.

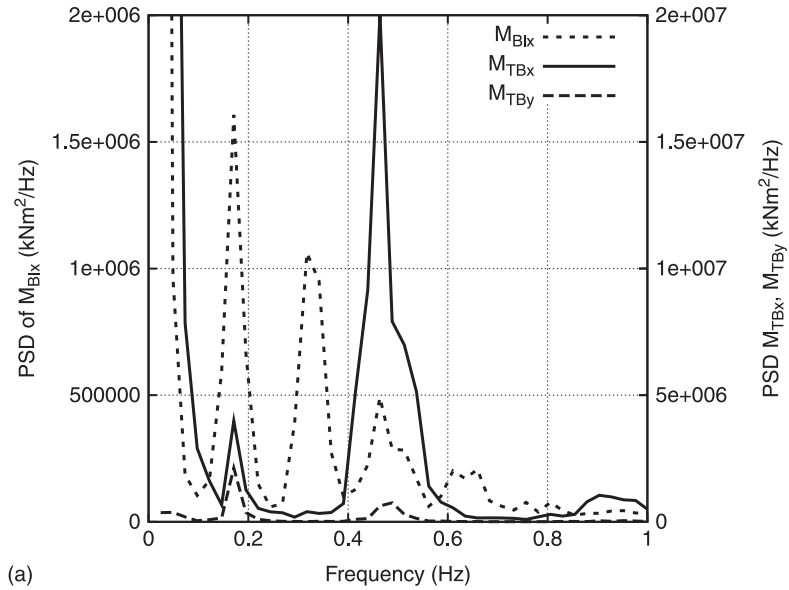

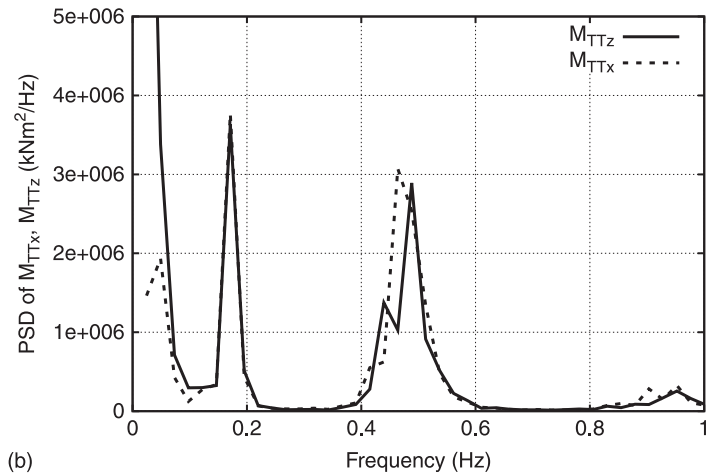

3.35 Turbulent load input. (a) Spectra of tower base moments in longitudinal and lateral directions and of the blade root flapwise moment based on time simulations with the HAWC2 code on the RWT turbine at 8 m/s, 15% turbulence and using a stiff structural dynamic model. (b) Spectra of tower top moments, the yaw moment M_{TT_z} and the tilt moment M_{TT_x} based on time simulations with the HAWC2 code on the RWT at 8 m/s, 15% turbulence and using a stiff structural dynamic model.

Wake loads

The standard IEC61400-3 (2005) specifies how to take operation in wind farms into account when certifying turbines for such sites. Basically, the concept works with an increase of the ambient turbulence to what is called an 'effective turbulence I_e', as formulated by Frandsen (2003). The effective turbulence is determined, for example, by the spacing of the neighboring wind turbines and their thrust coefficient, but also with a factor taking into account which component of the turbine is considered. An example of the variation of I_e in the wake of a single turbine and as a function of the distance from the wake generating turbine is shown in Fig. 3.36 (Frandsen, 2003).

However, it has turned out that there is a need in the industry to supplement the above procedure for more detailed simulations of the loading in wake operation. This led to the development of the dynamic wake meandering (DWM) model (Thomsen and Madsen, 2004; Larsen *et al*., 2008; Madsen *et al*., 2008), where the basic elements are the velocity deficit in the wake and the movement of this deficit determined by the big lateral turbulence components in the atmospheric flow. This modeling approach enables the computation of the mean turbine loads as well as the turbulence loads in wake operation and provides, in general, detailed information of the loading. An example is shown in Fig. 3.37 from Thomsen and Madsen (2004). Measured and simulated variation of average and standard deviation of electrical power, flapwise blade root moment and of yaw moment as a function of direction to an upstream 2 MW turbine aligned at 205° and at a distance of 3.5D are observed. In general, there is a good correlation between measured and simulated data, and one of the advantages of the DWM model compared with the model using an effective turbulence is that both the mean and

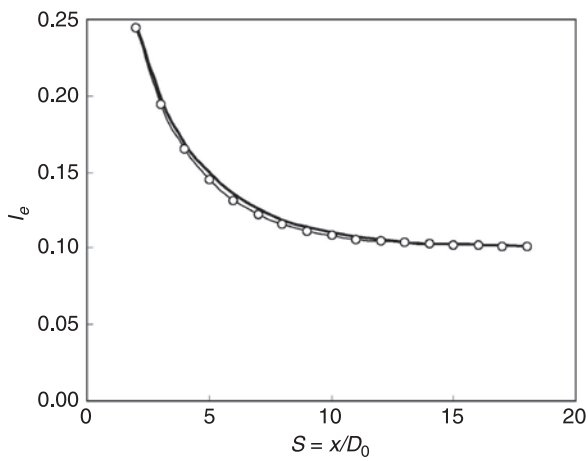

3.36 Variation of the effective turbulence I_e as a function of distance to the wake generating turbine for an ambient turbulence intensity of 10% (Frandsen, 2003).

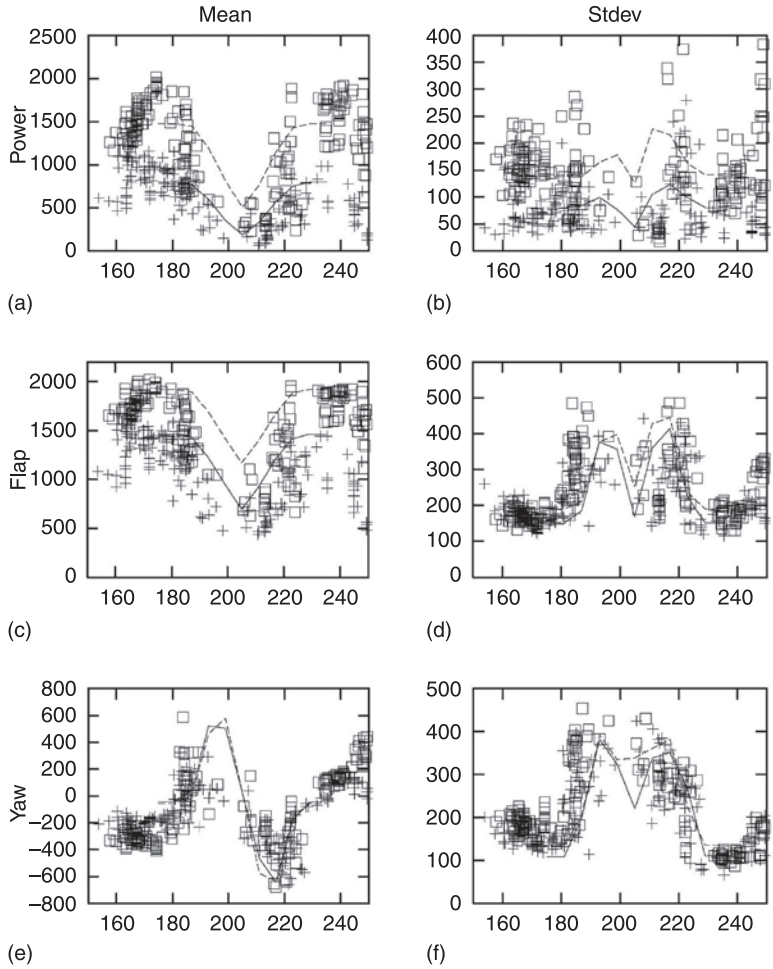

3.37 Measured and simulated variation of average (left panels) and standard deviation (right panels) of electrical power ((a) and (b)), flapwise blade root moment ((c) and (d)) and of yaw moment ((e) and (f)) as a function of direction to an upstream 2 MW turbine aligned at 205° and at a distance of 3.5D. Simulations with the dynamic wake meandering (DWM) model at two different wind speeds shown by dashed lines (Thomsen and Madsen, 2004).

the standard deviation can be computed which, for example, for the yaw loading, is important for providing more accurate design loads.

Extreme loads

Besides the load cases during normal operation with input from turbulence, waves or wakes, the standard IEC61400-3 (2005) also describes a number of extreme

external conditions that must be considered. Some of these extreme external conditions as, for example, cases 'extreme operating gust' (EOG), 'extreme direction change' (EDC) and 'extreme coherent gust with direction change' (ECD), have to be investigated for the turbine in normal operation or combined, for example with an emergency shutdown situation of the turbine. Another important extreme load case is the extreme wind speed for a 50-year recurrence period that has to be computed for the parked turbine, either with the rotor standing still or with the rotor idling.

Many of these extreme load cases are quite challenging in the wind turbine design process and will define the design loads for some components, while fatigue loads will be most important for other components or for part of a component. For a blade, it can often be a combination of fatigue and extreme loads that defines the design loads.

In the discussion below on optimized aeroelastic design, the focus will be on the normal operation cases leading to fatigue loading because this can be discussed in a more general sense, whereas the extreme load conditions are often closely linked to the specific design.

3.4.4 Methods for improved aeroelastic response

The methods for improved aeroelastic response can be divided into two major groups and then into a number of subgroups.

1 Reduction of load input/excitation:
   (a) active methods
      (i) pitch regulation (collective, cyclic or individual pitch)
      (ii) trailing edge flaps
   (b) passive methods
      (i) stall control
      (ii) stall strips
      (iii) flap/pitch coupling
      (iv) flexibility
      (v) hinges
2 Optimized wind turbine dynamics:
   (c) passive methods
      (i) separate excitation from frequency of aeroelastic modes
      (ii) increase coupling of modes with low damping to the higher damped modes
      (iii) increase structural damping
      (iv) passive dampers
   (d) active methods
      (i) powered dampers in tower, nacelle or blades
      (ii) pitch regulation (collective, cyclic or individual)
      (iii) generator torque regulation

However, there can be many designs in which methods from different groups are used on the same turbine.

Reduction of load input/excitation

It is obvious that reduction of the load input is a direct method to control or reduce the response and this can be done actively or passively. The best illustration of this is the difference between a stall-controlled and a pitch-controlled rotor. Basically, the two concepts make use of different operational points on the airfoil characteristics of the profile sections along the blade. For the power control, the stall-controlled rotor depends very much on the rise in airfoil drag when the power output will be limited around rated power. The lift forces do not necessarily decrease for increasing wind speed, so the thrust will increase as a function of wind speed, but the dynamic load input from the turbulence is reduced due to the small slope or even negative slope of the lift versus the angle of attack. The dynamic load and torque input on the pitch-regulated rotor is high, and it is therefore necessary to use variable speed in combination with pitch control.

The collective pitch of the blades is used for the power control, whereas the cyclic pitch can be used to reduce typically the 1p variation in flapwise blade and rotor moments (tilt and yaw moment). The individual pitch control has a higher load reduction potential as loads within a wider frequency range can be controlled and trailing edge flaps open for a distributed load control along the blade.

Regarding passive methods, hinges between the blades and the hub can reduce the load input, as well as the transmission of loads to the nacelle and the tower quite effectively. The two-bladed teetering rotor, eventually with a delta3 hinge, is a good example. Tilt and yaw moments can be reduced almost down to zero depending on the stiffness in the teetering system. On the other hand, the challenge is the considerable flapwise movement of the blade tips, and therefore the teetering rotor is mostly used in downwind turbines in order to keep clearance to the tower. However, it is possible to limit the teeter angle excursions considerably by use of pitch control of the blades using the teeter velocity (Larsen *et al*., 2007). Another major problem is to control the rotor during startup and shut down. During startup, the blades can easily be in a deep stalled mode, and if it is a rotor with low teeter stiffness, some additional mechanical system has to be used to limit the teeter excursions. Advanced pitch or flap control may be developed in the future to better control the aerodynamics of the blades during these conditions.

By increasing the teeter stiffness, there is a soft transition to rotors without a teeter hinge but with highly flexible blades and a flexible hub. Such designs could considerably benefit individual pitch or flap control.

Optimized wind turbine dynamics

It has been shown that the loads from turbulence are concentrated on peaks in the load spectra. One of the important objectives in the aeroelastic design of a turbine

is therefore to separate, as far as possible, the frequency of the aeroelastic modes from the peaks in the load input. On the other hand, this is quite challenging, as turbines – because of noise limitations and aerodynamic optimization – are operated at a variable speed, and then it is not only a number of load peaks that should be avoided but also a number of frequency bands. As an example, the aeroelastic response of the tower of the 5 MW RWT is shown in Fig. 3.38. For the same wind turbine, the load input for some components was presented previously in Fig. 3.35(a) and (b). Besides the response for the standard turbine, the response for three other tower configurations is shown, where the first longitudinal bending tower frequency has been changed from 0.34 to 0.30, 0.26 and 0.22 Hz. It is observed that lowering the tower eigen frequency reduces the tower response around the load input at 3p, and for the lowest tower frequency, the response around 3p is lower than the input (depicted in the spectrum of the stiff wind turbine). However, for this configuration, the response rises at 1p where there is some load input.

The results are shown in a different way in Fig. 3.39 where the amplification of the tower fatigue response (material factor $m = 3$) measured relative to the fatigue of the input is shown as a function of the ratio between the frequency of excitation (3p) relative to the first longitudinal bending tower frequency. When this ratio increases, the amplification decreases which is a well-known result from the basic vibration theory. In Fig. 3.39, the operational range of the RWT is also shown, and it is observed that the ratio of frequency of load input to tower eigen frequency

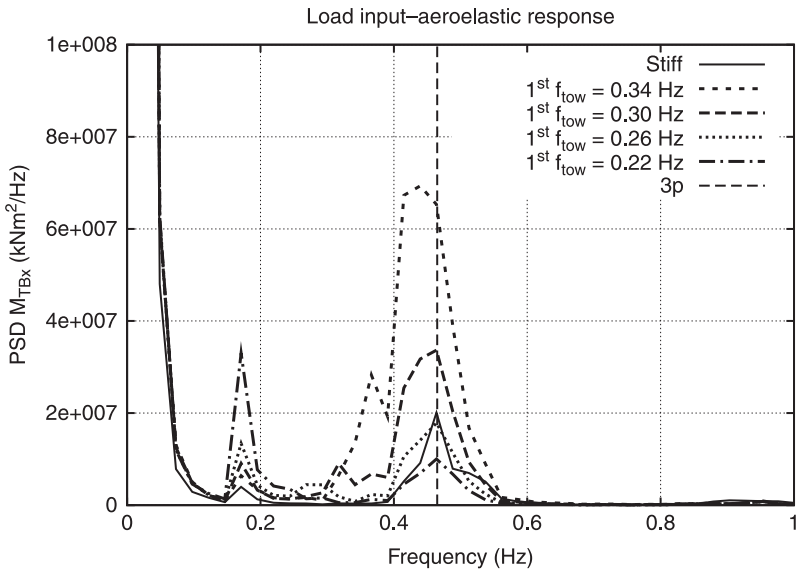

3.38 Power spectrum of the tower bottom bending moment M_{TBx} for different values of tower stiffness, based on simulations with the HAWC2 code on the 5 MW RWT turbine at 8 m/s and 15% turbulence.

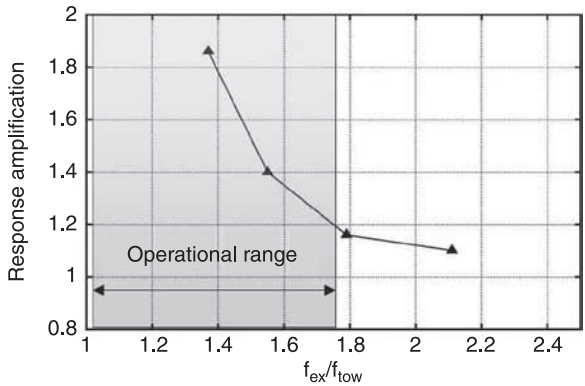

3.39 Aeroelastic tower response amplification as a function of the ratio between excitation frequency (3p) and first tower bending eigen frequency.

in the lower end is close to 1. However, this corresponds to the lowest wind speeds where the load input is low.

Moreover, in Fig. 3.40, the power spectrum of the blade root flapwise bending moment is presented for the same 5 MW RWT being infinitely stiff and flexible. Comparison of the two spectrums indicates that for the stiff design, the maximum energy is obtained at 1*P* which is reasonable, taking into account that the maximum energy from the wind is at the same frequency (see Fig. 3.34(b)). For the flexible wind turbine, the maximum peak in the spectrum is obtained at 2*P*, and this is because many of the wind turbine natural frequencies are close to this frequency.

The presented examples illustrate that it is important in the design process to keep track of a number of frequencies of aeroelastic modes relative to the load input bands. Considerable reduction in fatigue loads can be obtained by a suitable positioning of the eigen frequency of the different aeroelastic turbine modes.

Another important design procedure from the toolbox is to increase the coupling between a low damped aeroelastic mode and a mode with higher damping. Solutions for the edgewise vibration problem described previously are a good example. The task here is to increase the coupling of the edgewise modes with the flapwise modes as the latter often have a higher damping. Even in cases where the flapwise mode is negatively damped, non-linear aerodynamic effects, such as stall hysteresis, will typically limit the amplitudes of such vibrations to acceptable limits. The potential of design for optimal couplings seems big because this, for example, can be done with suitable orientation of the fibers in the blades. However, it requires advanced computational tools to model such couplings in detail.

Increased structural damping is also an important tool for optimized aeroelastic response, and this method has been studied intensively in the past, for example, to solve the problems of edgewise vibrations.

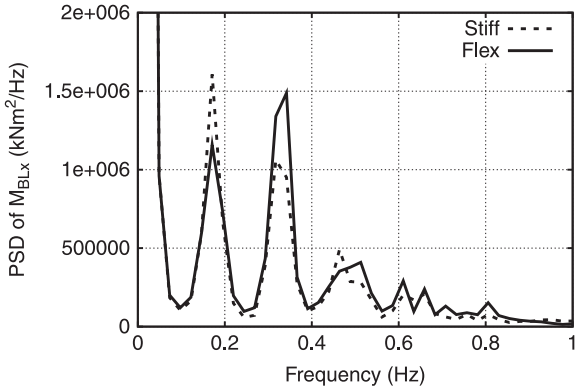

3.40 Power spectrum of flapwise blade root response for the 5 MW RWT based on time simulations with the HAWC2 code at 8 m/s, 15% turbulence and using a stiff structural and flexible structural dynamic model.

Passive and active dampers in different turbine components have been used widely in the past. Again, edgewise vibrations have not only been controlled with suitable dampers in the blades but also with suitable tuned damper systems in, for example, the rear of the nacelle. The last method is a very good illustration of how coupled the blade modes can be with the dynamics of the other part of the turbine. Also, tower vibrations are often controlled with damper systems.

Finally, the pitch system can be used to damp tower loads as well as rotor loads. The difference in the load reduction systems, which also make use of pitch control, is that the input to the control now is, for example, accelerations in the tower top. Lateral tower vibrations can effectively be controlled by the generator torque, as already discussed above.

3.5 Future trends

The future trends in wind turbine design and concepts are influenced by a variety of parameters and conditions and certainly not only determined by potential technology achievements. The ratio between the onshore and offshore market is, for example, an important parameter as the turbines for offshore application might take another development path, perhaps with bigger machines and higher tip speeds than onshore turbines.

3.5.1 Load reduction by control surfaces or boundary-layer control

During the last five to seven years, there has been an increasing research on control of the aerodynamic loads on the blades by control surfaces such as flexible

trailing edge flaps (Buhl *et al*., 2005) or by controlling the boundary layer with, for example, jets. The background for this development is that the biggest blades now have a length of around 63 m, and within a short time, it might increase to 70–80 m. For such blades, there is a need to have a distributed control along the blade as the turbulent inflow conditions can be quite different at different radial positions. Also, in order to be able to damp the individual aeroelastic modes, it is necessary to apply such distributed control techniques. Flexible trailing edge flaps could cover the whole trailing edge of a blade, as illustrated by Andersen *et al*. (2009) in Fig. 3.41, but only with a few sections being active. Andersen *et al*. (2009) report computed reduction in flapwise fatigue blade moments of 25%, 34% and 37% for one flap, two flaps and three flaps covering 10%, 20% and 30% of total blade span, respectively.

The challenge in increasing the load reduction more than 20–25%, which can be achieved with cyclic or individual pitch control as reported by Larsen, Madsen *et al*. (2004), is that it requires more and more accurate control signals. Sensors that can be used are those monitoring the strain in the blade and/or acceleration of the blade or those monitoring the flow over the blade (pressure sensors) or those measuring the inflow to the blade such as five-hole pitot tubes. Also, time delay and noise in sensor signals is critical for increasing the load alleviation by flaps as shown by Andersen *et al*. (2009). The main barrier at the moment in order to implement trailing edge flaps on MW turbines is that robust and reliable flap concepts have not yet been developed.

3.5.2 Flexible blades with bend/pitch coupling

Coupling the flapwise bending of the blade with pitch is an efficient way of changing the aeroelastic response of the blade. This is because a change in pitch directly couples to a change in effective angle of attack of the blade section and thus also to the aerodynamic load of the airfoil section. Recent results from Sandia Laboratories presented by Ashwill *et al*. (2010) show an increase in annual energy capture by 10–12% for the same loads as a baseline rotor on a Zond 750 test turbine. The new

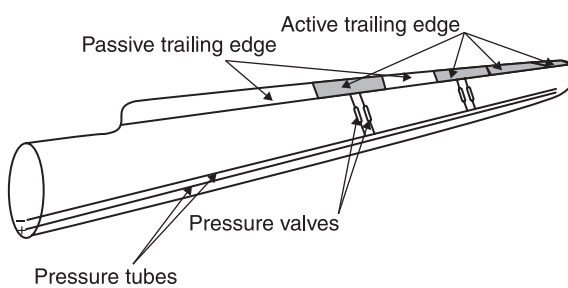

3.41 An illustration of a wind turbine blade with flaps for load alleviation (Andersen *et al.,* 2010).

blade had a flap twist coupling due to a sweep of the blade in the rotor plane and the lower loads were incorporated in the design by increasing the rotor diameter.

Bend/torsion coupling can also result from large blade deflections. Up-scaling of modern wind turbines to multi-MW sizes calls for lighter blade designs in order to reduce weight-induced loads (mass increases with the cube of the scaling factor) and increase cost efficiency. Reduction of weight can be achieved either by reducing the thickness of the blade walls while at the same time reinforcing the blade by using more advanced material or by slendering the blade (reducing the blade chords). Following current design trends, reduction in weight, for a certain blade planform, is followed by a loss in stiffness, and so the blades become more flexible.

It has been identified (Riziotis *et al*., 2008) that large flexible blades of MW wind turbines can undergo flapwise deflections, in normal operation, that exceed 10% of their radius. As indicated in Section 3.2.1, such high deflections can give rise to structural non-linear couplings not met in smaller and stiffer blades. One of the couplings that was found to have a significant contribution to blade torsion loads is the bending–torsion coupling, already addressed in Section 3.2.1. As illustrated in Fig. 3.4, when the blade exhibits very large flapwise deflections and blade curvature is high, the local edgewise bending moment comprises a twisting component with respect to the undeformed coordinate system. In Fig. 3.42, the time series of the

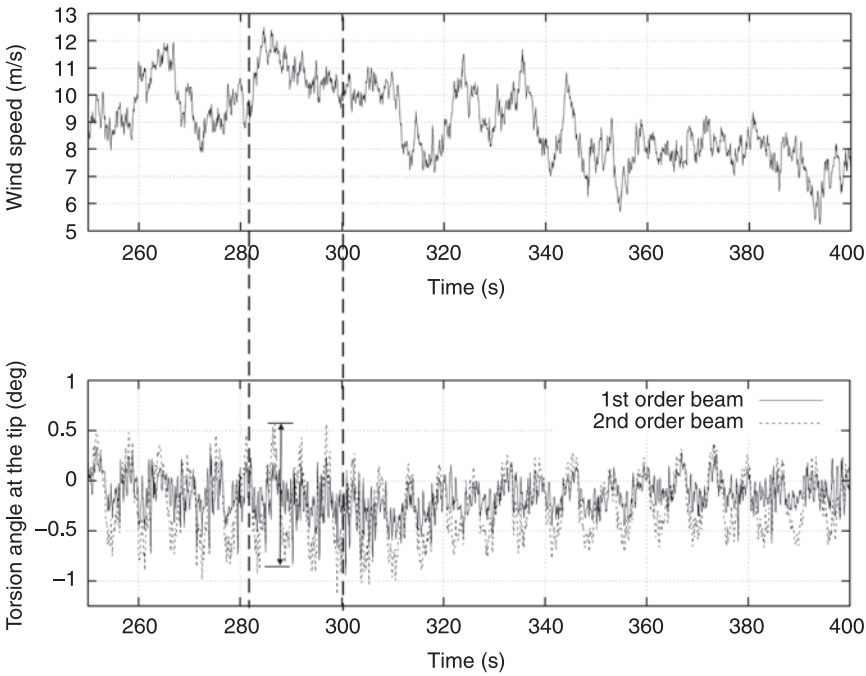

3.42 Time-series of wind speed and torsion angle at blade tip of a 5-MW wind turbine (mean wind speed 8 m/s).

torsion angle at the blade tip is shown for the RWT 5 MW wind turbine operating near the rated speed (around 11 m/s). Comparison of the torsion deformations predicted with a first- and a second-order model indicates that the amplitudes of the torsion angle variations obtained with the higher order model are much higher. It is also noted that they become higher when the wind turbine operates closer to the rated conditions where thrust and, therefore, flapwise deformations become maximum. Predictions of the equivalent blade root torsion moment presented in Fig. 3.43 indicate that pitch bearing loads can be more than twice as those predicted by a conventional first-order model near rated wind conditions.

3.5.3 Integrated design

Future turbine designs will probably have a number of subsystems, for example, for load alleviation, for vibration control or for noise reduction. The turbines will be optimized for low weight and flexibility in order to reduce load input and the transmission of loads between components. The design of such turbines must take place in an integrated environment, and this requires that the design tools and design procedures are developed such that the optimization of aerodynamic, aeroelastic and control properties can be carried out in a fully coupled system.

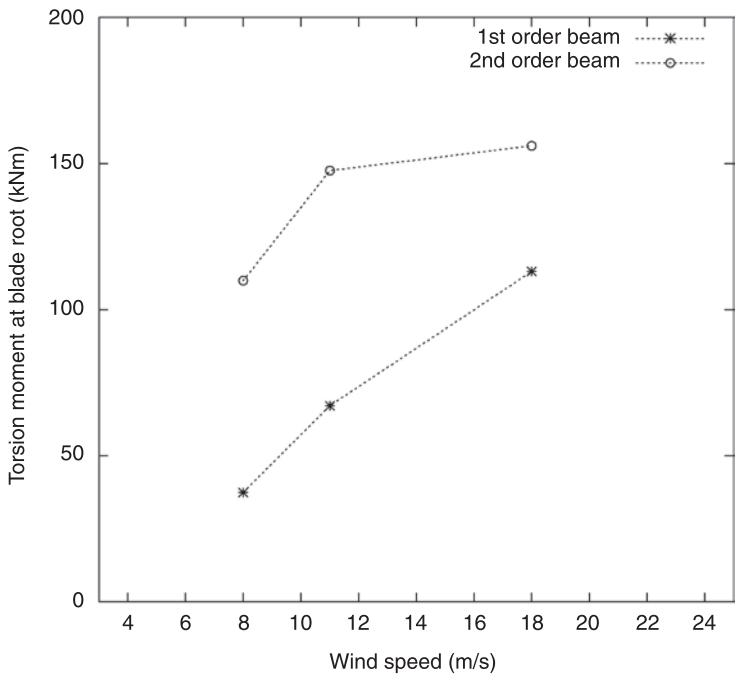

3.43 Equivalent fatigue loads of torsion moment at blade root (1 Hz, $m = 12$).

3.5.4 Pitch or stall control

The stall control concept, in combination with a fixed rotational speed and the use of an induction generator had, due to its robustness, a big success in the beginning of the modern wind turbine development in the 1980s and the 1990s. Later, active stall control was introduced in bigger machines in order to better regulate peak power and for the shutdown of the machines. Also, in recent wind farm installations, the concept has been used as an example for the Danish Rødsand 165 MW wind farm with 72 wind turbines from Bonus Energy, commissioned in 2003. Akhmatov and Nielsen (2005) describe the use of the active stall control in this wind farm temporarily to reduce the mechanical power and contribute to voltage re-establishment in the grid in the case of a short-circuit fault, as required by the Danish transmission system operator (TSO). This shows that a turbine without pitch control and variable speed can fulfill the grid requirements.

The active stall concept solved major problems of the fixed pitch stall machines, but on the other hand, it also became a more complicated system with a full pitch system of the blades and thus in a way comparable in complexity with the pitch-regulated turbines, but with much lower pitch activity than on a pitch-regulated turbine.

A rotor concept in which stall regulation fits well is the two-bladed turbine without a teetering hub. The advantage of the stall-controlled rotor is that the dynamic flapwise moments and also the tilt and yaw moments are smaller than on a pitch-regulated rotor. Therefore, acceptable levels of loading on shaft bending and on the yaw system can be obtained with this design.

3.5.5 Floating wind turbines

Most of the today's offshore wind energy capacity has been installed around the North and Baltic seas, at water depths not exceeding 20 m. For such shallow water applications, fixed-bottom wind turbines are installed using either monopiles driven into the seabed or concrete gravity bases. Recently, there has been a growing interest in exploiting the available wind resource potential at much higher depths (exceeding 30 m), where technologies already used in shallow water environments are no longer economical. For such deep water applications, the use of floating support platforms seems economically more feasible.

Designing of such floating wind turbines calls for integrated computational environments that are capable of simulating the aerodynamics of the rotor, the structural dynamics of the full wind turbine, the wave loads and the dynamics of the support platform, the loads from the mooring lines as well as their interaction (Jonkman and Sclavounos, 2006; Jonkman and Buhl, 2007).

3.6 Sources of further information and advice

Besides citations provided in the previous sections, the reader can get more information about the basic principles of aeroelasticity in the following general

textbooks (Bisplinghoff *et al*., 1955; Dowell, 1995; Fung, 1955). Specifically, for rotorcraft applications, the two textbooks by Johnson (1980) and Bielawa (2006) are excellent, although they focus on aeronautical applications (helicopter rotors and aircraft propellers). With respect to wind turbines, the literature for aeroelasticity is rather limited. Some information can be found in Hansen (2008). There are, nevertheless, many journal publications that deal with all the issues discussed in the chapter. Among those, special references should be made to some review papers providing information on the recent advances in the field of wind turbines aeroelasticity (Rasmussen *et al*., 2003; Hansen *et al*., 2006; Hansen, 2007). Finally, for the reader who would be interested in going deeper into FE analysis and beam modeling, some classic textbooks are those by Bathe (1996), Zienkiewicz and Taylor (1994) and Crisfield (1998).

3.7 References

Akhmatov, V and Nielsen, A H (2005), 'Fixed-speed active-stall wind turbines in offshore applications', *Euro Trans Electr Power*, 15, 1–12.

Andersen, P B, Henriksen, L, Gaunaa, M, Bak, C and Buhl, T (2009), 'Deformable trailing edge flaps for modern megawatt wind turbine controllers using strain gauge sensors', *Wind Energy*, 13(2–3), 193–206.

Ashwill, T D, Kanaby, G, Jackson, K and Zuteck, M (2010), 'Development of the swept twist adaptive rotor (STAR) blade', *Paper AIAA 2010–1582, 48th AIAA Aerospace Sciences Meeting Including the New Horizons Forum and Aerospace Exposition*, 4–7 January, Orlando, FL

Bathe, K J (1996), *Finite Element Procedures*, Prentice Hall, Upper Saddle River, NJ.

Bielawa, R L (2006), *Rotary Wing Structural Dynamics And Aeroelasticity*, AIAA education series, Reston, VA.

Bisplinghoff, R L, Ashley, H and Halfman, R L (1955), *Aeroelasticity*, Addison-Wesley, Cambridge, MA.

Buhl, T, Gaunaa, M and Bak, C (2005), 'Potential load reduction using airfoils with variable trailing edge geometry', *Journal of Solar Energy Engineering*, 127, 503–16.

Chaviaropoulos, P K (2001), 'Flap/lead-lag aeroelastic stability of wind turbine blades', *Wind Energy*, 4, 183–200.

Chaviaropoulos, P, Politis, E S, Sørensen, N N, Hansen, M, Bulder, B H, Winkelaar, D, *et al*. (2003), 'Recent advances on damped wind turbine rotor blades, the DAMPBLADE project', *Proceedings of the 2003 European Wind Energy Conference and Exhibition*, 16–19 June, Madrid, Spain.

Coleman, R P and Feingold, A M (1957), *Theory of Self-excited Mechanical Oscillations of Helicopter Rotors with Hinged Blades*, NASA TN 3844.

Crisfield, M A (1998), *Non-linear Finite Element Analysis of Solids and Structures, Essentials*, John Wiley and Sons, New York.

DNV-OS-J101 (2004), *Design of Offshore Wind Turbine Structures*, Det Norske Veritas, Offshore standard.

Dowell, E H (Ed.) (1995), *A Modern Course in Aeroelasticity*, Kluwer Academic, London.

Frandsen, S (2003), *Turbulence and Turbulence Generated Fatigue in Wind Turbine Clusters*, Risø report R-1188.

Fung, Y C (1955), *An Introduction to the Theory of Aeroelasticity*, John Wiley and Sons, New York.

Hansen, M H (2003), 'Improved modal dynamics of wind turbines to avoid stall-induced vibrations', *Wind Energy*, 6, 179–95.

Hansen, M H (2004), 'Aeroelastic stability analysis of wind turbines using an eigenvalue approach', *Wind Energy*, 7, 133–43.

Hansen, M H (2007), 'Aeroelastic instability problems for wind turbines', *Wind Energy*, 10(6), 551–77.

Hansen, M H and Buhl, T (2006), *Design Guidelines for Passive Instability Suppression – Task 11 Report*, Technical report of STABCON project (NNK5-CT 2002–00627 contract), Risoe-R-1575(EN), RISOE National Laboratory.

Hansen, M O L (2008), *Aerodynamics of Wind Turbines*, Earthscan, London.

Hansen, M O L, Soerensen, J N, Voutsinas, S, Sorensen, N and Madsen, H Aa (2006), 'State of the art in wind turbine aerodynamics and aeroelasticity', *Progress in Aerospace Sciences*, 42, 285–330.

Hodges, D H (1990), 'A mixed variational formulation based on exact intrinsic equations for dynamics of moving beams', *International Journal of Solids and Structures*, 26(11), 1253–73.

Hodges, D H (2003), 'Geometrically exact, intrinsic theory for dynamics of curved and twisted anisotropic beams', *AIAA Journal*, 41(6), 1131–37.

Hodges, D H and Dowell, E H (1974), *Nonlinear Equations of Motion for the Elastic Bending and Torsion of Twisted Non-Uniform Rotor Blades*, NASA TN D-7818.

Hodges, D H and Yu, W (2007), 'A rigorous, engineer-friendly approach for modelling realistic composite rotor blades', *Wind Energy*, 10, 179–93.

IEC61400-1 (2005), *Wind Turbines – Part 1: Design Requirements*, International Electrotechnical Commission, Geneva, Switzerland.

IEC61400-3 (2005), *Wind Turbines – Part 3: Design Requirements for Offshore Wind Turbines, IEC TC88 WG3*, International Electrotechnical Commission, Geneva, Switzerland.

Johnson, W (1980), *Helicopter Theory*, Princeton University Press, Princeton, NJ.

Jonkman, J M (2005), *NREL 5 MW Baseline Wind Turbine*, Technical report, NREL/NWTC.

Jonkman, J M and Buhl, M L Jr. (2007), 'Development and verification of a fully coupled simulator for offshore wind turbines', *AIAA Paper 2007–0212, 45th AIAA Aerospace Sciences Meeting and Exhibition, Wind Energy Symposium*, Reno, Nevada, 8–11 January.

Jonkman, J M and Sclavounos, P D (2006), 'Development of fully coupled aeroelastic and hydrodynamic models for offshore wind turbines', *AIAA Paper 2006–0995, 44th AIAA Aerospace Sciences Meeting and Exhibition, Wind Energy Symposium*, Reno, Nevada, 10–12 January.

Kaimal, J C, Wyngaard, J C, Izumi, Y and Cote, O R (1972), 'Spectral characteristics of surface-layer turbulence', *Quarterly Journal of the Royal Meteorological Society*, 98, 563–98.

Kallesøe, B S (2007), 'Equations of motion for a rotor blade, including gravity pitch action and rotor speed variations', *Wind Energy*, 10, 207–30.

Kallesøe, B S and Hansen, M H (2010), 'Lateral tower load mitigation by generator torque control', *Paper AIAA 2010–1001 presented at 48th AIAA Aerospace Sciences Meeting Including the New Horizons Forum and Aerospace Exposition*, 4–7 January, Orlando, FL.

Kristensen, L and Frandsen, S (1982), 'Model for power spectra of the blade of a wind turbine measured from the moving frame of reference', *Journal of Wind Engineering and Industrial Aerodynamics*, 10(2), 249–62.

Larsen, G C, Madsen, H Aa, Thomsen, K and Larsen, T J (2008), 'Wake meandering: a pragmatic approach', *Wind Energy*, 11, 377–95.

Larsen, T J (Ed.) (2009), *How 2 Hawc2, the User's Manual*. Risø-r-1597 (ver.3–7)(en), Risø National Laboratory, Roskilde, Denmark.

Larsen, T J, Hansen, A and Buhl, T (2004), 'Aeroelastic effects of large blade deflections for wind turbines', *Proceedings of the special topic conference: The science of making torque from wind*, Roskilde, Denmark, pp. 238–46.

Larsen, T J, Madsen, H Aa, Hansen, A M and Thomsen, K (2005), 'Investigation of stability effects of an offshore wind turbine using the new aeroelastic code HAWC2', *Proceedings (CD-ROM), Copenhagen Offshore Wind Conference 2005*, 25–28 September, Copenhagen, p. 6.

Larsen, T J, Madsen, H Aa and Thomsen, K (2004), 'Active load reduction using individual pitch, based on local blade flow measurements, *Wind Energy*, 8, 67–80.

Larsen, T J, Madsen, H Aa, Thomsen, K and Rasmussen, F (2007), 'Reduction of teeter angle excursions for a two-bladed downwind rotor using cyclic pitch control', *Proceedings of the 2007 European Wind Energy Conference and Exhibition, Milan (IT)*, EWEA, Brussels, 7–10 May, p. 9.

Leishman, J G and Crouse, G L (1989), *State-Space Model for Unsteady Airfoil Behavior and Dynamic Stall*, AIAA Paper 89–1319 CP.

Lobitz, D W (2005), 'Parameter sensitivities affecting the flutter speed of a MW-sized blade', *Journal of Solar Energy Engineering, Transaction of the ASME 2005*, 127, 538–43.

Madsen, H Aa, Larsen, G C, Mikkelsen, R and Troldborg, N (2008), 'Wake deficit and turbulence simulated with two models compared with inflow measurements on a 2 MW wind turbine in wake conditions', *Proceedings from EWEC2008*, 31 March – 3 April 2008, Scientific Track, Brussels, Belgium.

Mann, J (1994), 'The spatial structure of neutral atmospheric surface-layer turbulence', *Journal of Fluid Mechanics*, 273, 141–68.

Mann, J (1998), 'Wind field simulation', *Probabilistic Engineering Mechanics*, 13(4), 269–82.

Markou, H, Hansen, M H, Buhl, T, Engelen, T van, Politis, E S, Riziotis, V A, *et al*. (2007), 'Aeroelastic stability and control of large wind turbines – main results', *Proceedings of the 2007 European wind energy conference and exhibition*, 7–10 May 2007, Milan, Italy.

Petersen, J T, Madsen, H Aa, Björck, A, Enevoldsen, P, Øye, S, Ganander, H, *et al*. (1998), *Prediction of Dynamic Loads and Induced Vibrations in Stall. Risø-R-1045(EN)*, Risø National Laboratory, Roskilde, Denmark.

Petot, D (1989), 'Differential equation modelling of dynamic stall', *Recherché Aerospatiale*, 5, 59–72.

Politis, E S, Chaviaropoulos, P K, Riziotis, V A, Voutsinas, S G and Romero-Sanz, I (2009), 'Stability analysis of parked wind turbine blades', *Proceedings of the EWEC 2009*, 16–19 March, Scientific Track, Marseille, France.

Rasmussen, F, Hansen, M H, Thomsen, K, Larsen, T J, Bertagnolio, F, Johansen, J, *et al*. (2003), 'Present status of aeroelastcity of wind turbines', *Wind Energy*, 6, 213–28.

Riziotis, V A and Voutsinas, S G (1997), 'Gast: a general aerodynamic and structural prediction tool for wind turbines', *Proceedings of the EWEC 1997*, October 1997, Dublin, Ireland, pp. 448–52.

Riziotis, V A and Voutsinas, S G (2006), 'Advanced aeroelastic modeling of complete wind turbine configurations in view of assessing stability characteristics', *Proceedings of the EWEC*, 27 February–2 March, Scientific Track, Athens, Greece.

Riziotis, V A, Voutsinas, S G, Politis, E S and Chaviaropoulos, P K (2004), 'Aeroelastic stability of wind turbines: the problem the methods and the issue', *Wind Energy*, 7, 373–92.

Riziotis, V A, Voutsinas, S G, Politis, E S, Chaviaropoulos, P K, Hansen, A M, Madsen, H A, *et al*. (2008), 'Identification of structural non-linearities due to large deflections on a 5 MW wind turbine blade', *Proceedings of the EWEC*, 31 March–3 April, Scientific Track, Brussels, Belgium.

Schepers(editor), J G, Heijdra, J J, Foussekis, D, Øye, S, Rawlinson Smith, R, Belessis, M, *et al*. (2002), *Verification of European Wind Turbine Design Codes, VEWTDC: Final Report*. Technical report ECN-C-01-055, Netherlands Energy Research Foundation ECN. Available from: http://www.ecn.nl/publicaties/default.aspx?nr=ECN-C-01-055 [Accessed 7 Feb 2010].

Thomsen, K and Madsen, H Aa (2004), 'A new simulation method for turbines in wake – applied to extreme response during operation', *Wind Energy*, 8, 35–47.

Thomsen, K, Petersen, J T, Nim, E, Øye, S and Petersen B A (2000), 'A method for determination of damping for edgewise blade vibrations', *Wind Energy*, 3, 233–46.

Zienkiewicz, O C and Taylor, R L (1994), *The Finite Element Method Volume 1 and 2*, McGraw-Hill, London.

4

Wind turbine wakes and wind farm aerodynamics

J. N. SØRENSEN, Technical University of Denmark, Denmark

Abstract: This chapter presents various aspects of wind turbine aerodynamics. Wind turbine aerodynamics is the most central discipline for design and construction of wind turbine blades. Basics of the blade element momentum theory are presented along with guidelines for the construction of airfoil data. It provides a review of advanced numerical simulation (computational fluid dynamics) tools for wind turbine rotors and wakes. This includes rotor predictions as well as models for simulating wind turbine wakes and flows in wind farms. Finally, future trends concerning wind turbine aerodynamics are discussed.

Key words: rotor aerodynamics, blade element momentum (BEM) theory, computational fluid dynamics (CFD), wakes, wind farms.

4.1 Introduction

Aerodynamics concerns modeling and prediction of aerodynamic forces on the blades and the solid structures of a wind turbine. The aerodynamic model is normally integrated with models for wind conditions and structural dynamics. The integrated aeroelastic model for predicting performance and structural deflections is a prerequisite for design, development and optimization of wind turbines. Aerodynamics is the oldest science in wind energy. By using simple axial momentum and energy considerations, Lanchester (1915) and Betz (1920) predicted that even an ideal wind turbine cannot exploit more than 59.3% of the wind power passing through the rotor disk. A major breakthrough was achieved by Glauert (1935), who formulated the blade element momentum (BEM) theory. This theory, which has since been extended with many engineering rules, is today the basis for all rotor design codes in use by industry.

The forces acting on a wind turbine are dominated by an incoming wind that varies in time and space, hence a stochastic description of the wind field and a dynamical modeling of the blades and solid structures of the wind turbine form an intrinsic part of the aerodynamic design methodology. When the wind direction changes, misalignment with the rotational axis occurs. This causes periodic variations in the angle of attack that invalidates the assumption of axisymmetric inflow conditions. When a turbine is operating at its optimum condition, aerodynamic stall is always present on some part of the blades. In order to cope with all these different operating conditions the basic steady and axisymmetric BEM model, as it was formulated by Glauert (1935), has been extended with various empirically based modifications.

Alternatively, the BEM model may be replaced by Navier–Stokes computations. However, this type of computation still demands too much computing power to be a part of the design cycle. Aerodynamic modeling may also concern design of specific parts of wind turbines, such as rotor blade geometry or performance predictions of wind farms. In such a case, Navier–Stokes computations may be the only alternative that can provide sufficient detailed information.

4.2 One-dimensional momentum theory

We first discuss the simple axial momentum theory originated by Rankine (1865), W Froude (1878) and R E Froude (1889). Consider an axial flow of speed U_0 past an actuator disk of area A with constant axial load (thrust) T. Let u_R be the axial velocity in the rotor plane, u_1 the axial velocity in the ultimate wake where the air has regained its undisturbed pressure value $p_1 = p_0$ and let ρ denote the density of air. We now consider a one-dimensional (1D) model for the stream tube that encloses the rotor disc (see Fig. 4.1), where A_0 and A_1 are the cross-sectional areas of the wake far upstream and far downstream of the rotor, respectively.

The equation of continuity requires that the rate of mass flow $\dot{m}$ is constant in each cross section.

$$\dot{m} = \rho U_0 A_0 = \rho u_R A = \rho u_1 A_1. \quad [4.1]$$

Axial momentum balance for the considered stream tube, ignoring the influence of the pressure on the stream tube, results in the following equation for the thrust:

$$T = \dot{m}(U_0 - u_1) = \rho u_R A(U_0 - u_1). \quad [4.2]$$

Applying the Bernoulli equation in front of and behind the rotor, we find that the total pressure head of the air in the slipstream has been decreased by

$$\Delta p = \tfrac{1}{2}\rho(U_0^2 - u_1^2). \quad [4.3]$$

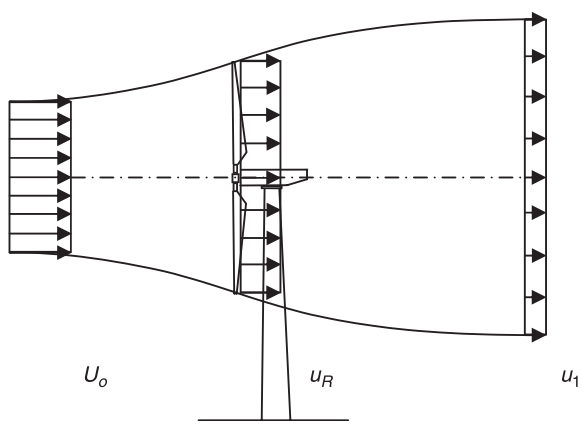

4.1 Control volume for one-dimensional actuator disk.

The pressure drop takes place across the rotor and represents the thrust $T = A\Delta p$. Combining equations [4.2] and [4.3] we get the well-known result

$$u_R = \tfrac{1}{2}(u_1 + U_0). \quad [4.4]$$

Introducing the axial interference factor as follows

$$a = \frac{U_0 - u_R}{U_0} \quad [4.5]$$

we get that $u_R = (1 - a)U_0$ and $u_1 = (1 - 2a)U_0$. From equation [4.2] we get the following expressions for thrust and power extraction:

$$T = 2\rho A U_0^2 a(1-a) \quad [4.6]$$

$$P = u_R T = 2\rho A U_0^2 a(1-a)^2. \quad [4.7]$$

Introducing the dimensionless thrust and power coefficient, respectively,

$$C_T \equiv \frac{T}{\tfrac{1}{2}\rho A U_0^2}, \quad C_P \equiv \frac{P}{\tfrac{1}{2}\rho A U_0^3} \quad [4.8]$$

we get

$$C_T = 4a(1-a), \; C_P = 4a(1-a)^2. \quad [4.9]$$

Differentiating the power coefficient with respect to the axial interference factor, the maximum obtainable power is obtained as

$$C_{P\max} = \frac{16}{27} = 0.593 \quad \text{for} \quad a = \frac{1}{3} \quad [4.10]$$

This result, usually referred to as the Betz limit, states that the upper maximum for power extraction is 59.3% of the kinetic energy contained in a stream tube having the same cross section as the disc. However, it does not include the losses due to rotation of the wake and therefore it represents a conservative upper maximum.

4.3 Blade element momentum theory

The blade element momentum method was developed by Glauert (1935) as a practical way to analyze and design rotor blades. The basic idea behind the model is to combine axial and angular momentum balance with forces and moments determined from a blade element strip theory. Applying the axial momentum equation on a differential element, i.e. an annulus comprising two stream surfaces, we get

$$dT = \rho u(U_0 - u_1)2\pi r dr + \int_{CV} p \, d\mathbf{A} \cdot \mathbf{e}_x, \quad [4.11]$$

where $2\pi r dr$ is the area of the rotor disk on which the local thrust dT acts and the integral is the axial component of the force exerted by the pressure on the annular

control volume. In BEM theory it is assumed, as an approximation, that the contribution from the pressure on the axial momentum is negligible, hence equation [4.11] is written as

$$\frac{dT}{dr} = \rho u_R (U_0 - u_1) 2\pi r. \quad [4.12]$$

Applying angular momentum balance, we get

$$\frac{dQ}{dr} = \rho u_R r u_\theta 2\pi r, \quad [4.13]$$

where u_θ is the azimuthal velocity behind the rotor. Assuming that $u_R \simeq \frac{1}{2}(U_0 + u_1)$ is valid also for a differential element and introducing the azimuthal interference factor as $a' = u_\theta/(2\Omega r)$, where Ω denotes the angular velocity of the rotor, equations [4.12] and [4.13] read

$$\frac{dT}{dr} = 4\pi\rho U_0^2 a(1-a). \quad [4.14]$$

$$\frac{dQ}{dr} = 4\pi\rho r^3 U_0 \Omega a'(1-a). \quad [4.15]$$

In the BEM technique the momentum theory is combined with local blade element considerations using tabulated 2D airfoil data. Employing blade-element theory, axial load and torque are written as, respectively,

$$\frac{dT}{dr} = BF_n = \frac{1}{2}\rho c B V_{rel}^2 \cdot C_n, \quad [4.16]$$

$$\frac{dQ}{dr} = BrF_t = \frac{1}{2}\rho c B r V_{rel}^2 \cdot C_t, \quad [4.17]$$

where B is the number of blades, c is the local chord length, V_{rel} is the relative flow velocity, as seen by the airfoil, F_n and F_t denote the loading on each blade in axial and tangential direction, respectively, and C_n and C_t denote the corresponding 2D force coefficients.

The force coefficients are related to the lift and drag coefficients as follows:

$$C_n = C_l \cos\phi + C_d \sin\phi, \quad [4.18]$$

$$C_t = C_l \sin\phi - C_d \cos\phi, \quad [4.19]$$

where ϕ denotes the angle between the rotor plane and the relative velocity (see Fig. 4.2). From the velocity triangle at the blade-element, we deduce that

$$\sin\phi = \frac{U_0(1-a)}{V_{rel}}, \quad \cos\phi = \frac{\Omega r(1+a')}{V_{rel}}, \quad [4.20]$$

where the induced velocity is defined as $W_i = (-aU_0, -a'\Omega r)$ and the relative velocity is given as

$$V_{rel} = \sqrt{U_0^2(1-a)^2 + \Omega^2 r^2 (1+a')^2}. \quad [4.21]$$

From equation [4.20] we get

$$V_{rel}^2 = \frac{U_0^2(1-a)^2}{\sin^2\phi} = \frac{U_0(1-a)\Omega r(1+a')}{\sin\phi\cos\phi}. \quad [4.22]$$

Inserting these expressions into equations [4.16] and [4.17], we get

$$\frac{dT}{dr} = \frac{\rho B c U_0^2(1-a)^2}{2\sin^2\phi} \cdot C_n, \quad [4.23]$$

$$\frac{dQ}{dr} = \frac{\rho B c U_0(1-a)\Omega r^2(1+a')}{2\sin\phi\cos\phi} \cdot C_t. \quad [4.24]$$

Combining equations [4.14]–[4.15] with equations [4.23]–[4.24], we get

$$a = \frac{1}{4\sin^2\phi/(\sigma C_n)+1}, \quad [4.25]$$

$$a' = \frac{1}{4\sin\phi\cos\phi/(\sigma C_t)-1}, \quad [4.26]$$

where $\sigma = Bc/2\pi r$ is the solidity of the rotor. To determine the flow conditions and loadings, these equations are solved at different radial cross sections along the blade. The equations are most efficiently solved as follows: 1) Guess appropriate values for a and a'; 2) compute the flow angle from equation [4.20] and determine the angle of attack, $\alpha = \phi - \gamma$, where γ is the local pitch angle (see Fig. 4.2); 3) determine the force coefficients from tabulated airfoil data; 4) compute a and a' from equations [4.25] and [4.26] and continue the iteration until convergence. Albeit simple to use, these equations are strictly speaking only valid for a rotor operating under steady axisymmetric flow conditions. In practice, they need to be adjusted to cope with realistic operational modes. In the following we will briefly go through the most relevant adjustments.

4.3.1 Tip correction

The BEM method is a 1D approach based on the actuator disc principle, which corresponds to a rotor with an infinite number of blades. To account for the difference in circulation between an N-bladed rotor and an actuator disc, a tip loss factor was derived by Prandtl (Betz, 1919) and introduced in the BEM technique by Glauert (1935). In Glauert's method a correction factor F is introduced as follows:

$$F = \frac{2}{\pi}\cos^{-1}\left[\exp\left(-\frac{B(R-r)}{2r\sin\phi}\right)\right], \quad [4.27]$$

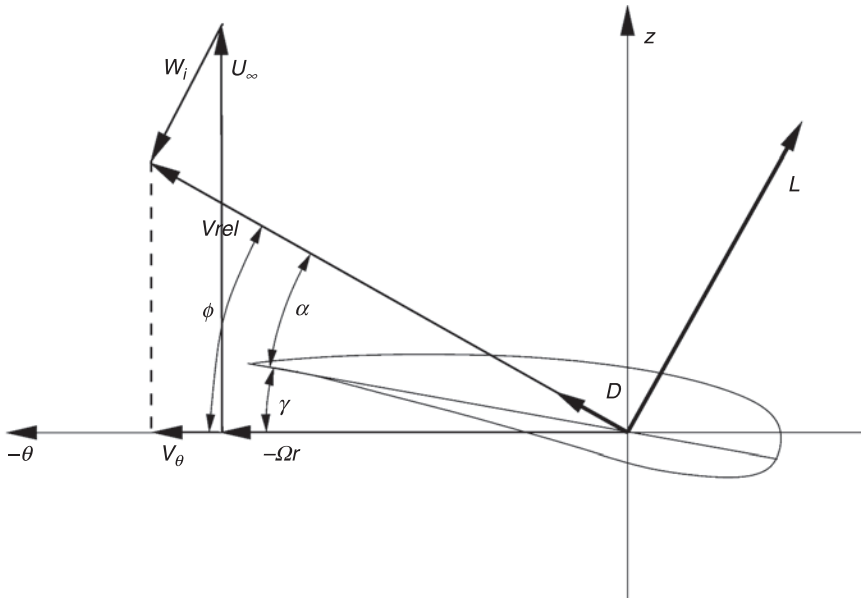

4.2 Cross-sectional airfoil element.

where B denotes the number of blades and $(R–r)$ is the distance from the tip to the considered radial cross section. The correction is introduced by dividing the force coefficients in equations [4.21] and [4.22] by F. Different tip loss correction models have been developed to calculate load and power of wind turbines (de Vries, 1979). Recently, some of the existing tip loss correction models were analyzed by Shen *et al*. (2005a) who found an inconsistency in their basic form, which results in incorrect predictions of the aerodynamic behavior in the proximity of the tip. To remedy the inconsistency, a new tip loss correction model was proposed and tested in combination with both a standard BEM model (Shen *et al*., 2005a) and a Navier–Stokes-based actuator disc model (Shen *et al*., 2005b).

4.3.2 Turbulent wake state

When the axial interference factor becomes greater than about 0.4 the rotor starts to run in the turbulent wake state and axial momentum theory is no longer valid (see e.g. Stoddard, 1977 or Sørensen *et al*., 1998). In the turbulent wake state, a solution can be found by using an empirical relationship between the thrust coefficient and the axial interference factor. Different relations can be used (e.g. Spera, 1994 or Eggleston and Stoddard, 1987). Below we show the expression proposed by Spera (1994):

$$\text{If } a < a_c,\ a = \frac{1}{\frac{4F\sin^2\varphi}{\sigma C_n} + 1}, \qquad [4.28]$$

$$\text{If } a > a_c,\ a = \frac{1}{2}[2 + K(1 - 2a_c) - \sqrt{(K(1 - 2a_c) + 2)^2 + 4(Ka_c^2 - 1)}], \qquad [4.29]$$

where $a_c = 0.2$ and $K = \frac{4F\sin^2\varphi}{\sigma C_n}$.

4.3.3 Yaw misalignment

When the rotor disc is not aligned with the incoming wind, yaw misalignment appears and the induced velocity will be subject to an azimuth variation. In this case, the wake is not in line with the free wind direction and it is impossible to apply the usual control volume analysis. A way of solving the problem is to maintain the control volume and specify an azimuth-dependent induction. In practice, it works by computing a mean induction and prescribing a function that gives the azimuthal dependency of the induction. The following simple formula has been proposed by Snel and Schepers (1995):

$$w_i = w_{i0}\left[1 + \frac{r}{R}\tan\left(\frac{\chi}{2}\right)\cos(\theta_{blade} - \theta_0)\right], \qquad [4.30]$$

where w_{i0} is the annulus-averaged induced velocity and χ is the wake skew angle, which is not identical to the yaw angle because the induced velocity in yaw alters the mean flow direction in the wake. In the notation used here, θ_{blade} denotes the azimuthal position of the blade and θ_0 is the azimuthal position where the blade is deepest in the wake.

4.3.4 Dynamic wake

Dynamic wake or dynamic inflow refers to unsteady flow phenomena that affect the loading on the rotor. In a real flow situation, the rotor is subject to unsteadiness from coherent wind gusts, yaw misalignment and control actions, such as pitching and yawing. When the flow changes in time the wake is subject to a time delay when going from one equilibrium state to another. An initial change creates a change in the distribution of trailing vorticity which then is convected downstream and first can be felt in the induced velocities after some time. However, the BEM method in its simple form is basically steady; hence unsteady effects have to be included as an 'add-on'. In the European CEC Joule II project 'Dynamic Inflow: Yawed Conditions and Partial Span Pitch' (see Schepers and Snel, 1995) various dynamic inflow models were developed and tested. Essentially a dynamic inflow model predicts the time delay through an exponential decay with a time constant

corresponding to the convective time of the wake. As an example, the following simple model was suggested,

$$Rf\,(r/R)\,\frac{du_i}{dt} + 4u_i(U_0 - u_i) = \frac{1}{2\pi r}\frac{dT}{dr}, \qquad [4.31]$$

where the function $f(r/R)$ is a semi-empirical function associated with the induction. The equation can be seen to correspond to the axial momentum equation [4.9], except for the time term that is responsible for the time delay.

4.3.5 Wind inflow

To include a realistic wind input in the computations, it is important to simulate a time history of the wind field that mimics a correct spatial and temporal variation. A method for simulating the time history of the wind as it is seen by a rotating blade was developed by Veers (1988). In a later method by Mann (1998) cross-correlation features are obeyed by using the linearized Navier–Stokes equations as basis for the model.

4.3.6 Airfoil data

As a pre-step to the BEM computations, 2D airfoil data have to be established from wind tunnel measurements or computations. For many years wind turbine blades were designed using well-tested aviation airfoils, such as the NACA 44xx and the NACA 63-4xx airfoils, as wind turbine manufacturers traditionally were reluctant to change to other airfoil types because of the fear of unexpected stall behavior. However, since the beginning of the 1990s various tailor-made airfoils have been designed for wind turbine rotors, e.g. Björk (1990), Tangler and Sommers (1995), Timmer and Rooij (2003), and Fuglsang and Bak (2004). In order to construct a set of airfoil data to be used for a rotating blade, the airfoil data further need to be corrected for 3D and rotational effects. Simple correction formulas for rotational effects have been proposed by Snel *et al.* (1993), Du and Selig (1998), Chaviaropoulos and Hansen (2000), and Bak *et al.* (2006) for incidences up to stall. As a simple engineering method, the following expression can be used to correct the lift data:

$$C_{l,3D} = C_{l,2D} + a(c/r)^b\left[C_{l,inv} - C_{l,2D}\right], \qquad [4.32]$$

where a and b are constants, with a values in the range from 2 to 3 and b values in the range from 1 to 2. A similar expression can be used for the drag coefficient. For higher incidences (>45°), 2D lift and drag coefficients of a flat plate can be used. These data, however, are too big because of aspect ratio effects and here the correction formulas of Viterna and Corrigan (1981) are usually applied (see also Spera, 1994). In Hoerner (1965), it is stated that the normal coefficient is approximately constant for angles of attack between 45° and 90° and that the

suction peak at the leading edge always causes a small driving force. Thus, as a guideline to construct airfoil data at high incidences one can exploit the following features:

$$C_n = C_l \cos\phi + C_d \sin\phi = C_d(\alpha = 90^\circ), \quad [4.33]$$

$$C_t = C_l \sin\phi - C_d \cos\phi > 0, \quad [4.34]$$

where a typical value for $C_d(\alpha = 90°)$ is 1.2. For angles of attack between stall and 45° the airfoil data may be determined using linear interpolation between the two sets of corrected data.

Since the angle of attack is constantly changing due to fluctuations in the wind and control actions, it is necessary to include a dynamic stall model to compensate for the time delay associated with the dynamics of the boundary layer and wake of the airfoil. This effect can be simulated by a simple first-order dynamic model, as proposed by Øye (1991), or it can be considerable more advanced, taking into account also attached flow and leading edge separation, as in the model of Larsen *et al*. (2007), and compressibility effects, as in the model of Leishman and Beddoes (1989).

4.4 Computational fluid dynamics modeling of wind turbine rotors

Computational fluid dynamics (CFD) has become an important supplement to the BEM technique. Although it is beyond the present day computer facilities to use CFD for the actual design process, after having obtained a design using BEM, CFD can be utilized to verify and check whether the design displays any unwanted aerodynamics features. Furthermore, CFD can be used when optimizing 2D airfoil shapes or in connection with simplified wake studies. During the past four decades a strong research activity within the aeronautical field has resulted in the development of a series of CFD tools. This research has focused on the development of efficient solution algorithms and numerical schemes for solution of the flow equations, grid generation techniques and modeling of boundary layer turbulence. These elements together form the basis of all CFD codes, of which some have long been available as standard commercial software.

Today, there are two main paths to follow when conducting CFD computations. The most popular is based on solving the Reynolds-averaged Navier–Stokes (RANS) equations, closing the system by introducing a suitable one-equation or two-equation turbulence model, such as the $k - \varepsilon$ or the $k - \omega$ model. Using this model, only the time-averaged flow field is computed, whereas the unsteady field is modeled through the turbulence model. If the flow is dominated by a broad spectrum of timescales, the low frequencies may be simulated partly by maintaining the time term in the RANS equations. In this case it is sometimes referred to as

unsteady RANS (URANS). The advantage of RANS or URANS is that a full resolved computation can be established with some few million mesh points, which makes it possible to reach a full 3D solution even on a portable computer. The accuracy of the computations, however, is restricted by the turbulence models' lack of ability of representing a full unsteady spectrum. Thus, for attached flow the accuracy is fully adequate, whereas for stalled flows it may degenerate completely. This is further rendered complicated by the laminar–turbulent transition process that also has to be modeled in order to compute the onset of turbulence. An alternative to RANS/URANS is large eddy simulation (LES). In LES the Navier–Stokes equations are filtered spatially on the computational mesh and only the sub-grid-scale part of the turbulence is modeled using a so-called sub-grid-scale (SGS) model. The advantage of LES is that all the dynamics of the flow fields are captures and that an accurate solution can be obtained even under highly separated flow conditions. The computational price, however, is often prohibitive, even when solving parallelized computing algorithms on large cluster systems, because of the large number of mesh points needed to resolve practical flows at high Reynolds numbers. As compared to direct numerical simulation (DNS), where the Navier–Stokes equations are solved directly without any modeling of the turbulence, LES is, however, still several orders of magnitude faster.

The first full Navier–Stokes simulation for a complete rotor blade was carried out by Sørensen and Hansen (1998) using the $k - \omega$ SST model of Menter (1993). These simulations were later followed by Duque *et al*. (1999, 2003) and Sørensen *et al*. (2002) in connection with the American NREL experiment at NASA Ames and the accompanying NREL/NWTC aerodynamics blind comparison test (Schreck, 2002). The NREL experiments have achieved significant new insight into wind turbine aerodynamics and revealed serious shortcomings in present day wind turbine aerodynamics prediction tools. In particular, it was found that performance computations using the BEM technique were extremely sensitive to the input blade section aerodynamic data. The Navier–Stokes computations generally exhibited good agreement with the measurements up to wind speeds of about 10 m/s. At this wind speed, flow separation sets in and for higher wind speeds the boundary layer characteristics is dominated by stall and the computations underestimate the power yield. Johansen *et al*. (2002) applied a hybrid LES/RANS technique on the NREL phase VI rotor under parked conditions. Good agreement with measurements was obtained at low angles of attack when the flow is largely attached. However, at high angles of attack the computations did not improve as compared to RANS computations. In the conclusion it was suggested that the inclusion of a laminar–turbulent transition model most likely will improve the quality of the results. To this end, a recent study by Sørensen (2009), using the correlation-based transition model of Menter *et al*. (2004), showed that a proper transition model indeed improves the results, but that the results at high wind speeds still underestimates the power.

4.5 Wind farm aerodynamics

Modern wind turbines are often clustered in wind parks in order to reduce the overall installation and maintenance expenses. An unwanted but inevitable effect, however, is that the power production of the interior turbines decreases and that the turbulence intensity in the wake increases because of the interaction from the wakes of the surrounding wind turbines. As a consequence, dynamic loadings are increased that may excite the structural parts of the individual wind turbine and increase fatigue loadings. The turbulence created from wind turbine wakes is mainly due to the dynamics of the vortices originating from the rotor blades. The vortices are formed as a result of the rotor loading. To analyze the genesis of the wake, it is thus necessary to include descriptions of the aerodynamics of both the rotor and the wake. Although many wake studies have been performed over the last two decades, a lot of basic questions still need to be clarified in order to elucidate the dynamic behavior of individual as well as multiple interactive wakes behind wind turbines (Vermeer *et al*., 2003).

Most attempts to model the flow field in wind farms are based on simple single wake calculations combined with assumptions regarding the superposition of merging wakes. Various superposition approaches have been devised, ranging from linear superposition of the wake (Lissaman, 1979) or of the square of the wake deficits (Katic *et al*., 1986) to more physical approaches based on momentum conservation considerations (Frandsen *et al*., 2006) or parabolized Navier–Stokes modeling (Schepers and van der Pihl, 2007). Common to the above-mentioned methods is that they are based on steady-state considerations and as a consequence disregard the various important dynamic wake effects that are known to take place in wind farms and that have a major impact on the wind turbine loadings. Even though some promising simplified dynamic wake models have been proposed (Frandsen, 2007; Larsen *et al*., 2008), these still remain to be combined with suitable models for wake interaction before they can be used for wind farm modeling. Another typical limitation of the existing wind farm models is that they only seek to predict the development of the mean velocity deficit and hence they do not take into account that the turbulence properties in the wake deviate significantly from that of the undisturbed atmospheric flow field.

Frandsen (2007) argued that the various changes in the turbulence properties usually correlate with the standard deviation of wind speed fluctuations and so proposed a model for the fatigue loading of rotors in wind farms in which a variable designated the effective turbulence intensity is the only governing parameter. The proposed expression for the effective turbulence intensity depends on the Wöhler exponent of the considered material in order to combine different load cases. Thus, the effective turbulence is a design variable rather than a physical quantity. Generally, the model was shown to be more accurate than existing engineering models, although it occasionally produces results with large discrepancies when compared to measurements.

A profound difficulty when seeking to validate models with field measurements is that the complicated and ever-changing inflow conditions generally are not fully known and that field measurements generally have inherent uncertainties due to, for example, the lack of stationary data. Therefore, numerical simulations constitute a valuable supplement since the inflow conditions are easily controlled and because all relevant flow properties are described in detail.

In connection with numerical wake studies actuator disk or line techniques and related methods, which combine a full set of Navier–Stokes equations with a blade element approach and airfoil data, are useful because the influence of the blades on the flow field is captured with a low number of grid points. This type of method, extended with a number of sub-models for coping with shear and turbulent inflow as well as the aero-elastic behavior of the turbines, has been used extensively for wake studies of both isolated turbines (Sørensen *et al*., 1998; Sørensen and Shen, 2002) and rows of turbines (Troldborg *et al*., 2006; Mikkelsen *et al*., 2007).

4.6 Simulation of flow and turbulence in wind farms

The following section presents some actuator line simulations of the flow field in the interior of a wind farm (Sørensen *et al*., 2007). The simulations are carried out using large eddy simulation (LES) technique in order to capture the small-scale turbulence without having to resolve all length scales. Thus the scales resolved by the grid are simulated directly by the Navier–Stokes equations, whereas scales below the grid scale are modeled using an eddy-viscosity-based mixed-scale sub-grid model. Two types of simulations are carried out. Initially the flow field between a row of three turbines is simulated in a case where the wind is in line with the common axis of the rotors. Thereafter, a row of 'infinitely' many rotors is simulated by applying periodic boundary conditions at the inlet and outlet of a computational domain inside which a turbine is located. In this way, the simulations cover the initial development of the flow field in a wind farm as well as the equilibrium state reached in the interior of large wind farms. The computations are conducted using airfoil data from the Tjæreborg wind turbine. The blade radius of this turbine is 30.56 m and it rotates at 22.1 RPM, corresponding to a tip speed of 70.7 m/s. The blade sections consist of NACA 44xx airfoils with a chord length of 0.9 m at the tip, increasing linearly to 3.3 m at hub radius 6 m. The blades are linearly twisted 1° per 3 m.

4.6.1 Three turbines in a row

Plate II (see between pages 286 and 287) depicts iso-vorticity contours in a cross section along the common axis of the three rotors. The wake behind the first turbine is seen to be dominated by organized tip and root vortices, whereas the flow undergoes massive separation over the second rotor, causing the most downstream rotor to operate in a completely separated flow. It should be mentioned that the highly separated flow is partly a result of the rotors being forced to operate at the

same rotational speed, whereby the tip speed ratio, and thus also the drag, becomes very high for the downstream rotors. To quantify the structure of the flow field the azimuthally and time-averaged axial velocities in the wake behind the three rotors are computed, and the outcome is shown in Figure 4.3, which depicts the velocity profiles for various downstream sections. The profiles in the wake of the most upstream turbine are nearly constant over most of the radial distance, i.e. from r/R = 0.3 to r/R = 1.0, which is indicative of the wake being dominated by the induction of distinct root and tip vortices. At the downstream position of the second rotor (z/R = 6) the presence of two systems of tip vortices originating from respectively the first and the second turbine is clearly observed in the velocity profile, which is consistent with the contour plot in Plate II. In between the second and the third rotor the wake deficit is observed to develop towards a bell-shaped profile, indicating that the wake is undergoing a transition from a flow field described by organized vortex structures to a flow field that is dominated by small-scale turbulence. From theoretical considerations, it is known that the axial velocity in the far field of a turbulent wake is described by a Gaussian distribution. The flow field is redistributed as it passes through the third rotor, but the strong unsteady mixing causes the deficit to develop rapidly back to the bell-shaped form.

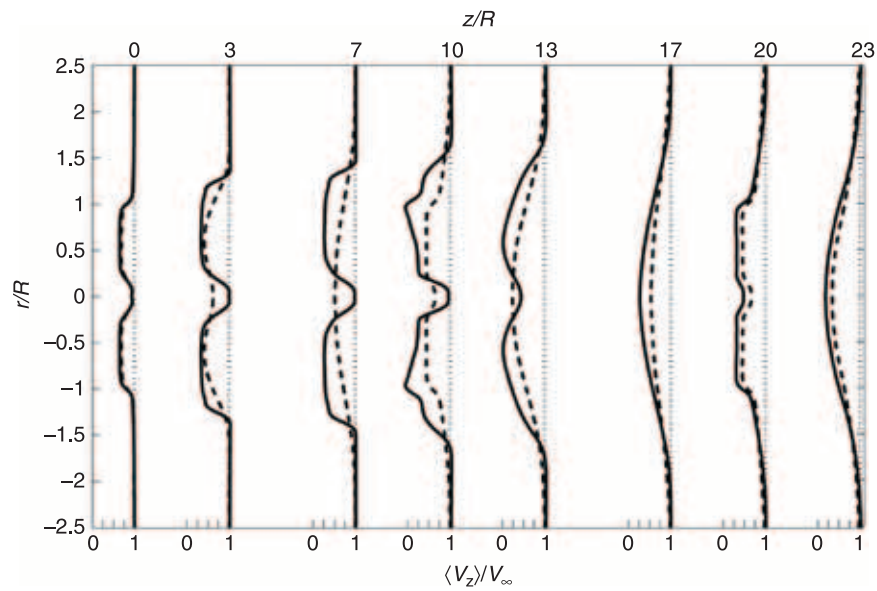

4.3 Azimuthally and time-averaged axial velocity profiles at different positions downstream of the first rotor. The second and third rotor are located at z/R = 6 and 12 respectively.

4.6.2 Multiple turbines in a row

To study the generation of turbulence in the interior of a large wind farm, a turbine operating in a domain imposed with periodic inflow and outflow conditions was considered. The introduction of periodic boundary conditions in the flow direction is a technique that has been largely used to study the generation of turbulence in boundary layers and in channels. In the present case the turbulence is generated by the 'mixing effect' of the rotor itself. Plate III(a)–(d) (see between pages 286 and 287) shows iso-vorticity contours illustrating how the flow develops as a function of time. As a time indicator the 'turn-around' time T is employed, which defines the time it takes for a flow structure to pass through the domain once. Designating the mean convective axial velocity in the wake as V_0, the approximate time it takes for a flow structure to be convected through the domain is $T = L_z/V_0$, where L_z is the length of the flow domain.

From Plate III(a) it is seen that the 'start-up' phase is associated with the development of distinct tip vortices and an inner vortex structure, corresponding to the usual transient for a single wind turbine starting up. After one 'turn-around' time, the wake that was developed in the initial phase goes through the rotor and creates a wake consisting of coherent tip vortices superposed a turbulent spot in the interior of the wake (Plate III(b)). This turbulent spot is subsequently convected downstream (Plate III(c)). When it passes through the rotor the second time, it starts to develop broadband turbulence superposed organized vortex structures. In the final stage, it is difficult to distinguish the various structures (Plate III(d)), although the influence of the rotor on the wake immediately downstream is still visible. The smallest length scales are determined here by the size of the computational grid, whereas the largest length scales are determined partly by the diameter of the rotor and partly by the length of the computational domain, corresponding to the distance between the turbines.

After the transients have died out, the flow becomes dominated by the development of turbulence. Due to the mixing of the rotor, turbulent kinetic energy is continuously added to the flow and statistics can be performed when the production of turbulence is in balance with the dissipation. When this happens the flow is statistically stationary and usual statistical tools can be applied.

In the following, the Reynolds stresses $\boldsymbol{R}$ in a cross section located one diameter upstream of the rotor are computed from the two-point correlation tensor:

$$R_{ij} = \langle v_i v_j \rangle = \frac{1}{N} \sum_{k=1}^{N} \left(v_i(t_k) v_j(t_k) \right), \qquad [4.35]$$

where $\langle \quad \rangle$ denotes ensemble averaging, $v_i = V_i - \langle V_i \rangle$ is the ith component of the fluctuating velocity and N denotes the number of statistically independent snapshots used for the time averaging. In the present work, $\boldsymbol{R}$ is estimated with $N = 750$. It should be mentioned, however, that the used sample rate was not sufficiently low to ensure statistically independent snapshots and so the statistics

presented in the following are not completely converged. Nevertheless, the used dataset is considered adequate to show the overall trend of the flow field. Defining the along-wind standard deviation of the turbulent wind speed fluctuations as

$$\sigma_{zz} = \sqrt{R_{zz}} = \left\langle v_z v_z \right\rangle^{\frac{1}{2}} \quad [4.36]$$

the turbulence intensity can be estimated as

$$I_{wake} = \sigma_{zz} / V_{\infty}, \quad [4.37]$$

where V_{∞} denotes the ambient wind speed at hub height.

In Plate IV(a) and (b) (see between pages 286 and 287), the contours of the turbulence intensity and its azimuthally averaged radial distribution are depicted. The turbulence intensity in the wake is found to vary from approximately 10% to 25%, with an average value of about 15%. Based on measurements and analytical considerations, and depending on operating conditions, Frandsen (2007) and Barthelmie *et al*. (2007) reported comparable values for a wind farm with a rotor spacing of approximately three diameters.

4.7 Future trends

The trend in the development of wind turbines is towards larger and more slender constructions, and turbines grouped in large wind farms. Further, because of limited space and problems with public acceptance, it is anticipated that wind turbines primarily will be installed in complex terrain and at offshore locations. Therefore, the development of aerodynamic models is directed partly towards development of engineering models that is capable of incorporating new phenomena and partly towards CFD models capable of dealing with complex physics, such as stall, fluid-structure interaction and wake modeling.

Within rotor aerodynamics it is expected that new 'intelligent' rotor blades equipped with sensors and various regulation and control equipment, such as trailing edge flaps, boundary layer blowing and extended use of vortex generators, will put new demands on the capability of the aerodynamic models. Thus, it is of utmost importance that future CFD tools are capable of treating boundary layer separation and laminar–turbulent transition with a greater accuracy than is possible today.

It is expected that a large proportion of future wind turbines will be installed in complex terrain. It is therefore important to incorporate the influence of the atmospheric boundary layer at the specific site in the aerodynamic analysis. An example of this is turbines erected in forests where the influence of the boundary layer formed by the forest greatly influences the final power production.

The tendency to install wind turbines at offshore locations puts new demands on the modeling of wakes and wake interaction. This concerns both engineering models for optimization of location with respect to minimizing installation expenses and maximizing the total power yield as well as advanced CFD models for computing turbulence and interaction between neighboring wind farms.

4.8 Sources of further information and advice

Brouckaert J-F (ed). 2007. Wind turbine aerodynamics: a state-of-the-art. *VKI Lecture Series 2007-05*. von Karman Institute for Fluid Dynamics, Belgium.

Burton T, Sharpe D, Jenkins N, and Bossanyi E 2001. *Wind Energy Handbook*. Wiley.

Crespo A, Hernández J, and Frandsen S 1999. Survey of modelling methods for wind turbine wakes and wind farms. *Wind Energy* 2:1–24.

Hansen A C and Butterfield C P 1993. Aerodynamics of horizontal-axis wind turbines. *Annu. Rev. Fluid Mech.* 25:115–49.

Hansen M O L 2008. *Aerodynamics of Wind Turbine*. Earthscan, London.

Hansen M O L, Sørensen J N, Voutsinas S, Sørensen N, and Madsen, H A 2006. State of the art in wind turbine aerodynamics and aeroelasticity. *Prog. Aerosp. Sci.* 42: 285–330.

Leishman J G 2002. Challenges in modeling the unsteady aerodynamics of wind turbines. *Wind Energy* 5:86–132.

Snel H 1998. Review of the present status of rotor aerodynamics. *Wind Energy* 1:46–69.

4.9 Acknowledgment

The author would like to acknowledge Robert Mikkelsen and Niels Troldborg for providing some of the figures.

4.10 References

Bak C, Johansen J, and Andersen P B 2006. Three-dimensional corrections of airfoil characteristics based on pressure distributions. *Proceedings of European Wind Energy Conference and Exhibition (EWEC)*. Athens, Greece.

Barthelmie R J, Frandsen S T, Nielsen M N, Pryor S C, Rethore P E, and Jørgensen H E 2007. Modelling and measurements of losses and turbulence intensity in wind turbine wakes at Middelgrunden offshore wind farm. *Wind Energy* 10, 517–28.

Betz A 1919. Schraubenpropeller mit geringstem Energieverlust, Dissertation, Gottingen Nachrichten, Gottingen.

Betz A 1920. Das Maximum der theoretisch möglichen Ausnützung des Windes durch Windmotoren. *Zeitschrift für das gesamte Turbinenwesen* 26, 307–9.

Björk A 1990. Coordinates and calculations for the FFA-w1-xxx, FFA-w2-xxx and FFA-w3-xxx series of airfoils for horizontal axis wind turbines. *FFA TN 1990-15*, Stockholm, Sweden.

Chaviaropoulos P K and Hansen M O L 2000. Investigating three-dimensional and rotational effects on wind turbine blades by means of a quasi-3D Navier–Stokes solver. *J. Fluids Eng.* 122, 330–36.

Du Z and Selig M S 1998. A 3-D stall-delay model for horizontal axis wind turbine performance prediction. *36th AIAA Aerospace Sciences Meeting and Exhibit. ASME Wind Energy Symposium. AIAA-98-0021*. Reno, NV, USA.

Duque E P N, van Dam C P, and Hughes S 1999. Navier–Stokes simulations of the NREL combined experiment phase II rotor. *AIAA Paper 99-0037*.

Duque E P N, Burklund M D, and Johnson W 2003. Navier–Stokes and comprehensive analysis performance predictions of the NREL phase VI experiment. *AIAA Paper 2003-0355*.

Eggleston D M and Stoddard F S 1987. *Wind Turbine Engineering Design*. Van Nostrand Rheinhold, New York.

Frandsen, S T 2007. Turbulence and turbulence-generated structural loading in wind turbine clusters. *Risø-R-1188(EN)*. Risø National Laboratory, Roskilde, Denmark.

Frandsen S T, Barthelmie R, Pryor S, Rathmann O, Larsen S, Højstrup J, and Thøgersen M 2006. Analytical modelling of wind speed deficit in large wind farms. *Wind Energy* 9, 39–53.

Froude W 1878. *Transactions Institute of Naval Architects* 19, 47.

Froude R E 1889. *Transactions Institute of Naval Architects* 30, 390.

Fuglsang P and Bak C 2004. Development of the Risø wind turbine airfoils. *Wind Energy* 7, 145–62.

Glauert H 1935. Airplane propellers. In Durand W F (ed). *Aerodynamic Theory*, vol. IV, Division L. Springer, Berlin.

Hoerner S F 1965. *Fluid Dynamic Drag*. Hoerner Fluid Dynamics, Bakersfield, CA.

Johansen J, Sørensen N N, Michelsen J A, and Schreck S 2002. Detached-eddy simulation of flow around the NREL phase VI blade. *Wind Energy* 5, 185–97.

Katic I, Højstrup J, and Jensen N O 1986. A simple model for cluster efficiency. In Palz W and Sesto E (eds). *Proceedings of EWEC'86*, pp. 407–10. Rome, Italy.

Lanchester F W 1915. A contribution to the theory of propulsion and the screw propeller. *Transactions of the Institution of Naval Architects* 57, 98.

Larsen C G, Madsen H A, Thomsen K, and Larsen T J 2008. Wake meandering – a pragmatic approach. *Wind Energy* 11, 377–95.

Larsen J W, Nielsen S R K, and Krenk S 2007. Dynamic stall model for wind turbine airfoils. *J. Fluids Struct*. 23, 959–82.

Leishman J G and Beddoes T S 1989. A semi-empirical model for dynamic stall. *J. Am. Helicop. Soc*. 34(3), 3–17.

Lissaman P B S 1979. Energy effectiveness of arbitrary arrays of wind turbines. *AIAA Paper 79-0114*.

Mann J 1998. Wind field simulation. *Probl. Eng. Mech.* 13, 269–82.

Menter F R 1993. Zonal two-equation $k - \omega$ turbulence models for aerodynamic flows. *AIAA Paper 93-2906*.

Menter F R, Langtry R B, Likki S R, Suzen Y B, Huang P G, and Völker S 2004. A correlation-based transition model using local variables, part I – model formulation. *Proceedings of ASME Turbo Expo 2004, Power for Land, Sea, and Air*, ASME, GT2004-53452, Vienna, Austria, 14–17 June 2004.

Mikkelsen R, Sørensen J N, and Troldborg N 2007. Analysis of power enhancement for a row of wind turbines using the actuator line technique. *The Science of Making Torque from Wind. J. Phys. Conf. Ser.* 75, 012044.

Øye S 1991. Dynamic stall, simulated as a time lag of separation. *Proceedings of Fourth IEA Symposium on the Aerodynamics of Wind Turbines. ETSU-N-118*. Harwell, UK.

Rankine W J 1865. *Transactions Institute of Naval Architects* 6, 13.

Schepers J G and van der Pihl S P 2007. Improved modelling of wake aerodynamics and assessment of new farm control strategies. *The Science of Making Torque from Wind. J. Phys. Conf. Ser.* 75, 012039.

Schepers J G and Snel H 1995. *Dynamic Inflow: Yawed Conditions and Partial Span Pitch Control, ECN-C-95-056*. ECN, Petten, The Netherlands.

Schreck S 2002. The NREL full-scale wind tunnel experiment introduction to the special issue. *Wind Energy* 5, 77–84.

Shen W Z, Mikkelsen R, Sørensen J N, and Bak C 2005a. Tip loss corrections for wind turbine computations. *Wind Energy* 8, 457–75.

Shen W Z, Sørensen J N, and Mikkelsen R 2005b. Tip loss corrections for actuator/Navier–Stokes computations. *J. of Sol. Energy Eng.* 121, 209–13.

Snel H, Houwink R, van Bussel G J W, and Bruining A 1993. Sectional prediction of 3D effects for stalled flow on rotating blades and comparison with measurements. *Proceedings of European Community Wind Energy Conference*, vol. 395–99. H.S. Stephens & Associates, Lübeck-Travemünde, Germany.

Snel H and Schepers J G 1995. Joint investigation of dynamic inflow effects and implementation of an engineering method. *ECN-C-94-107*. ECN, Petten, The Netherlands.

Sørensen J N, Mikkelsen R, and Troldborg, N 2007. Simulation and modelling of turbulence in wind farms. *EWEC 2007 – European Wind Energy Conference and Exhibition*. MIC, Milan, Italy.

Sørensen J N, Shen W Z, and Munduate X 1998. Analysis of wake states by a full-field actuator disc model. *Wind Energy* 1, 73–88.

Sørensen J N and Shen W Z 2002. Numerical modelling of wind turbine wakes. *J. Fluid Eng. – T. ASME* 124, 393–99.

Sørensen N N 2009. CFD modelling of laminar–turbulent transition for airfoils and rotors using the $\gamma - \tilde{\mathrm{Re}}_{\theta}$ model. *Wind Energy* 12, 715–33.

Sørensen N N and Hansen M O L 1998. Rotor performance predictions using a Navier–Stokes method. *AIAA Paper 98-0025*.

Sørensen N N, Michelsen J A, and Schreck S 2002. Navier–Stokes predictions of the NREL phase VI rotor in the NASA-AMES 80 ft × 120 ft wind tunnel. *Wind Energy* 5, 151–69.

Spera D A 1994. *Wind Turbine Technology*. ASME Press, New York.

Stoddard F S 1977. Momentum theory and flow states for windmill. *Wind Tech. J.* 1, 3–9.

Tangler J L and Somers D M 1995. NREL airfoil families for HAWTs. *Proceedings of WINDPOWER'95*, vol. 117–23. Washington D.C.

Timmer W A and van Rooij RPJOM 1992. Thick airfoils for HAWTs. *J. Wind Eng. Ind. Aerodyn.* 39, 151–60.

Troldborg N, Sørensen J N, and Mikkelsen R 2006. Numerical simulation of wakes of wind turbines in wind farms. *EWEC 2006 – European Wind Energy Conference and Exhibition*. Athens, Greece.

Veers P 1988. Three-dimensional wind simulation. *SANDIA Report SAND88-0152 UC-261*. Sandia National Laboratories, USA.

Vermeer L J, Sørensen J N, and Crespo A 2003. Wind turbine wake aerodynamics. *Prog. Aerosp. Sci.* 39, 467–510.

Viterna L A and Corrigan R D 1981. Fixed-pitch rotor performance of large HAWTs. *DOE/NASA Workshop on Large HAWTs*. Cleveland, Ohio.

de Vries O 1979. Fluid dynamic aspects of wind energy conversion. *AGARDograph 243*. AGARD, Brussels, Belgium.

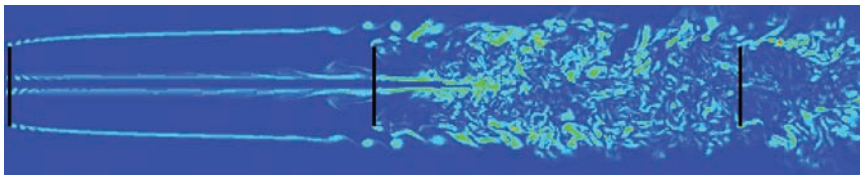

Plate II Development of the wake behind three rotors in a row. Regions of high vorticity appear as light colors. The rotors are indicated as black lines.

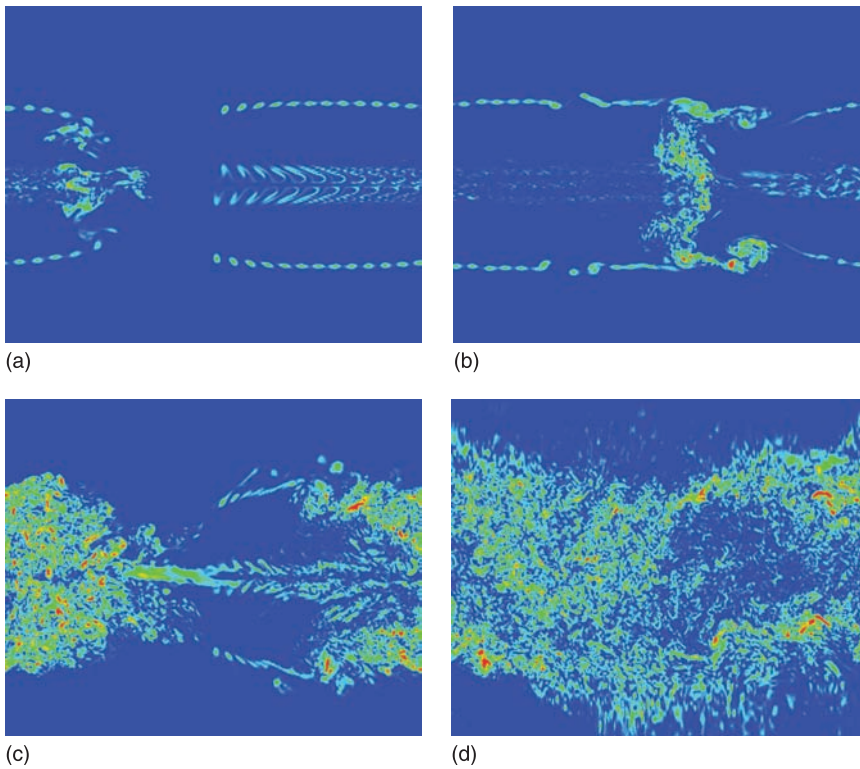

Plate III (a)–(d) Iso-vorticity contours at various stages of the transient. Regions of high vorticity appear as light colors. The rotor is placed in the center of the domain. For explanation of panels see text.

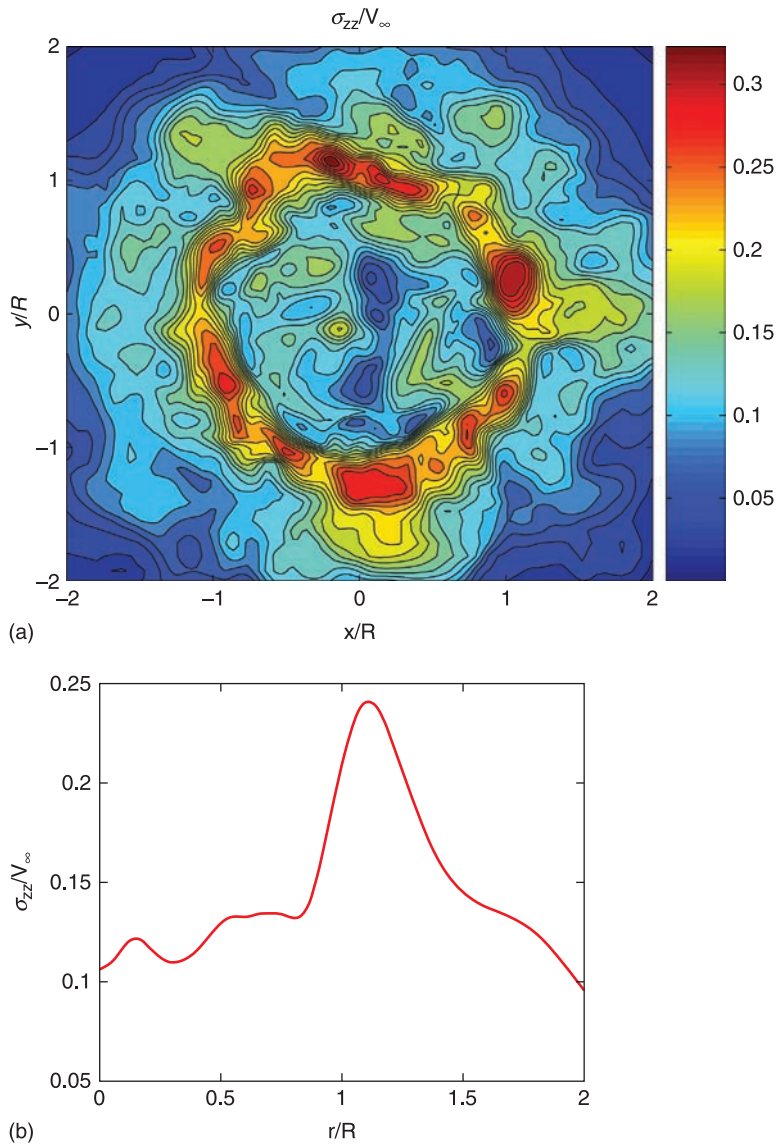

Plate IV (a) Turbulence intensity profile in a section located one rotor radius upstream from the rotor. (b) Circumferentially averaged turbulence intensity profile.

5

Fatigue loading of wind turbines

P. S. VEERS, Sandia National Laboratories, USA

Abstract: Wind turbine structures need to be designed with careful consideration of the fatigue strength and loading on critical load-bearing components. Each material in the various components of a wind turbine will potentially use different damage models to map the cyclic fatigue loadings into progressive deterioration of the material. In most cases, linear damage models using a Miner's Rule type approach are prevalent in design. The loadings of a particular turbine can be described as a function of the inflow conditions, which are considered to be weakly stationary for short periods, typically 10 minutes. These characteristic response statistics of the turbine are aggregated into a long-term distribution of loads using the theory of random variables and probability distribution functions. The long-term distribution is applied to the damage model to produce an estimate of fatigue lifetime. The design criteria require that the estimated stresses be amplified by safety factors to account for unfavourable deviations of action and material properties, as well as modeling uncertainties.

Key words: wind turbine, safety, reliability, fatigue, damage, Miner's Rule, loading, materials, stochastic, safety factors, structures, design criteria, standards.

5.1 Introduction and overview

Wind turbines are fatigue machines. A wind turbine is expected to operate almost continuously for its entire 20- to 30-year lifetime. The structure has a large stationary foundation and tower that is attached to a rotating portion with aeroelastic blades that pass through both a gradient wind shear (higher speed winds at the top of the rotor disk than at the bottom) and turbulence whenever it operates. A typical aircraft will fly through turbulence occasionally during flight, but a wind turbine always operates in the turbulent planetary boundary layer. An aircraft will experience a gravity cycle on its wings once per flight, while a wind turbine sees one gravity cycle every rotation. The result is that while a typical aircraft is designed to withstand on the order of one million major stress cycles in one design lifetime, the typical multi-megawatt wind turbine, operating at about 20 RPM, will see over 100 million revolutions in one design lifetime. And because of the stringent cost constraints on wind turbines, rather than aerospace composite materials that typically cost well over €200/kg, wind turbine blades must be manufactured for less than €20/kg. The combination of longer lives, lower cost and more turbulent loading makes the fatigue design of wind turbine components, but especially the blades, a significant challenge.

The long-lifetime requirement makes it a challenge to characterize the materials for a wind turbine structure. While most handbook data will stop at lifetimes of a million cycles, the wind turbine designer needs to know the behavior of the material out to one hundred times that life. It is very expensive to continue fatigue testing out to 10^8 cycles, so designers rely on a few data points with extrapolation from the shorter-life specimens carrying a great deal of weight.

The turbulence influence on loading requires the fatigue spectrum to be defined as a random variable with statistical fitting and extrapolation playing a major role. The intensity of the loading is directly related to the mean wind speed, so loading must be characterized across all wind speeds in the operating range. The statistical distribution of stresses at each wind speed must be defined. Then the relative amount of time spent at each wind speed is used to aggregate the loads into a long-term distribution of all incident wind speeds. Discrete load events such as starting and stopping must be included as well. All these design loads are estimated from complex aeroelastic calculations driven by three-dimensional simulations of the wind turbulence field.

The current state of the art in structural response simulation is quite good, providing the designer with time-series estimates of wind turbine response under all the critical conditions in the operational envelope (Jonkman and Buhl, 2005; Øye, 1999; Larsen and Hansen, 2007). The process begins with a simulation of a full field of turbulent winds for a ten-minute segment and than runs those winds through an aerodynamic code that calculates loads on the blades due to the combination of machine rotation and incident wind. The turbine dynamic response is simultaneously calculated in a time-marching manner, and elastic deformations are fed back into the aerodynamics code to update angles of attack and provide an aeroelastic capability. Internal moments and forces are calculated at all locations of interest and used to estimate local stress states for the components. The stress amplitude and mean are summarized into distributions that indicate the frequency of occurrence for a specific average wind speed. The process is repeated for all wind speeds of interest, as well as for important transients such as starts and stops. Then the aggregated distribution of all stresses is applied to a damage model that indicates the damage rate and estimated time to failure. Schematically, the process is illustrated in Fig. 5.1.

The intermediate steps in this process are best described using the language of random variables and probability. The short-term distribution of stress amplitudes is described by a probability density function (pdf). The probability that the random variable lies between any two values is the integral of the pdf between those limits. For example, with a distribution of stress amplitudes, S, the pdf is $p(S)$ and the probability that S is between s_1 and s_2 is

$$\Pr(s_1 < S < s_2) = \int_{s_1}^{s_2} p(S)\, dS. \qquad [5.1]$$

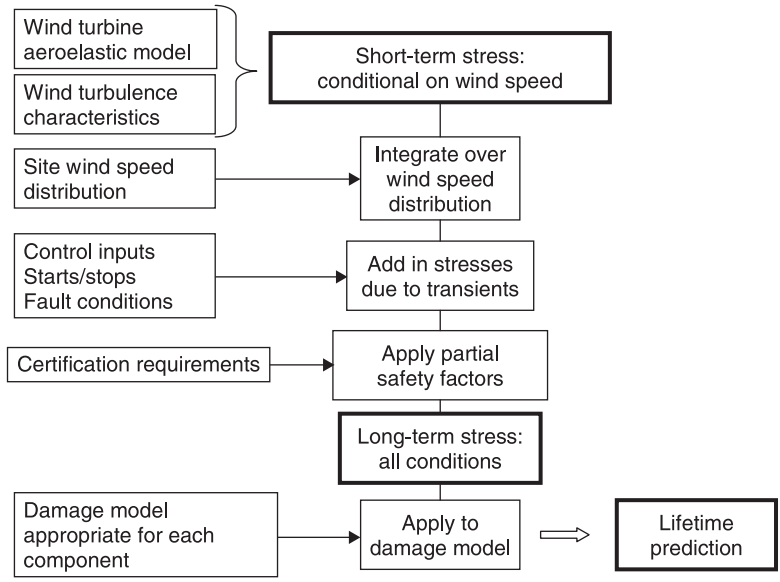

5.1 Schematic of the process to get from loading statistics to a lifetime prediction.

Two other functions are also used, the cumulative distribution function, or cdf, $P(S)$, is the integral of the pdf and indicates the probability that a particular stress amplitude is less than a given level.

$$P(S) = \int_0^S p(s)\,ds \qquad [5.2]$$

The inverse cdf or exceedence function indicates the probability that a particular stress amplitude is greater than a given level and approaches zero as amplitude gets large. It is mostly favored for clarity in plotting because it highlights the low probability high stress tail when plotted logarithmically.

$$P^{-1}(S) = 1 - P(S) \qquad [5.3]$$

The number of cycles, N, with stress amplitudes between s_1 and s_2 is equal to the total number applied in some time period T, N_T, times the relative probability of the range (assuming the cycle rates are relatively uniform).

$$N_i(s_1 < S_i < s_2) = N_T \int_{s_1}^{s_2} p(S)\,dS \qquad [5.4]$$

The short-term distribution depends on the mean wind speed, V, and the conditional pdf is written as $p(S|V)$. The normal operating stresses are aggregated into a long-term distribution by integrating the total probability expression over all operating wind speeds.

$$p_{LT}(S) = \int p_{ST}(S \mid V) p(V)\, dV \qquad [5.5]$$

In addition, the transient events with response levels high enough to cause damage need to be included in the long-term stress distribution. Since transient events may produce a different rate of stress cycles, the relative contribution needs to be accounted for as well.

The damage done in T, D_T, is calculated by multiplying the damage done by each stress cycle, $D(S)$, by the distribution of all stress cycles and integrating over all stresses described by the long-term distribution. Since the damage is characterized as damage per cycle, the integral needs to be multiplied by the total number of applied cycles, N_T.

$$D_T = N_T \int D(S) p_{LT}(S) dS \qquad [5.6]$$

Lifetime is estimated from the accumulated damage. The interpretation of the accumulation of damage depends on the model. It could be a physical quantity such as crack length or energy absorption, but is typically more simply interpreted using Miner's Rule with linear damage accumulation. Miner's Rule is an approach in which each cycle is assumed to consume $1/N_F$ of the lifetime, where N_F is the number of cycles to failure at the applied stress level due to constant amplitude loading. Failure is assumed when D_T exceeds unity.

Miner's Rule is an amazingly durable approach to fatigue life estimation, especially since it is known that in many if not most applications it is not capable of modeling important aspects of the fatigue damage process. If the damage caused by an applied cycle depends on the state of the material, there is an inherent sequence effect. The damage increment caused by that cycle is no longer equal to the average of the damage in each cycle that was determined in a constant amplitude test. However, these effects are typically very difficult to determine with enough certainty that improved lifetime calculations can be done by including the more physical effect. The difficulty is compounded by the fact that in a stochastic loading environment, it is not possible to determine the sequence of loading that the structure will encounter. So, in spite of the known shortcomings, the assumption of linear accumulation of damage independent of past loading remains the most common approximation used in fatigue calculations.

The major elements in the calculation of fatigue damage are: (1) the damage model, (2) the short-term load distribution, (3) aggregation into a long-term distribution using the wind speed distribution, and (4) calculation of fatigue life, either deterministically or probabilistically (Veers, 1982). The short-term distribution refers to the response of the turbine to quasi-steady stochastic inputs over durations of about ten minutes. Over these short time periods (typically ten minutes) the process is considered weakly stationary, even though this assumption is often poorly satisfied due to the continuous variation of the driving process of the input wind. The long-term distribution refers to the loads expected over the entire lifetime, aggregated over periods such as a full year. Each of these four

parts of the problem is discussed in turn in the following sections. Some comments on estimating fatigue reliability are included, although the application of reliability methods to fatigue of wind turbines is not yet a routine process for the industry, but is used in efforts to calibrate and fine-tune the safety factors applied to strength and loading estimates for design.

5.2 Damage model

A wind turbine is not a monolithic structure; rather it contains components with a wide range of materials possessing a variety of fatigue properties. The tower is typically welded steel, the hub is a very large steel casting, the drive train contains steel shafts and bearings with specially treated surfaces, and the blades are composites that combine resins with different fiber types (carbon and glass) in different fabric forms (woven, stitched, uniaxial, etc.) (Ronold and Echtermeyer, 1996). Each of these components has different fatigue characteristics. The fundamental nature of the fatigue process, however, is quite similar. The fatigue, or wear, or crack-growth in almost all materials can be described according to phenomenological models that relate the cyclic loading to the rate of damage according to a power law relationship. In simplified form, the damage is a summation of the effect of each fatigue event (typically a stress excursion) according to

$$\Delta D = C^* S^b, \tag{5.7}$$

where S is the loading intensity, ΔD is the increment in damage and C^* and b are material properties. Almost all material damage models are of this essential form, although specific models have much more complicated descriptions of the load amplitude (e.g. crack growth models use the stress intensity factor that combines the stress state with the crack length and shape). More sophisticated damage models have a physical interpretation for the damage, such as crack length or material strength degradation (Nijssen, 2006; Tsai, 2008).

Miner's Rule (Miner, 1945; Lundberg and Palmgren, 1952) is a simplification of the process that assigns a damage increment to each stress cycle and assumes that the material will fail when the sum of all the damage increments equals one. The increment is derived from constant amplitude coupon testing where the observed number of cycles to failure at stress level S is $N_F(S)$. Miner defines the damage from each cycle at that amplitude to be equal for each applied cycle, thus assuming damage accumulates linearly.

$$\Delta D(S) = \left(\frac{1}{N_F(S)} \right), \tag{5.8}$$

which implies that

$$N_F(S) = CS^{-b}, \tag{5.9}$$

where C is related to the coefficient from equation [5.7] by $C = 1/C^*$. The form fits test results fairly well in most applications, as shown in the example of Fig. 5.2. It is notable that the curve tends to change slope and flatten as lifetime increases and loads decrease. This is also commonly observed in a variety of materials (in steel it is referred to as the endurance limit), but is often associated with an artifact of constant amplitude testing. Fatigue damage progression is caused by a multitude of material mechanisms some of which can limit plastic deformation and damage until a sufficiently large load breaks the damage restriction. Afterward, damage can progress under lower level loads. A good example is in carbon steel where the carbon atoms in the crystal lattice lock the crystal dislocations that are responsible for consequent plastic deformation and damage. Below a certain load level, the mechanism for damage (dislocation motion) can not overcome the blockage of the carbon atoms. Once that load is exceeded, the dislocations move away from the locking atoms and are free to move and produce damage under much reduced loading (Cotrell, 1969; Brown, 1981; Mitchell, 1979). A similar example is when, in a composite material, fibers are broken or a delamination is initiated by a high load, after which the damage can progress under lower loads (Nijssen, 2006). The result is that under irregular loadings, the benefits of the flattened S-N curve found in constant amplitude test results are reduced and the dashed line extension shown in Fig. 5.2 is often used for design. Therefore, damage models such as

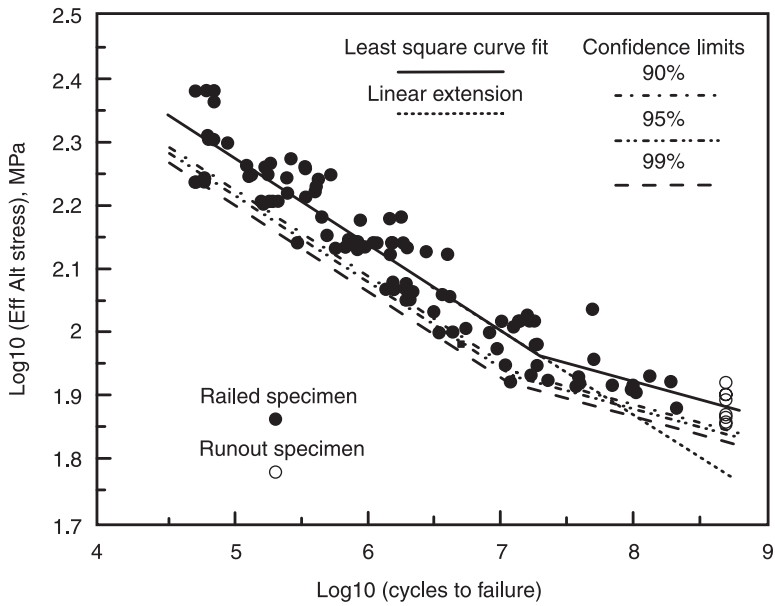

5.2 The number of cycles to failure found in constant amplitude coupons test results often follows a straight line relationship on a log-log graph, which is consistent with Equation [5.8] [Courtesy, Sutherland, 1999].

equation [5.9] that do not allow for changes in slope of the S-N curve are often much more applicable in a realistic, variable-amplitude loading environment than they might appear from the constant amplitude data alone.

Damage calculated from Miner's rule sums the increments in damage from each fatigue cycle applied to the material. The damage from each individual stress cycle, S_i, is added up so that the total damage done by any aggregation of N stress cycles is given by

$$D_N = \sum_{i=1}^{N} C^* S_i^b \qquad [5.10]$$

As noted before, the assumption is that failure occurs when the damage exceeds unity.

The applied stress is defined by both a mean, S_m, and amplitude, S_a, as shown in Fig. 5.3. In an irregular loading history, it may not be obvious where one cycle stops and another starts. The traditional approach is to use rainflow counting, which identifies cycles that would result in closed hysteresis loops in a plastically deforming material subjected to the stress history (Dowling and Socie, 1982). As shown in Fig. 5.4, each closed loop in stress–strain space is counted as a single cycle in the time series with its own mean and amplitude. This short example shows completed cycles defined by the peak–valley pairs of 1–2, 4–5 and 7–8. Although the 3–6 cycle has not yet closed, additional loading would most likely cause it to complete its loop so it is also counted as a cycle.

The mean stress effect can be approximated by a Goodman correction that relates an effective stress amplitude at zero mean to one at a non-zero mean by the ratio of the mean stress to the ultimate tensile strength of the material, S_{uts}.

$$S_{eff} = \frac{S_a}{\left[1 - \left(S_m / S_{uts}\right)\right]^{\varepsilon}} \qquad [5.11]$$

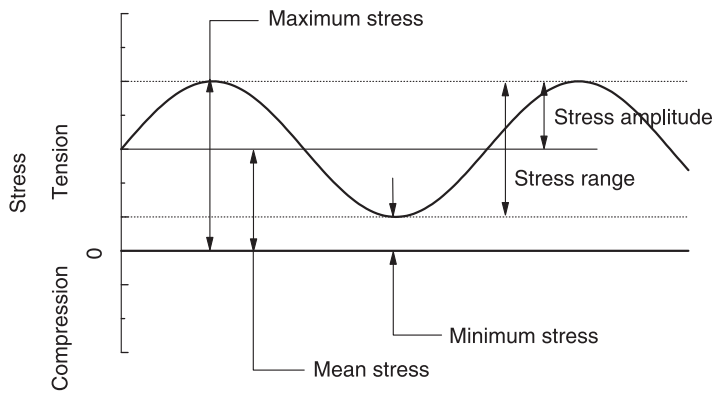

5.3 The damaging potential of an applied stress cycle depends on both the mean and amplitude of the cycle [Sutherland, 1999].

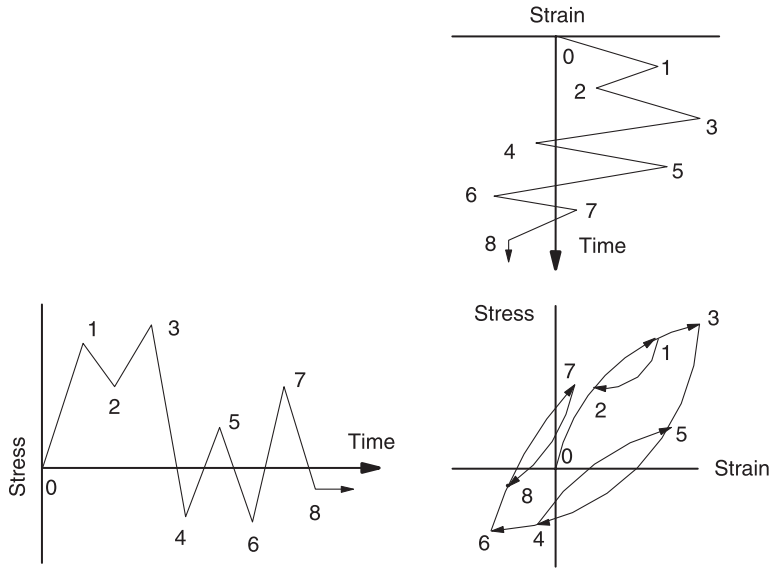

5.4 In an irregular stress history, the amplitudes and means of important stress cycles are defined using the rainflow algorithm that tracks closed hysteresis cycles in a material subjected to the stress history [Sutherland, 1999].

The parameter ε is a material constant that allows for curvature in the constant-life lines, but it is often set to unity.

A Goodman diagram is illustrated in Fig. 5.5 where lines of constant fatigue life are drawn on a plot with axes of mean and amplitude connecting the zero-mean vertical axis to the zero-amplitude horizontal axis. The material strength defines the zero amplitude fatigue strength. The radial lines emanating from the origin of the plot represent loci of constant R ratio, which is the ratio of the maximum stress to the minimum stress in a cycle.

$$R = \frac{S_{\min}}{S_{\max}} \qquad [5.12]$$

A fully reversed cycle with zero mean stress therefore has an R ratio of negative one – the vertical axis is therefore the locus of S_{eff}. Any reversal of tension and compression in the cycle results in a negative R, while both all-tensile and all-compressive loading have positive R.

Although the Goodman model of equation [5.11] predicts straight (or smoothly curving) constant-life lines as shown in Fig. 5.5(a), more often material tests are conducted at a great variety of mean and amplitude combinations and the constant-life lines are drawn to best fit the empirical test data as shown in Fig. 5.5(b). The empirical Goodman diagram rarely has continuously straight constant-life lines. In materials with different compressive and tensile ultimate strengths (such as

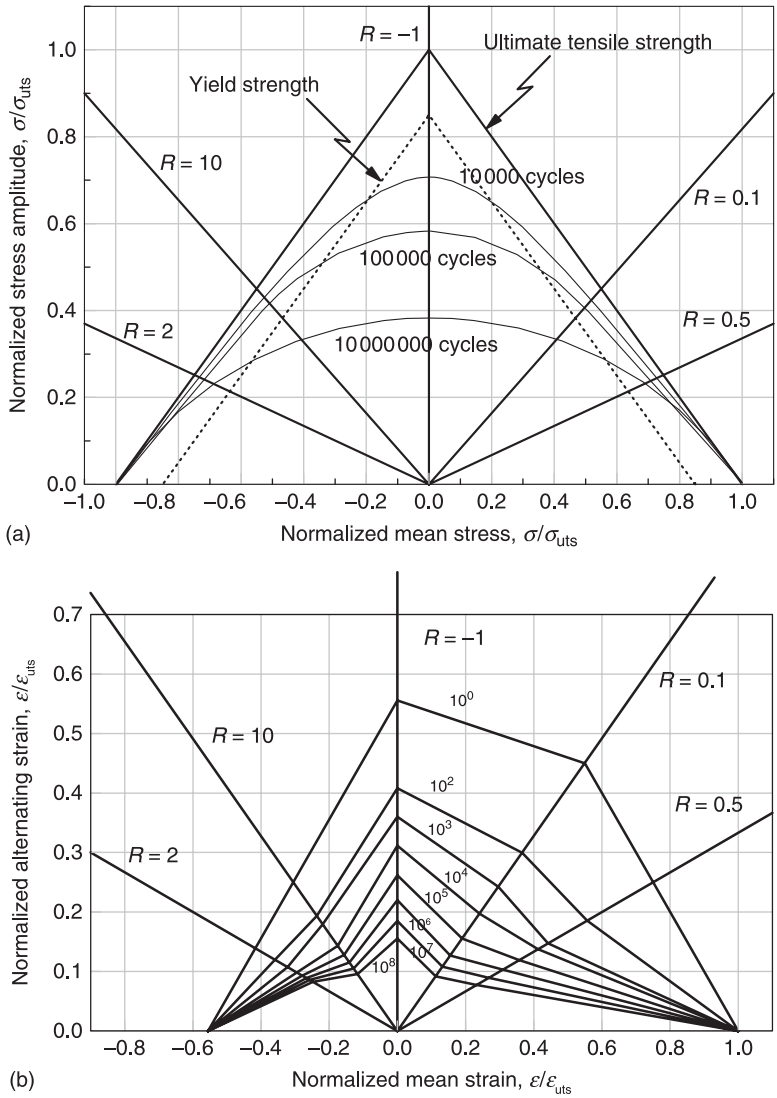

5.5 The Goodman diagram maps lines of constant fatigue lifetime over combinations of stress amplitude and mean stress [Sutherland, 1999]. (a) Goodman diagram concept; (b) empirical Goodman diagram based on material tests at multiple combinations of mean and amplitude.

most composites) the left and right sides will not be symmetric, and different composite materials will display different asymmetries.

After rainflow counting, the cycles can be aggregated into a histogram of frequency of occurrence within bins of combinations of mean and amplitude. The damage from all the cycles at each combination of mean and amplitude is simply the number of counts in that bin times the damage of a single cycle. The damage

from the entire loading history is then the damage summed over all combinations of mean and amplitude.

Miner's Rule does not model many of the physical properties of the fatigue process for some materials. Since fatigue is a process of continual degradation in strength, often measured by growth of cracks, fiber breakage, or surface wear, Miner's Rule remains a useful approximation for the average rate at which damage is accumulating. Also, the sequence of loading is not typically known and it would be therefore difficult or impossible to assess the actual accumulation of damage in a model that uses load sequence. Better physical models are likely to be used only when physical measures of damage, such as crack length, can be monitored with inspection methods and a damage tolerance approach to maintenance can be instituted. Damage tolerance is not yet used extensively in wind turbine design applications. Widespread adoption of these methods has been limited due to the expense of inspection and the tight constraints on wind plant operating cost. Also, in wind turbine applications, the uncertainties in the loading and material properties can be so large that the uncertainties produced by using a simple Miner's Rule damage summation in lieu of a more sophisticated approach can be overshadowed by other effects.

5.3 Short-term load distribution

A short-term load description will indicate the distribution of all stress cycles expected to be encountered by the machine under a particular set of inflow conditions (Thomsen, 1998). Many features of the atmospheric inflow will affect the magnitude of the structural response and consequent loading intensity on wind turbine components (Nelson *et al*., 2003). There are many more potential variables than can be realistically dealt with in a comprehensive design evaluation. Fatigue analyses are therefore routinely done using only the average wind speed as a descriptor of the inflow condition. Over time at a given wind speed, the turbine will experience a wide variety of wind shears, turbulence intensities, coherence levels and other factors that influence the nature of the inflow. Some of these effects will average out over time so that using the average value of the parameter will produce a loading that is quite close to the long-term average, but this may not always be the case. Design load distributions can either account for each of the variable inflow features explicitly, or can be averaged over most of the inflow parameters and characterize the wind turbine response as a function of wind speed alone. For example, the IEC design standard (IEC-1, 2005) normal turbulence model specifies an elevated intensity of turbulence as a characteristic value with the intent of producing a slightly conservative loading estimate. Further evaluation over a variety of turbulence levels is not required. Fatigue loading is tracked in this standard by defining the loading response as a function of mean wind speed alone while the other parameters of the inflow are defined according to the standard specification. Characteristic turbine response calculations are done by applying the normal turbulence model to aeroelastic simulations over a short time period such as ten minutes.

The stress cycle means and amplitudes are gathered in a histogram of frequency of occurrence at each critical location on a wind turbine structure to describe the damaging nature of the loading under a particular set of inflow conditions. Response histograms at different locations tend to have distinctive shapes as shown in the examples of a blade edge response (in the plane of the rotor) shown in Fig. 5.6(a) and flap response (perpendicular to the plane of the rotor) show in Fig. 5.6(b).

The edge response is unusual because it contains a deterministic sinusoidal gravity component that dominates the load and is independent of other wind-

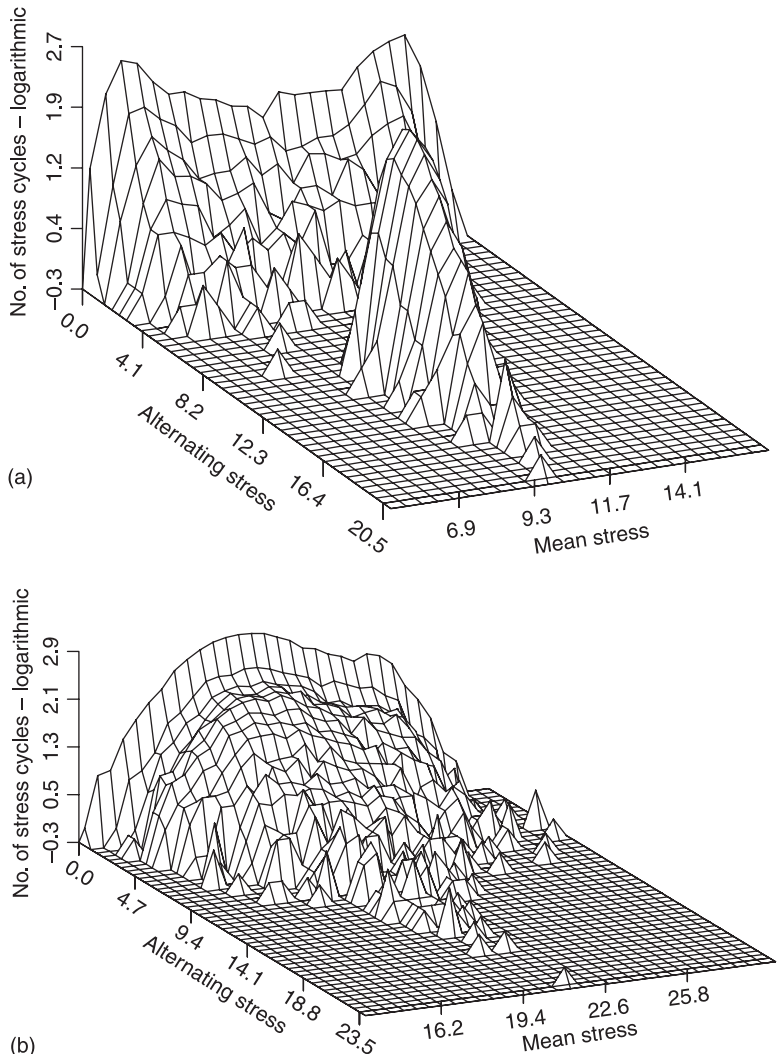

5.6 2-D histogram showing the number of rainflow counted ranges at each stress mean and amplitude [Sutherland, 1999]. (a) Edge loading; (b) flap loading.

related input conditions. Load distributions on components throughout most of the structure look more similar to the blade flap response.

Since the mean stress appears only as a ratio with the ultimate stress in the damage model (see equation 5.11), it can be well approximated by a single value for all stress amplitudes where the range of mean values is small compared to the ultimate stress. The oscillatory component can then be described by a one-dimensional plot of the magnitude of the stress or load amplitudes as shown in Fig. 5.7(a) and 5.7(b).

The limited amount of data that can be obtained from either field testing or aeroelastic simulation provides a good estimate of the expected counts in frequently occurring bins. However, rarely occurring high-amplitude stress cycles may not be observed in a limited data sample. The maximum *observed* cycle amplitude depends primarily on the length of the observations and should not be confused with the maximum *expected* cycle amplitude in *actual* operation over a typical 20-year lifetime. It is therefore necessary to extrapolate the observations from the limited

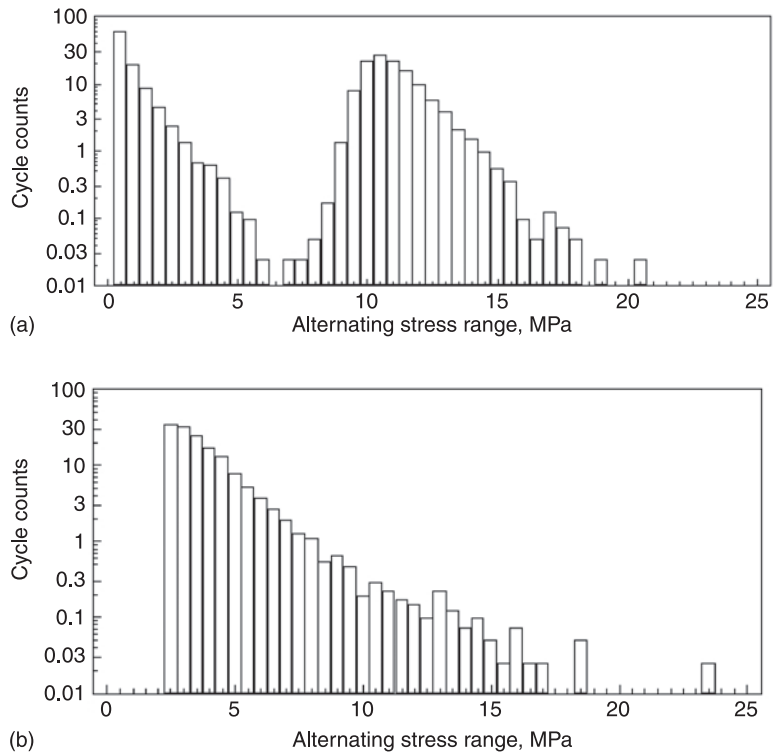

5.7 One-dimensional plot of the fatigue loading distribution for a typical blade out-of-plane (flapwise) component. These plots are for cycle counts per a selected time period, which results in less than one cycle in certain bins [Sutherland, 1999]. (a) Edge loading; (b) flap loading.

observation time to the turbine design lifetime (Sutherland, 1999). Figure 5.8 shows continually increasing observation times and illustrates how the maximum amplitudes continue to increase, usually along a smooth exponentially decreasing line.

Standard probability functions can be used to extrapolate from observations to 20-year distributions of stress amplitudes (Sutherland and Veers, 1995). Once an analytical distribution has been fitted to the existing data, the analytical distribution can be used to predict how many of the very large but not yet observed cycles are expected over the entire lifetime.

Rainflow counting produces a large number of low amplitude cycles that do not typically fit to any standard analytical distribution when combined with the largest cycles (Manuel *et al*., 2001). The number of counts in the lowest amplitude bin in Fig. 5.8(b) is about a thousand while no other bin has more than a hundred. The smallest amplitude cycles do not produce any appreciable damage and could be just as well ignored. Fitting a standard distribution to the data requires that the effect of the large number of smaller cycles does not destroy the quality of the fit

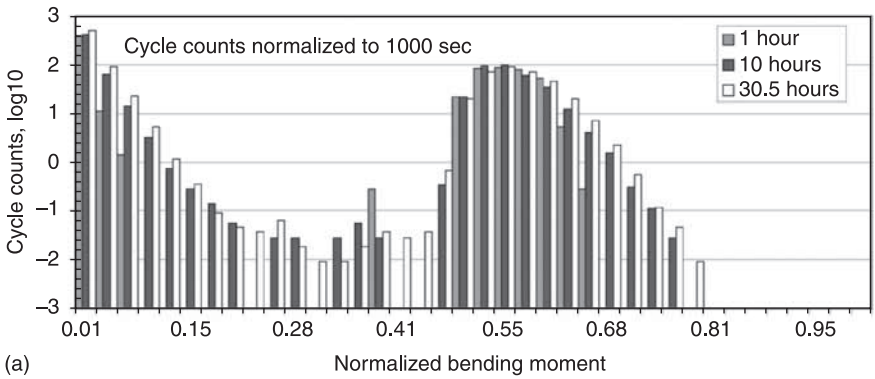

(a)

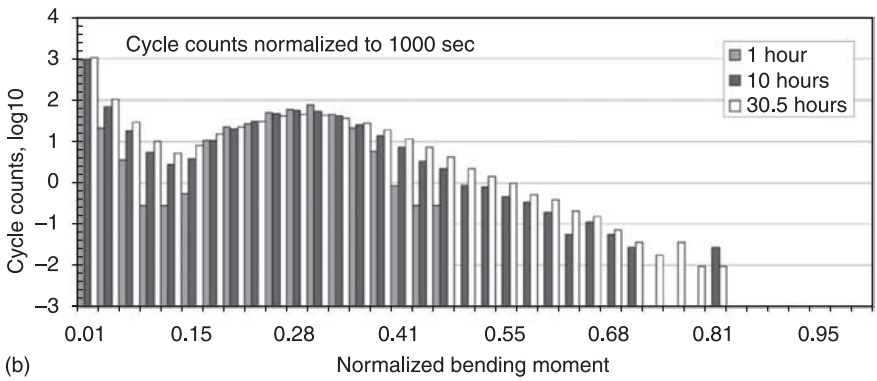

(b)

5.8 Fatigue loading distribution showing the increasing number of high amplitude cycles with longer observation times. (a) Edge loading; (b) flap loading.

to the larger and more important cycles. The extrapolation therefore needs to focus on the larger cycles that clearly represent a single population and which can be well approximated with a standard distribution type. A significant amount of work has been devoted to the issue of fitting distributions to fatigue data (Veers and Winterstein, 1998; Thomsen, 1998; Manuel *et al*., 2001; Fitzwater, 2002; Moriarty, *et al*., 2002). Figure 5.9 illustrates how the fit can be applied to the important cycles and used to extrapolate to less frequent, larger cycles while ignoring the low amplitude noise in the data.

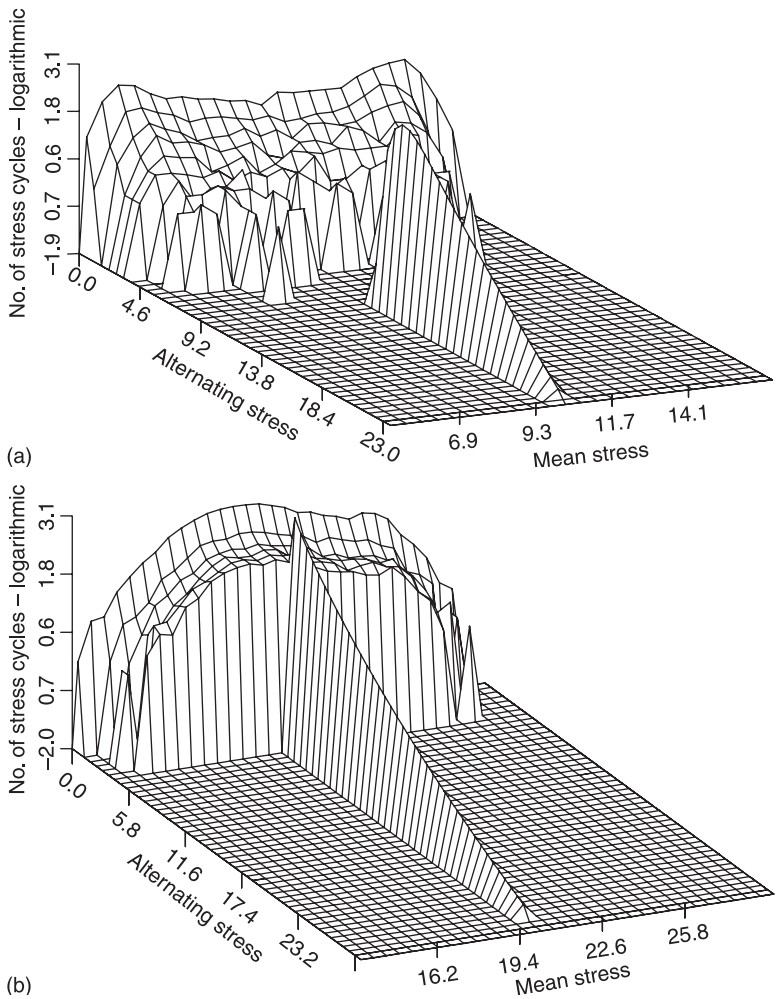

5.9 Smooth fitting to the high amplitude portion of the stress cycle distribution is used to extrapolate to higher amplitude cycles that are observed in the limited data. The relatively modest variation in mean stress is also approximated using a single value for mean stress [Sutherland, 1999]. (a) Edge loading; (b) flap loading.

The fatigue loading data is also better understood when probability distributions are used to represent the distribution of cycle amplitudes (Manuel *et al*., 2001). The histogram of the cycle counts in each range of amplitudes, when normalized by dividing by the total number of cycles, is itself an empirical probability distribution function of the cycle amplitudes. Thus, a normalized histogram of the short-term cycle counts can be used to describe the long-term expectation of cycle amplitudes. It is an unbiased estimate of the long-term distribution. The cdf is the integral of this pdf. The histogram provides a segmented distribution because the data has been stored in bins. A smoother distribution is generated if all the stress amplitudes are sorted from least to greatest, and the probability level assigned to each cycle is associated with the ranking in the list from 1 to N. The cdf or $P(S)$ is the probability that a given stress amplitude is less than S.

$$P(S) = \frac{r_i}{1+N} \quad S_{i-1} \le S \le S_i \quad i = 1,...,N \qquad [5.13]$$

r_i is the rank of the S_i stress amplitude in the sample. Although this distribution still has step changes at each S_i, N is now much larger than the number of bins and the distribution is usually quite smooth.

It is often also useful to plot the distribution in terms of the inverse of the cdf (1-$P(S)$) because it better highlights the distribution of largest cycles. This is often called the exceedence diagram and is used for both fatigue and extremes. Figure 5.10 shows exceedence plots of the same data as shown in the histograms of Fig. 5.8. In this view it is much clearer how the amplitudes behave at the highest end and how an extrapolation might continue to higher levels at lower probabilities. The logarithmic scale is also well suited to distributions that are approaching zero probability as the loads increase.

Empirical distributions have two major shortcomings: they are relatively inefficient since they require actual values of probability at many load levels to describe the full distribution, and there is no information on how the distribution might extend to higher amplitudes in the long term. Load extrapolation is a necessary part of the estimation of fatigue cycles since aeroelastic simulation results can rarely be generated for durations equal to a turbine lifetime. It is often useful, therefore, to fit a standard analytical distribution (such as a version of Weibull or Gumbel) to the empirical data before using it for long-term fatigue calculations. Analytical distributions define the loads over the entire range by just a few parameters. They are therefore useful for load extrapolation since they assign probabilities to loads at higher levels as the probability of occurrence goes to zero.

The fitted distributions need to be truncated at the low end and shifted to fit to the data that has the greatest percentage of the fatigue damage. Figure 5.11 shows examples of fits to shifted distributions after the lowest amplitude cycles have been eliminated. Over 80% of the cycles were eliminated from each of the flap

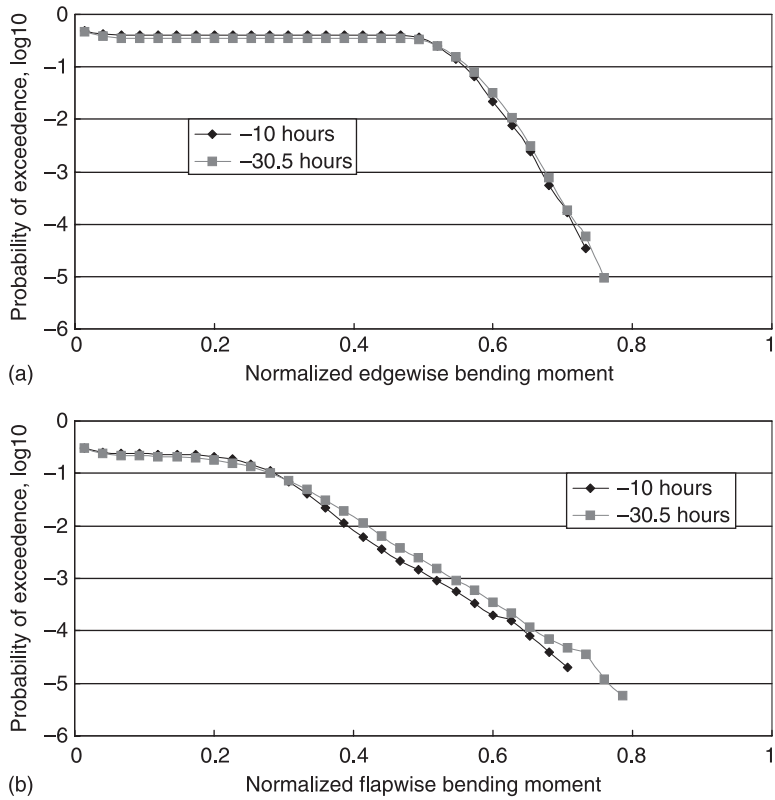

5.10 Exceedence plots are one minus the cdf of the distribution. These empirical distributions are taken from the same data as the histograms in Fig. 5.8. (a) Edge loading; (b) flap loading.

and edge loadings in this example. Yet the damaging potential of the loading was nearly unaffected. Figure 5.12 shows that the amount of damage lost in the low-end truncation depends on the exponent b used in calculating damage. Only the lowest exponent, $b = 3$, which is typical of welded steel, shows any measurable loss of damage. Even then, the loss in damage due to eliminating 80% of the smallest cycles is almost always less than 10%. For materials such as aluminium which typically has b of around 6 and fibreglass composites which has b of 9 or higher, the omitted damage is negligible and even more filtering could be applied without degrading the quality of the loading estimate.

If empirical distributions are used, it saves the effort of fitting distributions to the short-term data and at least theoretically, avoids the potential error of inappropriate distribution fits. However, the down side is that the empirical distribution is composed of only tables of numbers that define the distribution at each probability level and are not readily amenable to comparative analysis. By

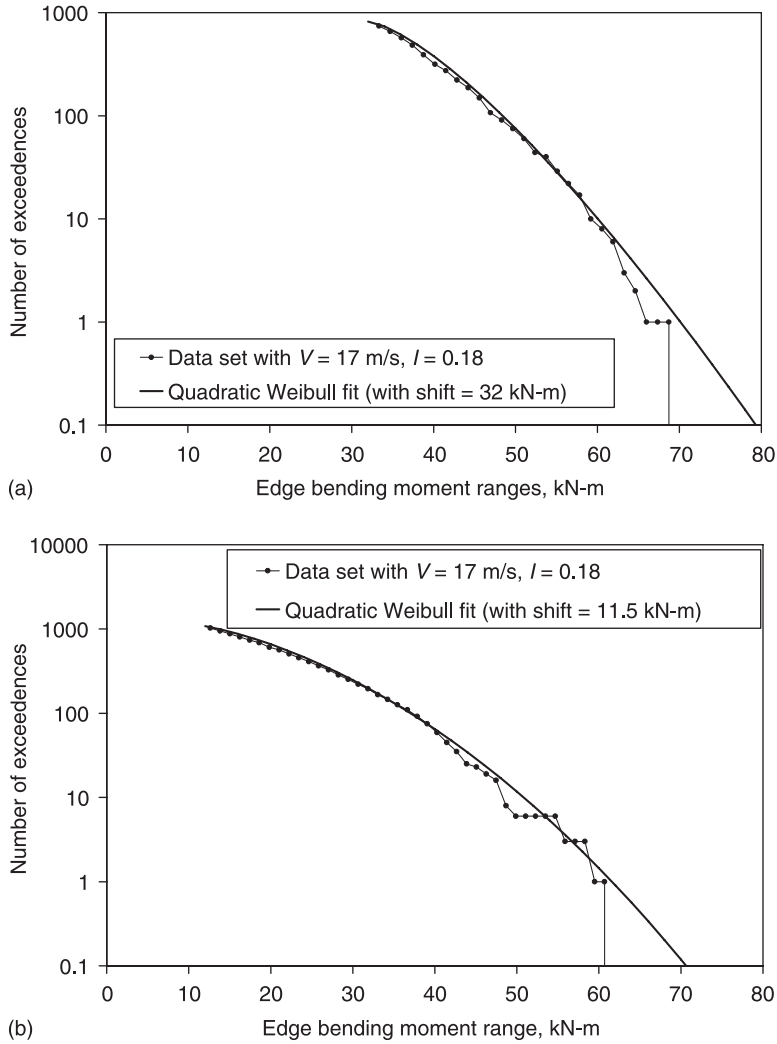

5.11 Examples of fatigue loads truncated at the low end to consider only those cycles that are significantly damaging, and fitted to quadratic Weibull distributions to represent the measured data and extrapolate to larger, less-frequent, load amplitudes [Manuel *et al.*, 2001]. (a) Edge loading; (b) flap loading.

taking the effort to fit analytical distributions, the behaviour of the turbine can be described parametrically as a function of average wind speed. The analysis is also readily extended to other inflow parameters, such as turbulence intensity and wind shear – if those properties are to be modeled explicitly in additional simulation studies.

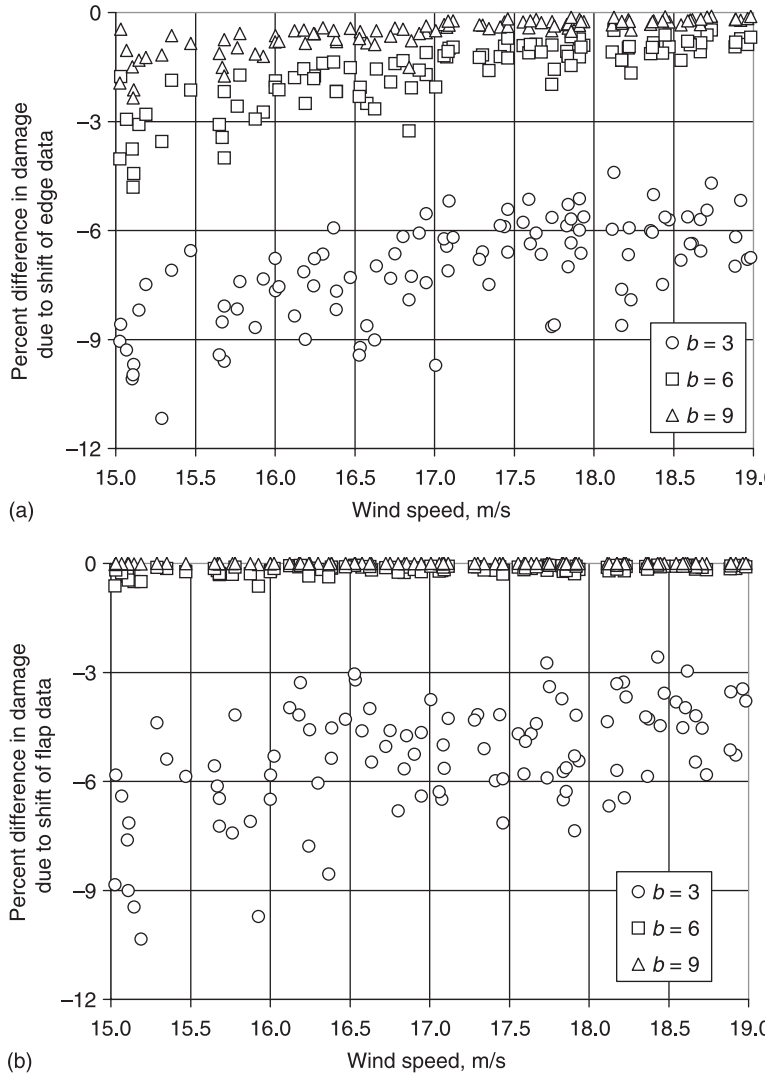

5.12 The amount of damage lost by ignoring the smallest amplitude cycles (using the shifts shown in Fig. 5.11) is negligible for high fatigue exponents (b) and still small even for the lowest fatigue exponents [Manuel *et al.,* 2001]. (a) Edge loading; (b) flap loading.

The next step in fatigue analysis is to aggregate all the loads over all operating conditions into a long-term loading distribution. The short-term distribution of fatigue loads should be viewed as a turbine-specific characteristic. The turbine can then be evaluated for its acceptability in various environments by summing these characteristic loads under specified inflow conditions that might be driven

by different design standards or that reflect site conditions for potential installations. The aggregation over the environment will be described in the next section.

5.4 Long-term load distribution

The long-term distribution of stress amplitudes starts with the estimate of turbine response due to specified short-term conditions and then adds up all the distributions of the cycle counts from all possibilities of occurrence of those specified conditions. The language and tools of probability are used to accomplish the feat, as described in the introduction to this chapter. If one has the probability of occurrence of a stress cycle under a specified set of inflow conditions, and one also has the probability of occurrence of those inflow conditions, it is a simple matter to apply the total probability theory to the situation. The short-term distribution of stress cycles, S, conditional on wind speed V is written as $p_{ST}(S|V)$. The long-term distribution of all stress cycles over all wind speed conditions, $p_{LT}(S)$, is obtained by multiplying by the wind speed distribution, $p(V)$, and integrating over all potential wind speeds.

$$p_{LT}(S) = \int p_{ST}(S \mid V) p(V)\, dV \qquad [5.14]$$

For design purposes, a standard distribution is typically used, such as the Weibull, or the Rayleigh, which is a special case of the Weibull with a shape parameter of 2.0.

$$p_{\text{Rayleigh}}(V) = \frac{V}{\sigma^2} \exp\left[-\frac{1}{2}\left(\frac{V}{\sigma} \right)^2 \right] \qquad [5.15]$$

The only parameter of the Rayleigh is then related to the annual average wind speed, $\overline{V}$.

$$\sigma = \sqrt{\frac{2}{\pi}}\overline{V} \qquad [5.16]$$

The wind speed distribution will depend on the site where terrain or turbine placement may produce differences in inflow for each machine in the wind plant. The expected wind speed distribution is usually measured at the site and described empirically. For design purposes, standard wind speed distributions are defined so that a class of turbine can be evaluated with respect to a single objective set of design criteria. Before any turbine can be installed at a particular site, the estimated loading produced by the actual site conditions must be evaluated with respect to the assumptions of the design. For site evaluation, standard wind speed distributions may not fit well enough to be used since as small distortion of the likelihood of high winds could make a substantial difference in fatigue damage estimates. Each site is evaluated in terms of whether it is expected to produce a long-term loading distribution that is more or less severe than the design loading distribution. This is one reason that the long-term fatigue load distribution function

is so important. The long-term design load distribution defines a load envelope within which all applications need to fall. If not, a design modification or retrofit will be required before the turbine can be certified as adequate for the application.

For simplicity, most design calculations use a single characteristic level of turbulence intensity selected to produce a reasonably conservative estimate of the fatigue load spectrum (or design envelope). However, it is also possible to evaluate the short-term distribution of loads as a function of both mean wind speed and turbulence intensity, and integrate over both variables to create the long-term fatigue load distribution.

$$p_{LT}(S) = \iint p_{ST}(S \mid V, I)\, p(V, I)\, dV dI = \iint p_{ST}(S \mid V, I)\, p(V)\, p(I \mid V)\, dV dI \qquad [5.17]$$

The joint distribution of wind speed and turbulence intensity, $p(I,V)$, is given by the product of the wind speed distribution and the turbulence intensity distribution conditional on the mean wind speed, $p(I \mid V)$.

Load extrapolation is a necessary part of the estimation of fatigue loads since aeroelastic simulation results can rarely be generated for durations equal to a turbine lifetime, even if limited to only those wind conditions severe enough to contribute to significant fatigue. The extrapolation is best done by fitting analytic distribution functions to the short-term loading distributions.

The empirical distributions can also be aggregated into an empirical long-term distribution before fitting and extrapolation. The advantage is that only one fit is required rather than one at each wind speed. The disadvantage is that the short-term distributions need to be aggregated with the appropriate relative proportion of time (and consequent number of data samples) in each wind speed bin. Otherwise the high amplitude end of the distribution will be distorted by the lack of cycle counts contributed by the upper tails of distributions from lower wind speeds. The computational effort in generating the appropriate number of simulations in moderate winds in order to have the correct ratio for even a few simulations at the highest wind speed is most often too great to make this approach practical.

The integration over wind speed runs from cut-in wind speed to cut-out wind speed, usually with the assumption that the turbine always operates in winds between these limits and never operates in winds outside the bounds. Only the high-wind cut-out boundary matters since relatively little damage occurs around cut-in. In reality, the high wind cut-out boundary is always greatly smeared due to the need for the turbine to shut down and stay off for some period when the winds get high. It would be far too damaging to allow the turbine to turn on and off repeatedly every time the instantaneous wind speed passed through the boundary. Since the turbine is likely to be off in winds below cut-out far more often than it is on in winds above, this approximation is considered conservative and is widely used.

Damage is also accumulated as the turbine transitions from one state to another. Damage can also occur during special events such as controls system failures, power outages, grid transients, icing, emergency stops and potentially many others, depending on site and turbine design. These events must also be accounted

for by estimating both the frequency of occurrence of the event and the loading distribution produced by the event. These are added to the long-term load distribution before a fatigue life calculation is conducted.

$$p_{LT}(S) = \left[N_T \iint p_{ST}(S \mid V, I) p(V, I)\, dV\, dI + \sum_i N_i p_i(S) F_T(E_i) \right] \frac{1}{N_{eff}} \qquad [5.18]$$

E_i is the event with a fatigue damaging potential, the $p_i(S)$ is the distribution of stress cycles caused by the event, N_i is the number of cycles caused by the event, and F_T is the frequency of occurrence of the event in time T. The total number of cycles during operation in time period T is N_T. An effective number of cycles in the time period must be chosen to aggregate the transients, but when operation cycles dominate, one could use N_T for the effective number of cycles.

The long-term load distribution is a mapping of a turbine with particular response to wind inflow conditions (defined by the suite of short-term load distributions at each set of inflow conditions) into a particular site by integrating over the probability of all conditions encountered at a site. A turbine designed for a particular standard class (IEC-1, 2005) has its characteristic short-term response mapped into a standard set of conditions to produce the design load envelope. When this turbine is evaluated for suitability at a particular site, the short-term loads are mapped into the site conditions to produce the site-specific load envelope. Fatigue life estimates are produced from both load envelopes, as described in the next section. With a complete set of short-term load distributions, conditional on inflow – preferably defined in terms of best-fit analytical distributions – this comparison can be done without the additional computational burden of aeroelastic simulations beyond what was needed in the design calculations.

5.5 Fatigue life evaluation

Lifetime can be estimated for design purposes only after appropriate safety factors have been applied to both the loadings and the fatigue properties of the materials. The prime motivation is to produce a design procedure that deals with the variability in both loads and resistance in such a way that the possibility of the coincidence of a very low strength with a very high load has a sufficiently small probability. For life-critical applications this probability must be very small, but for economic considerations alone, it might be tolerated at a somewhat higher level (Veers, 1996; Veldkamp, 2006). This is shown schematically in Fig. 5.13 (Manuel and Veers, 2008). The design condition is easier to visualize when extreme loads are being compared with ultimate strength, but it works for fatigue in very much the same way.

The governing equation of load and resistance factor design says that the characteristic resistance, R, divided by a safety factor greater than one, $\gamma_m > 1$, must be greater than the characteristic load, L multiplied by a safety factor, γ_f, also greater than one.

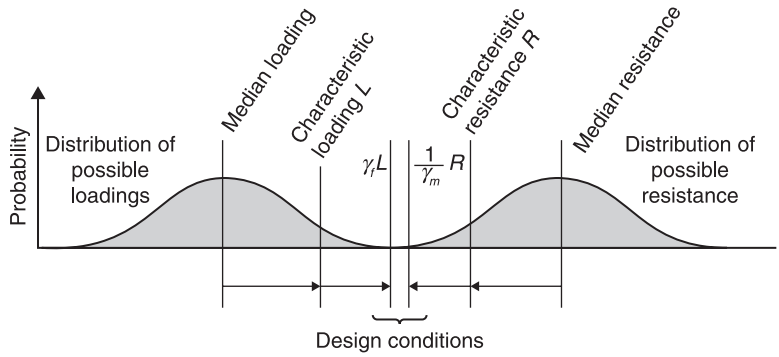

5.13 Schematic of the design philosophy of load and resistance factor design. The design condition is that the characteristic load factored by α must be less than the characteristic resistance factored by φ [Manuel and Veers, 2008].

$$\frac{1}{\gamma_m} R > \gamma_f L \qquad [5.19]$$

There is one important difference in the application of safety factors to fatigue life versus ultimate loading where the loads and resistance have the same units and are compared directly. In fatigue, the loads are applied to a damage model and used to generate an estimated lifetime, which is then compared with the design life. A safety factor applied to loads has a dramatic effect on lifetime, while safety factors on lifetime have a relatively lower effect on safety. The formulation of a safety factor system for fatigue needs to consider this nonlinearity and apply factors appropriately. For example the IEC Design Standard (IEC, 1998) moves all safety factors to the load side as amplifiers on the stresses and does not apply any factor to the damage, or lifetime, side.

$$\text{Damage} = \sum_i \frac{n_i}{N_F(\gamma_f \gamma_m S_i)} \leq 1.0 \qquad [5.20]$$

Characteristic loadings and resistances are not chosen to be at the median, but are selected to already hedge towards the more conservative end of the distribution of possible values. Usually, the characteristic values are intended to account for the known and measureable variability, such as the randomness in fatigue strength for a given material. The partial factors generally cover unfavorable deviations of action and material properties and model uncertainties – according to ISO 2394– which also form the reliability basis for the IEC standards. Therefore the partial safety factors are supplying additional margin for effects for which it can be difficult or even impossible to explicitly account. Both characteristic loads and safety factors are important and both must be applied to assure adequate margins for a durable design (Ronold *et al*., 1996; Tarp-Johansen *et al*., 2003).

There can be a trade-off between characteristic load and safety factor when comparing different standards. One system may require a very high percentile on the characteristic resistance, such as a 99% survival rate at a high confidence factor and then apply only a minimal safety factor. Another might pick a more modest level for the characteristic value and then specify a larger safety factor. In the end, adequate resistance depends only on the characteristic loading, and the ratio of the safety factors. Each certification standard will prescribe potentially different factors from others. It is not safe to pick and choose individual factors from different standards since each is designed to systematically cover all the uncertainties and might trade off strength and load factors differently. Great care must therefore be taken if you are taking design values (safety factors/partial factors) for loads from one standard and design values (safety factors/partial factors) for resistances from another standard.

The actual calculation of fatigue life is a matter of integrating over the pdf of the long-term stress cycle distribution and assigning the damage to each amplitude, A, and mean, M, that is defined in the Goodman diagram. If working with the empirical histograms of cycle counts as shown in Fig. 5.6 the calculation can be written as follows:

$$D = N_T \sum_{i=1}^{N_T} p_{LT}(M_i, A_i) D(M_i, A_i) \quad [5.21]$$

Or, one can convert the stress cycle of a given mean and amplitude into an equivalent stress amplitude at zero mean, S_{eff}, and use the fitted distributions of short-term loads to estimate a smooth long-term distribution of effective stress amplitudes and apply this to the fatigue curve that applies to the zero mean condition. The damage estimate is then written as

$$D = N_T \int p_{LT}(S_{eff}) C^* S_{eff}^b dS_{eff} \quad [5.22]$$

Following the IEC convention [see equation 5.20], stress amplitudes are multiplied by both the load and the resistance safety factors.

$$D = N_T \int p_{LT}(S_{eff}) \frac{(\gamma_f \gamma_m S_{eff})^b}{C} dS_{eff} \quad [5.23]$$

The calculated lifetime, T_{calc}, is estimated by the Miner's Rule assumption that failure occurs when $D = 1$. The total number of cycles at that time relates to lifetime by an average cycle frequency, f_{avg}.

$$T_{calc} = \frac{C}{f_{avg}} \left(\int p_{LT}(S_{eff}) (\gamma_f \gamma_m S_{eff})^b \, dS_{eff} \right)^{-1} \quad [5.24]$$

The design checking equation requires that the calculated lifetime must be greater than the specified characteristic life T_{calc}. The characteristic lifetime may itself be an inflated value to provide additional conservatism:

$$T_{calc} \geq T_{char} \quad [5.25]$$

It is often useful to apply the damage model to the short-term distributions to examine which wind speeds are responsible for the most damage. Damage is written as a function of wind speed by integrating over stresses conditional on each wind speed.

$$D(V) = f_{avg} \int p_{ST}(S_{eff}) C^* S_{eff}^{-b} dS_{eff} \quad [5.26]$$

When this damage is normalized to unit area over all wind speeds, it represents a damage density function that clearly shows where the damage in coming from in the operating envelope. Figure 5.14 shows how the exponent in the fatigue properties of the material has a major influence on the wind speeds in which most damage is accumulated. This example assumed a linear increase in the mean value of Weibull distributed stress amplitudes as wind speed increased. Some wind turbine components behave approximately in that manner, but some – notably flap loads and other loads related to the thrust on the turbine – can begin to decrease with wind speed when the controller feathers the blades in winds above the rated (Moriarty, 2008). Figure 5.15 shows the maximum, minimum and mean values of simulations over a wide range of wind speeds for drive train torque, tower base bending and blade flap bending, illustrating how different loads respond differently to wind speed.

Deterministic design criteria that allow the designer to evaluate whether the structure is on the safe or unsafe side of an objective checking equation (such as equations [5.19] and [5.20]) are very useful in the design and optimization process.

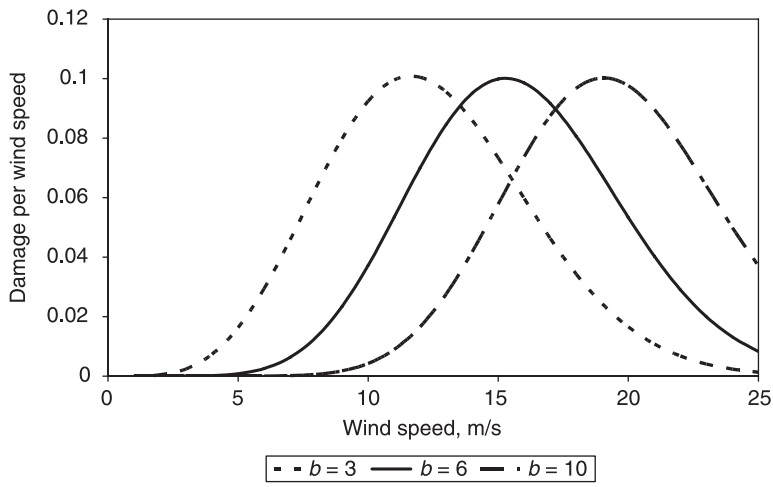

5.14 Damage density functions for Weibull distributed stress amplitudes, with the mean value of the Weibull distribution increasing linearly with wind speed. The wind speed distribution is Rayleigh with a mean value of 8 m/s. The plots are for different material fatigue exponents, *b*.

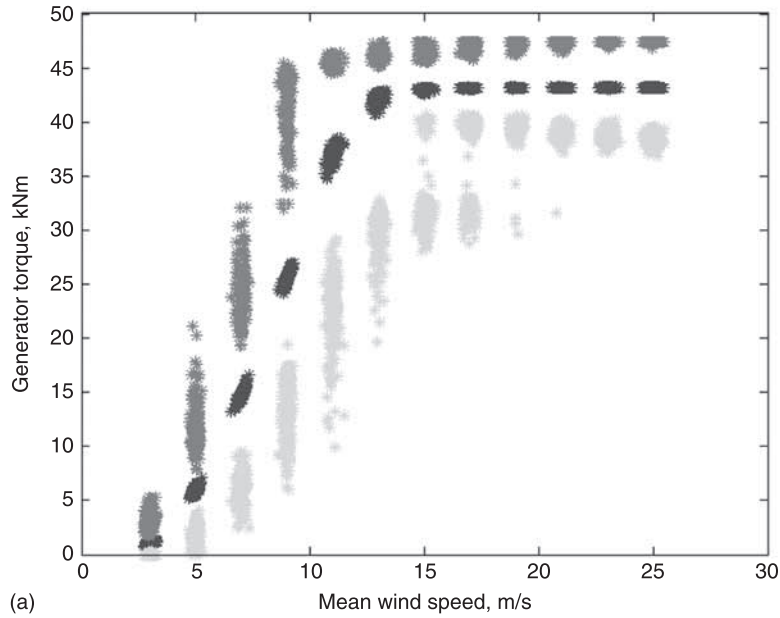

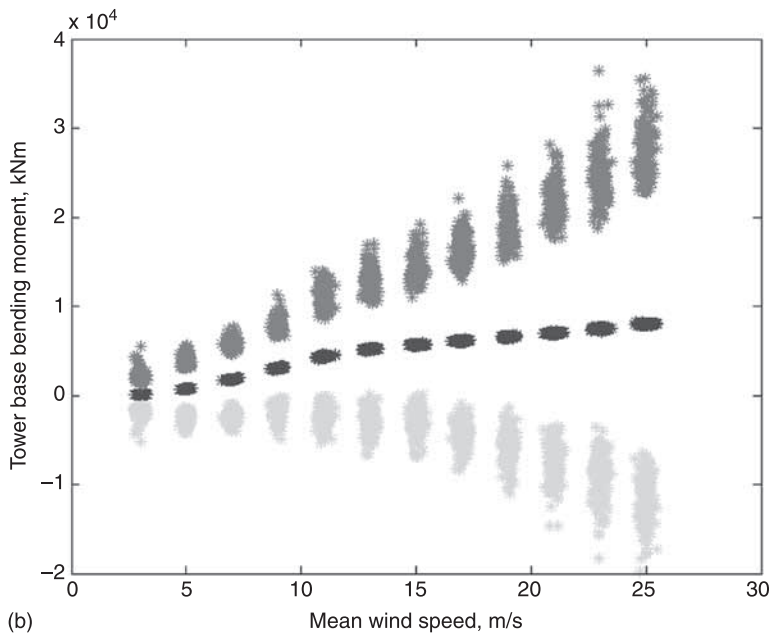

5.15 Examples of different load components showing the 10-minute maximum, minimum, and average from 200 simulations at each m/s wind speed bin [Courtesy Pat Moriarty, NREL]. (a) Generator torque (kNm) vs. mean wind speed (m/s); (b) tower base bending moment (kNm) vs. mean wind speed (m/s); (c) blade root shear force (kN) parallel to the mean wind direction vs. mean wind speed (m/s).

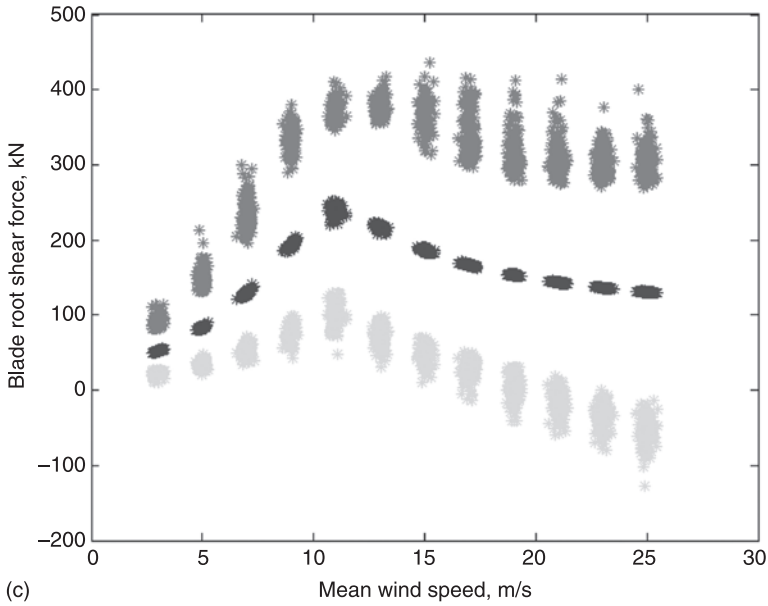

5.15 Continued.

The design criteria are based on some expectation for how low the probability of failure needs to be. The safety factors and characteristic values can be tuned to produce the desired probability of non-failure (Ronold and Larsen, 2000; Ronold and Christiansen, 2001; Sørensen and Tarp-Johansen, 2004; Sørensen and Tarp-Johansen, 2005; Veldkamp, 2008). This allows the designer to achieve a desired probabilistic outcome without going through all the difficulty of a probabilistic analysis. However, it is also useful to know what kind of margin really exists between the actual design evaluation and the specified design criteria. A large calculated lifetime is not necessarily a good measure of safety since with large fatigue exponents, a small change in stress level can produce orders of magnitude differences in lifetime (Sutherland, *et al*. 1994). Therefore, it is useful to estimate probability of failure by assessing the uncertainty in each of the controlling parameters and propagating that through into an estimate of the probability of failing to exceed the characteristic or required lifetime (Veers, *et al*., 1994; Veers and Winterstein, 2000; Veldkamp, 2006). It is very useful for these purposes to have developed a fully parametric model of the fatigue loading so that each parameter can be varied consistent with its inherent randomness and uncertainty to produce a suite of possible outcomes. Monte Carlo methods are reasonable approaches given the relative ease of repeated calculations (Rubinstein, 1981). It is also possible to estimate which parameters are most responsible for the probability of failure. Structural reliability methods are particularly good at not

only determining the probability of premature failure from a large number of uncertain parameters, but can also be used to assess which parameters are most important, as well as the sensitivity of the result to parametric variation (Madsen, *et al*., 1986; Lange, 1996; Braam, *et al*., 1999). Action on design adjustments for sites which exceed the allowable damage at the characteristic life can be made based on these sensitivity estimates.

5.6 Conclusion

Fatigue life estimates for wind turbines depend on accurate assessments of both the loading and the material fatigue durability. Loadings are estimated by defining the short-term distribution of stress cycles due to specified inflow conditions. Long-term distributions are determined by integrating the short-term distributions over all inflow conditions in the design criteria and then adding in transient and other special events. The lifetime is estimated by applying the damage rule to the long-term cycle distribution. Safety factors must be applied to all characteristic values for both the applied loads and the material properties. It would add greatly to the understanding of the drivers of the fatigue design to assess the probability that the calculated lifetime is less than the characteristic, or desired, lifetime. This process must be repeated for each turbine component that is susceptible to fatigue. The analysis of different components is greatly complicated by the fact that individual components are made of materials with widely different fatigue characteristics (e.g. welded steel versus fibreglass) and that they do not all share similar relationships between inflow conditions (wind speed) and stress response. The deterministic design checking equation in the load and resistance factor design approach allows designers to produce structures with acceptably low probability of failure by using the safety factors that have been tuned to achieve that end. Research on tuning those factors is an ongoing topic and critical to the ability to optimize design cost and durability.

5.7 References

Braam, H, Christensen, C J, Ronold, K O and Thøgersen, M L, 'PRODETO, a computer code for probabilistic fatigue design', *Proceedings of EWEC 1999: Wind Energy for the next Millennium*, Nice, France, 1–5 March 1999, eds. Petersen, E L, Hjuler Jensen, P, Rave, K, Helm, P and Ehmann, H, James & James Science Publishers, Sunnyvale, CA, 1999.

Brown, L M, *Dislocations and Fatigue Strength of Metals*, Pergamon Press, Sunnyvale, CA, 1981.

Cotrell, A H, *Mechanical Properties of Matter*, Wiley, New York, 1969.

Dowling, S D and Socie, D F, 'Simple rainflow counting algorithms', *Int J of Fatigue*, Vol. 4, No. 1, 1982.

Fitzwater, L M, 2002. 'Estimation of Fatigue and Extreme Load Distributions from Limited Data with Application to Wind Energy Systems', PhD thesis, Stanford University, Stanford, California, 2002.

IEC-1, '*Wind Turbine Generator Systems – Part 1: Safety requirements*', 61400-1, edition 2, International Electrotechnical Commission, IEC, 1998.

IEC-1, '*Wind Turbine Generator Systems – Part 1: Safety requirements*', 61400-1, edition 3, International Electrotechnical Commission, IEC, 2005.

ISO 2394, '*General principles on reliability for structures*', ISO 2394:1998, International Organization for Standardization, ISO, 1998.

Jonkman J M and Buhl M L, Jr., '*FAST User's Guide*', NREL/EL-500–38230 (previously NREL/EL-500–29798). NREL: Golden, CO, 2005.

Lange, C H, 'Probabilistic Fatigue Methodology and Wind Turbine Reliability', (Stanford University PhD thesis) SAND96-1246, Sandia National Laboratories, 1996.

Larsen, T J and Hansen, A M, '*How 2 HAWC2, the user's manual*', Risø-R-1597(ver. 3–1) (EN) Risø National Laboratory, Technical University of Denmark Roskilde, Denmark Dec. 2007.

Lundberg G, Palmgren A, 'Dynamic capacity of rolling bearings', *Acta Polytechnica Mech. Eng. Series*; Vol. 2, 96, 1952.

Madsen, H O, Krenk, S and Lind, N C, *Methods in Structural Safety*, Prentice-Hall, 1986.

Manuel, L, Veers, P S and Winterstein, S R, 'Parametric Models for Estimating Wind Turbine Fatigue Loads for Design', *Journal of Solar Energy Engineering, Trans. ASME*, Vol. 123, November, 2001.

Manuel, L and Veers, P S, 'Relating Site-Specific Risks to Standard Design Criteria and Extreme Events', *Prococeedings WindPower 2008*, American Wind Energy Association, Houston, TX, June 2–4, 2008.

Miner, M A, 'Cumulative Damage in Fatigue', *J Applied Mechanics, Trans. ASME*, Vol. 67, Sept. 1945.

Mitchell, M R, 'Fundamentals of Modern Analysis for Design', *Fatigue and Microstructure, ASM Material Science Seminar*, St. Louis, MO, October 1978, ASM, 1979.

Moriarty, P J, Holley, W E and Butterfield, C P, 'Effect of turbulence variation on extreme loads prediction for wind turbines', paper AIAA-2002-0050, 2002.

Moriarty, P, 'Database for Validation of Design Load Extrapolation Techniques', *Wind Energy*, Vol. 11, No. 6, 2008.

Nelson, L D, Manuel, L, Sutherland, H J and Veers, P S, 'Statistical Analysis of Inflow and Structural Response Data from the LIST Program', *Journal of Solar Energy Engineering, Trans. of the ASME*, Vol. 125, No. 4, November, 2003.

Nijssen, R P L, 'Fatigue Life Prediction and Strength Degradation of Wind Turbine Rotor Blade Composites', (Technical University of Delft PhD thesis) SAND06-7810, Sandia National Laboratories, November, 2006

Øye, S. '*FLEX 5 User Manual*', Technical University of Denmark, Lyngby, 1999.

Ronold, K O and Echtermeyer, A T, 'Estimation of fatigue curves of composite laminates', *Composites Part A*, 27A, Elsevier Science Ltd., 1996, pp. 485–491.

Ronold, K O, Wedel-Heinen, J, Christensen, C J, 'Calibration of partial safety factors for design of wind-turbine rotor blades against fatigue failure in flapwise bending', *1996 European Union Wind Energy Conference*, Goteborg, Sweden, 20–24 May, 1996.

Ronold, K O and Larsen, G C, 'Reliability-based design of wind-turbine rotor blades against failure in ultimate loading', *Engineering Structures*, Vol. 22, 2000, pp. 565–574.

Ronold, R O, Christiansen, C J, 'Optimization of a design code for wind-turbine rotor blades in fatigue,' *Engineering Structures*, Vol. 23, 993–1004, 2001.

Rubinstein, R Y, *Simulation and the Monte Carlo Method*, John Wiley & Sons, New York, 1981.

Sørensen, J D, Tarp-Johansen, N J, 'Optimal structural reliability of wind turbines', in *ICOSSAR Rome*, A G Schüller, M Ciampoli (eds), ICOSSAR, Millpress Science Publishers, Rotterdam, 2005.

Sørensen, J D and Tarp-Johansen, N J, 'Cost-optimal structural Reliability of offshore wind turbines', in *The Science of Making Torque from Wind*, G A M van Kuik (ed), EWEA, Duwind, Delft University of Technology, Delft, 2004.

Sutherland, H J, Veers, P S and Ashwill, T D, 'Fatigue Life Prediction for Wind Turbines: A Case Study in Loading Spectra and Parameter Sensitivity', *Case Studies for Fatigue Education, ASTM STP 1250*, R I Stephens, Ed., American Society for Testing and Materials, Philadelphia, 1994, pp. 174–207

Sutherland, H J and Veers, P S, 'Effect of Cyclic Stress Distribution Models on Fatigue Life Predictions', *Wind Energy –1995*, W Musial, Ed., ASME, SED – Vol. 16, 1995.

Sutherland, H J, 'On the fatigue analysis of wind turbines', SAND99-0089, Sandia National Laboratories, June, 1999.

Tarp-Johansen, N J, Madsen, P H and Frandsen, S, 'Background document for partial safety factors for extreme load effects, Proposal for the 3rd Ed. of IEC 61400: Wind turbine generator systems – Part 1: Safety Requirements', Risø report R-1319(EN), Risø National Laboratory, ISBN 87-550-3002-5, 2003.

Thomsen, K, 'The Statistical Variation of Wind Turbine Fatigue Loads', Risoe-R-1063, September 1998

Tsai, Steven W. (ed.), *Strength and Life of Composites*, Composites Design Group, Department of Aeronautics & Astronautics, Stanford University, Stanford, CA, 2008

Veers, P S, 'Blade Fatigue Life Assessment with Application to VAWTs', *Journal of Solar Energy Engineering, Trans. of the ASME*, Vol. 104, No. 2, May 1982, pp. 106–111.

Veers, P S, 'Three-Dimensional Wind Simulation', SAND88-0152, Sandia National Laboratories, March 1988.

Veers, P S, Winterstein, S R, Lange, C H and Wilson, T A, 'User's Manual for FAROW: Fatigue and Reliability of Wind Turbine Components', SAND94-2460, Sandia National Laboratories, November 1994.

Veers, P S, 'Fatigue Reliability of Wind Turbine Fleets: The Effect of Uncertainty on Projected Costs', *Journal of Solar Energy Engineering, Trans. of the ASME*, Vol. 118, No. 4, November 1996.

Veers, P S, and Winterstein, S R, 'Application of Measured Loads to Wind Turbine Fatigue and Reliability Analysis', *Journal of Solar Energy Engineering, Trans. of the ASME*, Vol. 120, No. 4, November 1998.

Veers, P S and Winterstein, S R, 'Theory Manual for FAROW Version 1.1: A Numerical Analysis of the Fatigue and Reliability of Wind Turbine Components', SAND94-2459, February 2000.

Veldkamp, H F, 'Chances in Wind Energy: A Probabilistic Approach to Wind Turbine Fatigue Design', PhD thesis, Delft Technical University, Delft, 2006.

Veldkamp, D, 'A Probabilistic Evaluation of Wind Turbine Design Rules', *Wind Energy*, Vol. 11, No. 6, 2008.

6

Aerodynamic design of wind turbine rotors

C. BAK, Risø National Laboratory for Sustainable Energy,
Technical University of Denmark, Denmark

Abstract: This chapter describes the process of aerodynamic rotor design for horizontal axis wind turbines. Apart from describing the state of the art, it describes the mathematical models, airfoil choice and rotor control required for the design, including common constraints. An example of a rotor design process is sketched from choice of rotor size, airfoil types and number of blades to the exact aerodynamic shape of the blades. At the end of the chapter, future trends are sketched, together with sources of further information.

Key words: rotor design, wind turbine rotor, wind turbine airfoils, aerodynamic design.

6.1 Introduction

The wind turbine rotor with its blades is the part of the wind turbine that extracts the kinetic energy from the wind and converts it into mechanical power and further into electricity, water heating and pumping. A result of extracting energy is that the flow speed of the air passing through the area through which the rotor sweeps is reduced in the rotor plane and behind the rotor. There are many different ways to extract energy from the wind. Wind turbine rotors can be divided into those which are driven by the lift on the airfoils and those which are driven by the drag on the blades. Also, rotors can be divided into those with low rotational speed, causing a high torque, and those with high rotational speed, which are common in electricity production. Further to this, wind turbines can be divided into horizontal axis wind turbines (HAWTs) and vertical axis wind turbines (VAWTs). The most common concept today is the HAWT (Fig. 6.1 left), with a different number of blades, driven by the lift on the airfoils and with high rotational speed. Also a VAWT is shown (Fig. 6.1 right), driven by the lift on the airfoils and with high rotational speed. The three-bladed HAWT with the rotor upstream of the tower is the absolute dominating concept today and the ten biggest suppliers of wind energy installing around 94% of the capacity in 2008[1] all use this concept. Because of the significant domination of the HAWT concept, this chapter will limit the description of aerodynamic design to HAWT rotors driven by the lift on the airfoils and with high rotational speed.

This chapter describes briefly the state of the art within the aerodynamic design of rotors and gives the basis for aerodynamic design of a rotor using simple but common methods. The introduction to rotor design is based on the blade element momentum (BEM) method followed by descriptions of the performance of the

6.1 Left, horizontal axis wind turbine (HAWT): Siemens 2.3 MW wind turbine, 69 m hub height, situated at Rødsand, Denmark (Photo by Christian Bak, Risø DTU). Right, vertical axis wind turbine (VAWT): Éole 4 MW wind turbine, height of 110 m, situated at Cap Chat, Quebec, Canada (Photo by Paul Gipe).

airfoil sections along the blade, decision of rotational speed, determination of the rotor size, rotor control, design constraints, determination of the number of blades, and how to evaluate the rotor design. Based on this introduction, an example of a rotor design process is described, where a first draft of a rotor for a 1 MW wind turbine is designed. At the end of the chapter, future trends and sources of further information are described.

Even though the scope of this chapter is about aerodynamic rotor design, it should be emphasized that the rotor design process should be considered as a part of the wind turbine design process, including the aeroelastic response of the entire wind turbine and the structural design of the blades. Therefore, along with the description of the aerodynamic rotor design in this chapter the reader will sometimes be reminded about the strong connection to the rest of the wind turbine to emphasize this issue.

6.2 State of the art

Many simulation tools have been developed for prediction of wind turbine rotor flow. They cover the range from the very simple models, such as the BEM method, requiring low computational means, to the very advanced models, such as three-dimensional computational fluid dynamics (CFD), resolving the boundary layers

on the rotor and the domain several rotor diameters upstream and downstream of the rotor plane, thus requiring high computational means. However, predictions with the very advanced methods are, despite the fast development of computer power, still in 2010, too time consuming and should be considered as tools for evaluating the rotor design, rather than a part of the inherently iterative rotor design process.

That is the reason for the extensive use of the BEM method implemented in tools for prediction of the rotor aerodynamics, but also implemented in tools for prediction of the aeroelastic response of the entire wind turbine. A common way of designing rotors in 2010 is to carry out a draft rotor design using a simple method such as the BEM method, and evaluate it using a so-called aeroelastic code. If the rotor design turns out to be efficient, it can be evaluated using advanced tools, such as CFD, if they are available.

The rotor design approach described above is a manual process based on trial-and-error and works with great success if the designer is experienced. However, the design can also be carried out using numerical optimization, where an object function is minimized or maximized. The object function could be the power coefficient or the annual energy production (AEP) subject to constraints, such as maximum loads below a certain level, and absolute thickness distribution of the blades above a certain level to ensure a certain minimum stiffness. In such a tool, coupling to an aeroelastic code is possible, which to some degree can automate the rotor and wind turbine design. However, the output of such a design study is dependent on the object function and the constraints, so carrying out such a design process requires an experienced user. Furthermore, such a design method is time consuming, especially if the design is based on aeroelastic calculations, and therefore certain simplifications are often needed to reduce the computational time. Despite the time consumption on using such a tool it can be profitable, because trends in the rotor design, which is not part of the experience, can be revealed. At least one tool can carry out designs based on both aerodynamic and aeroelastic calculations using numerical optimization.[2,37] If aerodynamic optimizations are sufficient, a few other tools exist.[3]

Because the simple BEM method is often used in the rotor design process, the design could, with great advantage, be evaluated using more advanced methods. The most time-consuming simulation method is based on an exact modeling of the surface geometry of the blade and rotor, where the boundary layer of the flow over the surface is resolved. Here, a significant part of the operator time is spent on generating a computational mesh that satisfies the conditions necessary for creating good solutions. Apart from commercially available CFD codes,[4–6] significant work has also been carried out to develop this technique dedicated for wind turbines since the start of the 1990s.[7–10] Reduced models exist as well, where the rotor is modeled by introducing volume forces into the flow either by lines simulating each blade (Actuator Line method)[11,12] or by a disk simulating the entire rotor, where the blade forces are smeared out on the entire rotor plane

(Actuator Disc method).[13] The results from these methods compare quite well with the full model, as described above, where, for example, power curves and force distributions along the blades are very similar. However, details such as airfoil characteristics and tip flow cannot be extracted. Finally, techniques using discrete vortices have been developed and are fairly fast as well, but depending on whether the wake behind the turbine is free to move or frozen.[14]

6.3 Models and elements used in the rotor design process

In the previous section, it appeared that the most common method for prediction of rotor performance and aerodynamic design of rotors was the BEM method and that it required low computational means. In this section, elements needed for aerodynamic design of rotors using BEM are described. Because the aerodynamic rotor design should be considered as integrated in the design of the entire wind turbine, aspects such as constraints relating to the aerodynamic rotor design process are also described. Furthermore, to make the rotor design process operational, a few rules of thumb are described, but these rules are based on the experience of existing rotor designs and may not work for all designs.

6.3.1 Rotor aerodynamics

The BEM method was developed in the 1930s,[15] and later other, but not very different, formulations have been developed.[16–18] In the following, this method will be described starting with a simplified model assuming that the flow through the whole rotor behaves the same way at all points, making the problem one-dimensional. Furthermore, the rotor has no losses such as friction caused by the air viscosity and losses caused by the flow at the tips. The description of the simplified one-dimensional model is followed by a description of the more advanced BEM model. This model is based on using the one-dimensional model in each annular element and also considering losses in terms of friction caused by air viscosity and by the flow at the tips.

One-dimensional momentum theory

In this first analysis of the rotor flow, it is assumed that the rotor is a disc and that it is ideal, i.e. the flow is inviscid (no air viscosity) and there are no losses at the tips. The disc has the characteristic that it reduces the flow speed and extracts all the energy resulting from the reduction of the flow speed. In Fig. 6.2, a sketch of the flow around an ideal wind turbine rotor is shown, where the development of the velocity and pressure from far upstream of the rotor to far downstream of the rotor is shown.

From Bernoulli's equation, it is possible to make a connection between pressure and velocity both upstream and downstream of the rotor. Bernoulli's equation

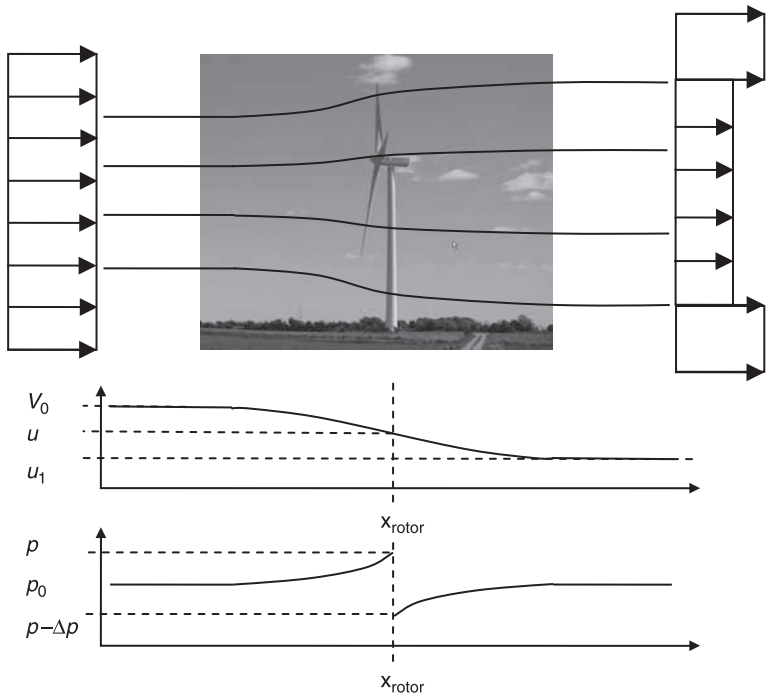

6.2 Sketch of flow around the ideal wind turbine rotor (Photo by Christian Bak: Vestas V80 at Tjæreborg Enge, Denmark).

states that along a stream line the dynamic pressure, determined by the flow speed, added to the static pressure equals the total pressure, Eq. 6.1:

$$\frac{1}{2}\rho u^2 + p = H \qquad [6.1]$$

From the equation, it is seen that when the velocity decreases, the pressure will increase and vice versa. However, this equation is not valid through the rotor plane, but the flow upstream and downstream of the rotor plane can be analyzed. Upstream, the connection is as described as:

$$p_0 + \frac{1}{2}\rho V_0^2 = p + \frac{1}{2}\rho u^2 \qquad [6.2]$$

Downstream of the rotor, the connection is as described as:

$$p_0 + \frac{1}{2}\rho u_1^2 = p - \Delta p + \frac{1}{2}\rho u^2 \qquad [6.3]$$

By subtracting Eqs 6.2 and 6.3 from each other, an expression of the pressure drop through the rotor plane is obtained:

$$\Delta p = \frac{1}{2}\rho\left(V_0^2 - u_1^2\right) \qquad [6.4]$$

The pressure drop can also be expressed as the change in momentum of the air passing through a unit area of the rotor per second:[18]

$$\Delta p = \rho u\left(V_0 - u_1\right) \quad [6.5]$$

Coupling Eqs. 6.4 and 6.5 gives:

$$u = \frac{1}{2}\left(V_0 + u_1\right) \quad [6.6]$$

Eq. 6.6 tells us that the air speed in the rotor plane has been decelerated to exactly half of the total velocity deficit that it will experience from far upstream to far downstream in the rotor wake. Thus, the other half of the deceleration of the wind takes place in the wake, downstream of the rotor.

In this context, a convenient entity to be defined is the axial interference factor, a:

$$u = (1-a)V_0 \quad [6.7]$$

Therefore, from Eq. 6.6 we get $u_1 = (1 - 2a)V_0$ and the expression for the extracted power, P, and the corresponding thrust, T, are given by:[18]

$$P = \frac{1}{2}\rho u\left(V_0^2 - u_1^2\right)A = 2\rho a(1-a)^2 V_0^3 A \quad [6.8]$$

$$T = \Delta p A = 2\rho a(1-a)V_0^2 A \quad [6.9]$$

The rate of the kinetic energy through the rotor disc, P_{wind}, and the stagnation pressure on the rotor disc, T_{wind}, are defined in as:

$$P_{wind} = \frac{1}{2}\rho V_0^3 A \quad [6.10]$$

$$T_{wind} = \frac{1}{2}\rho V_0^2 A \quad [6.11]$$

Non-dimensional coefficients for the power and the thrust are convenient to use and can be defined using Eqs. 6.10 and 6.11, as:

$$C_P = \frac{P}{P_{wind}} = \frac{P}{\frac{1}{2}\rho V_0^3 A} \quad [6.12]$$

$$C_T = \frac{T}{T_{wind}} = \frac{T}{\frac{1}{2}\rho V_0^2 A} \quad [6.13]$$

Using this definition Eqs. 6.8 and 6.9 can be written as:

$$C_P = 4a\,(1-a)^2 \quad [6.14]$$

$$C_T = 4a\,(1-a) \quad [6.15]$$

Eq. 6.14 is very important for understanding wind power extraction, because it tells us that the maximum obtainable power from the wind is C_P = 16/27

(approximately 0.593) and that this maximum value is obtained for an axial interference factor of $a = 1/3$. This means that not all of the existing wind power can be extracted, but only 59% at its very maximum. This maximum limit is usually called the Betz limit.[19] This means that the maximum power is extracted when the wind speed is decreased by 1/3 of the free wind speed in the rotor plane and is 2/3 of the free wind speed in the far wake. An explanation as to why not all power can be extracted is the need to transport the air away from the rotor after the power has been extracted. If the air were completely stopped and all existing power were extracted, the air would have to be accumulated somewhere. Thus, the remaining power in the wind is required to transport the air downstream and away from the power extraction device: the rotor disc. From Eq. 6.15 it is seen that the corresponding thrust coefficient, C_T, is 8/9 (approximately 0.89).

As shown in Fig. 6.3, both C_P and C_T are increasing for increasing a for small values of a. However, for $a > 1/3$ C_P decreases while C_T still increases. For $a > 1/3$, the theory is increasingly uncertain compared to real rotor aerodynamics. For $a = 0.5$, the far wake has reached a standstill and for $a > 0.5$ reversed flow in the far wake has resulted. Thus, for $a \geq 0.5$ the theory breaks down. According to the theory, $C_T = 1$ for $a = 0.5$ and the rotor is said to be highly loaded. However, in reality the rotor may be even more loaded, because the assumptions used in the derivation of the theory no longer hold for $a > 1/3$. Corrections for $a > 1/3$ will be given in the next section.

Blade element momentum theory

Even though the flow through a wind turbine is very complex with its tip and root vortices, and the mutual interaction between the rotor blades, it is possible to

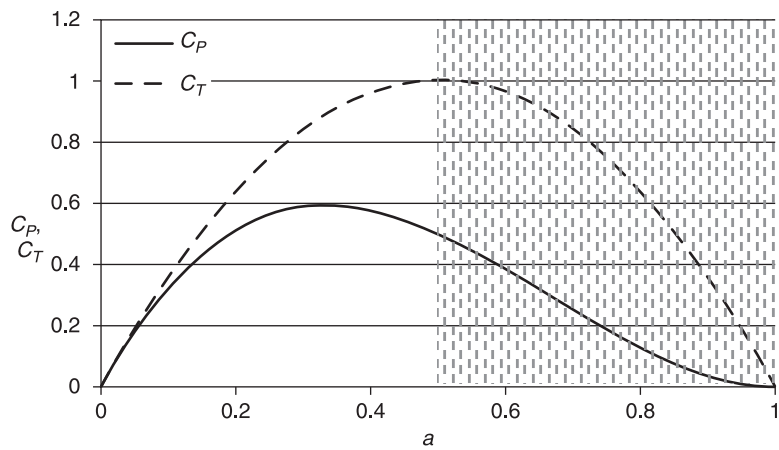

6.3 The power coefficient (C_P) and thrust coefficient (C_T) for one-dimensional momentum theory as a function of axial interference factor (a).

simplify the mechanisms in a very efficient way. As shown in Fig. 6.4, the rotor can be divided into annular elements of span width dr. Because the theory that will be developed in this section is based on the one-dimensional momentum theory, it must be assumed that there is no interaction between neighboring elements, which one-dimensional momentum theory can show to be a good assumption.[18] Also, it must be assumed that the axial and tangential velocities all over the annular element are uniformly distributed. This means that the forces are not concentrated on the blades, but are smeared out over the annular element.

Figure 6.5 shows a section on the rotor blade illustrating the symbols used in the BEM formulation. The blade section is exposed to the axial velocity (wind speed), V_0, and the tangential velocity (eigen velocity), $r\omega$. Because of the forces from the rotor on the wind, where the total induced velocity is parallel to the lift force but in the opposite direction, the axial velocity is reduced to $(1–a)V_0$, and the tangential velocity is increased to $(1+a')r\omega$. The resulting velocity that the blade section experiences, the relative velocity, W, is the vector sum of the axial and

6.4 Sketch of the division of a wind turbine rotor into annular elements (Photo by Christian Bak: NM80 at Tjæreborg Enge, Denmark).

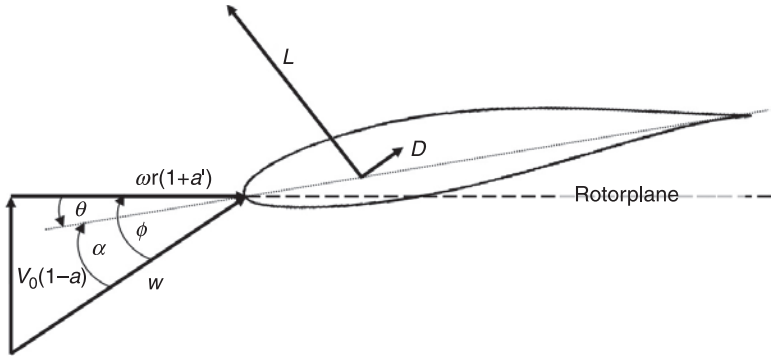

6.5 Sketch of a section on the rotor blade illustrating the symbols used in the blade element momentum formulation. The arrows show the direction of positive values.

tangential velocity. The angle from W to the rotor plane is called the inflow angle, ϕ, positive in the clockwise direction. The blade section is in general twisted, θ, positive in the anticlockwise direction. The twist is defined as the angle from the rotor plane to the airfoil chord line, which is from the very leading edge of the airfoil to the very trailing edge of the airfoil. The angle from the relative velocity, W, to the chord line is called the angle of attack, α, positive in the clockwise direction.

Based on the sketch in Fig. 6.5, the following relations can be derived:

$$\alpha = \phi - \theta \qquad [6.16]$$

$$\tan\phi = \frac{1-a}{1+a'}\frac{V_0}{r\omega} \Leftrightarrow \phi = \arctan\left(\frac{1-a}{1+a'}\frac{V_0}{r\omega}\right) \qquad [6.17]$$

From the *Theory of Wing Section*, see for example Abbot and Doenhoff,[20] the lift and drag forces on each blade section, respectively, can be expressed in terms of lift and drag coefficients:

$$L = \frac{1}{2}\rho W^2 c c_l \qquad [6.18]$$

$$D = \frac{1}{2}\rho W^2 c c_d \qquad [6.19]$$

Here, c is the chord length and c_l and c_d are the lift and drag coefficients, respectively. These coefficients will be described further in Section 6.3.3, 'Airfoil performance'. For each annular element the thrust and torque, respectively, are given as:

$$dT = \frac{1}{2}\rho W^2 cBc_y dr \qquad [6.20]$$

$$dQ = \frac{1}{2}\rho W^2 cBc_x r dr \qquad [6.21]$$

Here, the force coefficients normal to the rotor plane, c_y, and parallel to the rotor plane, c_x, have been used:

$$c_y = c_l \cos\phi + c_d \sin\phi. \qquad [6.22]$$

and

$$c_x = c_l \sin\phi - c_d \cos\phi. \qquad [6.23]$$

In order to couple the forces from the blade elements with momentum theory, the response from the tangential forces must be taken into account. Therefore, the one-dimensional theory described above, where the wake rotation is not part of the theory, must be extended with a rotational part reflecting the momentum in the tangential direction. Furthermore, a correction for the finite number of blades will be included as

$$dT = \rho u\left(V_0 - u_1\right) F dA \Leftrightarrow dT = \frac{1}{2}\rho V_0^2 4Fa(1-a)2\pi r dr \qquad [6.24]$$

$$dQ = \rho u u_t r F dA \Leftrightarrow dQ = \frac{1}{2}\rho V_0^2 4F(1-a)a'\frac{\omega r}{V_0} r 2\pi r dr \qquad [6.25]$$

Here, u_t is the tangential velocity caused by the wake rotation in the far wake, a' is the tangential interference factor, and F is the Prandtl correction for a finite number of blades described by Glauert:[15]

$$F = \frac{2}{\pi}\arccos e^{-f} \text{ with } f = \frac{B}{2}\frac{R-r}{r\sin\phi} \qquad [6.26]$$

The above formulation of thrust and torque for an annular blade element, Eqs 6.20 and 6.21, can now be used in combination with the extended momentum theory, Eqs 6.24 and 6.25. The result can be written as

$$\frac{a}{1-a} = \frac{1}{4}\frac{1}{F\sin^2\phi}\frac{cB}{2\pi r}c_y \qquad [6.27]$$

$$\frac{a'}{1+a'} = \frac{1}{4}\frac{1}{F\sin\phi\cos\phi}\frac{cB}{2\pi r}c_x \qquad [6.28]$$

With the solidity of the rotor defined as

$$\sigma = \frac{cB}{2\pi r}, \qquad [6.29]$$

the axial and tangential interference, respectively, can be written as

$$a = 1\Big/\left(\frac{4F\sin^2\phi}{\sigma c_y} + 1\right) \qquad [6.30]$$

$$a' = 1 \Big/ \left(\frac{4F \sin\phi \cos\phi}{\sigma c_x} - 1 \right) \qquad [6.31]$$

These equations have to be solved iteratively because F, θ, c_y and c_x are all dependent on the interference factors, a and a'. Also, the equations are not in agreement with real rotor flow when an axial interference value, a, greater than approximately 0.4 is obtained. Interpreting this, it means that the wind speed in the rotor plane is reduced to 60% of the free wind speed and to only 20% of the free wind speed in the far wake. The BEM theory assumes no or small expansion of the wake. Therefore, the thrust coefficient must be corrected for $a > 1/3$ to be in agreement with real rotor flows. Glauert[15] showed that such a correction and different empirical relations between the axial interference, a, and the thrust coefficient, C_T, can be made so as to fit to measurements, such as the one described by Hansen:[18]

$$C_T = \begin{cases} 4a(1-a)F & a \le 1/3 \\ 4a(1-\frac{1}{4}(5-3a)a)F & a > 1/3 \end{cases} \qquad [6.32]$$

Thus, using the above equations, Eqs 6.16–6.21, 6.26, 6.30–6.32, the rotor aerodynamics can be predicted for all wind speeds. However, before doing this, knowledge of, for example, important parameters in the rotor design and the airfoil characteristics should be obtained. This will be given in the following sections.

6.3.2 Important parameters in aerodynamic rotor design

The momentum theory described in the previous section provides the basis for the aerodynamic design of wind turbine rotors. As described earlier, the main driver in the wind turbine design is to minimize the cost per energy. This is done by obtaining the right ratio between manufacturing cost (e.g. material cost and rental of workshop) and energy production. However, irrespective of the constraints that are required to reduce the wind turbine cost, it is important to maximize the power with respect to the constraints. Therefore, the approach in this section is to make a design for maximum energy production without any constraints.

The power coefficient in an annular element of the rotor disk can be expressed as Eq. 6.33, where $F_{tangential}$ describes the force per length unit in the tangential direction on an airfoil section and in the rotor plane

$$C_P = \frac{r\omega F_{tangential} dr}{\frac{1}{2}\rho V_0^3 dA} \Leftrightarrow$$

$$C_P = \frac{r\omega \frac{1}{2}\rho((1-a)V_0)^2 + ((1+a')r\omega)^2 c_x c B dr}{\frac{1}{2}\rho V_0^3 2\pi r dr} \Leftrightarrow$$

$$C_P = \frac{(((1-a)V_0)^2 + ((1+a')r\omega)^2)}{V_0^2}\frac{r\omega}{V_0}\frac{cB}{2\pi r}c_x \quad [6.33]$$

Defining

$$\lambda = \frac{\omega R}{V_0} \quad [6.34]$$

as the tip speed ratio between the eigen speed of the blade tip and the free wind speed and

$$\lambda_{loc} = \lambda\frac{r}{R} \quad [6.35]$$

as the local speed ratio between the eigen speed of the blade at a certain radius and the free wind speed, and using Eq. 6.29 results in the following expression for the power coefficient:

$$C_P = ((1-a)^2 + \left(\lambda,\frac{r}{R}\right)^2(1+a')^2)\lambda\frac{r}{R}\sigma c_x = f(\lambda,\frac{r}{R}\sigma,c_x,a,a') \quad [6.36]$$

This equation is important in aerodynamic blade design because it tells us that the power coefficient at a certain rotor radius is dependent on the tip speed ratio, λ, the position relative to the tip, r/R, the solidity of the rotor, σ, the force coefficient in the rotor plane, c_x, and interference factors in axial and tangential direction, a and a', respectively. Deriving the thrust coefficient the same way results in the following expression, Eq. 6.37:

$$C_T = ((1-a)^2 + \left(\lambda,\frac{r}{R}\right)^2(1+a')^2)\sigma c_y = f(\lambda,\frac{r}{R}\sigma,c_y,a,a') \quad [6.37]$$

Even though this relation for the thrust coefficient is somewhat different from the relation for the power coefficient, it tells us that the thrust coefficient is dependent on the same parameters as the power coefficient except that the force coefficient normal to the rotor plane, c_y, and not in the rotor plane, c_x, contributes to the thrust. Because the forces and the interference factors are unambiguously connected, and σ and c_x (and c_y) are always used together as in, for example, Eqs 6.30, 6.31, 6.36, and 6.37, C_P and C_T in an annular element can briefly be described by the functions $f(\lambda,r/R,\sigma c_x)$ and $f(\lambda,r/R,\sigma c_y)$, respectively, meaning that only the three parameters in each function control the rotor design. Since c_x and c_y are strongly correlated to c_l (see Eqs 6.23 and 6.22, respectively) the rotor design can, with very good approximation, be described by the function $f(\lambda,r/R,\sigma c_l)$.

Based on Eq. 6.14, we found that maximum C_P is ideally 16/27 and that this value is obtained for $a = 1/3$. Using Eq. 6.29 and isolating σ while putting $a = 1/3$ in Eq. 6.30 gives the following expression:

$$\frac{2\sin^2\phi F}{c_y} = \frac{Bc}{2\pi r}$$

$$c = 4\pi r \sin^2\phi F \frac{1}{c_y}\frac{1}{B} \qquad [6.38]$$

$$\frac{c}{R} = 4\pi\frac{r}{R}\sin^2\left(\arctan\left(\frac{(2/3)}{(1+a')}\frac{1}{\lambda}\frac{1}{r/R}\right)\right)F\frac{1}{c_y}\frac{1}{B} = f\left(\frac{r}{R}, a', \lambda, F, c_y, B\right)$$

Here, also Eqs 6.17 and 6.35 are used for expressing the chord of the blade using the same parameters as in Eqs 6.36 and 6.37. Thus, as stated in Eq. 6.38, the normalized chord, c/R, is dependent on the normalized radius, r/R, the tangential interference factor, a' (the axial interference factor, a, is locked to 1/3), the tip speed ratio, λ, the correction for number of blades, F, the force coefficient normal to the rotor disc, c_y, and the number of blades, B. Furthermore, Eq. 6.38 shows that the planform is independent of rotor size and should simply be scaled with the rotor radius, R.

The equations need to be solved iteratively and a few results are shown in Fig. 6.6 assuming that the chosen c_l (closely correlated to c_y) and α are constant for the whole blade. Apart from solving Eqs 6.16 and 6.38, also Eq. 6.31 must be solved. Note that increasing c_l (and thereby c_y), B and λ (TSR) leads to a reduction in the chord distribution.

Further to the aerodynamic design also the twist of the blade is needed. This can be derived from Eq. 6.16, which shows the relation between the inflow angle, the angle of attack and the twist. The inflow angle is known when predicting the interference factor, a', and the angle of attack is determined from the airfoil characteristics, where good airfoil performance in combination with a robust operation is part of the decision when choosing the design angle of attack.

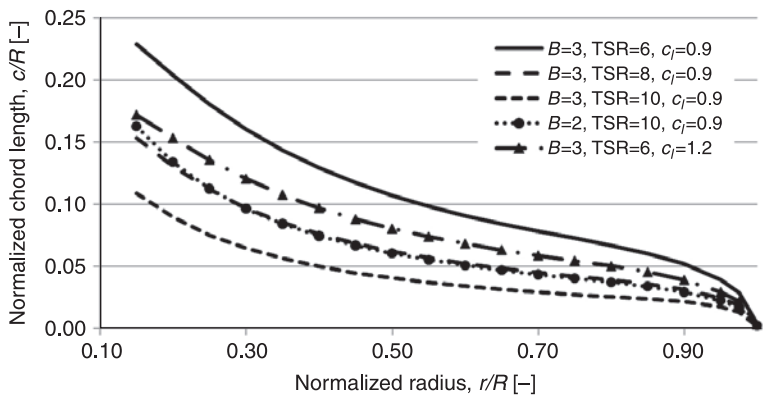

6.6 Example of the chord distribution with different numbers of blades, different force coefficients normal to the rotor plane and different tip speed ratios, TSRs.

6.3.3 Airfoil performance

As seen in the previous section, the important parameters in aerodynamic blade design are the force coefficients in the rotor plane, c_x, and out of the rotor plane, c_y. It is seen from Eqs 6.22 and 6.23 that these coefficients are derived from the coefficients c_l and c_d, the lift and drag coefficients, respectively. In Fig. 6.5 the directions of lift and drag are shown. The lift is always normal to the incoming flow whereas the drag is always in the direction along the flow. Thus, the angle of attack, α, gives these directions. In Fig. 6.7 a sketch of the airfoil characteristics is seen.

To the right is the lift coefficient, c_l, versus angle of attack, α, and to the left is c_l versus the drag coefficient, c_d, where the coefficients are normalized according to Eqs 6.18 and 6.19. For low α and low c_l, c_d is fairly constant and corresponds to a flow around the airfoil which is mainly attached to the surface. For higher α and c_l and approaching maximum c_l, c_d is increasing, which reflects the start of separation typically from the trailing edge. Increasing α will increase the amount of separation, which eventually will cause the airfoil to stall from the leading edge with massively separated flow. Because c_l can be interpreted as a production term and c_d as a loss term, a convenient measure for the airfoil efficiency is the lift–drag ratio, c_l/c_d. The fine dashed line in the left plot illustrates this. The steeper the slope of this line starting from its origin, the more efficient the airfoil is. According to Eqs 6.22 and 6.23, the normal and tangential force coefficients can be written as

$$c_x = c_l \sin\phi - c_d \cos\phi \Leftrightarrow c_x = c_l(\sin\phi - \frac{1}{c_l / c_d}\cos\phi) \qquad [6.39]$$

$$c_y = c_l \cos\phi + c_d \sin\phi \Leftrightarrow c_y = c_l(\cos\phi + \frac{1}{c_l / c_d}\sin\phi) \qquad [6.40]$$

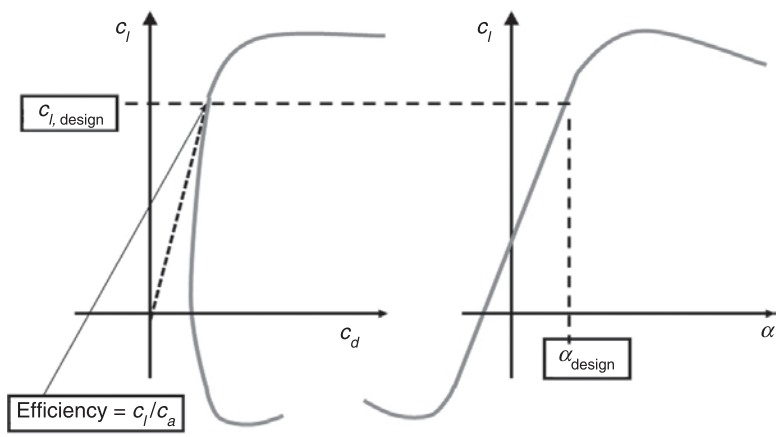

6.7 Sketch of the airfoil characteristics measured by c_l, c_d, and α.

These equations reflect that the in-plane force coefficient contributing to the power is dependent of the lift coefficient, c_l, the inverse lift–drag ratio, c_l/c_d, and the inflow angle ϕ. Thus, an airfoil for use on a wind turbine should operate at a point with high lift–drag ratio to reduce the influence from the second term in the parentheses. Commonly, the point at which we find maximum lift–drag ratio is called the design point, with the corresponding design lift, $c_{l,design}$, and design angle of attack, α_{design}. Furthermore, from Eq. 6.39 it is seen that for increasing inflow angle, ϕ, there will be an increasing contribution to c_x and thereby to the power from the term $\sin\phi$. Thus, even though c_l/c_d in all cases is important, it is seen that the lower λ_{loc} is, corresponding to high inflow angles, ϕ (e.g., on the inner part of the rotor), the less relatively important is c_l/c_d when maximizing the power.

However, the airfoil characteristics, c_l and c_d, are not a fixed set of data, but depend mainly on three parameters:

- the Reynolds number
- the leading edge roughness
- the relative thickness of the airfoil

The airfoil characteristics are also dependent on the actual airfoil shape, so an explanation of these parameters, how to choose airfoils and how to establish the final airfoil characteristics, are described as follows.

The Reynolds number

Judging the airfoil performance, knowledge of the Reynolds number is important. The Reynolds number is a dimensionless number that characterizes the relation between the flow momentum in the boundary layer around the airfoil surface and the flow viscosity. It is defined as $Re = Wc/\nu$, where W is the relative velocity, c is the chord length and ν is the dynamic air viscosity. Low Reynolds number flows result in flows highly affected by the viscosity resulting in rather high drag and weak boundary layers with the risk of, for example, sudden separation. High Reynolds number flows result in flows with rather low drag and strong boundary layers. Thus, high Reynolds numbers are highly desirable. In particular, the boundary layer becomes significantly stronger for Reynolds numbers greater than 0.5×10^6 to 1.5×10^6.

The leading edge roughness

Wind turbines are typically designed for 20 years of operation. In the 20-year period a relatively small number of maintenance checks will be carried out. Thus, in contrast to airplanes, the blades are in general not accessible and will not be cleaned when they are contaminated with, for example, dust and bugs, especially on the leading edge. Therefore, it is very important to consider the performance of the airfoils with contaminated leading edges, which is also called leading edge roughness (LER). An example of the performance is seen in Fig. 6.8, showing the

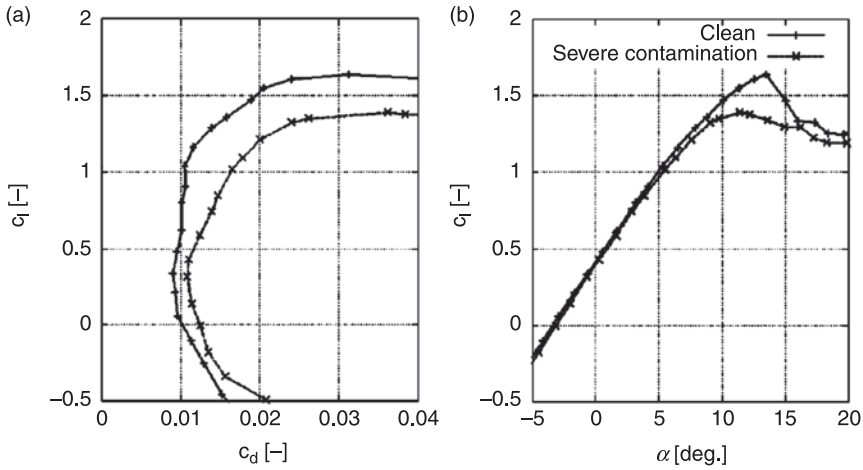

6.8 Airfoil characteristics of Risø-B1-18 measured in the VELUX wind tunnel, Denmark, at $Re = 1.6 \times 10^6$ with and without severely contaminated leading edge.

characteristics for the Risø-B1-18 airfoil. Here, c_l versus c_d is seen to the left and c_l versus α is seen to the right. Even though this airfoil is known to be quite insensitive to LER, a loss of performance is unavoidable if the surface is severely contaminated.

When designing a blade it is important that it does not operate too close to maximum c_l, $c_{l,max}$. If the angle of attack, α, gets too close to $c_{l,max}$ it will have difficulties in performing well when the turbine is approaching rated power. This is due to the risk of separation, which will cause an increase in noise emission, an increase in drag, c_d, and a decrease in lift, c_l. This risk is mainly caused by possible LER. Therefore, as a rule of thumb the value of the lift coefficient chosen in the design of a blade should be as a maximum $c_{l,max}$–Δc_l, with Δc_l between 0.4 and 0.6. The exact value of Δc_l, however, depends on the expected turbulence intensity of the free wind, the control strategy of the rotor, the degree of separation until maximum lift (because separation is often undesirable), and the certainty of the airfoil characteristics with LER.

The relative thickness

Caused by the high loading of the blade towards the tip, the root part of the blade requires high strength. This strength can be obtained by increasing the distance between the bottom and top part of the airfoil as shown in Fig. 6.9. The ratio between this distance (the thickness) and the chord length is the relative thickness.

Therefore, increasing the thickness of the blade without increasing the chord length requires higher relative thickness. Thus, not just one type of airfoil but a series of airfoils is in general needed in the blade design process. However, this depends on the structural evaluation of the blade. The minimum relative thickness

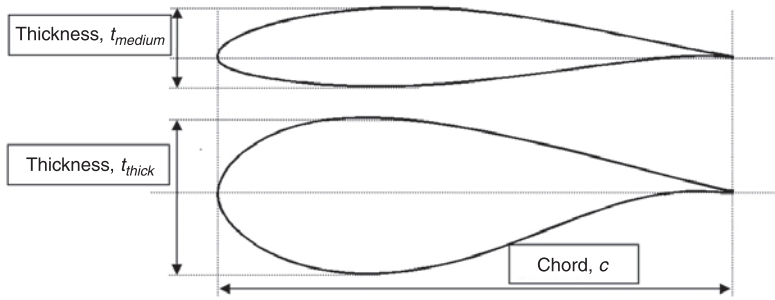

6.9 Airfoils with different thicknesses: medium thick airfoils with relative thickness t_{medium}/c between 15% and 24% and thick airfoils with relative thickness t_{thick}/c greater than 24%. Two airfoils extensively used for wind turbine rotors are shown, the NACA 63_2-415 airfoil with t/c = 15%[20] and the FFA-W3-301 airfoil with t/c = 30%.[25]

for large rotors should generally be chosen to t/c = 15% because this airfoil thickness often show high lift–drag ratio and a relatively smooth stall characteristics. This airfoil thickness should be used on the outer part of the blade. On the inner part of the blade high relative airfoil thicknesses should be used. Only a few relatively efficient thick airfoils exist, because thick airfoils are commonly not used in applications other than wind turbines. However, even though the contribution to the power per length unit of the blade at, for example 20% tip radius compared to 100% tip radius is only 20%, and even though many rotor designs for that reason put more weight to the structural efficiency than on the aerodynamic efficiency at the inner part of the rotor, the efficiency of the inner part of the rotor is important because the total rotor power can be increased by several percent with special attention to the aerodynamics of the thick airfoils.

Choosing the airfoils

Airfoils needed in the rotor design process can, for example, be found in work of Abbott Doenhoff[20], Althaus[21] and Selig,[22] where mainly airfoils for airplanes and gliders are described. Also, airfoils specifically designed for wind turbines can be found in work of, for example, Tangler and Somers,[23] Timmer and van Rooij,[24] Björck,[25] Fuglsang and Bak,[26] and Bak *et al*.[27] The important characteristics that should be investigated are as follows:

1 Maximum lift ($c_{l,max}$) with and without LER.
2 Lift–drag ratio (c_l/c_d) with and without LER.
3 Lift value where maximum lift–drag ratio is found, also called design lift ($c_{l,design}$).

The choice of airfoil series depends on the rotor design philosophy. It should be decided whether the blades should be slender or wide. Analyzing Eq. 6.38 shows

that slender blades require high design tip speed ratio, high design lift and/or a high number of blades, whereas wide blades require low design tip speed ratio, low design lift and/or a low number of blades. Potentially, slender blades can, for example, ensure both low extreme and fatigue loads, but suffer structurally because the thickness of the blade decreases for decreasing chord length and constant relative thickness. On the other hand, wide blades can ensure high structural strength, but higher extreme and fatigue loads can potentially be a result. Deciding whether the blades should be slender or wide depends on the design of the structure and concept of the complete wind turbine.

Establishing the data

Measurements often do not exist at the right Reynolds number and sometimes measurements do not exist at all. Therefore, it is important to be able to check the airfoil characteristics using computations. This can be done by simulating the flow assuming two-dimensional conditions. The simulation can be carried out either by using computational fluid dynamics (CFD), where the velocity and pressure in the domain is resolved into hundreds of thousands of cells, or panel codes, which are semi-empirical and require very few computational resources. The publicly available panel code XFOIL[28] is very efficient and results in airfoil characteristics quite close to wind tunnel tests. However, there is a trend towards over prediction of maximum lift and too low drag at all angles of attack especially if free transition from laminar to turbulent flow is assumed. Thus, when investigating the airfoil performance it is important to simulate the flow both with free transition from laminar to turbulent flow, which corresponds to a clean surface, and forced transition from, for example, $x/c = 0.001$ on the suction side and $x/c = 0.1$ on the pressure side, which corresponds to LER. It should be noted that wind turbine aerodynamicists are still discussing how to simulate LER, because the roughness can vary substantially between fine salt crystals and large insects. Using XFOIL in the evaluation process the model for free transition, the so-called 'e to the nth' method, requires the factor n as an input. For very low turbulent flow $n = 9$, which corresponds to a turbulence intensity of 0.070%. However, for comparison of XFOIL computations to many high-quality wind tunnels, the 'e to the n^{th}' method should have $n = 6$ or 7 as input, corresponding to a turbulence intensity of 0.245% and 0.161%, respectively. When interpreting the simulation results, reliable data for use in the blade design are needed. Therefore, most emphasis should be put on those simulations assuming LER, because the rotor performance should be trustworthy even with contaminated blades. The blade design should then be evaluated using the assumption of clean blades. However, if trustworthy data from wind tunnel tests exist at or close to the right Reynolds number, these data should be used.

Measurements and computations on airfoil sections are typically assuming two-dimensional conditions. However, on a rotating blade the flow is exposed to,

for example, centrifugal forces, Coriolis forces, tip effects and root effects, resulting in a high degree of three-dimensional flow, especially if separations occur. Models exist for correction of two-dimensional airfoil characteristics taking centrifugal forces and Coriolis forces into account[29–33] and should be applied, when a trustworthy set of two-dimensional data is established.

6.3.4 Design tip speed ratio

As seen in Section 6.3.2 the tip speed ratio, λ, is an important parameter when designing a rotor. When analyzing the influence of λ on the power performance it turns out that one should increase λ to reduce the tip loss. For ideal rotors in inviscid flow, λ should be increased as much as possible and in theory to infinity if the target is to maximize the power. However, for real viscous flows the lift–drag ratio of the airfoils limits λ to between 5 and 12 for rotors between 1 kW and 5 MW depending on the lift–drag ratio and the number of blades.[34] Figure 6.10 shows the relation between the power coefficient, C_P, and λ assuming that the lift–drag ratio is constant for the entire blade. Thus, knowing the approximate lift–drag ratio of the airfoils used on the blades, Fig. 6.10 indicates which λ to choose with respect to C_P. However, other aspects than the power can be important, such as reducing the load, considerations concerning the blade structure, and noise caused by high tip speed.

6.3.5 Rotor size, control and constraints

Size of rotor/generator

As described earlier, the design of a rotor is part of an integrated process of designing the entire wind turbine. The overall goal is to manufacture a wind

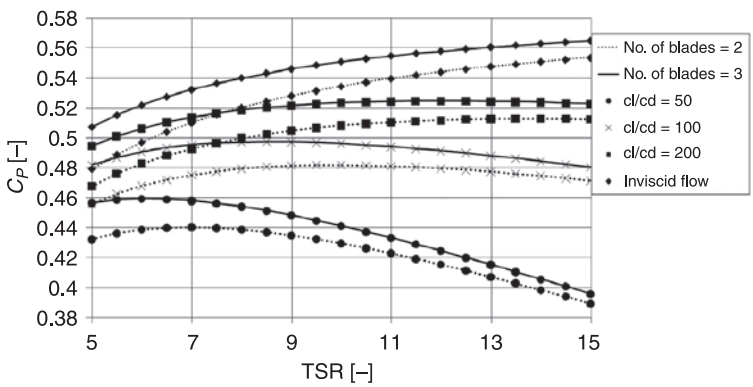

6.10 Power coefficient C_P vs. tip speed ratio (TSR), λ.

turbine at lowest cost per energy. Therefore, the target when designing a wind turbine rotor is not necessarily to capture the maximum energy on a certain site or the maximum power at a certain, typical wind speed, but rather to capture as much energy as possible at the lowest cost of all components from generator and tower to foundation and grid connection. The size of the rotor is of primary importance, when considering the total cost of the wind turbine. With a bigger rotor more energy can be captured, however, probably at the expense of higher loads and a larger generator. At least it is very important to determine the so-called rated power, which is the maximum of the mean power output averaged over a period of ten minutes. In general, the rated power correlates with the maximum loads in normal operation of the wind turbine. Also, it is important to determine the so-called rated wind speed, which is the wind speed at which the rated power is obtained. This wind speed depends on the wind climate at a certain site and therefore a decision is needed for which type of sites the wind turbine should be erected. Often, the rated wind speed is chosen as the mean wind speed at a site plus approximately 6 m/s. Thus, if the mean wind speed is 8 m/s, the rated wind speed will be around 14 m/s. This is, however, a rule of thumb and should be based on considerations of the specific wind climate and cost estimations. Cost modeling for wind turbines has been investigated by several researchers,[35–40] but is not within the scope of this chapter.

A simple way to determine a rough estimate of the rotor size is to decide on the rated power and rated wind speed, and use the following procedure. Based on analysis of existing rotor designs the mechanical power coefficient (which is the efficiency without the loss in generator and gearbox), $C_{P,rated}$ (see Eq. 6.13), is between 0.25 and 0.30 at rated wind speed. The radius of the rotor will then be

$$R = \sqrt{\frac{P_{rated}}{\frac{1}{2}\rho V_{rated}^3 C_{P,rated}\pi}} \qquad [6.41]$$

Here the rotor area or the area through which the blades sweep, the so-called swept area, A, from Eq. 6.12 is $A = \pi r^2$. Choosing P_{rated} to 1 MW and V_{rated} = 14 m/s, which corresponds to a site with medium to high wind speed, and assuming the air density at standard conditions, ρ = 1.225 kg/m^3, we get R = 27.5 m and a rotor diameter of 55.0 m if $C_{P,rated}$ is chosen to be 0.25.

A simpler rule of thumb exists, where the rotor size is simply determined so that P_{rated}[kW] = $1.2R^2$. Using this rule, the 1 MW rotor should be designed with a diameter of 57.7 m irrespective of the wind climate. Thus, this rule does not take into account the dependency of the specific wind climate that the wind turbine will be designed for.

Rotor control

As shown in Sections 6.3.2 and 6.3.4 the rotor design is dependent on, for example, the tip speed ratio. Therefore, a certain tip speed ratio, λ, must be chosen. To

operate the rotor so as to extract maximum power, the ratio between the tip speed and wind speed must be constant. This means that for increasing wind speed, the tip speed should be increased correspondingly if this is possible according to the choice of generator. However, because of, for example, noise and erosion of the leading edge, the tip speed should not increase too much. For large modern wind turbines, maximum tip speeds of 70–80 m/s are common. Also, increasing the tip speed results in increasing loads on the entire wind turbine structure, which again increases the total cost of the wind turbine. Therefore, for several reasons it is desirable to limit the tip speed and therefore the rotational speed. Which maximum rotational speed to choose should also depend on an analysis of the total wind turbine cost as described at the beginning of Section 6.3.5.

Apart from choosing λ, it should also be decided how to limit the power. The size of the generator and the allowable loads on the turbine determine at which level the power should be limited. This limitation is carried out by increasing the drag or decreasing lift on the airfoil sections. On modern wind turbines each blade will limit the forces that contribute to the power and thrust, which can be done actively by pitching the blades or passively by letting the blades stall.

It is now clear that making an aerodynamic design for a wind turbine rotor requires knowledge of the rotor control, so that it is known if the turbine should, for example, operate with or without stalled condition and if the airfoils have the required reserve from design lift to maximum lift. Several different methods of control are possible, among which a few common ways are described below.

- *Constant/variable rotational rotor speed:* This degree of freedom in the control depends on the characteristics of the generator. If a constant rotor speed is chosen, a simpler and less costly generator can be chosen than if a variable speed rotor is chosen. However, the variable speed rotor makes the possibility of optimising the power for a large range of wind speeds. Also, using this kind of generator creates more flexibility in the connection to the power grid.
- *Pitchable/fixed blades:* Pitchable blades allow freedom to limit and optimize the power very precisely and also make it possible to stop the turbine, such as in emergency situations. When limiting the power, the pitchable blades can be used to reduce the lift by either decreasing or increasing the angle of attack. Decreasing the angle of attack ensures that the flow is attached to the airfoils so that the operation of the airfoils will be in the linear part of the lift curve; this is called pitch regulation. Increasing the angle of attack to stall/deep stall ensures a nearly passive limitation of the power because only minor changes to the pitch setting are commonly needed; this is called ‘active stall control’.
- *Pitch/stall control*: Turbines limit the power by reducing the lift coefficient for increasing wind speeds either in the linear part of the lift curve by reducing the angle of attack (pitch control) or in the stall part of the lift curve by increasing

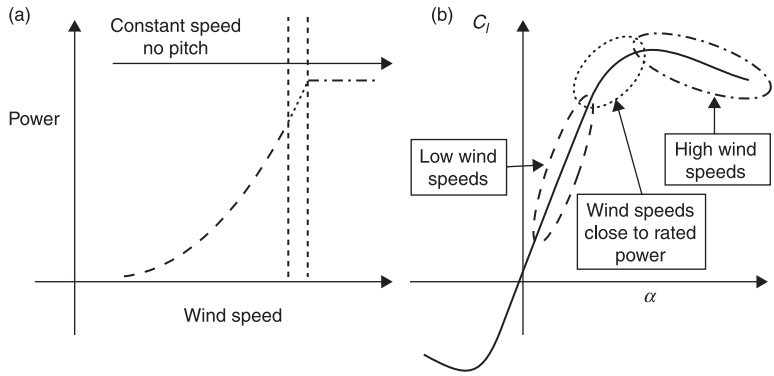

6.11 Sketch of the principle behind stall regulation shown on (a) the power curve (power vs. wind speed), and (b) the lift curve (lift coefficient vs. angle of attack).

the angle of attack (stall control). Using fixed blades and constant rotational rotor speed, one is forced to use stall control. This is illustrated in Fig. 6.11, where the power curve is shown to the left with the corresponding airfoil operation in terms of a lift curve to the right. At low wind speeds the angle of attack is low and the lift is thereby also low (dashed lines) operating around maximum lift–drag ratio. The dotted line shows operation at wind speeds close to rated power and at corresponding lift values close to and at maximum lift. The dot-and-dash line shows the operation at high wind speeds where rated power is obtained and the corresponding operation at high angles of attack in stall resulting in a (nearly) passive limitation of the power. The stall regulation was a common concept for wind turbines of size up to around 2 MW.

Using pitchable blades both pitch and stall control are possible. However, the (active) stall controlled rotors for the bigger rotors between 500 kW and 2 MW in some cases showed negative aerodynamic damping, which caused undesirable vibrations. Also, the (active) stall controlled rotors experience relatively high loads at high wind speeds compared to the pitch controlled rotors. Using pitch control requires much higher pitch activity, but because stall is avoided, the flow is more reliable and predictable. The pitch control concept is illustrated in Fig. 6.12, where variable rotor speed is also used at low wind speeds. This kind of control is pitch control in combination with variable rotor speed and is called pitch regulated variable speed (PRVS). Apart from variable rotor speed at low wind speeds, which is used to obtain constant tip speed ratio (λ or *TSR*), the blades will be pitched to limit the power at high wind speeds. However, the blades can in some cases also be pitched for wind speeds between the region of variable rotor speed and the region with power limitation. In Fig. 6.12, it is seen that the angle of attack is

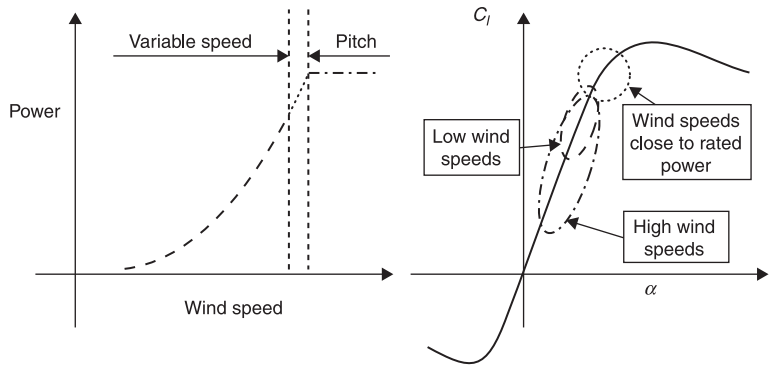

6.12 Sketch of the principle behind Pitch Regulated Variable Speed (PRVS) showed on the power curve (power vs. wind speed), left, and the lift curve (lift coefficient vs. angle of attack), right.

low at high wind (dotted-and-dashed lines) and high (but not entering stall), close to rated power (dotted lines). Furthermore, the rotor load decreases at high wind speeds. Therefore, the loads for a pitch controlled wind turbine will in general be less than for an (active) stall-controlled wind turbine. In Fig. 6.12 the dashed line shows operation at low wind speeds at the power curve where the rotor operates at constant tip speed ratio and corresponding operation at a lift value with high lift–drag ratio.

The common way of controlling MW turbines of today is by using PRVS. However, in the 1970s, 1980s and 1990s when the rated power of most turbines was below 2 MW, the turbines did not work as a significant part of the power grid and there were lower requirements for the power quality. Also, the structural dynamics were less sensitive to the aerodynamic damping of the blades. Therefore, the dominant method of control was stall regulation, with constant rotational speed combined with fixed blades – the so-called Danish concept.

Thus, it is necessary to know the choice of rotor control:

- to select airfoils that have proper design lift, maximum lift and stall characteristics;
- to design the rotor in such a way that it can start up at a fairly low wind speed;
- to design the rotor in such a way that rated power can be kept fairly constant at all high winds; or
- to design the rotor at the right tip-speed ratio.

Design constraints

In the previous sections, it has been stated that the rotor design should focus not only on maximizing the power, but also on other aspects, because the main

objective is to reduce the cost of energy. Many constraints exist in this process, but they are dependent on, for example, the rotor size and the selected materials. Examples of such constraints are the following:

- The maximum chord has to be less than a certain value to be able to be transported, e.g., by trucks on roads below bridges.
- The maximum chord should be such that the extreme loads at, for example, stand still do not cause high loads on other components such as the tower.
- The inner part of the blade has to be designed with thicker airfoils than on the outer part of the blade, to withstand the loads.
- The rotor should be able to cut in at a fairly low wind speed.
- In order to reduce noise emission, the outer part of the blade can be twisted towards lower lift coefficients, because, in general, noise emission increases for increasing angle of attack.[41]
- The maximum rotor speed should be limited to limit the noise emission, because noise emission is highly dependent on the tip speed.
- The rotor speed has to be limited to reduce loads on the whole wind turbine. However, for a given power the shaft torque will be reduced with increasing rotor speed. Therefore, the maximum rotor speed should be selected appropriately.
- As illustrated in Fig. 6.3 the thrust coefficient, which in general relates to the loads on many components on the wind turbine, can be reduced somewhat by reducing the axial interference factor, a, slightly below $a = 1/3$ with only a small reduction in C_P. In this way, loads on the turbine can be reduced without losing too much energy production.
- Pre-bend and/or pre-twist of the blade are options for blades to increase the blade–tower clearance and obtain the desired twist irrespective of the torsional deformation, respectively. However, these options do not affect the aerodynamic design because the pre-bend ensures the intended maximum rotor area and the pre-twist ensures the intended twist distribution.

There will probably be other design constraints depending on the manufacturing process, the rotor control concept, and the wind turbine concept in general. Thus, the above is not an exhaustive list of issues, but only indicates different aspects to be considered in the rotor design process.

6.3.6 Choice of number of blades

When choosing the number of blades, several considerations have to be taken into account, such as esthetics, tip loss, structural constraints and Reynolds numbers. Even though the rotor designer will often find that the number of blades has been decided before the design is carried out, a few considerations are described in the following to draw a complete picture of the various aspects of the rotor design process.

- *Esthetics*: The design of the complete turbine, such as the shapes of the nacelle, the spinner and the tower, is important. Thus, also the visual impression of the rotating blades is important. This item poses the question: Do two, three, or four rotating blades (or even more) look nice?
- *Tip loss*: The rotor becomes more aerodynamically efficient when the number of blades is increased. This is because the distance between the vortex sheets in the wake of the rotor becomes smaller for an increasing number of blades, and flow outside the wake therefore does not flow in between the vortex sheets creating a more diffuse wake and thereby introducing loss. The loss of power efficiency when reducing the number of blades from three to two blades is illustrated in Fig. 6.10.
- *Structural considerations*: Increasing the number of blades for fixed design lift along the blade will reduce the chord length of each blade since the solidity of the rotor should be kept constant. With decreasing chord length, either the relative thickness may need to be increased or is maintained requiring more material for the entire rotor for structural reasons. The increasing relative thickness generally makes the blade less aerodynamically efficient and increasing material makes the blade heavier.
- *Reynolds number*: The Reynolds number is proportional to the chord length of the blade and the rotational speed. Therefore, an increase in the number of blades with fixed solidity of the rotor, σ, will result in a decrease of the chord length and thereby in a decrease of the Reynolds number. Thus, in terms of Reynolds number, it is desirable to minimize the number of blades.

6.3.7 Evaluation of the rotor design

When a rotor is aerodynamically designed, it needs to be evaluated to reveal the response on power and loads. For this purpose aerodynamic or aeroelastic codes should be used. Several aerodynamic codes exist, but if an aerodynamic or aeroelastic code is not available, the background for creating an aerodynamic code can be found.[18] Commonly used aeroelastic codes in the wind turbine industry in 2010 include FLEX,[42] Bladed,[43] Phatas,[44] FAST[45] and HAWC2.[46]

An aerodynamic code requires the blade planform in terms of chord and twist as function of radius, rotational speed and pitch as function of wind speed, airfoil characteristics in terms of c_l, c_d and c_m as function of α for the different relative thicknesses along the blade, and possibly also losses in the drive train (gearbox and generator) to predict the electrical power. Thus, as a part of the aerodynamic rotor design process this information should be provided.

6.4 An example of the rotor design process

In this section, a rotor for a 1 MW PRVS wind turbine will be designed. The design process is simplified so that the power is maximized with no considerations of load

reduction, even though this is very important to save loads on all the components on the turbine. The process is divided into steps, but in reality each step can appear more than once because the process is iterative since knowledge gained during the process sometimes proves to have been relevant for an earlier step in the process. The process described for designing the blade does not require any other tools than a spreadsheet or access to a programming language such as Matlab, FORTRAN or C. However, in the evaluation process an aerodynamic or aeroelastic computer code would be of great advantage to obtain a detailed evaluation of the rotor and the wind turbine. The resulting rotor is not meant as an example of an optimal rotor, but should only be perceived as an illustration of the method.

6.4.1 Step 1: wind climate

Even though the wind turbine under consideration can potentially be erected at many different sites, a representative wind climate should be decided. Standards exist[47] where the turbines are classified in site characteristics such as low/high wind speeds and low/high turbulence. However, in this example for demonstration purposes, it has been decided to erect the turbine on an inland site in Denmark, Værløse as stated by Troen and Lundtang[48] with a Weibull distribution in 10 m height given as:

$$F\left\{V_{10\,\mathrm{min}} \le V\right\} = 1 - \exp\left(-\left(V/A\right)^{k}\right)$$

with $A_{h,measured} = 4.7$ m/s, $k_{h,measured} = 1.55$, and $A_{h,measured} = 10$ m. The roughness length in Værløse is estimated to $z_0 = 0.01$ m corresponding to airport runway areas and terrain surface characteristics between very smooth surfaces such as water areas and smooth surfaces such as farmland. Because the hub height of the wind turbine is set to 60 m (approximately the rotor diameter for a 1 MW turbine), Weibull parameters for this height should be predicted. Assuming that the wind shear is logarithmic and there are no changes in roughness close to the site, the parameters will be:

$$A_h = A_{h,measured}\frac{\ln\left(h/z_0\right)}{\ln\left(h_{measured}/z_0\right)} = 5.9\ \mathrm{m/s}$$

$$k_h = k_{h,measured} = 1.55$$

6.4.2 Step 2: size of rotor/generator

Estimating the size of the rotor and generator requires an estimate of the fixed cost such as rent of workshop, tools and salary of employees. A thorough study should be carried out based on experience of the wind turbine cost or the models referred to at the beginning of Section 6.3.5. However, in this case the problem is simplified and, based on the knowledge of factor A_h, which is fairly low, it is decided to choose 12 m/s as the rated wind speed, which is approximately 6 m/s higher than the average

wind speed on the site. Maximum C_P at rated wind speed is set to $C_P = 0.25$, which will be used to estimate the rotor diameter. The rotor size can be predicted using Eq. 6.41. With $P_{rated} = 1.0$ MW, $V_{rated} = 12$ m/s, $\rho = 1.225$ kg/m^3 and $C_P = 0.25$, the rotor must be designed with a diameter of approximately 70 m or a radius of 35 m.

6.4.3 Step 3: rotor control

Even though the rotor control in this case is given as a PRVS, it is important at this stage to consider the type of control to be used as stated in the subsection 'Rotor control' in Section 6.3.5. The rotor control will be dependent on the size of the rotor and wind turbine and dependent on the philosophy of the design. Also, the components forming part of the rotor control, such as the pitch bearings and the variable speed generator, should be considered in order to take the total cost of the turbine with its operation and maintenance into account.

6.4.4 Step 4: design constraints

There are some constraints which the rotor design should fulfill:

- The maximum chord is set to 3 m for transportation reasons. However, this limit depends on the possibilities for the blade manufacturer to transport the blade.
- The maximum tip speed is set to 75 m/s. This is to reduce the maximum noise emission. The tip speed of 75 m/s corresponds to a maximum rotational speed of 20.46 rpm.
- The initial guess for the thickness of the blade is based on structural considerations. Often the aerodynamic rotor design will be based on a distribution based on experience from an earlier design. The structural design should fulfill different requirements, such as a maximum tip deflection and minimizing the weight (i.e. increasing the thickness) without losing too much aerodynamic efficiency. An example of such a thickness distribution is shown in Fig. 6.13. In this example the thickness distribution should simply be

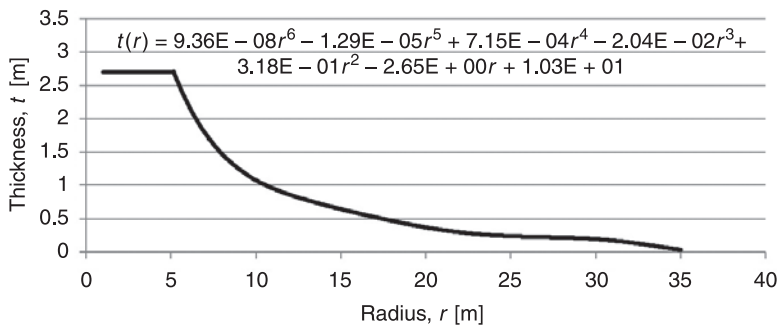

6.13 Initial guess of the thickness distribution of the blade.

considered as an input to the aerodynamic design process. However, when evaluating the rotor design after the aerodynamic rotor design process has been carried out, the weighting between the structural and the aerodynamic performance could possibly change the thickness distribution. In Fig. 6.13, a polynomial is shown to describe the thickness distribution from 5.14 m and outwards. For radii less than 5.14 m, the thickness is constantly 2.70 m.

6.4.5 Step 5: choice of number of blades

For this size of turbine, the number of blades influences transportation cost, maintenance cost, and rotor cost significantly. Therefore, the number of blades should be reduced as far as possible without compromising the energy production, loads, noise emission or esthetics. This analysis should be based on thorough cost and market estimations. However, since the cost estimation is beyond the scope of this chapter, a traditional three-bladed rotor is assumed in this case.

6.4.6 Step 6: choice of design lift and airfoils

As stated in Section 6.3.3, several different airfoils exist which can be used for wind turbine rotors. For this rotor, airfoils common in rotor design will be used: the NACA 63-4xx from relative thicknesses t/c = 15–21% and FFA-W3-xxx from relative thicknesses t/c = 24–36%. The airfoil characteristics are shown in Fig. 6.14–6.17. When evaluating possible airfoils it is important to know at which

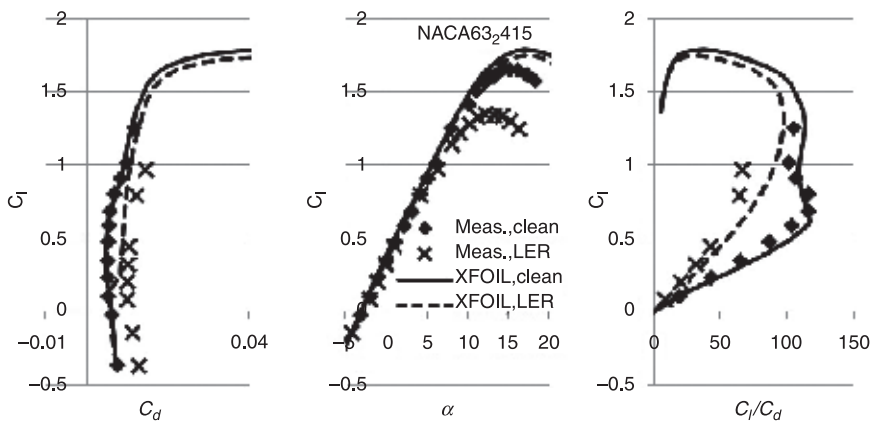

6.14 Two-dimensional airfoil characteristics for NACA $63_2$415 at $Re = 6 \times 10^6$. Measurements from the work of Abbott and von Doenhoff[20] and data from the work of Bertagnolio *et al.*[49] Computations using XFOIL. XFOIL,clean is free transition and XFOIL,LER is forced transition and computed according to the description in Section 6.3.3, 'Airfoil performance'.

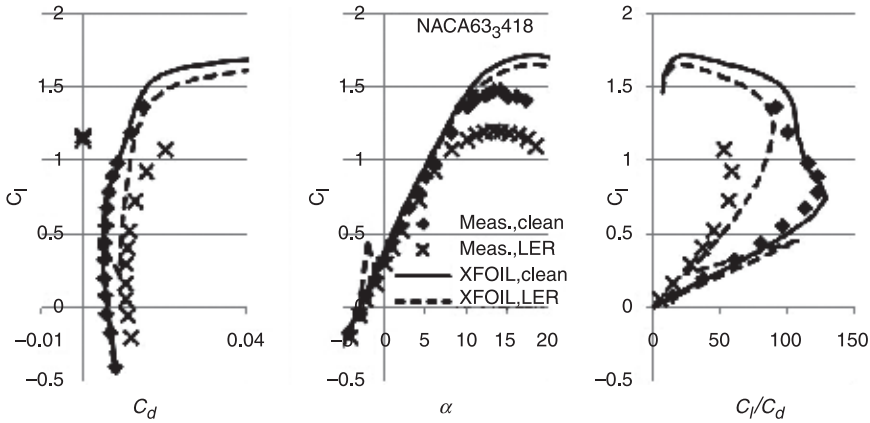

6.15 Two-dimensional airfoil characteristics for NACA 63$_3$418 at *Re* = 6 × 10^6. Measurements from the work of Abbott and von Doenhoff[20] and data from the work of Bertagnolio *et al.*[49] Computations using XFOIL. XFOIL,clean is free transition and XFOIL,LER is forced transition and computed according to the description in Section 6.3.3 'Airfoil performance'.

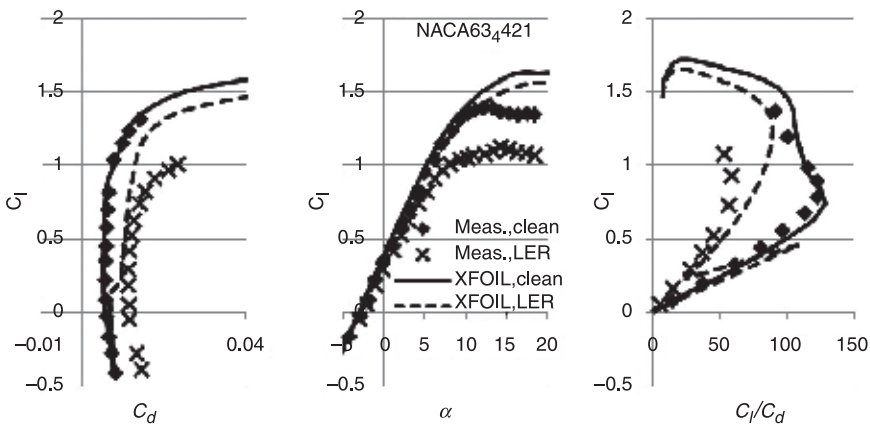

6.16 Two-dimensional airfoil characteristics for NACA 63$_4$421 at *Re* = 6 × 10^6. Measurements from the work of Abbott and von Doenhoff[20] and data from the work of Bertagnolio *et al.*[49] Computations using XFOIL. XFOIL,clean is free transition and XFOIL,LER is forced transition and computed according to the description in Section 6.3.3 'Airfoil performance'.

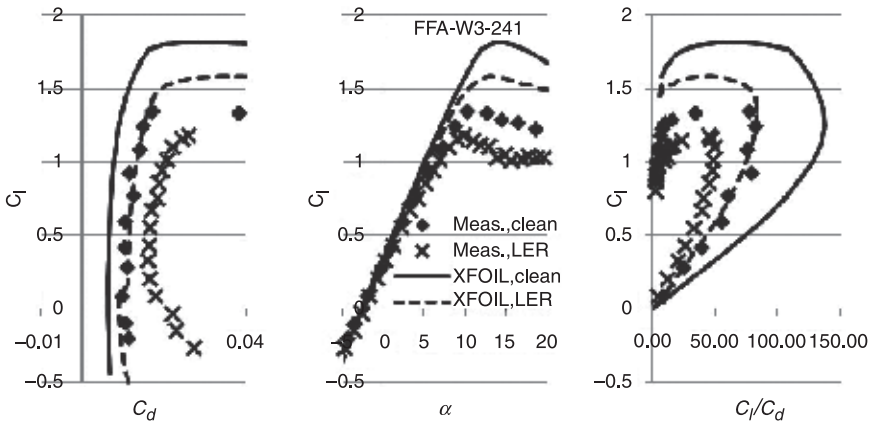

6.17 Two-dimensional airfoil characteristics for FFA-W3-241 at $Re = 1.6 \times 10^6$ for the measurements and $Re = 6 \times 10^6$ for the computations. Computations using XFOIL. XFOIL,clean is free transition and XFOIL,LER is forced transition and computed according to the description in Section 6.3.3, 'Airfoil performance'.

Reynolds numbers the blade will operate. As a rule of thumb, the Reynolds number will be between $Re = 75\,000\,R$ and $150\,000\,R$, which in this case with $R = 35$ m is between 2.6×10^6 and 5.3×10^6.

Wind tunnel measurements exist for most of the chosen airfoils. Measurements on the NACA 63-4xx airfoils are described by the work of Abbott and Doenhoff.[20] They are measured at $Re = 3 \times 10^6$ and 6×10^6. For this purpose $Re = 6 \times 10^6$ has been chosen, because measurements with LER also exist and most of the energy will be produced for the airfoils operating at the higher end of the Reynolds number interval.

The FFA-W3-xxx airfoils are measured in a wind tunnel for only 24% and 30% relative thickness. Thus, the thicker airfoils have not been wind tunnel tested. However, the existing wind tunnel tests have been carried out at $Re = 1.6 \times 10^6$, so the design has to rely on measurements at too low Reynolds numbers. Furthermore, data for LER for the 30% airfoil were not available.

When analyzing the airfoil characteristics, much emphasis should be put on the performance of LER, because the rotor will most probably frequently operate with bugs and dust on the blade leading edge, which will reduce the airfoil efficiency.

As seen in Fig. 6.14–6.18 it is obvious that the computations by XFOIL do not predict the airfoil characteristics very well for the thick airfoils, whereas the predictions are quite good for the thinner airfoils. Even though uncertainties exist for wind tunnel data, most emphasis should be put on these data, because XFOIL as well as other kinds of flow simulation tools do not predict separated flows very well. However, if data are missing for airfoils, a rule of thumb is to simulate the

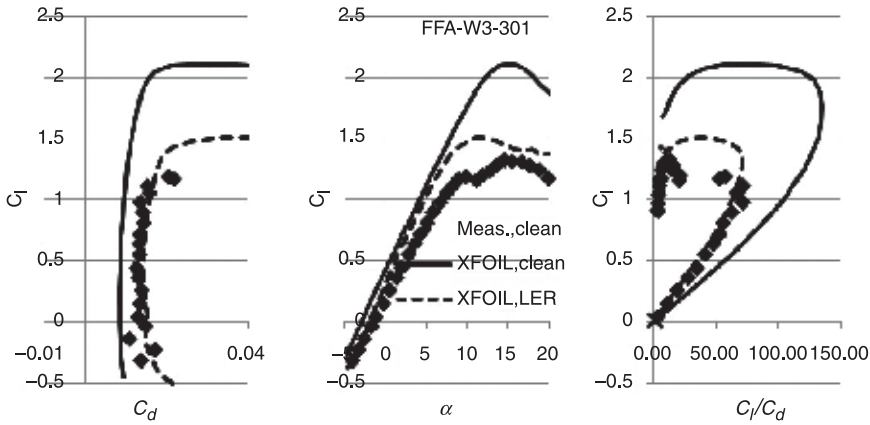

6.18 Two-dimensional airfoil characteristics for FFA-W3-301 at Re = 1.6×10^6 for the measurements and $Re = 6 \times 10^6$ for the computations. Measurements from the work of Fuglsang *et al.*[50] and data from the work of Bertagnolio *et al.*[49] Computations using XFOIL. XFOIL,clean is free transition and XFOIL,LER is forced transition and computed according to the description in Section 6.3.3, 'Airfoil performance'.

airfoil performance assuming fully turbulent flow, i.e., 'XFOIL,LER', to be a bit conservative and use these data as a basis for the blade design.

The airfoil characteristics should be used for the rotor when the performance of the wind turbine is going to be simulated at more wind speeds. However, for the blade design process, the airfoil characteristics should be analyzed to find the lift coefficient used in the blade design, $c_{l,design,blade}$, and the corresponding lift–drag ratio, $(c_l/c_d)_{design,blade}$, and angle of attack, $\alpha_{design,blade}$. Figures 6.19–6.21 show the distribution of these entities as a function of relative airfoil thickness, which will be used in the blade design process. These values are mainly based on the maximum lift with LER reduced with Δc_l of approximately 0.4 to include a reserve in the operation, so that gusts or further reduction in maximum lift caused by even more severe LER will not cause premature separation or stall. Thus, it should be noted that the lift coefficient used in the blade design, $c_{l,design,blade}$, ought to be equal to the lift coefficient for each airfoil at which the maximum lift–drag ratio exists, $c_{l,design}$. However, this is in general not possible because of the requirements of attached flow at all wind speeds. Since the data with LER are based on severe contamination, the chosen values of design lift are however somewhat conservative and some designers would choose a higher design lift because this will result in a more slender blade, which again will result in reduced extreme and fatigue loads for the entire wind turbine.

As shown in Fig. 6.19–6.21, it has been chosen to describe the distribution of the entities using polynomial functions as trend lines because these are relatively smooth and are easy to use. The smoothness of the functions will result in a

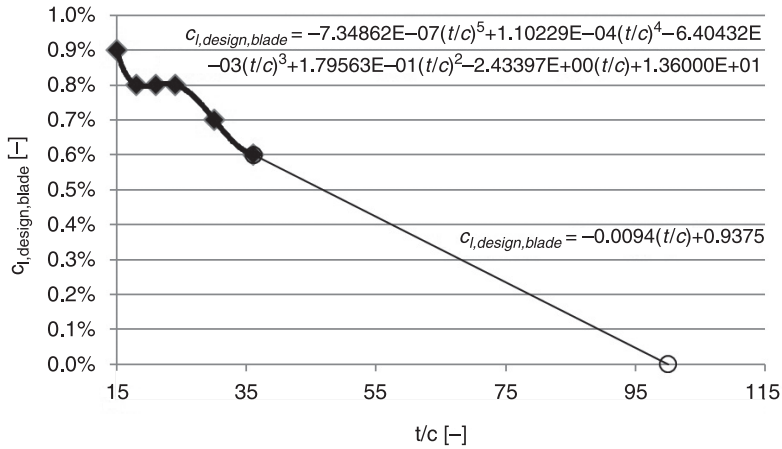

6.19 Distribution of $c_{l,design,blade}$ as a function of the relative thickness of the airfoil. A fifth-order polynomial describes $c_{l,design,blade}$ from t/c = 15% to 36% and for t/c between 36% and 100% a linear relation is used as shown on the plot.

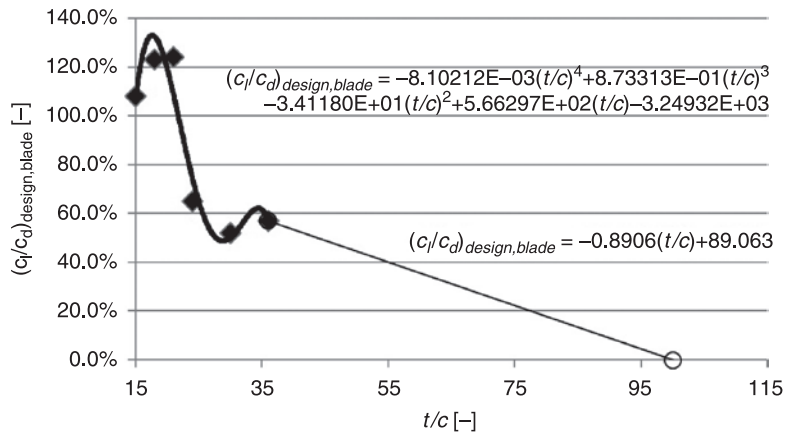

6.20 Distribution of $(c_l/c_d)_{design,blade}$ as a function of the relative thickness of the airfoil. A fourth-order polynomial describes $(c_l/c_d)_{design,blade}$ from t/c = 15% to 36% and for t/c between 36% and 100% a linear relation is used as shown on the plot.

smooth shape of the blade. Other trend line functions exist and can be used as well. Despite the relatively smooth functions, they show abrupt changes between 21% and 24% airfoil for the blade design lift–drag ratio distribution and between 30% and 36% airfoil for the blade design angle of attack distribution. It should be noted that care should be taken for ensuring that the smooth function should be close to the actual values and that no under- or overshoots of the function appear.

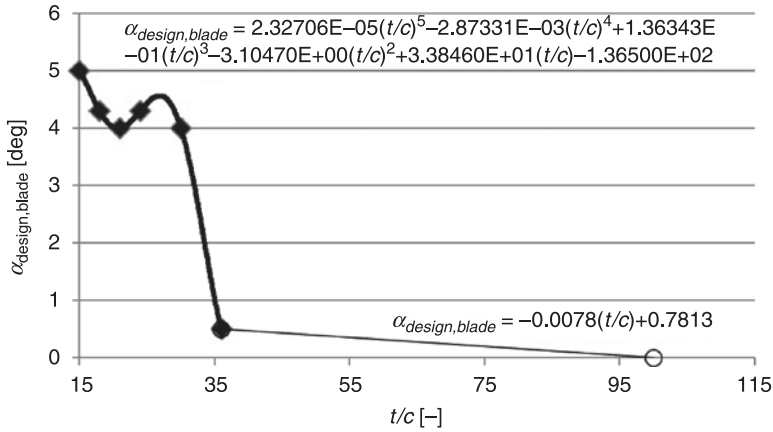

6.21 Distribution of $\alpha_{design,blade}$ as a function of the relative thickness of the airfoil. A fifth-order polynomial describes $a_{design,blade}$ from t/c = 15% to 36% and for t/c between 36% and 100% a linear relation is used as shown on the plot.

6.4.7 Step 7: choice of design tip speed ratio

The choice of design tip speed ratio will in this case be simplified and as previously mentioned it will only be based on maximizing the power coefficient C_P. No considerations concerning load reduction are taken into account. From Step 6 it is known that the rotor operates with a lift–drag ratio for the thin airfoil sections of around 120. According to Fig. 6.10, a design TSR of nine is appropriate for this lift–drag ratio to obtain maximum power efficiency.

6.4.8 Step 8: one-point design of blade

In the previous steps, the basis of the blade design has been created. To summarize, we now know that the rotor has:

- a radius of 35 m,
- three blades,
- a maximum chord length of 3.0 m,
- a tip speed ratio of 9,
- a description of the blade design lift and the corresponding blade design angle of attack and blade design lift–drag ratio, and
- an initial guess of the thickness distribution.

Based on this information, it is possible to design a blade in one point, i.e., at one tip speed ratio. Because the rotor is decided to operate with PRVS control this one-point design will work well at low wind speeds, as long as the variable speed control is active. The planform is shown in Table 6.1 in the first four columns and

Table 6.1 Entities used in the blade design process

R	c	θ	t/c	ϕ	$\alpha_{design,\ blade}$	f	F	a'	σ	c_x	c_y	$c_{l,design,\ blade}$	$(c_l/c_d)_{design,\ blade}$	λ_{loc}	t
	Eq. 6.38 or 6.29	Eq. 6.16		Eq. 6.17	Fig. 6.21	Eq. 6.26	Eq. 6.26	Eq. 6.31	Eq. 6.29	Eq. 6.23	Eq. 6.22	Fig. 6.19	Fig. 6.20	Eq. 6.35	Fig. 6.13
5.250	3.000	26.03	87.77	26.12	0.10	19.304	1.000	0.007	0.273	0.040	0.105	0.112	10.891	1.35	2.633
7.000	3.000	19.65	59.26	19.97	0.32	17.566	1.000	0.019	0.205	0.120	0.361	0.380	36.283	1.80	1.778
8.750	3.000	15.73	43.04	16.18	0.45	16.149	1.000	0.021	0.164	0.138	0.515	0.533	50.728	2.25	1.291
10.500	3.000	11.77	33.75	13.60	1.83	14.881	1.000	0.020	0.136	0.137	0.607	0.622	61.550	2.70	1.012
12.250	2.963	7.35	28.31	11.73	4.38	13.703	1.000	0.019	0.115	0.133	0.716	0.728	48.769	3.15	0.839
14.000	2.583	5.86	27.52	10.34	4.48	12.533	1.000	0.015	0.088	0.118	0.732	0.741	49.197	3.60	0.711
15.750	2.244	4.67	26.76	9.24	4.57	11.415	1.000	0.012	0.068	0.109	0.758	0.766	52.839	4.05	0.600
17.500	1.974	3.88	25.26	8.35	4.47	10.331	1.000	0.010	0.054	0.102	0.783	0.789	62.801	4.50	0.499
19.250	1.774	3.44	23.00	7.61	4.16	9.268	1.000	0.008	0.044	0.097	0.797	0.803	85.370	4.95	0.408
21.000	1.644	2.98	20.31	6.99	4.01	8.218	1.000	0.007	0.037	0.090	0.792	0.797	116.427	5.40	0.334
22.750	1.523	2.25	18.47	6.46	4.21	7.175	1.000	0.006	0.032	0.084	0.792	0.797	130.888	5.85	0.281
24.500	1.407	1.66	17.77	6.01	4.35	6.140	0.999	0.005	0.027	0.078	0.798	0.802	132.764	6.30	0.250
26.250	1.314	1.28	17.84	5.62	4.34	5.110	0.996	0.004	0.024	0.072	0.798	0.801	132.693	6.75	0.234
28.000	1.230	1.01	18.19	5.27	4.26	4.083	0.989	0.004	0.021	0.067	0.795	0.798	131.929	7.20	0.224
29.750	1.136	0.67	18.05	4.96	4.29	3.059	0.970	0.003	0.018	0.063	0.797	0.799	132.306	7.65	0.205
31.500	0.992	0.12	16.86	4.69	4.57	2.038	0.917	0.003	0.015	0.061	0.816	0.818	130.863	8.10	0.167
33.250	0.720	–0.53	15.00	4.45	4.98	1.018	0.765	0.003	0.010	0.061	0.889	0.891	108.681	8.55	0.108
34.125	0.536	–0.67	15.00	4.33	5.00	0.509	0.589	0.003	0.007	0.060	0.898	0.900	105.847	8.78	0.074
34.983	0.120	3.49	35.50	4.23	0.74	0.010	0.091	0.002	0.002	0.034	0.601	0.602	60.019	9.00	0.043

Note: In each column there is a reference to an equation that describes the entity.

the corresponding quantities are shown in the right side of the table. In each column of the table, a reference is found to the corresponding equation needed to describe the entity. The planform is plotted in Figs 6.22–6.24. In Fig. 6.22, it is noted that the root part, from around $r = 8$ m and inwards, has an unusual shape. Often the blade needs a transition from the airfoil part to a cylindrical part to connect the blade to the hub and the pitch bearings. This is not taken into account in this design, where only the aerodynamic performance is in focus. However, this transition should be corrected for in the final blade design.

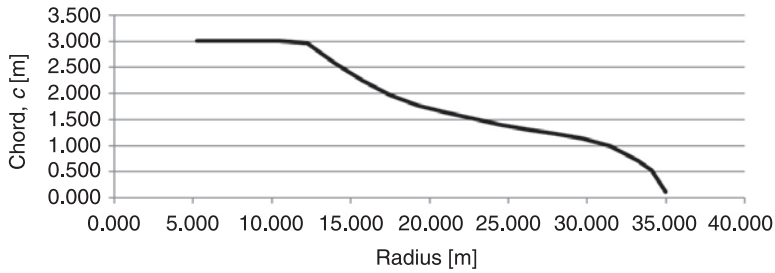

6.22 Chord distribution.

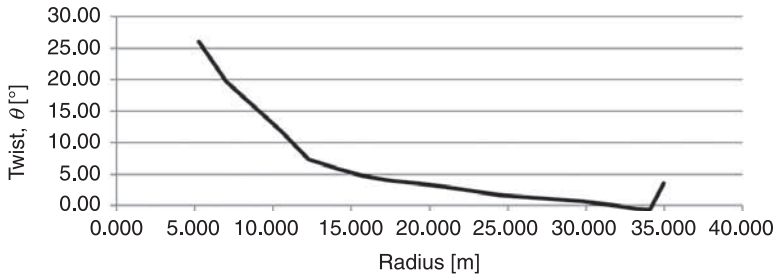

6.23 Twist distribution.

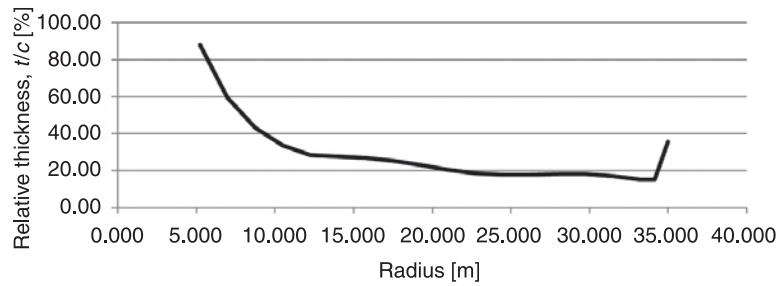

6.24 Relative thickness distribution.

6.4.9 Step 9: evaluation of the blade design

The blade as designed in Step 8 should be evaluated not only to reveal the aerodynamic performance, where power performance and load performance should be investigated, but also the AEP. In the following, the aerodynamic tool HAWTOPT,[2] developed at Risø DTU, Denmark, will be used. However, before commencing the evaluation, the airfoil characteristics should be corrected for three-dimensional flow effects, such as centrifugal and Coriolis forces, which appear when the flow starts to separate. For this purpose the models mentioned in Section 6.3.3[29–33] can be used. In general, these corrections will increase the maximum lift the closer the airfoil sections are to the hub. The corrections are important for precise estimation of the rotor performance for a PRVS concept, but because most of the rotor experiences attached flow in normal operation the influence of the three-dimensional effects is fairly small. However, if a rotor for a stall-regulated turbine was designed, the rotor would experience separated flow on the entire rotor and the three-dimensional corrections would be crucial for making fair predictions of power and load. In this example, the three-dimensional correction model by Bak *et al*.[33] was used.

The power without drive train losses and the thrust are shown in Fig. 6.25. Also, Fig. 6.26 shows the corresponding rotational speed and pitch. It is seen that rated power is obtained slightly above a wind speed of 10 m/s and not 12 m/s as estimated. This might be due to a relatively optimistic power curve, where the power at the 'knee' of the power curve is not obtainable on real turbines because

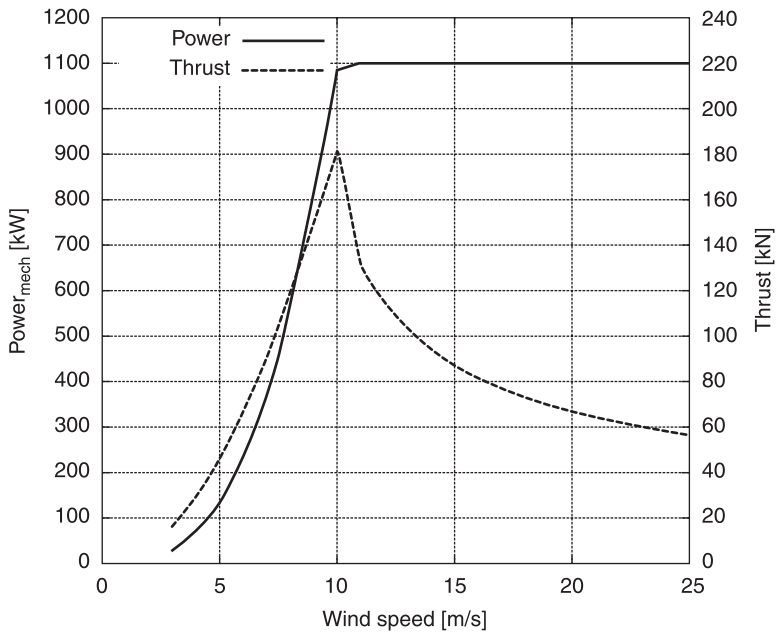

6.25 Mechanical power and thrust as a function of wind speed – so-called power and thrust curves.

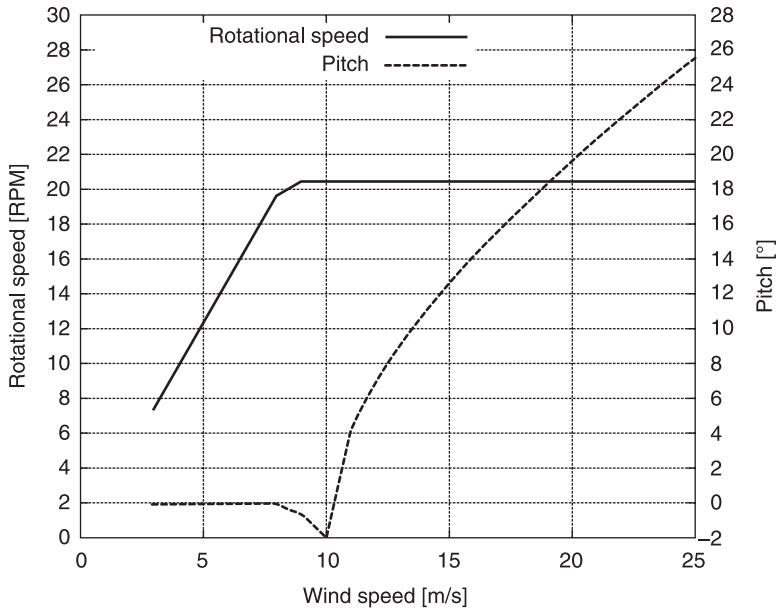

6.26 Rotational speed and pitch as a function of wind speed.

of the rapid changes in the pitch curve at these wind speeds. Furthermore, the losses from the drive train will decrease the efficiency, which will result in a slightly higher rated wind speed. However, it should be considered whether the rotor has the right size compared to the generator to obtain minimum cost of energy. For this purpose, the AEP is important to predict. For this rotor with the given control settings and on the given site it is AEP = 2270 MWh. Relating AEP to the number of hours in a year, the mean mechanical power for the rotor in this wind climate is 259 kW. This is 25.9% of the rated power, which agrees well with the rule of thumb of 25% for wind turbine rotors in general.

Figure 6.27 shows the power coefficient and the thrust coefficient. It is noted that the power coefficient is somewhat below the Betz limit. Analyzing this, Fig. 6.28 shows the local power and thrust coefficient reflecting how the efficiency is distributed along the blade at a wind speed of 8 m/s. In terms of the power coefficient, the blade is rather inefficient on the inner part of the blade, especially from r = 12 m and inwards. This is partly due to the conservatism in the airfoil characteristics for the FFA-W3-xxx airfoils because they were measured at a lower Reynolds number than the number at which the rotor actually operates. Also, a negative power coefficient is seen at the tip and at the root, which is due to the thick airfoil section of 35.5% relative thickness at the tip and approximately 60% relative thickness close to the root.

To ensure that the rotor will not result in too much noise and possibly lose power, the angle of attack during operation should be investigated. This is shown in Fig. 6.29 for the situation of mean wind speeds. The corresponding lift coefficients, c_l,

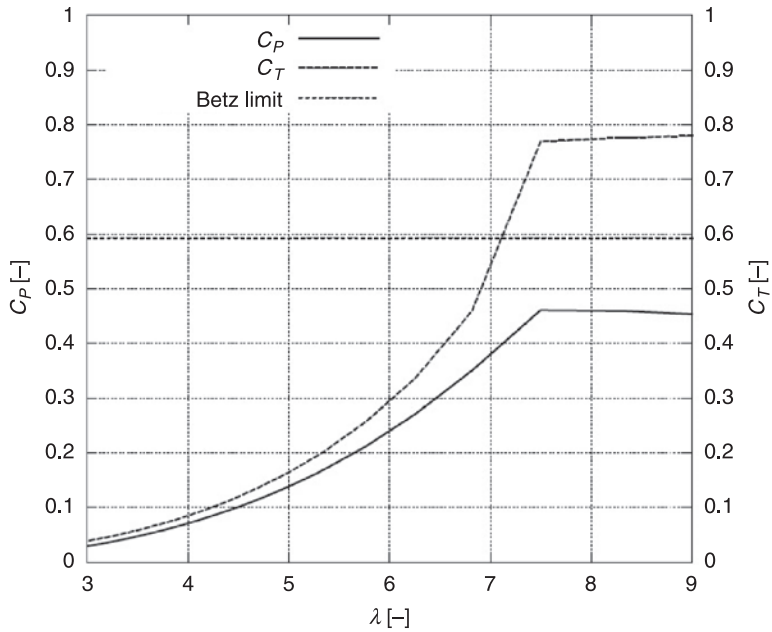

6.27 Power and thrust coefficient as a function of tip speed ratio, λ. The Betz limit is also shown.

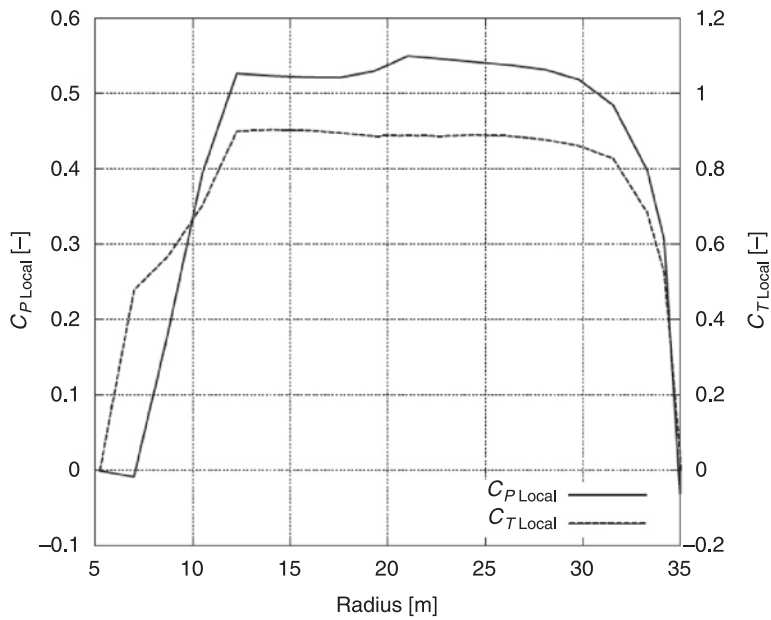

6.28 Local mechanical power and thrust coefficient as a function of rotor radius at a wind speed of 8 m/s corresponding to $\lambda = 9.0$.

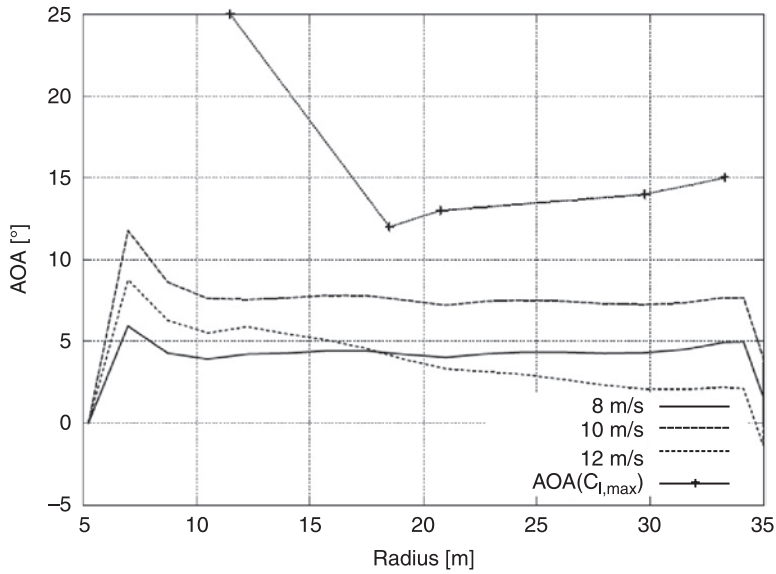

6.29 Angle of attack (AOA) as a function of radius.

is shown in Fig. 6.30. However, gusts entering the rotor will result in a sudden increase of the angle of attack and can potentially cause separation and corresponding noise and loss of power. Thus, even though Figs 6.29 and 6.30 show that the operation at a wind speed of 10 m/s is closest to maximum lift and that the rotor even at this wind speed will be free of separation and far from maximum lift, the performance in terms of, for example, load, power and risk of separation should be investigated using an aeroelastic code using the wind climate in terms of turbulence intensity and the Weibull distribution for which it is designed.

Figure 6.31 shows the Reynolds numbers as a function of radius at wind speeds from 8 m/s to 12 m/s. At 8 m/s the rotor is still operating in the variable speed range, but at 10 m/s and 12 m/s maximum rotational speed is obtained. It shows that the Reynolds numbers used from the wind tunnel tests correspond fairly well for the 18% and 21% relative thickness, where it is maximum $Re = 5 \times 10^6$ on the blade instead of $Re = 6 \times 10^6$ in the tunnel. However, for the thicker airfoils, $Re = 1.6 \times 10^6$, as measured in the tunnel, is too low compared to $Re = 5 \times 10^6$ on the blade. For the 15% airfoil $Re = 3 \times 10^6$ on the blade, whereas $Re = 6 \times 10^6$ was used, which is too high.

Analyzing the geometry of the blade planform, the chord distribution is relatively smooth and should cause no significant problems when creating the structure. However, the twist and the distribution in relative thickness are not as smooth, so there might be some requirements set up to let the distribution of the different parameters be smooth and continuously changing. Finally, the structural design should be analyzed to find potential improvements concerning, for example, strength, stress strain and manufacturing process.

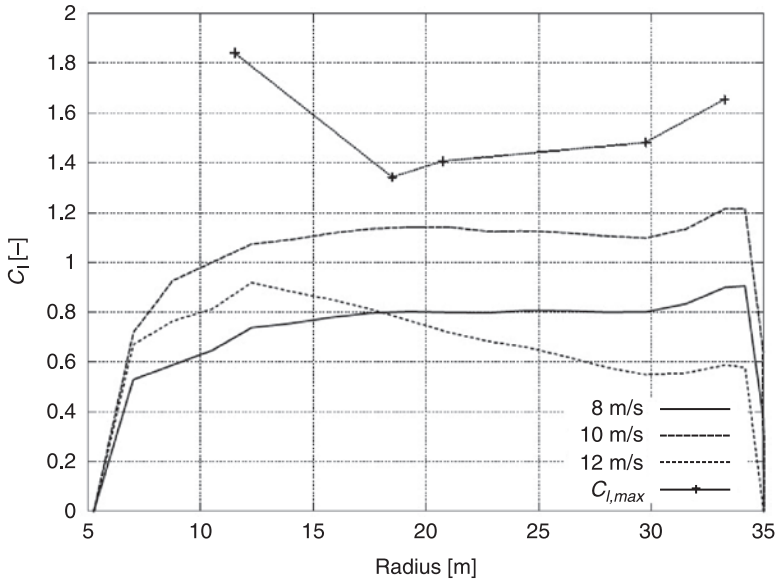

6.30 Lift coefficient as a function of radius.

Using the evaluation of the design as stated in this Step 9, evaluation of the blade design, a new iteration in the blade design process is carried out starting from the step at which the findings in the evaluation influence the design for the first time in the process. For the above design we should obtain new airfoil

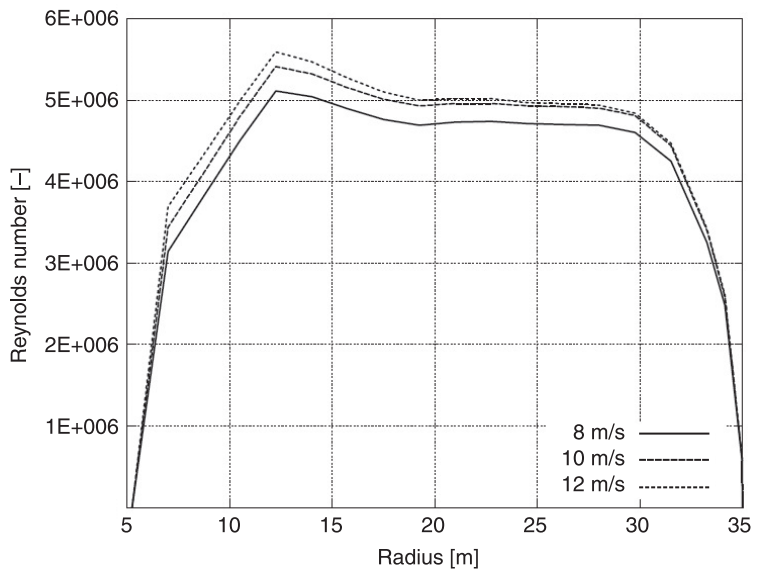

6.31 Reynolds number as a function of radius.

characteristics for $t/c = 15\%$ and for $t/c \geq 24\%$, because they seem to affect the design too much. Therefore, a new iteration in the rotor design process should be carried out starting at Step 6. However, if an aeroelastic code was used to reveal the load response from the entire wind turbine and if a proper cost function was set up, a new iteration in the rotor design process could start at an even earlier step, possibly starting at Step 2 to scale the rotor diameter.

6.5 Future trends

With the number volume of wind turbines on the world market and the increasing interest in wind energy, it seems that several development lines will be followed in rotor design. One line is a new market being developed for small wind turbines in the kW range (in 2010). Many different concepts are being tested as was the case at the end of the 1970s and in the early 1980s. Thus, for this size of rotors, the trend is not clear. Another line of development is the large MW wind turbines, which are based on experience and up-scaling from the early 1980s. Concerning blade design for MW wind turbines, different shapes exist at the moment. The difference in shape is related to the extent of required load reduction. Some blades are designed with rather thin airfoil sections from tip to root and rather large chord lengths are allowed. Other blades are designed with rather thick airfoil sections close to the root with a transition from airfoil sections to a cylinder part and a correspondingly small allowable maximum chord length. This difference is due to the predictions of the loads on the entire wind turbine in certain conditions, such as with the rotor idling in extreme wind. In the past few years, there has been a trend towards slender blades to reduce the loads on the entire turbine. Another way to reduce the loads is to equip the blades with trailing edge flaps, to be able to actively reduce fluctuating loads. This technique is being developed and has been investigated for use on wind turbines since 2003.[51–54] Also, the greater use of sensors will probably affect the blade design, such as using strain gauges embedded in the blade or laser measurements upstream of the rotor, such as the Wind Scanner.[55]

With the increasing number of wind turbines on the market, it seems increasingly cost effective to design wind turbines and rotors for specific wind climates. Thus, different aspects need to be considered, such as whether the turbine is erected offshore, in complex terrain or in wind farms, or on low-wind sites or high-wind sites. Therefore, there is a trend towards designing turbines and rotors specialized for particular sites.

Irrespective of whether the blades are designed with large or small maximum chord lengths close to the root, there is a trend towards making the blades more aerodynamically efficient. Especially on the inner part of the blade, where thick airfoils are used, much effort is put into the understanding and correct modeling of this part of the rotor, where high thrust close to the root has been observed to result in suction of the flow through the rotor caused by swirl in the wake close to

the hub.[56] Thus, more focus on the performance of both thicker airfoils and the rotor aerodynamics on the inner part of the rotor will probably be seen.

6.6 Sources of further information

The design of rotors requires the use of different tools. In particular, mechanisms that cannot be described by the BEM method have been investigated since the 1980s and in latter years also supported by advanced tools such as computational fluid dynamics. Wind tunnel tests on rotors have been carried out[57,58] and rotor tests in atmospheric flow have also been carried out.[59–61] Recently, an experiment on a rotor for a 2.3 MW modern wind turbine was carried out to measure both pressure distributions on the blade surface and fast pressure fluctuations up to 10 kHz to investigate the smallest eddies in the turbulence characteristics around wind turbine blades in operation.[62] Details of the aerodynamic rotor design have been investigated at different research institutions such as NREL (USA), UC Davis (USA), ECN (The Netherlands), Delft (The Netherlands), Stuttgart (Germany), FOI (Sweden), CRES (Greece), Mie University (Japan), Imperial College (UK), DTU MEK (Denmark) and Risø DTU (Denmark). Overviews of aerodynamic rotor design have been given by Tangler[63] and Snel.[64]

6.7 Acknowledgements

I wish to thank my colleagues at Risø DTU, Denmark, particularly the Aeroelastic Design Program of the Wind Energy Division which is a continuous source of inspiration. I especially wish to thank Mac Gaunaa and Flemming Rasmussen from the Aeroelastic Design Program for fruitful discussions in the writing of this chapter.

6.8 Nomenclature

Symbol	Unit	Description
a	[–]	Axial interference factor in rotor plane
a'	[–]	Tangential interference factor in rotor plane
A	[m^2]	Area of rotor plane
A_h	[m/s]	Parameter in Weibull distribution relating to the mean wind speed
B	[–]	Number of blades on rotor
c	[m]	Chord length or distance from extreme leading edge to extreme trailing edge of airfoil
c_d	[–]	Drag coefficient
c_l	[–]	Lift coefficient
$c_{l,design}$	[–]	Lift coefficient at which $(c_l/c_d)_{design}$ is obtained (design lift)
$c_{l,design,blade}$	[–]	Lift coefficient used to design the blade (blade design lift)
$c_{l,max}$	[–]	Maximum lift coefficient
c_l/c_d	[–]	Lift–drag ratio
$(c_l/c_d)_{design}$	[–]	Maximum lift–drag ratio for airfoil section

$(c_l/c_d)_{design,blade}$	[–]	Lift–drag ratio at which $c_{l,design,blade}$ is obtained
c_x	[–]	Force coefficient on airfoil driving the rotor – parallel to rotor plane
c_y	[–]	Force coefficient on airfoil contributing to rotor thrust – orthogonal to rotor plane
C_P	[–]	Rotor power coefficient
C_T	[–]	Rotor thrust coefficient
D	[N]	Drag on airfoil
f	[–]	Exponent in the Prandtl tip correction formula
F	[–]	Prandtl tip correction
$F_{tangential}$	[N/m]	Force per length unit in tangential direction on an airfoil section
h	[m]	Height above ground at which the wind speed will be modeled
$h_{measured}$	[m]	Height above ground at which the wind speed is measured (commonly 10 m)
H	[Pa]	Stagnation pressure
k_h	[–]	Parameter in the Weibull distribution
$k_{h,measured}$	[–]	Parameter in the Weibull distribution determined from measurements
L	[N]	Lift on airfoil
p	[Pa]	Pressure in the rotor plane on the upstream side
p_0	[Pa]	Pressure far upstream and downstream of the rotor
P	[W]	Mechanical power from the rotor
P_{wind}	[W]	Power available from the wind
Q	[Nm]	Torque from the rotor
r	[m]	Radius locally on the blade
R	[m]	Tip radius
Re	[–]	Reynolds number
t	[m]	Maximum thickness of airfoil measured orthogonal to the chord
T	[N]	Thrust on rotor
T_{wind}	[N]	Thrust from the wind
TSR	[–]	Tip speed ratio = λ
u	[m/s]	Wind speed in the rotor plane
u_1	[m/s]	Wind speed far downstream in the rotor wake
V_0	[m/s]	Wind speed far upstream of the rotor
W	[m/s]	Relative velocity on the airfoil which is the combination of the axial and the tangential inflow
z_0	[m]	Terrain roughness length
α	[°]	Angle of attack
α_{design}	[°]	Angle of attack at which $c_{l,design}$ is obtained
$\alpha_{design,blade}$	[°]	Angle of attack at which $c_{l,design,blade}$ is obtained
Δp	[Pa]	Pressure jump over the rotor disk
ϕ	[°]	Angle between the relative inflow and the rotor plane
λ_{loc}	[–]	Ratio between the local tangential velocity of the rotor and the wind speed far upstream
λ	[–]	Ratio between the tangential velocity at the tip of the rotor and the wind speed far upstream (tip speed ratio)
ν	[m^2/s]	Air dynamic viscosity
ω	[rad/s]	Rotational speed of the rotor
ρ	[kg/m^3]	Air density
σ	[–]	Solidity of the rotor
θ	[°]	Pitch angle

6.9 References

1 BTM Consult ApS, 'International Wind Energy Development', *World Market Update 2008. Forecast 2009–2013*, BTM Consult ApS, March 2009.
2 Fuglsang, P, Thomsen, K, 'Site-specific design optimization of 1.5–2.0 MW wind turbines', *J. Solar Energy Eng.* 123 (2001), 296–303.
3 Xudong, W, Shen, W Z, Zhu, W J, Sørensen, J N, Jin, C, 'Shape optimization of wind turbine blades', *Wind Energy* 12(8) (2009), 781–803.
4 ANSYS Fluent, www.ansys.com
5 ANSYS CFX, www.ansys.com
6 STAR-CD, www.cd-adapco.com
7 Michelsen, J A, *Basis3d – A Platform for Development of Multiblock PDE Solvers*, Technical Report AFM 92-05, Technical University of Denmark, 1992.
8 Michelsen, J A, *Block Structured Multigrid Solution of 2D and 3D ELLIPTIc PDE's*, Technical Report AFM 94-06, Technical University of Denmark, 1994.
9 Sørensen, N N, *General Purpose Flow Solver Applied to Flow Over Hills*, Risø-r-827(en), Risø National Laboratory, Denmark, June 1995.
10 Sørensen, N N, 'CFD modelling of laminar-turbulent transition for airfoils and rotors using the γ-Re_θ model', *Wind Energy* 12 (2009), 715–33.
11 Sørensen, J N, Shen, W Z, 'Numerical modelling of wind turbine wakes', *Journal of Fluids Engineering* 124(2) (2002), 393–9.
12 Mikkelsen, R, *Actuator disc methods applied to wind turbines*, MEK-FM-PHD 2003-02, Technical University of Denmark, 2003.
13 Madsen, H A, 'A CFD analysis of the actuator disc flow compared with momentum theory results', *10th IEA Meeting on Aerodynamics*, 16–17 December, University of Edinburgh, 1996.
14 Voutsinas, S G, Riziotis, V A, 'Vortex particle modeling of stall on rotors: application to wind turbines', *Proceedings of the Fluids Engineering Division Summer Meeting*, ASME, San Diego, CA, 1996, pp. 25–32.
15 Glauert, H, 'Airplane propellers', in *Aerodynamic Theory*, Volume IV, ed. W F Durand, The Dover edition, New York, 1963.
16 Wilson, R E, Lissaman, P B S, *Applied Aerodynamics of Wind Power Machines*, Oregon State University, May 1974.
17 Andersen, P S, Krabbe, U, Lundsager, P, Petersen, H, *Basismateriale for Beregning af Propelvindmølle*, Risø-M-2153(rev.), Risø, Januar, 1980. (in Danish)
18 Hansen, M O L, *Aerodynamics of Wind Turbines*, 2nd ed., Earthscan, London, 2008.
19 Prandtl, L, Betz, A, *Schraubenpropeller mit geringstem Energieverlust*, Göttinger Nachrichten, 1919.
20 Abbott, I H, von Doenhoff, A E, *Theory of Wing Sections*, Dover Publications, New York, 1959.
21 Althaus, D, *Niedrig-geschwindigkeits-profile*, Friedr. Vieweg & Sohn Verlagsgesellschaft mbH, Braunschweig/Wiesbaden, 1996.
22 Lyon, C A, Broeren, A P, Giguere, P, Gopalarathnam, A, Selig, M S, *Summary of Low-Speed Airfoil Data*, Volumes 3, Department of Aerospace Engineering, University of Illinois at Urbana-Champaign, Urbana, IL.
23 Tangler, J L, Somers, D M, 'Nrel airfoil families for HAWTs', *Proceedings of the Windpower'95*, 26–30 March, Washington, DC, 1995, pp. 117–23.
24 Timmer, W A, van Rooij, R P J O M, 'Summary of the Delft University wind turbine dedicated airfoils', *Proceedings of the AIAA-2003-0352*, 2003.

25 Björk, A, *Coordinates and Calculations for the FFA-w1-xxx, FFA-w2-xxx and FFA-w3-xxx Series of Airfoils for Horizontal Axis Wind Turbines*, FFA TN 1990-15, FFA, Stockholm, Sweden, 1990.
26 Fuglsang, P, Bak, C, 'Development of the Risø wind turbine airfoils', *Wind Energy* 7 (2004), 145–62.
27 Bak, C, Andersen, P B, Madsen, H A, Gaunaa, M, Fuglsang, P, Bove, S, 'Design and verification of airfoils resistant to surface contamination and turbulence intensity', *AIAA 2008-7050, 26th AIAA Applied Aerodynamics Conference*, 18–21 August, Honolulu, HI, 2008.
28 Drela, M, XFOIL: an analysis and design system for low reynolds number airfoils', *Low Reynolds Number Aerodynamics*, Volume 54, Lectures Notes in Engineering, Springer-Verlag, 1989.
29 Snel, H, Houwink, R, van Bussel, G J W, Bruining, A, 'Sectional prediction of 3D effects for stalled flow on rotating blades and comparison with measurements', *Proceedings of the European Community Wind Energy Conference*, 8–12 March, H S Stephens & Associates, Lübeck-Travemünde, Germany, 1993, pp. 395–9.
30 Du, Z, Selig, M S, 'A 3-D stall-delay model for horizontal axis wind turbine performance prediction', *AIAA-98-0021, 36th AIAA Aerospace Sciences Meeting and Exhibit, 1998 ASME Wind Energy Symposium*, 12–15 January, Reno, NV, USA, 1998.
31 Chaviaropoulos, P K, Hansen, M O L, 'Investigating three-dimensional and rotational effects on wind turbine blades by means of a quasi-3D Navier–Stokes Solver', *Journal of Fluids Engineering* 122 (June 2000), 330–6.
32 Lindenburg, C, 'Modelling of rotational augmentation based on engineering considerations and measurements', *European Wind Energy Conference*, 22–25 November, London, 2004.
33 Bak, C, Johansen, J, Andersen, P B, 'Three-dimensional corrections of airfoil characteristics based on pressure distributions', *Presented at the European Wind Energy Conference & Exhibition (EWEC)*, 27 February–2 March, Athens, Greece, 2006.
34 Bak, C, 'Sensitivity of key parameters in aerodynamic wind turbine rotor design on power and energy performance', *Proceedings of the Science of Making Torque from Wind, Journal of Physics: Conference Series* 75 (2007).
35 Collecutt, G R, Flay, R G J, 'The economic optimisation of horizontal axis wind turbine design', *Journal of Wind Engineering and Industrial Aerodynamics* 61(1) (June 1996), 87–97.
36 Fingersh, L, Hand, M, Laxson, A, *Wind Turbine Design Cost and Scaling Model*, Technical Report NREL/TP-500-40566, December 2006.
37 Fuglsang, P, Bak, C, Schepers, J G, Bulder, B, Cockerill, T T, Claiden, P, Olesen, A, van Rossen, R, 'Site-specific design optimization of wind turbines', *Wind Energy* 5(4) (2002), 261–79.
38 Diveux, T, Sebastian, P, Bernard, D, Puiggali, J R, Grandidier, J Y, 'Horizontal axis wind turbine systems: optimization using genetic algorithms', *Wind Energy* 4(4) (2001), 151–71.
39 Griffin, D A, Zuteck, M D, 'Scaling of composite wind turbine blades for rotors of 80 to 120 meter diameter', *Journal of Solar Energy* Engineering 123(4) (November 2001), 310–9.
40 Zaaijer, M B, Kooijman, H J T, Herman, S A, Hendriks, H B, 'How to benefit from cost modeling of offshore wind farms', *EWEC2003*, Madrid, Spain, 2003.
41 Brooks, T F, Pope, D S, Marcolini, M A, *Airfoil Self-Noise and Prediction*, NASA Reference Publication No. 1218, USA, 1989.

42 Øye, S, 'FLEX 4 – simulation of wind turbine dynamics', *Proceedings of the 28th IEA Meeting of Experts – State of the Art of Aeroelastic Codes for Wind Turbine Calculations*, 11–12 April, Technical University of Denmark, Lyngby, Denmark, 1996, pp. 71–6.
43 Bossanyi, E A, *GH-Bladed User Manual*, Issue 14, Garrad Hassan and Partners Ltd, Bristol, UK, 2004.
44 Lindenburg, C, Schepers, J G, 'Phatas-IV Aero-elastic Modelling, Release "DEC-1999" and "NOV-2000" ', *ECN-CX-00-027*, 2000.
45 Jonkman, J M, Buhl, M L Jr., 'FAST user's guide', *NREL/EL-500-29798*, National Renewable Energy Laboratory, Golden, CO, 2005.
46 Larsen, T J, Madsen, H A, Hansen, A M, Thomsen, K, 'Investigations of stability effects of an offshore wind turbine using the new aeroelastic code HAWC2', *Proceedings of the Conference on Copenhagen Offshore Wind 2005, Copenhagen*, 2005, pp. 25–8.
47 IEC 61400-SER ed1.0, www.iec.ch
48 Troen, I, Lundtang, E L, *European Wind Atlas*, Risø National Laboratory, Roskilde, Denmark.
49 Bertagnolio, F, Sørensen, N N, Johansen, J, Fuglsang, P, *Wind Turbine Airfoil Catalogue*, Risø-R-1280(EN), 2001.
50 Fuglsang, P, Antoniou, I, Dahl, K S, Madsen, H A, *Wind Tunnel Tests of the FFA-W3-241, FFA-W3-301 and NACA 63-430 Airfoils*, Risø-R-1041(EN), Risø National Laboratory, Roskilde, Denmark, December 1998.
51 Buhl, T, Gaunaa, M, Bak, C, 'Potential load reduction using airfoils with variable trailing edge geometry', *Journal of Solar Energy Engineering*, 127 (November 2005), 503–16.
52 Andersen, P B, Henriksen, L, Gaunaa, M, Bak, C, Buhl, T, 'Deformable trailing edge flaps for modern megawatt wind turbine controllers using strain gauge sensors', *Wind Energy*, 2009.
53 Barlas, A, van Kuik, G A M, 'State of the art and prospectives of smart rotor control for wind turbines', *Proceedings of the Science of Making Torque from Wind*, Lyngby, Denmark.
54 Yen Nakafuji, D, van Dam, C, Smith, R, Collins, S, 'Active load control for airfoils using microtabs', *Journal of Solar Energy Engineering* 123 (2001), 282–9.
55 Mikkelsen, T, Mann, J, Courtney, M, Sjöholm, M, 'Windscanner: 3-D wind and turbulence measurements from three steerable doppler lidars', *14th International Symposium for the Advancement of Boundary Layer Remote Sensing, Earth and Environmental Science*, Volume 1, 2008.
56 Johansen, J, Aagaard Madsen, H, Gaunaa, M, Bak, C, Sørensen, N N, '3D Navier–Stokes simulations of a rotor designed for maximum aerodynamic efficiency', AIAA-2007-217, in [Technical papers] *Presented at the 42th AIAA Aerospace Sciences Meeting and Exhibit 45th AIAA Aerospace Sciences Meeting and Exhibit; 26th ASME Wind Energy Symposium*, Reno, NV (USA), 8–11 January 2007, American Institute of Aeronautics and Astronautics, Reston, VA, 2007.
57 Hand, M M, Simms, D A, Fingersh, L J, Jager, D W, Cotrell, J R, Schreck, S, Larwood, S M, 'Unsteady aerodynamics experiment phase VI: wind tunnel test configurations and available data campaigns', *NREL/TP-500-29955*, National Renewable Energy Laboratory, Golden, CO, USA, December 2001.
58 Snel, H, Schepers, J G, Montgomerie, B, 'The MEXICO project (model experiments in controlled conditions): the database and first results of data processing and interpretation', *Proceedings of the Science of Making Torque from Wind, Journal of Physics: Conference Series* 75 (2007).

59 Schepers, G, Brand, A, Aagaard Madsen, H, Simms, D, Hand, M, Stefanatos, N, Bruining, A, van Rooy, R, Maeda, T, Shimizu, Y, Graham, M, 'IEA Annex XIV/XVIII, field rotor aerodynamics, wind energy for the new millennium', In Helm, P, Zervos, A (Eds), *Proceedings of the 2001 European Wind Energy Conference and Exhibition (EWEC'01)*, 2–6 July 2001, Copenhagen, Denmark, WIP Renewable Energies, München, 2001, pp. 457–61.
60 Schepers, J G, Brand, A J, Bruining, A, Graham, J M R, Hand, M M, Infield, D G, Madsen, H A, Paynter, R J H, Simms, D A, *Final Report of IEA Annex XIV: Field Rotor Aerodynamics*, ECN-C-97-027, ECN Solar Energy, 1997.
61 Schepers, J G, Brand, A J, Bruining, A, van Rooij, R, Graham, J M R, Paynter, R J H, Hand, M M, Simms, D A, Infield, D G, Madsen, H A, Maeda, T, Shimizu, Y, Stefanatos, N, *Final Report of IEA Annex VIII: Enhanced Field Rotor Aerodynamics Database*, ECN-C-02-016, ECN Wind Energy, 2002.
62 Madsen, H A, Bak, C, Paulsen, U S, Gaunaa, M, Sørensen, N N, Fuglsang, P, Romblad, J, Olsen, N A, Enevoldsen, P, Laursen, J, Jensen, L, 'The DAN-AERO MW experiments', AIAA 2010-645, *48th AIAA Aerospace Sciences Meeting Including the New Horizons Forum and Aerospace Exposition*, 4–7 January 2010, Orlando, FL.
63 Tangler, J, 'The evolution of rotor and blade design', *Presented at the American Wind Energy Association WindPower 2000*, April 30–May 4, Palm Springs, CA, 2000.
64 Snel, H, 'Review of aerodynamics for wind turbines', *Wind Energy* 6 (2003), 203–11.

7

Wind turbine drive train systems

Z. CHEN, Aalborg University, Denmark

Abstract: This chapter describes drive train systems of modern wind turbines. Various types of systems, including gears, generators, power electronics and the integrated overall power transmission systems, are discussed, and an optimization design study of electrical conversion systems is presented.

Key words: wind turbines, gearbox, generator topologies, variable speed, direct drive, power electronics.

7.1 Introduction

This chapter describes the wind turbine drive train systems. The main function of a drive train is power transmission, i.e. to convert the mechanical energy at the rotor hub of the wind turbine to electrical energy, and to send it to the load/grid. The main components include the gearbox, generator and power electronic converters.

Along with the rapid development of wind power application and significant growth of wind turbine installation capacity worldwide, research and development are being conducted actively; various wind turbine concepts have been developed to make wind energy conversion systems even more cost-effective.

Figure 7.1 shows a typical drive train of modern wind turbines (Vestas A/B, Denmark), where a gearbox converts the low speed, high torque power into the high speed and low torque power to drive a normal generator. However, the generator type would determine the type of drive train. The gearbox may be omitted if the generator is a direct-drive type which can produce electricity at the low speed of the wind turbine's rotor.

This chapter is organized into the following sections: Section 7.2 describes gearbox and bearing systems, Section 7.3 presents power electronic system, followed by Section 7.4 where generators are introduced; in Section 7.5, the integrated wind power conversion systems are discussed, then the system optimal design is reported in Section 7.6; finally, conclusions and future trends are given in Section 7.7.

7.2 Gearbox and bearing systems

7.2.1 Gearboxes, shafts, bearings

Gears are used to transmit power between shafts rotating at different speeds. In a wind turbine, a combination of gears may be used to increase the low rotational

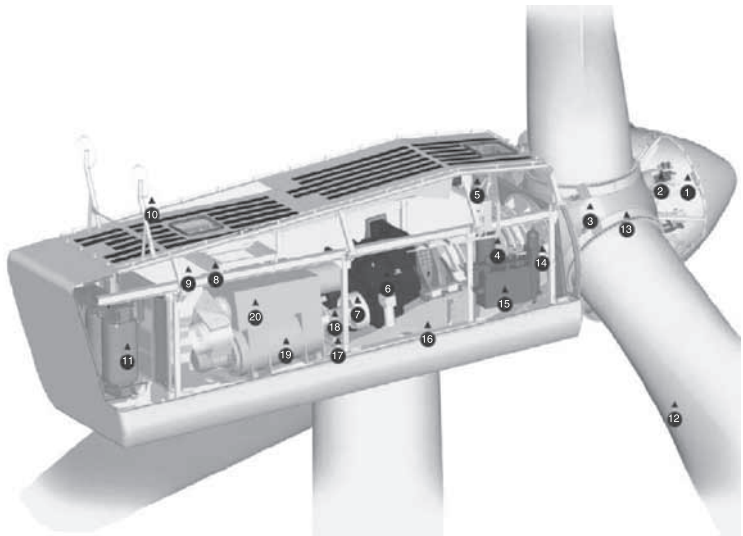

① Hub controller
② Pitch cylinders
③ Blade hub
④ Main shaft
⑤ Oil cooler
⑥ Gearbox
⑦ Mechanical disc brake
⑧ Service crane
⑨ VMP-Top controller with converter
⑩ Ultrasonic wind sensors
⑪ High voltage transformer
⑫ Blade
⑬ Blade bearing
⑭ Rotor lock system
⑮ Hydraulic unit
⑯ Machine foundation
⑰ Yaw gears
⑱ Composite disc coupling
⑲ OptiSpeed® generator
⑳ Air cooler for generator

7.1 Vestas V90-1.8 MW and 2.0 MW DFIG wind turbine (Courtesy Vestas A/B).

speed of the turbine blades to a high speed for a standard generator, normally, 1000 rpm or 1500 rpm. There are various types of gears, the following three types are often used in wind turbine gearboxes:

1 *Spur gear* is the simplest and most common type of gear, where teeth are parallel to the rotational axis of the gear as shown in Fig. 7.2(a). Tooth contact is primarily rolling, with sliding occurring during engagement and disengagement.
2 *Single helical gear* has cylindrical shaped gear with angled teeth shown in Fig. 7.2(b), and is designed so that the teeth come in contact with one another with gradually increasing pressure, rather than engaging the entire tooth at once as in spur gears. At any time, the load on helical gears is distributed over several teeth, resulting in reduced wear. Helical gears operate with less noise and vibration than spur gears.

(a) (b) (c)

7.2 (a) Spur gear, (b) helical gear, and (c) herringbone ('V' shape teeth).

3 *Double helical gear*, also known as herringbone gear, may have both left-hand and right-hand helical teeth set in a 'V' shape, as two standard single helical gear and one is mirror image of the other as shown in Fig. 7.2(c).

Gears can be combined in different configurations; the following two types are often used for wind turbines:

1 *Parallel stage*: In this configuration, two different size gears are fixed on two parallel shafts as shown in Fig. 7.3(a) (Peeters *et al*., 2006). The speed ratio is inversely proportional to the number of teeth.
2 *Planetary stage*: The main components of a planetary stage are illustrated in Fig. 7.3(b) (Peeters *et al*., 2006), including:
   (i) an interior toothed gear wheel (ring gear)
   (ii) two or three smaller toothed gear wheels (planet gear)
   (iii) a common carrier arm (planet carrier)
   (iv) a centrally placed toothed gear wheel (the sun gear).

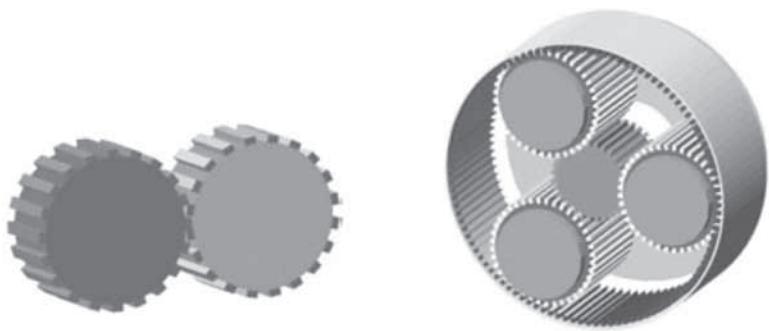

(a) (b)

7.3 (a) Parallel gear stage, (b) planetary gear stage (Peeters *et al.*, 2006; Courtesy Wiley Interscience).

The ring gear is stationary while the planet carrier is mounted on the turbine rotor shaft rotating with the same speed as the rotor shaft. The planet carrier transmits the driving torque to the planet gears that move around inside the inner circumference of the ring wheel. The number of the planet gears is a design variable which is often chosen as three. The speed-up ratio for this configuration can be expressed by the following:

$$\frac{n_{HSS}}{n_{LSS}} = 1 + \frac{D_{ring}}{D_{sun}} \qquad [7.1]$$

where n_{HSS} and n_{LSS} are respectively the rotational speed of the sun and the planet carrier, D_{ring} is the diameter (or number of teeth) of the ring wheel and D_{sun} is the diameter (or number of teeth) of the sun.

Planetary gear stages are more compact and produce a higher torque density than parallel gear stages, so that they may transfer more torque for the same amount of used material.

Spur gears and helical gears are used in both parallel gear stages and planetary gear stages for wind turbine gearboxes.

7.2.2 Multistage gearbox

As power and rotor diameter increase, the torque and gear ratio also increase and often one single gear stage is not sufficient. Multistage gears are required to obtain the desired ratio. A wind turbine gearbox typically contains one low-speed planetary stage with two parallel stages or two planetary stages with one high-speed parallel stage. In general, a planetary stage is designed for gear ratio up to seven and a parallel stage usually up to five.

Figure 7.4 shows a cross section of a gearbox for an MW level wind turbine with one planetary stage and two parallel gear stages (Todorov *et al*., 2009). The planetary stage has spur gears and its ring wheel is fixed in the gearbox housing. The second gear stage is a helical parallel stage. Its wheel is driven by the sun of the first stage and its pinion drives the wheel of the third stage, which is also a helical parallel stage.

The following components are associated with the gearbox and may contribute to its failures:

1 *Bearings*: The main function of bearings is reducing frictional resistance between two surfaces with relative motion, either linear or rotational. According to the type of motion, bearings can be either linear/axial or rotational/radial.
2 *Shafts*: Shafts are cylindrical elements used to transmit torque; a drive train may have several shafts, for example, the low-speed shaft on the turbine rotor side, high-speed shaft on the generator side, and intermediate shafts in the gearbox housing to carry the gears.
3 *Couplings*: These are elements used to connect and transmit torque between two shafts, for example, the generator and the high-speed shaft of the gearbox.

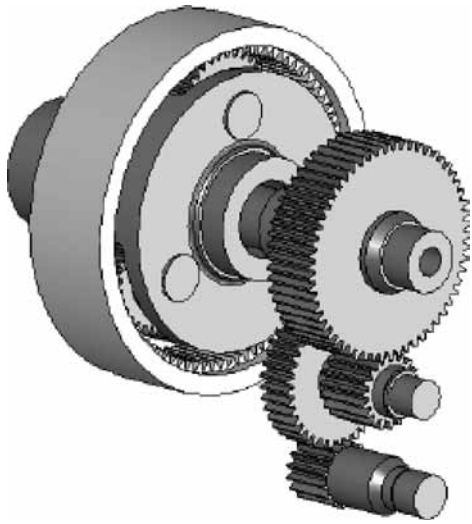

7.4 Illustration of three-stage gearbox, one planetary stage, and two parallel stages (Todorov *et al.*, 2009; Courtesy IEEE, © 2009 IEEE).

In some designs, a safety clutch is integrated into the coupling to protect the gearbox by preventing the transfer of a torque transient caused possibly by a short circuit.

4 *Mechanical brakes*: Aerodynamic brakes (by pitching the blades or turning the blade tip) are used to limit the turbine speed or to stop a wind turbine. The aerodynamic brake is the preferred brake for stopping as less stress is being placed on the system than if mechanical brakes are applied. The brakes are usually spring or hydraulic operated and constructed to work even during electrical power failure.

   However, a mechanical braking system, including a friction brake and its hydraulic system, can bring the rotor to a complete stop and halt the turbine blades during maintenance and overhaul, or in emergency cases. The mechanical brake is built with a fail-safe mechanism. For instance, the reduced hydraulic oil pressure can be used to activate the brakes to stop the wind turbine. The brake disk is made of a special metal alloy that can endure temperatures of up to 700°C and is normally installed on the high-speed shaft, i.e. between gearbox and generator, to keep the brake disk diameter as small as possible.

5 *Yaw mechanism*: It is used to align the rotor axis with the wind in order to extract as much energy from the wind as possible. An electrical or hydraulic system is used to align the machine with the wind. A wind vane on top of the nacelle may be used to the yaw drive.

7.2.3 Drive train bearing concepts

In a wind turbine, the rotor hub transfers the mechanical energy from the wind into the drive train with several loading components. Only the torque component is useful for the generator to produce electricity. The other loading components are transferred towards the tower. The stiffness and damping characteristics of the suspension play an important role in the dynamic response of the drive train. Figure 7.5 shows three possible supporting structure examples (Harrison *et al.*, 2000; Hau, 2000).

Figure 7.5(a) shows a concept with two separate bearings supporting the main shaft. Both bearings carry radial loads and transfer bending moments towards the tower. The bearing near the wind turbine's rotor also carries axial loads. The torque is transferred to the gearbox through the main shaft. The gearbox suspension may only carry the reaction torque towards the bed plate. Torque arms are equipped with vibration dampers and give the gearbox some flexibility.

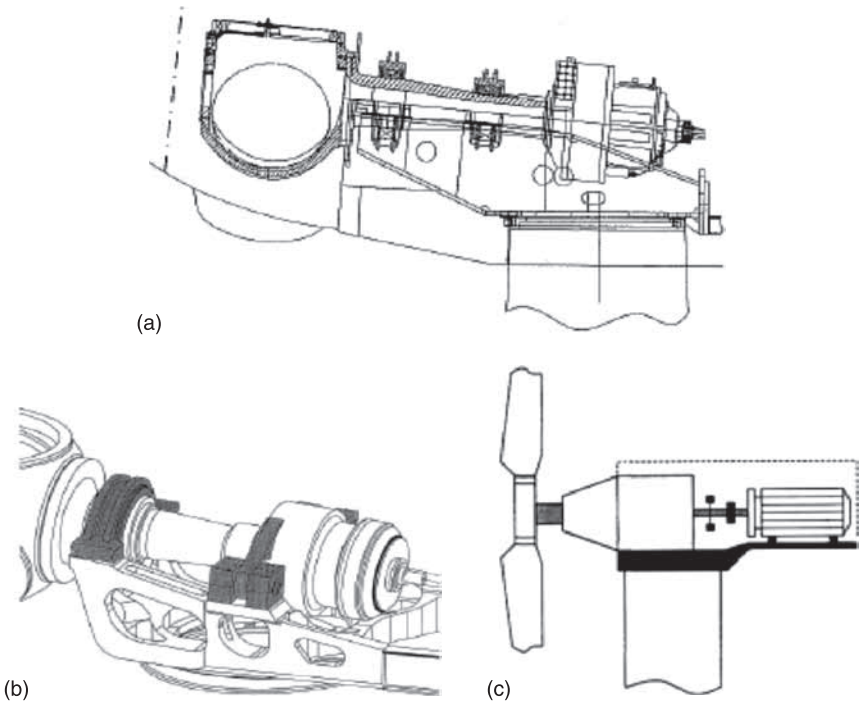

7.5 Drive train bearing concept examples: (a) two bearings outside the gearbox supporting the main shaft, reproduced from Hau, 2000; (Courtesy Wind turbines, Springer-Verlag). (b) Three-point suspension: one bearing integrated in the gearbox (Hau, 2000; Courtesy Wind turbines, Springer-Verlag). (c) Main bearing integrated in the gearbox (Harrison *et al.*, 2000).

Figure 7.5(b) shows that one axial bearing supports the main shaft near the rotor and one radial bearing is integrated in the gearbox. The gearbox suspension, typically of two torque arms, is mounted on the bed plate. The drive train concept is often referred to as a 'three-point-suspension' system.

Figure 7.5(c) shows another drive train concept: the rotor hub is hanging in one large bearing carrying radial and axial loads as well as all bending moments. The gearbox is an integrated part of the whole nacelle. This design may lead to a considerable weight reduction of the nacelle.

7.2.4 Possible drive train mechanical failure and prediction and mitigation

Similar to other gear applications, the wind turbine gearbox and bearings could have the following failures:

- fatigue cracks
- teeth breakage
- wear
- plastic flow
- scoring (scuffing)
- surface fatigue
- spalling.

The aerodynamic torque and the electromagnetic torque are applied on a wind turbine drive train and determine the loading on the mechanical system. Drive train failures, including spalled bearings and fractured gear teeth, are largely caused by unexpected and/or excessive loading conditions. Such drive train failures often resulted in expensive repairs and can have catastrophic consequences for the turbine. Therefore, wind turbine gearboxes may be designed to have strength a few times the rated torque for preventing the damage caused by unpredictable torques and stresses. However, electrical system faults, such as a short circuit fault may cause a high torque peak in the drive train. In order to protect the gearbox and the rotor shaft, overload clutches are built into the high-speed shaft in most cases.

Different drive train concepts, gearbox and generator designs, and power electronic control strategies will affect the drive train loading, for example, individual blade pitch control and power electronic optimal torque control, etc. Numerical modeling and simulation methods are used to analyze the impacts and evaluate the fatigue effects of dynamic loading under various situations, including emergency stop, power system faults (Heege *et al*., 2007), etc. Based on such studies, the control strategies could be developed to reduce the damaging loading and the risk of system failure, and improve drive train fatigue mitigation.

Wind turbine monitoring can be used for control applications as well as preventive measures. Preventive monitoring is necessary to extend turbine lifecycle, schedule maintenance and predict fault conditions. Also state monitoring, fault prediction and

diagnoses techniques are being developed to predict the possible failure so that the maintenance or repairs could be performed effectively to reduce the cost and the risk of system breakdown (Amirat *et al*., 2009; Hameed *et al*., 2009; Zaher *et al*., 2009).

The condition monitoring of the gearbox and main bearing is attracting more interest because the gearbox is problematic and the costs of replacement are high. There are various condition-monitoring techniques which may be applied on a wind turbine, some most relevant to the mechanical part of a drive train system are:

- vibration analysis
- oil analysis
- acoustic measurements.

7.2.5 Vibration

Vibration monitoring is used in wind turbines to determine the condition of rotating equipment, including the main bearing gearbox and generator. The vibration sensors may be placed in the axial and radial directions. Depending on the applicable frequency range, the position sensors (low range), velocity sensors (mid range), or accelerometers (high range) may be used. These vibration sensors are rigidly mounted to the component of interest and return an analog signal proportional to the instantaneous local motion. Various sensors with different frequency ranges can be used for different situations, including shafts, bearings, gearbox and generators, as well as other equipments, such as pumps and compressors. The measured data are analyzed, such as by harmonic analysis, then the health condition of the monitored components can be determined before they are damaged (e.g., cracked gear tooth, broken bearing, and so on).

7.2.6 Oil quality

Oil analysis is mainly used for checking the condition of oil for lubricating or insulating equipment such as bearing, gearbox, transformer and other electrical distribution equipment. The analysis enables the detection of some possible problems, including arcing, aging insulating paper, and other latent problems. Improper lubrication can reduce efficiency and cause mechanical failures. Most bearing and gear wear results from incorrect oil lubrication and can lead to more serious problems in the turbine drive train. This monitoring can be conducted with oil particle counting and measurements of moistness, viscosity, acidity and temperature.

By using instruments such as a particle counter the quality of the oil and the possible existence of contaminants can be identified. Water contamination in industrial oil plays an important role; high moisture levels can cause components to overheat, corrode or fatally malfunction. Based on the oil analysis, an oil management scheme can keep the oil in an optimal condition to reduce the costs of oil replacement as well as the wear of the components.

7.2.7 Acoustic monitoring

Acoustic monitoring has some relationship with vibration monitoring. The vibration sensors are rigidly mounted on the component concerned, record the local motion and analyse the frequencies in relation to the rotational speeds. On the other hand, the acoustic sensors are attached to the component by flexible glue with low attenuation. These sensors are based at higher frequencies which give an indication of developing defects.

Acoustic monitoring measures the noise from the turbine both internally and externally. An acquisition device with antialiasing, a high sampling rate and dynamic range should ideally be used. The gearbox and the main bearing are important when monitoring internally, while the overall turbine noise is monitored externally. From the measured results, the higher frequency components can be determined to predict possible faults.

7.3 Power electronic systems

Power electronic, being the technology of efficiently converting electric power, plays an important role in wind power systems. It is an essential part to integrate the variable speed wind power generation units to achieve high efficiency and high performance. Even in a fixed speed wind turbine system where wind power generators are directly connected to the grid, thyristors are used as soft-starters. The power electronic interfaces are used to match the characteristics of wind turbines with the requirements of grid connections, including frequency, voltage, active and reactive power, harmonics, ride-through requirement, etc.

Power electronics have been developed rapidly in recent years in the semiconductor devices, circuit topologies and control technologies; the performance is improving and price is falling, and the applications areas have significantly been increased.

Power electronic device technology is still undergoing important progress. The breakdown voltage and/or rated current of the components are continuously increasing. Important research is also going on into the use of silicon carbide. This may dramatically increase the power density of the converters. Commonly, switchable power semiconductor devices available for wind power applications may include IGCTs (insulated gate commutated thyristor), SGCTs (symmetrical gate commutated thyristor), GTOs (gate turn-off thyristor), IGBTs (insulated gate bipolar transistor) and IEGTs (injected enhanced gate transistor).

IGBTs are one of the most widely used devices for power electronics converters. They are available from 600 V to 4500 V, and the current rating is up to 2400 A. Higher voltage IGBTs up to 6500 V are also available but with reduced current capability, e.g., 650 A. The IGBT power rating can achieve 3600 V, 1700 A and 4500 V, 1200 A, while state-of-the-art asymmetric blocking IGCT devices are available with 6500 V, 3000 A and 6000 V, 4500 A (Badrzadeh *et al.*, 2009), which could be used for large high power wind turbines.

Power electronic converters are constructed by semiconductor devices driving, protection and control circuits, to perform voltage magnitude and frequency conversion and control. Self-commutated converter systems use the switchable semiconductors and normally adopt pulse width modulated (PWM) control methods. This type of converter may transfer active power in both directions (AC-DC or DC-AC), and the reactive power demand on the AC side can also be delivered by a PWM converter.

Self-commutated converters may be further divided into two types: voltage source converters (VSC) and current source converters (CSC), depending on the types of DC link. A VSC has a DC capacitor to keep a smooth DC voltage, and commonly IGBTs are used as switching devices. The AC output of VSC is a PWM voltage waveform. A CSC has a DC reactor to keep a smooth DC current and generates a current PWM waveform at its AC terminal. Both self-commutated VSC and CSC may provide four-quadrant operation (transferring active power and reactive power in both directions with reference to an AC grid). Both types of self-commutated converter systems can use PWM high frequency switching, which may produce harmonics and interharmonics in the range of some kHz. These harmonics are relatively easy to be removed by small-size filters. Presently, most of the power electronic converters used in wind power are VSC.

VSC may have various configurations, but two-level converters are the simplest configurations and are widely used in various areas, including wind power applications. Figure 7.6 shows a two-level VSC, consisting of self-commutated semiconductors, such as IGBTs.

Multi-level converters are developed for high voltage and high power applications. There are various multi-level converter circuit topologies, for example, the neutral point clamped (NPC) converter and flying capacitor (FLC) converter. The one-leg circuits of NPC and FLC converters are shown in Fig. 7.7. In a multi-level converter, dynamic voltage sharing is built into the structure through either clamping diodes or clamping capacitors. Multi-level VSCs can

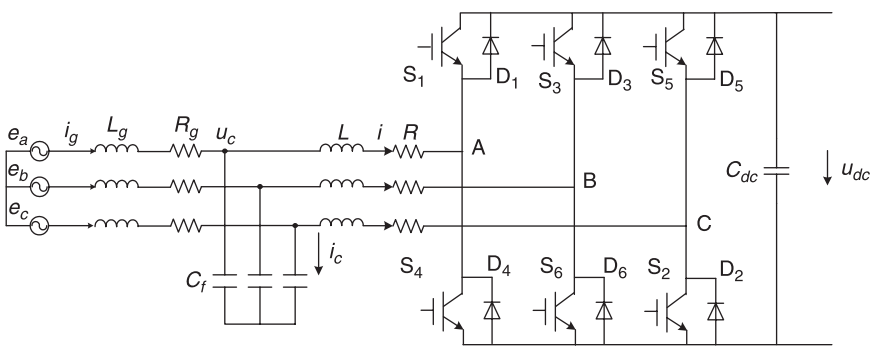

7.6 Circuit diagram of a two-level voltage source converter (VSC) with IGBTs.

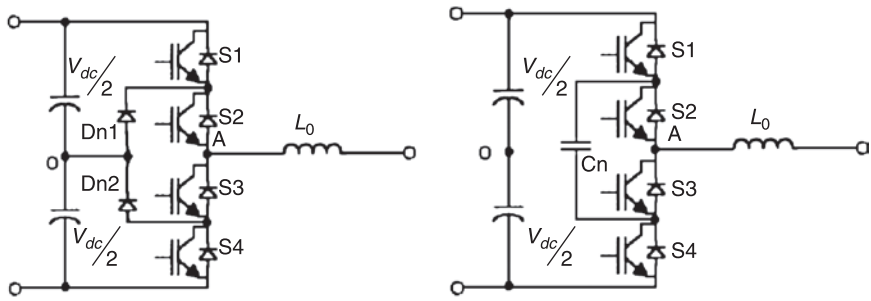

7.7 Legs of voltage source converters: (a) three-level neutral point clamped VSC, and (b) three-level flying capacitor VSC.

vary their output between several voltage levels, which provides the improved voltage waveforms, reduced filtering requirements, and reduced common mode voltage and EMI issues.

Other multi-converter system may also be used, such as the cascaded H-bridge (CHB) converter and the interleave converter systems, which have several converters connected in parallel; the output waveforms of these converters are phase shifted to reduce the harmonics with the increased power delivery.

Medium voltage converter systems may be more suitable for larger wind turbines. For example, ABB has made a PCS 6000 converter for 5 MW wind turbines (Eichler *et al*., 2008). The converter has two NPC (neutral point connected) phases based on high power semiconductors IGCT–PEBB (modular power electronics building blocks) technology, which enable the development of compact converters.

7.4 Electrical generator basic characteristics

A generator plays a very important role in wind turbine technical solutions. The integration of the generator and power electronics significantly affects the performance of the wind power systems, and affects both the mechanical part as well as the electrical grid.

A generator consists of two main components: a stator and a rotor. The space between the rotor and stator is called the 'air gap', where a rotating electromagnetic field is produced by three-phase AC current flowing in the machine windings. The rotating speed of the magnetic filed is related to the synchronous speed n_s, which depends on the frequency of AC terminal voltage and on the number of pole pairs in the generator:

$$n_s = 60 f_{ac} / pp \qquad [7.2]$$

n_s = synchronous rotational speed (rpm)
f_{ac} = AC system frequency (Hz)
pp = number of pole pairs.

Generators can be mainly divided into two types: synchronous generator and asynchronous generator, also called an induction generator. A synchronous generator always rotates at the synchronous speed while an induction generator can operate at a varying speed different from the synchronous speed. Figures 7.8 and 7.9 show the torque characteristics of the two types of generators.

Synchronous generators may be excited either by an externally applied direct current (electromagnet) or by permanent magnets (PMs) and can be made with a large number of pole pairs, yielding a low synchronous speed, as low as the wind turbine's rotor speed, then a gearbox is no longer needed. There is considerable interest in the application of multiple-pole synchronous generators (either electrical excitation or with PM) driven by a wind-turbine without a gearbox or with a low ratio gearbox. However, the vertical torque characteristic of the synchronous generator (Fig. 7.8) indicates that it works at a constant speed. This means that the wind power fluctuations may be translated into heavy torque fluctuations and high peak loads in the drive train. Therefore, synchronous generators powered by wind turbines may not be directly connected to the AC grid due to the lack of damping.

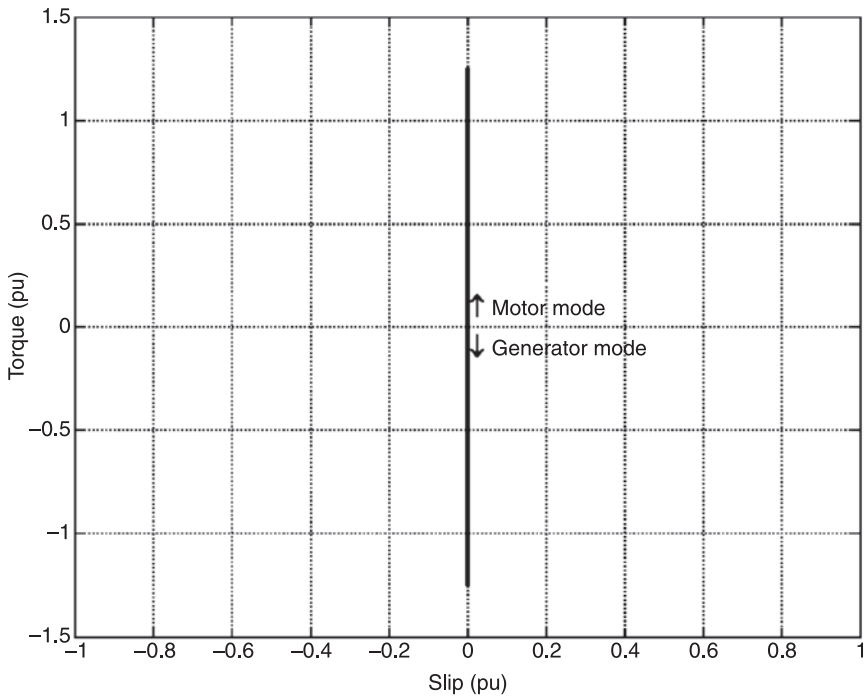

7.8 Torque characteristic of a synchronous generator.

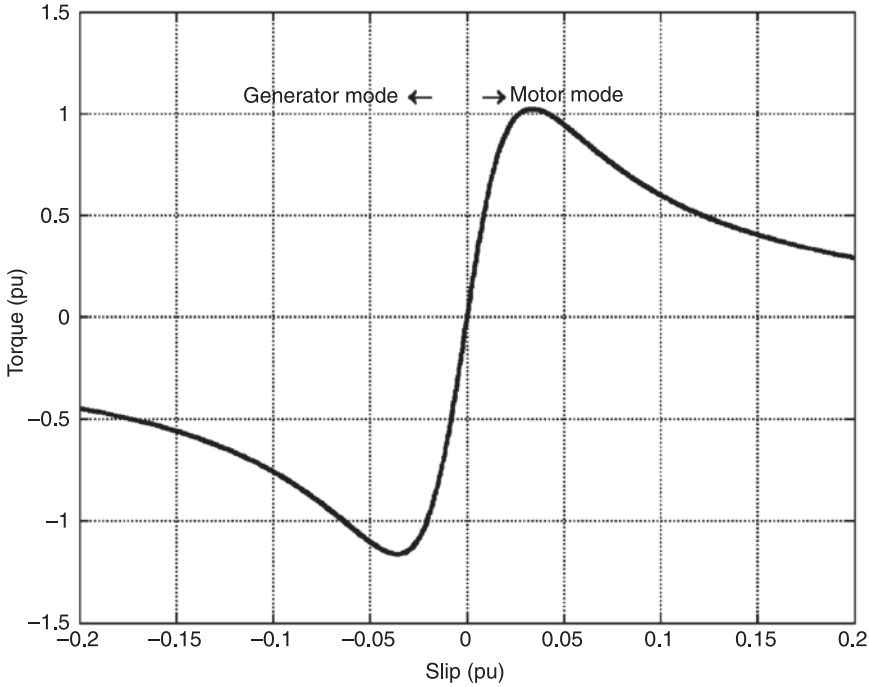

7.9 Torque characteristic of an asynchronous (induction) generator.

For an induction machine, the slip, s, is defined as

$$s = (n_s - n_r)/n_s \quad [7.3]$$

n_r = speed of the generator (rpm).

For a generator operation of an induction machine, ignoring the other power losses, the power balance may be expressed as

$$P_m = P_s + P_r \quad [7.4]$$

$$P_r = -sP_s \quad [7.5]$$

P_m is the mechanical power, P_s is the stator power and P_r is the rotor power. The torque of the asynchronous generator is a function of the slip, s (Fig. 7.9), which is negative if the machine is in super synchronous speed, and a higher slip (absolute value) means a larger amount of electrical energy in the rotor circuit. The slip is small for a short-circuited rotor such as the squirrel cage rotor with the speed variation being limited (e.g., 1%). Within this limited speed range, a linear characteristic may be used to represent the relation between the torque and the slip of the generator, which corresponds to a damper characteristic. The small speed

variation characteristic of the cage rotor asynchronous generator makes the machine suitable for wind turbine application.

The number of pole pairs, *pp*, of an induction generator in wind applications is usually two or three, resulting in a synchronous speed of 1500 rpm or 1000 rpm. A higher pole pair number is rarely used because the induction generator efficiency decreases with increasing *pp*. Normally, a gearbox is needed to reduce generator speed to the speed of the wind turbine's rotor.

Both induction generators and synchronous generators have some varieties, which are presented in the following parts of this section (Li and Chen, 2008).

7.4.1 Squirrel cage rotor induction generators

For a long time, squirrel cage induction generators (SCIGs) have been the most used generators for wind turbines. A three-stage gearbox in the drive train is usually required. The generator may be directly grid connected, which was the conventional concept applied by Danish wind turbine manufacturers during the 1980s and 1990s, i.e., an upwind, stall regulated, three-bladed wind turbine with an SCIG, which is sometimes referred to as the 'Danish concept'. Though the stall control method is usually used in combination with the fixed speed SCIG, the active stall control or pitch control may also be applied. More details about the system will be presented in a later section.

7.4.2 Wound rotor induction generators

The stator of a wound rotor induction generator (WRIG) is constructed in the same way as that of the SCIG, but the rotor is no longer a squirrel cage rotor; rather it is equipped with a three-phase winding. In wind power applications, the rotor of a WRIG may be either connected to a resistor which consumes some power while changing the slip and the generator speed, or connected to a power electronic system which exchanges the power between the machine and the AC grid. The latter is also called doubly fed induction generator (DFIG), i.e., both the stator and rotor of the WRIG can transfer power to the AC system.

Wound rotor induction generator with rotor resistance control

The torque characteristics are shown in Fig. 7.10 for an induction generator with and without an external rotor resistor. It can be seen that, for the same level of torque, the higher resistance of the rotor windings, the higher the slip is. Therefore, one way of varying the slip is to vary the resistance of the rotor. The basic idea of this concept is to control the rotor resistance using a variable external rotor resistor by means of a power electronic converter. The suitable torque–speed characteristic can be chosen to obtain the desired speed at an operating point. Only speeds higher than synchronous speed are possible for generator operation,

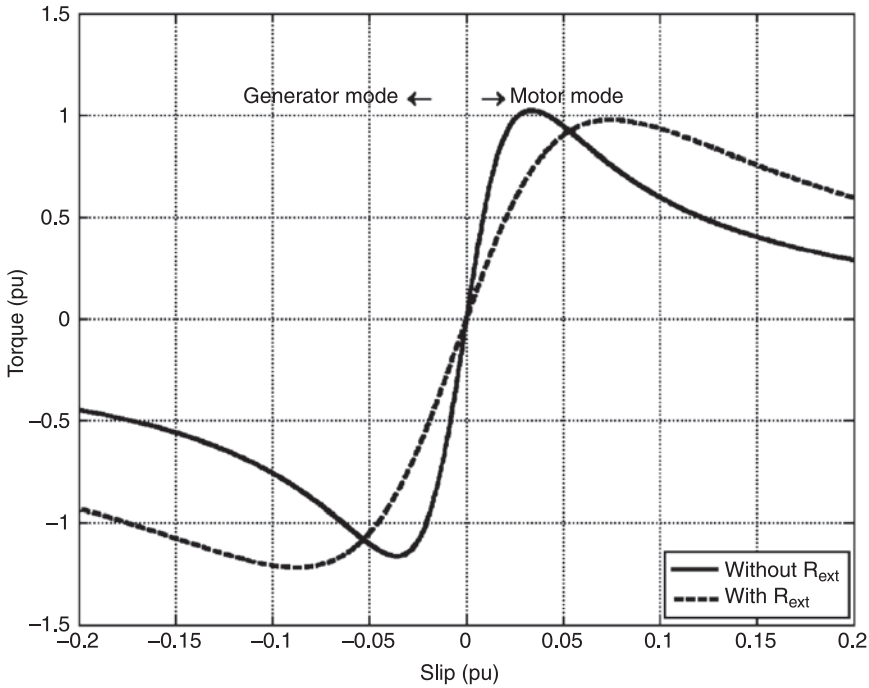

7.10 Torque characteristics of asynchronous (induction) generators with and without external rotor resistance.

and the rotor power is not fed back into the grid. It is basically a single-fed induction generator with similar characteristics to an SCIG. Variable speed operation can be achieved by controlling the energy extracted from the WRIG rotor; however, this power must be dissipated in the rotor resistor. With the increase of variable speed range, a higher slip means more power consumed by the rotor, and a lower generator efficiency, so that the rating of the resistor must also be higher. Therefore, the dynamic speed control range depends on the size of the variable rotor resistor. A typical limited variable speed range is less than 10% above the synchronous speed. Conventionally, the connection is usually done with brushes and slip rings, which introduce parts and raise the maintenance requirements, and are a drawback in comparison with the simple technical design of a cage rotor induction machine, but a larger speed variation range is an advantage.

Wound rotor induction generator with power electronic converters

An alternative to the energy dissipation in the generator's rotor is to exchange energy between the rotor and the electricity grid. The stator of a DFIG is connected

to the grid directly, while the rotor of the generator is connected to the grid by electronic converters through slip rings, i.e., a DFIG. The power converter controls the rotor active power flow and thus the rotor speed. This concept supports a wide speed range operation, depending on the size of the frequency converter. The choice for the rated power of the rotor converter is a trade-off between the cost and the desired speed range. The generator can operate as a generator in both super synchronous speed ($s < 0$) and sub-synchronous speed ($s > 0$).

7.4.3 Synchronous generators

A synchronous generator may not be directly connected to the grid as discussed above, unless a variable ratio gearing system is implemented. Therefore, most commercially available synchronous generators in wind power applications use a full-scale power electronic converter. Compared with the variable speed concept with a partial-scale power converter, the full-scale power converter can perform smooth grid connection over the entire speed range but all the generated power has to go through the power converter. Consequently, it has a higher cost and a higher power loss in the power electronics which need intensive cooling.

Like the SCIG and WRIG, the synchronous generator generally has a stator magnetic circuit made of laminations provided with uniform slots that house the stator winding. For the rotor excitation, there are two main possibilities. One type is a rotor winding supplied by a DC current from a separate circuit, usually called the electrically excited synchronous generator (EESG); and the other type is permanent magnets (PMs) attached to the rotor, and named as the permanent magnet synchronous generator (PMSG).

7.4.4 Multipole synchronous machines

The most important difference between gear drive wind turbines and the direct-drive types is the generator rotor speed. The direct-drive generator rotates at a low speed, because the generator rotor is directly connected to the hub of the turbine rotor. To deliver a given power, the lower speed makes it necessary to produce a higher torque. A higher torque means a larger size of the generator. The direct-drive generators (either field excited or PM generator) demand a larger diameter for the implementation of a large number of poles with a reasonable pitch. Moreover, for a larger direct-drive generator, considering the limitations on the current loading and air gap flux density makes the torque density not to be further significantly increased. To increase the efficiency, to reduce the weight of the active parts and to keep the end winding losses small, direct-drive generators are usually designed with a large diameter and small pole pitch. However, the pole pitch must be large enough for the field-excited machine in order to arrange space for the excitation windings and pole shoes. So the larger number of parts and windings probably make it a heavy and expensive solution.

The advantages of direct-drive wind turbines are the simplified drive train, the high overall efficiency and the high reliability and availability by omitting the gearbox. These machines provide good fault ride-through capability due to the use of a synchronous generator and a fully rated converter, but have a very large diameter, which may cause transportation and installation problems.

7.4.5 Electrically excited synchronous generator

The EESG is usually built with a rotor carrying the field system for a dc excitation. The stator may carry a three-phase winding quite similar to that of induction machines. The rotor may have salient poles, or cylindrical. Salient poles are more usual in low-speed machines, and may be the most useful version for application to direct-drive wind turbines.

Because the excitation current is controllable, for example, with a DC supply and slip rings and brushes, or brushless exciter, employing a rotating rectifier, the EESG has the opportunities of controlling the flux for a minimized loss in different power ranges, but the field losses are inevitable. Moreover, it does not require the use of PMs, which might suffer from performance loss in harsh atmospheric conditions.

7.4.6 Permanent magnet synchronous generator

In a three-phase sinusoidal PM machine, the stator winding is the same as the wound field synchronous machine, but the rotor is replaced with PMs which provide excitation instead of a field winding. The use of rare-earth PMs with high-energy density reduces the generator weight associated with copper windings, eliminates problems associated with insulation degradation, and reduces electrical losses; however, generator cooling needs to be appropriately designed to prevent permanently degrading magnetic field strength of the rare-earth magnets.

PMSGs have recently been manufactured achieving a lower kg/kW (approximately a two-to-one weight advantage over the wound field synchronous machines) (Badrzadeh *et al.*, 2009). These machines can be manufactured with a large number of poles for a low rotational speed to eliminate a gearbox.

PM machines require less cooling since the rotor losses are predominantly removed and this allows the PM machine to be built with smaller frame than an equivalent induction or wound field synchronous machine. These advantages are achieved at the expense of losing field voltage/current control, but the problem is alleviated with the use of power electronics converters which provide the machine with voltage control. The low-speed PM machines are more expensive than a high-speed generator using a gearbox, but have a higher efficiency, a higher reliability and lower maintenance requirements.

PMSG is becoming more attractive for direct-drive wind turbines. Compared with electrically excited machines, PM machines have a number of economical and technical advantages, such as the following:

- higher efficiency and energy yield
- no additional power supply for the magnet field excitation
- improvement in the efficiency and thermal characteristics of the machines due to absence of the field losses
- higher reliability due to the absence of slip rings
- higher torque density and improvement in the dynamics due to the replacement of wound iron mover with high-energy PM.

However, PM machines have some disadvantages, such as the following:

- high cost of PM material
- difficulties to handle in manufacture
- demagnetization of PM at high temperature.

According to the magnet location, PM machines are classified as interior or surface PM machines. In surface-magnet machines, the magnets are glued to the surface of the rotor, and machines feature non-salient pole characteristics. In an interior PM machine, the magnets are buried inside the rotor, giving salient pole characteristics.

PM machines are not standard off-the-shelf machines, and allow a great deal of flexibility in their geometry; various topologies may be used. Common types of PM machines may be classified into the radial-flux, the axial-flux and the transversal flux machines by the direction of flux penetration. Some basic structures and features of the machines are briefly described here.

Radial-flux PM (RFPM) machines

The PMs of radial-flux machines are radially oriented. In manufacture, the simple way of constructing the machine with a high number of poles is gluing PMs onto the rotor surface. In RFPM machines, the length of the machine and the air-gap diameter can be chosen independently. If necessary, the radial-flux machine may be made with a small diameter by using a long machine. RFPM machines have a better torque density than the EESG. The slotted surface-mounted PM machine is shown in Fig. 7.11.

Axial-flux PM (AFPM) machines

The AFPM machine has its magnetic flux in the axial direction, instead of the radial direction. AFPM machines may have slotless or slotted surface-mounted PMs. Compared with RFPM machines, the advantages of AFPM machines can be summarized as follows:

- simple winding
- low cogging torque and noise (in slotless machine)
- short axial length
- higher torque/volume ratio.

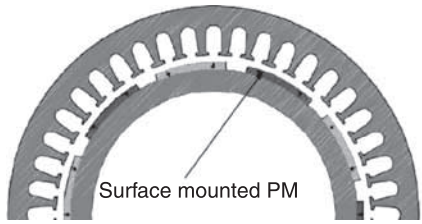

7.11 Basic configuration of RFPM machine with surface-mounted magnets.

However, the disadvantages of AFPM machines in comparison with RFPM machines are as follows:

- lower torque/mass ratio
- larger outer diameter, large amount of PM and structural instability (in slotless machine)
- difficult to maintain air-gap in large diameter (in slotted machine)
- difficult production of stator core (in slotted machine).

Various structures of AFPM machines with surface-mounted PMs have been investigated, including slotless machine and slotted machines, also different combinations of stator and rotors, such as single-stator-double-rotor or single-rotor-double-stator configurations.

The slotless single-stator-double-rotor, which is often referred to as a torus machine, is shown in Fig. 7.12 (Aydin *et al*., 2001; Spooner and Chalmers, 1992). The two rotor disks are made of mild steel and have surface-mounted PMs to produce an axially directed magnetic field in the machine air gaps. The machine stator comprises a slotless toroidally wound strip-iron core that carries a three-phase winding in a toroidal fashion by means of concentrated coils. The slotless, toroidal-stator, AFPM generator has several advantages, such as the lightness, compactness, short axial length and the suitable integration with the engine.

Transversal-flux PM (TFPM) machines

The magnetic flux path of a TFPM machine is perpendicular to the direction of the rotation. A TFPM machine is a synchronous machine in nature, and functions in a similar manner to other PMSGs. There are various rotor structures, such as the rotor with single-sided surface magnets, with single-sided flux concentration, and with double-sided flux concentration. Figure 7.13 shows the configuration of a surface-mounted TFPM (Huang *et al*., 1997). Compared with RFPM or AFPM machines, a major difference is that TFPM machines allow an increase in the space for the simple windings without decreasing the available

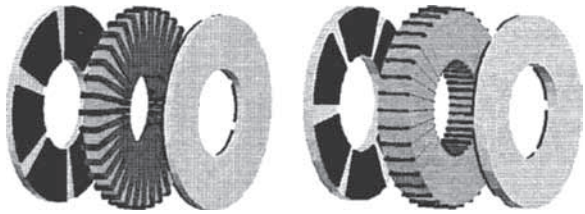

(a) (b)

7.12 Axial flux torus type surface-mounted PM motor configuration: (a) non-slotted stator and (b) slotted stator (Aydin *et al.*, 2001; Courtesy IEEE, © 2001 IEEE).

space for the main flux, so that the machines have very low copper losses. TFPM machines can also be made with a very small pole pitch; however, the structure is much more complicated. TFPM machines have low power factor, which leads to an increase in the necessary rating of the power electronic converter.

Among the above PM machines in axial flux, radial flux and transverse flux structures, the radial flux machines are widely used for direct-drive PM generators. The radial flux machines have the highest cost/torque ratio. Transverse flux machines have been researched extensively, but have some disadvantages which need to be improved, such as the complex structure, poor power factor (due to the large leakage inductance), difficulty in fault detection, and lower torque density for high power applications.

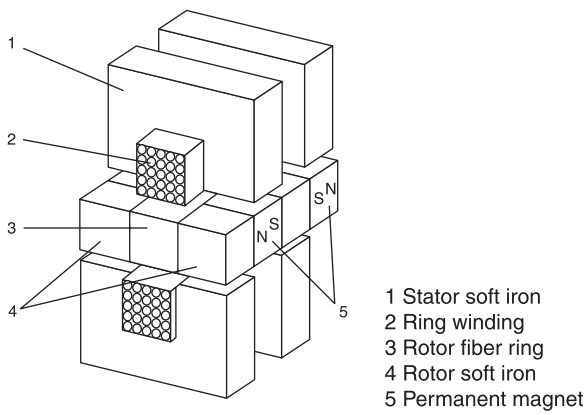

7.13 Transverse flux circumferential current PM (TFCCPM) machine (Huang *et al.*, 1997; Courtesy IEEE, © 1997 IEEE).

7.4.7 Other potential generator types

A new stator interior permanent magnet machine (SIPM), as shown in Fig. 7.14, derived from the doubly salient PM machine has been studied for wind power application (Zhang *et al*., 2007). The machine has the split stator pole and full pitched windings, where tooth-shoe is adopted and the PM is inserted into the stator pole. This configuration may offer higher power density and lower cogging torque ripple than the doubly salient machine.

Many other types of wind generators are also investigated, such as linear induction generators, switched reluctance generators, claw pole generators and brushless doubly fed induction generators (BDFIG). The BDFIG requires double stator windings with different number of poles, respectively. The output of the induction generator is directly connected to the grid; the second stator winding is connected through a power electronic converter, which is rated at only a fraction of the generator rating (Fig. 7.15). Compared with the DFIG system, the BDFIG concept does not require slip rings, while the BDFIG system has the capability of realizing the variable speed operation and independently controls the stator active and reactive power (Carlson and Voltolini, 2008). However, the machine structure, operation and control are relatively complex.

Multi-phase induction machine

A conventional variable speed drive has a three-phase machine with a three-phase converter. In a multi-phase machine drive system more than one set of three-phase winding may be housed in the same stator. For example, a six-phase machine

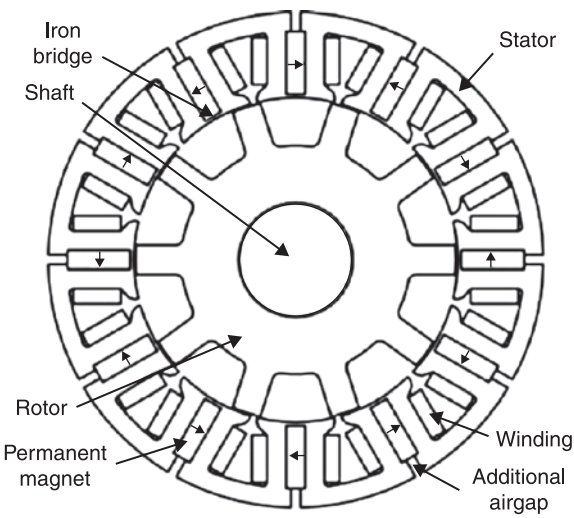

7.14 Cross-section of 12/10-pole SIPM generator (Zhang *et al.*, 2007).

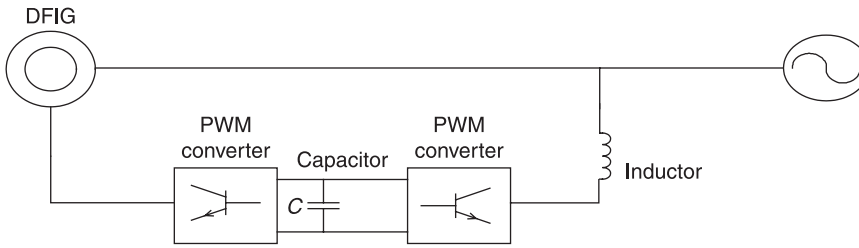

7.15 Illustration of a brushless doubly fed induction generator (BDFIG).

comprises two sets of three-phase winding spatially shifted by 30 electrical degrees and connected to two VSCs. The configuration may provide high torque density, improved fault ride-through capability, reduced torque pulsation, reduced noise and vibration, and improved efficiency and reliability (Singh, 2002; Zhao and Lipo, 1996). A loss of a phase should be less of a problem in multi-phase systems compared to a conventional three-phase system. This arrangement has been used for high-torque direct-drive naval propulsion motors and is available for up to 20 MW. Such a configuration may find applications in wind power systems.

High-temperature superconducting (HTS) generator

HTS allows significant increase in power density compared to wound copper or PM machines. Different types of rotating machine using HTS have been proposed, including synchronous, homopolar and induction machines, while most large HTS projects have been synchronous machines with an HTS DC field winding on the rotor.

Using HTS wires in the field winding of a synchronous machine, current densities up to 100 A/mm^2 can be achieved compared to about 5 A/mm^2 for conventional wound field synchronous generators. The high current density achieved with superconductive materials makes it possible to produce very compact and dense rotating machines. HTS machines can handle larger harmonic currents than conventional machines due to their attenuation of harmonic fields in the larger air gap. Other advantages of the HTS machines include improved efficiency due to elimination of rotor losses, and reduced noise and vibration (Fogarty, 2004). It is a promising technology for direct-drive generator in very large turbines; the second generation coated conductor HTS wire has the potential to meet the price and performance targets for wind energy (Lewis and Müller, 2007).

7.5 Electrical conversion systems

The structures and topologies of gearbox, generator, power electronic converters, and their integration determine the characteristics and performance of the electrical conversion systems in a wind turbine (Chen *et al*., 2009). The commonly used

systems are listed in Table 7.1, where high speed refers to speed of 1000 rpm or 1500 rpm, medium speed is in the range of around 100 rpm, and low speed is normally below 20 rpm depending on wind turbine design. In this section, the five types of systems listed in Table 7.1 will be described.

7.5.1 Multistage geared induction generators without power electronic interfaces

Induction generators, including squirrel cage rotor, wound rotor and DFIG normally use multistage gearbox drive trains. A synchronous generator system (either electrically excited or with PM excitation) may also use a multistage gearbox to reduce the generator's volume and improve the generator efficiency. The squirrel cage rotor induction generators and WRIGs connected directly to the grid are introduced respectively in this subsection.

Multistage geared squirrel cage rotor induction generator

The 'Danish Concept' of directly connecting a wind turbine to the grid is widely used in early wind turbine systems. The scheme consists of an SCIG, connected via a transformer to the grid and operating at an almost fixed speed. Since the speed range of the induction generator is very small, it is referred to as a 'fixed speed wind turbine'. The power can be limited aerodynamically either by stall control,

Table 7.1 Summary of commonly used wind turbine systems

System	Gearbox	Generator	Power electronics	Wind turbine speed
1	Multistage gear	High-speed cage rotor or wound rotor induction generators	Direct connection to grid without power electronic interface	Nearly fixed
2	Multistage gear	High-speed doubly fed induction generators	Partially rated power electronics	±30% variable
3	Multistage gear	High-speed cage rotor induction generators or synchronous generators	Fully rated power electronics	Fully variable
4	Direct drive without a gear	Multipole lower-speed synchronous generators	Fully rated power electronics	Fully variable
5	Hybrid drive (one- or two-stage gear)	Multipole medium-speed synchronous generators	Fully rated power electronics	Fully variable

active stall or pitch control. The basic configuration of the fixed speed system is shown in Fig. 7.16. The advantages of wind turbines with induction generators are the simple, robust and cheap construction, and no synchronization device is required. Some drawbacks are: (1) the wind turbine has to operate at almost constant speed, (2) it requires a stiff power grid to enable stable operation, and (3) it may require a more expensive mechanical construction to absorb high mechanical stress, since wind gusts may cause torque pulsations on the drive train.

Rotating at a fixed speed under all wind speeds is disadvantageous for the aerodynamic efficiency, and the noise from the rotor blades may be a problem at low wind speeds. In addition, the fixed-speed operation yields higher loads on the drive train. This concept may also cause flicker due to resulting varying power to the grid.

Connecting the induction generators to power system may produce transients with very high inrush currents which cause both disturbances to the grid and high torque spikes in the drive train of wind turbines. Such a transient disturbs the grid and limits the acceptable number of wind turbines. The high starting currents of induction generators are usually limited by a thyristor soft-starter. The current limiter or soft-starter, based on thyristor technology, typically limits the RMS value of the inrush current to a level below two times of the generator rated current. The soft-starter has a limited thermal capacity and it is short-circuited by a contactor, which carries the full load current, when the connection to the grid has been completed. In addition, to reduce the impact on the grid, the soft-starter also effectively dampens the torque peaks associated with the peak currents and hence reduces the loads on the gearbox.

The SCIG always draws reactive power from the grid, capacitors are connected in parallel to the generator to compensate for the reactive power consumption. However, the capacitor bank may cause self-excitation when the connection to the network is lost. In such a case, the terminal voltage or reactive power may not be directly controlled, and the induction generators may suffer from voltage instability problems, which is a concern for large-scale wind power penetration.

Changing the number of pole pairs could provide some improvement, which may be considered as switching to another generator. In practice, it is normally

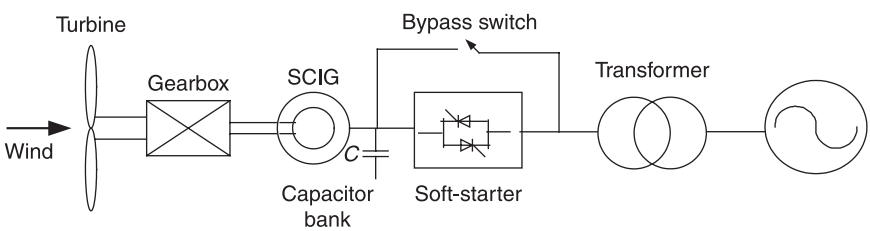

7.16 A cage induction generator based fixed-speed wind turbine with power electronic soft-starter.

applied in one single generator by changing the connection of the stator windings: at low wind speeds, the generator operates with a higher number of pole pairs (e.g., $pp = 3$), but a limited capacity. At higher wind speeds, it switches to a lower number of pole pairs (e.g., $pp = 2$) and operates, consequently, at a higher rotational speed. A lower rotational speed at low wind speeds yields a higher aerodynamic efficiency and a lower noise emission.

Multistage geared wound rotor induction generator

Figure 7.17 shows a wound rotor induction generator with rotor resistance control (dynamic slip control). In this scheme, the rotor windings are connected through slip rings and brushes with an external variable resistor. The equivalent resistance in the circuit can be adjusted by an electronic control system, the slip of the generator can be affected and the rotor speed is changed. The generator can have a speed variation up to 10% above synchronous speed; however, the design is vulnerable to wear at the slip rings and requires sufficient maintenance. The rotor resistance may also be such controlled in power system transients to help the fault ride-through of the wind turbine (Chen *et al*., 2007).

The slip rings, brushes and associated maintenance may be eliminated by mounting the resistors and associated electronic control system on the rotor (Vestas OptiSlip). The requirement of changing the slip is communicated to the rotor by using optical fiber communication.

Both cage induction generators and rotor resistance controlled WRIGs need a soft-starter, and they need to operate at a super-synchronous speed to generate electricity. Both of them draw reactive power which might be supplied from the grid or from installed compensation equipment, such as capacitor banks or additional power electronic equipment. Modern MW-class turbines have thyristor-switched capacitors allowing for a more dynamic compensation. A static var compensator (SVC) or similar technology may be needed to improve the dynamic response of the wind farm.

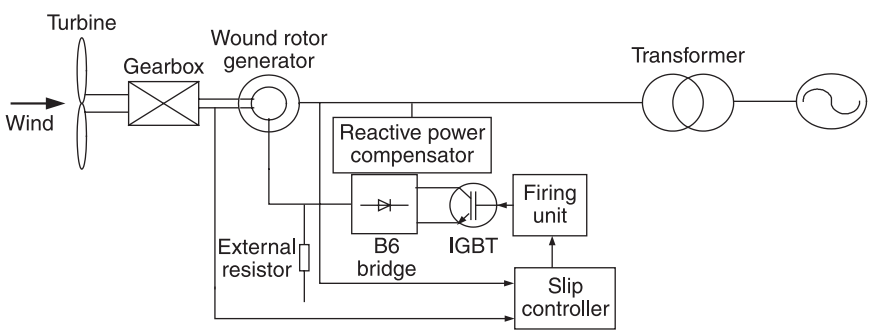

7.17 A wound rotor induction generator with rotor resistance converter.

7.5.2 Multistage geared doubly fed induction generator (DFIG) system

The DFIG is popular for modern wind turbines applications. A DFIG circuit connection is shown in Fig. 7.18. The generator can deliver energy to the grid at both super-synchronous and sub-synchronous speeds. The advantages of a DFIG are that the speed is variable within a sufficient range, and the limited converter costs. Compared with the OptiSlip concept, the rotor energy, instead of being dissipated, can be fed into the grid by the power electronic converter. The nominal power of the power electronic converter system can be less than the nominal power of the wind turbine. In general, the nominal power of the converter may be about 30% of the wind turbine power, enabling a rotor speed variation in the range of about ±30% of the synchronous speed. The slip is varied with the power flowing through the power electronic circuit. By controlling the active power of the converter, it is possible to vary the rotational speed of the generator and, thus, the speed of the wind turbine rotor.

The rotor circuit of DFIG normally uses a back-to-back converter, which consists of two bidirectional converters sharing a common DC-link, one connected to the rotor and the other one to the grid. The power electronic converters for variable speed generators have the ability to control both the active and reactive power delivered to the grid (Pena *et al*., 1996). This gives potential for optimizing the grid integration with respect to steady-state operation conditions, power quality and voltage control. The reactive power to the grid from the generation unit can be controlled as zero or to a value required by the system operator within the converter rating limit.

The DFIG system also enables the application of special operation strategies and provides the high-quality power to the grid. The acoustical noise from the wind turbines can effectively be reduced since the system can operate at a lower speed when the wind becomes quiet. The DFIG solution needs neither a soft-starter nor

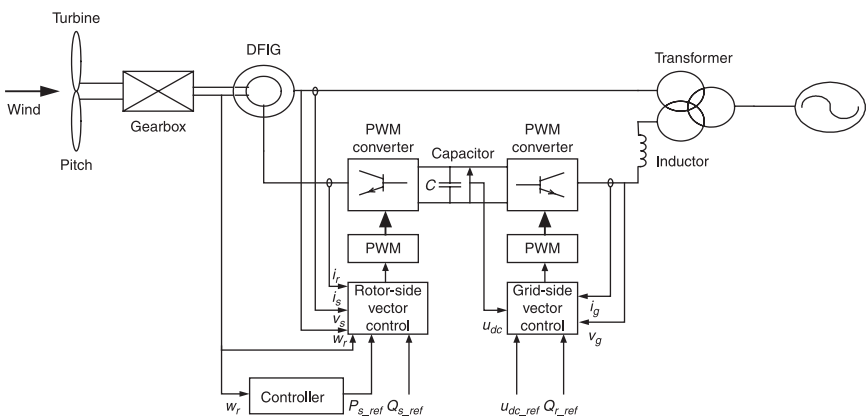

7.18 Wind turbine topologies with doubly fed induction generator (DFIG).

a reactive power compensator. A Vestas V90 DFIG wind turbine is shown in Fig. 7.1.

The drawbacks of a DFIG system are the following:

- A multistage gearbox is necessary in the drive train because the speed range for DFIG is far from a common MW turbine speed of 10–25 rpm. A gearbox is inevitably associated with some drawbacks, such as heat dissipation from friction, regular maintenance and noise.
- The control of the rotor power by means of a power converter requires an electrical connection between the rotating system and the stationary system; such a connection is given by carbon brushes (on the stationary system) pressing against slip rings (rotating system). These require regular maintenance, are a potential cause of machine failure and increase the electrical losses.
- In case of a grid voltage dip, the stator and rotor currents may dramatically increase for a short time (~100 ms). The high stator currents may cause high torque loads on the drive train. The insulated winding on the rotor may be subjected to a stress that may reduce the lifetime of the generator.
- The fault ride-through and post-fault restoration of DFIG requires complex control strategies.

7.5.3 Multistage geared high-speed generators and fully rated power electronic system

Cage rotor induction generators and synchronous generators may be integrated into power systems with fully rated power electronic converters as shown in Fig. 7.19. The wind turbines with a full-scale power converter between the generator and the grid give the added technical performance. Usually, a back-to-back VSC system is used to achieve full control of the active and reactive power, though with synchronous generators, diode rectifiers plus a boost may be used as the generator side converter (Chen and Spooner, 1998). In this concept, the operation speed may vary from zero to the maximum speed limit. The generator can operate at a wide variable frequency range for optimal operation.

In this configuration, the grid performance of the wind turbine system is largely determined by the power electronics and control; therefore, the system with different types of generators may have almost the same characteristics viewed from the grid since the generator is decoupled from the grid by the power electronic interface. The power electronic converter enables the system to control active and reactive power very fast. However, the negative side is a more complex system with more sensitive electronic parts. Also the losses in the converter are higher because all power is processed by the power electronic converter.

Compared with the fixed speed system, the SCIG in this concept has the flexible control with a variable speed operation for all wind speeds, better performances of

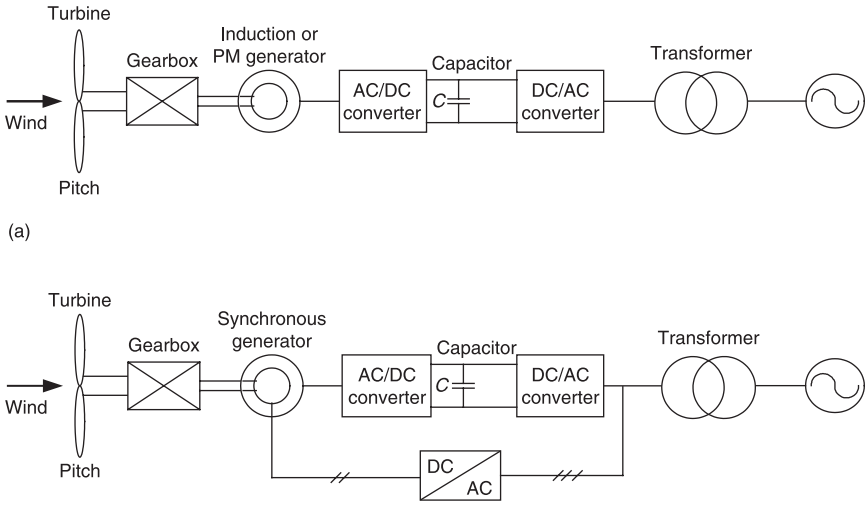

7.19 Wind turbine systems with high-speed generator and full-scale power converters: (a) PM synchronous and induction generator, and (b) field excited synchronous generator.

reactive power compensation, and smooth grid connection. However, its disadvantage is the high cost and the losses of the full-scale converter.

Compared with the multistage geared DFIG system, a multistage geared PM synchronous generator is a brushless generator and has better efficiency and grid-fault ride-through capability due to the fully rated power electronic converter, while the converter is larger and more expensive.

7.5.4 Direct-drive low-speed synchronous generator and fully rated power electronic system

Historically, gearboxes have been problematic for wind turbines. The fluctuating aerodynamic loads are difficult to accurately predict, therefore, large safety factors are often used. The gearboxes for large wind turbines are more expensive per kW than for smaller turbines because the torque, which is the key cost factor, increases more quickly than the power for a given increase in rotor diameter. The rotor torque tends to increase faster than the power, which only increases with the square of the diameter. This is because large wind turbine rotors operate at low rotational speeds (to limit aeroacoustic noise).

The direct-drive approach can simplify the drive train and nacelle systems, increase reliability and efficiency, and avoid the expensive gearbox and associated problems. Multipole systems with the synchronous generators without a gear are shown in Fig. 7.20(a) for a PM generator and Fig. 7.20(b) for a field-excited generator.

As discussed above, the fully rated power electronic system determined the grid performance of the system, while the simplified drive train could remove the cost and maintenance requirement of the gearbox, but the required diameter of the synchronous generator increases with the torque density.

Enercon produces direct-drive synchronous generators with electrically exited rotor windings; the generator size is large, for example, the Enercon E-66/15.66 1.5 MW, wound rotor, direct-drive wind turbine has a 5.3 m generator diameter (Cotrell, 2002). The Enercon E-112 wind turbine has a power capacity of 4.5 MW, a tower head mass of 500 tonnes and a generator diameter of 12 m (de Vries, 2005). While most other direct-drive designs are based on PM generator technology. An illustration of an ENERCON E-112 is shown in Fig. 7.21.

7.5.5 Hybrid gear drive medium-speed synchronous generator and fully rated power electronic system

Owing to the low-speed operation, direct-drive generators have large diameter, heavy weight and tend to be more expensive. With the increase of rated power levels and the decrease of wind turbine rotor speeds, these direct-drive systems are becoming even larger and more expensive, with more difficulties for transport and assembly. Between the conventional drive train with a three-stage gearbox at

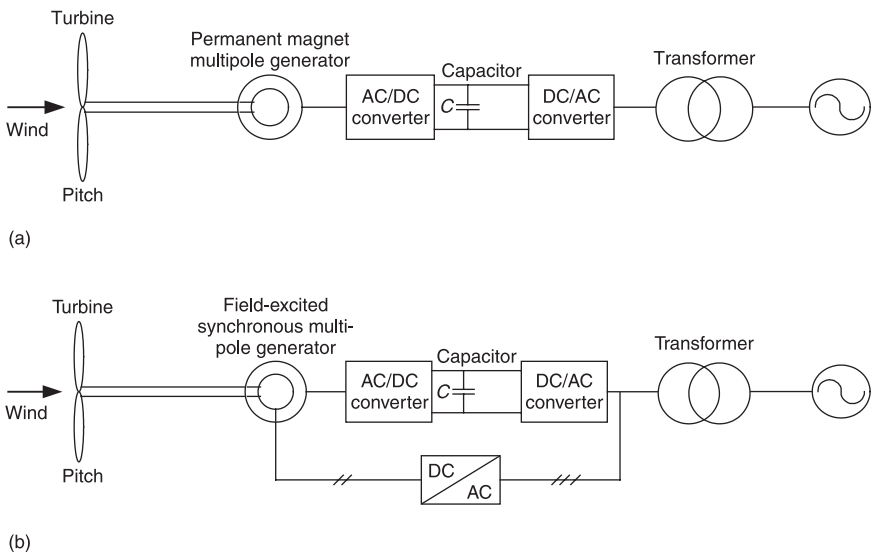

7.20 Wind turbine systems with direct drive generators: (a) multipole PM synchronous and (b) multipole field-excited synchronous generator.

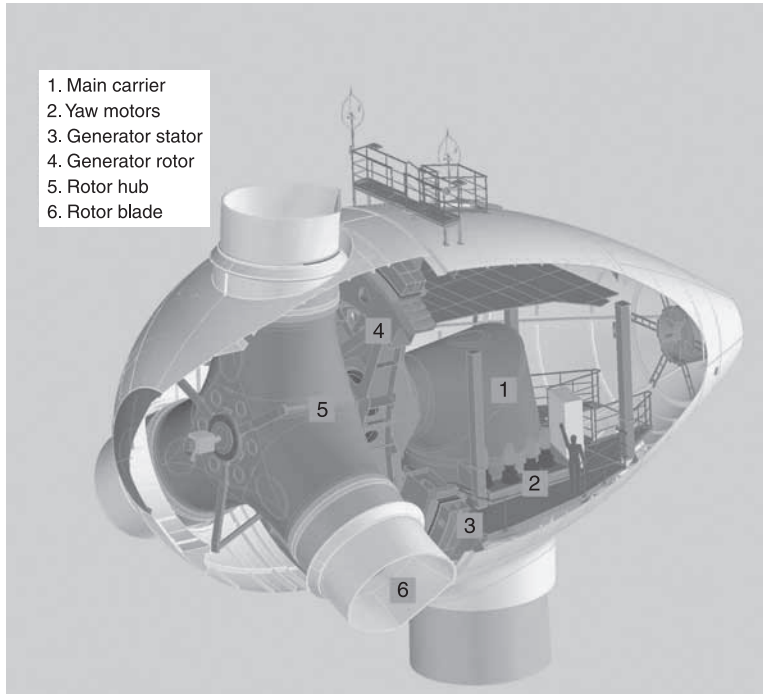

7.21 Enercon E-112 direct drive wind turbine (Courtesy Enercon GmbH).

MW scale and direct-drive solutions, a hybrid system may have a one- or two-stage gearbox with a medium-speed generator (as shown in Fig. 7.22). The intention is to have a simple and more reliable gearbox with a not very large size generator leading to a dimensionally balanced and compact drive train. In this wind turbine concept, the generator, gearbox, main shaft and shaft bearing may all be integrated within a common housing. The common generator–gearbox housing is supported by a tubular bedplate structure. This concept has lower generator costs than the direct-drive concept, and lower gearbox costs, and higher availability and operating reliability than the multiple-stage geared drive concept. An overall optimal system design may be obtained by an optimal design (Li *et al*., 2009). The aim is to minimize capital costs and maximize reliability to realize the goal of minimizing the cost/kWh of the wind power.

The Multibrid M5000 5 MW wind turbine is an example of a single stage gear drive train. It has a highly compact integrated slow-rotating drive system, comprising a single main bearing, a single-stage gearbox, and a medium-speed PM generator (58–147 rpm). With a tower head mass of 310 tonnes, the M5000 is a relatively light wind turbine rated around 5 MW (European Wind Energy Association, EWEA, 2009).

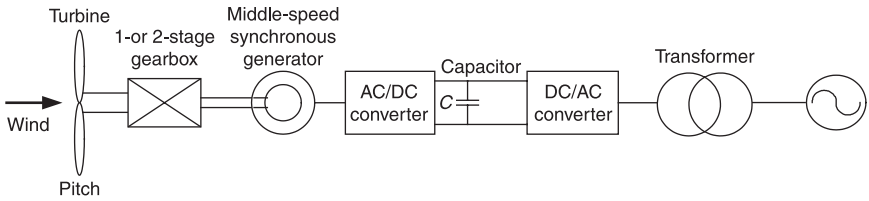

7.22 Wind turbine systems with a hybrid drive system.

7.5.6 Condition monitoring of electrical systems

Similar to the mechanical system, condition monitoring of the generator and power electronics is necessary for early detection of failures. The generator bearing can also be monitored by vibration analysis techniques, similar to those used with the gearbox. Furthermore, the condition of the rotor and stator windings can also be monitored by the temperatures.

Thermography may be applied for monitoring and failure identification of electronic and electrical components. Hotspots due to failure or malfunction of components or bad contact can be identified. The technique could be used for electrical systems such as the generator and power electronics. Also the measurements and analysis of voltage and current waveform can be used to identify some problems.

7.6 Generation system optimization

Various optimization methods can be used for optimizing a generator design. The optimization of different wind generators in variable speed wind generation systems using an improved genetic algorithm (IGA) is reported by Li *et al.* (2008). The objective function is the minimization of the generator system cost, including the costs of generator active materials, generator structures, gearbox, power electronic converters and other electrical subsystem, as given.

$$C_w = C_{g\_act} + C_{g\_str} + C_{con} + C_{subsystem} + C_{gear} \quad [7.6]$$

where

$C_{g\_act} = c_{cu} G_{cu} + c_{Fe} G_{Fe} + c_m G_m$ is active material cost;

c_{cu}, c_{Fe}, c_m are the unit costs of the copper, the active iron and the PMs, respectively;

G_{cu}, G_{Fe}, G_m are the weight of the copper, the active iron and the PMs, respectively;

C_{g_str} is the generator structure cost;

C_{con} is the cost of the power electronic converter;

$C_{subsystem}$ is the other electrical subsystem cost, which includes transformer, cable, switchgear and so on; and

C_{gear} is the gearbox cost (if present).

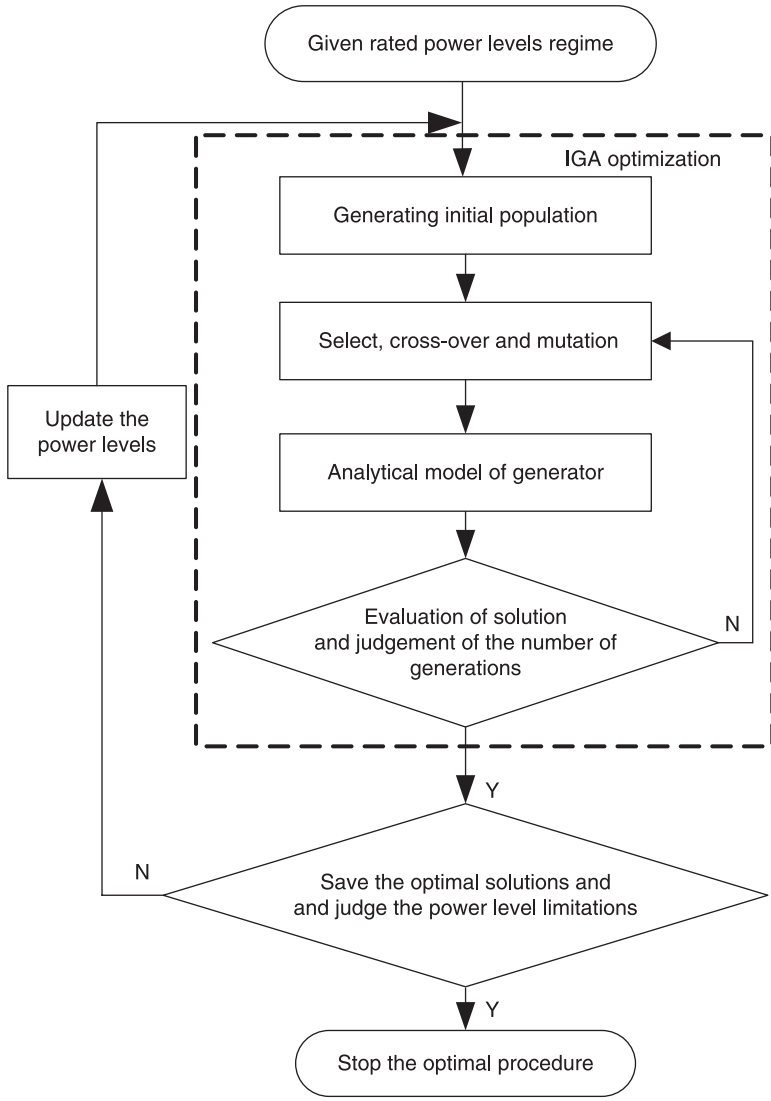

7.23 Flow chart of the optimization procedure.

In order to optimize the objective function (equation 7.6), six generator design variables are considered, including the air gap radius (r_s), the stator length (L), the slot height (h_s), the pole pitch (τ_p), the peak air-gap flux density ($\hat{B}_{g0}$), and the peak stator-yoke flux density ($\hat{B}_{ys}$).

Figure 7.23 shows the flow chart of the optimization procedure. Firstly, at a given rated power and a gearbox (if present), the initial population is randomly generated for the six variables within a specified range. Then, according to the

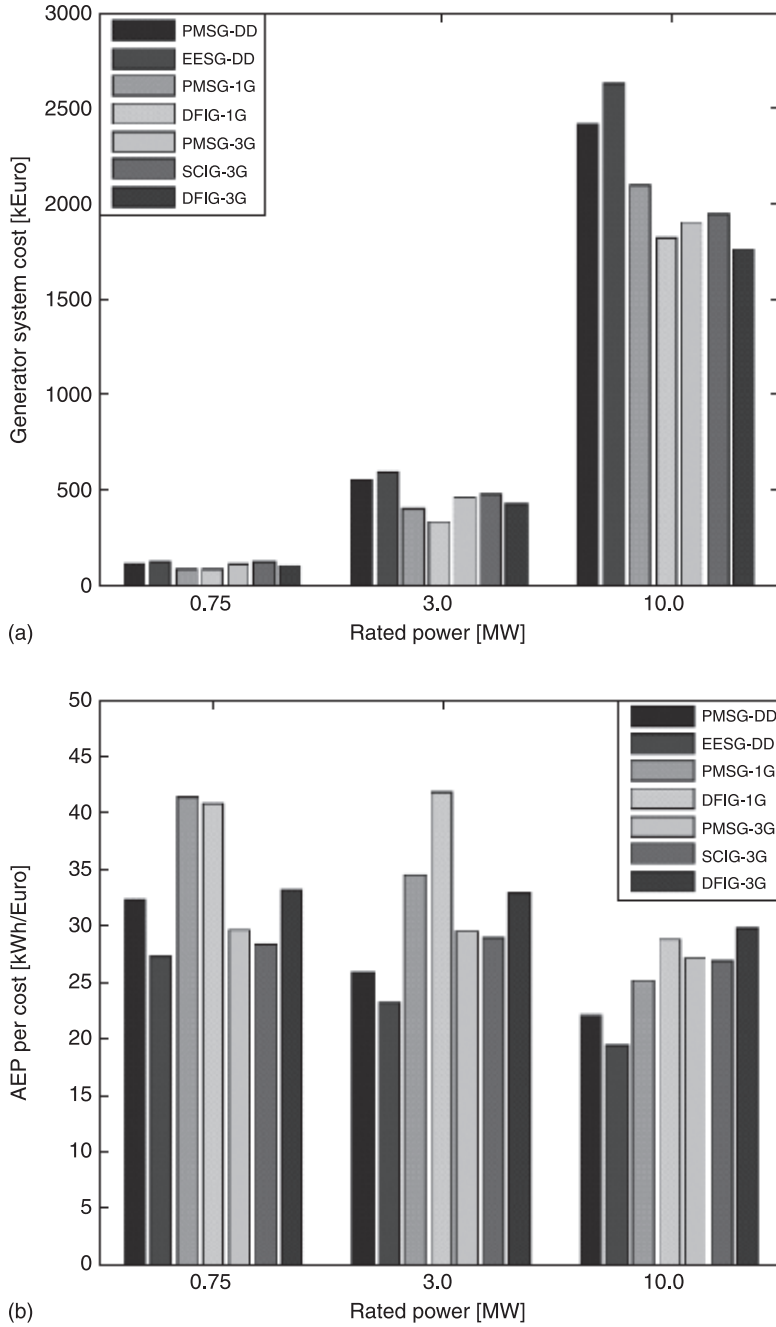

7.24 Comparison of seven wind generator systems: (a) system cost and (b) AEP per cost.

IGA models and the analytical models of the generator, the optimization is performed for minimizing the generator system cost under constraint conditions. Once the best design is obtained, the program will update the power level and repeat the optimization until the optimal designs in a given range have been finished. In addition, when the gear ratio is taken as an optimized variable, the optimal gear ratios of the most cost-effective system are also obtained.

A comparative design study example is given below. The considered generators include:

- squirrel cage induction generator (SCIG)
- doubly fed induction generator (DFIG)
- electrically excited synchronous generator (EESG)
- permanent magnet synchronous generator (PMSG).

Different drive train concepts are considered, such as direct drive (DD), single-stage gear (1G), and multi-stage gear (3G).

Some results of the generator system's cost and the annual energy yield (AEP) per cost are summarized in Fig. 7.24 for the rated powers of 0.75 MW, 3.0 MW and 10 MW. It can be seen that the single-stage geared wind generator system has the lowest cost in small and medium power ranges; however, the DFIG_3G system may be the cheapest when the rated power increases towards 10 MW, while the direct drive generator systems are most expensive. On the other hand, it can be seen that the single-stage geared wind generator systems (DFIG_1G and PMSG_1G) have the highest AEP per cost at small and medium rated power levels, but when the rated power increased towards 10 MW, the DFIG_3G and DFIG_1G systems seem to be more attractive solutions. In addition, it can also be observed that the EESG_DD system has the lowest AEP per cost for each rated power level. Although the optimization is a preliminary study, many factors are simplified; the developed procedure and methods could be a guide. It should be noted that an important factor for choosing the type of system is the grid performance which is not considered in the above economic evaluation.

7.7 Conclusion and future trends

This chapter has described drive trains of modern wind turbines. Various concepts of wind turbine system, including gears, generators and power electronics, are presented. Some work on the optimization of the electrical conversion system is also introduced.

An important distinction between different drive train types is related to the type of the generator. The simplest wind turbines is the combination of a gearbox with an induction generator, the stator winding being directly connected to grid. For a WRIG, changing the generator slip continuously and varying the rotational speed accordingly can be implemented either by dissipating the rotor energy in a

controllable rotor resistance (dynamic slip control system) or by exchanging power between the rotor and the grid through a partially rated frequency converter (DFIG system). The allowable speed variations are typically about 10% above synchronous speed for the dynamic slip control system, and ±30% around the synchronous speed for the DFIG. The latter alternative is very popular in modern multi-MW wind turbines. The variation in speed can lead to a higher aerodynamic efficiency, and reduced noise and mechanical stress. Asynchronous generators, including squirrel cage rotor, wound rotor with dynamic slip control and DFIG, are normally designed with a synchronous speed of 1500 rpm or 1000 rpm (two or three pairs of poles), so a multi-stage gearbox is required.

Gearbox reliability is a major issue, and gearbox replacement is quite expensive. A direct-drive system with a full-scale power electronic interface without a gearbox has good potential. The power electronic can also enhance the system performance.

However, a direct-drive multi-MW class wind turbine leads to large, heavy generators. An alternative hybrid drive approach, with one or two gear stages and a medium-speed generator, makes the generator dimensions reasonably small and improves the reliability by reducing the parts count. The degree of systems integration is also increased: the bearing, gearbox and PM generator may be fitted directly into the main cast-iron frame with the generator bearings being part of the gearbox assembly. The compactness could enable full enclosure of the sensitive components for high reliability. An optimization of the system could result in a cost-effective system.

The fundamental gearbox topology may also be improved; for example, Clipper Wind power developed a system having a gearbox with outputs to four PM generators. This design is a compact drive train with multiple-drive-path gearbox and decreases individual drive-path load, which eases erection and maintenance, and improves reliability by its inherent redundancies.

With the increase of wind turbine size and the installed capacity, the condition monitoring and fault detection attract more attention. The operational and maintenance cost of wind turbine compose a part of the overall cost, especially for offshore wind turbines. One way to reduce the cost, in particular for corrective maintenance, is the application of condition monitoring for early failure detection. The degradation or incipient faults can be detected and dealt with at an early stage before they result in more serious and costly failures; the consequent damage can be less to lead to the less expensive repair, shorter downtimes and lower revenue losses. Also, healthy turbines can be left to operate, thereby reducing outages.

A condition monitoring, aiming to identify the turbine health condition, can help to improve operational efficiency by conducting cost-effective maintenance, for example, the condition-based maintenance instead of the typical scheduled maintenance used in most industries today. However, it takes time to gain practical experience since component degeneration is a slow process.

Power losses in a wind turbine, especially during low power generation period, may be significant; reducing the power losses could have an important impact on raising the capacity factor. The improvements may be made by using new power electronic devices, circuits and control, permanent magnet generators and matching the turbine size for a particular site. Modular versions of the generation systems may also help increasing the productivity during low wind speed period.

Some other interesting systems are also under development, for example, a wind turbine which includes a closed loop hydraulic transmission system, where the wind turbine's rotor is directly coupled to a low-speed high torque hydraulic motor, which is pressure reversible to act as a pump, a 15–20 rpm digital displacement hydraulic pump, which then produces enough high-pressure fluid to power a hydraulically coupled hydraulic digital displacement motor that drives a generator at 1500 rpm. This continuously variable transmission allows the turbine rotor to be operated at its optimal speed for maximum power capture, that is, a synchronous generator can be run at a standard constant high speed. The drive train may be compactly located in the nacelle of wind turbine tower (Cunningham, 2009).

Another fluidic systems development is the Voith transmission system. In this concept, a synchronous generator directly coupled with hydrodynamically controlled gearbox is directly connected to the AC grid, without the application of any power electronics converter (Müller *et al*., 2006). Variable speed operation of the turbine is mechanically achieved by the gearbox with continuously controllable variable gear ratio. The Voith WinDrive system uses a hydrodynamic torque converter to provide the variable speed relationship between the shafts. WinDrive is essentially a mechanical solution to variable speed operation, based on a torque converter in combination with a planetary gear system. The fluid machine decouples the input and output shafts, absorbs input torque spikes, and provides damping. The added mechanical complexity and cost in the gear system may be compensated by elimination of the cost, mass and losses of the electrical power converter.

Most of the next generation wind turbines are expected to be applied in large wind farms, possibly situated offshore. Higher power turbines in the range between 7 MW and 10 MW are expected in the future. Future plants may support the grid by delivering not only fault ride-through capability, frequency, voltage and VAR control, but will also carry a share of power dispatch capability for the grid. Wind plants would become active power plants, instead of a simple energy source. Plants can be designed to perform some of the traditional duties of conventional power plants, and would trade some energy capture for grid ancillary services. Paying for this trade-off will require a lower capital cost and highly reliable system.

Power electronics have already played an important role in enhancing the system performance. The modern power semiconductor switches, including press-pack IGBT (PPI) or IGBT IPM (intelligent power module), IGCT or

SGCT, have been used in the power electronic converters such as multi-level converters, NPC converters. New silicon carbide (SiC) devices could allow operation at higher temperature and higher frequency, while improving reliability and lowering cost. New circuit topologies are to be developed to provide better control of power quality, enable higher voltages to be used, and increase overall system efficiency. Medium-voltage electrical systems may be used for optimizing multi-MW turbines to reduce the cost, weight and volume of turbine electrical components, as well as reduce electrical losses.

PMSGs, including a new type of generator with PM, HTS generators, multi-phase induction generators, have good potential for large wind turbines. Furthermore, high-voltage machines may also be developed for wind power generators to eliminate the step-up transformer.

In summary, the following possible further research and developments could be interest of the application in the wind turbine drive train power transmission system (gearbox, generator and power electronics):

- fewer gear stages or direct-drive system
- distributed gearbox topologies
- new drive train concepts (variable gear ratio systems, magnet gears)
- permanent magnet generators
- medium/low-speed generators and new type generators (HTS, etc.)
- medium-voltage equipment
- new semiconductor devices
- new high-power circuit topologies
- new control methods of power electronic systems
- system monitoring and fault prediction methods.

7.8 References

Amirat, Y, Benbouzid, M EH, Al-Ahmar, E, Bensaker, B and Turri, S (2009), 'A brief status on condition monitoring and fault diagnosis in wind energy conversion systems', *Renewable and Sustainable Energy Reviews*, 13, 2629–36.

Aydin, M, Huang, S and Lipo, T A (2001), 'Design and 3D electromagnetic field analysis of non-slotted and slotted TORUS type axial flux surface mounted permanent magnet disc machines', *IEEE International Electric Machines and Drives Conference*, IEMDC 2001, Boston, pp. 645–51.

Badrzadeh, B, Smith, K S and Wilson, R C (2009), 'Alternatives for high-power electronic converters, switching devices and electric machines for very large wind farms: a technological and market assessment', *EWEC2009 Proceedings*, 17 March 2009, Transmission and Distribution Division, Mott MacDonald Ltd, Glasgow, UK.

Carlson, R and Voltolini, H (2008), 'Grid synchronization of brushless doubly fed asynchronous generators in wind power systems', *IEEE, 7 encuentro de Energía, Potencia, Instrumentación y Medidas*, 16 y 17 de Octubre del 2008, Montevideo-Uruguay, PAG. 194

Chen, Z, Guerrero, M J and Blaabjerg, F (2009), 'A review of the state-of-the-art of

power electronics for wind turbines', *IEEE Transactions on Power Electronics*, 24(8), 1859–75.

Chen, Z, Hu, Y and Blaabjerg, F (2007), 'Stability improvement of induction generator-based wind turbine systems', *IET Proceedings on Renewable Power Generation*, 1(1), 81–93.

Chen, Z and Spooner, E (1998), 'Grid interface options for variable-speed, permanent-magnet generators', *IEE Proceedings on Electric Power Applications*, 145(4), 273–83.

Cotrell, J (2002), 'A preliminary evaluation of a multiple-generator drive train configuration for wind turbines', *Symposium of the 21st American Society of Mechanical Engineers (ASME) Wind Energy*, Reno, Nevada.

Cunningham, J (2009), *Hydraulic gearless transmissions for large wind turbines*. Available from: http://www.eurekamagazine.co.uk/article/20433/Hydraulic-gearless-transmissions-for-large-wind-turbines.aspx (accessed January 2010).

de Vries, E (2005), *Thinking bigger*. Available from: www.ewea.org

Eichler, M, Maibach, P and Faulstich, A (2008), 'Full size voltage converters for 5MW offshore wind power generators', *EWEC2008 Proceedings*, ABB Switzerland Ltd., Turgi, Switzerland.

European Wind Energy Association (EWEA) (2009), *Wind energy: the facts*. Available from: *http://www.ewea.org/index.php?id=91* (accessed January 2010).

Fogarty, J M (2004), 'Development of a 100 MVA high temperature superconducting generator', *IEEE Power Engineering Society General Meeting*, 6–10 June 2004, Denver, CO, Vol. 2: 2065–67.

Hameed, Z, Hong, Y S, Cho, Y M, Ahn, S H and Song, C K (2009), 'Condition monitoring and fault detection of wind turbines and related algorithms: a review', *Renewable and Sustainable Energy Reviews*, 13, 1–39.

Harrison, R, Hau, E and Snel, H (2000), *Large wind turbines*, John Wiley and Sons, Chichester.

Hau, E (2000), *Wind turbines*, Springer Verlag, New York.

Heege, P, Prats, J, Betran, L, Bastard, R, Santos, R and Castell, S D (2007), 'Impact of wind turbine drive train concepts on dynamic gearbox loads', *EWEC 2007*, 7–10 May, Milan, Italy.

Huang, S, Luo, J and Lipo, T A (1997), 'Analysis and evaluation of the transverse flux circumferential current machine', *IEEE Industry Application Society Annual Meeting*, New Orleans, Louisiana.

Lewis, C and Müller, J (2007), 'A direct drive wind turbine HTS generator', *IEEE Power Engineering Society General meeting*, 24–28 June 2007, Tampa, FL, 1–8.

Li, H and Chen, Z (2008), 'Overview of generator topologies for wind turbines', *IET Proceedings on Renewable Power Generation*, 2(2), 123–38.

Li, H, Chen, Z and Polinder, H (2008), *Numerical Evaluation of Various Variable Speed Wind Generator Systems*, UPWIND Project Research Report No D 1B2.b.3.

Li, H, Chen, Z and Polinder, H (2009), 'Optimization of multibrid permanent magnet wind generator systems', *IEEE Transactions on Energy Conversion*, 24(1), 82–92.

Müller, H, Pöller, M, Basteck, A, Tilscher, M and Pfister, J (2006), 'Grid compatibility of variable speed wind turbines with directly coupled synchronous generator and hydro-dynamically controlled gearbox', *Sixth International Workshop on Large-Scale Integration of Wind Power and Transmission Networks for Offshore Wind Farms*, 26–28 October 2006, Delft, NL.

Peeters, J L M, Vandepitte, D and Sas, P (2006), 'Analysis of internal drive train

dynamics in a wind turbine', *Wind Energy*, 9, 141–61. Available from: *www.interscience.wiley.com*

Pena, R, Clare, J C and Asher, G M (1996), 'Doubly fed induction generator using back-to-back PWM converters and its application to variable speed wind-energy generation', *IEE Proceedings on Electric Power Applications*, 143(3), 231–41.

Singh, G K (2002), 'Multi-phase induction machine drive research – a survey', *Electric Power Systems Research*, 61, 139–47.

Spooner, E and Chalmers, B J (1992), ' "TORUS": a slotless, toroidal-stator, permanent-magnet generator' *Electric Power Applications, IEE Proceedings B*, 139(6), 497–506.

Todorov, M, Dobrev, I and Massouh, F (2009), 'Analysis of torsional oscillation of the drive train in horizontal-axis wind turbine', *8th International Symposium on Advanced Electromechanical Motion Systems & Electric Drives, Joint Symposium*, Electromotion 2009, 1–3 July, Lille, France.

Zaher, A, McArthur, S D J, Infield, D G and Patel, Y (2009), 'Online wind turbine fault detection through automated SCADA data analysis', *Wind Energy*, 12, 574–93.

Zhang, J, Chen, Z and Cheng, M (2007), 'Design and comparison of a novel stator interior permanent magnet generator for direct-drive wind turbines', *IET Proceedings on Renewable Power Generation*, 1(4), 203–10.

Zhao, Y and Lipo, T A (1996), 'Modeling and control of a multi-phase induction machine with structural unbalance', *IEEE Transactions on Energy Conversion*, 11(3), 570–7.

8

Wind turbine control systems and techniques

T. VAN ENGELEN and S. KANEV, Energy Research Centre of the Netherlands (ECN), The Netherlands

Abstract: This chapter begins by discussing the sensor/actuator equipment of modern wind turbines. It then gives a detailed overview of the conventional control loops for rotor speed and power control at below-rated and above-rated wind speed conditions, as well as the transients between these two regimes. Advanced control options for fatigue load reduction are then reviewed, such as drive-train damping, tower fore–aft and sideward damping and blade load reduction.

Key words: wind turbine control, fatigue load reduction, sensors, actuators.

8.1 Introduction

Most modern wind turbines have a three-bladed rotor that operates with variable speed and has the possibility to adjust the setting angle of the blades for reduction of the captured aerodynamic power: the so-called pitch regulated variable speed (PRVS) wind turbine type. The PRVS wind turbine type is usually equipped with an electric system that allows adjustment of the generator torque to any desired value within a broad range of rotational speeds. In partial load conditions PRVS wind turbines can adapt the rotor speed to the wind speed in order to maximize power production. In full load conditions, the generator torque is used to keep the power production at its rated level. The adjustment of the setting angle of the rotor blades (blade pitching) enables to deal with slower wind speed fluctuations. A well-chosen combination of generator torque setting and blade pitching allows for reduced in-plane and out-of-plane load variations in comparison with constant speed wind turbines while operation on any desired speed and power level is possible. More refined methods for load reduction by dynamically influencing of the rotor aerodynamic behavior are undergoing a fast development trajectory.

Well-proven technology for wind turbine control involves servo units for pitch actuation and generator torque setting. Measurement devices for the rotational speed, pitch angles, generator power and tower acceleration are also in common use. The mapping of measurement to control signals nowadays occurs in an embedded process computer or PLC that is accessible via a high-level programming language like C or Structured Text. Feedback loops based on the mentioned sensing and actuation equipment enable to comply with baseline control requirements for production operation. Recent developments focus on add-ons to the baseline controller for load reduction. These comprise additional

actuation options such as individual blade pitching, variable edge geometry, synthetic jets, etc., as well as direct sensing of the blade loads or motions or even of the instantaneous inflow conditions.

The conventional wind turbine control involves regulation of the power yield and rotor speed control. In above-rated wind conditions, the generator power should lie as close as possible to the rated value. In below-rated wind speeds the rotor speed should 'track' the wind speed in order to gain maximum energy yield. This type of control is usually set up by a so-called torque/rotor-speed curve for generator control and proportional-integral (PI) feedback of the rotor speed for pitch angle control. The latter is only active in above-rated wind speeds and in case of any severe gust; it involves synchronized adjustment of the pitch angles of all blades (collective pitch control) and can also be implemented as proportional-differential (PD) feedback for pitch speed control. It is worthwhile to achieve so-called 'peak shaving' in the aerodynamic thrust just around the rated wind speed by already starting to pitch the blades at some rotor speed below the rated speed. This allows for significant peak thrust force reduction at the expense of just a slight energy loss. Excessive vibrations are to be avoided, so low-pass and band-stop filters are included to avoid undesired feed through of turbulence effects in the pitch actuators and unwanted excitation of the structural dynamics. An additional lead–lag filter is used for compensation of the dynamic behavior of the wake. Further, faster reaction to gusts can be achieved by feed-forward control of the estimated wind speed. For the design of the baseline control, a rather simple wind turbine model is sufficient, including simple rotor aerodynamics and structural degrees of freedom for the first deformation modes of the tower and the drive-train.

The aim of advanced control is to achieve significant reduction of the structural loads. The tower bottom loads can be reduced at and around the frequency of the first fore-aft and sideward deformation mode. Actuator signals are the collective pitch angles and generator torque, respectively. Proper band filters are very important in order to avoid interference between different control loops. When a gearbox is present, the vibrations in the drive-train are usually damped via band pass feedback of the rotational speed of the generator to the generator torque setpoint. The mitigation of blade loads at and around the rotational frequency (1p) is also a viable option, although the actuator loadings are high in the case of full-span individual blade pitching. Nevertheless, commercial implementations exist. Suitable measurement signals are the blade root bending moments, blade tip motions, rotor shaft bending moments or yawing and tilting torque on the nacelle. The design and stability analysis of such advanced control loops now requires a more elaborate aero-servo-elastic model, including at least the three deformation modes of the rotor at and around the first flapwise natural frequency, as well as the first deformation modes of the tower and the drive-train.

8.2 Instrumentation

The control loops, discussed in this chapter, require sensors for the measurement of the rotational speed on the generator shaft, tower motion and blade root moments, and actuators for adjusting the pitch angle of the blades and the torque of the generator. These devices are discussed in this section.

8.2.1 Sensors

This section discusses sensors for measurement of the rotational speed on the generator shaft, tower motion and blade root moments.

Rotational speed measurement

The rotational speed is measured for both power regulation and active damping of the first drive-train mode. It is common practice to measure the rotational speed with a rotary encoder on the generator shaft. This is a digital device that consists of a fixed part and a rotating part. The rotating part is equipped with a number of equidistant markers (usually a power of two) and is mounted on the generator shaft with a typical speed range from 750 to 1500 rpm. The fixed part usually contains three 'pulse factories', which generate N pulses per shaft revolution accompanied by a single pulse for detection of the reference position. The generator shaft position is thus measured with resolution $2\pi/N$.

Tower-top motion measurement

The sideward and fore–aft tower motions are usually measured with accelerometers, which yield the linear acceleration in the two directions. The basic principle consists of measuring the force that is required to accelerate a small measurement mass at the same rate as the object (in this case the tower top) itself. Different methods exist for measurement of this required force (Klaasen, 1986), which are discussed below in the context of control.

Mechanical transducers include a spring in order to realize a displacement between the measurement mass (m) and the measurement device housing. This relative displacement is measured with a strain gauge or a differential transformer and is converted to a force via the spring stiffness (s). A differential transformer exploits the principle of varying mutual inductance between two coils when the position of the relatively small-sized core changes. In both cases, a 'stable' (low impedance) device output voltage becomes available to be used for control. The mass–spring configuration puts an upper frequency limit on the measurable acceleration: up to ca. 10% of the natural frequency the required force is up to 98% proportional to the acceleration of the object with negligible phase shift (<1°) for exponential damping rates less than 0.1. The natural frequency is

$\sqrt{s/m}$. At higher frequencies, the dynamics of the transducer itself disturb the proportionality and cause phase shift. However, internal compensation may be included because of the known parameters of the measurement device.

Piezoelectric transducers include a piece of material that exhibits electrical polarization when externally loaded. Via its capacitance, a voltage is associated with the rate of electrical polarization. If so desired, the electrical polarization is available as the 'stable' (low-impedance) device output voltage. This can be realized in two ways. The first method uses only passive elements, viz. a resistor and capacitors, and performs straightforward amplification of the transducer voltage to the device output voltage (passive method). The second method exploits an operational amplifier as active element with a resistor (R) and capacitor (C) in the feedback loop in parallel configuration (active method).

Both methods put a lower frequency limit on the measurable acceleration. Above ca. 10 times the high-pass frequency (ω) of the overall measurement device, the device output voltage is more than 99.5% proportional to the required force for accelerating the device, and thus proportional to the acceleration of the object with small phase shift (5.7° at 10ω down to 0.6° at 100ω). The high-pass frequency amounts to 1/(RC) rad/s. At lower frequencies, the dynamics of the overall device disturb the proportionality and cause phase shift; internal compensation may be included but never allows for measuring constant acceleration levels. The lower the high-pass frequency, the higher the product RC. In the passive method, the capacity C can never significantly exceed the capacitance of the piezoelectric material piece while in the active method, C equals the capacitance to be chosen in the feedback loop of the operational amplifier. The resistance R in the passive option can never exceed the leakage resistance while in the active option, R equals the resistance in the feedback loop, which can be much larger than the leakage resistance.

Blade load measurement

Conventionally, blade loads are measured with wire strain gauges. The measurement principle is simple: under elastic deformation conditions (regular operation) the strain in the blade surface is proportional to the blade loading and can be transformed straightforwardly into a 'stable' (low-impedance) device output voltage, which can be used for control. However, the layout of a wind turbine and the conditions in which a wind turbine works make installation difficult and operation unreliable while the potential danger of damage due to lightning is high. In addition, strain gauges are subject to calibration drift.

The calibration drift is not such a large problem since only variations in the load measurements around the mean value are used in the control loops. Of course, some way of calibration is still required as otherwise the operation range of the overall load measurement device can be exceeded.

Recent developments in the field of optical strain gauges are likely to overcome the problems with wire strain gauges. The measurement principle is based on

variation in the wavelength of light when it is reflected from the surface which deforms. Very high frequency data processing is required to generate the desired measurement signals with a reasonable sample rate. This measurement technique exploits fiber Bragg gratings (FBG), which allows separate measurement locations in one optical fiber. Thus, functionally separated sensors can be realized in an elegant way. In Wernicke *et al*. (2004), measurement results from wired and optical strain gauges on a rotating blade have been compared. The results with optical strain gauges were obtained with 16 FBGs on the blade. Both measurements showed sufficient accuracy but the results with optical strain gauges showed 0.07 s more delay. This delay is significant in the context of individual pitch control (IPC). However, the use of fewer FBGs is likely to reduce the delay to an acceptable value of 0.025 s or lower.

Local blade flow measurement

The local blade inflow measurements, i.e. the local angle of attack and local flow velocity, can be used for individual blade pitching to alleviate blade loads. A multi-hole pitot tube enables the measurement of both the flow velocity and the flow direction. The measurement is not a standard feature on wind turbines at the moment but a five-hole pitot tube, as described in Madsen (1991), has been previously used in an experimental set-up to directly measure local inflow conditions on a rotating wind turbine blade. Pitot tubes can be mounted at different radial positions to obtain the required measurements for the flow-based controller. A recommended radial position is 2/3 out from the blade root, as close to the tip as possible without influences from tip vortices.

The pitot tube is mounted on a tube equal to the length of the chord at the mounting position, on the leading edge of the blade, pressure side. The considerations in defining the length of the tube are:

- the measurement point should be as close as possible to the airfoil to measure angle of attack;
- there should be a minimum influence from the bound circulation; therefore it is placed further out from the airfoil.

The influence of bound circulation on the magnitude of the local velocity is insignificant, whereas the upward deflection of the flow is considerable at 1–2 chord lengths from the leading edge. The pitot tube is connected to four differential pressure transducers and the output gives the magnitude of velocity, the angle of attack and the sideslip angle.

8.2.2 Actuators

The control loops discussed in this chapter require actuators for the realization of desired values for the generator torque and the pitch angles of the rotor blades.

The full-span pitch actuators are dealt with as pitch *speed* servo systems instead of pitch *angle* servo systems. Within a pitch servo actuator, pitch *angle* control is always realized via a feedback loop that contains a pitch *speed* servo loop. This additional feedback loop significantly lowers the bandwidth for pitch angle control in comparison with pitch speed control. The higher bandwidth of the speed servos introduces much less parasitic dynamics in the pitch control loops and thus allows for stronger and faster control.

Generator torque control

The majority of wind turbines are equipped with an electric conversion system consisting of a doubly fed asynchronous machine, power electronics and control loops for the desired generator torque and reactive power in the stator of the machine. This kind of conversion system is commonly used in variable speed wind turbines that are equipped with a gearbox. So-called direct-drive wind turbines, which do not include a gearbox, are usually equipped with conversion systems based on a permanent magnet synchronous machine. A survey of electric conversion systems is given in Pierik *et al.* (2008).

Electric blade pitching

Electric actuators for pitch control are usually driven by a DC motor or a vector-controlled synchronous machine with permanent-magnet rotor (AC drive). In the context of control, the AC drive can be assumed to act as a DC motor.

Figure 8.1 shows the configuration of a pitch speed servo system with AC drive. The effect of aerodynamic forces on the blade torsion moment is not included in the figure. The feedback block for the speed servo controls the effective AC-motor current in an inner loop and the rotor speed in an outer loop.

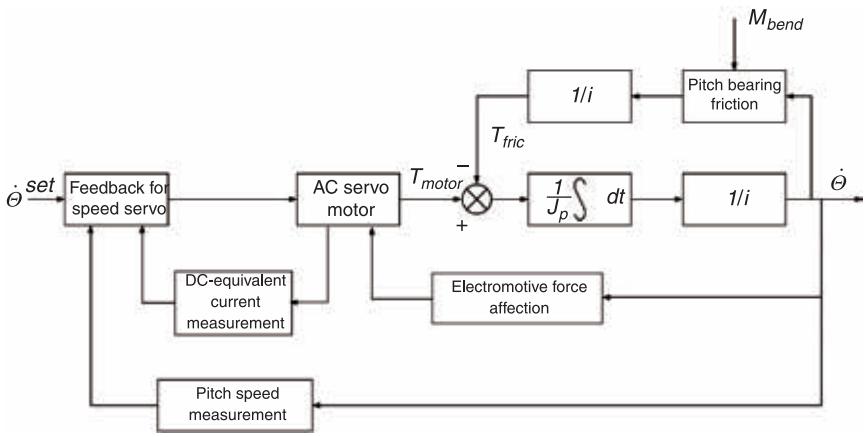

8.1 Pitch speed servo system with vector controlled AC motor.

The current control loop of the AC motor compensates for changes in the electromotive force caused by rotor speed variation. The resulting motor torque T_{motor} accelerates the pitch-wise blade rotation via a gearbox with transmission ratio i. The load inertia J_P as felt by the motor amounts to $J_M + J_B/i^2$, with J_M the moment of inertia of the rotor of the AC motor and J_B the pitch-wise inertia of the rotor blade. The friction torque T_{fric} caused by the pitch bearings counteracts this acceleration.

Hydraulic blade pitching

Hydraulic actuators for pitch control are usually equipped with a proportional servo valve that controls a double-acting hydraulic cylinder. The double-acting cylinder guarantees similar performance in both pitching directions. The proportional servo valve allows for fast control of the oil flow in a continuous range of values.

Figure 8.2 shows the layout of a hydraulic pitch speed servo actuator. The effect of aerodynamic forces on the blade torsion moment is not included in the figure. The compensation scheme translates the desired pitching speed $\dot{\theta}^{set}$ into a servo valve position v^r that gives rise to the desired oil flow ϕ_{oil}. A crankshaft mechanism converts the linear speed of the piston rod to the angular pitching speed with an approximately constant transmission ratio of $1/i$. The oil column in the hydraulic cylinder effectively behaves as a very stiff spring-damper system. A change in ϕ_{oil} causes a rate of change F_{hydr} in the force on the piston as long as its changed position has not yet fully compensated for the changed height of the oil column. These transient dynamics are very fast.

8.3 Control objectives

The control capability of a PRVS wind turbine adapts the operation to the wind conditions and reduces the varying loads that result from wind speed fluctuations. This section defines the considered control objectives.

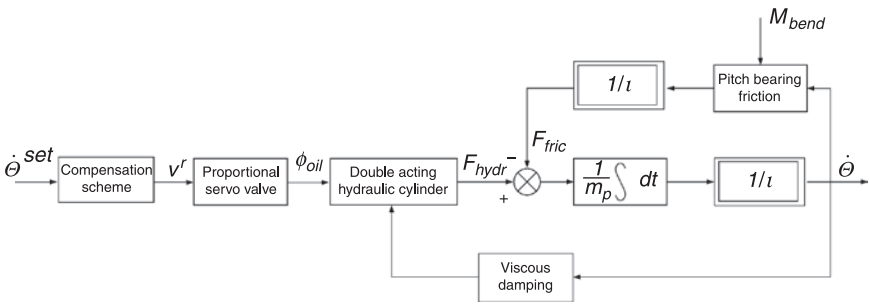

8.2 Pitch speed servo system with double-acting hydraulic cylinder and servo valve.

Though modern low-solidity horizontal axis wind turbines show good aerodynamic performance in a broad range of tip speed ratios, it remains worthwhile to adapt the rotor speed to the wind speed in order to achieve maximum power capture.

This can be accomplished by adjusting the generator torque. The generator torque setting also has a strong influence on the collective lead–lag modes of the turbine rotor that result from in-plane blade bending and drive-train torsion (drive-train modes). In addition, the poorly damped sideward tower bending modes are affected by the generator torque setting. So, from a control viewpoint, the generator torque setting has a threefold effect on the wind turbine behavior.

The aerodynamic power captured by wind turbines is limited in high wind speeds by pitching the blades simultaneously to a feathering position (collective blade pitching). In this way, the angle of attack is reduced at increasing wind speed. However, collective blade pitching also affects the rotor thrust, which in turn influences the fore–aft tower bending modes. This opens up the possibility of using blade pitching to enhance the damping of the tower fore–aft motion.

Another important aspect of wind turbine behavior concerns cyclic load variations due to rotational sampling of the wind field and the passage of the tower by the rotor blades. Wind shear and tower shadow give rise to harmonic bending moment variations in the rotor blades at rotor speed angular frequency and integer multiples of it, generally referred to as nP (n = 1, 2, . . .). Rotational sampling of atmospheric turbulence gives rise to stochastic blade load variations that have a broad frequency content with peaks centered around nP. The driving torque and thrust of a three-bladed rotor only experience the 3nP harmonic content of these (pseudo) periodic load variations. This also applies to the tilt and yaw moments on the nacelle. Individual (cyclic) blade pitching is a suitable way of reducing these loads (see e.g. Bossanyi, 2004; Larsen *et al*., 2005).

With these considerations in mind we can define aeroelastic control objectives which are focused on dynamic load reduction, stability and performance enhancement.

1. Adjustment of the generator torque based on the rotational speed Ω_{gen} for optimal tip speed ratio operation in partial load.
2. Collective pitch control based on the rotational speed Ω_{gen} for rated power operation in full-load conditions.
3. Adjustment of the generator torque based on the rotational speed Ω_{gen} for enhanced damping of the first drive-train mode.
4. Adjustment of the generator torque based on tower sideward acceleration $\ddot{y}$ for enhanced damping of the first sideways bending mode.
5. Collective pitch control based on tower fore–aft acceleration $\ddot{x}$ for enhanced damping of the first fore–aft bending mode in full-load conditions.
6. IPC based on blade flapwise moments $M_{z,1}$, $M_{z,2}$, $M_{z,3}$, for reduced flapwise blade loading and tilt-wise and yaw-wise nacelle loading.

Objectives 1 and 2 represent conventional wind turbine control objectives, while objectives 3 and 6 will be treated separately in the section on advanced control methods (section 8.5).

8.4 Conventional wind turbine control

The main control loops, called here *conventional wind turbine control*, concern the regulation of the power production and rotor speed control. Power control is achieved by both pitch control and electric torque control, at both below-rated and above-rated wind speed conditions. Figure 8.3 gives a block-schematic representation of the feedback structure for conventional rotor speed regulation and power control. The different blocks are explained below.

8.4.1 Generator speed filtering

The quality of the measured generator speed is crucial for generator speed feedback control. The following turbine effects disturb the generator speed and should be sufficiently suppressed by means of digital filtering, which usually includes a series interconnection of one or more of the following filters.

- Filter for 3p and 6p effects, resulting from tower shadow and rotational sampling. A typical filter for this is a fourth-order inverse Chebyshev type II filter with cut-off frequency of 2.5p rad/s and reduction of 20 dB.

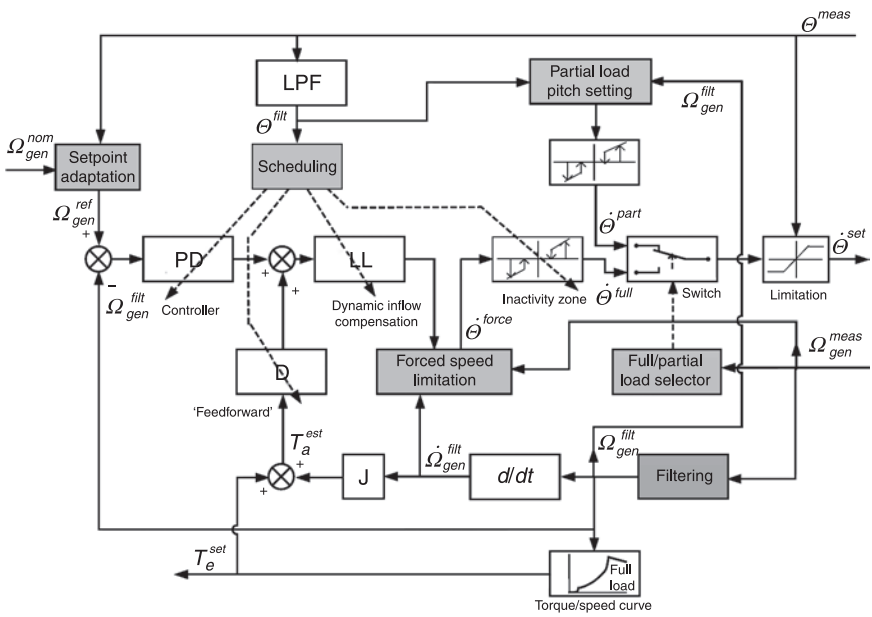

8.3 Block-schematic representation of the conventional pitch control.

- Notch filter at the collective lead–lag (drive-train) frequency, e.g. a second-order elliptic filter with stop-band of 10% around the drive-train frequency, 30 dB reduction and 1 dB ripple.
- Notch filter at the first sideways tower frequency, such as a second-order elliptic filter with stop-band of 15% around the first tower frequency, 20 dB reduction and 1 dB ripple.

Besides the positive effect of smoothing, the measured generator speed signal and preventing undesired actuation at the above-mentioned natural frequencies, these filters also introduce phase shift that has a negative effect on the achievable performance. For that reason, the filter selection/tuning process is turbine-specific and should be done carefully.

8.4.2 Below-rated control

In the *below-rated* region, the aim is to produce as much energy as possible. This is achieved by maintaining an optimal tip speed ratio λ_{opt}, and keeping the pitch angle at its *working position*, i.e. at the position where the power coefficient is maximal, that is

$$\theta_{opt} = \arg\max_{\theta} C_P(\theta, \lambda_{opt})$$

Assuming pitch speed (rather than pitch angle) as the signal sent to the blade pitch actuators, a simple proportional (P) compensator can be used to eliminate any deviation of the measured blade pitch angles with the setpoint value θ^{set}, as depicted in Fig. 8.4. The setpoint θ^{set} equals the working point value θ_{opt} up to a certain value of the generator speed, after which it starts to increase linearly with Ω_{gen}, reaching about 4°–6° when the generator speed rises to rated. This is called *peak-shaving* and its purpose is to reduce the axial force on the rotor at around rated wind speed conditions (where it achieves its maximum). This reduces the load on the tower bottom at the expense of a negligible power loss. This effect is realized by the block 'rotor speed dependent pitch angle setpoint' in Fig. 8.4.

Clearly, the best option to achieve optimal tip speed ratio would be to control the rotor speed Ω at the reference value $\Omega_{opt} = \lambda_{opt}.V/R$, where V is the undisturbed wind speed, and R is the rotor radius. However, because the undisturbed wind is

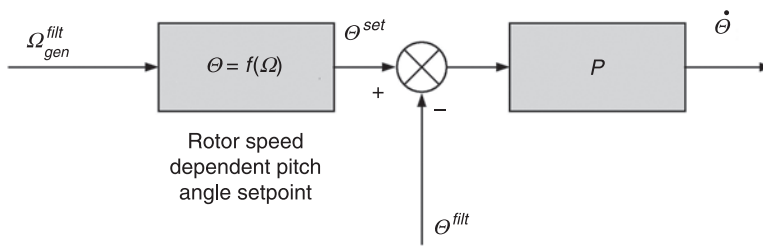

8.4 Pitch angle control at partial load conditions.

not measured, Ω_{opt} is unknown. Direct rotor speed control at below rated wind conditions would thus only be possible through some estimate of the undisturbed wind V. Instead, the usual approach is to set the generator torque demand based on the measured generator speed Ω_{gen} using the so-called optimal torque/speed-curve (QN-curve). The optimal QN-curve is formed by defining the maximal power as a function of the rotor speed (when $\lambda = \lambda_{opt}$),

$$P_{opt}(\Omega) = \frac{1}{2}\rho\pi R^2 C_P(\theta_{opt}, \lambda_{opt})V^3 = \frac{1}{2}\rho\pi R^5 C_P(\theta_{opt}, \lambda_{opt})\frac{\Omega^3}{\lambda_{opt}^3}$$

so that, by neglecting the drive-train dynamics ($\Omega_{gen} = i\Omega$, i being the gearbox ratio), the optimal generator torque would be

$$T_g(\Omega_{gen}) = P_{opt}\left(\frac{\Omega_{gen}}{i}\right)\Big/\Omega_{gen}$$

which represents the QN-curve. It can easily be shown that at constant wind speed V this generator torque control approach leads to optimal tip speed ratio and, hence, also maximal power. Dynamically, the power fluctuates around the optimal value due to wind variations. Several options have been proposed in the literature to improve the energy yield, including a reduction by a few percent of the optimal torque according to the QN-curve (Johnson *et al.*, 2004), tip speed ratio estimation (Bossanyi, 2000) or by achieving reduced effective rotor inertia by including a differential term in the generator torque set-point (Burton *et al.*, 2001). These approaches achieve 0.5–1% increase in energy capture. Still, due to the simplicity of the QN-curve for generator torque control and the fact that it works well in practice, it represents an often-used industrial solution.

8.4.3 Above-rated control

During *full load* operation, the conventional control objective is to keep the rotor speed at its rated value and produce rated electric power. To control the electric power at its rated value, the generator torque demand is set to

$$T_g = \frac{P_{rat}}{\Omega_{gen}^{rat}}$$

Here, the filtered generator speed Ω_{gen}^{filt} is used, as explained in Section 8.4.1. Filtering is used to avoid excessive excitation of the drive-train and the tower, as well as unnecessary actuation at frequencies 3p (and higher). It should be pointed out that this constant-power generator torque demand approach has a destabilizing effect on the generator speed, since generator speed increase leads to generator torque decrease, leading to additional increase in Ω_{gen}. The loop is stabilized with pitch control. However, due to the limited pitch bandwidth, this leads to increased rotor speed fluctuations. An alternative generator torque control approach is to

keep it at its rated value, i.e. $T_g = \dfrac{P_{rat}}{\Omega_{gen}^{rat}}$, where Ω_{gen}^{rat} is the rated rotor speed. This gives rise to larger power fluctuations, but allows the pitch control algorithm to achieve better generator speed regulation.

Rotor speed regulation is achieved by controlling the blade pitch angle in such a way that the lift force is reduced by decreasing the angle of attack. This pitch control concept is called *pitch-to-vane* control in this chapter (another often-used term in the literature is *pitch-to-feather*). This is discussed in more detail below.

Full-load pitch controller design

For rotor speed control, the conventionally used controller structure is of PD type when pitch speed is used as the control signal (and PI type when pitch angle is the output of the controller). Without loss of generality, in this chapter the pitch speed is assumed to be the control signal.

For the design of the parameters of the PD controller, a very simple model of the rotational speed of the generator is sufficient:

$$J_t \dot{\Omega}_{gen} = T_a(\theta, \lambda) - T_g$$

Here, $J_t = J_g + i^2 J_r$ is the total moment of inertia, being the sum of the fast-shaft equivalent moments of inertia of the generator and rotor, and T_a denotes the aerodynamic torque, given by

$$T_a(\theta, \Omega, V) = \frac{1}{2}\rho\pi R^3 C_Q(\theta, \lambda) V^2$$

In this model for the rotor speed dynamics, the tower and drive-train are assumed rigid, which is acceptable since the controller will act on the *filtered* generator speed (see the previous section), from which dynamic influences from the tower and drive-train are removed. After linearization of the aero dynamic torque around a given working point (θ^*, Ω^*, V^*), the transfer function describing the dynamics from the pitch speed θ^* to the filtered generator speed Ω_{gen}^{filt} has the form

$$H_0(s) = \frac{\dfrac{\partial}{\partial\theta} T_a\left(\theta^*, \Omega^*, V^*\right)}{J_t s^2} . F(s),$$

where $F(s)$ represents the generator speed filtering, described in Section 8.4.1.

Usually, the working point (θ^*, Ω^*, V^*) at which the PD controller is designed is selected such that $\dfrac{\partial}{\partial\theta} T_a\left(\theta^*, \Omega^*, V^*\right)$ is maximal. When designing the controller it is important that the *data processing delay* τ (representing computer calculation time, measurement and actuation delay time) is also taken into account, so that the final model for PD controller design then becomes

$$H(s) = H_0(s)e^{-\tau s}$$

The parameters of the PD compensator, $C_0(s) = k_P + k_D S$, are selected to achieve the given desired gain and phase margins (typically a gain margin of 2 and a phase margin of 45°).

Gain scheduling

The PD compensator is designed for the selected working point (θ^*, Ω^*, V^*). In order to cover the whole operating region of the wind turbine, its coefficients are scheduled. To this end, the inverse of the aerodynamic torque sensitivity to pitch angle, $\frac{\partial}{\partial\theta}T_a(\theta,\Omega,V)$, is used. As the wind speed V is unknown, the idea is to define a gain-scheduling parameter (θ, Ω) such that, for all relevant wind speeds, rotor speeds and pitch angles

$$\mu(\theta,\Omega)\frac{\partial}{\partial\theta}T_a(\theta,\Omega,V) \approx \frac{\partial}{\partial\theta}T_a\left(\theta^*,\Omega^*,V^*\right)$$

The gain-scheduling parameter (θ, Ω) is derived by first choosing some two-dimensional polynomial, such as

$$\mu(\theta,\Omega) = \sum_{i=0}^{N_\theta}\sum_{j=0}^{N_\Omega} c_{ij}\theta^i\Omega^j$$

and then selecting the coefficients by least-squares fitting

$$c_{ij} = \arg\min \sum_{\theta,\Omega,V}\left\|\mu(\theta,\Omega)\frac{\partial}{\partial\theta}T_a(\theta,\Omega,V) - T_a\left(\theta^*,\Omega^*,V^*\right)\right\|_2$$

Sufficient accuracy is usually achieved for $N_\theta = 2, N_\Omega = 1$. The final gain-scheduled PD controller becomes

$$C(s) = \mu\left(\theta,\frac{\Omega_{gen}}{i}\right)\left(k_P + k_D s\right)$$

Setpoint adaptation

Basically, the generator speed setpoint Ω_{gen}^{ref} is controlled at its rated value Ω_{gen}^{rat} for generation of rated electric power. In the higher wind speed regions, the pitch angle will be feathered and far away from the 'working position'. In case of sudden falling wind gusts, each rotor speed decrease will then cause loss of electric power, in spite of above-rated mean wind speed.

To prevent this loss of production, in the higher wind speed region the rotor speed setpoint can be raised slightly by a few rpm's, dependent on the pitch angle. Using the mechanism of 'kinetic buffering' (flywheel), rated power can be maintained longer during falling gusts.

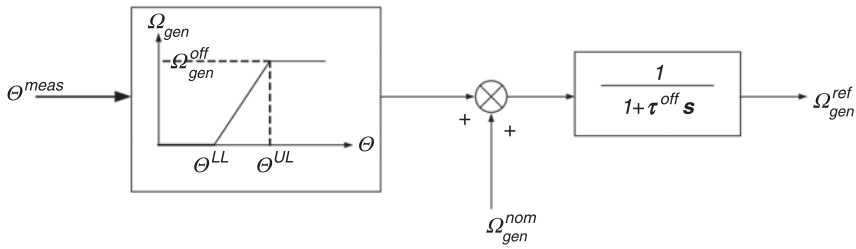

8.5 Generator speed setpoint adaptation.

To realize a smooth reference value towards the rotor speed controller, the setpoint offset Ω_{gen}^{off} is only implemented between the lower θ^{LL} and the upper pitch limit θ^{UL} in a linear way, using a first-order filter with large time constant (see Fig. 8.5). Setting Ω_{gen}^{off} to a value of 0.5–1 rpm, and θ^{LL}, θ^{UL}, to a value of 5° and 12°, respectively, usually improves the power production during sudden falling wind gusts. Another approach to 'kinetic buffering' is treated in Section 8.4.4.

Dynamic inflow compensation

Due to dynamic inflow effects, a fast variation of the blade pitch angle will result in a dynamic transition of the aerodynamic torque and trust to the steady-state values. Since this effect is neglected in the model used for the PD compensator design, it can be (partially) compensated for by extending the controller C(s) with the inverse of a linearized model of the dynamic inflow phenomenon. This is described in detail in van Engelen (2004).

Inactivity zone and limitation

Small pitch actions due to, for example, remaining noise (despite of rotor speed filtering), are undesired because they will cause considerable mechanical loads on the actuation system. To prevent this, an inactivity zone can be introduced, that performs the following operations before the pitch setpoint is sent to the actuators:

- ignore small pitching actions (inactivity zone);
- pass on effective pitching actions undisturbed (passing zone);
- avoid too many transitions into and out of the inactivity zone (hysteresis);
- enforced pitching when leaving the inactivity zone for compensation of temporal inactivity (catch up).

Further, the pitch speed is limited to its maximum values, and pitch actions are ignored if it would drive a blade beyond an extreme position:

- limit the pitch speed to its maximum values (pitch speed limitation),
- ignore pitching actions if maximum of minimum blade position is already reached (pitch angle limitation).

All the above-mentioned functions aim to reduce mechanical loads of the pitch actuation system without loss of control performance as intended by the pitch control algorithm.

The inactivity zone should be scheduled by taking into account the actual turbulence.

Forced rotor speed limitation

A maximum rotor speed has to be guaranteed in order to limit wind turbine loading and to minimize the variable speed range of the generator and converter. Commonly, exceeding the rotor speed alarm value will lead to intervention of the turbine supervisory control system and result in a turbine shut down. To prevent this whenever possible, the pitch control algorithm can include a 'forced rotor speed limitation' algorithm, a mechanism that ensures limitation of the rotor speed by forcing the rotor blades towards feathering direction. The principle of forced rotor speed limitation is shown in Fig. 8.6.

As soon as the switch condition is enabled, the pitch speed setpoint is set to the target value $\dot{\theta}_{FRL}$. It occurs as soon as the measured generator speed value exceeds the forced generator speed limit value, Ω_{gen}^{lim}, and the rotor speed is still increasing. To minimize loss of energy yield, the forced rotor speed limitation is disabled as soon as the generator speed starts to decrease or the pitch angle gets larger than some (variable) limit θ_{FRL}. Setting θ_{FRL} to a few degrees (e.g. 3°–4°) higher than the pitch angle at which the rotor speed limitation was enabled is usually sufficient.

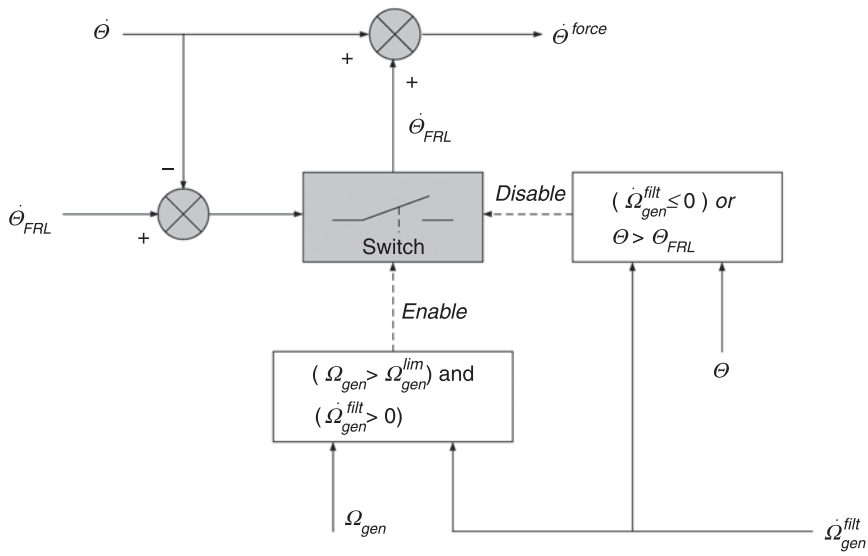

8.6 Principle of forced rotor speed limitation.

Feed-forward control of estimated wind speed

The principle of wind speed feed-forward control is based on the estimation of a rotor effective wind speed from rotor speed measurements. The purpose is to react better to wind gusts. The simplest way to estimate the wind speed is through the reconstruction of the aerodynamic torque from the (low frequency) power balance,

$$\hat{T}_a = J_t \frac{\dot{\Omega}_{gen}^{filt}}{i} + T_g + T_L$$

In the above equation, T_L represents losses. The wind speed can then be estimated by solving the following non-linear least squares problem:

$$\hat{V} = \arg\min_V \left\| \hat{T}_a - \frac{1}{2}\rho\pi R^3 C_Q\left(\theta, \frac{R\Omega_{gen}^{filt}}{iV}\right)V^2 \right\|_2$$

Note that in the estimation of the aerodynamic torque the filtered rotor acceleration is used. The reason for that is that the tower dynamics and drive-train dynamics are simply neglected in the equation for T_a, although they do affect the generator speed. By using the filtered generator acceleration $\dot{\Omega}_{gen}^{filt}$ instead of the measured one, these dynamics do not influence the aerodynamic torque estimate, and hence also have no effect on the estimated wind speed. Unfortunately, a delay is introduced by the filtering, which is effective in the corresponding control action. A better alternative is, therefore, to include the tower and drive-train dynamics in the estimation scheme. To this end, a Kalman filter can be used to either estimate the aerodynamic torque with a linear Kalman filter and then extract the wind speed suggested above (Østergaard *et al.*, 2007) or directly estimate the wind speed from a non-linear model, including the aerodynamics, with an augmented state extended Kalman filter. In Kanev and van Engelen (2009), a generalized framework is developed for estimation of blade-effective wind speeds by non-linear Kalman filtering, which can readily be simplified for the rotor effective wind speed estimation.

The estimated wind speed can be used to realize an additional pitch control action, that improves the turbine power production and its response to sudden wind gusts. A target pitch speed value $\dot{\theta}^{FF}$ is determined from the desired condition to maintain stationary rated power production,

$$P^{rat} = \frac{1}{2}\rho\pi R^2 C_P\left(\theta^{FF}, \frac{R\Omega_{gen}^{filt}}{i\hat{V}}\right)\hat{V}^3$$

Differentiation with respect to time gives

$$\dot{\theta}^{FF} = -\frac{1}{\dfrac{\partial C_P}{\partial\theta}\hat{V}^3}\left(\frac{\partial C_P}{\partial\Omega}\dot{\Omega}_{gen}^{filt} + \left(\frac{\partial C_P}{\partial V}\hat{V}^3 + 3C_P\hat{V}^2\right)\dot{\hat{V}}\right)$$

The estimated wind speed $\hat{V}$ is mapped to the pitch speed action $\dot{\theta}^{FF}$ through the feed-forward controller

$$C_{FF}(s) = -\frac{\dfrac{\partial C_P}{\partial V}\hat{V}^3 + 3C_P\hat{V}^2}{\dfrac{\partial C_P}{\partial \theta}\hat{V}^3} \cdot \frac{K_{FF}\tau_{FF}s}{\tau_{FF}s+1}$$

The differentiation time constant τ_{FF} and the gain K_{FF} should be carefully selected to guarantee stability and sufficiently smooth pitch actions. Time-consuming online computations are avoided when the fraction in the controller with the derivatives of the power coefficient is approximated offline by a polynomial through least squares fitting. $1/\tau_{FF}$ should be smaller than the 3p and drive-train frequencies, but high enough to create sufficient bandwidth. A typical value is τ_{FF} = 0.5 – 1 s. The gain K_{FF} must be smaller than 1 (typically 0.5–0.8).

8.4.4 Full/partial load selector

The transitions between full load and partial load should be implemented with care in order to prevent excessive transitions due to turbulence at mean wind speeds around rated. Transition from full to partial load could be triggered when the blade pitch angle has reached its working position value θ_{opt}, while the (filtered) generator speed is below rated and falling, that is

$$\left(\theta \le \theta_{opt}\right) \text{ and } \left(\Omega_{gen}^{filt} < \Omega_{gen}^{rat}\right) \text{ and } \left(\dot{\Omega}_{gen}^{filt} < 0\right)$$

The transition back to full load could be effected whenever the generator speed exceeds some given above-rated value, e.g. $\left(\Omega_{gen}^{rat} + 1 \text{ rpm}\right)$, or the generator acceleration exceeds some limit $\dot{\Omega}_{gen}^{\lim}$. The acceleration condition is added to prevent the generator speed from passing the rated speed with high acceleration as a result of wind gusts. The following condition could be used for transition from partial to full load:

$$\left(\Omega_{gen}^{filt} > \Omega_{gen}^{rat} + 1 \text{ rpm}\right) \text{ and } \left(\dot{\Omega}_{gen}^{filt} > \dot{\Omega}_{gen}^{\lim}\right)$$

The generator torque behavior at full load, which is based on the QN-curve described above, can be improved by extending the full load operating region as depicted in Fig. 8.7 (Schaak and van Engelen, 2004). The purpose is to keep rated power production even when the generator speed drops below its rated value, as long as the pitch controller works in full load. This gives rise to the extended full load operation curve for the generator in Fig. 8.7, which guarantees rated power yield even when $\Omega_{gen} < \Omega_{gen}^{rat}$ as long as the torque demand is below its allowed maximum T_g^{max}. The transient zone, depicted by the shaded area in the figure, is used for transition from the extended full load curve to the optimal-λ partial load torque curve. The generator torque leaves the extended full load curve whenever a full to partial load transition takes place, or when the generator speed reaches some minimal value $\Omega_{gen}^{full,min}$. The torque demand then follows a straight line from the point at which the extended full load curve is left to the point $\Omega_{gen}^{tr,min}$ on the optimal-λ curve.

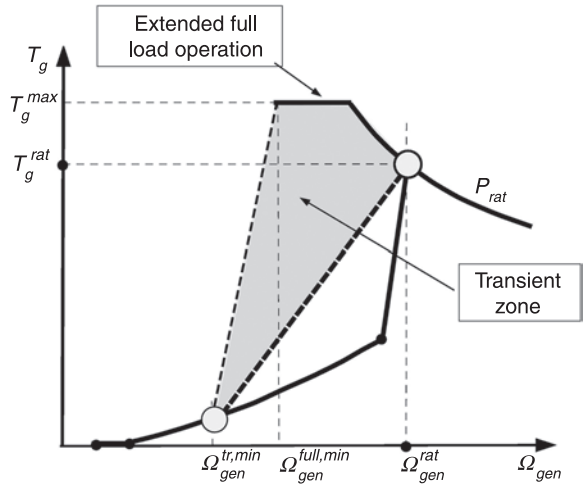

8.7 Generator torque full load region.

8.5 Advanced control for load reduction

We have already discussed the idea that generator torque variations can be used to reduce drive-train resonances and sideways tower vibrations, while collective pitch speed variations enable additional damping of fore–aft tower vibrations, and individual pitch actions can be used to reduce blade loads. All these control add-ons are active in different frequency bands and can thus be designed as independent control loops under the condition that separation is guaranteed by means of proper filtering. These load reduction control strategies are discussed below.

8.5.1 Drive-train damping

For variable speed turbines with a gearbox transmission, there are serious risks of severe rotor shaft vibrations. These vibrations can be reduced with the generator torque.

Figure 8.8 represents a schematic representation of the drive-train, in which the flexibility is modeled as a spring-damper pair interconnecting the moments of inertia of the rotor J_r and generator J_g (via the gearbox). This model can be used to describe the first drive-train mode, higher modes and the coupling with the tower 'naying' motion. The following equations of motion hold:

$$J_r\dot{\Omega} = T_a - c_d\gamma - k_d\dot{\gamma}$$

$$J_g\dot{\Omega}_{gen} = \frac{1}{i}\left(c_d\gamma + k_d\dot{\gamma}\right) - T_g$$

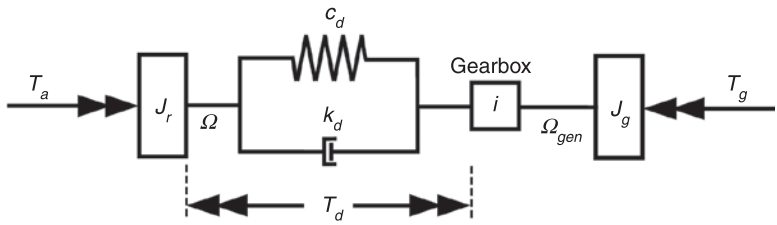

8.8 Block-schematic representation of the drive-train model.

where the torsion speed is defined as $\dot{\gamma} = \Omega - \frac{\Omega_{gen}}{i}$. Drive-train vibrations are defined as the varying shaft torsion.

The stiffness c_d and damping k_d parameter can be chosen such that they model the first coupled drive-train/collective lead–lag blade vibration mode. This coupled mode dominates the in-plane vibration behavior.

The above equations can be rewritten in the following form:

$$\frac{i^2 J_g J_r}{i^2 J_g + J_r}\ddot{\gamma} = -c_d\gamma - k_d\dot{\gamma} + \frac{i^2 J_g}{i^2 J_g + J_r}T_a + \frac{J_r i}{i^2 J_g + J_r}T_{gen}$$

This equation, in combination with the equation of motion for the generator speed above can be used to build a Kalman filter for the estimation of the torsion speed, $\hat{\dot{\gamma}}$, which can be used in a feedback loop for achieving the desired effective damping parameter k_d^{des}. This is achieved by the following feedback law:

$$T_{gen} = \frac{i^2 J_g + J_r}{i J_r}\left(k_d - k_d^{des}\right)\hat{\dot{\gamma}}$$

This drive-train damping control loop does not influence the low-frequency behavior of the power control loop if a high-pass filter is used to filter the low-frequency components of the measured generator speed. Setting the cut-off frequency sufficiently small yields close to zero-phase shift in the vicinity of the first drive-train frequency.

Since $\dot{\gamma} = \Omega - \frac{\Omega_{gen}}{i}$ and the variations in Ω are small compared to those in Ω_{gen}, it is often possible to feed-back Ω_{gen} instead of torsion speed (Burton *et al.*, 2001).

8.5.2 Tower fore–aft damping

Reduction of fore–aft movements (nodding) of the tower will become more relevant for larger turbines, due to the lower frequency of the first bending mode. The active damping of the first tower fore–aft mode is discussed below.

Consider the following simplified model for the first fore–aft bending mode of the tower, in which tower torsion, yawing effects and higher bending modes are neglected

$$m_t\ddot{x} + k_t\dot{x} + c_t x = F_{ax}(\theta, V - \dot{x}, \Omega)$$

$$F_{ax}(\theta, V - \dot{x}, \Omega) = \frac{1}{2}\rho\pi R^2 C_T(\lambda, \theta)(V - \dot{x})^2, \quad \lambda = \frac{\Omega R}{V - \dot{x}}$$

where x is the tower top position in the longitudinal direction, and F_{ax} is the axial force on the rotor. Note that the effect of the tower top speed $\dot{x}$ on the rotor-effective wind speed is also included in the expression for the axial force. Linearization of the axial force around a given working point (θ^*, V^*, Ω^*) gives

$$m_t\ddot{x} + k_t\dot{x} + c_t x = F_{ax,0} + \frac{\partial F_{ax}}{\partial \theta}\theta - \frac{\partial F_{ax}}{\partial V}\dot{x}$$

$$F_{ax,0} = F_{ax}(\theta^*, V^*, \Omega^*) - \frac{\partial F_{ax}}{\partial \theta}\theta^* + \frac{\partial F_{ax}}{\partial V}(V - V^*) + \frac{\partial F_{ax}}{\partial \Omega}(\Omega - \Omega^*)$$

By feeding back the measured tower top acceleration to the blade pitch speed via a proportional gain, $\dot{\theta} = K_{fa}\ddot{x}$, the following equation of motion is obtained:

$$m_t\ddot{x} + \left(k_t + \frac{\partial F_{ax}}{\partial V} - \frac{\partial F_{ax}}{\partial \theta}K_{fa}\right)\dot{x} + c_t x = F_{ax,0}$$

This allows for achieving some desired effective damping k_t^{des} through the feedback gain

$$K_{fa} = \frac{1}{\dfrac{\partial F_{ax}}{\partial \theta}}\left(k_t + \frac{\partial F_{ax}}{\partial V} - k_t^{des}\right)$$

A bandpass filter around the first tower frequency strongly reduces the influence on the rotor speed control loop. A possible choice for this filter is a fourth-order inverse Chebyshev type II filter with about 40 dB reduction. Its phase shift will be zero at the tower frequency. Since in practice the tower frequency is not exactly known (and may vary slightly), the phase shift of the filter will only be exactly zero if the actual tower frequency is estimated online from the zero-crossings of the measured tower top acceleration $\ddot{x}$.

Note that the feedback gain depends on $\dfrac{\partial F_{ax}}{\partial \theta}$ and $\dfrac{\partial F_{ax}}{\partial V}$, which in term vary with the working point (θ^*, V^*, Ω^*). Hence, gain-scheduling needs to be implemented.

8.5.3 Tower sideways damping

Reduction of sideways tower movement (naying) is important because it is naturally badly damped due to the absence of aerodynamic rotor damping. Active damping through the generator torque is discussed below.

Using similar simplifying assumptions as above, the following equation of motion describes the first sideways tower mode,

$$m_t \ddot{y} + k_t \dot{y} + c_t y = \frac{1}{h} T_g$$

where y is the sideways tower top position, and h is a parameter relating the generator torque to the resulting sideways force on the tower top. For notational simplicity in the above equation the same mass, stiffness and damping parameters are used as in the equation of motion in the fore–aft direction, although this need not be the case. An effective damping k_t^{des} can be achieved by feeding the measured sideways acceleration $\ddot{y}$ back to the generator torque signal through integral action,

$$\dot{T}_g = h\left(k_t - k_t^{des}\right)\ddot{y}$$

To prevent interaction with the feedback loop for power regulation through the AN-curve, two filters are needed: a band-pass filter around the first tower sideways eigen frequency in the damping loop, and an additional low-pass filter in the power loop. A first-order elliptic filter with a pass band of about 10% around the tower frequency, 20 dB reduction and 2 dB ripple is sufficient in the damping loop, and it has a favorable phase shift around the tower frequency. The low-pass filter in the power loop for power control should have as little phase shift at low frequencies as possible, and could be implemented as a high-order inverse Chebyshev filter with cut-off frequency about 15–20% below the tower frequency and 10dB reduction.

8.5.4 Blade load reduction

Modern wind turbines have the possibility of individually pitching the blades. This opens the road towards the use of advanced IPC algorithms for achieving fatigue load reduction. Different effects (such as tower shadow, wind shear, yaw-misalignment and rotational wind field sampling) result in blade loads at the rotational frequency (1p) and multiples of it (2p, 3p, etc.). Blade load reduction by IPC can be achieved by using additional measurements, such as blade root bending moments, shaft bending moments or tower-top bending moments measured at the yaw bearing. Below we will assume that measurements of the blade root bending moments are available, since these are rather common in modern wind turbines. The use of other moment measurements (at the shaft or at the yaw bearing) is straightforward.

The starting point is the closed-loop interconnection, depicted on Fig. 8.9, where C_{CPC} denotes the collective pitch control algorithms (including rotor speed control and tower fore–aft damping), and C_G is the generator torque controller (including power control, drive-train damping and tower sideways damping). The blocks in the shaded area in the figure representing the IPC controller will become clear in the following.

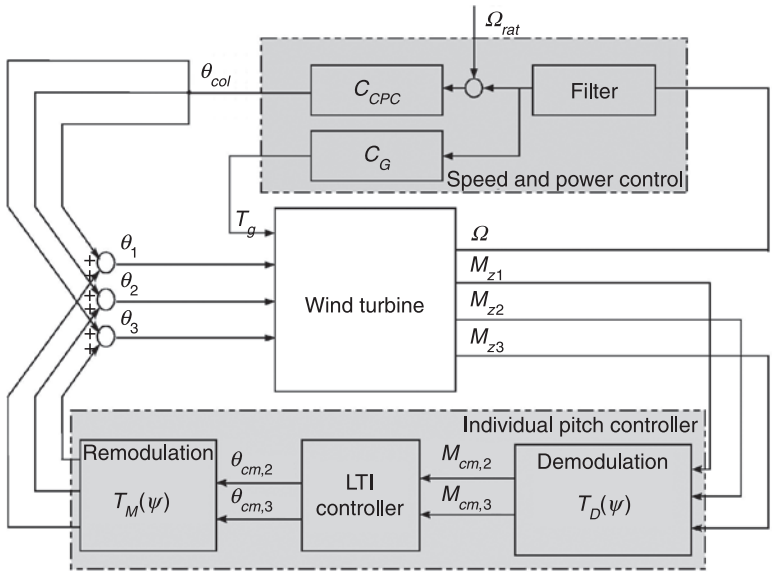

8.9 Wind turbine individual pitch control.

Suppose that the following linear parameter varying model describes the relevant dynamics of the wind turbine (possibly including the basic controllers C_{CPC} and C_G) from the three blade pitch angles θ_i, and axial blade effective wind speeds w_i, to the three flapwise blade root bending moments M_{zi}, $i = 1, 2, 3$.

$$\dot{x}(t) = A(\psi, p)x(t) + B(\psi, p)\theta(t) + E(\psi, p)w(t)$$
$$M_z(t) = C(\psi, p)x(t) + D(\psi, p)\theta(t) + F(\psi, p)w(t)$$

where ψ is the rotor azimuth angle,

$$M_z = \left[M_{z1}, M_{z2}, M_{z3}\right]^T,$$
$$\theta = \left[\theta_1, \theta_2, \theta_3\right]^T,$$
$$w = \left[w_1, w_2, w_3\right]^T.$$

The parameter $p = \{\Omega, \theta_{col}, w_{ax}\}$ defines the operating point of the turbine, wherein $\theta_{col} = \frac{1}{3}(\theta_1 + \theta_2 + \theta_3)$ is the collective blade pitch angle, and $w_{ax} = \frac{1}{3}(w_1 + w_2 + w_3)$ is the driving torque effective wind speed. Although not explicitly denoted in the model, the parameters $\psi = \psi(t)$ and $p = p(t)$ are functions of time. The blade-effective wind speeds w_i are fictitious signals defined in such a way that they approximate (in a statistical sense) the effects of full 3D longitudinal turbulence on the driving moments of the three blades (van Engelen, 2007).

For a fixed operating point $p(t) = p^*$, the above model represents a periodic system, which complicates the controller design process. However, by transforming the signals M_z, θ and w (and the states x), defined in the rotating coordinate frame, to the fixed reference frame, one can convert this model into a linear time-invariant (LTI) system. This so-called Coleman transformation is based on the matrix:

$$T_D(\psi) = \frac{2}{3}\begin{bmatrix} \sin(\psi) & \sin\left(\psi + \frac{2\pi}{3}\right) & \sin\left(\psi + \frac{4\pi}{3}\right) \\ \cos(\psi) & \cos\left(\psi + \frac{2\pi}{3}\right) & \cos\left(\psi + \frac{4\pi}{3}\right) \end{bmatrix}$$

which is used to demodulate the signals defined in the rotating coordinate frame into non-rotating *multi-blade coordinates*,

$$\left[\begin{array}{c|c|c} M_{cm,2} & \theta_{cm,2} & w_{cm,2} \\ M_{cm,3} & \theta_{cm,3} & w_{cm,3} \end{array}\right] = T_D(\psi)\left[\begin{array}{c|c|c} M_{z,2} & \theta_2 & w_2 \\ M_{z,3} & \theta_3 & w_3 \end{array}\right]$$

It has been shown in van Engelen (2006) and Van Engelen (2007) that this transformation gives an azimuth independent model in the resulting non-rotating coordinates,

$$\dot{x}_{cm}(t) = A_{cm}(p)x_{cm}(t) + B_{cm}(p)\theta_{cm}(t) + E_{cm}(p)w_{cm}(t)$$
$$M_{cm}(t) = C_{cm}(p)x_{cm}(t) + D_{cm}(p)\theta_{cm}(t) + F_{cm}(p)w_{cm}(t)$$

This model takes the form of an LTI system for a fixed operating point (i.e. for fixed p), allowing the use of conventional control design techniques. Once designed, the IPC controller should be connected to the original system using the Coleman demodulation matrix T_D and its (pseudo) inverse modulation matrix, given by

$$T_M(\psi) = \begin{bmatrix} \sin(\psi) & \cos(\psi) \\ \sin\left(\psi + \frac{2\pi}{3}\right) & \cos\left(\psi + \frac{2\pi}{3}\right) \\ \sin\left(\psi + \frac{4\pi}{3}\right) & \cos\left(\psi + \frac{4\pi}{3}\right) \end{bmatrix}$$

By actuating $\theta_{cm,2}$ and $\theta_{cm,3}$, the IPC controller adds up deviations around the collective pitch angle θ_{col}, which is controlled by the CPC (see Fig. 8.9). Moreover, it can be shown that the rotor tilt and yaw moments are approximately proportional to the second and third multiblade coordinates of the blade root flapwise moments. More specifically, when the influence of tensile and shearing forces and pitch-wise moments in the hub center are neglected, $M_{tilt} = \frac{3}{2}M_{cm,2}$ and $M_{yaw} = \frac{3}{2}M_{cm,3}$. For that reason, the second multiblade components of the input signals, $\theta_{cm,2}$ and

$w_{cm,2}$, are referred to as *tilt-oriented* components (having most effect on the rotor tilt moment), while the $\theta_{cm,3}$ and $w_{cm,2}$ are called *yaw-oriented* components.

Finally, it should be pointed out that, due to rotational wind field sampling, tower shadow and wind shear, the original blade effective wind speeds w_i contain frequency components at multiples of the rotational frequency, 1p, 2p, etc. This results in similar (np) components in the blade root moments M_{zi}. In multiblade coordinates, however, these (np) frequencies in w_i are demodulated into (3 np) frequencies in $w_{cm,2}$ and $w_{cm,3}$, resulting in 3p, 6p, 9p, etc. components in $M_{cm,2}$ and $M_{cm,3}$. More specifically, 1p components in M_z are transformed into static 0p tilt and yaw moments, 2p and 4p frequencies in M_z become 3p components in the fixed frame, 5p and 7p are modulated to 6p, and so on. Interestingly, 3 np components in the flap moments cancel out and have no influence on the rotor moments. For more insight into the effects of the Coleman transformation, see van Engelen (2006).

Hence, blade load reduction around the 1p frequency can be achieved by means of reducing the static (0p) rotor moments $M_{cm,2}$ and $M_{cm,3}$. Due to the negligible coupling between these at low frequencies, a single-input-single-output approach with two simple I-compensators is sufficient:

$$\theta_{cm,2} = \frac{k_2}{s} F_{IPC}(s) M_{cm,2},$$

$$\theta_{cm,3} = \frac{k_3}{s} F_{IPC}(s) M_{cm,3}$$

where $F_{IPC}(s)$ is a series of band-stop filters around the 3p and 6p frequency that prevents unnecessary propagation of these components in M_{cm}. A filter at the first tower frequency might also be needed. Note that constant $\theta_{cm,2}$ and $\theta_{cm,3}$ will yield, after modulation to rotating coordinates, cyclic variations of the three blade pitch angles around θ_{col}, shifted by 120°:

$$\theta_i = \theta_{col} + \sin\left(\psi + \frac{(i-1)2\pi}{3}\right)\theta_{cm,2} + \cos\left(\psi + \frac{(i-1)2\pi}{3}\right)\theta_{cm,3}$$

The controller gains k_2 and k_3 can be selected to achieve some desired gain margin m_g (e.g. $m_g = 2$). The phase margin cannot be influenced with k_j. To compute the gains, denote $T_j(s)$, $j = 2, 3$, as the transfer function from $\theta_{cm,j}$ to $M_{cm,j}$, and consider the open-loop transfer

$$L_j(s) = \frac{k_j}{s} F_{IPC}(s) T_j(s)$$

Due to the lack of poles of $L(s)$ in the open right-half plane (assuming, of course, stability of T_j), a standard Nyquist stability analysis indicates that gain-margin of m_g is achieved by selecting

$$k_j = \frac{1}{m_g \left| L_j\left(w_{180^o}\right)\right|}$$

where w_{180^o} is such that $p = \left\{\Omega^*, \theta^*_{col}, w^*_{ax}\right\}$.

Designed in this way, the IPC controllers will only achieve the specified design criteria at the working point where the model is valid. To achieve improved performance throughout the whole operation range of the turbine, a gain-scheduling approach can be used. Assuming that IPC is only active in full load conditions, the operating point is (statically) defined by θ_{col}. Hence, the gain of the IPC controller can be scheduled as a function of the collective pitch angle in such a way that the DC gain of the resulting open-loop transfer function remains constant. More specifically, let the IPC controller $C_{IPC}(s)$ be designed for linear the model $T_j(s)$ in operating point $p = \{\Omega^*, \theta^*_{col}, w^*_{ax}\}$, defined by θ^*_{col}, and let $T^l_j(s)$, $l = 1, 2, \ldots, L$, denote the dynamics from $\theta_{cm,j}$ to $M_{cm,j}$ defined at operating points with corresponding θ^l_{col}. By computing off-line the gains

$$K^l_{gs,j} = \frac{T_j(0)}{T^l_j(0)}, \quad l = 1, 2, \ldots, L$$

one can gain-schedule the IPC controller based on the current collective pitch angle $\theta_{col}(t)$ as follows

$$j = \left\{ l : l = 1, 2, \ldots L, \theta^l_{col} \le \theta_{col}(t) \le \theta^{l+1}_{col} \right\},$$

$$\alpha_j(t) = \frac{\theta_{col}(t) - \theta^j_{col}}{\theta^{j+1}_{col} - \theta^j_{col}},$$

$$C_{IPC,j}(s) = \left(\alpha_j(t) K^{l+1}_{gs,j} + (1 - \alpha_j(t)) K^l_{gs,j} \right) \frac{k_j}{s} F_{IPC}(s).$$

8.6 Future trends

At present, different IPC algorithms are available for the reduction of blade loads (Bossanyi, 2003; van Engelen, 2006). Although these can lead to large reduction of the 1p blade loads, the resulting cyclic pitching of the blades easily reaches the speed limits of the blade pitch actuators. For achieving 2p, 3p and higher blade load reduction with IPC, a much wider bandwidth of the pitch actuators is required (van Engelen, 2006).

To circumvent this bandwidth restriction, different actuation mechanisms that influence the local aerodynamic characteristics of the blades can be used, such as micro-electromechanical translational tabs and trailing edge flaps. Such actuation devices have a much broader bandwidth, allowing for higher harmonics control (2p, 3p, etc. blade load reduction).

So far, the question of achieving fatigue load reduction using sensors and actuators distributed over the blade span has received little attention. In the framework of the Danish project AdapWing research has been done to the application of trailing edge control surfaces for load alleviation (Basualdo, 2005; Andersen *et al*., 2006; Buhl *et al*., 2007). It has been demonstrated that (under

idealized conditions) the use of flaps throughout about 1/3 of the blade length, together with local flapwise deflection measurements, can achieve load suppressions of up to 63% (Andersen *et al*., 2006). An even larger potential is suggested to be achievable by using angle of attack measurements as input to the controller (Buhl *et al*., 2007). Angle of attack measurements can be obtained by using a five-hole pitot tube. A proof of concept of the so-called smart rotor blade was presented in van Wingerden *et al*. (2008), where the experiment included an elastic, non-rotating blade equipped with blade root flapwise bending moment sensor (piezoelectric patch) and a trailing edge flap actuator.

Although these first efforts show promising results, further research is needed on the (optimal) design of the control structures, on the stability and the interaction between the local control loops, the use of more sophisticated (multivariable) control design techniques, the interactions between the blades, and the effect on the loads of other turbine components, etc.

8.7 References

Andersen, P, Gaunaa, M, Bak, C and Buhl, T (2006), Load alleviation on wind turbine blades using variable airfoil geometry. *Proceedings of the European Wind Energy Conference and Exhibition (EWEC)*, 27 February–2 March, Athens, Greece.

Basualdo, S (2005), 'Load alleviation on wind turbine blades using variable airfoil geometry', *Wind Engineering*, 29(2), 169–82.

Bossanyi, E (2000), 'The design of closed loop controllers for wind turbines', *Wind Energy*, 3, 149–63.

Bossanyi, E (2003), 'Individual blade pitch control for load reduction', *Wind Energy*, 6, 119–28.

Bossanyi, E (2004), 'Developments in individual blade pitch control'. *Proceedings of special topic conference on 'the Science of Making Torque from Wind'*, April 2004, Delft, The Netherlands, pp. 486–97.

Buhl, T, Bak, C, Gaunaa, M and Andersen, P (2007), 'Load alleviation through adaptive trailing edge control surfaces: ADAPWING overview', *Proceedings of the European Wind Energy Conference and Exhibition (EWEC)*, 7–10 May, Milan, Italy, pp. 20–23.

Burton, T, Sharpe, D, Jenkins, N and Bossanyi, E (2001), *Handbook of Wind Energy*, John Wiley & Sons, Chichester.

Johnson, K, Fingersh, L, Balas, M and Pao, L (2004), 'Methods for increasing region 2 power capture on a variable speed HAWT', *Proceedings of the 23rd ASME Wind Energy Symposium*, 5–8 January, Reno, Nevada, pp. 103–113.

Kanev, S and van Engelen, T (2009), 'Wind turbine extreme gust control', *Wind Energy*, 13(1), 18–35.

Klaasen, K (1986), *Elektrotechnisch Meten* (in Dutch), Delftse Uitgevers Maatschappij B.V., Delft, The Netherlands

Larsen, T, Madsen, H and Thomsen, K (2005), 'Active load reduction using individual pitch, based on local blade flow measurements', *Wind Energy*, 8(1), 67–80.

Madsen, H (1991), *Aerodynamics of a horizontal-axis wind turbine in natural conditions*, Technical Report Risϕ-M-2903, Risϕ National Laboratory.

Østergaard, K, Brath, P and Stoustrup, J (2007), 'Estimation of effective wind speed', *Proceedings of the Conference on the Science of Making Torque from Wind*, 28–31 August, Lyngby, Denmark.

Pierik, J, Bauer, P and Zhou, Y (2008), *Wind Farm as Power Plant: Dynamic modelling studies*. Technical Report ECN-E-08-017, ECN Wind Energy, Petten, The Netherlands. Available from '*http://www.ecn.nl/docs/library/report/2008/e08017.pdf*

Schaak, P and van Engelen, T (2004), 'Torque control for variable speed wind turbines', *Proceedings of the European Wind Energy Conference and Exhibition* (*EWEC*), 22–25 November, London, UK.

van Engelen, T (2004), 'Dynamic inflow compensation for pitch controlled wind turbines', *Proceedings of the European Wind Energy Conference and Exhibition* (*EWEC*), 22–25 November, London, UK.

van Engelen, T (2006), 'Design model and load reduction assessment for multi-rotational mode individual pitch control (higher harmonics control)', *Proceedings of the European Wind Energy Conference and Exhibition* (*EWEC*), Athens, Greece. Available from *http://www.ecn.nl/publicaties/default.aspx?nr=ECN-RX-06-068*

van Engelen, T (2007), 'Control design based on aerohydro-servo-elastic linear models from TURBU (ECN)', *Proceedings of the European Wind Energy Conference and Exhibition (EWEC)*, 7–10 May, Milan, Italy.

van Wingerden, J, Hulskamp A, Barlas, T, Marrant, B, van Kuik, G, Molenaar, D-P, *et al*. (2008), 'On the proof of concept of a 'smart' wind turbine rotor blade for load alleviation', *Wind Energy*, 11, 265–80.

Wernicke, J, Shadden, J, Kuhnt, S, Byars, R, Rhead, P and Damaschke, M (2004), 'Field experience of fibre optical strain sensors for providing real time load information from wind turbine blades during operation', *Proceedings of the European Wind Energy Conference and Exhibition* (*EWEC*), London, UK.

9

Wind turbine tower design, erection and maintenance

M. VELJKOVIC, Luleå University of Technology, Sweden, M. FELDMANN, J. NAUMES and D. PAK, RWTH Aachen University, Germany, L. SIMÕES DA SILVA and C. REBELO, University of Coimbra, Portugal

Abstract: Higher towers for wind turbines are the main trend to achieve better effectiveness in the conversion of wind energy to electrical energy. This leads to an increasing contribution of the tower costs to the total investment costs. Optimization of the structural design by improving the design of connections in the tower is an important issue for the competitiveness of the wind energy sector. The basis of the design model of the flange connection and the possibilities of retrofitting are shown.

A short overview of the main structural solutions for towers and the most common criteria for the design are provided in the text.

Key words: towers, structural design, flange connection, retrofitting, fatigue.

9.1 Introduction

Wind is one of the most important sources of renewable energy. One of its main advantages is very low CO_2 emission during production. Wind power stations convert kinetic energy from wind into electrical energy. During the last few years, wind energy has had an increase of about 30% annually. The installed wind power capacity all over the world increased from 6 GW in 1996 up to 121 GW in 2008, of which about 60% was produced in OECD-Europe.

This continuing trend requires a growing production, which can be achieved by building towers higher than 80 m in regions with higher wind speeds and installing wind turbines with larger potential, more than 4 MW. The wind's power rises up to the power of 3 as a function of wind velocity. It is not only the height above the ground level that influences the wind speed. The location where the station is constructed and daily/seasonal changes play decisive roles, as well as long-term variations in wind speed over decades. The latter are not fully understood yet.

The height of the tower and the installed capacity have to be balanced against maintenance and tower production costs. The tower accounts for about 15–20% of the overall investment.

Most towers for wind turbines are fabricated of steel. Recently, concrete towers were promoted by a couple of companies, but their use is limited due to certain

conditions where the production costs are competitive. These conditions are mostly dependent on the transport costs and local building tradition as well as the price and availability of the steel. Steel towers may be either a part of a hybrid tower (lower part in concrete and upper part in steel) or solely as a lattice tower or a tubular tower which is the focus of this chapter because it is the most common design.

9.2 Lattice towers

9.2.1 General

Lattice towers were a common structural solution in the past, mostly because of the simplicity of design and construction. Even today they are rather common for towers up to 30 m high. The outer appearance of a lattice tower from a nearby place, larger footprint and maintenance issues are the main disadvantages. Although lattice towers become indistinct from far away, they have almost disappeared for aesthetic reasons. The main structural advantages, compared to tubular towers, are larger bending stiffness for the same amount of material, more flexible supply chain, less expensive transport to the site and simpler foundations (see Fig. 9.1).

For extreme situations, the very high towers with heights over 120 m, lattice towers are certainly the most competitive solution because they are not limited by their base diameter as most common tubular towers are.

9.2.2 Assembly

Lattice towers are constructed of many pre-assembled sections, which are hot-dip galvanised. They are bolted together on the construction site and lifted by a crane. Lattice towers are more costly and difficult to assemble than tubular towers. Complex terrain can complicate assembly because a staging area for assembly is necessary. The base section is bolted to the foundation.

9.3 Tubular towers

Most of the existing tubular steel towers are constructed as cantilevers and just a few guyed towers can be found. The latter are mostly used for down-wind rotors since in this case their low self-weight is advantageous. The foundations are rather expensive and the guys need more free area around the tower.

Cantilever tubular steel towers are mostly constructed as tapered towers, as can be seen in Fig. 9.2. This saves the weight of the steel used in the structure. The diameter decreases and the thickness of the steel shells is reduced for the higher segments of the tower.

9.1 Lattice tower. Photo by Marcus Klose, Germanischer Lloyd.

9.3.1 Tower erection

The towers consist of a number of sections, which are transported to the construction site where they are assembled using bolted connections (see Chapter 4). The prefabrication of the sections at the steel workshops shortens the time of the tower erection on site to just three to five days. But the transportation of the steel tubes limits the maximum base diameter of the tower to about 4.5 m; a small variation exists for different countries. At present the tower sections are connected by flange connections which require rather thick machine-produced rings, with small out-of-plate tolerances which make them a rather expensive detail. Recently

9.2 Tubular tower.

an alternative solution for in situ tower connection was proposed: using friction connections with long opened slotted holes instead of flange connections – which is more economical. The solution was developed within the European project HISTWIN (High Strength Tubular Tower for Wind Turbines, 2006–9). These types of connections are less prone to fatigue and less expensive to produce, which reduces total tower costs by about 10%. A major advantage of tower connections is that they are assembled inside the tower and all accessories are protected from the weather conditions.

9.3.2 Short towers

Small capacity turbines are often placed on short towers, mostly for private use, which may be erected in one piece. The tower structure may be either lattice or tubular, guyed or clamped tower. The tower is fabricated at a steel workshop and transported to the site.

9.3.3 Offshore towers

A fairly new area is a wind farm built offshore. The wind power is more constant with higher average speed and less air turbulence compared to onshore wind farms. All towers look alike above the sea level: a turbine placed on a steel tubular tower about 100 m high. However, the foundation of offshore towers differs depending on the water depth. They may be designed as fixed or floating support structures. The most common are fixed support structures including monopole, gravity-based and tripod structures (IEC 61400-3). The choice of the foundation structure is governed by soil conditions, water depth, type of wind turbine and installation/fabrication costs.

A monopole is a welded steel pile 4–6 m in diameter which penetrates into the sea bed. No preparation of the sea bed is required which is the biggest advantage of the system. One limitation is water depth: 25–30 m, above which the tower often becomes too flexible.

Gravity-based support foundation is suitable for shallow water up to 10 m water depth. It is often necessary to include post-installed ballast to stabilise the structure. The main advantage is that the structure can be fabricated onshore, transported to the installation site and installed as a whole.

Development of the foundation structures for deep water, 30–60 m deep, is mostly based on tripod and quadropod structures, the latter widely used in the oil/gas offshore industry.

Floating structures are considered for deep waters and where the fixed supports are too expensive due to work on the sea bed. Technical difficulties are related to the minimisation of the wave-induced motion and coupling of supported structure and wind turbine in order to satisfy requirements of static and dynamic stability.

Investment and maintenance costs are roughly twice the onshore costs, installations which leads to requirements for higher capacity turbines. Turbines with capacity of at least 5 MW are recognised as sufficiently economical.

The structural design of offshore towers is much more complicated than onshore towers. In addition to dynamic loads of the rotor, the loads from waves and ice pressure during wintertime in areas with colder climate have to be taken into account.

The installation of an offshore wind energy converter is much more complicated than onshore. These difficulties are not only the weather conditions but also the conditions of the sea, for example the swell. Firstly, the foundation, which is the most complicated part, is set into place. The tubular tower and the nacelle, which are pre-assembled onshore to keep the offshore work at a minimum, are installed faster. Finally the pre-installed rotor blades are fixed to the structure.

9.4 Load cases on towers for wind turbines

The definition and the quantification of load cases depend mainly on the wind conditions at the construction site. Turbine classes defined in IEC (2005), in terms

of wind speed and turbulence parameters, cover most practical applications independently of particular wind conditions. For a certain turbine class, the complete set of design situations can be defined, such as normal situations, fault situations, transportation, installation and maintenance situations. Within each design situation a number of load cases have to be considered. For each load case the analysis of ultimate loads (U) with reference to material strength, deflection or stability, and the analysis of fatigue loads (F) in the assessment of the fatigue strength are performed.

The load calculation and the load application on the towers for wind turbines are usually performed by the wind turbine designer using sophisticated tailor-made programs. These programs have to be capable of simulating the loads in the time domain considering the turbulent wind characteristics, the dynamic behaviour of the structural components as well as the operational behaviour of the wind turbine. Based on such analysis, the turbine producer provides load tables pertinent to tower design in the form of section loads at different tower heights.

For a free-standing tubular tower, the shear force in the wind direction and the corresponding bending moment are usually design driving. Considering that bending moment along the tower height depends directly on the shear force, the load case that delivers the extreme shear force becomes design driving for the whole tower except for the upper parts close to tower top where the load case resulting in maximum bending moments must be used.

More detailed information on design load cases (DLC) can be found in Chapter 4 of the design guidelines (GL Wind, 2004) and in Chapter 7 of the electrotechnical standard (IEC, 2005).

9.4.1 Analysis of fatigue loads

Time series of section resultants along the tower for different load cases based on numerical simulations of the adequate wind speed are made in time domain (Burton *et al*., 2001). To derive suitable loads for fatigue analysis the 'rainflow' counting is performed and Markov matrices are issued. However, information about the mean value of the section resultants contained in those matrices together with the load range and the number of cycles, is usually not necessary for performing fatigue calculations. The load cycles within predefined ranges are merged together, and the fatigue load spectrum is developed, which represents the number of cycles for each load range considered in Markov matrices.

Usually, a further simplification of the fatigue loading quantification is performed by converting the fatigue load spectrum into a damage equivalent load range ΔR_e. This is a constant load range which, in an equivalent number of cycles N_e, will produce the same amount of damage as the actual fatigue load spectrum with different load ranges ΔR_i and cycles N_i. The equivalent load range ΔR_e is defined as (Hansen, 2008):

$$\Delta R_{\mathrm{e}} = \left(\sum_{i=1}^{N} \frac{N_i \Delta R_i^m}{N_{\mathrm{e}}} \right)^{\frac{1}{m}} \quad [9.1]$$

where N is the total number of amplitude ranges. According to EN1993-1-9 CEN, 2005) $N_{\mathrm{e}} = 2 \times 10^6$ and values of m vary between 3 and 5, $m = 4$ being normally used. Turbine producers often provide the equivalent load range for $N_e = 2 \times 10^8$ cycles. Nevertheless, the conversion of the damage equivalent load range ΔR_e to the reference value given in EN1993-1-9 is straightforward.

When using damage equivalent moments in two orthogonal directions, these can be combined to obtain the resultant equivalent bending moment in order to compute the corresponding equivalent fatigue stress range $\Delta\sigma_{\mathrm{S,equ}}$ given in EN1993-1-9.

9.4.2 Design requirements

The most common failure criteria of steel tubular towers are: buckling failure due to extreme loading and fatigue failure. According to Burton *et al*. (2001) fatigue is more likely to be critical for pitch-regulated machines and at low-wind-speed sites. Pitch-regulated machines have increased thrust fluctuations above rated and reduced loading at standstill. On the other hand, in comparison to high-wind-speed sites, low-wind-speed sites tend to generate lower extreme wind gusts while maintaining the fatigue load spectra. Stress concentrations at the door opening must be checked. It is very common for fatigue loading to govern the design near openings. A fatigue strength curve, detail 71, according to EN1993-1-9, is used for a full penetration butt weld.

Local buckling

The main objective of the tower design is to make the cylinder thickness as thin as possible which often leads to design against local instability. Assuming a perfect geometry without any imperfections, the critical buckling stress of the axially loaded tubular tower is:

$$\sigma_{cr} = 0.605 \cdot C \cdot E \cdot \frac{t}{r} \quad [9.2]$$

where
C = coefficient due to length of the shell
E = E-modulus
t = wall thickness
r = radius of cylinder

Since in reality no structure has a perfect geometry, semi-empirical coefficients are determined for axial and bending loading (Eurocode 3; CEN, 2005). For axial loading this is:

For $r/t < 212$

$$\alpha_0 = \frac{0.83}{\sqrt{1 + 0.01\frac{r}{t}}} \quad [9.3]$$

For $r/t > 212$

$$\alpha_0 = \frac{0.70}{\sqrt{0.1 + 0.01\frac{r}{t}}} \quad [9.4]$$

And for bending loading:

$$\alpha_B = 0.1887 + 0.8113\alpha_0 \quad [9.5]$$

With these factors the ultimate strength ends up as:

For $\alpha_B \sigma_{cr} > \frac{f_y}{2}$

$$\sigma_u = f_y \cdot \left[1 - 0.4123 \cdot \left(\frac{f_y}{\alpha_B \sigma_{cr}} \right)^{0.6} \right] \quad [9.6]$$

For $\alpha_B \sigma_{cr} < \frac{f_y}{2}$

$$\sigma_u = 0.75 \alpha_B \sigma_{cr} \quad [9.7]$$

Eigen frequency of the tower

Dynamic loading on the wind tower is composed of periodic loading, mainly generated by the turbine rotation, and random loading due to the wind turbulence. Resonance effects due to the cyclic loading can be minimised by tuning the natural frequencies of the tower.

The rotor of a horizontal-axis wind turbine rotates in close proximity to the tower, since the clearance between the rotational plane and the tower axis is kept as small as possible to minimise bending moments induced by low-speed shaft and nacelle bedplate in the tower. Therefore, the most important periodic loading is induced by the blades when passing in front of the tower. This blade-passing frequency is equal to the turbine rotational frequency multiplied by the number of blades on the turbine rotor, in general three. On the other hand, periodic excitation due to the turbine rotational frequency appears very rarely, because this would mean that the individual blades of the rotor are different in shape or mass, which is usually avoided using tight tolerances.

To avoid resonant excitation of the tower by thrust fluctuations at blade-passing frequency or, to a lesser extent at rotational frequency, the lowest natural frequencies of the tower should be tuned to not coincide with those excitation frequencies. This constraint requires in general a specific check involving the mass

and stiffness of the tower since it is not met by the ultimate limit state design. According to the first natural frequency of the tower, it can be classified as (Burton *et al*., 2001):

- *Soft-soft tower*, for which the natural frequency is lower than the rotational frequency.
- *Soft tower*, for which the natural frequency falls between the rotational frequency and the blade-passing frequency.
- *Stiff tower*, for which the natural frequency is greater than blade-passing frequency.

When increasing the tower height, it becomes unfeasible to conceive stiff towers, since the greater the ratio between height and diameter, the smaller the stiffness of the tower. Therefore, soft towers have become the current solution.

Wind turbines develop their peak efficiency at one particular ratio between the rotational speed of the tip of a blade and the wind speed – the tip speed ratio. For a wide range of wind speeds the maximisation of efficiency is reached when two-speed or variable-speed wind turbines are used. The latter present several advantages when compared to fixed-speed or two-speed turbines (Hau, 2006).

In the case of two-speed operation wind turbines, the constraint on the first natural frequency can be stated in order to minimise the near-resonant dynamic amplification. Considering that the amount of viscous damping of the tower is relatively small, usually less than 2% of critical, and that the ratio between upper and lower rotational frequency is 1.5, the first natural frequency should be about 2.6 times the upper rotational frequency, and the second natural frequency should be greater than 3.36 times the same frequency in order to keep the amplification factor below 4.

For a three-blade turbine operating with continuously variable speed between the lower and the upper rotational frequencies, the minimisation of the dynamic amplification is achieved when the first natural frequency falls between the upper rotational frequency and three times the lower rotational frequency. Concerning the second natural frequency, the minimisation of dynamic amplification is achieved when it is greater than the upper blade-passing frequency. If for a two-speed operation, a minimum ratio of 3.36 is used then the amplification factor in the second natural frequency is kept below 4.

Consider, for example, the Repower MM92 wind turbine, for which the manufacturer gives operating limits of 0.13 Hz and 0.25 Hz, for the lower and the upper rotor speeds, respectively. With a possible error of 12.5%, the tower first natural frequency should fall in the range 0.281–0.341 Hz and the second frequency above 0.85 Hz in order to minimise dynamic amplification (Fig. 9.3). An experimental model identification of one of this type of towers (HISTWIN, 2010) delivered values of 0.34 Hz and 2.8 Hz, respectively, for the first and second tower natural frequencies.

Besides the stiffness and mass distribution of the tower, natural frequencies depend on the stiffness of the foundation and on the soil–structure interaction. Figure 9.4 illustrates the dependency of the first and second natural frequency

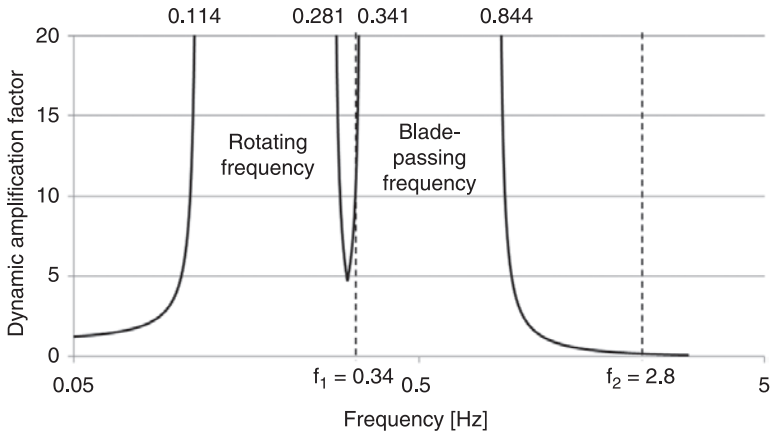

9.3 Dynamic amplification factor for % of critical damping and natural frequencies for Repower MM 92 wind turbine (80m high and 4,3 m base diameter steel tower.

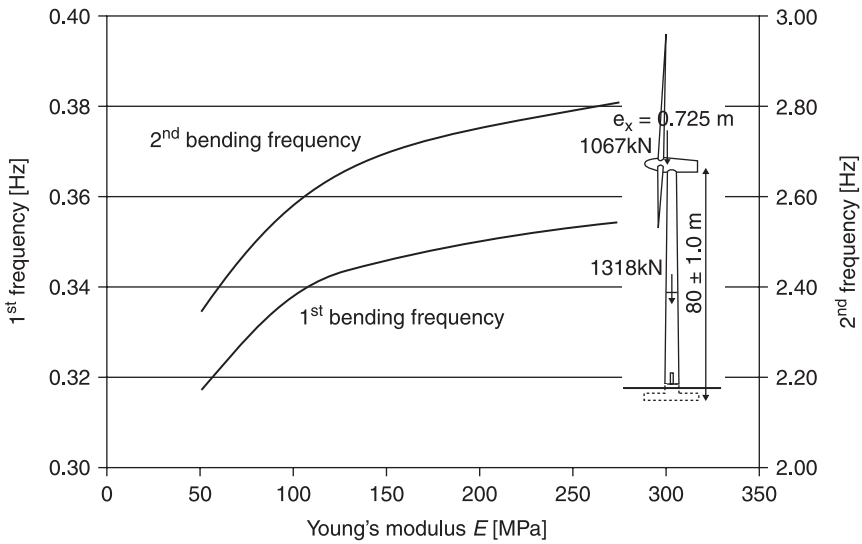

9.4 The first and second tower natural frequencies versus modulus of elasticity of the soil for Repower MM92 wind turbine.

of an 80 m tall wind tower on the modulus of elasticity E_s of the soil. To ensure allowable range for the integrated structure's first natural frequency a minimum rotational stiffness of the interaction of soil and foundation should be established by the wind tower fabricant. This implies a minimum subgrade reaction modulus that must be checked using adequate site tests such as SPT, cross-hole or seismic refraction tests.

9.5 Ring-flange connection

9.5.1 General

Bolted ring-flange connections are the most common type of joints in tubular wind turbine tower constructions. Fast assembly during erection and easy disassembling at the end of lifetime are reasons for that, especially for onshore towers.

Due to the high fatigue loading with about 10^8–10^9 cycles during lifetime, special focus has to be set on the fatigue resistance of the bolts as well as the welded joints between tower shell and flanges. For both details the type of the flange connection, which can be different, plays an essential role in the fatigue resistance.

9.5.2 Flange types

Conventional ring-flange connections

The detailing and specific geometry of a ring-flange has a significant influence on the fatigue behaviour of the connection. Single-sided, resp. L-shaped, ring-flanges, which can be regarded as state-of-the-art joints between tower segments, cause additional local bending moments in the bolts and in the shell. Figure 9.5 shows four different types of conventional L-shaped ring-flange connections. The main differences between the particular flange connections are summarised in Table 9.1.

Alternative solutions for bolted joints

The eccentricity of the L-shaped flange connections described above causes additional axial bolt forces, which in simple terms depend on the leverage between compressed flange area C, bolt load F_s and tower shell tension force Z (cf. Fig. 9.6). Furthermore, the bolts are subjected to bending moments in function of the opening angle φ of the joint, which additionally decreases the maximum load as well as the fatigue resistance of the joint.

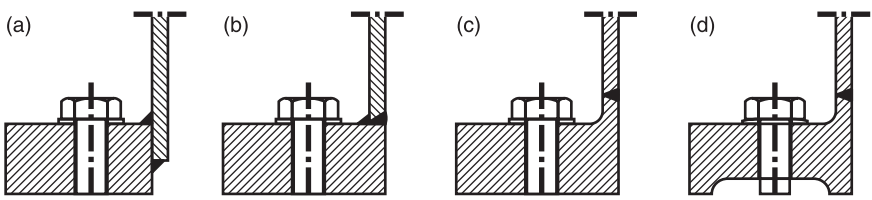

9.5 Scheme of different model types of conventional ring-flange connections: (a) slip-on flange, (b) welding-on flange, (c) welding-neck flange and (d) welding-neck flange with defined contact area.

Table 9.1 Comparison of different conventional flange-connection types

(a) Slip-on flange	(b) Welding-on flange	(c) Welding-neck flange	(d) Welding-neck flange with defined contact area
Common connection type for free-standing steel stack constructions and antenna towers	Used to be standard choice for tubular wind turbine towers	Recently standard connection detail for tubular wind turbine towers	Rarely used connection detail; machining of contact area has to be done for one flange of each flange connection
(+) Low production costs (+) High lamellar-tearing safety due to geometry and residual stress pattern in flanges (+) No joint preparation needed (–) Difficult to weld due to wide difference in material thicknesses; flange-sided weld penetration small (–) Low fatigue safety; detail category 40 according to Eurocode 3 Part 1-9	(+) Low production costs (+) Higher fatigue safety than flange type (a); detail category 71 according to Eurocode 3 Part 3-2 (o) Easy joint preparation (tower shell sided; can be done in the same production step as cutting of plate) (–) Difficult to weld due to wide difference in material thicknesses; flange-sided weld penetration small	(+) Easy to weld; equal material thicknesses of tower shell and flange neck lead to equal weld penetration on both sides of the butt joint (+) Higher fatigue safety than flange type (a); detail category 71 according to Eurocode 3 Part 1-9 (+) Good assessment of weld quality due to several inspection techniques to find inner and outer flaws.	(+) Defined bolt-load function $F_s(Z)$ due to clearly defined contact areas (+) More favourable bolt-load function compared to conventional flanges with full contact areas (Schmidt and Neuper, 1997) (+) Easy to weld due to equal shell thickness on both sides of the weld (+) Higher fatigue safety than flange type (a); detail category 71 according to Eurocode 3 Part 1–9
(+) Weld inspections only by surface inspection techniques	(0) Good assignment of weld quality due to several inspection techniques to find inner and outer flaws. However, it is difficult to find flaws of the weldroot.	(–) 30% higher flange production costs due to machining of the flange compared to solution (a) and (b) (Seidel, 2001)	Good assessment of weld quality due to several inspection techniques to find inner and outer flaws. (–) 45% higher flange production costs compared to solution (a) and (b) due to double-sided machining of the flange (Seidel, 2001)

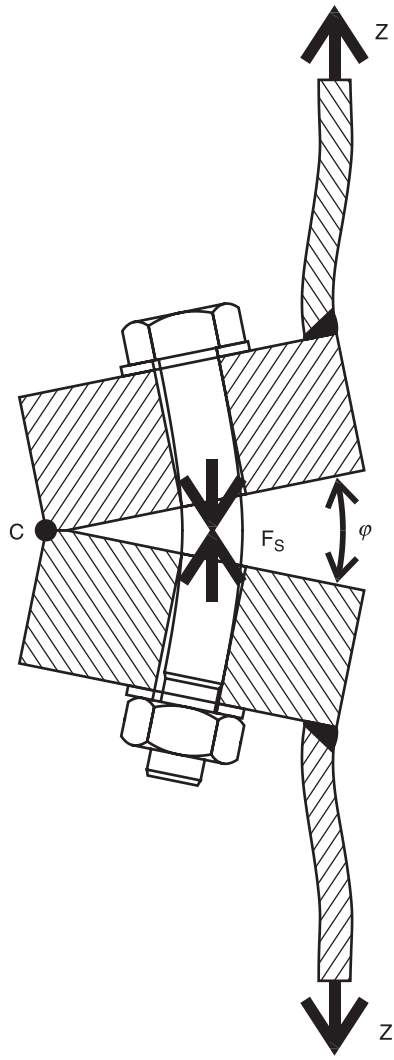

9.6 Scheme of opened joint.

Therefore, several alternative site-joint designs have been proposed to avoid or decrease additional loads and bending moments in the bolts. Figure 9.7 gives an overview of those different alternative proposals. However, such proposals do not show only advantages; in particular attention must be paid when having blind bolts to be prestressed.

Alternatives (a) and (b) represent 'tension-free' connection details developed by Schlemenat (2001), which have already been used for all kinds of industrial applications with great demands on tightness and fatigue safety of the joints, such

as steam generators. All internal forces of the shell are transferred from one segment to the other via contact pressure. The pre-loaded bolts of the connection are not subjected to significant additional axial tension or bending stresses (see also Schlemenat and Burmann, 2009). The application of tension-free joints for tubular wind turbine towers has been considered, but to the knowledge of the authors still not realised.

Figure 9.7(c) and (d) represent 'eccentric-free' flange systems from MECAL (1997), which lead to more favourable loading of the bolts compared to conventional ring-flange connections. One disadvantage of system (c) is the inclined boreholes, which are difficult to realise. Furthermore, for both flange connections (c) and (d) it is problematic that threads have to be drilled into the blind holes and the prestressing is uncertain. However, a realisation of the flange on wind turbine towers is not known, probably due to economic reasons (see also Jakubowski, 2003). Figure 9.7(e) shows a friction joint, developed within the research project (see Velskovic *et al*., 2010) in period 2006–2009 HISTWIN.

9.5.3 Design

General

The analytical determination of the real structural behaviour of a pre-loaded ring-flange connection of tubular tower segments under bending is rather complicated (see Jakubowski and Schmidt, 2005; Lehmann, 2003; Schaumann and Seidel, 2002). Currently the best way to consider all redistribution and load-shifting effects within the 3D structure is by numerical simulations. Thereby the entire joint is to be discretised by means of volumetric brick-elements. However, due to the large number of contact surfaces needed, such finite element simulations are too labour-intensive for the usual tower design. Therefore, common practice is to

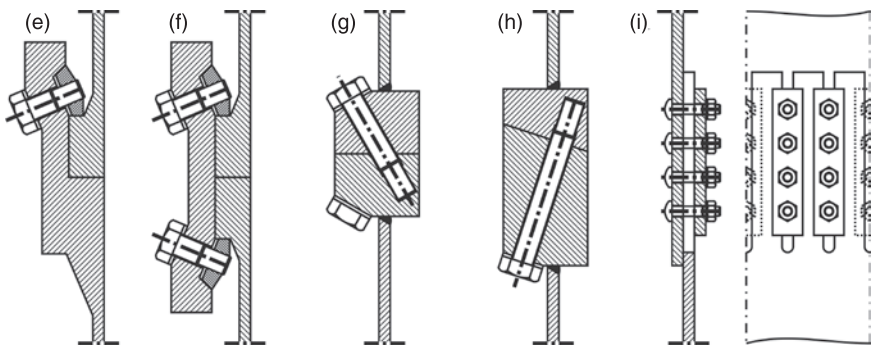

9.7 Proposal for alternative connection details for on-site segment joints: (a) and (b) 'tension-free' joint, (c) and (d) 'eccentric-free' joint and (e) friction joint.

use segment models, allowing for a simple and realistic determination of the relevant internal forces, such as bolt loads (see Fig. 9.8(a)). As a result of these segment models the tension force Z in the shell can be obtained by the integral of the axial stress σ_x over the cross-sectional area of the shell strip with c.

By means of this simplified 2D model the design for ultimate and fatigue limit state can be realised in a more reasonable way. Thereby the smaller the radius R of the tube the more the ring effects that have to be taken into account. The general procedure for both design verifications is described in sections 9.5.4 and 9.5.5, respectively.

For the fatigue limit state the determination of the exact bolt loads as a function of the shell force Z plays an essential role. The general behaviour of a pre-loaded bolt in L-shaped ring-flange connections can be described as follows (see Fig. 9.8(b)):

1 For segment forces $Z \leq 0$ the flange zone under compression (solid clamp) has the shape of a paraboloid of revolution (VDI 2230) and the bolt loads F_s keep almost constant at the level of F_v, thus $F_s \approx F_v \approx$ constant.
2 With increasing segment force $Z \leq Z_1$ the solid clamp begins to move in the direction of the flange edge and the bolt load F_s slightly increases.
3 From a certain segment force Z_1 onwards the shifting of the clamp solid develops faster and the flange connection begins to open, which leads to an expeditious increase of bolt load F_s.
4 On reaching segment force Z_2 the interface of the flanges stays only in contact at the flange edges, and the structural behaviour of the connection corresponds to the pure edge-bearing model illustrated in Fig. 9.6. The bolt load F_s increases linearly as a function of the tension force Z in the shell.
5 When reaching the elastic limit of the bolt (Z_3) the slope of the bolt-load function $F_s(Z)$ decreases and the connection reaches its limit due to plastification of the bolt.

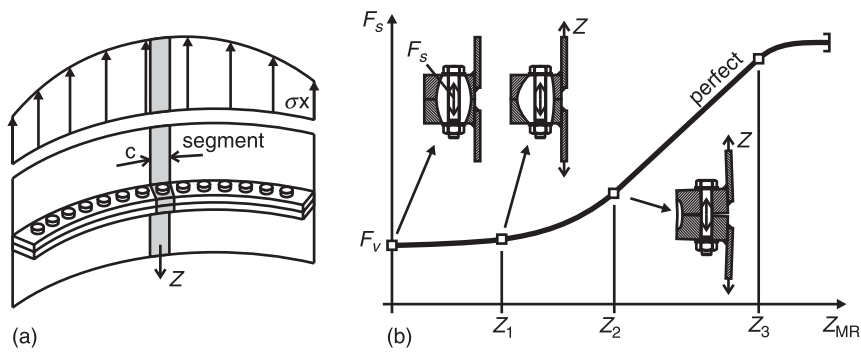

9.8 Segment model of L-shaped ring-flange connection.

Flange imperfections

Imperfections due to manufacturing, such as inclinations or gaps between the flanges, cannot be avoided. These imperfections can significantly influence the actual loads in the bolts in the region affected and thus the performance of the entire connection. Figure 9.9 shows the qualitative shape of the solid clamp after pre-loading of the bolt for different types of imperfection.

Jakubowski (2003) indicates the following three types of imperfection, which can occur in any combination:

1 rotation symmetric or local taper with flange-sided gap – case (b) in Fig. 9.9
2 rotation symmetric or local taper with tube-sided gap – case (c) in Fig. 9.9
3 local parallel gap – case (d) in Fig. 9.9

Local taper and parallel gap imperfections have the most detrimental impact on ultimate as well as fatigue resistance of the flange connection. Figure 9.10 shows the influence of these imperfections on the bolt load. The shift of bolt-load function $F_s(Z)$ considerably increases the load variation ranges in the bolt δF_s and thus the fatigue load. This fact should be considered to gain a conservative and prudent fatigue design.

9.5.4 Ultimate limit state

The verification of the ultimate limit state (ULS) is usually performed according to the plastic hinge theory. Even though bolts in ring-flange connections are pre-loaded, the pre-tensioning load in bolts is not to be considered in the ULS verification. According to Petersen (1988), three different failure mechanisms

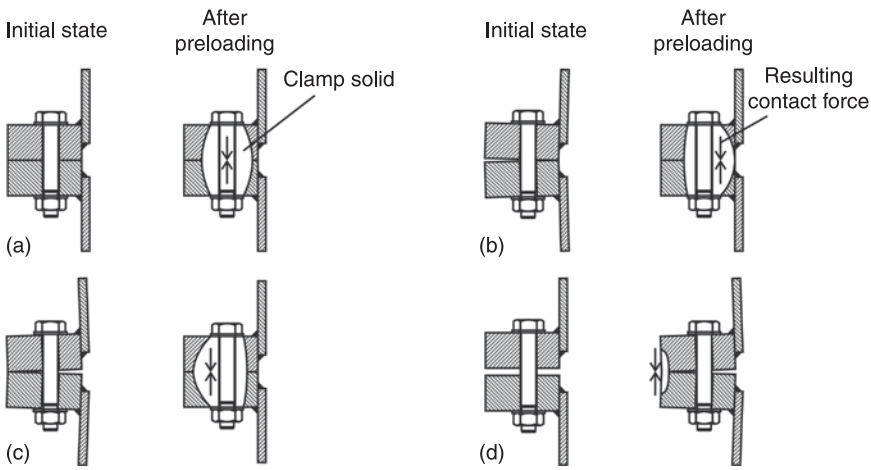

9.9 Qualitative shape of clamp solid in L-flange in a perfect (a) and different imperfect connections (b–d) (Jakubowski, 2003).

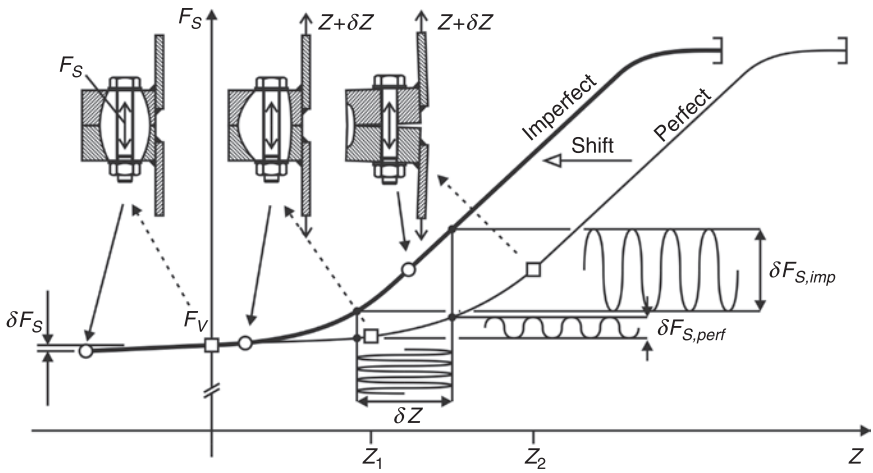

9.10 Influences of flange imperfections on the bolt-load function.

must be checked in L-shaped ring-flange connections, whereas the lowest resistance $Z_{ult,i}$ governs the design (cf. Fig. 9.11):

1 Yielding of the bolt – this failure mechanism governs if flanges and shells are rather stiff compared to the bolt. The ultimate resistance of the segment is equal to the tensional resistance of the bolt:

$$Z_{ult,1} = F_{t,Rd}$$

2 Yielding of the bolt and at the same time plastic hinge in the shell; the ultimate resistance of this failure mode is given by:

$$Z_{ult,2} = \frac{F_{t,Rd} \cdot a + M_{pl,Rd,sh}}{a+b}$$

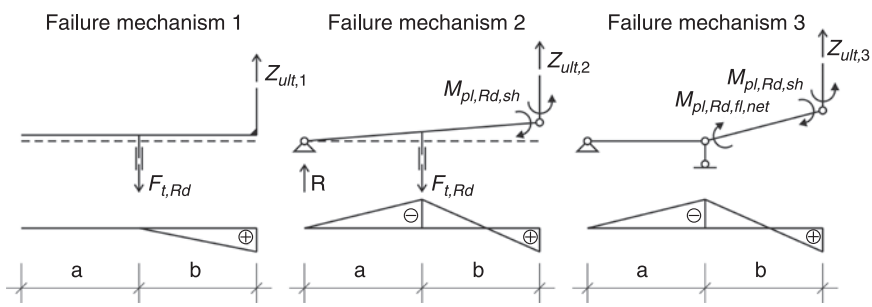

9.11 Plastic hinge models for the determination of the ultimate resistance of L-shaped ring-flange connections according to Petersen (1988).

3 Plastic hinge in shell and flange; the bolt load stays below its tensile resistance ($F_{s,Ed} < F_{t,Rd}$). The ultimate resistance of this failure mode thereby reads:

$$Z_{ult,3} = \frac{M_{pl,Rd,sh} + M_{pl,Rd,fl,net}}{b}$$

where

Z_{ult} = Ultimate tensile resistance force of the segment
$F_{s,Ed}$ = Design value of bolt load
$F_{t,Rd}$ = Design tensile resistance of the bolt
$M_{pl,Rd,sh}$ = Design plastic bending resistance of the shell
$M_{pl,Rd,fl,net}$ = Design plastic bending resistance of the flange with deduction of bolt hole
a = Distance between flange edge and axis of bolt
b = Distance between axis of bolt and shell

9.5.5 Fatigue limit state

General

With regard to high fatigue safety, ring-flange connections should be designed elastically in such a way that the bolted joint does not open during the relevant fatigue cycles, which requires a sufficient high pre-loading of the bolts. The fatigue limit state can then be verified by means of a conventional fatigue verification. The ranges $\Delta\sigma_i$ of the stress-spectrum are to be determined as a function of the tower-loads, e.g. by a rainflow matrix. In doing so the non-linear relation between bending moments $M_{Ed,i}$ in the tower shell and detail stresses should be regarded, e.g. by using an adequate calculation method for the determination of the bolt-load function (cf. Fig. 9.10).

Secondly the design lifetime $N_{R,i}$ for each stress range $\Delta\sigma_i$ is calculated by taking into account the detail category. The assessment usually takes into account the accumulated damage according to Palmgren-Miner (see also CEN, 2005):

$$D_D = \sum_i^n \frac{n_{Ei}}{N_{Ri}} \leq 1,0$$

with D_D = Damage index of entire lifetime
n_{Ei} = Expected load cycles on stress range $\Delta\sigma_i$ according to rainflow matrix
N_{Ri} = Endurance (in terms of life cycles) obtained from the fatigue strength curve of the detail for the stress range
n = number of stress ranges considered

Depending on the design model used for the determination of the stress ranges $\Delta\sigma_i$, different detail categories may be used for the fatigue assessment of the bolts. The German guidelines (DIBt-Ri, 2004; GL Wind, 2004) recommend the use of

detail category 36* for the bolt, if a simplified calculation method is used for the determination of the bolt-load function. If the bending moments in the bolts are taken into account by the model, the regular detail category 50 for bolts in tension according to EN 1993-1-9 (CEN (2005)) may be used.

According to GL Wind (2004) the cut-off limit for endurance $N_{Ri} > 10^8$ given in EN 1993-1-9 (CEN (2005)) has to be neglected, whereas a constant slope of $m = 5$ has to be used for load cycles $n_{Ei} > 2 \times 10^6$.

A brief summary of different calculation methods for the determination of bolt-load functions is given in the following sections. More detailed explanations can be taken from the quoted sources or from Zein El Dine (2007).

Elastic structural behaviour of L-shaped flange connections

All methods for the determination of bolt-load functions summarised in the following have in common that two spring stiffnesses are to be determined as input parameters, the bolt stiffness C_S and the equivalent clamp solid stiffness C_D. According to the elastic model given in Fig. 9.12, these spring values are given by:

$$C_S = \frac{1}{\int_0^{\ell_S} \frac{\bar{1}}{EA_S(x)}\,\mathrm{d}x} \qquad C_D = \frac{1}{2 \cdot \int_0^{t_F} \frac{\bar{1}}{EA_D(x)}\,\mathrm{d}x}$$

where

$A_S(x)$ = Cross-sectional area of the bolt along the bolt axis
$A_D(x)$ = Cross-sectional area of the clamp solid along the bolt axis
ℓ_S = Bolt length
t_F = Flange thickness
$\bar{1}$ = Unit load

The exact calculation procedures for the determination of C_D and C_S can be taken from VDI-Ri 2230 (2003). Simplified methods are given in Seidel (2001).

Figure 9.13 gives the dimensions used by following segment models.

Bolt-load function according to Petersen (1988)

A widely used method for the determination of bolt loads is the simplified, bilinear model derived by Petersen (1988) given in Fig. 9.14. Compared to a real bolt-load function this assumption is conservative and on the safe side in the range of the first slope but may become unsafe in the case of imperfect ring-flanges when reaching the second slope, as ideal elastic and pure edge-bearing behaviour of a perfect connection is assumed.

Furthermore, the method does not consider bending stresses in the bolt. Therefore, the use of detail category 36* is recommended in various guidelines.

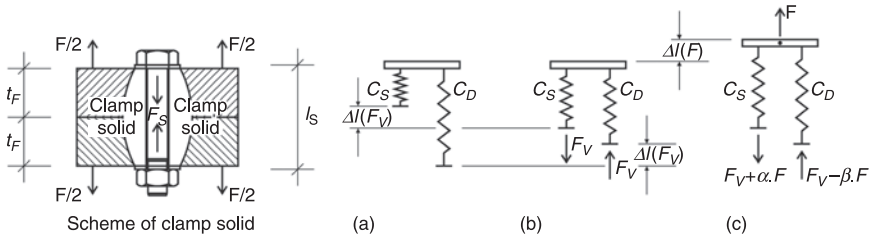

9.12 Scheme for different load situations of clamp solid: (a) unloaded model, (b) pre-loaded spring model and (c) pre-loaded spring model under external load (Zein El Dine, 2007).

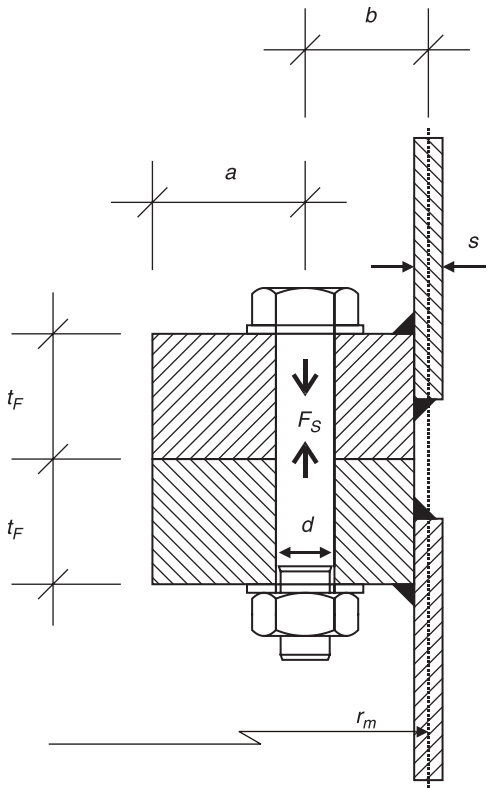

9.13 Dimensions of flange.

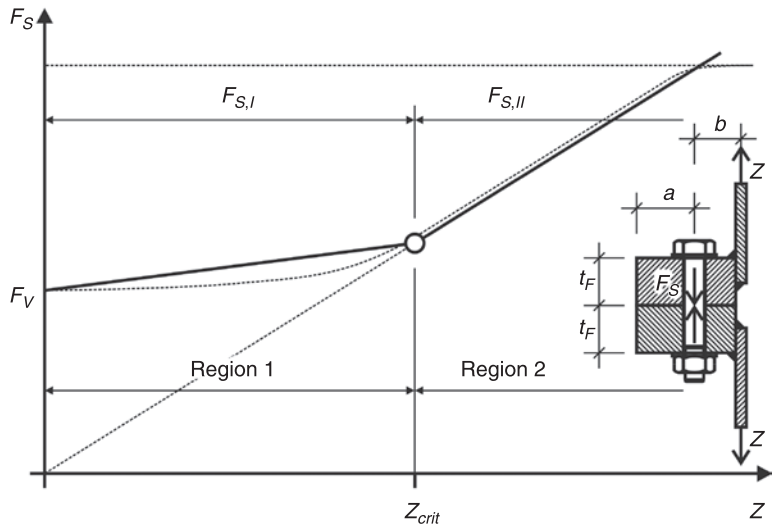

9.14 Scheme of a bolt-load function according to the Petersen model taken from Seidel (2001).

$$p = \frac{C_S}{C_S + C_D} \quad q = \frac{C_D}{C_S + C_D}$$

$$\lambda = \frac{a+b}{a}, \; Z_{krit} = \frac{F_v}{\lambda \cdot q}$$

$$F_{S,I} = F_v + p \cdot \lambda \cdot Z$$

$$F_{S,II} = \lambda \cdot Z$$

Bolt-load function according to Schmidt and Neuper (1997)

The tri-linear model developed by Schmidt and Neuper (1997) is, apart from the Petersen model, the most commonly used bolt-load function. Due to the small slope of the first part of the function ($F_{S,I}$) (see Fig. 9.15), this method is less conservative for low shell forces, Z, than the Petersen approach. The part of the function, which considers the final edge-bearing behaviour ($F_{S,III}$) of the flange-connection, is modified in such a way that small imperfections are directly considered. The limit of this approach is given by the ratio:

$$\frac{a+b}{t_F} \leq 3$$

As the method does not consider bending stresses in the bolt, the use of detail category 36* is recommended in various guidelines.

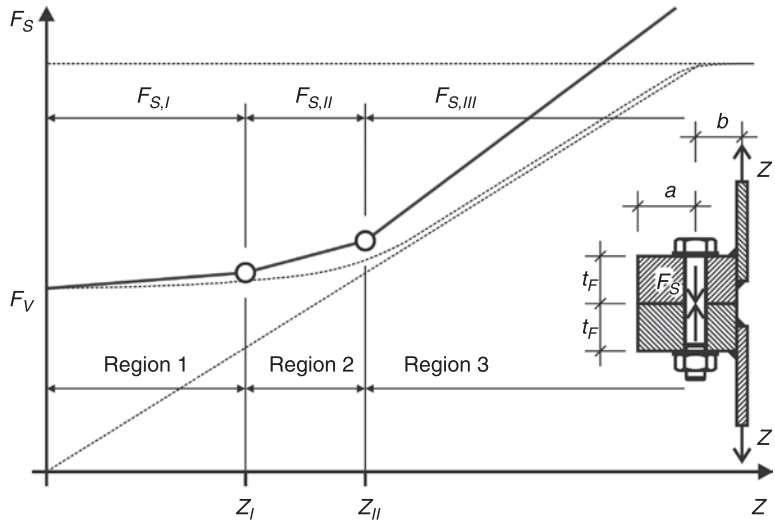

9.15 Scheme of a bolt-load function according to Schmidt and Neuper (1997).

$$p = \frac{C_S}{C_S + C_D},\ q = \frac{C_D}{C_S + C_D}$$

$$\lambda^* = \frac{0.7 \cdot a + b}{0.7 \cdot a},$$

$$Z_I = \frac{a - 0.5 \cdot b}{a + b} \cdot F_v,\ Z_{II} = \frac{1}{\lambda^* \cdot q} \cdot F_v$$

$$F_{S,I} = F_v + p \cdot Z$$

$$F_{S,II} = F_v + p \cdot Z_I + \left[\lambda^* \cdot Z_{II} - \left(F_v + p \cdot Z_I\right)\right] \cdot \frac{Z - Z_I}{Z_{II} - Z_I}$$

$$F_{S,III} = \lambda^* \cdot Z$$

Bolt-load function according to Faulhaber and Thomala (1987)

A quite close estimation of the real bolt-load function of perfect ring-flange connections can be found in the circular arc approach according to Faulhaber and Thomala (1987) (shown in Fig. 9.16). As the final slope of the function corresponds to pure edge-bearing of a perfect flange, this method leads to unsafe results in the case of high tension forces Z in the shell. The limit of this approach is given by the ratio $\varphi_{en}\ a + b \leq D_{washer} + t_F$.

Bending stresses in the bolt can only be considered for the closed flange-joint; thus, the use of detail category 36* is also recommended here.

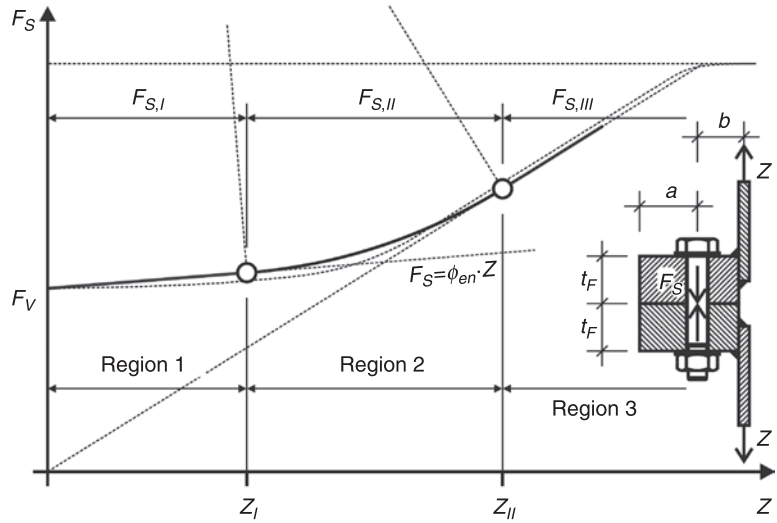

9.16 Scheme of a bolt-load function according to Faulhaber and Thomala (1987).

$$F_{S,I} = \varphi_{en} \cdot Z + F_v$$

$$F_{S,II} = F_v + n_k - \sqrt{r_k^2 - \left(Z - m_k\right)^2}$$

$$F_{S,III} = \frac{v + a}{v + s_{sym}} \cdot Z$$

Input values can be taken from VDI-Ri 2230.

Bolt-load function according to Seidel (2001)

Another method, which allows for the determination of the additional bending stresses in the bolt, is the numerical procedure according to Seidel (2001). The flange is assumed to be a stocky cantilever fixed at the intersection of the flanges, with an identical bending line as for the pre-loaded bolt (cf. Fig. 9.17). Due to the eccentric tension force Z in the shell the cantilever is bent, which leads to the rotation φ at its end. The elongation Δl of the bolt can then be determined as a function of the eccentricity between the bolt and the cantilever axis. However, the width of the cantilever b_c is iteratively reduced about the length of the gap l_{gap} until the system is in a balanced condition.

The limit of application of the Seidel approach is given by:

$$t \geq \sqrt[4]{\frac{8 \cdot a^2 \cdot b^2 \cdot A}{c \cdot (a + b)}}$$

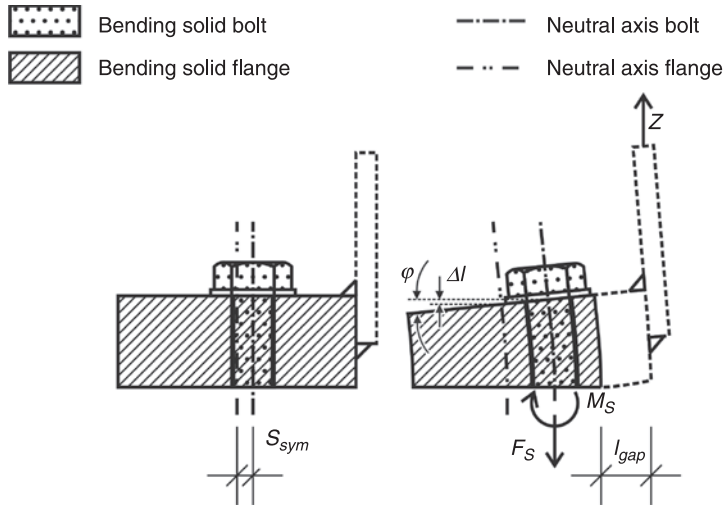

9.17 Stocky cantilever approach according to Seidel (2001).

9.6 Periodic monitoring

Periodic monitoring is a specified technical inspection of the whole structure, tower and foundation, which should be exclusively done by technical experts. The inspection intervals have to be defined in the certification report of the tower. They should not exceed a time period of more than two years (cf. DIBt-Ri, 2004; GL Wind, 2004).

The tower has to be controlled in view of eventual defects, whereby covered and soiled parts have to be uncovered and cleaned, including:

- Corrosion: tower-shell, flanges and bolts
- Cracks: concrete and welds
- Pre-load in bolts
- Deviation from allowable inclination of the tower
- Required covering of foundation

The pre-load in the bolts has to be controlled at least manually not only in view of looseness but also of existence of pre-load. However, an acoustic verification via weak hammer stroke against the bolts is an appropriate and easy method to detect large differences in the pre-loads. Loose or broken bolts have to be replaced, and the pre-loads of the replaced and the adjacent bolts have to be checked via a specified method, e.g. additional rotation angle method (see EN 1090, CEN, 2008).

Periodic monitoring has to be documented in inspection reports, which should be appended to the maintenance manual.

9.6.1 Retrofitting of flange imperfections

Imperfections in form of a flange-sided taper or parallel gap, as specified in subsection 'Flange Imperfections' (page 289), can be retrofitted using lining plates (see Fig. 9.18). The lining plate packages may consist of galvanised or stainless steel plates with different thicknesses. The provided plates should allow a maximum grading of 0.5 mm (e.g. by combining plates with a thickness of 2 mm, 1 mm and 0.5 mm). The following sequence of work steps should be followed:

1 Replacement of all bolts in the affected zone and low pre-loading by hand
2 Fitting of lining plate packages
3 Full pre-loading of the bolts up to F_v using a pre-tensioning tool
4 Readjustment of the pre-loads F_v in the bolts in the imperfection zone within six months after retrofitting via appropriate method, but not directly afterwards to ensure settling has stopped.

The shape and recommended dimensions of the lining plates are given in Fig. 9.19.

Length of lining plate: $\ell_{lp} \leq b_{fl}$

Widths of lining plate: $w_{lp} \leq \dfrac{2 \cdot \pi \cdot \left(R - s - b_{fl}\right)}{n_{bolts}} - 5 \text{ mm}$

Width of cut: $w_{\text{cut}} = d_h$, with d_h = diameter of bolt-hole

Length of cut: $\ell_{\text{cut}} \leq \ell_{lp} - \left(a + \dfrac{d_h}{2}\right)$

All dimensions in mm; definitions of R, b_{fl}, s and a are given in Fig. 9.18

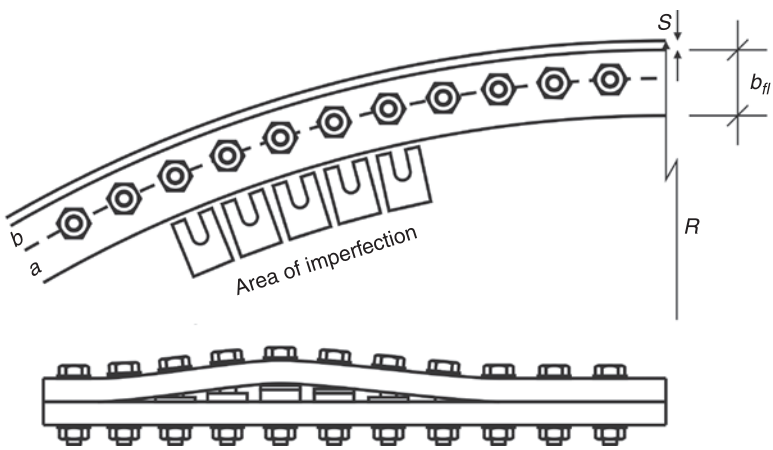

9.18 Lining plate packages before insertion.

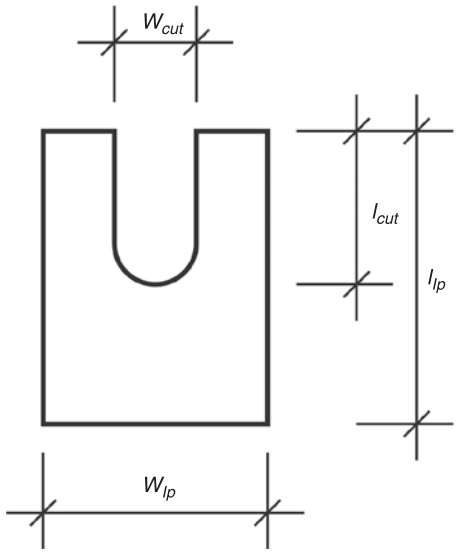

9.19 Recommended shape and dimensions of lining plates.

In the same way flange imperfections can be adjusted during erection. The method specified above has been checked within the scope of the research project HISTWIN, where almost all perfect bolt-force functions have been obtained after retrofitting (see Naumes *et al*., 2009).

9.7 References

Burton, T, Sharpe, D, Jenkins, N and Bossanyi, E (2001), *Wind energy handbook*. Chichester: Wiley.

CEN (2005), *Eurocode 3 – Design of steel structures. Part 1-9, 2005: Fatigue*. Brussels: European Committee for Standardisation (CEN), Technical Committee 250, Subcommittee 3.

CEN (2007), *Eurocode 3 – Design of steel structures. Part 3-2, 2007: Towers, masts and chimneys*. Brussels: European Committee for Standardisation (CEN), Technical Committee 250, Subcommittee 3.

CEN (2008), *EN 1090, 2008 – Execution of steel structures and aluminium structures. Part 2: Technical requirements for steel structures*. Brussels: European Committee for Standardisation (CEN), Technical Committee 135.

DIBt-Ri (2004), *Richtlinie für Windenergieanlagen – Einwirkungen und Standsicherheitsnachweise für Turm und Gründung*. Berlin, Germany: Deutsches Institut für Bautechnik.

Faulhaber, A and Thomala, W (1987), 'Erläuterungen zur Richtlinie VDI 2230 Blatt 1 (1986): Der nichtlineare Berechnungsansatz', *VDI-Z – Zeitschrift des Vereins Deutscher Ingenieure*, 129 (9), 79–84.

GL Wind Guideline (2004), *Guideline for the certification of wind turbines*. Hamburg, Germany: Germanischer Lloyd WindEnergie GmbH.

Hansen, M O L (2008), *Aerodynamics of wind turbines*. 2nd ed. UK: Earthscan.

Hau, E (2006), *Wind turbines – Fundamentals, technologies, application, economics*. Berlin: Springer

IEC 61400-3 (2009), *Wind turbines – Part 3: Design requirements for offshore wind turbines*, Geneve.

International Electrotechnical Commission (IEC) (2005), *International standard IEC 61400-1: Wind turbines, design requirements*. Geneva.

Jakubowski, A (2003), 'Ermüdungssichere Bemessung geschraubter Ringflanschstöße in turmartigen Stahlbauten unter besonderer Berücksichtigung von Flanschimperfektionen', Doctoral thesis, Essen University, Germany.

Jakubowski, A and Schmidt, H (2005), 'Ermüdungssichere Bemessung vorgespannte Ringflanschstöße unter Berücksichtigung von Flanschimperfektionen', *Stahlbau*, 74 (6), 452–61.

Lehmann, D (2003), 'Nichtlinearer Längskraft- und Biegemomentenverlauf in der Schraube vorgespannter L-Flansche – Teil 1 und Teil 2', *Stahlbau*, 72 (9), 653–66/(10), 734–43.

MECAL (1997), 'Flanged joint with in-line load transfer', *Mecal Mail*, Newsletter of engineering company Mecal BV.

Naumes, J, Pak, D and Feldmann, M (2009), *Large scale 4-point-bending tests*. RFCS Background Report HISTWIN.

Petersen, C (1988), *Stahlbau – Grundlagen der Berechnung und baulichen Ausbildung von Stahlbauten*. Braunschweig, Germany: Vieweg-Verlag.

Schaumann, P and Seidel, M (2002), 'Ermüdungsbeanspruchung geschraubter Ringflanschverbindungen bei Windenergieanlagen', *Stahlbau*, 71 (3), 204–11.

Schlemenat, A (2001), 'Kraft- und formschlüssig verspannen statt schrauben', *Erneuerbare Energien*, 11 (5), 36–40.

Schlemenat, A and Burmann, K (2009), 'Innovative connections for steam generators – Elimination of leakages and minimisation of assembly and idle times', *VGB PowerTech – International Journal for Electricity and Heat Generation*, 89, 49–57.

Schmidt, H and Neuper, M (1997), 'Zum elastostatischen Tragverhalten exzentrisch gezogener L-Stöße mit vorgespannten Schrauben', *Stahlbau*, 66 (3), 163–8.

Seidel, M (2001), 'Zur Bemessung geschraubter Ringflanschverbindungen von Windenergieanlagen', Doctoral thesis, Hannover University, Germany.

Veljkovic, M. et al (2010), 'High-strength steel tower for wind turbine, HISTWIN' Final Report RFSR-CT-2006-00031, Brussels: RFCS Publications, European Commission, to be published.

VDI-Ri 2230 (2003), *Systematic calculation of high duty bolted joints – Joints with one cylindrical bolt*. VDI-Gesellschaft, Fachbereich Konstruktion, Ausschuss Schraubenverbindungen.

Zein El Dine, S (2007), 'Ermüdungssicherheit der Schweißnähte an Ringflansch-verbindungen in turmartigen Stahlbauten', Doctoral thesis, Duisburg-Essen University, Germany.

10

Wind energy system reliability and maintainability, and operation and maintenance strategies

I. ALSYOUF, Linnaeus University, Sweden

Abstract: This chapter discusses the reliability, operation and maintenance strategies for wind power systems. It examines the role of systems engineering in optimising the aspects of a system relating to reliability, supportability and maintainability. It considers various maintenance approaches and the role of proper maintenance practices in providing a secure and reliable energy supply at the right cost. It discusses the importance of identifying and understanding the relevant cost factors associated with wind power systems, based on lifecycle costing and using relevant performance measures to help select a cost-effective maintenance approach. It then reviews some efforts aimed at improving the design, production, construction, operation and maintenance of wind power systems. Finally, some future trends are discussed in the areas of operation and maintenance of wind power systems.

Key words: reliability, maintainability, supportability, wind power systems, maintenance approaches.

10.1 Introduction

The safe and reliable operation of wind energy systems depends on the right design, manufacture, construction, smooth operation and proper maintenance of several components that comprise these systems. Engineering for reliability and maintainability plays a key role in the production capacity achieved by wind farms and in their financial returns. Poor reliability directly affects the outcome of a project through increased operational and maintenance costs and reduced availability to generate power as a result of turbine downtime. Usually, the downtime period is a function of the supportability and maintainability characteristics of the system. Reliability and maintainability engineering attempts to study, characterise, measure and analyse the failure and repair of systems in order to improve their operational use by increasing their design life, eliminating or reducing the likelihood of failures and safety risks, and reducing downtime, thereby increasing available operating time. In this chapter, we present and discuss the main operational and maintenance issues relating to optimising the design and construction of wind energy systems. First, there is a basic introduction of the 'bathtub curve concept'. There is then a discussion of the importance of considering the reliability and maintainability issues at the design stage, due to its impact on the system's lifecycle costs. In this context, reliability practices include 'classical' reliability methods, mainly used for electrical and mechanical components such

as failure mode effect and criticality analysis (FMECA), event sequence analysis and fault tree analysis (FTA). Additionally, structural reliability methods are reviewed, such as probabilistic safety assessment (PSA), and asymptotic techniques, known as first- and second-order reliability methods (FORM/SORM), used for the structural constituents (tower, blades, foundations, towers, hub and safety systems (see e.g. Lange and Flint, 2007; Seebregts *et al*., 1995). Next, we discuss the role of systems engineering in optimising the aspects of a system relating to reliability, supportability and maintainability. We will subsequently introduce various maintenance approaches and discuss the role of proper maintenance practices in providing a secure and reliable supply of energy. Following this is a discussion of the importance of identifying and understanding the relevant cost factors associated with wind power systems, based on lifecycle costing (LCC) and using relevant performance measures to help select a cost-effective maintenance approach. We then present some efforts aimed at improving the design, production, construction, operation and maintenance of wind power systems. Finally, we discuss future trends in the areas of operation and maintenance of wind power systems.

10.2 Bathtub curve concept

When a system fails, the cause of the failure can usually be traced to a failed part or an interaction between components which failed to perform their intended function. Components degrade with age and usage and they fail when they are no longer capable of functioning as they should. These failures can result in downtime and serious safety or environmental consequences. In the following section, we discuss the concept of the bathtub curve. The bathtub curve is perhaps the oldest and best-known concept in the field of reliability (Sherwin and Bossche, 1993). The bathtub curve consists of three periods: an infant mortality period, with a decreasing failure rate, followed by a normal life period, known as the 'useful life', with a low and relatively constant failure rate, and finally a wear-out period that exhibits an increasing failure rate (see Fig. 10.1).

It is necessary to distinguish between components and systems. Here, we use a hazard rate z(t) to represent the failure rate of a component, while we use the overall rate of occurrence of failures (ROCOF) to represent the 'failure rate' for repairable and maintained systems. Each component in a system has its bathtub curve. Populations of new components always contain a proportion of defective items which fail early and give the z(t) bathtub curve its initial downward trend, due to a relatively high initial failure rate. However, this part of the curve, that is the decreasing failure rate, does not appear in practice, due to recent advances in manufacturing and quality control that try to eliminate all infant mortality failures. Therefore, in Fig. 10.1, we assume that the useful life of all components in the system is defined from time zero. We then have a constant z(t) portion of the curve when the component is at or near its inherent or random average failure rate.

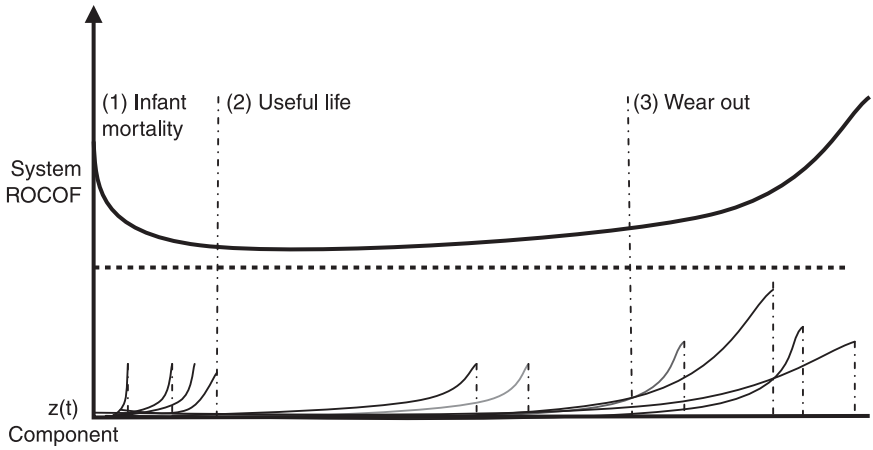

10.1 Bathtub curve for a system (adapted from Sherwin and Bossche, 1993).

Finally, we have a rising portion of the curve, when the deterioration mechanisms begin to dominate (see Ireson *et al*., 1995). Components generally have only one mode of failure and are renewed or restored to their standard condition following each failure or replacement.

In contrast, systems fail in many different ways, corresponding with the failure of the components from which they are assembled. The overall ROCOF in a system that consists of many components is the instantaneous sum of all the hazard rates z(t) of those components (Sherwin and Bossche, 1993).

Looking at the bathtub curve, we see that the initial phase is usually falling. This could be due to a combination of design errors, substandard material, poor manufacturing methods, poor processes, poor quality control, assembly faults, poor workmanship, poor installation quality or human errors. As these problems are rectified (which is usually done during the warranty period) the system starts its useful life period. Failures may occur during this period for various reasons, such as poor design with a low safety factor, an extreme load (higher than expected random stress), undetectable defects, human errors – such as misuse – and natural failures. Finally, as the long-life components exceed their design lifetime, they start to fail. These failures may be due to the following: wear caused by friction, wear caused by aging, poor maintenance, incorrect overhaul practices, fatigue, corrosion and creep, or a short item life, which may be part of the way it was designed (Dhillon, 2006).

The shape of the bathtub curve of a system may be altered by applying certain measures within each phase (Sherwin and Bossche, 1993). This means that in principle, and for the right price, initial problems in the infant mortality phase may be reduced, for example, by selecting the right materials, using well-designed components and quality manufactured parts, and employing highly skilled

assembly, installation, operational and maintenance personnel. The constant level of the bathtub curve can be lowered by applying the right preventive maintenance approach for the critical parts of the system. Finally, in the wear-out phase, it is usually the case that failures become more frequent as well as more expensive. In this case, one should consider whether the system should be renewed, replaced by a better system or overhauled to extend its life, which is usually between 20 and 25 years in the case of a wind turbine. Walford (2006) reported that wind turbines are commonly designed so that the design lives of the major components are the same as the turbine's design life. However, there are numerous examples where the design life of major components is not achieved in practice. The reasons for this difference include inappropriate design assumptions, inadequate knowledge about the true operating environment and manufacturing quality control issues.

10.3 The role of reliability and maintainability engineering in wind energy systems

Maintenance costs for wind energy systems have been hitting manufacturers and will soon start to hit the owners of these systems, since the maintenance warranty periods for large (greater than 1 MW) turbines are beginning to lapse. While scheduled wind turbine maintenance costs are relatively low, unscheduled maintenance can weaken a company's bottom line (Teresa, 2007). The productive capability of wind energy systems may be affected by reducing output and increasing operational and maintenance costs. Decisions made during the design and acquisition phases, (i.e. conceptual preliminary design and detailed design development) can dramatically influence the inherent reliability, supportability and maintainability aspects of a system, which in turn influence the ROCOF, time to support and time to maintain. Consequently, the performance of operational, logistics and maintenance functions is affected and this influences the system's lifecycle costs (i.e. production, construction, operation and maintenance and disposal costs). Blanchard (2004) emphasised that including lifecycle considerations from the start of the decision-making process is critical. Although improvements to reduce cost can be initiated at any stage of a system's lifecycle, the greatest impact (80–90%) on lifecycle costs (e.g. maintenance and support costs) can be achieved during the early phases of system design and development. This means that design for reliability (operation), supportability (logistics), and maintainability (maintenance) must be inherent within the early design and development process if the results are to be cost-effective.

It is very important to distinguish between reliability, maintainability and maintenance. Reliability is defined in a variety of ways. The most widely accepted definition of reliability states that it is the ability or capability of the product to perform the specified function in the designated environment for a minimum length of time or a minimum number of cycles or events (Ireson *et al.*, 1995).

Reliability engineering, starting from the design and development stage, seeks to select the best design compromise which balances the cost of failure reduction with the value of enhancement (David, 2001). Dhillon (1999) clarified the idea that maintainability refers to measures taken during the design and development of a product to include features that will increase the ease of maintenance, and will ensure that, when used in the field, the product will have minimum downtime and lifecycle support costs. Maintenance refers to the measures taken by the users of a product or a system to keep it in an operable condition, or to repair it in order to restore it to an operable condition.

It can be seen in Fig. 10.2 that the availability of a system, which can be calculated as Uptime/(Uptime + Downtime), is a function of the mean time to failure (MTTF), the mean time to support (MTTS) and the mean time to repair (MTTR). Supportability and maintainability issues are important factors here to improve the availability of wind farms – i.e. system uptime. For example, the eventual maintenance and support infrastructure selected for a wind power system throughout its period of utilization can significantly affect the overall cost effectiveness of that system. It is very important that future wind power system design and development efforts start by defining wind power system requirements, as determined by stakeholder needs (e.g. owners or operators of wind farms, original equipment manufacturers (OEMs), service providers). This should be done early in the conceptual design phase. In addition, it is imperative that feedback information, based on experience gained during the various phases of a system's lifecycle, especially during the operation and maintenance phase, be considered in new designs; see Fig. 10.3.

Investigating the root cause of a major component failure is essential and it assists the manufacturer in determining if the problem is an isolated instance or a systematic problem that needs a retrofit or redesign (Walford, 2006). Therefore, more cooperation between owners, operators and maintainers of wind farms and OEMs is needed to improve design, based on the needs of the various stakeholders.

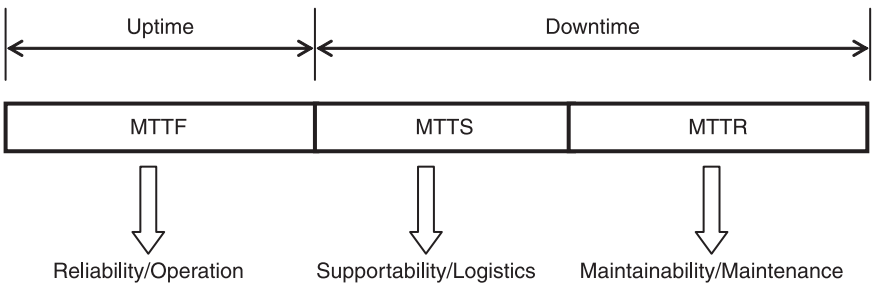

10.2 The impact of reliability, supportability and maintainability on a system's availability.

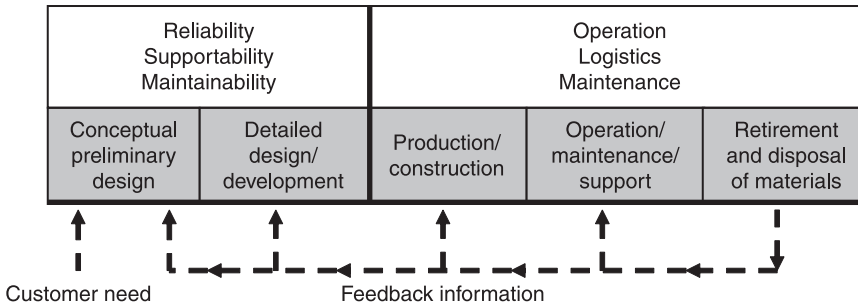

10.3 The role of feedback information in improving the cost effectiveness of a system's design.

10.3.1 Reliability and maintainability aspects of wind energy systems

When designing wind energy systems, we have a situation in which there are various stakeholders having opposing interests, with multiple and sometimes conflicting constraints. For example, manufacturers have a vested interest in reducing maintenance expenses during the guarantee period, which normally lasts two years. When turbines start to come out of their maintenance warranty periods, it is the owners who pay the maintenance costs. Prior to 2005, turbine buyers could generally base their procurement decisions purely on site characteristics and price; however, recent turbine shortages have made availability a key element in choosing suppliers (EWEA, 2009). Consequently, OEMs have started taking more responsibility for the lifecycle – selling working hours, that is uptime, instead of the machines. Turbine manufacturers now offer their customers options to select from a range of service packages that include an availability guarantee. Such manufacturers are very motivated to take maintenance issues into account during the early planning and conceptual design phases for wind energy systems.

Key issues to be addressed to run a wind farm economically are the minimization of maintenance requirements and the maximization of ease of access, which is critical for an offshore farm. The dilemma for the designers is how best to balance the cost of minimizing maintenance by increasing reliability – often at an added cost in redundant systems or greater design margins – against the cost of systems for facilitating and increasing maintenance capability (EWEA, 2009). Design for maintenance, the design of a condition monitoring system (CMS) and diagnostic instrumentation, maintenance data acquisition systems, design for service crew safety and the integration of measurement and control systems are among the important factors that should be considered early in this phase.

The provisioning and acquisition of reliability and maintenance support elements is considered very critical at this stage. This influences the ROCOF, the time to support and the time to maintain (Blanchard, 2004). For example, tasks

that are considered essential for reducing the ROCOF are: reliability requirements analysis, reliability modelling and analysis, reliability prediction, FMECA, event sequence analysis and FTA. Additionally, structural reliability methods are important, such as PSA and asymptotic techniques, known as FORM/SORM, which are used for structural components. As a result, one can identify a list of system-critical items and system-critical failure modes and causes (EWEA, 2009). These critical components will stand out as high-risk items, either because they are 'weak items' that are demonstrably failure prone, or because they are absolutely essential to turbine operation, or are expensive and time-consuming to diagnose and repair. Identifying the critical components (such as gearboxes, generators and power converters, and minor components with a high failure frequency) allows the operation and maintenance (O&M) staff to direct their monitoring, training, inventory and logistics efforts to areas that provide the most benefit (Walford, 2006). For example, according to a study that investigated failure statistics from two farms in Sweden, one in Finland and one in Germany, the gearbox is the most critical, because downtime per failure is high, compared to the other components (Ribrant and Bertling, 2007).

Blanchard (2004) illustrated that, to reduce the time to support, the following tasks should also be considered at the design stage: definition of the operational support concept; system component inter-changeability; analysis of the human–machine interface, as related to training; analysis of vendors and suppliers, from a maturity and stability perspective; analysis of technology from a proprietary maturity perspective; level of repair analysis; and maintenance task analysis. Consequently, the following deliverables can be provided: maintainer and operator training, spare and repair parts list, technical documentation, test and support equipment and a definition of required facilities.

To improve maintainability (time to maintain), the following tasks should be carried out: system maintenance concept definition; maintainability modeling and analysis; maintainability prediction; failure diagnosis; human factors and accessibility analysis; and reliability-centred maintenance (RCM). Accordingly, the following output can be generated: planned maintenance requirements, maintenance personnel and skill level requirements (Blanchard, 2004). Usually, maintenance personnel are very good at finding efficient ways of performing routine tasks and they often have an understanding of the equipment that can only be gained from hands-on experience. Therefore their suggestions and comments should be routinely incorporated into the continuous improvement process (Walford, 2006).

Despite the fact that there is reasonable adherence to the internationally recognised gearbox wind turbine design standards, gearboxes have yet to achieve their design life goals, and most systems still require significant repair or overhaul well before the end of their intended lifespan, as cited by Musial *et al.* (2007). They attempted to shed light on the nature of gearbox failures and found that most of the problems were generic in nature. Therefore, there is an opportunity for the

many stakeholders in the wind turbine gearbox supply chain to collaborate with each other; poor adherence to accepted gear industry practices, or poor workmanship, is *not* the primary source of failure. Therefore, there is a need to identify and correct deficiencies in the design process; most gearbox failures do not begin as gear failures or gear-tooth deficiencies. Field-failure assessments indicate that up to ten percent of gearbox failures may be manufacturing anomalies and quality issues that are gear related, but this is not the primary source of the problem; the majority of wind turbine gearbox failures appear to initiate in the bearings, although most gearboxes have been designed and developed using the best bearing-design practices available. This means that it is very important to analyse why gearboxes fail and to investigate the root cause of the gear problems. The Danish Wind Power Academy (DWPA) reported the following examples of reasons for gearbox failure (DWPA, 2008):

- Wrong or bad oil, which creates unnatural wear and tear
- Dirty oil restricting oil flow and clogging up coolers
- Dust and brake dust clogging up internal coolers
- Oil level too low, creating air in the oil pump
- Oil temperature too low, blowing hoses and coolers or destroying couplings
- Mechanical wear and tear on hoses
- Faulty bypass valves
- Bent hoses, restricting oil flow
- Changing standard parameters when dealing with problems
- Disabling alarms completely
- Ignoring 'filter clogged' alarms
- Incorrect reassembling when changing parts
- Not closing oil sample valves, thus destroying gearboxes
- Continuing remote restarts without inspection
- Standstill marks, slowly causing the breakdown of bearings

Many of the gearbox problems discussed above may be due to the institutional barriers that hinder communication and feedback during the design, operation and maintenance of turbines. Hence, widespread collaboration of the diverse stakeholders is needed to bring together the various parts of the design process and to share information that is needed to address the problems. Here, we suggest systems engineering as an approach that can help in solving these problems.

10.4 Systems engineering

A comprehensive approach is required to tailor the optimization process to specific business variables and objectives. The word 'holistic' is defined by The Merriam-Webster dictionary as 'relating to or concerned with wholes or with complete systems rather than with the analysis of, treatment of, or dissection into parts.' Applying this principle to wind power systems means looking at all lifecycle

components as a whole and considering their interactions and conflicts. The wind energy industry has learned from its accumulated knowledge and experience over the past decades, with stakeholders such as researchers, wind turbine manufacturers, gear designers, bearing manufacturers and consultants all working together to improve load prediction, design, fabrication, operation and maintenance. However, there is an ever-increasing challenge to achieve the highest level of economic efficiency. Thus, there is a need to engage a wide range of stakeholders, including researchers, consultants, manufacturers of rotor blades, bearings, gearboxes, controls, generators, castings and towers, wind turbine owners/operators and service providers/maintainers, each of whom holds a piece of the answer and seeks to provide a safe and balanced wind energy system. This means that we are faced with a situation where there may be opposing interests, with multiple and sometimes conflicting constraints. Thus, there is a need for an approach which reveals the big picture. It is very important to achieve the stakeholders' requirements for functional, physical and operational performance in the intended use environment throughout the planned life of the systems, in a cost-effective way. Thus, in this context, systems engineering may be used as a holistic, integrated discipline, where the inputs of various stakeholders are evaluated and balanced against each other to produce a coherent whole that is not dominated by the perspective of a single stakeholder.

In the following section, we present an overview of systems engineering and its role in transforming operational and maintenance needs and requirements into an integrated wind energy system design, through the concurrent consideration of all lifecycle needs. A system is defined by NASA (2007) as 'the combination of elements that function together to produce the capability to meet a need. The elements include all hardware, software, facilities, personnel, processes, and procedures needed for this purpose.' Systems engineering may be defined differently depending on one's background and personal experience (Blanchard, 2004). Buade (2000) presented many definitions of systems engineering. For example, the International Council on Systems Engineering (INCOSE, 2004) defines systems engineering as 'An interdisciplinary approach and means to enable the realization of successful systems'. NASA (2007) defines systems engineering as 'a robust approach to the design, creation, and operation of systems'. The approach consists of a top-down, iterative process of requirements analysis, functional analysis and allocation, design synthesis and verification, and systems analysis and control. Blanchard (2004) illustrated that systems engineering principles influence the balance between performance, risk, cost and schedule. More specifically, they will:

1. transform approved operational needs and requirements into an integrated system design solution through concurrent consideration of all lifecycle needs (i.e. development, manufacturing, testing and evaluation, deployment, operations, support, training and disposal);
2. ensure the interoperability and integration of all operational, functional and physical interfaces. Ensure that system definition and design reflect the

requirements for all system elements: hardware, software, facilities, people, and data; and
3. characterize and manage technical risks.

The systems engineering approach consists of the identification and quantification of system goals, the creation of alternative system design concepts, the performance of design alternatives, the selection and implementation of the best design, the verification that the design is properly built and integrated, and the post-implementation assessment of how well the system meets (or met) the goals (NASA, 2007). Blanchard (2004, 29) preferred and cited the following definition for systems engineering: '*the application of scientific and engineering efforts to:*

1. *Transform an operational need into a description of system performance parameters and a system configuration through the use of an iterative process of definition, synthesis, analysis, design, test and evaluation, and validation.*
2. *Integrate related technical parameters and ensure the compatibility of all physical, functional, and program interfaces in a manner that optimises the total definition and design.*
3. *Integrate reliability, maintainability, usability (human factors), safety, producibility, supportability (serviceability), disposability, and other such factors into a total engineering effort to meet cost, schedule, and technical performance objectives.*'

Ignoring any part of the system's lifecycle while engineering the system can lead to a number of negative consequences, including failure at the extreme. Maes and Faber (2008) reported that decision making can be seen as being equivalent to participating in a game, with nature acting as the main opponent. Knowing the rules of the game, that is the (success or acceptance) criteria, the system, the boundaries of the system, the possible consequences for the system and how all these factors are influenced by the world outside the system, is essential to winning the game. They emphasised that, for this reason, a very significant part of risk-based decision making is, in practice, concerned with system identification/definition as well as the identification of acceptance criteria, possible consequences and their probabilities of occurrence. The Joint Committee on Structural Safety (JCSS, 2008, 5) emphasised that 'Only when an integral approach is taken to risk assessment it can be ensured that the significant risk contributions originating from the interactions between the different agents are accounted for'. The integral approach implies that explicit consideration is given to the interaction between all relevant agents, that is technical systems, nature, humans and organizations, in the assessment of the risks associated with the system under consideration. Here we can see the relationship between systems engineering as an integral methodology and its role in improving the effectiveness of decision making. Risk management is considered an important part of the systems engineering process, where effective risk management depends on a well-defined project.

10.5 Operation and maintenance issues and strategies

In this section, we will discuss some appropriate maintenance approaches and the role of proper maintenance practices in providing a secure and reliable energy supply.

10.5.1 Maintenance approaches

Several maintenance approaches, that is strategies and concepts, have been implemented by practitioners or suggested by intellectuals. For a further discussion of maintenance approaches and their development see Alsyouf (2009). Jardine and Tsang (2006) illustrated that there are two complementary methodologies that focus on different areas with regard to increasing the uptime of physical assets. These methodologies are:

1. Total productive maintenance (TPM) – a people-centred methodology that has proven to be successful for optimizing equipment effectiveness and eliminating breakdown. It has a strong focus on people and the basics, such as cleaning, tightening and lubrication, for ensuring the well-being of equipment. Its emphasis is on early detection of wear-out to prevent in-service failures.
2 Reliability-centred maintenance (RCM) – an asset-centred methodology that focuses on design to enhance asset reliability. It is a structured methodology for determining the maintenance requirements for a physical asset in its operating context.

Usually, maintenance tasks are aimed at minimizing failures and the consequences of failure of industrial plant, machinery and equipment. The taxonomy of maintenance is illustrated in Fig. 10.4.

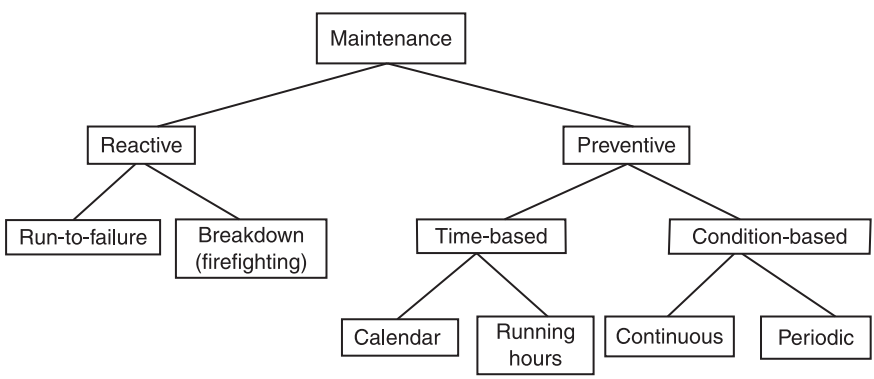

10.4 Taxonomy of maintenance approaches.

Maintenance can be described as 'reactive' or 'preventive'. Under the *reactive approach*, which is also denoted as 'corrective maintenance', there are two types. The first is *run to failure*, where the failure has little or no effect. In this case we may decide to do no routine maintenance beyond the basic cleaning or lubrication, if needed. The second type is *breakdown maintenance*, where we have unplanned maintenance due to the failure of critical components and where we need to act quickly to fix the problem(s) – that is firefighting. These failures should be avoided by performing preventive maintenance because they could have safety, environmental or operational consequences.

Preventive maintenance is defined by Sherwin (2000) as 'any task designed to prevent failures or mitigate their effects'. It is divided into time-based maintenance (i.e. replacing components at a pre-specified (calendar or running) time, using statistical models based on recorded historical failure data, and condition-based maintenance (CBM), where there is a continuous or periodic monitoring of the condition of a critical component using one (or more) condition-monitoring techniques. CBM is also described in much of the literature as *predictive maintenance*. Put simply, it means the use of advanced technologies to determine equipment condition, and to potentially predict failure. There are many condition-monitoring methods used for the detection and diagnosis of defects in equipment. They include, but are not limited to, technologies such as: vibration and acoustic measurements, temperature measurements, wear debris analysis, machine performance monitoring, and the use of human senses (look, listen, feel and smell – see Dunn, 2000). The reliability of detecting a defect, given that a defect is present, varies with each of the condition-monitoring techniques. Vibration analysis is the most well-established technique. However, acoustic emission is often thought to be more sensitive for the detection of early stage damage (Fan *et al*., 2005). A detailed review and comparison of different vibration and acoustic methods for the detection of defects in rolling element bearings have been presented by Tandon and Choudhury (1999) and Tandon *et al*. (2007). Dunn (2000) emphasized the need for a holistic view of equipment condition to improve the accuracy of failure prediction. This requires the effective integration of condition-monitoring inspection results, including the condition-monitoring techniques used, visual inspection results, fixed-interval 'preventive' maintenance actions and equipment performance monitoring.

Hameed *et al*. (2009) summarized the main condition monitoring techniques used for wind turbines as follows:

1. Vibration analysis: Vibration analysis is the most widely known technology that is applied to condition monitoring. For wind turbines, this type of monitoring is applicable for monitoring the wheels and bearings of the gearbox, the bearings of the generator and the main bearing. The application of vibration monitoring techniques and working methods for wind turbines differ from other applications with respect to the dynamic load characteristics and low rotational speeds.

2. Oil analysis: This has two purposes – safeguarding the oil quality (contamination by parts, damp) and safeguarding the components involved (characterization of parts).
3. Thermography: This is often applied to the monitoring and failure identification of electronic and electric components. Hot spots, due to the degeneration of components or a bad contact, can be identified in a simple and fast manner.
4. Physical condition of materials: This mainly focuses on crack detection and growth. The methods applied are normally off-line and are not suitable for the on-line condition monitoring of wind turbines. An exception might be the usage of optical fuses in the blades and the acoustic monitoring of the structure.
5. Strain measurements: Measurement by strain gauges is a common technique.
6. Acoustic monitoring: This has a close relationship with vibration monitoring. While vibration sensors are rigidly mounted on the component involved, and register the local motion, the acoustic sensors 'listen' to the component.
7. Electrical effects: Various methods are used for monitoring electrical machines. For accumulators the impedance can be measured. For medium- and high-voltage grids, a number of techniques are available, such as discharge measurements and velocity measurements for switches. For cabling, isolation faults can be detected. These types of inspection measurements do not directly influence the operation of wind turbines.
8. Process parameters: For wind turbines, safeguarding based on process parameters is, of course, common practice. However, safeguarding is still largely based on level detection or the comparison of signals, which immediately results in an alarm when the signals exceed predefined limits. At present, more intelligent usage of the signals, based on parameter estimation and trending, is not common practice for wind turbines.
9. Performance monitoring: For safeguarding purposes, the relationship between power, wind velocity, rotor speed and blade angle can be used and, for large deviations, an alarm is generated. The detection margins for the alarm thresholds are large, in order to prevent false alarms. As with the estimation of process parameters, more sophisticated methods, including trending, are not often used.

10.5.2 Classification of maintenance practices

Maintenance practices are classified and described empirically, based on a survey conducted within the Swedish industry (see Alsyouf, 2009):

1. The reactive approach is focused mainly on firefighting, installing new equipment, using work-in-progress inventory between machines to guarantee the running of production lines, and performing an annual overhaul.
2. The preventive approach is characterised by performing maintenance tasks only, based on the OEM and the usage of statistical methods to model the life function of critical components, based on failure data.

3. The predictive approach is characterised by the usage of computerised maintenance and management systems, investment in training and improving the competence of personnel, using condition monitoring technology and using methods suggested by RCM, such as failure analysis, FMECA and statistical modeling.
4. The diagnostic (expert systems) approach is characterised by the use of remote and automatic diagnostic technology.
5. The autonomous approach is based on the philosophy of TPM, which mainly relies on measuring overall equipment effectiveness (OEE).
6. The lean approach focuses on reducing losses resulting from, for example, having a high level of spare parts inventory and requiring a long time to repair the machines.
7. The proactive approach is characterised by the following practices: improving the production process; purchasing new equipment and selecting suppliers, based on their previous experience; using cross-functional groups to solve production problems; supporting efforts to design and improve production processes; using the information available within a company to perform maintenance tasks and carry out the periodic, planned replacement of critical components.

The classification presented above was used as the basis for reviewing maintenance practices in wind power systems (see Alsyouf and El-Thalji, 2008). It was found that most of these practices are relevant in the wind energy industry. Only the reactive and lean approaches were found not to be relevant in this context.

However, in all cases, the decision-maker needs to select the right policy for each component, module or piece of equipment from all the applicable maintenance approaches. The identification and implementation of the appropriate maintenance policy will enable managers to avoid premature replacement costs, maintain a stable production capacity, and prevent the deterioration of the system and its components (Alsyouf, 2004).

10.6 Cost-effective maintenance for sustainable and competitive energy supply

According to a report published in 2006 by Sandia National Laboratories, the cumulative costs for O&M may represent as much as 65–90% of a turbine's investment cost. Efforts to minimise O&M costs must start from a holistic approach, based on LCC, to identify current costs and gain a better understanding of those costs and the factors that drive them, and must not just look at the tip of the iceberg. Some of these factors will be common to wind power projects in general, but other factors will be site specific. Thus, using the right economic factors, one can estimate the savings expected from productivity improvement suggestions, compare this to the investments needed, and make a cost-effective

decision. Al-Najjar and Alsyouf (2004) developed a model for identifying, monitoring and improving the economic impact of the implemented maintenance approach, for example vibration-based maintenance. It provides an additional opportunity to identify where, why and how much capital should be invested, and judges whether or not the investment was cost effective.

To improve the reliability and safety of wind farms and reduce the O&M costs, there is a need to measure wind farm performance using holistic performance indicators that provide the required information for continuous improvement efforts, that is establish a sound foundation for comprehensive maintenance practice improvements using quantitative and qualitative data. Alsyouf (2006) suggested a balanced scorecard framework to assess the contribution of maintenance to strategic business objectives. Using the suggested framework it was possible to identify and measure the cause-and-effect relationship of using an effective maintenance strategy, and assess its impact on a company's competitive advantage. There is a need for an adapted holistic performance measurement system to measure the performance of wind energy systems, so that one can:

- assess the contribution of the maintenance function to strategic business objectives
- identify the strengths and weaknesses of the implemented maintenance strategy
- establish a sound foundation for a comprehensive maintenance improvement strategy using quantitative and qualitative data.

Furthermore, by selecting suitable performance measures, it would be possible to detect deviations at an early stage, and to identify and trace the root cause of any deviation, thereby achieving cost-effective and continual improvements.

Based on both the LCC and performance measurement assessment, the decision-maker can select the right maintenance policy. For example, a very critical decision should be made regarding which event (failure, time-based, condition-based) triggers what type of maintenance task (e.g. repair, replacement or inspection). The decision-maker should select the right approach, that is the cost-effective task. In practice these decisions are based on informed opinions, such as following the recommendations of the OEM or introducing a preventive maintenance program, such as CBM. However, while such procedures may improve a wind farm's reliability, it is by no means guaranteed to provide a cost-effective solution. Therefore, there is a need to help the decision-maker to select the right, that is, the most cost-effective, maintenance approach (Al-najjar and Alsyouf, 2003). El-Thalji *et al*. (2009) discussed the importance of using a lifecycle cost approach for the design, construction, operation and maintenance of wind energy systems. They developed a model for assessing the operation and maintenance costs, based on the OEE. They showed how lifecycle cost analysis can help decision-makers make cost-effective decisions (at every stage of the lifecycle of a wind energy system).

10.7 Efforts towards improved design and construction for wind power systems

This section presents part of the results of a literature review of maintenance practices in wind power systems. It is based on a review paper written by Alsyouf and El-Thalji (2008). The following is a summary of the main results of this review, presented according to the relevant wind power system lifecycle processes:

10.7.1 Design and development

An integrated design approach for offshore wind farms is presented by Kühn *et al*. (1999). The authors discussed three conceptual directions for future wind turbines and their associated maintenance strategies: a base case wind turbine; a disposable wind turbine; an advanced control wind turbine. These conceptual directions represent different compromises for the desirable features of turbines intended for offshore use. Various maintenance strategies applicable to the concepts were analysed, using Monte Carlo simulations. It was concluded that it is very important to have a well-adapted maintenance strategy with respect to machine design, in order to obtain an optimal design solution.

The design modifications necessary for future offshore wind turbines were discussed by Bussel van *et al*. (2001). The authors emphasized that an effective design approach is needed to reduce major maintenance costs and increase availability through, for example: improvement of access methods, reduction of the time required for offshore maintenance, turbine design for reduced maintenance and the development of appropriate maintenance strategies for servicing and repair.

The objectives and results of the Dutch offshore wind energy converter (DOWEC) project were discussed by Bussel van and Zaaijer (2001). The authors assessed the opportunities and the drawbacks of the application of different designs of very large wind turbines.

The differences between two development approaches to wind turbines, that is the proven technology approach and the integrated design approach, were discussed by Bussel (2002). The author emphasized that the use of proven technology is often considered as a requirement for the technology that is to be used offshore. However, with regard to current maintenance requirements, this may not be the best approach. There is a need for a design with significantly higher reliability specifications.

The importance of considering maintenance when designing wind turbines was discussed by Teresa (2007). The author illustrated how maintenance costs can weaken the bottom line for wind energy companies. As large (greater than 1 MW) turbines are beginning to come out of their maintenance warranty periods, so maintenance and repair work becomes a bigger issue for facility owners. There

was additionally a discussion of some of the difficulties and obstacles faced by maintenance operations departments. For example, the maintenance and rebuild of the critical components of some turbines, such as the gearbox and the generator, is very expensive. This can be attributed to a number of things: the high price of replacement components, the need to obtain and mobilise a large crane, the cost of the crane, as well as other difficulties that result in longer-than-planned downtime. The author suggested that this may be avoided by including on-board service cranes in new machines.

10.7.2 Production and construction

Some of the difficulties associated with maintaining offshore wind farms were discussed by Wood (2004). He highlighted that poor quality control in the production and construction phases were the root cause of the problems that forced manufacturing companies to reassess the entire design and retrofit. He reported that technical failures in wind systems are, in many cases, due to a combination of manufacturing problems, weather conditions and quality problems due to the way in which the wind energy equipment is transported and stored.

The current state of safety within construction processes and operations for wind energy equipment at sea was presented and discussed by Robb (2005). He emphasized that, although the operation of these farms can be supervised remotely, there is still a need to perform planned and unplanned maintenance tasks. These activities bring with them particular risks, such as personnel travelling from on shore, working at night, moving large objects, including machinery, diving operations that may be required, and the risk of fire, with limited means of escape. The importance of implementing appropriate safety and operational guidelines was emphasized, including a specification of actions for each site and for employee training.

10.7.3 Operation and maintenance

The operation and maintenance of wind power systems has been discussed in many sources. In the following section, we summarise the main issues discussed and present them according to the classification of maintenance practices presented previously in section 10.5.2:

Preventive

Operational problems and their effect on the performance of wind power systems were studied and discussed by Iniyan *et al.* (1996). The authors analysed the technical availability, real availability, capacity factors and maximum downtime of wind turbine generators over the course of a year. They found that the total downtime fluctuates over the months, mainly dependent on wind velocity.

Therefore, the availability of the system can be improved by planning maintenance tasks properly. Besnard *et al*. (2009) presented an opportunistic maintenance optimisation model for offshore wind power systems. The model takes advantage of wind forecasts and corrective maintenance activities in order to perform preventive maintenance tasks at low cost.

Predictive

The integration of CMS into offshore wind technology was discussed by Caselitz *et al*. (1997). The authors presented an approach to integrate the required hardware and software extensions of CMS into wind energy converter technology to perform a predictive maintenance and repair strategy. This approach is based on using fibre optic technology to exchange data between the CMS and the offshore wind farm. They raised the challenge of integrating fault prediction data into databases, in order to generate a condition-dependent maintenance and repair strategy for offshore wind farms.

The wind turbine industry is young, with limited operational experience (Jefferies *et al*., 1998). The blades are a crucial and expensive component of a wind turbine. The authors explored the application of a normalised bi-spectrum or bi-coherence to the problem of condition monitoring for wind turbine blades. They reported that bi-coherence condition monitoring can successfully detect small physical changes in the machine from a very noisy signal.

Machine dynamics and electrical machine theory were studied by Wilkinson and Tavner (2004). The authors tried to link the causes of faults to detectable effects on the rotor dynamics of the overall drive train.

Condition monitoring instrumentation, data acquisition systems and a data analysis methodology for a small-scale wind turbine system are described by Khan *et al*. (2006). A lifecycle cost analysis of maintenance strategies for single wind turbine onshore and offshore farms were presented by Nilsson and Bertling (2007). A lifecycle cost methodology was used to compare alternative maintenance strategies. The analysis of two case studies showed that current maintenance planning is not optimised, and it is possible to make maintenance more efficient. CMS could resolve the growing need in the wind power industry for better maintenance management and increased reliability. They suggest, as a future task, studying how to combine CMS and RCM in wind power systems.

The impact of using the right maintenance policy, that is condition monitoring, on the cost per kilowatt-hour of producing energy by wind power was discussed by Anon. (2005a). The paper discussed technological developments for monitoring the condition of critical components in a wind turbine, that is mechanical parts and blades. It suggests the implementation of continuous autonomous condition monitoring as a solution for the technical problems associated with wind power systems.

Diagnostic (expert systems)

On-line condition monitoring in induction generators for small hydro stations and wind farms was discussed in (Albizu *et al*., 2004). The authors highlighted the importance of using on-line diagnostic techniques in the maintenance schemes. The latest version of SKF wind turbine CMS, that is WindCon 2.0, was presented and discussed in (Anon., 2005b). WindCon 2.0 works continuously in real time; it consists of an intelligent monitoring unit, a supervisory and analysis system, and a data transmission hotline that provides engineers with remote access to the system.

Autonomous (TPM)

A mathematical model to quantify wind farm production losses, in terms of planned and unplanned downtimes and speed losses, was derived in (Krokoszinski, 2003). The model is based on a total OEE method suggested by the TPM methodology. These losses are related to the theoretical maximum of annual wind park revenues. This approach can highlight the O&M cost contributions required prior to any investment decision.

Practical methods of predicting large wind turbine reliability using grouped survey data were discussed in (Tavner *et al*., 2007). The authors illustrated how turbine design, turbine configuration, time, weather and possibly maintenance can affect the results obtained.

Proactive

The role of research and development (R&D) efforts in achieving a more structured approach to O&M issues, and the optimization of maintenance strategies for wind farms were discussed by Rademakers *et al*. (2003). The authors emphasised that, in order to gain more benefit from R&D results, industrial parties should collaborate in collecting and exchanging O&M data. Furthermore, R&D is still needed to demonstrate the added value of condition monitoring and to develop algorithms for predicting the remaining life of components. Also, there is a need to develop tools that assist operators in making cost-effective decisions in their day-to-day work, especially for offshore work.

The question of whether a cost-effective integrated CMS can be realised in practice was investigated by Braam *et al*. (2003). The authors discussed how to improve available condition monitoring techniques by using new algorithms for data processing, which are based not only on condition monitoring data, but also on data and signals that are available in the turbine already. These include the temperature of the generators and the gearbox, variations in the power curves, trends in the pitch and yaw speeds.

10.8 Future trends

In the following section we will discuss future trends with regard to the operation and maintenance of wind energy systems.

According to a report published by the European Wind Energy Association (EWEA), the average cost per kWh of wind-generated power is estimated to be about 7 c€/kWh at a wind site with average wind speed (EWEA, 2009). It is estimated that O&M costs for a wind turbine are on average about 20–25% of the total cost per kWh produced; this figure is higher for offshore farms. According to the European Wind Energy Association's scenarios, the market's annual wind power investments are expected to be stable at around €10 billion up to the year 2015, with a gradually increasing share of the investment going offshore. By 2030, annual wind energy investments in EU-27 will reach almost €20 billion, with 60% of the investment offshore. For an onshore installation, the energy production indicator is normally around 2000–2500 full load hours per year. For a typical offshore installation this figure reaches up to 4000 full load hours per year, depending on the site, due to higher offshore wind speeds (Krohn *et al*., 2009). The economics of the performance of wind energy systems is highly dependent on the reliability and availability of the wind energy systems that have previously been installed. In the case of offshore wind farms, maintenance and service work have a considerable impact on the cost of energy (CoE) per kWh of generated power, due to issues related to their relative inaccessibility. Therefore, more attention is given to wind turbine reliability, and operation and maintenance. Consequently, different approaches have been tried to decrease operation and maintenance costs, and various measures have been applied to bring operation and maintenance activities and their costs under control. Due to the environmental conditions under which these activities are performed, and because of accessibility difficulties for offshore sites, efforts are now being focused on identifying risks, adapting new quality methods and investigating new technical solutions using, for example, remote condition monitoring and e-maintenance.

Condition monitoring is an essential component of an effective maintenance program. A comprehensive maintenance program provides diagnostic information on the health of the various subsystems of a farm and alerts the maintenance staff to trends that may be developing into failures or critical malfunctions. Usually, one can use the basic operational data available from the turbine's control (SCADA) system, such as temperatures, speeds, fluid levels, line phase imbalance, voltage levels and tower vibration. In recent years, more sophisticated on-line monitoring systems have been introduced for wind turbines. These systems use technologies that were initially developed for other industries. For example, vibration monitoring is used to detect faults in the bearings and gearing. Similarly, shock-pulse or acoustic systems that use high-frequency, narrow-band vibration sensors are used to detect structure-borne pulses. These systems are component-specific and require significant knowledge to select the optimal sensor configuration and to develop algorithms for

interpreting the data collected from the sensors. There are many intelligent methods (known as soft computing) that are used for diagnostic and prognostic purposes (see Alsyouf and Alzoghoul, 2009). Soft computing is a collection of artificial intelligence techniques that uses the human mind as a model; it works synergistically and aims to exploit the tolerance of imprecision, uncertainty, approximation and partial truth to achieve tractability, robustness and a low solution cost (see as examples Zadeh, 1994; Mitra *et al*., 2002). Soft computing provides intelligent processing techniques which overcome the time-consuming and complex problems of hard computing techniques (Cabrera *et al*., 2009).

There are several soft computing methods, such as fuzzy logic, artificial neural networks (ANN), genetic algorithms (GA) and rough sets. The application of soft computing techniques is extensively found in the data mining step of the 'knowledge discovery in databases' (KDD) process, as shown in Fig. 10.5.

While neural networks, which are used for learning and curve fitting, and rough sets, which are used for handling uncertainty, are widely used for classification and rule generation, genetic algorithms are mostly used in various optimization and search processes, for example query optimization and template selection. On the other hand, case-based reasoning and decision trees are widely used to solve data mining problems, while fuzzy logic deals with imprecision and uncertainty (Zadeh, 1994). These methods have been applied successfully in the industrial sector. However, there is much to be done within wind power systems.

We present below part of the results (related to operations and maintenance) of a review of the available literature on soft computing applications in the field of wind power systems (see Alsyouf and Alzoghoul, 2009):

- An intelligent system for predictive maintenance (SIMAP) software and its features was presented in (Garcia *et al*., 2006). SIMAP uses different intelligent methods such as: ANN, fuzzy expert systems and fuzzy genetic algorithms for the purpose of supporting predictive maintenance. SIMAP is able to perform online condition monitoring, failure detection and diagnostic, and predictive maintenance scheduling, and to measure the effectiveness of the applied maintenance actions. The software was applied successfully to monitor the health condition of the gearbox of a wind turbine; moreover, the results showed that the artificial intelligence methods applied are capable of achieving the aims of a predictive maintenance strategy.
- An integrated maintenance management system, Terology Integrated Modular System (SMIT), applied to a form of renewable energy, was introduced by

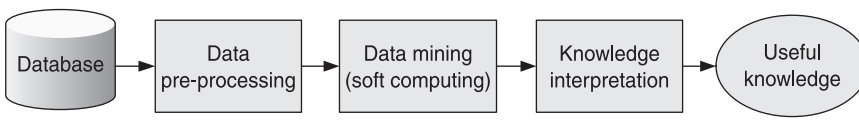

10.5 Flow chart showing the Knowledge Discovery in Databases (KDD) process.

Fonseca *et al*. (2008). SMIT manages the integration of the prediction algorithms developed, such as: support vector regression (SVR), autoregressive moving average (ARMA) and autoregressive integrated moving-average (ARIMA), along with the information system and the hardware itself. SMIT, which can be accessed through a client–server system, includes useful modules such as a fault diagnosis module, a non-periodic maintenance planning module and a generic on condition maintenance module, and it has the facility to add more modules. The results showed that SMIT is a powerful tool for maintenance management and can be used as the basis for new developments.

- The design of a vibration data acquisition system, along with an intelligent fault diagnostic system for wind turbines, was presented by Dongxiang *et al*. (2007). For early detection of wind turbines faults, a wavelet neural network (WNN) was used to predict vibration trends. Additionally, the C Language Integrated Production System (CLIPS) expert system tool was used for diagnostic purposes. The results showed that the system is effective for wind turbine vibration fault diagnostics.
- An application of an artificial neural network for predicting the power produced by different wind turbines was presented by Li *et al*. (2001). The predicted power generation can be used for diagnostic purposes. This can be achieved by comparing the expected power generation, which can be found by checking the manufacturer's rating for a given wind speed, against the predicted power generation. If the predicted power is less than the expected power, this is an early warning indicator to carry out maintenance.
- A wave forecast method based on an artificial neural network was presented by Londhe and Panchang (2005). A wave forecast is helpful in planning O&M work for offshore wind power systems. The results showed that the artificial neural network was able to perform well for 6–12 hours' wave prediction, and moderately well for 18–24 hours.

10.9 Sources of further information and advice

For additional information on major professional bodies and research groups within the wind energy sector, a useful source is The European Academy of Wind Energy's web site (EAWE) http://www.iset.uni-kassel.de/eawe/partners/hannover.html. There is a link to all EAWE partners in Europe on this web site. An additional source is the web site of Sandia National Laboratories (SNL) http://www.sandia.gov/wind/.

Below, we list selected references that could be used for obtaining further information concerning topics related to maintenance engineering and management:

Dekker, R (1996), Applications of Maintenance Optimisation Models: A Review and Analysis, *Reliability Engineering and System Safety*, 51, 229–40.

Duffuaa, S, Campbell, J D and Raouf, A (1998), *Planning and Control of Maintenance Systems: Modelling and Analysis*, John Wiley, New York.
Ireson, W G Jr., Coombs, C F and Richard, Y M (1995), *Handbook of Reliability Engineering and Management*, second ed., McGraw-Hill.
Kelly, A (1998), *Maintenance Strategy*, Butterworth Heinemann, UK.
Mckone, K and Wiess, E (1998), TPM: planned and autonomous maintenance – bridging the gap between practice and research. *Production and Operations Management*, 7(4), 335–51.
Mann, L, Saxena, A and Knapp, G M (1995), Statistical-based or condition-based preventive maintenance? *Journal of Quality in Maintenance Engineering*, 1(1), 46–59.
Moubray, J (1991), *Reliability Centred Maintenance*, Butterworth Heinemann, Oxford, UK.
O'Connor, P D T (2002), *Practical Reliability Engineering*, fourth ed., Wiley, West Sussex, England.
Swanson, L (2001), Linking maintenance strategies to performance. *International Journal of Production Economics*, 70(3), 237–44.
Sherwin, D J (2000), A review of overall models for maintenance management, *Journal of Quality in Maintenance engineering*, 6(3), 138–64.
Tsang, A H C (2002), Strategic dimensions of maintenance management, *Journal of Quality in Maintenance Engineering*, 8(1), 7–39.
Vineyard, M, Amoako-Gyampah, K and Meredith, J (2000), An evaluation of maintenance policies for flexible manufacturing systems: a case study, *International Journal of operations and production management*, 20(4), 409–26.
Waeyenbergh, G and Pintelon, L (2002), A framework for maintenance concept development. *International Journal of Production Economics*, 77(3), 299–313.
Williams, J, Davies, A and Drake, P (1994), *Condition-Based Maintenance and Machine Diagnostics*, Chapman & Hall.

10.10 Acknowledgements

I would like to thank the authors of all the published sources that I have read and made use of while writing this chapter. I would also like to thank the co-authors of my previously published sources, which I reused in this piece of work.

10.11 References

Albizu, I, Tapia, A, Saenz, J, Mazon, A J and Zamora, I (2004), *On-Line Stator Winding Fault Diagnosis In Induction Generators For Renewable Generation*, IEEE MELECON, Dubrovnik, Croatia.
Al-Najjar, B and Alsyouf, I (2003), Selecting the most efficient maintenance approach using fuzzy multiple criteria decision making. *International Journal of Production Economics*, 83(3), 81–96.
Al-Najjar, B and Alsyouf, I (2004), Enhancing a company's profitability and competitiveness using integrated vibration-based maintenance: a case study. *European Journal of Operational Research*, 157, 643–57.
Alsyouf, I (2004), *Cost Effective Maintenance for Competitive Advantages*. PhD Thesis (Terotechnology), School of Industrial Engineering, Vaxjo University Press, Acta Wexionensia, Sweden, ISBN: 91-7636-401-1.

Alsyouf, I (2006), Measuring maintenance performance using a balanced scorecard approach. *Journal of Quality in Maintenance Engineering*, 12(2), 133–49.

Alsyouf, I and Alzghoul, A (2009), Soft computing applications in wind power systems: A review and analysis, *The European Offshore Wind Conference & Exhibition, Offshore Wind 2009*, Stockholm, 14–16 September.

Alsyouf, I and El-Thalji, I (2008), Maintenance practices in wind power systems: a review and analysis, *The European Wind Energy Conference & Exhibition Brussels Expo*, Belgium, 31 March–3 April 2008.

Alsyouf, I (2009), Maintenance practices in Swedish industries: Survey results. *International Journal of Production Economics*, 121, 212–23.

Anon (2005a), Managing the wind: Reducing kilowatt-hour costs with condition monitoring. Refocus.

Anon (2005b), Web based data access lower costs, Modern Power Systems October, 34.

Besnard, F, Patrikssont, M, Strombergt, A-B, Wojciechowskit, A and Bertling, L (2009), An optimization framework for opportunistic maintenance of offshore wind power system, *IEEE*, 1–7.

Blanchard, B (2004), *Logistics Engineering and Management*, Pearson Education International: Upper Saddle River, NJ.

Braam, H, Rademakers, L W M M and Verbruggen, T W (2003), CONMOW: condition monitoring for offshore wind farms, ECN-RX-03-036, *Presented at European Wind Energy Conference 2003*, Madrid, Spain, 16–19 June 2003.

Buade, D (2000), *The Engineering Design of Systems – Models and Methods*, Wiley series in systems engineering, John Wiley & Sons, Inc, USA.

Bussel, van G J W, Henderson, A R, Morgan, C A, Barthelmie, R, Argyriadis, K, Arena, A, Niklasson, G and Peltola, E (2001), State of the art and technology trends for offshore wind energy: operation and maintenance issues. Presented at the *EWEA special topic conference on Offshore Wind Energy*, Brussels, 10–12 December 2001.

Bussel, van G J W and Zaaijer, M B (2001), DOWEC concepts study, reliability, availability, and maintenance aspects, *European Wind Energy Conference and Exhibition* (EWEC).

Bussel, van G J W (2002), Offshore wind energy, the reliability dilemma, *Proceedings of the World Wind Energy Conference*, Berlin, Germany, 2–6 July 2002.

Cabrera, I P, Cordero, P and Ojeda-Aciego, M (2009), Fuzzy Logic, Soft Computing, and Applications, *Lecture Notes in Computer Science, Bio-Inspired Systems: Computational and Ambient Intelligence*, 5517, 236–44.

Caselitz, P, Giebharht, J and Mevenkamp, M (1997), applications of condition monitoring systems in wind energy converters, *EWEC*.

DWPA. (2008), Technical training for the wind turbine industry, DWPA presentation at the workshop '*Drift och underhåll av Vindkraftvrk*' organised by Teknologisk Institut, 12 June 2009, Stockholm.

David, J S (2001), *Reliability, Maintainability and Risk: Practical Methods for Engineers* [including reliability centred maintenance safety-related systems], sixth ed., Oxford, Butterworth-Heinemann.

Dhillon, A S (2006), *Maintainability, Maintenance, and Reliability for Engineers*, CRC Press, Houston, Texas, USA.

Dhillon, A S (1999), *Engineering Maintainability: How to Design for Reliability and Easy Maintenance*, CRC Press, New York, USA.

Dongxiang, J, Liangyou, H, Yongshan, D and Qian, H (2007), *The Design of Vibration Data Acquisition and Intelligent Fault Diagnostic System for Wind Turbine*. Tsinghua University, Beijing 100084, China.

Dunn, Sandy (2000), Condition monitoring in the 21st century. The Plant Maintenance Resource Centre (*http://www.plant-maintenance.com/articles/ConMon21stCentury.shtml*).

El-Thalji, I, Alsyouf, I and Ronsten, G (2009), A model for assessing operation and maintenance cost adapted to wind farms in cold climate environment: based on Onshore and offshore case studies, *The European Offshore Wind Conference & Exhibition, Offshore Wind 2009*, Stockholm 14–16 September.

EWEA. (2009), Wind Energy – *The Facts: a Guide to the Technology, Economics and Future of Wind Energy*, London, Earth Scan.

Fan, Y E, Gu, F and Ball, A (2005), A comparative study of the vibration and acoustic emission techniques to detect early stage damage of rolling element bearings, *International Conference on Condition Monitoring*, Cambridge, UK, 18–21 July,

Fonseca, I, Farinha, T and Barbosa, F M (2008), On-condition maintenance of wind generators: from prediction algorithms to hardware for data acquisition and transmission 2008. *WSEAS transactions on circuits and systems*, 7(9), 909–18.

Garcia, M C, Sanz-Bobi, M A and Pico, J D (2006), SIMAP: Intelligent System for Predictive Maintenance: Application to the health condition monitoring of a wind turbine gearbox, Elsevier, *Computers in Industry*, 57(6), 552–68.

Hameed, Z, Hong, Y S, Cho, Y M, Ahn, S H and Song, C K (2009), Condition monitoring and fault detection of wind turbines and related algorithms: A review, *Renewable and Sustainable Energy Reviews*, 13, 1–39.

INCOSE (2004), *Systems Engineering Handbook: A 'What To' Guide For All SE Practitioners*, INCOSE-TP-2003-016-02, Version 2a, 1 June 2004, Technical Board International Council on Systems Engineering, INCOSE.

Iniyan, S, Suganthi, L and Jagadeesan, T R (1996), Fault analysis of wind turbine generators in India. *Renewable Energy*, 9(1–4), 772–75.

Ireson, G W, Coombs, C F and Moss, R Y (1995), *Handbook of Reliability Engineering and Management*, second ed., McGraw-Hill, New York, USA.

Jardine, A K S and Tsang, A H C (2006), *Maintenance, Replacement, and Reliability Theory and Application*, Taylor&Francis, USA.

Jefferies, W Q, Chambers, J A and Infield, D G (1998), Experience with bicoherence of electrical power for condition monitoring of wind turbine blades. *IEE Proceedings – Vision, Image and Signal Processing*, 145(3), 141–48.

JCSS (2008), Risk Assessment in Engineering – Principles, System Representation & Risk Criteria (*http://www.jcss.ethz.ch/publications/publications_background.html*).

Khan, M M, Iqbal, M T and Khan, F (2006), Reliability and condition monitoring of a wind turbine, *Electrical and Computer Engineering, Canadian Conference*, 1978–81.

Krohn, S, Morthorst, P-E and Awerbuch, S (2009), The Economics of Wind Energy, A report by the European Wind Energy Association.

Krokoszinski, H J (2003), Efficiency and effectiveness of wind farms – keys to cost optimized operation and maintenance, *Renewable Energy*, 28(14), 2165–78.

Kühn, M, Bierbooms, W, Bussel, G J W, Cockerill, T T, Harrison, R, Ferguson, M C, Goransson, B, Harland, L A, Vugts, J H and Wiecherink, R (1999), Towards a mature offshore wind energy technology – Guidelines from the Opi-OWECS Project, *Wind Energy*, 2, 25–58.

Lange, C H and Flint, A (2007), Structural reliability methods for improved designs against fatigue. *Proceedings – Annual Reliability and Maintainability Symposium IEEE*, 386–91.

Li, S, Wunsch, D C, O'Hair, E A and Giesselmann, M G (2001), Using neural networks to estimate wind turbine power generation. *IEEE Transactions on energy conversion*, 16(3), 276–82.

Londhe, S and Panchang, V (2005), One-day wave forecasts using buoy data and artificial neural networks, OCEANS, *Proceedings of MTS/IEEE*, 3, 2119–23.

Maes, M A and Faber, M H (2008), Utility, Preferences, and Risk Perception in Engineering Decision Making: Background Documents on Risk Assessment in Engineering, Joint Committee of Structural Safety (JCSS), Document #6, November 2008.

Mitra, S, Pal, S K and Mitra, P (2002), Data mining in soft computing framework: A survey. *Neural Networks, IEEE Transactions*, 13(1), 3–14.

Musial, W, Butterfield, S and McNiff, B (2007), Improving wind turbine gearbox reliability, an article by National Renewable Energy Laboratory. *Presented at the European Wind Energy Conference*, Milan, Italy.

NASA (2007), *NASA Systems Engineering Handbook*, NASA/SP-2007-610S Rev1.

Nilsson, J and Bertling, L (2007), Maintenance management of wind power systems using condition monitoring systems – lifecycle cost analysis for two case studies. *IEEE Transactions on Energy Conversion*, 22(1), 223–29.

Rademakers, L W M M, Braam, H and Verbruggen, T W (2003), R&D needs for O&M of wind turbines. ECN-RX-03-045.

Ribrant, J and Bertling, L (2007), 'Survey of failures in wind power systems with focus on Swedish wind power plants during 1997–2005', *IEEE transactions on energy conversion*, 22(1), 167–73.

Robb, D (2005), Wind energy at sea. *Refocus* March/April 2005.

Seebregts, A J, Rademakers, L W M M and van den Horn, B A (1995), 'Reliability analysis in wind turbine engineering', *Microelectronics Reliability*, 35(9–10), 1285–1307.

Sherwin, D J and Bossche, A (1993), *The Reliability, Availability and Productiveness of Systems*, Chapman & Hall, London, England.

Sherwin, D J (2000), A review of overall models for maintenance management. *Journal of Quality in Maintenance Engineering*, 6(3), 138–64.

Tandon, N and Choudhury, A (1999), A review of vibration and acoustic measurement methods for the detection of defects in rolling element bearings, *Tribology International*, 32, 469–80.

Tandon, N, Yadava, G S and Ramakrishna, K M (2007), A comparison of some condition monitoring techniques for the detection of defects in induction motor ball bearings, *Mechanical Systems and Signal Processing*, 21, 244–56.

Tavner, P J, Xiang, J and Spinato, F (2007), Reliability analysis for wind turbines. *Wind Energy*, 10(1), 1–18.

Teresa, H (2007), 'Wind turbines: designing with maintenance in mind', *Power Engineering*, May 2007.

Walford, C A (2006), Wind turbine reliability: understanding and minimizing wind turbine operation and maintenance costs, Sandia National Laboratory, SAND2006-1100, Springfield, VA 22161.

Wilkinson, M R and Tavner, P J (2004), Extracting condition monitoring information from a wind turbine drive train, *Universities Power Engineering Conference (UPEC) 2004, 39th International*, 2, 591–94.

Wood, J (2004), Up and Running: as the Offshore Wind Industry Develops, It's Learning From Some Painful Experiences, *IEE Power Engineer*, August: 27–29.

Zadeh, L A (1994), Soft computing and fuzzy logic, *Software, IEEE*, 11(6), 48–56.

11

Wind turbine condition monitoring systems and techniques

J. GIEBHARDT, Fraunhofer Institute for Wind Energy and Energy System Technology (IWES), Germany

Abstract: This chapter describes the main aspects of condition monitoring and fault prediction for large onshore and offshore wind turbines and gives an overview of the quantities to be measured for condition monitoring purposes. Examples are given for data processing and evaluation algorithms. The most relevant standards and technical guidelines are introduced. A discussion on the future of condition monitoring in wind turbines closes the chapter.

Key words: condition monitoring, fault prediction, spectral analysis, algorithms, component faults.

11.1 Introduction

This chapter discusses the main aspects of condition monitoring and fault prediction in large onshore and offshore wind turbines. Condition monitoring in the context of this chapter should be understood as a measure to observe the development of faulty conditions in wind turbine components and to give the operator of a wind turbine or wind farm information for the planning and organising of maintenance and repair activities.

Since there are various commercial solutions for condition monitoring systems (CMS), technical details of the hardware and software will not be discussed in this chapter. Such information can be obtained from the CMS manufacturers, for example from their Internet home pages. Section 11.2 gives an overview of the physical quantities, which are of interest for condition monitoring and fault prediction purposes, and their measurement. In Section 11.3, algorithms for data processing and evaluation are discussed. Using an example of typical faults in the main components of wind turbines, time signal-based algorithms as well as those based on spectral analysis and frequency domain calculations are introduced. Section 11.4 introduces the most relevant standards and technical guidelines with respect to condition monitoring. An outlook to the future challenges, developments and requirements of condition monitoring in wind turbines closes the chapter.

11.2 Metrology for condition monitoring

To perform online condition monitoring and fault prediction functions, robust sensor and data acquisition equipment for continuous (i.e. ‘online’) measurements

is required. The following sections describe the required measurement hardware. The measurement principles and the major specifications according to bandwidth, sensitivity, etc., of the most common sensor types will be discussed. Table 11.1 shows a selection of the most relevant measures and the basic requirements for the respective sensors. A detailed description of the required measurements for condition monitoring in wind turbines can be found in Upwind-Report 2008.[1]

11.2.1 Measurement of power and wind speed

Measurement of the wind speed and the power output of a wind turbine yields information about the overall condition and is used as a classification measure for other fault descriptive quantities. For wind speed measurement to be used for condition monitoring, the integral anemometer of the wind turbine can be used. Active power output is measured by use of commercial power transducers. Typically, the anemometer output is a pulse signal, where the pulse frequency is proportional to the wind speed. Values will be taken by measuring the anemometer pulse frequency and calculating the wind speed according to the anemometer's

Table 11.1 Measurement requirements for condition monitoring (selection)

Quantity	Base unit	Accuracy	Bandwidth	Sensitivity	Range	Signal type
Power output	kW	5%	0–2 Hz	Depends on turbine size	–100 kW to +20 MW	Analogue or data
Wind speed	m/s	5%	3 Hz RR[a]	–	0–50 m/s	Pulse
Acceleration	m/s^2	5%	0–20 Hz	2 V/g[b]	± 2 g	Analogue
Vibration	m/s^2	5%	3–20 kHz	100 mV/g	± 20 g	Analogue
RPM	RPM or Hz	1%	3 Hz RR	–	0–3000 RPM	Pulse
Shaft position	Degree	5%	3 Hz RR	–	0–360 degrees	Analogue, pulse, data
Oil particle number	Number	10%	1 Hz RR	–	–	Pulse or data
Oil conductivity and pH value	S and pH	10%	1 Hz RR	1 V/Sm 500 mV/pH	0–10 Sm 0–14 pH	Analogue or data

[a] RR: refresh rate of the signal, i.e. number of measured values per second.
[b] g: gravitational constant g = 9.81 m/s^2.

characteristics. The output signal of the power transducer is represented by a voltage or current loop signal and is measured with analogue to digital conversion (ADC) inputs of the used CMS.

11.2.2 Measurement of nacelle oscillations

Nacelle oscillations can be used for indirect monitoring of the rotor condition. The measurements to be used for this are the transverse and axial nacelle oscillations related to the rotor shaft. Figure 11.1 shows a typical sensor configuration for measuring the nacelle oscillation of a horizontal axis wind turbine. Since rotor-induced nacelle oscillation frequencies are very low (typically from 0.1 Hz to 10 Hz), the acceleration sensors must be able to measure within a bandwidth of 0 Hz (DC) to a maximum of about 20 Hz. This covers the required frequency band for rotor condition monitoring data analysis very well. For more detailed technical specifications about condition monitoring see Table 11.1.

There are three oscillation modes that a wind energy converter's nacelle can perform, which are relevant for rotor condition monitoring and fault prediction: transverse to the rotor axis, in line with the rotor axis and as torsion around the vertical tower axis. These oscillation modes are shown in Fig. 11.1 (see arrows). To monitor these oscillations, three acceleration sensors are required. The sensor

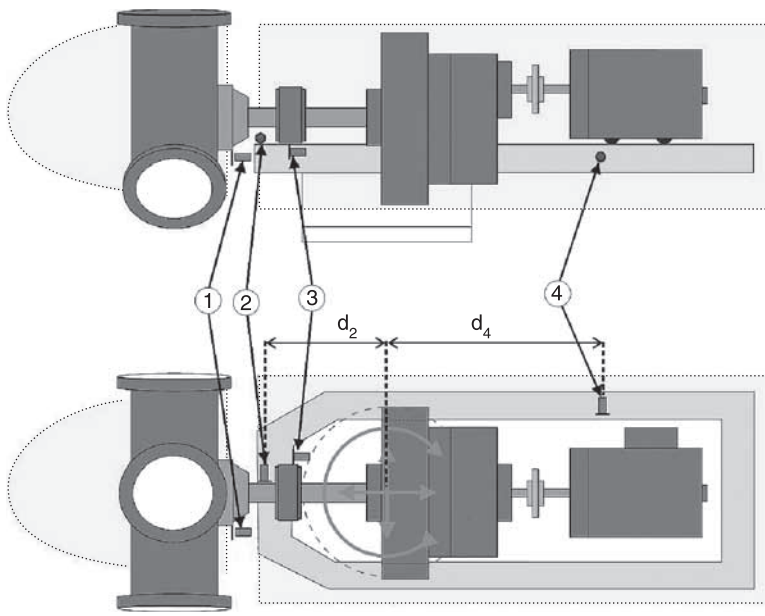

11.1 Sensor configuration for measurement of low frequency nacelle oscillations with accelerometers.

with label 3 in Fig. 11.1 is sensitive in the axial direction (related to the rotor axis). Sensors at labels 2 and 4 are sensitive in the transverse direction to the rotor axis. The sensor shown at label 1 is an inductive distance sensor. This sensor gives a reference signal for the absolute rotor position, when one blade is in the vertical upright position. This blade by definition is blade 1. Rotor position information is required to calculate the phase information, which helps to detect the rotor faults mass imbalance and aerodynamic asymmetry.

The acceleration sensors provide a voltage output signal, which is connected to the respective analogue input channels of the CMS. Appropriate low-pass filtering of the signals has to be done before ADC to allow the application of spectral analysis-based algorithms. The digitised values then contain information of all relevant nacelle oscillation frequencies to perform the rotor condition monitoring tasks.

11.2.3 Vibrations

Vibration measurement is used to evaluate the condition of bearings and gear wheels. For this purpose, piezoelectric vibration sensors are suitable. These sensors can measure mechanical vibrations in a frequency range of 3Hz–20 kHz. Detailed information about condition monitoring of bearings and gear wheels is given in various publications, for example in Final Public Report of the EC Project (2006).[2] Table 11.1 shows the technical requirements for vibration measurement.

11.2.4 Shaft RPM and position

Some of the characteristic values used for condition monitoring and fault prediction are correlated to the RPM and absolute position of rotating components. For RPM measurement, an easy and very reliable way is to use inductive approximation sensors, which face the bolts of a shaft coupling or the mounting bolts of the rotor hub. This will generate a pulse signal, where the pulse frequency (as the product of the rotational shaft frequency and the number of bolts) gives the RPM value. To achieve a reasonable signal resolution, the minimum pulse frequency should not be less than 5 Hz. Table 11.1 shows the measurement requirements. The given bandwidth means that there should be at least three readings of the RPM value per second possible (refresh rate). This corresponds to the minimum required pulse frequency of 5 Hz as mentioned above.

To perform some specialised fault prediction algorithms, the absolute position of the rotating component under test has to be measured. In most of the cases, a single pulse per shaft revolution is sufficient. Such a pulse signal can be derived from the above-described measurements with an inductive approximation sensor. It only has to be modified in a way that a single pulse per shaft revolution is generated by passing only one bolt or a small metal object on the rotating shaft or

hub. If a higher resolution with interim values over one revolution is required, an electronic position encoder can be used. From these sensors, the actual position value can be read out via a communication line (e.g. RS485 with the SSI protocol). Some of them have an additional analogue output, which gives a ramp-shaped output signal (e.g. 0–360 degree corresponds to 4–20 mA).

11.2.5 Oil monitoring

Wear of bearings and gear wheels causes particles to develop in the oil of wind turbine gearboxes. If the number and/or size of particles (above a minimum size) in the oil increases, a developing fault can be assumed. Therefore, the oil particle number counting (see Table 11.1) can be used for condition monitoring purposes. The output of an oil particle sensor can be a pulse signal or a counter data value.

11.3 Algorithms for condition monitoring

This section describes the functionality of several condition monitoring algorithms developed for online signal processing, fault detection and fault classification. In section 11.3.1 the monitoring of the wind turbine's power characteristic as an indicator for the overall health/performance is described. Section 11.3.2 describes the monitoring of the nacelle oscillations which are used to detect rotor faults. In section 11.3.3 the algorithms for monitoring of the drive train are described. Section 11.3.4 gives some basic information of the monitoring of the electrical system. Finally, section 11.3.5 gives an overview of the data classification, which has to be applied to all the condition monitoring algorithms mentioned.

11.3.1 Monitoring of power characteristic

The relation between wind speed and active power output of a wind energy converter provides information about the overall rotor condition, which for example can be influenced by blade pollution, increased surface roughness, icing and so on. To obtain this information from the raw data, the calculation of five-minute mean values (i.e. 300s mean values) of wind speed and power have been proven to be suitable, with N = (number of samples per seconds) × 300s:

$$\overline{v}_W = \frac{\sum_{i=1}^{N} v_{Wi}}{N} \text{ and } \overline{P} = \frac{\sum_{i=1}^{N} P_i}{N} \qquad [11.1]$$

The power characteristic monitoring starts with a learning phase. In this phase, the calculated pairs of mean values as described in equation [11.1] are classified in wind speed classes of a width of 0.5 m/s. Once there is a sufficient number of values binned in each class, the class mean value $\overline{P}_{Class}$ and the standard deviation

$\sigma(\bar{P})$ are calculated. The resulting curve $\bar{P}_{Class}(\bar{v}_W)$ is called the power characteristic of the wind energy converter.

For monitoring the power characteristic, the anemometer on the nacelle can be used for wind speed measurement. The measurements described above then do *not* represent the nominal power performance curve of the wind energy converter (e.g. as measured by certification institutes according to the IEC61400-12 standard). Nevertheless, to monitor the overall rotor performance these measurements are sufficient, since only deviations from the faultless condition as determined in the learning phase have to be considered.

As soon as the learning phase is completed, alarm limits will be calculated and the monitoring phase starts. Figure 11.2 shows the power characteristic of a 600 kW wind turbine with stall power limitation. The dots result from pairs of $\bar{P},\bar{v}_W$ and the dark grey circles represent the calculated (learned) class mean values $\bar{P}_{Class}$. The light grey circles represent the certified power curve provided by the wind energy converter manufacturer. The outer thin lines are absolute alarm limits which have to be determined by an application programmer of the used CMS. The inner thin lines are calculated alarm limits. The distance of the calculated (inner) alarm limits (named here as L_{dist}) to the class mean values $\bar{P}_{Class}$ have to be determined by an application programmer who sets up the CMS. For definition of the distances a heuristic approach has been chosen:

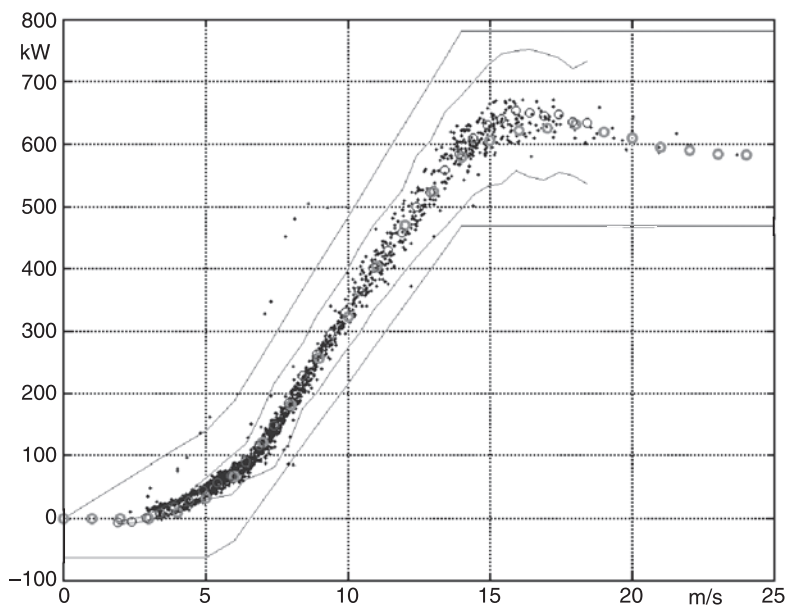

11.2 Power characteristic of a 600 kW wind energy converter with absolute and learned alarm limits.

$$L_{dist}(\overline{v}_W) = K_1 \cdot \overline{P}_{Class}(\overline{v}_W) + K_2 \cdot \sigma\left(\overline{P}_{Class}(\overline{v}_W)\right) \quad [11.2]$$

With the calculated distances the curves for the upper and lower alarm limits L_{UP} and L_{LO} as a function of the wind speed class mean value are given by:

$$\begin{aligned} L_{UP}(\overline{v}_W) &= \overline{P}_{Class}(\overline{v}_W) + L_{dist}(\overline{v}_W) \\ L_{LO}(\overline{v}_W) &= \overline{P}_{Class}(\overline{v}_W) - L_{dist}(\overline{v}_W) \end{aligned} \quad [11.3]$$

As mentioned above, the distances will be calculated within a learning phase. The length of this phase is individual for each class. It ends either when more than a given number of pairs of $\overline{P},\overline{v}_W$ have been evaluated or after a defined time period. Experiences from field tests with several CMS have shown that a number of 20–50 learned values for each class is suitable. The learning period should not exceed three months. After the end of the learning phase (i.e. either the maximum number of values are learned in the respective class or the three-month period has expired) the monitoring phase starts individually for each class. In this phase every incoming pair of $\overline{P},\overline{v}_W$ is classified and $\overline{P}$ is checked against the alarm limits.

The learned alarm limits can be parameterised by an application programmer. The parameter K_1 in equation [11.2] considers the higher turbulence intensity of power output at higher wind speeds by spreading up the alarm limits. Parameter K_2 considers the scatter of the measured mean values. Since the scatter results from random effects (measurement uncertainties and wind field turbulences) it can be assumed that the values are normal (Gauss) distributed. A value of 3 for K_2 then would assure that 99% of the values for pairs $\overline{P},\overline{v}_W$ will be inside the alarm limits at faultless operation of the wind energy converter. Since the alarm limits already have a certain distance given by the factor $K_1 \cdot \overline{P}_{Class}$, the value for K_2 should be slightly reduced. From the experiences from several field tests, it seems that a parameter setting of $K_1 = 0.1$ and $K_2 = 2.0$ is a good choice.

To avoid false alarms caused by one extreme values of a pair $\overline{P},\overline{v}_W$, a threshold criterion is used. This criteria means that an alarm is triggered only when more than a determined number (to be set up by the CMS application programmer) of subsequent values of $\overline{P},\overline{v}_W$ exceed the alarm limit. Since measurement of every pair of $\overline{P},\overline{v}_W$ takes 5 minutes, a compromise between the robustness of the algorithm against extreme data points causing false alarms and the reaction time in case of a fault must be found. A number of three subsequent alarm limit overruns (corresponding to a reaction time of 15 minutes) will give a reasonable threshold criterion in this respect. This means that if the fourth subsequent value of $\overline{P},\overline{v}_W$ exceeds an alarm limit, a problem with the rotor performance is detected and an alarming action is triggered by the CMS.

11.3.2 Monitoring of nacelle oscillations

Rotor faults in wind turbines induce specific oscillations of the nacelle. A mass imbalance of the rotor will bend the tower in the transverse direction (relative to

the rotor axis) with the rotational frequency. An aerodynamic asymmetry of the rotor will induce a complex nacelle oscillation pattern (for details see Giebhardt, 2006[6]). This section describes the relevant algorithms to monitor the nacelle oscillations and to derive fault information from it.

Spectral analysis and order analysis

To analyse periodic nacelle oscillations, the fast Fourier transform (FFT) algorithm is used. For constant speed wind turbines the FFT algorithm is directly applied to the measured acceleration time signals $a(t)$. To analyse nacelle oscillations of variable speed wind turbines, a modified algorithm has to be used which is called order analysis. This algorithm is based on samples recorded at equidistant rotational angles φ_R instead of time-equidistant samples. If the measurement equipment does not allow proper samples directly triggered according to the rotor angle φ_R, the required data samples for order analysis can be generated by applying an interpolation algorithm to the time series of the acceleration signals. This algorithm uses the rotor position signal as a reference. The continuous variables t and φ are replaced by their time-discrete counterparts defined by the sample time T and the sample angle Φ_R ($k = 0, 1, 2, 3, \ldots$):

$$a(kT) \xrightarrow{Interpolation} a(k\Phi_R) \qquad [11.4]$$

Applying the FFT algorithm to $a(k\Phi_R)$ generates the complex discrete order spectrum $A(f_O)$ with the discrete 'order frequency' f_O as the abscissa. For details of the spectral order analysis refer to the extensive literature in this field (e.g. Oppenheim and Schafer, 1989).[3]

The frequencies of nacelle oscillations to be evaluated are quite small. Especially for large wind energy converters the frequency range in scope is from about 0.1–3 Hz. To evaluate these low frequencies with a reasonable spectral resolution Δf, the time window length T_{WIN} for the FFT and order analysis should be at least 100 s ($\Delta f = 1/T_{\mathrm{WIN}}$). An advantage of these long evaluation time windows is that the random influences resulting from incoherent wind fields will be damped in the calculated spectra. Another way to reduce these influences is to average the calculated spectra over several time windows, using Welch's method (refer to Oppenheim and Schafer, 1989).[3]

Calculation and monitoring of 1p nacelle oscillations

To monitor the 1p (i.e. at the rotational frequency of the rotor) nacelle oscillations of a wind turbine, amplitude and phase of the 1p spectral components have to be analysed. The axial nacelle oscillation can be derived directly from the order spectrum at 1p frequency of the respective acceleration sensor time signal, that is, the component at $A_{AXIAL}(1p)$.

The transverse and torsion components of the 1*p* nacelle oscillations can be calculated out of the order spectra of the two transverse acceleration signals. With the configuration shown in Fig. 11.1, both of the transverse sensitive sensors (labels 2 and 4) measure the pure transverse oscillation of the nacelle with the same phase.

Since one of the sensors is mounted in front of the tower's vertical axis and the other one is at the rear of it, torsion oscillation of the nacelle generates an acceleration signal contribution in the front sensor, which is in opposite phase (or in other words: the phase shift is π) to the acceleration signal contribution in the rear sensor.

Therefore, transverse and torsion oscillations can be separated by adding or subtracting the complex spectral components of the sensor signals at 1*p* frequency respectively:

$$A_{TRANS}(1p) = \frac{d_4 \cdot A_{Sensor\,2}(1p) + d_2 \cdot A_{Sensor\,4}(1p)}{d_2 + d_4} \quad [11.5]$$

$$A_{TORS}(1p) = \frac{A_{Sensor\,2}(1p) - A_{Sensor\,4}(1p)}{d_2 + d_4} \quad [11.6]$$

The weight factors d_2 and d_4 in equations 11.5 and 11.6 represent the distance of the sensors 2 and 4 (see Fig. 11.1) from the vertical tower axis as a projection to the rotor axis. Weighting is required for calculation of the transverse oscillation, since the measured acceleration amplitude of the torsion nacelle oscillation, which has to be eliminated from the spectrum, depends on the distance of the acceleration sensor mounting position from the vertical tower axis. For calculation of the torsion oscillation, no weighting is required, since the transverse acceleration signal contribution and, therefore, the amplitude in the spectrum does not depend on the sensor distance projection from the vertical tower axis.

Trend analysis and alarm generation

Trend analysis and alarm generation for complex values require special algorithms. To monitor 1*p* nacelle oscillations, both amplitude and phase of the complex spectral components have to be analysed. Figure 11.3 shows the principle of functionality of a trend analysis and alarm generation algorithm for monitoring complex spectral components. To monitor amplitude and phase simultaneously, the alarm limit is represented by a circle around the tip of the complex mean value $\underline{X}_0$, which represents the faultless condition of the rotor. The differential vector $d\underline{X}_1 = \underline{X}_1 - \underline{X}_0$ represents the case of changes in phase with a constant amplitude. Vector $d\underline{X}_2 = \underline{X}_2 - \underline{X}_0$ shows a case where only the amplitude increases, whereas the phase angle remains almost unchanged. This means that these two extreme conditions for changes of complex values are covered by the algorithm. Therefore, with the proposed circular alarm limit, obviously all other changes in between the two extremes will also be recognized by the algorithm.

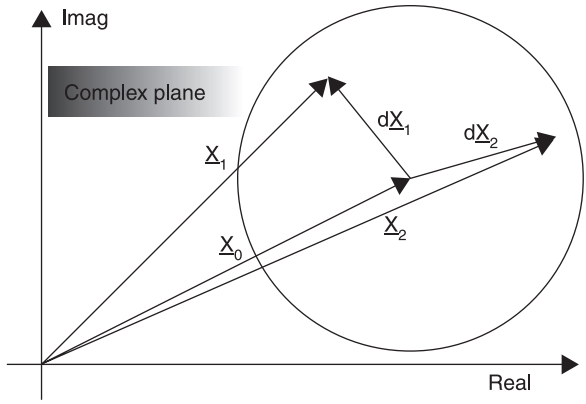

11.3 Monitoring of complex spectral components with a circle-shaped alarm limit.

A physical application of the above-described complex trend analysis is the monitoring of a wind turbine's rotor. Looking at the faults related to mass imbalance and aerodynamic asymmetry of the rotor, the first type of fault will increase the amplitude of the 1*p* transverse nacelle oscillation (i.e. the spectral component at rotor rotational frequency resulting from an order analysis), but will leave the phase nearly unaffected. An aerodynamic asymmetry will result in a phase shift of the axial 1*p* nacelle oscillation with only a small increase of the related amplitude. A detailed description of the mentioned rotor faults and their monitoring is given by Giebhardt (2006)[6].

X_0 as the absolute value of the complex number $\underline{X}_0$ results from a learning phase, which is performed under faultless condition of the rotor to be monitored. In this phase the incoming complex values $\underline{X}_i$ will be averaged by averaging the real part and imaginary part separately:

$$\mathrm{Re}\left\{\underline{X}_0\right\} = \frac{\sum_{i=1}^{N} \mathrm{Re}\left\{\underline{X}_i\right\}}{N} \quad \textit{and} \quad \mathrm{Im}\left\{\underline{X}_0\right\} = \frac{\sum_{i=1}^{N} \mathrm{Im}\left\{\underline{X}_i\right\}}{N} \qquad [11.7]$$

After a user-specified number N of values has been averaged, the radius of the alarm limit circle is calculated from the scatter of the learned $\underline{X}_i$. Since the scatter is caused only by random effects (measurement uncertainties and wind field turbulences) in faultless operation of the wind turbine, it can be assumed that the values are normally distributed. The radius r_{AL} of the alarm limit circle is calculated as a multiple of the standard deviation of X_0:

$$r_{AL} = K \cdot \max\left(\sigma\left(\mathrm{Re}\left\{\underline{X}_0\right\}\right), \sigma\left(\mathrm{Im}\left\{X_0\right\}\right)\right) \qquad [11.8]$$

To keep the calculation of radius r_{AL} simple, the maximum value of the two possible standard deviations is used. Experiences from field tests have

recommended a value of 20 for the number N of averaged X_i in equation [11.7]. For the parameter K in equation [11.8], a value between 3.5 and 4.5 is recommended.

Once the alarm phase is activated, exceeding of the alarm limit is checked continuously by calculating the actual differential vector from the actual amplitude and phase measurements of $\underline{X}$ with respect to $\underline{X}_0$. An alarm is triggered when the absolute value of the calculated difference $d\underline{X} = \underline{X} - \underline{X}_0$ exceeds the alarm limit circle radius. As a threshold parameter a number of three subsequent alarm limit overruns is required to cause the CMS to trigger an alarming action.

11.3.3 Monitoring of the drive train

This section describes the different approaches for monitoring drive train components. There are low-level algorithms used as well as those for advanced spectral analysis. The latter are based on the same principles as those described in section 11.3.2, but applied in a completely different frequency range (10 Hz < f < 10000 Hz).

Faults in drive train bearings and gear wheels

In the scope of the condition monitoring, there will be bearings on shafts, in the gearbox and in the generator. Most of the bearings used in wind turbines are roller bearings. Therefore, all the following statements according to fault description, causes and detecting algorithms will be related to the elements of roller bearings. Common causes for roller bearing faults and damage as well as their consequences are given in Table 11.2. In Table 11.3, some typical faults are described, which can occur with gear wheels.

Statistical algorithms

Statistical algorithms are used to analyse the time signals of vibration sensors. The approach is to calculate statistical values for a trend analysis and to learn more about the shape of the vibration signal. It is assumed that vibration signals taken from intact bearings are normally distributed, since the sonic pulses will be generated by the rolling elements and surfaces in a random way. If a fault on the bearing starts to develop, sonic pulses with higher energy (spikes) can be found in the vibration signals. The presence of those spikes can be identified with the statistical analysis algorithms as described below. Advantages of these statistical algorithms are that they give an absolute measure for the condition of the respective bearing; there is no training phase required to learn the baseline values, which correspond to a fault-free condition of the component. Disadvantages of these algorithms are the relatively poor selectivity, which means that a change in the value does not point to a certain faulty component of a bearing, for example the inner ring surface. Here are some examples for statistical characteristic values

Table 11.2 Typical roller bearing faults

Category	Damage	Cause	Consequences
Abrasion	Wear	Abrasion of surfaces under design loads, increased wear due to lubrication problems	Increased bearing clearance
	Fatigue	High loads, eventually beyond design loads	Cracks and break-out of particles from surfaces
Overload	Deformation	Extreme loads, ongoing wear	Plastic surface deformation of roller elements and rings, pitting
	Fracture		Fracture of roller cages and rings
Overheating	Heat stress cracks	Overheating and cooling within short periods	Cracks in bearing components
	Overheated operation	Over RPM, dimension changes by heat extension, lubrication problems (too much, too little, pollution)	
Corrosion	Corrosion of surfaces	Lubricant humidity, environmental influences (salt water in offshore WECs)	Increased wear, lubricant pollution
Electrical current conduction	Surface break-out and adherence	Bearing has to conduct high electrical currents due to lightning strikes, electrical problems (induced currents)	High abrasion, surface adherence due to sparks and surface welding

WEC, wave energy converter.

used for bearing condition monitoring. The time signal to be analysed is represented by its discrete form $x(t) \rightarrow x(iT)$ or x_i, ($i = 0, 1, 2, 3, \mathrm{N}$) with T as the sample time interval. The number of intervals is $N = T_{\mathrm{Meas}}/T$ (T_{Meas} is the measured length of the time signal). This results in the following representations of the statistic values:

Maximum value: $\hat{x} = \max(x_i)$

Mean value: $\overline{x} = \frac{1}{N}\sum_{i=1}^{N} x_i$

Table 11.3 Typical faults on gear wheels

Category	Damage	Cause	Consequences
Cracks	Tooth base cracks	Extreme torque loads, blocking due to debris inside gearbox	Cracks or complete break-out of teeth
	Tooth face cracks		Pitting, surface peeling
Tooth face	Cracks, pitting, grey marks, surface peeling, wear, erosion	Wrong geometry, torque overload, vibrations	Ductile surface deformation of teeth, pitting on contact surfaces
Overheating	Heat stress cracks	Overheating and cooling within short periods	Cracks in teeth
	Overheated operation	Over RPM, dimension changes by heat extension, lubrication problems (too much, too little, pollution)	High abrasion, surface adherence
Corrosion	Corrosion of surfaces	Lubricant humidity, environmental influences (salt water in offshore wind turbines)	Extreme wear
Current	Teeth have to carry high electrical currents	Lightning strikes, electrical problems	Surface adherence

$$\text{RMS value: } x_{RMS} = \sqrt{\frac{1}{N}\sum_{i=1}^{N} x_i^2}$$

$$\text{Crest factor: } CF = \frac{\hat{x}}{x_{RMS}}.$$

The crest factor has a value of approximately 3 for an ideal normally distributed signal. This is because the maximum value in a normally distributed signal (the so-called 'white noise') is nearly 3σ, the RMS is 1σ. If a fault is developing in a bearing, the spike amplitudes and, therefore, the maximum value of the signal increases. In an early occurrance of the faulty condition, this will not affect the RMS value, since the spike energy is small related to the overall energy of the signal. Therefore, the RMS value does not change significantly and the crest factor increases. Fault detection and the generation of CMS alarms is done by trend analysis of the crest factor. Although calculation of the statistic values of vibration signals is not dependent on the measurement time, an appropriate time

window should be measured, for example 1 s. In any case, the measurement time should be a multiple of the grid frequency (20 ms in Europe), because this will help to eliminate signal distortions related to grid EMC effects.

Time series based algorithms

An approach using only the pure time signal $a(t)$, for example from a vibration sensor, for detection of bearing faults is the calculation of the bearing condition unit (BCU). This approach is based on a special signal conditioning within the time domain which gives a signal proportional to the spike energy in a time signal. The algorithm in principle uses the effect that a fault on a bearing element induces spike pulses. These pulses excite the Eigen resonance of the attached vibration sensor. The signal conditioning unit will perform a bandpass filtering of the sensor signal, for example in a frequency range of 5–30 kHz (the Eigen resonance frequency of the sensor must be in this interval!). The filter output will be rectified and low-pass filtered (see Fig. 11.4). The mean value of the resulting signal is the BCU value and gives a measure for the spike energy in the sensor signal. The trend analysis of the BCU will detect developing bearing damage.

Spectral analysis based algorithms

1. Fault frequency calculation: All moving elements in a bearing or a gearbox generate vibration at defined frequencies, the so-called fault frequencies. They

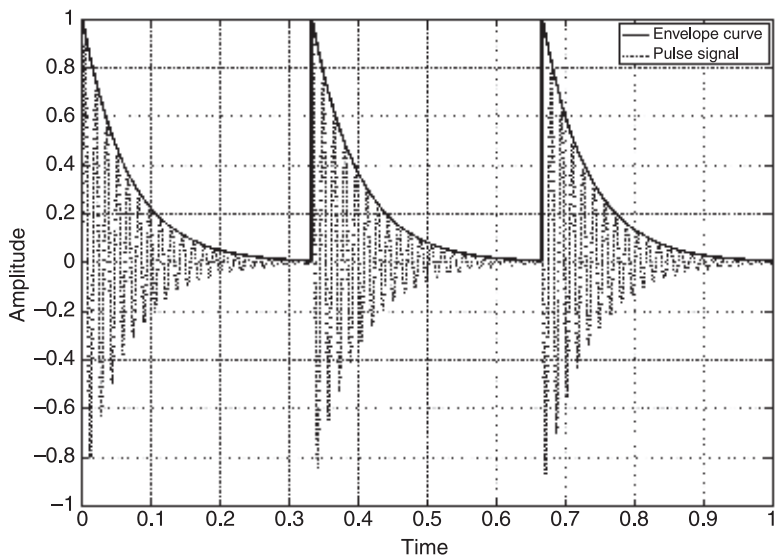

11.4 Principle of the BCU filtering.

depend on the geometry of the bearing, the roller elements and the wheels as well as on the rotational frequency of the shaft attached to the bearing under consideration. Algorithms for the calculation of fault frequencies can be found in the literature or can be obtained from the manufacturer's technical documentation.

2. Standard FFT: The standard FFT algorithm computes the complex spectrum of a time signal. To get characteristic values for the monitoring of bearings, the amplitudes and phase values of the spectral components at the respective fault frequencies will be analysed. For this, normally the absolute value of the spectrum is calculated and a trend analysis is performed. To analyse faults in gear wheels, the sideband amplitudes of fault frequencies (in that case they are called 'tooth mesh frequencies') and their trend development can be of interest.
3. Order analysis: Since most of today's wind turbines work at variable speed, the FFT algorithm faces some problems. When the frequency of the spectral component to be monitored varies within the analysed time window, the spectral peak related to it is no longer a peak but is 'stretched' to some kind of a knoll. Defined analysis of this particular spectral component is no longer possible. To get an idea of the problem, consider the following example: to monitor a spectral component at a fault frequency of 100 Hz with a resolution of 0.1 Hz, a time window of 10 s length has to be analysed. If the RPM of the wind turbine's drive train varies by ten per cent (which can easily happen during normal operation) within this 10 s interval, the 'peak' at 100 Hz will be stretched over a frequency range of about 10 Hz, for example from 95 Hz to 105 Hz.

   The problems described are avoided by use of the order analysis. For the order analysis, an equidistant sampled time signal will be transferred to a signal, which is equidistant sampled according to the rotational angles of the respective rotating component (shafts) in the drive train. For this, one of the shafts in the drive train must be the reference shaft. Applying the FFT to a shaft angle equidistant sampled signal, there will no longer be a spectrum produced with a frequency abscissa but with an 'order' abscissa. The (variable) rotational frequency of the reference shaft is as per definition related to 'order = 1'. The fault frequencies can be calculated by multiples of this order 1, for example for a bearing with 10 rolling elements on the reference shaft, the passing frequency will be at order = 10. For fault frequencies on other shafts, the gear ratio according to the reference shaft must be taken into account.

   The order analysis in its various forms of appearance is a very useful instrument to perform condition monitoring and fault prediction for variable speed offshore wind turbines. There are different approaches to get the above-mentioned 'rotational angle' equidistant sampled signal. One way is to use trigger pulses deduced from one of the shafts in the drive train, which then should also be the reference shaft. This can be realised quite easily with modern type data acquisition equipment. But this method is quite inflexible according to the sampling resolution. Therefore, another way is to measure the RPM of the reference shaft and interpolate a normal time signal to an order

signal by use of digital interpolation algorithms. This requires a very accurate RPM measurement with a high resolution according to the shaft angle, but is much more flexible since several of the above-mentioned FFT based analysis methods can be applied to the same time series input signals.

4. Envelope curve spectral analysis: This type of analysis is very sensitive for detecting bearing faults. The output of this algorithm is a spectrum with a significant peak at the dominant fault frequency and its harmonics. For calculation of an envelope curve spectrum (ECS), a high-pass filter eliminates signal components below the acceleration sensor's resonance frequency. The resulting time signal is rectified and low-pass filtered. From this signal, an FFT/order analysis is performed. Figure 11.5 shows a comparison of the standard FFT (a) and the ECS algorithm (b). As can be seen, the fault frequency in question (here a bearing fault frequency at 103 Hz) can be seen much more clearly in the ECS.

Drive train fault prediction

The prediction of faults in the drive train faces some particular problems. The above-described algorithms for calculation of fault describing values and their

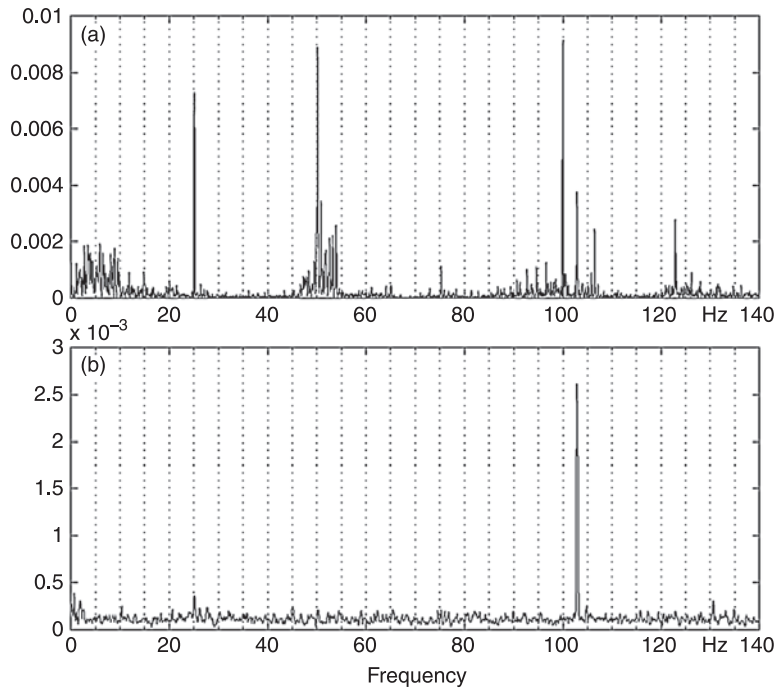

11.5 Comparison between (a) standard FFT and (b) ECS algorithm for a bearing fault.

analysis can be automated in principle. But to ensure safe fault recognition, a lot of testing and long-term experience is required. This would require a high personnel effort as well as a wide database of measurements, causing high demand for database storage capacity.

Therefore, an often-used approach to predicting faults in wind turbine drive trains is to monitor some basic scalar values (temperature ratios, CF and RMS of vibration signals, oil particle counting, etc.). As soon as one of those basic values show an increasing trend, an expert will trigger and analyse more detailed measurements as the described various spectral analysis algorithms. Such an approach provides a large number of wind turbines with appropriate condition monitoring at a reasonable personnel and data handling level.

11.3.4 Monitoring of electrical components

The main electrical component in a wind turbine is the generator and, depending on the concept, the power electronic equipment. Some promising concepts for monitoring the electric parts of a generator are described in Tavner *et al* (2008).[4] For monitoring of cabling, switching gear, contacts in electrical cabinets, etc., thermography is a newly introduced method. A loss of conductivity due to contact corrosion or loosening in the above-described components will lead to higher thermal power loss caused by the faulty location. This can be clearly seen with IR cameras. Figure 11.6 shows a thermo image of an electrical cabinet with a temperature hot spot in the upper left corner, pointing to a fault in a circuit breaker.

11.3.5 Classification

Depending on the particular type of the wind turbine to be monitored, the above-described fault descriptive measurements can depend on the actual load condition

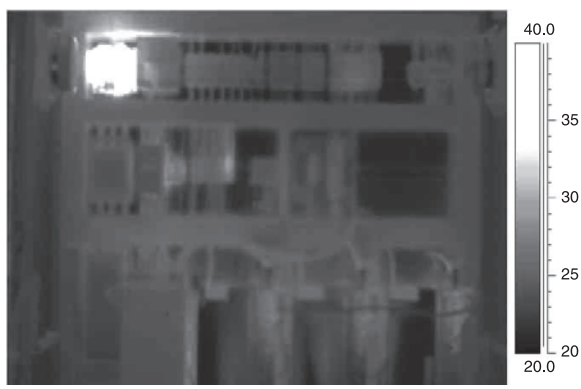

11.6 Thermo image of an electrical cabinet.

and the RPM of rotating components. A measure of the load condition is the active power output, so it can be used to classify the calculated fault describing values, for example spectral amplitudes. The number of classes and class width to be used depends strongly on the type of measurement, so no generalised parameters can be given here. This is a matter of experiences of the CMS application programmers. The same is true for rotating component RPM.

Besides the regular classification algorithms, fuzzy classification can be used. This allows the application programmer of a CMS to include expert knowledge about the correlation between spectral amplitudes and power output. This expert knowledge is defined in the 'rule base' of a fuzzy classification algorithm. An example for such rules could be:

> 'If *power output is high* and *amplitude of 1p transverse nacelle oscillation is medium* then *rotor mass imbalance alarm condition is OK*'

or

> 'If *power output is low* and *amplitude of 1p transverse nacelle oscillation is high* then *rotor mass imbalance alarm condition is FAULT*'.

For a detailed description of fuzzy classification algorithms and classification results refer to Bothe (1995) and Giebhardt (2006).[5,6]

11.4 Condition monitoring standards and technical guidelines

11.4.1 Communication standard IEC 61400-25

The IEC 61400 is a comprehensive standard, covering most of the relevant technical items of wind turbines. The relevant part for CMS applications is Part 25 'Communications for monitoring and control of wind power plants' with its subparts (see structure given below). Once implemented, the given definitions of the internal communication between the different wind turbine components will allow easy access to the internal data of the controller by a CMS. This can be used to get information about the actual load condition of the wind turbine, for example to classify fault descriptive measurements like vibration levels according to the power output. Furthermore, the different temperatures and environmental conditions measured by the controller can be made available for the CMS.

The subpart 6, which is under development at the moment, deals with the communication of CMS itself with the outside world. Among others, the format and contents of CMS data (time series, spectra, trends, warnings, alarms, etc.) to be transmitted to a database server or an operator are defined here. More information about the IEC 61400-25 can be found on the IEC web site (www.iec.ch, type '61400-25' into the search engine).

Structure of IEC 61400 Part 25 'Communications for monitoring and control of wind power plants'
Subparts published (Status: 2009-05):

- IEC 61400-25-1 Overall description of principles and models
- IEC 61400-25-2 Information models
- IEC 61400-25-4 Mapping to communication profile
- IEC 61400-25-3 Information exchange models
- IEC 61400-25-5 Conformance testing

Subparts under editing:

- IEC 61400-25-6 Logical node classes and data classes for condition monitoring

11.4.2 Certification of condition monitoring systems

The certification process for CMSs was initiated by the German insurance company Allianz. Due to the growing number of faults on the gearboxes and bearings of wind turbines, Allianz insisted on installing a CMS for the respective components or, alternatively, replacing these components regularly every 5 years. To ensure a minimum functionality of the CMS, a certification procedure was worked out by the German Allianz Zentrum für Technik (AZT) in cooperation with Germanischer Lloyd (GL), wind energy department, Germany. The outcome of this is a certification guideline (2007).[7] This certification is now accepted all over Europe as a standardised functional description of CMS for wind turbines. The GL certificate is mandatory, if the CMS is to meet the requirements of the German wind turbine insurance regulations. The main manufacturers/suppliers of CMS for wind turbines have achieved the certificate for their systems. A regularly updated table, which shows the certificated systems, can be found on the GL web site at: (http://www.gl-group.com/pdf/certlist_cms.pdf).

11.5 Future trends in condition monitoring

11.5.1 New sensor technologies

Newly developed sensor technologies allow new monitoring and fault prediction tasks in wind turbines. As an example, monitoring of the bending moments in the blade root as an indication for the rotor condition will be discussed here. With classic resistance-based strain gauges (SGs), measurement of the blade root bending moment is problematic. Those SGs are hard to attach to the FRP surface of rotor blades. Experience from field tests has shown that resistor SGs did not survive more than about five years on wind turbine rotor blades. For condition monitoring purposes, the SGs must survive as long as the blade being monitored, that is at least about 15 years. Meanwhile, SGs have been developed, which work

on an optical principle, the so-called fiber Brag gratings (FBG) SGs. These sensors measure strain exposed to an optical fibre. The technology allows up to 20 measurement positions in a single fibre. Therefore, one rotor blade can be equipped with full two-axis strain measurement with four sensors at the blade root and at one or two more positions along the blade's length. An application example for FBG strain measurement in wind turbines can be found in Verbruggen (2004).[8] Other innovative developments are expected with new wind speed measurement systems, based on sonic (SODAR) or light reflection (LIDAR) effects.

11.5.2 Condition monitoring system integration

Today's CMSs are normally installed with their own computing hardware for data acquisition and processing. This is due to historical reasons, since the turbine controllers of older turbines have no computing capacity left for calculating condition monitoring algorithms and tasks. In modern type wind turbine of the multi-megawatt class, the performance of wind turbine controllers has increased significantly. This would allow integrating condition monitoring and fault prediction functionalities into the controller system of a wind turbine. Advantages of such integration are a reduction of hardware and installation costs and direct and fast communication between condition monitoring and controller tasks. A disadvantage of integrating the condition monitoring functionalities into the turbine controller is that there will be less hardware redundancy.

11.5.3 New challenges for condition monitoring

The main challenge for future CMSs is the increasing size of the wind turbines and their components. The next generation of wind turbine is expected to have a rated power of 20 MW with a rotor diameter and hub height of 200 m or more. This results in very low eigen (natural) and rotating frequencies of the structural components. Monitoring of the related oscillations requires the development of new sensor technologies and new algorithms for fault prediction. For the latter, system identification methods will be a promising approach.

The next generation of wind turbines will also require new control strategies, for example with active damping of the tower oscillations. A CMS must consider the different behaviour of the wind turbine controller in the different load states. For example, when the controller performs damping activities, the oscillation behaviour of the structural components can change. This must be considered in the fault prediction algorithms of a CMS to avoid false alarms.

11.6 References

1. Rademakers, L, Stavely, C, Borum, K and Giebhardt, J, 2008. 'Condition Monitoring for Wind Turbines – State of the Art', Upwind-Report, Brussels (Web-Link: *http://www.upwind.eu/Shared%20Documents/WP7%20-%20Publications/UpWind-WP7_SOTA_CMS.pdf*).
2. Lyrner, T, Pahlke, T, Ley, C, Giebel, G, Gram-Hansen, K, Ahlf, A, Myszkowski, M and Giebhardt, J, 2006. 'Advanced Maintenance and Repair for Offshore Wind Farms using Fault Prediction and Condition Monitoring Techniques (OffShoreM&R)', Final Public Report of the EC Project, Brussels (Web-Link: *http://ec.europa.eu/energy/renewables/wind_energy/doc/offshore.pdf*).
3. Oppenheim, A V and Schafer, R, 1989. '*Discrete-Time Signal Processing*', Prentice Hall, Englewood Cliffs, NJ.
4. Tavner P, (Editor), Ran, L, Penman, J and Sedding, H, 2008. '*Condition Monitoring of Rotating Electrical Machines*, 2nd Edition', The Institution of Engineering and Technology, London, UK.
5. Bothe, H, 1995. '*Fuzzy-Logic*', Springer-Verlag, Berlin, Germany.
6. Giebhardt, J, 'Evolutionary Algorithm for Optimisation of Condition Monitoring and Fault Prediction Plattern Classification in Offshore Wind Turbines', Proceedings of the EWEC 2006, Athens, Greece (Web-Link: *http://www.ewec2006proceedings.info/allfiles2/75_Ewec2006fullpaper.pdf*).
7. Germanischer Lloyd (GL), 2007. 'Guideline for the Certification of Condition Monitoring Systems for Wind Turbines, Edition 2007', published by GL Indus, Germany.
8. Verbruggen, T, 2004. 'Fiber Optitrial Services GmbH Renewables Certification, Hamburgc Blade Monitoring' Proceedings of the European Wind Energy Conference 2004. 22–25 November, London, UK.
9. Caselitz, P and Giebhardt, J, 2005. 'Rotor condition monitoring for improved operational safety of offshore wind energy converters', *Journal of Solar Energy Engineering*, Vol. 127, 253–61.

12

Wind turbine performance assessment and knowledge management for aerodynamic behaviour modelling and design: IEA experience

T. MAEDA, Mie University, Japan and G. SCHEPERS, Energy Research Centre of the Netherlands (ECN), The Netherlands

Abstract: During the 1990s, several institutes cooperated within the International Energy Agency (IEA) Annexes XIV and XVIII in order to perform aerodynamic experimental programmes on full-scale horizontal axis wind turbines in field conditions. In these experimental programmes, local aerodynamic quantities (forces, velocities) are measured at several locations along a rotor blade. As a result of the international collaboration within the IEA Annex XIV, it has been possible to coordinate data processing and to create a database of measured data. The detailed aerodynamic measurements obtained on very different turbines gave a unique opportunity to better understand the aerodynamic behaviour of a wind turbine and resulted in the development and validation of more accurate aerodynamic models. Moreover, the extreme wind in the Pacific Ocean region in Asia damages wind turbines every year. To promote the installation of wind turbines in such a severe wind region, the Extreme Wind Speed Database was constructed by Japanese New Energy and the Industrial Technology Development Organization. The database includes the extreme wind speed distribution in Japan for users who want to examine more detailed information on, for example, the local terrain effects.

Key words: horizontal axis wind turbine, aerodynamics, full-scale aerodynamic experiments, extreme wind condition.

12.1 Introduction

In the past, the accuracy of wind turbine design models has been assessed in several validation projects, see for example Schepers *et al*. (2002b). They all showed that the modelling of a wind turbine response (i.e. the power or the loads) is subject to large uncertainties. These uncertainties mainly find their origin in the aerodynamic modelling, where several phenomena, like three-dimensional geometric and rotational effects, instationary effects, yaw effects, stall, tower effects, etc., contribute to unknown responses, in particular at off-design conditions. These unknown responses make it very difficult to design cost-effective and reliable wind turbines. Turbines behave unexpectedly, experiencing instabilities, power overshoots or higher loads than expected. Alternatively, the loads may be lower than expected, which implies an over-dimensioned (and costly) design.

The availability of high-quality measurements is considered to be the most important prerequisite to gain insight into these uncertainties and to validate and improve aerodynamic wind turbine models. However, in a conventional measurement programme, only integrated total (blade or rotor) loads are measured and this does not provide sufficient information to fully understand the very complicated details of wind turbine aerodynamics. For this purpose, it is necessary to have measurements of the underlying sectional aerodynamic loads, and for this, the pressure distribution and the resulting normal and tangential forces, together with the inflow angles, should be measured at different radial positions.

For this reason, many institutes initiated full-scale aerodynamic field experiments. These measurements were stored in a common database within the International Energy Agency (IEA) Annex XIV and XVIII projects. A well-known problem in these (and all field) experiments is the uncertainty due to the instationary, inhomogeneous and uncontrolled wind conditions, on the one hand complicates the interpretation of results significantly but on the other hand, opposite to measurements taken in a wind tunnel, makes the results representative for the conditions 'felt' by a wind turbine where wind speed variations and flow non-uniformities form important design drivers.

In this respect, it should be realised that it is not only the aerodynamic response to turbulence (and extreme wind speeds) that is largely uncertain but the input, that is the turbulence and extreme wind speeds, are also uncertain. As an example, extreme winds associated with typhoons are approaching and passing in the Pacific Ocean region in Asia and various regions in the world every year. To promote the installation of wind turbines to such severe wind regions, the Extreme Wind Speed Database was constructed by the Japanese New Energy and Industrial Technology Development Organization.

12.2 Aerodynamic measurements

12.2.1 Inflow conditions

Ideally, wind turbines are installed in flat terrain where the inflow is uniform without the influence of geographical features, such as hills or obstacles. However, for aerodynamic performance assessment, the inflow to the wind turbine is measured by anemometers set up in meteorological masts upwind the wind turbine because the actual wind turbine is operated in the unsteady flow environments. In these measurements, it is difficult to understand the detailed distribution of the inflow wind to the rotor plane because the number of masts and anemometers is limited. Moreover, because the masts are located at some distance upstream the wind turbine and because they are usually fixed at a certain position, the inflow condition at the position of the wind turbine is estimated using time-averaged data (e.g. one minute). However, the instantaneous inflow velocity and direction to the rotor plane remain unknown. Therefore, detailed measurements of the inflow

conditions with high resolution in time and space, also close to the rotor plane, are necessary for the clarification of high-frequency phenomena (e.g. dynamic stall).

Nowadays, the free-stream inflow condition is often measured with a sonic anemometer. Such a device can measure the three-dimensional flow velocity with high accuracy and response, and it can be used in combination with measurements from cup-type anemometers and wind vanes used in standard wind assessment. Also, other methods, for example the remote sensing technology of the Doppler sonic detection and ranging (SODAR) and the Doppler light detection and ranging (LIDAR), can measure the inflow conditions for a large-scale wind turbine. These remote sensing devices can measure the wind profile with a high spatial resolution, and as such, they can be useful to provide the inflow condition over the rotor plane. To exploit these remote sensing devices, the improvement of the rate of data acquisition is still a problem to be solved when used in regions where the spatial non-uniformity of the wind is large, for example regions of complex geographical features and/or regions where changes in the ambient environment are large due to the weather changing by the seasons.

12.2.2 Aerodynamic forces

In general, the only performance indicator, as measured on wind turbines, is the electrical power. This quantity, however, hardly provides information on the aerodynamic behaviour of the rotor for which, as a minimal requirement, measurements of rotor torque and rotational speed of the rotor are also needed. This is due to the fact that the mechanical losses and generator losses depend on the rotational speed. Additional information on the aerodynamic characteristics of the rotor or the blade can be obtained from measurements of blade flap bending moment, blade lead–lag moment and rotor thrust.

The rotor torque is measured with the torque sensor installed at the rotor shaft or the generator shaft. There are methods for obtaining rotor thrust using a thrust sensor or estimating the tower bending moment from strain gauges mounted on the tower. Strain gauges mounted on the blade root can measure the blade root lead–lag bending moment and the blade flap bending moment.

These quantities make it possible to assess the aerodynamics of the whole rotor or blade in a global way. However, the loads consist of an aerodynamic and a mass-induced component and they are integrated over a certain spanwise length. This gives only indirect information about the aerodynamics at blade element level. In order to measure the aerodynamic properties relevant for dynamic load codes directly (i.e. lift, drag and moment coefficients, inflow angle, inflow velocity at several radial positions), the forces that act on a small area of the blade surface need to be measured. One method of measuring the local stress is to use strain gauges on the blade surface.

Another method of obtaining local forces on the blade is to measure normal forces and skin friction on separate segments on the blade surface using balances built in the blade. The most common (though still relatively rare) method is to

measure the aerodynamic forces on a blade surface with pressure taps that are led through pressure tabs to pressure sensors (scanners) inside the blade. By the use of these methods, the net local aerodynamic characteristics can be determined where corrections may be needed for effect of the centrifugal force by the rotor rotation that acts on the air in the pressure tubing, pressure sensors and the balances. Moreover, it is necessary to consider the response time governed by the inertia of the surface segment or the response of the pressure signal, which depends on the tubing length, since the aerodynamic forces on the blade surface change during the field measurement. The inflow to the rotor plane of the wind turbine is influenced by the non-uniformity of the atmospheric boundary layer as well as of the unsteadiness of the natural wind. Thus, it is necessary to measure the aerodynamic forces, which act on the blade and the rotor, with high speed sampling and to synchronise them with the azimuth angle, in order to ensure enough resolution in time and space.

The pressure or stress that acts on the blade surface is transmitted to the stationary system after it is converted into an electrical signal, detecting it with the sensor built inside the blade by the slip rings or the telemeter installed in the hub or the rotor shaft and sampled by the computer.

12.2.3 Angle of attack

The angle of attack is an important parameter in most three-dimensional aerodynamic models of rotating wind turbines. However, the definition of the angle of attack is based on the wind tunnel environment as the angle between the chord line and the wind velocity vector, which has the same direction as the uniform flow along the wind tunnel walls. However, for a wind turbine situation, no such equivalent of the angle of attack is known. This is due to the fact that the ambient wind velocity vector far upstream is not the only determining parameter in the angle of attack definition, but the wake-induced velocity (at the rotor plane!) should also be taken into account. This implies that the angle of attack should be measured in the rotor plane.

This could be accomplished by measuring the local flow angle ahead of the blade profile with a measuring device (i.e. a five-hole pitot probe, windvane, etc.). However, the local inflow angle as measured with such a device is considerably different from an actual angle of attack because of the bending of the stream lines, caused by the upwash from the bound vortex of the blade. It is then necessary to subtract this upwash to obtain the angle of attack from the local inflow angle.

It is possible to determine the upwash from two-dimensional wind tunnel experiments or numerical analyses. However, corrections using data from two-dimensional wind tunnel experiments suffer from the question whether such correction is representative of the three-dimensional rotational environment. An argument against correcting the angle of attack with numerical analysis is found in the idea that the measurements are meant to be material for validation and model improvement and they should not be obscured by uncertainties from the

calculational codes that they are supposed to validate! Besides probes, other methods have been tried to measure the inflow angle. A popular method is to use the pressure distribution or the position of the stagnation point. The angle of attack is then determined by comparing the position of the stagnation point or the entire pressure distribution with the corresponding results obtained from wind tunnel experiments. It is then assumed that the pressure distribution (and stagnation point) remains unchanged in rotational situations.

12.2.4 Dynamic pressure and non-dimensionalisation

The aerodynamic forces are often presented as coefficients that are non-dimensionalised with the dynamic pressure. This dynamic pressure is determined by the local wind speed at the airfoil that, however, cannot be derived straightforwardly from the free-stream wind speed and the rotational speed since the wake-induced velocities should also be included as well these induced velocities are not known a priori. At first sight, one could think of determining the dynamic pressure from the maximum in the pressure distribution around the airfoil or from a five-hole pitot probe measurement, but then it should be known that in most aerodynamic experiments on wind turbines, the pressures are measured as *differentials* relative to a reference pressure in, for example, the rotor hub that is not known precisely on an instantaneous level. As such, a dynamic pressure from the probe measurements, written as $q = p_{\text{pitot}} - p_{\text{ref}}$ or $q = p_{\max} - p_{\text{ref}}$, when determined from the maximum in pressure distribution, suffers from the uncertainty in reference pressure. The uncertainty in reference pressure does not affect the value of the dimensional aerodynamic forces since, for instance, the normal force on an airfoil is determined as the difference between the pressure force on the suction side and the pressure force on the pressure side that cancels out the uncertainty in the reference pressure. However, the non-dimensionalisation of forces is affected by the uncertainty in reference pressure, as this is written as the (accurate) dimensional force divided by the (uncertain) dynamic pressure.

12.2.5 Flow visualisations

It is useful to measure pressure distributions and local aerodynamic forces on the blade surface of wind turbines in operation to determine the in-situ aerodynamic characteristics of the blade. On the other hand, it is equally important for understanding the unsteady phenomena of wind turbines in operation to investigate the flow pattern on the blade surface and the pressure distribution on the whole blade.

Although it is not easy to make flow visualisations on the blade surface of a full-scale wind turbine, averaged flow behaviour on the blade surface can be observed by the oil film method. Using this method, separated areas on the blade surface can be observed from the pattern of the liquid after operation by painting

liquid or fine particles on the blade surface. It would also be possible to monitor boundary layer transition on a rotating blade with a sublimation technique, like using naphthalene, where the sublimation takes place much faster in the turbulent part of the boundary. To observe the dynamic behaviour of the flow on the blade surface, there is the visualisation method of determining the behaviour of tufts, such as short strings glued on the blade surface, and recording them by a video camera mounted on the hub. The dynamic influence of the unsteadiness of the inflow, the spatial variance with the atmospheric boundary layer and the yaw operation on the flow on the blade surface can be observed by this method. Because the video camera is installed in the rotating hub, the picture is transmitted to the stationary system by slip rings or a telemeter, or it is stored by a recorder located on the hub – a method to detect stall is the so-called stall flag technique (Corten, 1998). In attached flow, an optical reflector is hidden by a stall flag, but in a stalled boundary layer, the reversed flow tips up this flag so that the reflector becomes visible, enabling an optical detection of the stalled region.

12.3 Field rotor aerodynamics database

As mentioned before, conventional experimental programmes on wind turbines generally do not provide sufficient information for the purpose of validating and improving aerodynamic design methods, as they only measure the integrated, total (blade or rotor) loads. These loads consist of an aerodynamic and a mass-induced component and they are integrated over a certain spanwise length. In the late 1980s and the 1990s, it was realised that more direct aerodynamic information was needed in order to improve the aerodynamic modelling. For this reason, several institutes initiated experimental programmes in which pressure distribution and the resulting normal and tangential forces together with the inflow angle and velocity at different radial positions were measured.

However, such aerodynamic field experiments are typically very time-consuming, expensive and complicated through the large volumes of data and the extensive data reduction that is required. Furthermore, each turbine configuration that is investigated experimentally may exhibit a very different aerodynamic response characteristic. Hence, the results that are obtained from the very time-consuming, expensive and complicated experiments may have only a limited validity.

For this reason, it was considered very advantageous to cooperate in these experiments. Under the auspices of the IEA Wind, this cooperation was established in Annex XIV and Annex XVIII (Schepers *et al*., 1997; Schepers *et al*., 2002a). These projects started in 1992 and ended in 2001. The so-called Operating Agent (coordinator) of these projects was the Energy Research Center of the Netherlands.

The cooperation led to an extensive database of aerodynamic measurements. This database provides unique aerodynamic data for a large number of wind turbine

configurations, which has been used for model validation and model development. The combination of insights and models had more general validity than those obtained from the experimental programmes independently. Furthermore, the project served as a platform where very specific knowledge associated with aerodynamic measurements could be exchanged. This has been very instructive for all participants by which the experimental programmes could be accelerated.

12.3.1 Test matrix

The full-scale aerodynamic experiment programme involved the following seven organisations in IEA Annex XIV and/or IEA Annex XVIII.

- *Delft University of Technology, DUT, The Netherlands*: The DUT experiments were carried out on a two-bladed, 10 m diameter turbine. The blades were untwisted and untapered.
- *The Energy Research Center of the Netherlands, ECN, The Netherlands*: The ECN experiments were carried out on a two-bladed, 27.4 m diameter turbine. The blades were twisted and tapered.
- *Imperial College, IC and Rutherford Appleton Laboratory, RAL, UK*: The IC/RAL experiments were carried out on a three-bladed, 16.9 m diameter turbine. The blades were twisted and tapered.
- *National Renewable Energy Laboratory, NREL, USA*: The NREL experiments were carried out on a three-bladed, 10 m diameter turbine. Measurements on two types of blades have been supplied:
  - An untwisted and untapered blade;
  - A similar blade, without taper, but with twist.
- *Mie University, Japan*: The Mie experiments were carried out on a three-bladed, 10 m diameter turbine. The blades were twisted and tapered.
- *Risø National Laboratory, Denmark*: The Risø experiments were carried out on a three-bladed, 19 m diameter turbine. The blades were twisted and tapered.

Note that the Centre for Renewable Energy Systems (CRES, GR) was also participating in the IEA Annexes.

The database constructed with IEA Annexes XIV and XVIII is arranged by the condition shown in Table 12.1.

Hence, the data included in this database can be summarised as follows:

- The diameter of the rotor ranges from 10 to 27 m.
- The number of blades is two or three.
- There are two kinds of local aerodynamic force measurements: by measuring segment forces with balances (applied by Risø) and by measuring the pressure distributions with pressure taps along the blade connected to pressure scanners (applied by the other participants).

Table 12.1 Test matrix of IEA Annexes XIV and XVIII

Participants	ECN	DUT	NREL	IC/RAL	Risø	Mie
Diameter (m)	27.44	10	10.06	16.9	19	10
Number of blades	2	2	3	3	3	3
Blade configuration	Twist and taper	Untwist and without taper	(1) Without twist and without taper (2) Without taper but with twist	Twist and taper	Twist and taper	Twist and taper
Profile	NACA 44xx	NLF 0416	S809	NACA 632xx	NACA 632xx	DU91-W2-250 and DU93-W-210
Aerodynamic measurement	Pressure distribution	Pressure distribution	Pressure distribution	Pressure distribution	Segment force by balance	Pressure distribution
Instrumented radial stations of pressure taps	3 (30%, 60%, 82%)	4 (30%, 50%, 70%, 90%)	4 or 5 (30%, 47%, 62%, 80%, 95%)	6 (20%, 30%, 40%, 50%, 65%, 80%)	3 (37%, 68%, 98%)	4 (32.5%, 50%, 70%, 90%)
Number of taps per station	47	59	28 or 32	26	—	50
Inflow angle and inflow velocity	Five-hole probe	Three-hole probe or six-hole probe	Five-hole probe and/or wind vanes	Five-hole probe	Five-hole probe	Five-hole probe
Instrumented radial stations of inflow measurements	1 (42%)	4 (36%, 56%, 76%, 96%)	4 (30%, 47%, 63%, 80%, 95%) or 5 (34%, 51%, 67%, 84%, 91%)	3	1 (72%)	5 (21%, 39%, 56%, 76%, 96%)

(*continued*)

Table 12.1 Continued

Participants	ECN	DUT	NREL	IC/RAL	Risø	Mie
Measurement speed (Hz)	128 or 64	333	520	625	25	95
Section measurement	Simultaneous	Partly	Simultaneous	Two stations simultaneous	—	Partly
Re	1.8×10^6	0.9×10^6	0.7×10^6	1.0×10^6	1.0×10^6	0.5×10^6
Averaged local inflow angle (degrees)	–5 to +40	–5 to +40	–5 to +40	–5 to +40	–5 to +40	–5 to +40
Yaw angle (degrees)	±30	±30	±30	—	±30	±30
Rotor speed (min^{-1})	Fixed but various rotor speeds were possible	Fixed	Fixed 71.63 min^{-1}	Fixed 38.2 min^{-1}	Fixed 35.6 min^{-1} and 47.5 min^{-1}	Fixed 90 min^{-1}

Note: Reynolds number at rotating conditions at 70% R.

- The number of segments on which measurements of aerodynamic forces are performed ranges from three to six sections. The measurements are carried out at two or more sections simultaneously or partly.
- Often, the inflow angle was measured with a multi-hole probe mounted in front of the blade leading edge to which several corrections were applied to obtain the angle of attack.
- The sampling speed is from 64 to 625 Hz for the pressure measurements and 25 Hz for the segment force measurement.
- The Reynolds number at the 70% radius section varies from 0.5×10^6 to 1.8×10^6.

12.3.2 Supplied data

The measurement results are supplied in the form of time series (rotating and parked conditions). In order to facilitate the selection of signals from a file, it was considered essential that all the files were supplied in the same format. It was agreed that three types of files had to be supplied:

- *Log files*: these files contain general information about the measurement procedure. It should also contain:
  - date and time of measurement;
  - air density, pressure and temperature;
  - information that is needed to read the other files (like the number of pressure taps, the number of anemometers, etc.).
- *Profile files*: these files contain information about the wind speeds, the wind directions, the rotor speed, the pitch angle, the mechanical loads, the angles of attack and the inflow velocities, and the profile coefficients, all as a function of time and azimuth angle.
- *Pressure files*: these files contain the pressure recordings.

The format of the files and the filenames are synchronised. The files start with the statistics (mean, max, min, standard deviation) of every signal.

Note that the aerodynamic sectional characteristics, as measured during rotation, are also specified. Where possible, as a reference, the two-dimensional wind tunnel experimental data are added.

The database is open to the public, see http://www.ecn.nl/nl/units/wind/rd-programma/aerodynamica/projects/field-rotor-aerodynamics-database/, and the data are supplied to third parties on the condition that they inform the IEA Annex XIV/XVIII groups on the experiences gained with the data.

12.3.3 Results

The IEA Annex XIV/XVIII measurements have been used for several analyses. The most successful activities have been:

- Investigations on stall delay: It was clearly shown that at the inner blade section of wind turbine blades, the aerodynamic normal forces are much higher than expected from two-dimensional wind tunnel measurements. It could be shown (and, as a result of that, explained) that these phenomena depend on the pitch angle. Better stall delay models could be developed on the basis of these measurements.
- The validation of computational fluid dynamics (CFD) codes (NS-codes, free wake panel methods and RFOIL) on the basis of pressure distributions;
- The validation of yaw models on the basis of azimuthally binned averaged $c_n - \alpha$ data.

Most comparisons between calculations and measurements showed a good-to-reasonable agreement below stall, but above stall the agreement is poor. The main problems in the interpretation of the measurements are almost all associated with the angle of attack (and to a lesser extent with the non-dimensionalisation of the aerodynamic forces with an uncertain dynamic pressure). Some studies have been done where these uncertainties are avoided by using an aeroelastic code to simulate time series from the IEA Annex database, and then the calculated and measured, time-averaged, dimensional, aerodynamic segment loads are compared (Schepers *et al*., 2004).

Another problem lay in the fact that the incoming inflow conditions are very instationary and partly unknown by which, for example, very chaotic dynamic stall loops were identified (Bjorck, 1995). These dynamic stall measurements have limited value as validation material for dynamic stall models because these models require precise knowledge of the flow within the rotor plane. For validation of some CFD methods, the modelling of transition turned out to be a problem. Retrospective measurements at fixed transition were also desired, but no such measurements have been made available in the IEA Annex XIV/XVIII database.

12.4 Databases for special wind climates/high wind regimes

These databases concern data from strong and extreme winds, resulting from, for example, typhoons or cyclones appearing in the Pacific Ocean region in Asia and various regions in the world every year. Moreover, the turbulence of such winds affects the fatigue load of wind turbines considerably in a complex terrain.

The worldwide production of commercial wind turbines is based on the IEC61400-1 standard, and the wind turbines suitable for the installation site are selected according to the specification decided by the averaged wind velocity and turbulence intensity. IEC61400-1 is based on the wind situation in Europe and USA, and it is not intended for the extreme wind regions appearing in monsoon regions, such as Japan.

However, the damage caused by typhoons has increased recently, and the influence of local wind characteristics and the terrain configuration has become obvious in Japan. To avoid damage to the wind turbine by these extreme winds, it is necessary to estimate the turbulence and extreme wind speed and to select or design a wind turbine taking into account these extreme wind characteristics. Therefore, a manual covering a wind turbine selection procedure that is appropriate for the wind situation, and the process for the problem clarification, in Japan has been written by the Japanese New Energy and Industrial Technology Development Organization. In the manual, the following material is being provided for evaluating extreme wind speeds in detail and supporting material for a convenient evaluation of siting aspects (New Energy and Industrial Technology Development Organization, 2008).

- The outline of the extreme wind speed distribution in Japan: 'Extreme Wind Speed Atlas' and
- Database for users who examine more detailed information such as the influence of local terrain: 'Extreme Wind Speed Database'.

These data are given for the whole of Japan, which was covered with 1 km meshes, and the influence of large-scale terrain configuration on the scale of several kilometres that is expressed by 1 m altitude data. In addition, the users need to examine the influence of small-scale terrain features based on the data from the Extreme Wind Speed Atlas if the site includes the special local feature.

Extreme Wind Speed Atlas and Extreme Wind Speed Database have the following features.

1 The value from the mesh of the meteorological station (hereafter, meteorological station mesh value) was obtained by statistically processing observed values and typhoon simulation results. Values from other meshes were obtained by interpolation from meteorological station mesh values and the resulting numerical wind analysis.
2 The values from the meteorological station mesh are converted into wind speed at 250 m height from the expected value of a 50-year span based on the Recommendations for Loads on Buildings by Architectural Institute of Japan (2004). This was calculated using the exponential law and the roughness class obtained from a vertical wind speed profile, according to the numerical flow analysis for wind direction sectors. It is used to construct the Extreme Wind Speed Atlas and the Extreme Wind Speed Database.
3 The effects of acceleration and deceleration by large-scale terrain features located several kilometres upstream of the turbine, taking into account the arbitrary position between meteorological stations.
4 The Extreme Wind Speed Atlas plots the maximum extreme wind speed in all wind direction sectors. The Extreme Wind Speed Database provides the extreme wind speed data according to eight wind direction sectors.
5 The Extreme Wind Speed Database is given as wind speed at 250 m height.

12.4.1 Complexity of terrain

It is necessary to check and evaluate the wind conditions when they do not correspond to standard conditions of a smooth terrain. In the Japanese wind power generation guideline, the complexity of terrain is judged by the following indicators:

1 The slope of the terrain is 10° or more.
2 The standard deviation in the altitude of the terrain cross-section in the upwind side, measured within 5 km from the installation site, is greater than 1.5 times the hub height.
3 The standard deviation in the altitude of the terrain cross-section in the upwind side within 5, 10 and 20 times the hub height exceeds 0.5, 0.8 and 1.4 times the hub height, respectively.
4 The acceleration rate of the wind speed exceeds by 1.1 of the local terrain.
5 More than 30% of the area is very steep (where very steep means a slope in the terrain of more than 30%).

The conditions from items 1 to 3 constitute indices in accordance with the IEC standard. It is judged that there is a possibility that the wind speed is influenced by the local terrain by item 1, and by the terrain complexity by items 2 and 3. Owing to the possibility of mountains located upwind of wind turbines at high altitudes, turbulence may increase, although it is thought that the possibility for an acceleration of the wind speed at the hub height is small. Item 4 is an item that is related to the effect of wind speed increase by the local terrain effects in item 1. It depends on the additional wind speed determined by the Recommendations for Loads on Buildings about the evaluation of acceleration rate. The acceleration rate is usually large close to the ground surface and becomes small at increasing heights above ground level, although the possibility of acceleration of the wind speed is shown in item 1. Therefore, the influence on the evaluation of strength of a large-scale wind turbine due to the vertical wind profile is thought to be small even if it is assumed that the wind speed in the higher layer is equivalent to that on a flat ground, provided that the wind speed at a hub height is corrected by the acceleration ratio. The typical one is the ruggedness index, RIX, as the index related to item 5 used with the wind simulation software WASP, developed by Risø National Laboratory. RIX is an index to judge the coverage of WASP, which provides the occupation rate of terrain more steep than the slope at which the separation of the flow will occur, according to the wind direction sector. The threshold of the slope gradient for the separation judgement used to calculate RIX is usually set to 0.3, which is 30% in slope gradient or 17° in slope angle.

After the indices mentioned above are evaluated according to the wind direction in 16 sectors, the maximum value of the index is used to judge the terrain complexity. The complexity is judged by the following indices:

1 *Low complexity*: None of the items 1, 2, 3, 4 and 5 are fulfilled.

2 *Middle complexity*: One or more of the items 1, 2, 3 and 4 are fulfilled and item 5 is not fulfilled.
3 *High complexity*: One or more of the items 1, 2, 3 and 4 are fulfilled and item 5 is also fulfilled.

However, the judgement procedure discussed above is a standard of the complexity of the terrain, and there is a possibility of taking the high values of the turbulence and/or the extreme wind speed according to terrain features even when the complexity is judged as low or middle. Moreover, when the field observations are greatly different from standard wind conditions and/or from wind speed data, corrected by adding the influence of local terrain on the standard wind condition, it is necessary to know the wind characteristics at the site in detail and to include the surrounding areas in the numerical simulations, regardless of the result of the judgement of the terrain features mentioned above.

12.4.2 Extreme Wind Speed Atlas

The Extreme Wind Speed Atlas provides an extreme wind speed at which the whole of Japan is covered with 1 km mesh. The features of the extreme wind speed distribution around the wind turbine installation site can be analysed by the Extreme Wind Speed Atlas.

The Extreme Wind Speed Atlas has the following features for the users in order to use it properly:

1 The wind speed at three levels of 30, 50 and 70 m height is provided.
2 The effect of the ground roughness is based on the national digital land information, which is provided by the Japanese Geographical Survey Institute.
3 It is provided so that the numerical wind speed distribution can be understood in the form of a distribution map.

The Extreme Wind Speed Atlas is constructed by considering the effect on the averaged altitude data of the 1 km mesh and the wind speed affected by the ground roughness distribution. Therefore, the user should locally examine it in a region where terrain configurations smaller than 1 km are predominant, although the effect of large-scale terrain features in the scale of several kilometres or more to which 1 km mesh is expressed as a minimum unit is considered.

12.4.3 Extreme Wind Speed Database

When it is judged that the wind turbine installation site is not flat, it is necessary to evaluate the influence of the local terrain by the equation of wind acceleration due to terrain features, numerical simulations and wind tunnel experiments using the Extreme Wind Speed Database, and to calculate the extreme wind speed. It is necessary to examine the effect of the terrain by using the extreme wind speed

according to the wind direction sector of the Extreme Wind Speed Database, as the effect of the terrain on the extreme wind speed depends on upwind terrain features, and the degree of influence depends on the wind direction.

The Extreme Wind Speed Database provides extreme wind speeds on a 1 km mesh, depending on the following conditions and the Extreme Wind Speed Atlas:

1 The extreme wind speed in eight wind directions is provided.
2 The wind speed at 250 m height is provided.
3 It is provided in the form of numeric information as a database to evaluate the influence of small geographical features.

12.5 Future trends

An obvious problem in aerodynamic (and other) field experiments is the uncertainty due to the instationary, inhomogeneous and uncontrolled wind conditions. In order to understand unsteady three-dimensional aerodynamic phenomena, statistical techniques, such as time and ensemble averaging, need to be used to translate the results from field rotor experiments into more reliable aerodynamic design methods.

The problem of the uncertain inflow was overcome in follow-up projects in which detailed aerodynamic measurements on model rotors placed in the wind tunnel were carried out (e.g. NREL's NASA-Ames and the EU Mexico project, http://wind.nrel.gov/amestest/, http://www.ecn.nl/nl/units/wind/rd-programma/aerodynamica/projects/mexico/). The known, stationary, homogenous and controllable conditions of these tests facilitated the interpretation of results considerably. Within the Mexico project, it was even possible to map the details of the three-dimensional flow field around the rotor with the particle image velocimetry technique, in addition to aerodynamic blade measurements. Such detailed flow field mapping is still difficult to image in the field. On the other hand, it should be acknowledged that the 'smooth' wind tunnel conditions are not fully representative of the conditions 'felt' by a wind turbine where wind speed variations and flow non-uniformities form important design drivers. Also, disturbing scaling and tunnel effects can be considered as drawbacks of wind tunnel measurements.

The authors believe that a full understanding of wind turbine aerodynamics can only be established by combining the information from detailed aerodynamic measurements on wind turbines placed in the wind tunnel with similar information on wind turbines placed in the field where larger size turbines than the IEA Annex XIV/XVIII turbines should be applied in combination with more advanced measurement techniques; see for example the DanAero experiment. For aerodynamic field measurements, it is essential to combine them with very detailed inflow measurements to determine the response of the aerodynamics to unsteady conditions, where an attempt should be made to capture extreme wind conditions. Wind tunnel measurements are supporting in generating the basic

aerodynamic characteristics. Moreover, wind tunnel experiments could be used to investigate the aerodynamics of wind turbines under high mean wind speeds, and arbitrarily high turbulence intensities where the protected wind tunnel environment allows applying the most advanced measurement techniques in a relatively easy way. The combination of all this information will make it possible to improve aerodynamic models and design more reliable wind turbines that need less maintenance.

12.6 References

Architectural Institute of Japan (2004), *Recommendations for Loads on Buildings* (in Japanese), Architectural Institute of Japan, Tokyo.

Bjorck, A (1995), *Dynamic Stall and Three Dimensional Effect*, FFA-TN-1995-31, FFA.

Corten, G P (1998), *The Stall Flag method: Proof of Concept*, ECN-RX-98-001.

New Energy and Industrial Technology Development Organization (2008), *Report on the Japanese type wind power generation guideline*. Available from: *http://www.nedo.go.jp/library/furyokuhoukoku/index.html* (in Japanese) [Accessed 7 Feb 2010].

Schepers, J G, Brand, A J, Bruining, A, Graham, J M R, Hand, M M, Infield, D G, *et al.* (1997), *Final report of IEA Annex XIV: Field Rotor Aerodynamics*, ECN-C-97-027.

Schepers, J G, Brand, A J, Bruining, A, Rooij van, R, Graham, J M R, Paynter, R J H, *et al.* (2002a), *Final report of IEA Annex XVIII: Enhanced Field Rotor Aerodynamics Database*, ECN-C-02-016.

Schepers, J G, Feigl, L and Rooij van, R (2004), 'Analysis of detailed aerodynamic field measurements using results from an aeroelastic code', *Wind Energy*, 7, 357–71.

Schepers, J G, Heijdra, J J, Foussekis, D, Øye, S, Rawlinson Smith, R, Belessis, M, *et al.* (2002b), *Verification of European wind turbine design codes, VEWTDC final report*. ECN-C-01-055, Energy Research Center of the Netherlands. Available from: http://www.ecn.nl/publicaties/default.aspx?nr=ECN-C-01-055 [Accessed 7 Feb 2010]

13

Optimising wind turbine design for operation in low wind speed environments*

M. CLIFTON-SMITH, Garrad Hassan Pacific, Australia, D. WOOD, University of Calgary, Canada and A. WRIGHT, Hydro Tasmania Consulting, Australia

Abstract: This chapter considers wind turbines at low wind speed and the optimising of blade design to improve performance in these conditions. The key aim is to achieve fast acceleration of the blades when the wind starts blowing because the average wind speed for starting is higher than the cut-in wind speed, which is the conventional measure of low wind performance. A blade element method for starting is described and shown to give good agreement with the measured starting sequences of a three-bladed 500 W turbine. Analytic expressions for starting time appear possible only for simple and unrealistic situations. Using a numerical, differential evolutionary strategy, however, blades can be designed to reduce starting time at the same time as maintaining high efficiency of power extraction. The most efficient blade designs are always very slow to start but, typically, a small trade-off in efficiency is associated with a large decrease in starting time. A practical application of this methodology is described for the blade design of a 5 kW turbine. This chapter shows that reducing starting time is also possible in the context of noise minimisation.

Key words: wind turbines, low wind speed, starting, optimisation, blade design, wind turbine blade design, low wind performance, optimisation, noise.

13.1 Introduction

It is important to state immediately that there is no magic solution to the problem of extracting significant power at low wind speeds from wind turbines; the wind speed sets the upper limit on that power. In other words, the Betz limit for conventional turbines applies equally at 5 m/s as at 25 m/s. The difference, for any turbine, is a factor of 125 in power output. This limitation was recognised in the US programme on low wind speed technology, Calvert *et al*. (2002), which aimed at general improvements to wind turbine technology, including cheaper but taller towers and lighter blades. Of course, there must be an improvement in 'low wind' economics if costs are reduced, but we concentrate here on the specific engineering issues of blade design and construction.

There are at least three reasons why good low wind performance is important for conventional turbines:

* Most of the work described in this chapter was done at the University of Newcastle, Australia.

1. For stand-alone power systems, turbine siting can then be biased in favour of the load rather than the resource.
2. It ensures that a turbine is ready to extract the available energy at higher wind speeds. We will see that this can be an important issue since the wind speed at which turbine blades start rotating from rest can be significantly higher than the cut-in wind speed.
3. Customers want to see their blades turning when the wind is blowing but are less fussy about the actual power production.

Low wind performance is usually discussed in terms of the cut-in speed, defined in the International Electrotechnical Commission (IEC) standards for large and small turbines as 'the lowest mean wind speed at which the turbine produces power' as determined by 10-minute averages of wind speed and power output, IEC (2006). Actual low wind performance is more complex than this single measure indicates. Figure 13.1(a) shows a plot of rotor speed against wind speed for a three-bladed, 2 m diameter, 500 W turbine taken from Wright (2005): an earlier version is given by Wright and Wood (2004). Each data point was assessed as being 'steady', 'accelerating', or 'decelerating' according to the method described in Wright and Wood (2004) and this determined the symbol used for plotting. The 'steady' points giving the maximum rotor speed for

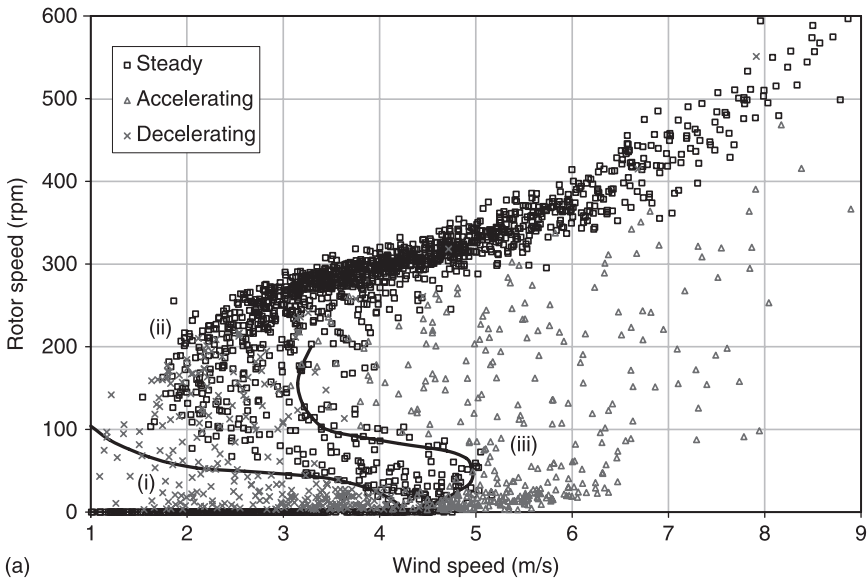

(a)

13.1 (*a*) Low speed behaviour of a three-bladed 500 W turbine, taken from Wright (2005). (*b*) Simplified representation of hysteresis in rotor behaviour, adapted from (2005). The solid lines show the boundaries between region (i) decelerating, region (ii) steady, and region (iii) accelerating, as found by blade element theory.

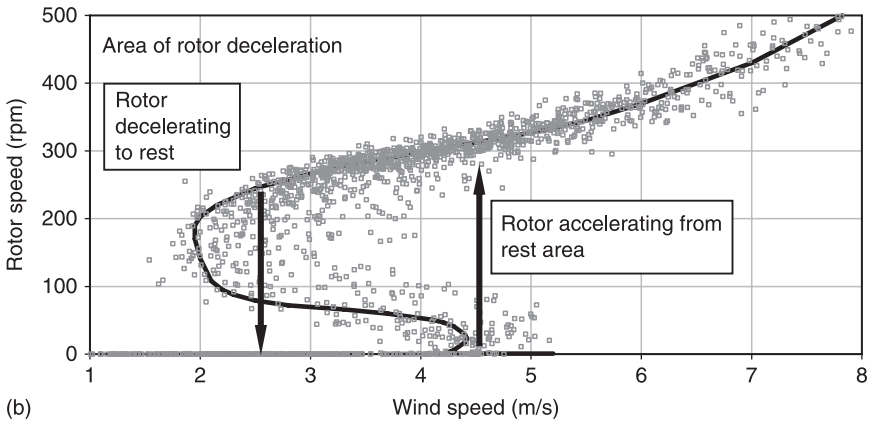

13.1 Continued.

each wind speed are bunched around the trajectory of power production as the wind speed changes. Below them are the (mostly) accelerating points at relative high wind speed and the decelerating points at low speed. There is significant hysteresis in the turbine passing between the operational curve and the stationary state (zero rotor speed) as indicated schematically in Fig. 13.1(b). The average speed at which the rotor starts from rest is 4.5 m/s, and the average speed at which it comes to rest is 2.5 m/s. The conventional cut-in wind speed is 3.5 m/s. These differences are well known anecdotally to manufacturers, installers and owners of small turbines and it is surprising that they have attracted so little academic attention.

The solid lines in Fig. 13.1(a) are the boundaries between the three regions as estimated by blade element theory: it does remarkably well for reasons that will be explained. It is clear from Fig. 13.1 that the major difficulty in achieving good low wind performance is starting the blades. The aerodynamic torque on stationary blades must overcome any resistive torque in the drive-train and generator. Starting is made more difficult by most small wind turbines having no blade pitch adjustment. This is usually considered too expensive but condemns the stationary or slowly rotating blades to high angles of attack, low lift and high drag.

Figure 13.2 shows a typical starting sequence for the turbine used to obtain Fig. 13.1, for an average wind speed at which the blades will just start. The origin for time is arbitrary. At around 5 seconds, a small gust causes the stationary blades to accelerate. There follows a long period, up to about 85 seconds, where the rotor accelerates slowly and the blade angles of attack decrease slowly. This is the 'idling period' whose length scales as U^{-2}, where U is the wind speed (Wright and Wood, 2004). The last short period of rapid acceleration is also typical.

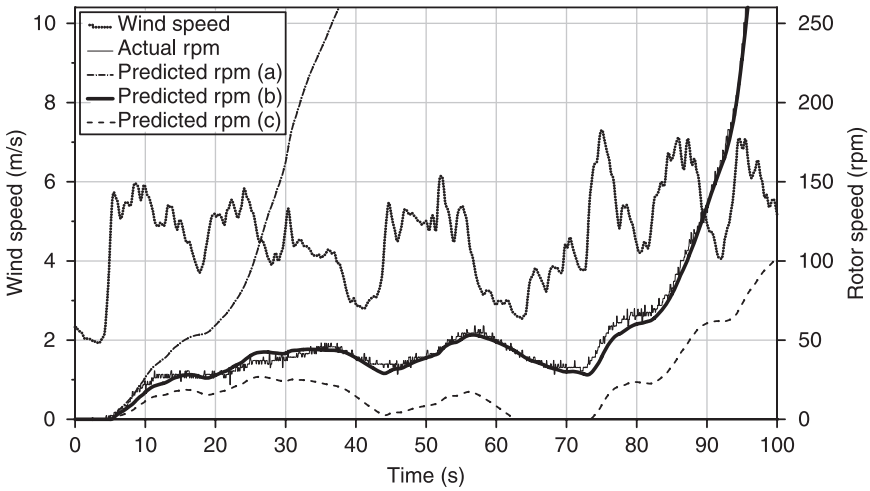

13.2 Low speed start of a three bladed 500 W turbine, taken from Wright (2005).

13.2 Aerodynamic modelling for starting

It is a straightforward task to turn the standard blade element method (BEM) for calculating power output, e.g. Burton *et al*. (2001), into a quasi-steady prediction of the rotor acceleration in the idling period. Somewhat surprisingly, Fig. 13.2 shows that the quasi-steady analysis remains accurate for the last period as well. The (related) assumptions for idling are:

1. the rotor extracts insignificant energy from the wind which, therefore, does not slow down through the blades;
2. the rotor acceleration is so slow that a quasi-steady analysis can be used; and
3. the aerodynamic torque acts only to accelerate the rotor.

These assumptions will hold for small values of the ratio of the rotor kinetic energy at the end of the idling period, $\frac{1}{2}NJ\Omega^2$ (where N is the number of blades, J is the inertia of one blade, and Ω is the rotor angular velocity) to the kinetic energy of the wind that passed through the rotor during the idling period of length T_s, $\frac{1}{2}\rho U^3 A T_s$ (where ρ is the air density, U is the average wind speed during starting, the rotor area, $A = \pi R^2$, and R is the tip radius). There is a further assumption that the blades provide the overwhelming contribution to the turbine inertia, which in our experience is always the case. For the sequence in Fig. 13.2, with $NJ = 0.43$ kgm^2, $\Omega = 75$ rpm, $U = 4$ m/s and $T_s = 80$ s, the ratio is 0.0014.

Quasi-steadiness allows the use of steady lift and drag data to evaluate the rotor torque at any time.

With knowledge of the resistive torque, the third assumption leads to an ordinary differential equation for Ω by equating the net torque to NJ times the angular acceleration. The equation can be solved easily by standard methods such as the Runge–Kutta scheme. For the turbine used to obtain Fig. 13.1 and 13.2, the static resistive torque was 0.36 Nm, which is two orders of magnitude lower than the power-producing torque at rated wind speed. This value was used in the calculations shown in Fig. 13.2. The remaining issue is to categorise aerofoil lift and drag at angles of attack, α, up to 90°. This is difficult for two reasons: first as shown by curves (a), (b) and (c) in Fig. 13.2, which will be explained below, the calculations are very sensitive to the lift and drag values. Second, there is little information on aerofoil behaviour at high α, particularly in combination with the low Reynolds numbers, Re, typical of small wind turbines. Mitigating these is the reasonable assumption that, at high α, all aerofoils tend to behave as flat plates. Furthermore, the drag on a stationary blade does not influence the aerodynamic torque, so it is the lift that must be modelled accurately. A corollary is that aerodynamic torque *decreases* as the blades start rotating and the drag becomes important.

The tip chord of the 500 W blade is only 43 mm, and its twist angle relative to the plane of rotation is fixed at 3°. At a wind speed of 3.5 m/s the stationary blade has a tip $Re = 10^4$ and $\alpha = 87°$. Needless to say, there are no lift and drag data for these conditions for the SD7062 section used for the blade; the only available data, from Lyon *et al.* (1997), cover $Re \geq 6\times10^4$ and $\alpha \leq 20°$. The SD7062 section has a maximum thickness of 14% and the most relevant aerofoil data that could be found for higher angles were those of Ostowari and Naik (1985) for the 18% thick NACA4418 at $Re \geq 2.5 \times 10^5$. The values of C_l and C_d used to obtain the results labelled as (a) in Fig. 13.2 and 13.3 are an amalgam of the two sources with the high-α data being for infinite aspect ratio, AR, defined as the square of the length of the blade divided by the planform area.

Viterna and Corrigan (1981) produced equations for high-α lift and drag that are matched to the measured low-α values for any aerofoil. Estimate (b) was obtained using their equations as a guide; see Wright (2005) for more details. One interesting feature is that both C_l and C_d are dependent on AR at high α. C_d is determined from the maximum value, given by

$$C_{d,\max} = 1.11 + 0.018(AR) \qquad [13.1]$$

which is an approximation to the drag coefficient of a normal flat plate given in many fluid dynamics textbooks, e.g. White (1999), for $AR \leq 20$ typically. It is entirely reasonable to expect that $C_{d,\max}$ depends on AR, as suggested by the NACA4418 data of Ostowari and Naik (1985) in Fig. 13.3, but equation [13.1] may give a too great variation at the high AR typical of blades as $C_{d,\max}$ for a two-dimensional plate is 2.0. Furthermore, but probably of less importance, $C_{d,\max}(AR)$ must equal $C_{d,\max}(1/AR)$ for a flat plate, but equation [13.1] obviously does not give this. It is unclear whether C_l, which is *not* corrected for AR at low α in blade element theory for power production, should be modified at high α for the analysis

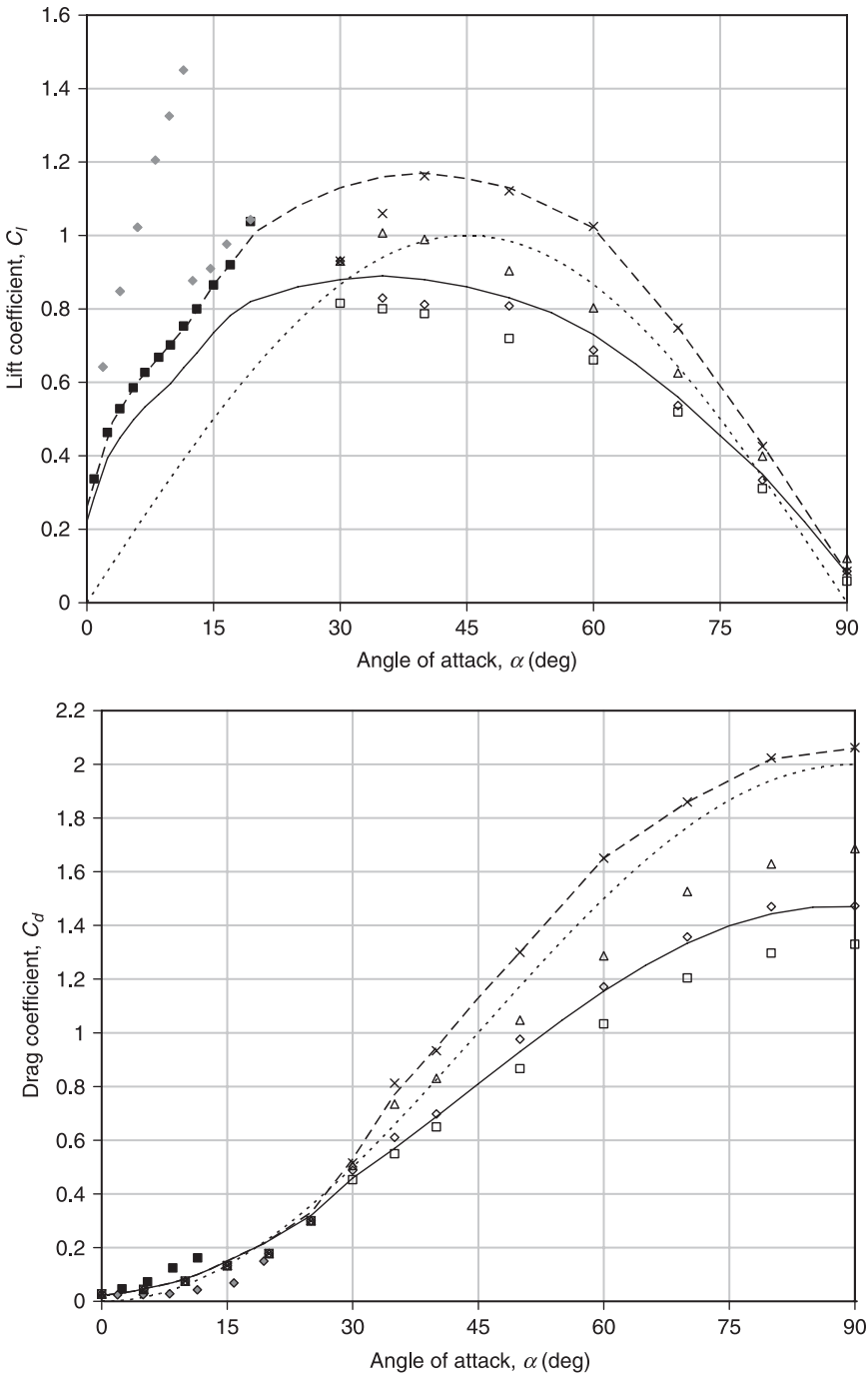

13.3 Lift and drag over the full range of angles of attack, taken from Wright (2005). Symbols and lines defined in Table 13.1, except that estimate (c) is shown dotted.

Table 13.1 Symbols for lift and drag data in Fig. 13.3 and details of predictions shown in Fig. 13.2

Symbol	Reference	Aerofoil	Re	AR
■	Lyons *et al.* (1997)	SD7062	6×10^4	Infinite
♦	Lyons *et al.* (1997)	SD7062	10^5	Infinite
□	Ostawari and Naik (1985)	NACA4418	2.5×10^5	6
◊	Ostawari and Naik (1985)	NACA4418	2.5×10^5	9
Δ	Ostawari and Naik (1985)	NACA4418	2.5×10^5	12
×	Ostawari and Naik (1985)	NACA4418	2.5×10^5	Infinite
---------	Estimate (a) – aerofoil data			Infinite
_____	Estimate (b) – based on Viterna and Corrigan (1981)			Blade *AR*
.....	Estimate (c) – flat plate equations [13.2] and [13.3] with $A_l = A_d = 2$			Infinite

of starting. Nevertheless, estimate (b) gives remarkably accurate predictions of starting, not just for the data in Fig. 13.2, but for most of the over two hundred starting sequences analysed by Wright (2005).

Estimate (c) comes from the infinite-*AR* 'flat plate' equations,

$$C_l = A_l \sin\alpha \cos\alpha \qquad [13.2]$$

$$C_d = A_d \sin^2\alpha \qquad [13.3]$$

used, *inter alia*, by Strickland and Graham (1987) with $A_l = 2.25$ and $A_d = 3.25$, Meyer and Kroger (2001) with $A_l = A_d = 1.98$, and Wood (2001) with $A_l = A_d = 2$. These equations underestimate starting performance partly because they are the only ones that give zero C_l at $\alpha = 90°$, which is correct for a flat plate but apparently not for a cambered aerofoil: note that the lift is solely responsible for the initial blade rotation. Wood (2004) and Clifton-Smith and Wood (2007) used equations [13.2] and [13.3] with an ad hoc additional term to improve accuracy for the particular aerofoil.

The simple equations [13.2] and [13.3] with $A_l = A_d = 2$ allow the quasi-steady torque acting on the rotor, Q, to be written in the simple closed form

$$Q = N\rho U^2 R^3 \int_{r_h}^{1} (1 + \lambda^2 r^2)^{1/2} \sin\theta_p (\cos\theta_p - \lambda r \sin\theta_p)\, c\, r\, dr \qquad [13.4]$$

where λ is the tip speed ratio, θ_p is the blade twist angle relative to the plane of rotation, c is the blade chord, r is the radius, and r_h is the hub radius, all normalised by R (Wood, 2004). Equation [13.4] shows that the aerodynamic torque is proportional to U^2, and so is consistent with the finding that starting time depends on the inverse square of wind speed. Strictly, this is true only in the case of zero resistive torque. In that case, equation [13.4] also shows that Q is linear in N, and

if blade inertia dominates the turbine inertia then starting becomes independent of N. This limiting result has some important consequences which will be mentioned later. It appears that resistive torque becomes more important as turbine size decreases, which may explain why micro-turbines for yachts etc. often have five or seven blades. Equation [13.4] also shows that increasing rotor size is a sensible way to improve starting. If equation [13.4] is combined with the high-λ approximation to the equations for c and θ_p for an optimal power extracting rotor,

$$rcC_l \approx \frac{16\pi}{9N\lambda^2} \qquad [13.5a]$$

$$\tan\theta_p \approx \frac{2}{3r\lambda} \qquad [13.5b]$$

which are the limiting forms of equations [3.67] and [3.68] of Burton *et al*. (2001), the constancy of rc results in a simple analytical expression for Q. No analytic expressions for Q appear to be available for other formulations of lift, drag, chord and pitch, so that starting and its optimisation in practice must be studied numerically.

A major consequence of the analyses is that starting torque is generated mainly near the hub (Wood, 2001; Wright and Wood, 2004; Wright, 2005), for two main reasons. First, the rotational contribution to the effective velocity seen by the blade is small or zero. Second, equation 13.5(b) shows that the pitch angle is usually highest in the hub region. On the other hand, it is well known that power-producing torque comes from the tip region. This suggests the possibility of designing a blade to start quickly *and* be very efficient. However, it also means that considerable care needs to be exercised in designing the root section of small turbine blades for starting at low *Re*. Numerous studies, such as Sunada *et al*. (1997), have shown that thick aerofoils perform poorly at high α and low *Re*, so their use near the hub, which is common for large blades, must be avoided.

Finally, starting time depends on blade inertia and resistive torque, neither of which is important for power production.

13.3 Optimising blade design for power and starting

Blade design consists mainly of selecting the aerofoil section(s) that comprise the blade, and then determining the chord and twist distribution to optimise power output, for example. There are also localised structural and other requirements, such as the use of thick sections to ease the transition to circular blade attachments for large blades and chord modifications to reduce tip noise.

The observation that starting torque and power come from different regions of a blade suggests that dual optimisation is possible, but the method to do so is not immediately obvious. As shown above, analytical expressions for starting are possible only in restricted situations, so some form of numerical optimisation is required. Our work has been based on differential evolution (DE), Price *et al*.

Table 13.2 Parameters for blade optimisation

Population size: 2000 blades	U = 10 m/s
Number of generations: 200	N = 3
Maximum lifetime of one member: 20	R = 1.5 m
Aerofoil: SG6043	r_h = 0.15
Blade density: 550 kg m^{-3}	Resistive torque: 0 or 0.5 Nm
λ_f = 1	λ = 5.5
Maximum chord: 0.3	Minimum chord: 0.02
Maximum θ_p: 25°	Minimum θ_p: –5°
No. blade elements: 15	$0 \le a_s \le 0.5$

(2006), one of the myriad of 'evolutionary strategies' for numerical optimisation. It was used by Wood (2004) and Clifton-Smith and Wood (2007) for starting and power optimisation, Clifton-Smith (2010a) for power optimisation including tip losses, Clifton-Smith (2010b) for noise minimisation, and Clifton-Smith and Wood (2010) for tower optimisation. Evolutionary strategies require the random selection of an initial population, which is then 'evolved' over a large number of generations with the aim of achieving convergence of the best performing members of the population. Most of our calculations have used a population of 2000, as shown in Table 13.2 along with the other main parameters used in the design examples to be given below. λ_f is the tip speed ratio at which the idling period is assumed to finish. The restrictions on chord and pitch may well be partly set by manufacturing requirements. A single aerofoil section was used: the SG6043, specifically designed for small turbines (Giguère and Selig, 1998). Continuing with the evolutionary terminology, we speak of the blade 'genes' which are the chord and twist of the blade elements. In all our work, we have used the same aerofoil section for the whole blade, largely on the grounds that increasing section thickness near the hub, which is a standard practice for large blades, may cause serious loss of lift and increased drag at low Reynolds number as described above. If the optimisation required different sections or a variation in thickness along the blade, then the number of blade genes would increase, but the change would be easy to incorporate in the optimisation.

DE generates a potential replacement, or comparison vector, $\mathbf{c}_i$, for the ith member of the current population, by randomly choosing genes either from a basis vector, $\mathbf{b}_i$, or from a trial vector, $\mathbf{t}_i$. This trial vector is constructed by the addition of $\mathbf{b}_i$ and a weighted difference vector as follows:

$$\mathbf{t}_i = \mathbf{b}_i + w(\mathbf{u}_i - \mathbf{l}_i) \qquad [13.6]$$

where, w is the weighting factor and $\mathbf{b}_i$, $\mathbf{u}_i$ and $\mathbf{l}_i$ are randomly chosen members of the current population. The 'differential' in the name DE refers to this method of 'breeding' the next generation using the weighted difference vector. Genes are chosen as follows:

```
FOR j = 1, number of genes                    ! for every gene
        IF (rand < CR)
                                  c_i(j) = t_i(j)     ! take gene from trial vector
        ELSE
                                  c_i(j) = b_i(j)     ! take gene from basis vector
END
```

where *rand* is a random number, $0 < rand < 1$, and *CR* is a crossover factor taken here 0.1. If the trial blade has a higher fitness score than the original blade, the new replaces the old. Fitness is defined by

$$fitness(i) = a_s \frac{\min(T_s)}{T_s(i)} + (1 - a_s)\frac{C_p(i)}{\max(C_p)} \qquad [13.7]$$

where the values of factor a_s used in the calculations to be presented are given in Table 13.2, C_p is the standard power coefficient calculated using a BEM model (e.g. Burton *et al*., 2001), and the minimum and maximum values are taken over the current population. All the graphical results presented in this chapter are for the blades defined by Table 13.2. For all calculations, 15 blade elements were used. Figure 13.4 shows a typical convergence history over 400 generations for an optimisation that did not include tip losses. It is clear that 200 generations is sufficient to obtain results that are close to convergent. The rapid increase in the starting time around Generation 50 corresponds to an *increase* in the maximum

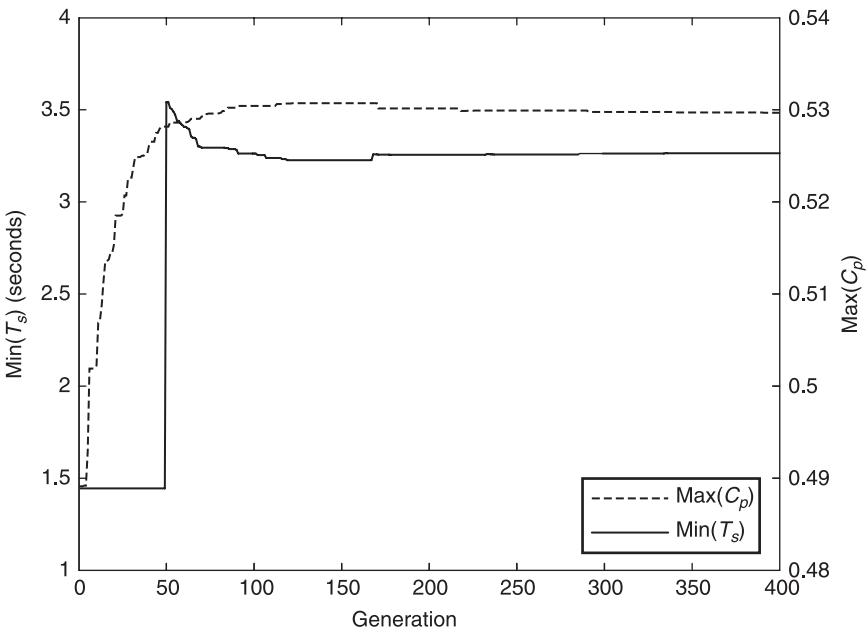

13.4 Typical convergence of C_p and T_s for $a_s = 0.1$ over 400 generations, taken from Clifton-Smith (2009).

fitness (not shown) indicating that the fastest starting blades were a small fraction of the population and had very low efficiency. Around Generation 170, T_s increases again, this time by a much smaller amount, largely because of the death of the fastest starting, but old, blade.

For the dual optimisation of starting and power, the aim of the DE calculations is to populate the 'Pareto front' on a graph of C_p versus T_s. For discrete calculations, the front is the sub-population that has either C_p higher than or T_s lower than all other blades. Typically, 1–10% of the final population lie on the front, and as demonstrated in Fig. 13.5, multiple runs of the program with different values of a_s are required to map it. This is because the results from each run of the DE tend to converge on a small section of the two-dimensional space of C_p and T_s. It is an assumption that implementing DE for 200 generations is sufficient to map the front. Apart from finding that test runs with more generations did not produce any significant changes, e.g. Fig. 13.4, there are several reasons to expect that the assumption is valid. The first is that DE accurately reproduces equation [13.5] for blade chord and twist when C_p is the only objective function, Wood (2004), Clifton-Smith (2009) and the results to be presented below. Secondly, the situation

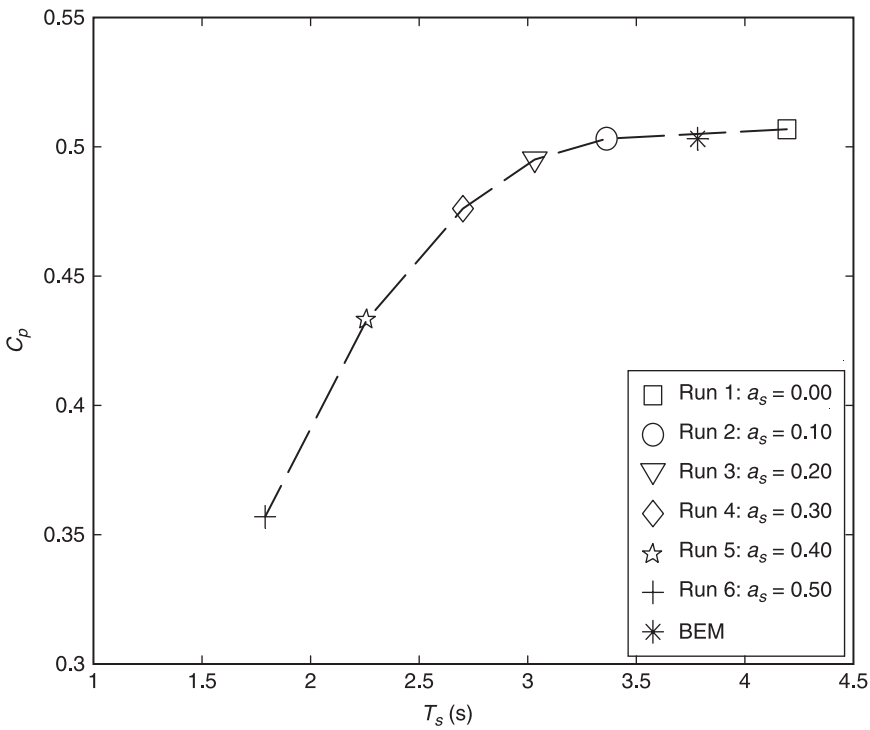

13.5 Typical Pareto front for λ = 5.5, resistive torque = 0.5 Nm, including tip loss corrections, taken from Clifton-Smith (2009).

shown in Fig. 13.5 looks to be a relatively simple optimisation problem, at least in comparison to the very difficult ones that DE has tackled successfully (Price at al., 2006).

The Pareto front is the locus of all optimal blades from which the designer must choose one. The C_p values in Fig. 13.5 have been reduced from those in Fig. 13.4 by the introduction of the tip loss correction of de Vries (1979). Note that the optimal blade equation [13.5a] and [13.5b] ignore tip losses. Figure 13.5 shows the most important feature of all the dual optimisations that we have done: the 'BEM' blade, defined only by the optimal power producing equations as explained above, always has very poor starting performance. Furthermore, the shape of the Pareto Front is such that a small decrease in efficiency can be traded against a very large decrease in starting time.

Typical evolved chord (Fig. 13.6) and twist distributions (Fig. 13.7) are labelled as follows. Run 1 is the validating case, i.e. the result of DE optimisation ignoring starting time minimisation, or $a_s = 0$. Run 1 and the BEM chord and twist distributions (see equation 13.5) are in very good agreement except for the DE blade's twist near the tip, which has been altered by the implementation of the de Vries (1979) tip loss correction. There is no correction for the BEM distributions.

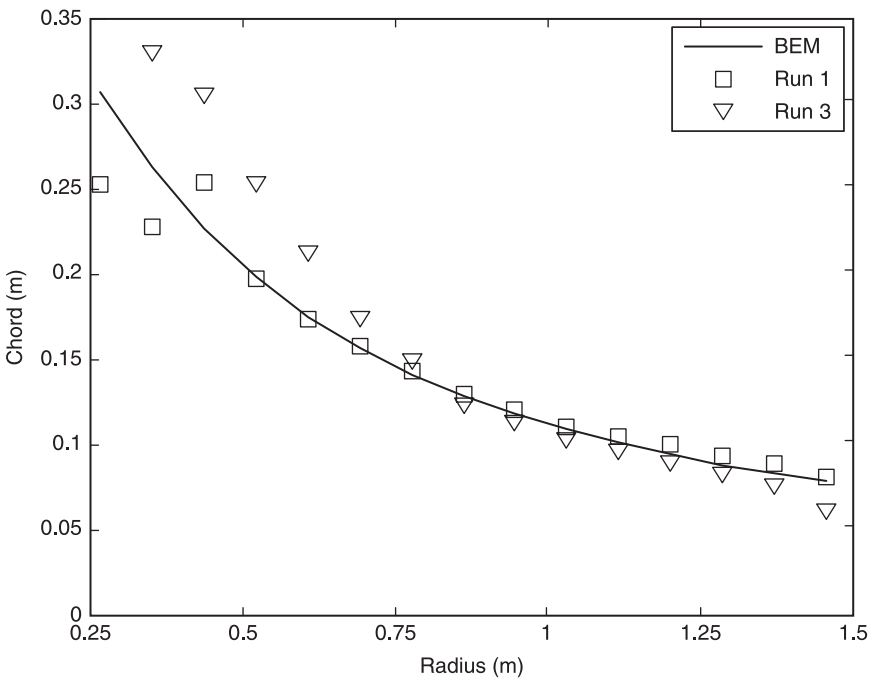

13.6 Chord for efficient, slowly starting blade (Run 1) and a less efficient but faster starting blade (Run 3), taken from Clifton-Smith (2009).

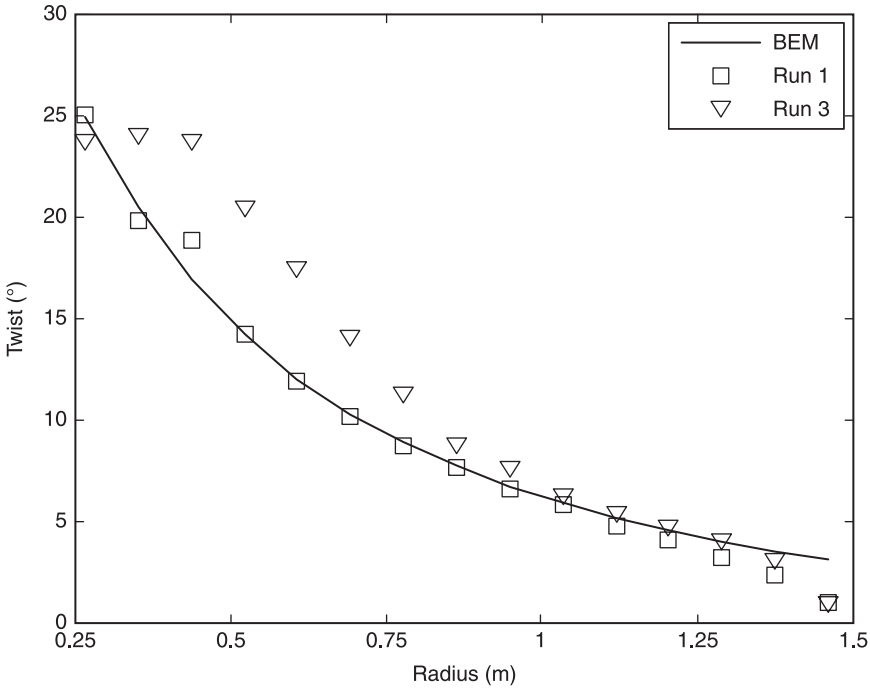

13.7 Twist distribution for an efficient, slowly starting blade (Run 1) and a less efficient but faster starting blade (Run 3), taken from Clifton-Smith (2009).

There is some disagreement and scatter in the chord distribution near the hub, but this region produces little power and hence exerts little evolutionary pressure on the evolving blades. For Run 3, $a_s = 0.2$. As shown in Fig. 13.5, there is a significant improvement in starting time for a small decrease in C_p. This is primarily due to an increase in chord and twist in the hub region. The difference in the tip region of the blade is again due to the DE calculations including a tip loss correction in determining C_p.

13.4 Actual blade design, construction and performance

The first practical application of the dual optimisation design methodology was the 2.5 m long blade for the Aerogenesis 5 kW wind turbine shown in Fig. 13.8 (Wood, 2008). This turbine has two, rather than three, blades partly to reduce cost. A standard electric motor and gearbox combination is used for the same reason. Induction motors or generators usually have little resistive torque but the gearbox may have a substantial amount that must be overcome by good blade design. Figure 13.8 shows that the blade has a much wider chord near the hub than is

common for large blades. Large blades have thick aerofoils near the hub, partly to withstand the large centrifugal loads. These loads scale as $\Omega^2 R$, whereas tip speed ratio does not change significantly with R, so ΩR is constant. Thus, both Ω and the centrifugal loads increase with decreasing turbine size. However, as pointed out above, it is dangerous aerodynamically to use thick aerofoils at low Re, so the structural design of the 2.5 m blade was a major challenge. Previous versions of the blade were attached to the blade disk via a flat, rectangular section. The rapid twist required to connect to the aerodynamic section of the blade was the weak point of the blade. Blade failure occurred through delamination along the trailing edge as well as more normal fatigue cracking and fibre pullout on the pressure surface. The new blade has most of that twist removed, requiring it to be mounted at 20° to the plane of rotation as can be seen in Fig. 13.8.

Finite element modelling (FEM) was used to design the blade layup. In turn, the finite element modelling was calibrated for material properties using static dead load and torsion tests as well as determination of the blade natural frequency. Conventional fibreglass (mainly unidirectional glass for the centrifugal load) produced a sufficiently strong blade so that no carbon fibres or other advanced materials were needed. The blade is made, as are many large blades, by gluing together two halves made separately by vacuum infusion. A machined PVC foam core is used as an alternative to a spar or a shear web to keep the surfaces apart and to form a glue dam at the

13.8 The Aerogenesis 5 kW wind turbine with cup anemometer and wind vane.

leading edge. Each blade weighs 5.43 kg, which compares to the value of 5.74 kg from the data correlation of large blade mass and length shown in Fig. 13.3 of Brøndsted *et al*. (2005). This comparison suggests that we have been successful in achieving low blade inertia to improve starting performance. A static fatigue test programme, based on the work of Epaarachchi and Clausen (2006), and similar to those used on larger blades, is underway using the rig shown in Fig. 13.9. The first

13.9 Fatigue test rig with 2.5 m blade. The safety cage has been removed to show blade driven by the hinged arm in the middle of the photo. Strain gauges and their electrical connections can be seen on the pressure (upper) surface.

blade to be tested has successfully survived the equivalent of twenty years of service life; the full results of the programme will be reported later.

There is a powered-off brake behind the motor, and this influenced the choice of blade number by the following reasoning. The brake serves two purposes: emergency stopping in the unlikely event that the control system fails, and parking the blades in high winds. The first requires a relatively low brake torque to minimise blade stresses during braking, whereas the second requires a higher torque; both, however, are significantly larger than the static resistive torque. In terms of blade number, emergency stopping would probably require *less* brake torque if three blades were used. This is because the turbine's rated power would occur at a lower angular velocity and therefore a higher torque, but the increase would be more than counterbalanced by the increase in the rotor inertia, provided that the brake torque still exceeded the aerodynamic torque. However, parking in high winds would require a *higher* brake torque as the aerodynamic torque would be raised by 50% for the same wind speed. The range of available brake torques favoured the use of two blades.

The beginning of an actual starting sequence for the two-bladed rotor is shown in Fig. 13.10 along with the wind speed and predictions of the rotor acceleration. The gearbox resistive torque was established from static tests and from measurements of the time required to stop with a known inertial load when the motor power was turned off. The computed rotor speed (the heavy solid line) is greater than that measured, possibly because of turbine yaw which is ignored in the starting analysis described above, but the comparative value of the starting analysis is likely to be unaffected. Using three blades (the long-dashed prediction) would significantly improve the starting performance. Recall, however, that in the absence of resistive torque, starting performance is independent of blade number. Thus, the difference between two- and three-bladed starting is an indication that the 1.9 Nm static resistive torque is significant. Since the turbine was installed we have purchased, but not yet received, gearboxes from another manufacturer with a resistive static torque of 0.9 Nm. The short-dashed lines in Fig. 13.10 suggest that using these units would improve starting significantly, and using three blades would then result in a much smaller additional advantage. However, there is a further indirect advantage of using three blades: they can be pitched out relative to two blades while maintaining the rated power. The final calculation in Fig. 13.10 (the second long-dashed line) shows that this arrangement would produce the fastest start.

Another way of assessing starting performance and drive train resistance is through the plots of net (aerodynamic – restive) torque against rotor speed for varying wind speeds shown in Fig. 13.11 for the 5 kW turbine with two blades and the original gearbox. As mentioned previously, the aerodynamic torque decreases once the blades start – the short, sudden drop from the static value is a consequence of a slight mismatch between the measurements of static and dynamic resistive torque – so the wind speed needs to be at least 5 m/s to ensure positive net torque

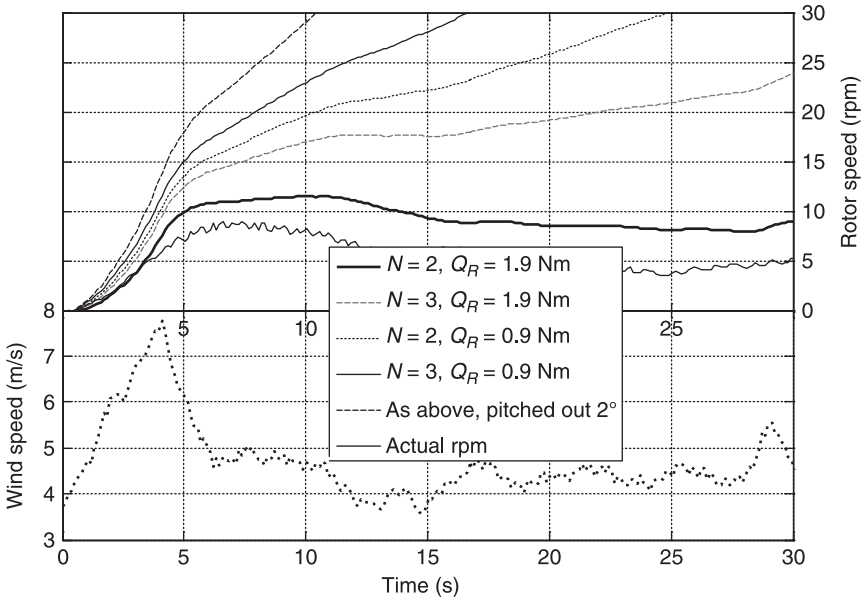

13.10 Measured and predicted starting of the Aerogenesis 5 kW turbine. Q_R is the resistive torque.

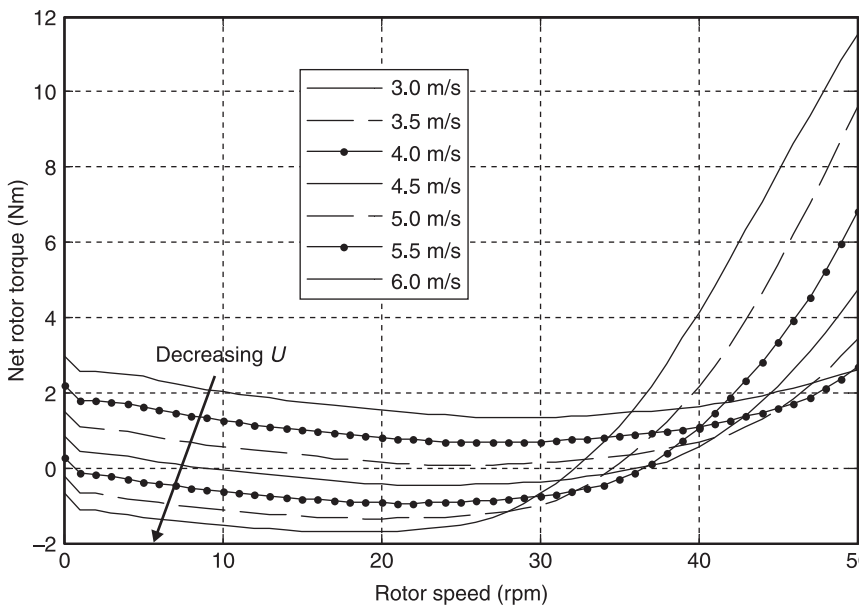

13.11 Net rotor torque as a function of rotor speed and wind speed for the two-bladed 5 kW Aerogenesis wind turbine.

for all rotor speeds. Assuming a similar reduction in the dynamic resistance as in the resistive torque, the new gearboxes would reduce the minimum wind speed to somewhere between 3.5 and 4 m/s.

It is clear from these considerations that starting is a complex process and its influence on blade and machine design involves a number of trade-offs, of which only the major aerodynamic ones were covered. Of the rest, we note that gearbox friction is temperature dependent and may be reduced by judicious choice of lubricant.

13.5 Multi-dimensional design of larger blades

So far, very little has been written about noise. The reason is simply that a well-designed blade of around 2–3 m in length will not be noisy during normal operation. No particular attention was paid to noise in designing the 5 kW blade.

As blade size increases, however, resistive torque becomes less important but noise more so. Whilst the above results focused only on dual optimisation, the numerical nature of DE and the use of a weighted fitness function means that the method can be expanded to any number of objective functions. For example, a possible fitness function combining starting performance, C_p, and sound pressure level is:

$$fitness(i) = a_s \frac{\min(T_s)}{T_s(i)} + a_p \frac{C_p(i)}{\max(C_p)} + a_n \frac{\min(SPL)}{SPL(i)} \qquad [13.8]$$

where $a_p = (1 - a_s - a_n)$ and the factors, a_s and a_n, are the starting and noise weightings and can be varied between 0 and 1, such that the condition $a_n + a_s < 1$ is satisfied. This, of course, assumes, as with power and starting, that noise production can be modelled simply enough to allow many thousands of evaluations of the objective function during an evolutionary optimisation. Our work, Clifton-Smith (2009, 2010b), used the noise model of Zhu (2002) and Zhu *et al.* (2005). They developed a Class III model in the classification of Wagner *et al.* (1996) for the turbulent boundary layer trailing edge noise, the laminar boundary layer vortex shedding noise, the trailing edge bluntness vortex shedding noise, and the inflow turbulence noise. Boundary layer thickness calculations were done using XFOIL, Drela (1989). Mechanical and other noise sources were not considered. For consistency in presentation, the extended design used the blade parameters in Table 13.2.

Results from Clifton-Smith (2010b) suggest that it is possible to reduce both noise and starting time for a negligible reduction in C_p. The use of three objective functions maps out an optimal fitness surface for minimal noise, minimal starting time and maximum C_p, and is shown in Plate V (between pp. 286 and 287). Figure 13.12 shows an optimal fitness front for minimal noise and minimal starting time where only blades with a C_p within 1% of the BEM-optimal bladed were considered. Note that the C_p calculations included the de Vries (1979) correction for tip losses, and the starting calculations included a resistive torque of 0.5 Nm as in Fig. 13.5.

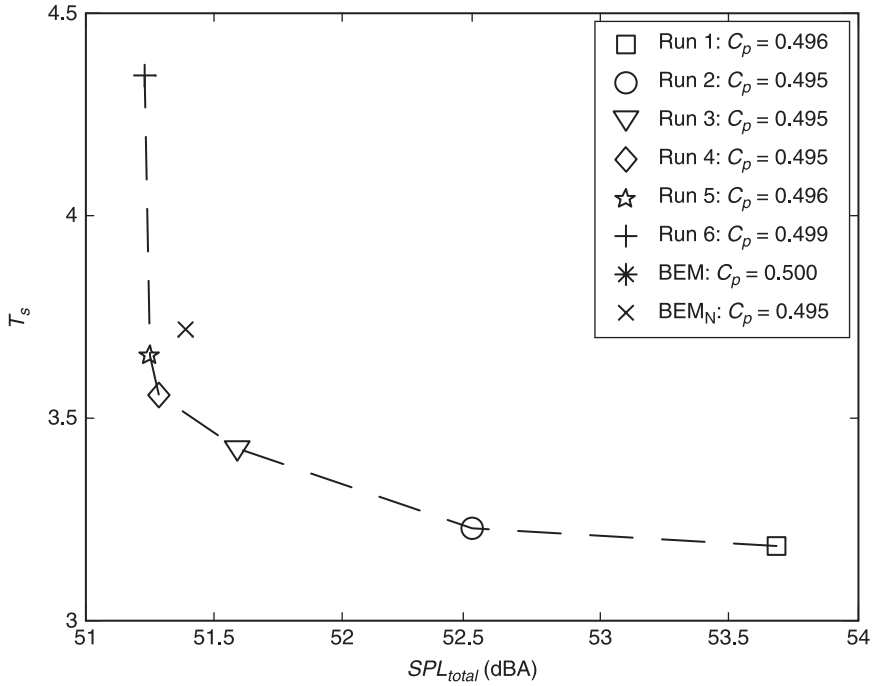

13.12 Typical Pareto front for SPL and T_s for blades within 1% of maximum C_p, taken from Clifton-Smith (2009).

Whilst the quietest blade is the slowest to start and the fastest starting blade is the loudest, there is an area in between where starting performance and noise levels can be improved simultaneously. In particular, significant improvement in the starting time and sound pressure level can be made relative to the BEM optimal blade.

13.6 Conclusion

The results presented in this chapter show that many of the desirable features of wind turbine blade design, such as high efficiency, fast starting and low noise are determined by specific regions on the blade. In addition, and somewhat surprisingly, blades designed solely to maximise power extraction tend to be very slow to start and relatively noisy. It is possible, for example, to make significant improvements to the starting performance of blades by trading off only a small loss in efficiency as measured by the standard power coefficient.

Low wind performance is a particular requirement of small blade design because the drive train and generator resistive torque appears to become more

important as turbine size decreases. Furthermore, large wind turbines are usually sited in windy areas whereas small turbines tend to be placed near the load they supply. Very little research has been done on low wind speed performance. It has been shown here that it is much harder to start blades as the wind starts blowing than it is to keep them spinning as the wind decreases, so the major emphasis on analysing and improving low wind performance has been on starting. Fortunately, the simple BEM used routinely to predict power extraction can be readily adapted to provide an accurate calculation of starting. Further, the two forms of BEM for starting and power extraction are sufficiently simple to be used for many thousands of evaluations of the objective functions during numerical optimisation for blade design.

It is assumed that no power is produced during starting so that the net torque acts solely to accelerate the rotor. The key data required are the lift and drag of the appropriate aerofoil sections at high incidence and low Reynolds number. Even though there is very little applicable data, it was shown that starting could be accurately simulated and was useful in making major design decisions for small turbines.

Optimisation of small blades using the methodology outlined in this paper produces large chords and requires thinner profiles in the root area than is common for large blades. Particular care is required to preserve blade integrity in the face of much higher centrifugal loads on small blades. Section 13.4 described the design of blades for a 5 kW wind turbine. The actual starting performance was described along with the construction and testing of the blades to ensure that they had low inertia, and a fatigue life of at least 20 years.

The optimisation was extended to include noise minimisation in Section 13.5. The trade-offs are harder to judge than in the two-dimensional case, but a decrease in starting time and reduction in noise level can be made for a small decrease in efficiency from the maximum as determined by the standard BEM.

13.7 Acknowledgements

The development of the Aerogenesis 5 kW turbine is supported by a grant from the Australian government under the Asia-Pacific Partnership for Clean Development. We thank Mitchell Gibbs and Paul Peterson for their major contributions to the field testing of the turbine. They and Philip Clausen made similar contributions to the fatigue testing of the blades. Callan Wilson measured the static and dynamic friction in the gearboxes. Sturt Wilson developed the blade manufacturing techniques and provided the blades for field and fatigue testing. Part of the presented work was funded through a University of Newcastle Research Scholarship (UNRS-C) and a CSIRO Energy Technology Postgraduate Scholarship. We thank Wei Jun Zhu for providing source code for the noise model.

13.8 References

Brøndsted, P, Lilholt, H and Lystrup, A (2005), 'Composite materials for wind power turbine blades', *Annual Review of Materials Research*, 35, 505–38.

Burton, T, Sharpe, D, Jenkins, N and Bossanyi, E (2001), *Wind Energy Handbook*, John Wiley & Sons, Chichester.

Calvert, S, Thresher, R, Hock, S, Laxson, A and Smith, B (2002), 'Wind energy research program for low wind speed technology of the future', *Journal of Solar Energy Engineering*, 124, 455–60.

Clifton-Smith, M J (2009), *Multi-purpose Design of Small Wind Turbine Systems*, Ph.D. thesis, Univ. Newcastle, Australia.

Clifton-Smith, M J (2010a), 'Tip loss corrections for wind turbine blade optimisation', *Wind Engineering*, 33, 477–96.

Clifton-Smith, M J (2010b), 'Aerodynamic noise reduction for small wind turbine rotors, *Wind Engineering* (to appear).

Clifton-Smith, M J and Wood, D H (2007), 'Further dual purpose evolutionary optimisation of small wind turbine design', *Journal of Physics Conference Series*, 75, 012017.

Clifton-Smith, M J and Wood, D H (2010), Optimisation of Self-Supporting Towers for Small Wind Turbines, *Wind Engineering*.

de Vries, O (1979), *Fluid Dynamic Aspects of Wind Energy Conversion*. Technical report. AD-A-076315.

Epaarachchi, J A and Clausen, P D (2006), 'The development of a fatigue loading spectrum for small wind turbine blades', *Journal of Wind Engineering and Industrial Aerodynamics*, 94, 207–23.

Drela, M (1989), 'An analysis and design system for low Reynolds number airfoils', *Conference on Low Reynolds Number Aerodynamics, Lecture Notes in Engineering*, 54, Springer-Verlag, Heidelberg.

Giguère, P and Selig, M S (1998), 'New airfoils for small horizontal axis wind turbines', *Journal of Solar Energy Engineering*, 120, 108–14.

IEC (International Electrotechnical Commission) (2006) *Wind Turbines – Part 2: Design Requirements for Small Wind Turbines*, 61400-2 revision 2, Switzerland.

Lyon, C A, Broeren A P, Giguere P, Gopalarathnam A and Selig M S (1997), *Summary of Low-Speed Airfoil Data*, Vol. 3, Soartech Publications, Virginia Beach.

Meyer, C J and Kroger, D G (2001), 'Numerical simulation of the flow field in the vicinity of an axial flow fan', *International Journal for Numerical Methods in Fluids*, 36, 947–69.

Price, K, Storn, R and Lampinen, J (2006), *Differential Evolution – A Practical Approach to Global Optimization*, Springer-Verlag, Heidelberg.

Strickland, J H and Graham, G M (1987), 'Force coefficients for a NACA-0015 airfoil undergoing constant pitch rate motions', *American Institute of Aeronautics and Astronautics Journal*, 25, 622–24.

Sunada, S, Sakaguchi, A and Kawachi, K (1997), 'Airfoil section characteristics at low Reynolds number', *Journal of Fluids Engineering*, 119, 129–35

Viterna, L A and Corrigan, R D (1981), Fixed Pitch Rotor Performance of Large Horizontal Axis Wind Turbines, *DOE/NASA Workshop on Large Horizontal Axis Wind Turbines*, July 1981, Cleveland, Ohio.

Wagner, S, Bareiss, R and Guidati, G (1996), *Wind Turbine Noise*, Springer-Verlag, Heidelberg.

White, F M (1999), *Fluid Mechanics*, 4th ed., McGraw Hill, New York.

Wood, D H (2001), 'A blade element estimation of the cut-in wind speed of a small turbine', *Wind Engineering*, 25(4), 249–55.

Wood, D H (2004), 'Dual Purpose Design of Small Wind Turbine Blades', *Wind Engineering*, 28, 511–27.

Wood, D H (2008), *Wind Turbine and Wind Turbine Blade*, International Patent Application, WO 2008/070917.

Wright, A D (2005), *Aspects of the Aerodynamics of Small Wind Turbines*, Ph.D. thesis, Univ. Newcastle, Australia.

Wright, A D and Wood, D H (2004), 'The starting and low wind speed behaviour of a small horizontal-axis wind turbine', *Journal of Wind Engineering & Industrial Aerodynamics*, 92, 1265–79.

Zhu, W J (2002), *Modelling of Noise from Wind Turbines*. Master's Thesis, Denmark Technical University, 2002. Available from: *http://www.fm.mek.dtu.dk/upload/institutter/mek/fm/eksamensprojekter/wei%20jun%20zhu%20mek-fm-ep%202004-01.pdf*.

Zhu, W J, Heilskov, N, Shen, W Z and Sørensen, J N (2005), 'Modeling of aerodynamically generated noise from wind turbines', *Journal of Solar Energy Engineering*, 127, 517–28.

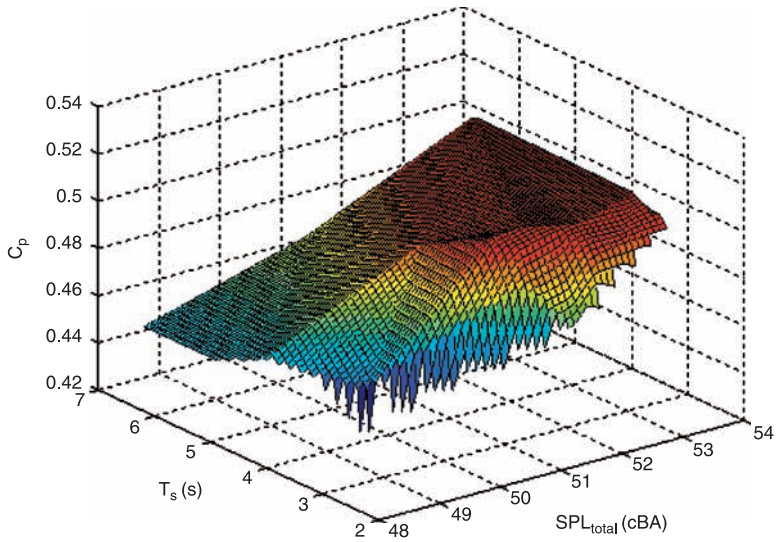

Plate V Typical Pareto front for SPL and T_s and C_p, taken from Clifton-Smith (2009).

14

Optimising wind turbine design for operation in cold climates

L. BATTISTI, University of Trento, Italy

Abstract: There is still a lack of basic information on the conditions causing ice formation on wind turbines, and of technical solutions for turbines operating at low temperatures and in icy climates, despite more and more installation taking place in recent years. Icing of wind turbines affects three different aspects: the design (aerodynamics, loads, control system, materials), safety (ice throw, unbalance, over power, fatigue), and cost-effectiveness (annual energy output expectations, reliable wind sensor, ice detection, wind turbine equipment and lifetime). Cold weather packages provided by turbine manufacturers are typically adopted. The aim of these technical solutions is to widen the operating temperature range of a given wind turbine. However, at sites with a high probability of icing – e.g. several weeks per year – systems that ensure the operation of turbines are needed in order to avoid long stoppages during icing weather events. Active or passive de-icing or anti-icing systems for the rotor blades are then recommended. In this chapter, a general review of the main effects of cold climates on wind energy conversion systems is provided. The wide array of solutions that have been used to reduce the impact of cold weather and ice events on wind turbine design and operation are presented and discussed. Finally, approaches to evaluating and minimising safety and economic risks from ice shedding, and operation and maintenance costs related to the exploitation of wind energy in cold climates are presented.

Key words: cold climates, ice accretion, ice prevention systems, ice shedding risk, economic feasibility.

14.1 Effect of cold climates on wind turbine design and operation

14.1.1 General effects of cold climates on wind turbines

Certification guidelines, that is GL Wind, arbitrarily define low temperature as an hourly averaged temperature of less than –20°C that happens in an average year on the wind energy conversion system (WECS) site on more than nine days per year, and/or the yearly average temperature being below 0 °C (GL Wind, 2005, pp. 4–21). The IEA XIX Annex, Wind Energy in Cold Climates, more consistently defines cold climates as: 'sites that have either icing events or low temperatures outside the operational limit of standard wind turbines' (Laakso *et al*., 2003).

The principles of operation of wind turbines under icing conditions have been compiled in several projects within the EU-funded WECO project, 'Wind Energy

Production in Cold Climates' (Tammelin *et al*., 2000). However, since finishing the research work, many more larger wind turbines have been installed and more experience has been gained.

It has to be recognised that the retrieval of reliable data on characteristics of cold climate sites is still crucial. Although several maps of average site temperatures and frost are available (Fig. 14.1a and 14.1b shows an example of typical maps), there is a substantial lack of icing maps that can be used to assess the severity of the phenomenon for preliminary design. The fact that the common icing evaluation for meteorological purposes is of limited help in forecasting the severity of the icing process on the wind turbine parts is not stressed enough. As will be explained in more detail in the following paragraphs, it is the dimensions of the object being struck (i.e. the blade) and its relative velocity with regard to the water droplet dimension and speed that drive the ice formation on the surface. Therefore, indications of icing maps are indicative of the presence of conditions favourable for icing, but direct measurements of icing parameters to be used in models are necessary for the safe design of wind farms in cold climates.

There are several contributory effects of cold climates on WECSs. In mountainous sites, temperatures lower than the standard (15 °C) associated with high altitude reduce the annual energy harvest, both directly (effect on density) and indirectly (effect on blade Reynolds number) due to the aerodynamic forces. Additionally, this resource, being strongly influenced by the lay of the land, is

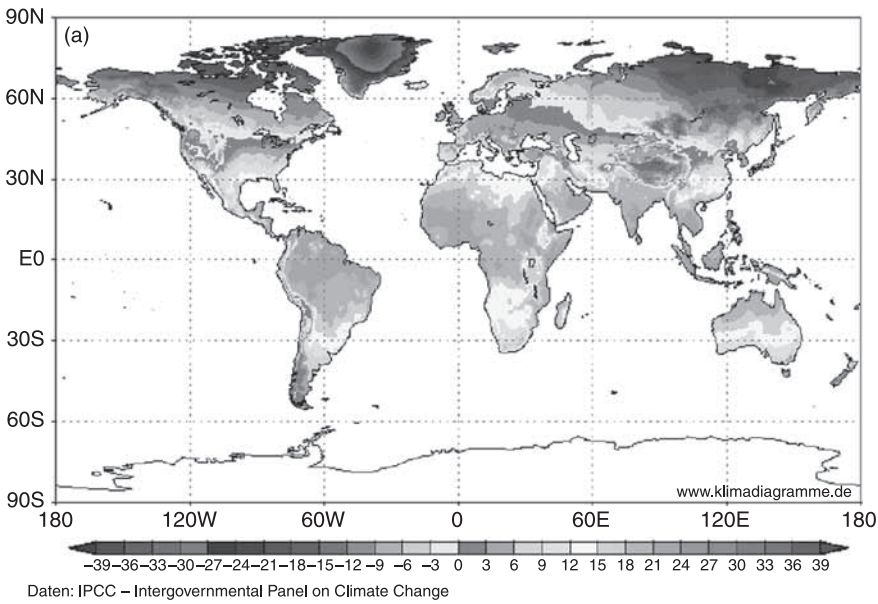

14.1 (a) Mean minimum temperature (in °C) in January (1961–1990).

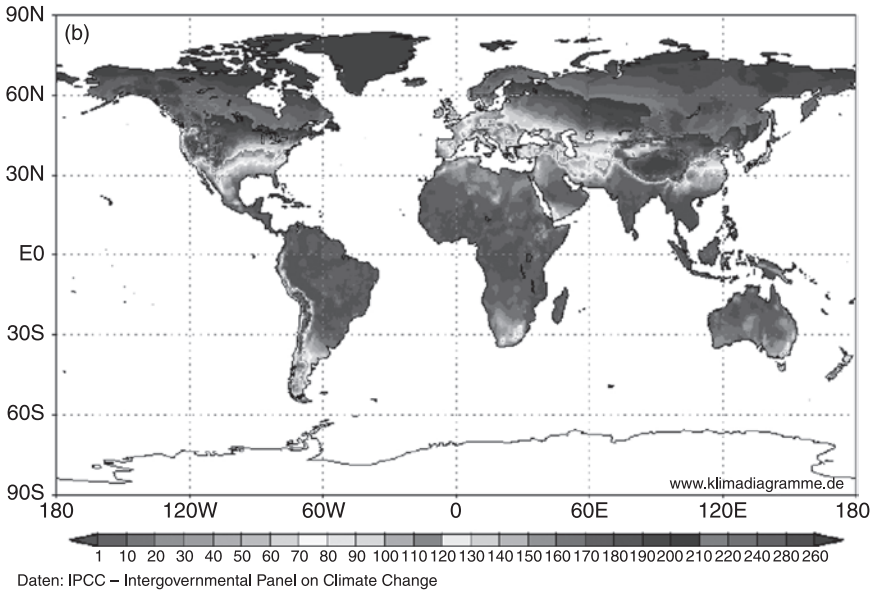

14.1 (b) Average frost days (source: www.klimadiagramme.de.).

characterised by complex turbulence mechanisms, and, in winter, very cold temperatures and clouds favour ice accretion. Figure 14.2 (Battisti and Giovannelli, 2006) shows the trend of the relationship between the relative air density (density at the site to the standard value, ρ_{ST} = 1.225 kg/m^3) and elevation. The effect of different stability conditions is shown. Note that the density at 1000 metres a.s.l. is approximately 90% of the standard density for standard atmosphere, and about 82% at 2000 m a.s.l.

However, this value depends on the degree of stability of the atmosphere, and may drop considerably in the presence of local conditions of thermal inversion (approximately 2% every 100 m) compared to the vertical gradient based on the United States Standard Atmosphere (0.65°C/100 m) implying care evaluations for the structural stresses and plant capacity.

The dual dependence of the Reynolds number on the density and dynamic viscosity prompts the considerations of Fig. 14.3, where the dependence of the Reynolds number on site temperature at different locations is shown.

For the same characteristic velocity and dimensions, blades operating in the mountains experience lower Reynolds numbers, which can drop by as much as 8% at 1000 m a.s.l, while at subarctic sites (considered at the sea level) with mean temperatures around 0 °C, they increase by around 10%, leading to an increase in the performance and forces. The Reynolds number affects the static curves of the lift and resistance coefficient of the profiles and can consequently have a further

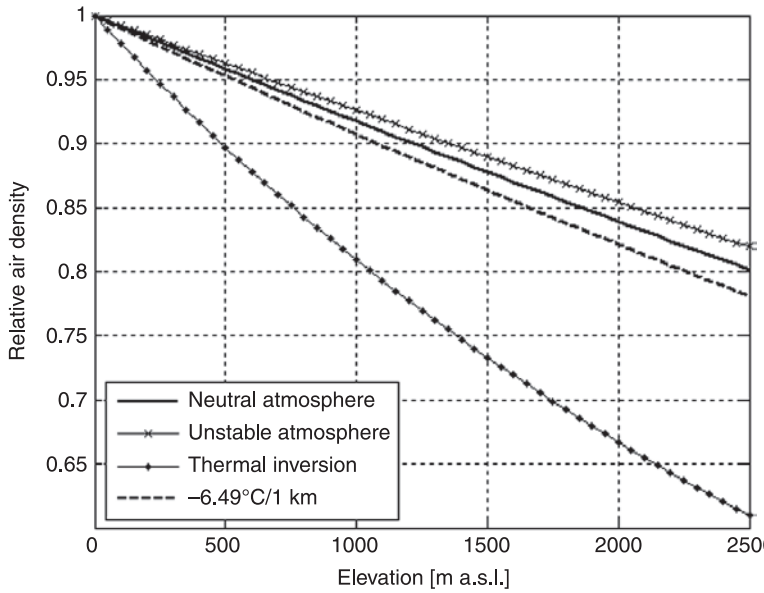

14.2 Dependence of air density on site elevation.

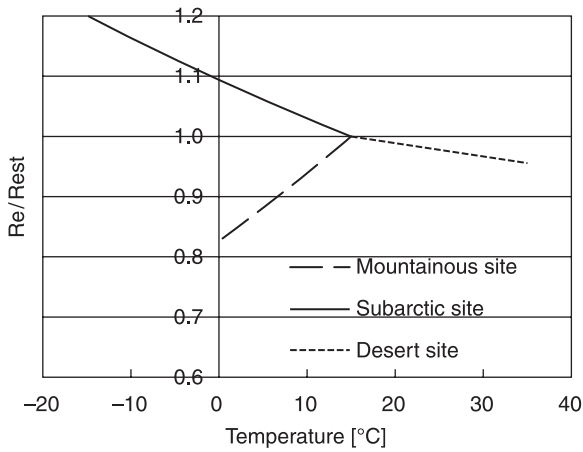

14.3 Dependence of Reynolds number on site temperature.

effect on the capacity prediction. This effect is particularly relevant for small blade chords, where changes in maximum lift and lift-AOA slope do not vary linearly with the Reynolds number. In Fig. 14.4, the dependence of maximum lift and lift-to-drag coefficient as a function of the Reynolds number for the NACA0015 profile are given (Sheldahl and Klimas, 1980).

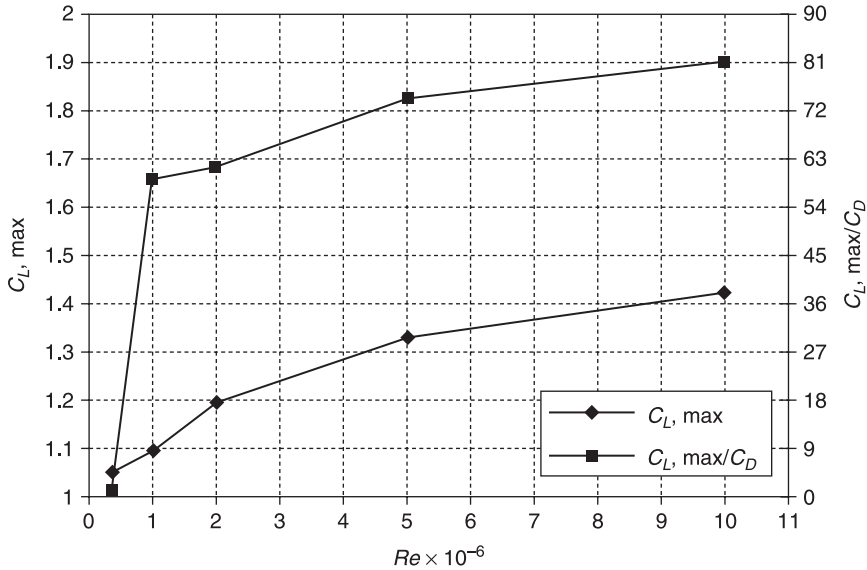

14.4 Dependence of maximum lift and lift-to-drag coefficient on Reynolds number for the NACA0015 profile. (Data collected from Sheldahl and Klimas, 1980.)

To analyse the effect of density on power, power coefficient, thrust and thrust coefficient, three main typologies of wind turbines, stall, pitch and variable speed-controlled wind turbines of the same diameter have been designed and their behaviour analysed for standard and altered density conditions. The wind turbine characteristics have been recomputed for three environmental situations that are described in Table 14.1. Class A is stall regulated, class B is pitch regulated and class C is fully variable speed. Item 1 represents design with standard density, item 2 design with reduced density, item 3 reduced density where the rotor diameter has been increased by means of hub extenders and keeping the same blade, and finally item 4 is an increased density environment compared to the standard. The magnification of the rotor size is a common procedure to recover part of the energy losses due to the reduced density. This operation is actually limited in efficacy for large rotors, as the maximum feasible root elongation for the blades is about 1.5 m. All the cases presented have been computed by optimising the power coefficient. A diameter of 66 m has been used for the computations. The blade pitch and rotational speed have been optimised to deliver the maximum power coefficient for each operational case. The Reynolds number effect on the blades' lift and drag is also considered.

The effect of density variation on power, power coefficient, thrust and thrust coefficient for the same three typologies of wind turbines is presented in Fig. 14.5.

Table 14.1 Data and results for the operation of a 66 m diameter wind turbine in different environments

	Stall regulated				Pitch regulated				Full variable			
	A1	A2	A3	A4	B1	B2	B3	B4	C1	C2	C3	C4
ρ [kg/m3]	1.225	1	1	1.35	1.225	1	1	1.35	1.225	1	1	1.35
D [m]	66	66	66	66	66	66	66	66	66	66	66	66
N [RPM]	20	20	19.27	20	20	20	19.27	20	(30.85)	(33.85)	(31.10)	(29.87)
Pitch angle [°]	–4.6	–4.6	–5.1	–4.6	–4.5	–4.5	–5.25	–4.5	–4.6	–4.6	–5.1	–4.6
V_{tip} [m/s]	69.11	69.11	69.62	69.11	69.11	69.11	69.62	69.11	106.6	114.1	112.3	103.2
Cp_{max}	0.527	0.527	0.516	0.527	0.527	0.527	0.516	0.527	0.527	0.527	0.516	0.527
V_{nom} [m/s]	–	–	–	–	14.47	16.73	15.78	13.55	12.19	13.04	12.75	11.8
P/Pst [m/s]	1	0.816	0.860	1.102	1	1	1	1	1	1	1	1
$\lambda/\lambda st$	1.00	1.00	0.98	1.00	1.00	1.00	0.98	1.00	0.98	0.98	0.99	0.98

Note: A – stall regulated, B – pitch regulated, C – fully variable speed. Item 1 – standard density environment, 2 – reduced density environment, 3 – reduced density with enlarged rotor size, 4 – increased density environment compared to standard.

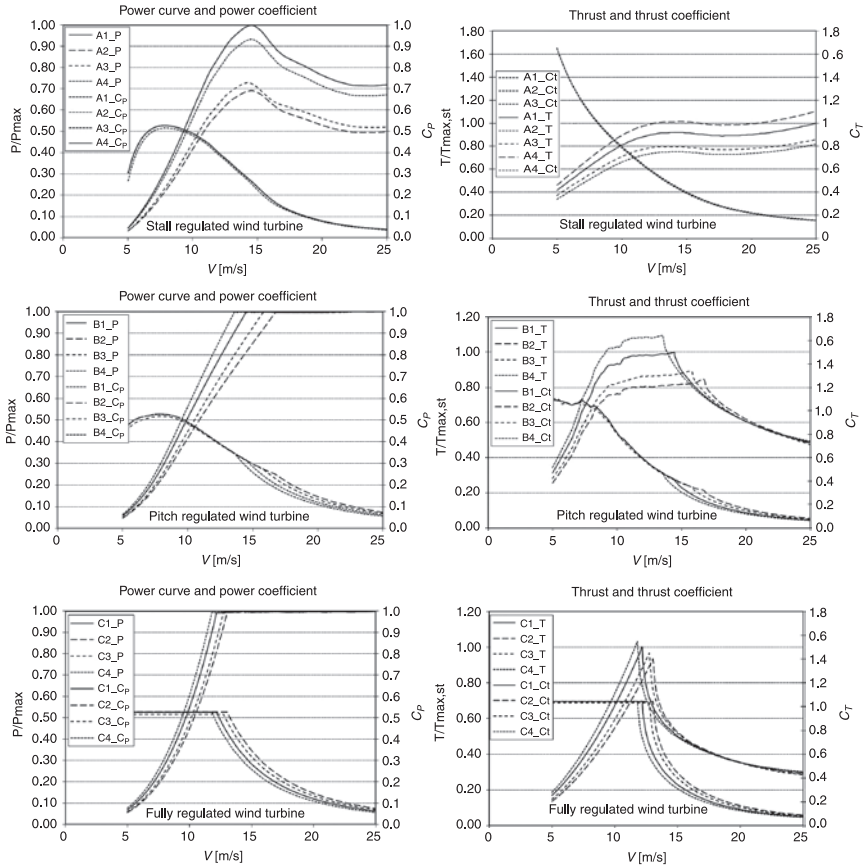

14.5 The effect of density variation on power, power coefficient, thrust and thrust coefficient for the three typologies of wind turbines (A – stall regulated, B – pitch regulated, C – fully variable speed).

For stall-regulated wind turbines, the reduction of the density (case A1) brings general decrease of power, while an increase (A4) in the density results in extra power at each wind speed. The same trend is also confirmed for the thrust. The wind speed at which the maximum power occurs remains almost unaffected. The extended diameter of the rotor (A3) allows recovering almost all the power, but it has to be mentioned that a structural verification of the tower for the bigger rotor size and thrust is necessary. In pitch-regulated and fully variable speed wind turbines, the rotor will deliver the maximum power in all conditions, but the rated wind speed will shift to higher values for reduced density sites (B2, C2) and to lower values for higher densities (B4, C4). The peak thrust is also reduced as the density drops. Note that for higher density, the control lets the thrust increase well

above the maximum setting given for the standard conditions. This shift of the power curve also has an adverse effect on the siting of the wind turbine, which can be completely mismatched. The general conclusion is that without any correction of the control settings, the power curves are generally altered and both siting and mechanical problems are expected.

Cold climates are also characterised by conditions that could potentially lead to ice formation. Generally speaking, icing refers to both atmospheric icing, due to precipitation of water and sea spraying, and it consists of the accretion of ice over both stationary and moving parts, thus determining and altering the fluid dynamic behaviour of the aerodynamic profiles and the mass of the ice-contaminated components. In particular, the lift and drag of both the single profile and the blade as a whole with its three-dimensional development, and therefore the pressure distribution along the blade, are considerably changed. Often, it is very difficult to foresee how lift and drag will change as a result of the deposit of ice on the surfaces, this issue being dependent on the type of ice and its growth history. In the instance of ice accretion, which always happens unevenly, the blade in operation undergoes different flexional and torsional stresses with respect to the uniced conditions, which are transferred to the hub and bearings. These conditions cause unbalanced loads on the mechanical train, and excessive vibration that can reduce the power production and even lead to a stopping of the turbine.

Ice detection is still an unresolved issue for wind energy applications, and potentially effective existing means of de-icing have a poor effect in mitigating the consequences of icing. Moreover, in such operating conditions, a WECS safety concern arises, in terms of the safety of both people and goods that are near to the system.

Due to the increased size of the latest generation of WECSs, once the conditions are created for the ice to come off, sudden and unpredictably sized ice masses can take off like bullets from the blades, causing damage to the surrounding environment. This can lead to the operator having to stop the WECS as soon as the ice presence on the blades is detected. The length of such stops will depend on the seriousness of the problem. In fact, if the ice cannot be adequately removed by means of the available de-icing devices, the consequence is that the systems can be used only for a limited number of days during the potential icing period. In the field, reports indicate an electrical power loss of 1–20% of a normal year's production with continuous system working.

A qualitative scheme of the effect on harvested energy in cold climates with reference to mountainous sites is depicted in Fig. 14.6. The relative figures are compared to the wind resource available at sea level (100% expected production). Ice causes a direct reduction in energy harvest due to the presence of ice on the blades (alteration of power curve, stop, anti-icing system supply) and an indirect reduction due to the more prolonged maintenance times and additional source of damage induced by operation with ice. The figure shows that operation in icing conditions can lead to a significant decrease of energy delivered – as high as about

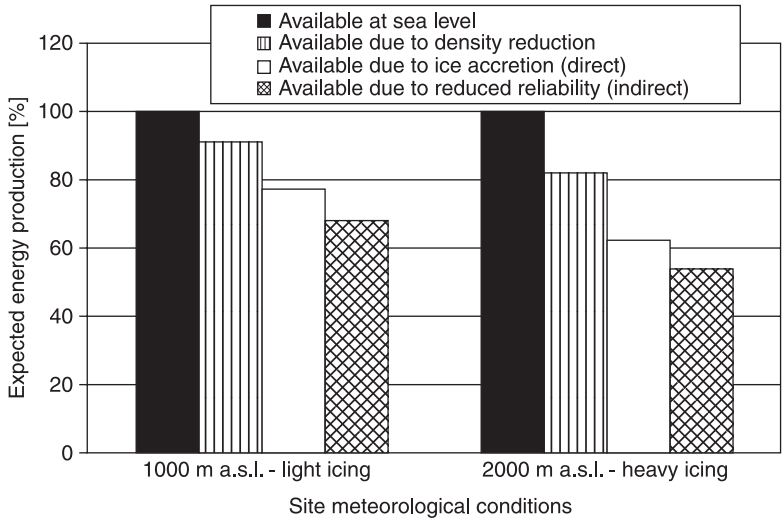

14.6 Qualitative scheme of the effect of iced sites on harvested energy.

50% compared to the same resource at sea level. Lower utilisation factor and non-competitive energy prices can result.

At harsh sites, annual power loss may increase by up to 20–50% (Laakso *et al.*, 2003; Maissan, 2001; Seifert, 2003). How future large offshore plants will be affected by icing events is not clear at the moment.

14.1.2 Special requirements of wind turbines in cold climates

Besides general certification stating that the design and construction of a given turbine/tower assembly are to conform to accepted standards (in terms of design load assumptions, construction materials and methods, control systems and safety measures), operations in cold climates need further caution in ensuring the applicability of the system design and construction to the site-specific conditions.

Usually, manufacturers refer to the standstill temperature as the temperature the turbine can withstand while not operating. This temperature reflects a limit on the turbine material's ability and design philosophy to withstand stress without exceeding normal or acceptable wear and tear. According to the specifications of many manufacturers, most turbine models are designed for operation in ambient temperatures down to –20°C, although some companies indicate operational ranges as low as –30°C and structure ranges down to –40°C. Specially designed versions exist for such applications (cold climate version, Arctic version, cold weather packages, etc.). The wind turbines equipped with such systems allow widening of their operating temperature range (Fig. 14.7).

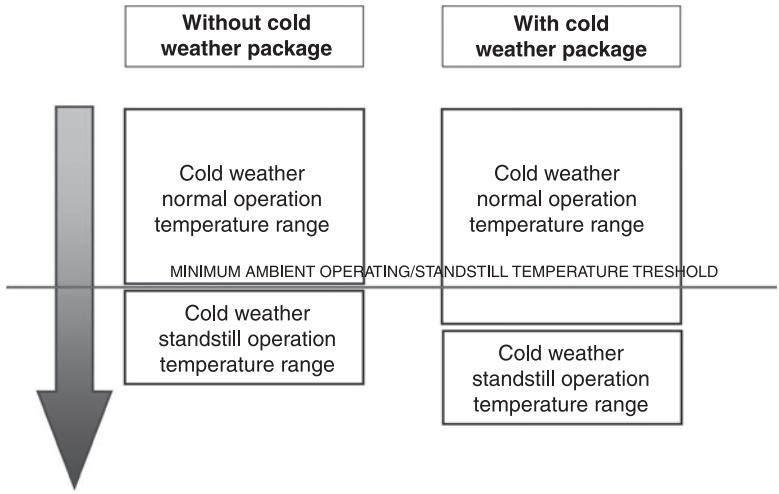

14.7 Schematic of the effect of cold weather packages.

The cold weather packages will normally include:

- heaters (various services, such as oil, gearbox and electric generator);
- additional control cabinet heaters;
- nacelle space heaters;
- improved ambient sealing;
- special alloy ductile iron for hub and machine frame;
- special alloy tower steel;
- low temperature lubricants;
- heated anemometry;
- ice detectors;
- diagnostic package;
- modified start-up procedure;
- increased ventilation systems (in sites with density lower than standard).

As icing is expected during operations, anti-icing or de-icing systems, synthetically classified as IPS (ice prevention systems), are necessary. These systems usually require a source of power to be operated, which is taken from the online production of the turbine or from the electrical grid. As a consequence, operation in cold climates needs a cold station service to provide energy for both the cold weather package and the ice prevention system and to prevent damage during the turbine standstill or shut-down periods.

All such issues need to be examined in the design phase preceding the installation of the turbines in their working environment. Not doing so would mean lower

Table 14.2 Strategies suggested for operations in cold climates

Climate characteristic	Strategy
Low temperatures (0°C to –3°C) and light icing	None and occasional stopping of the WT
Very low temperatures (less than –3°C) and moderate icing	Cold weather package
Real icing risks	Ice prevention system

energy production than expected and prolonged periods of inactivity required for safety reasons or because of the turbines' inability to perform satisfactorily.

Turbines operating in cold climates have to be designed for safe operation: dedicated strategies and special equipment could be considered according to the scheme summarised in Table 14.2, showing the climate characteristics and the suggested strategy.

Generally, the adoption of icing mitigation strategies (such as the IPS, increased preventive maintenance, pre-stocking replacement parts on the site or near each turbine) aims to increase the WT's availability and performance. As a consequence in cold climates, additional costs and the different performance scatter with respect to a wind project on a conventional site have to be taken into account. The major economic risk is due to:

- increased initial costs (limited installation schedules, higher equipment costs, higher installation costs);
- additional costs for installation of dedicated equipment (such as cold weather packages or an anti-deicing system) and their operational costs;
- increased periodic (e.g. after snowfalls and icing events) and unscheduled (premature failures due to increased fatigue loading) maintenance costs;
- increased downtime or power penalty due to icing events;
- increased downtime due to extremely low temperatures (only in very cold weather);
- increased downtime between repairs due to turbine inaccessibility;
- increased turbine downtime for public and labour safety (blades and tower ice throw).

14.1.3 Installed or planned wind farms in cold climates

Despite the mentioned technical problems, there is a growing interest in installing wind farms on cold climate sites. There are two reasons for this. The first lies in the fact that nowadays, the more favourable sites for wind energy have been exploited in historically wind-developing countries (i.e. Europe), and the second is that for some countries, cold-climate sites are the only available land. The

majority of potential cold climate sites are located in open and forested terrain with average wind speeds higher than 7 m/s. The total potential is estimated to be ten times more than for easily accessible offshore sites (personal evaluation based on unpublished market analysis). A wide market potential is located in Sweden, Finland, Norway, Iceland, other European mountainous areas (Pyrenees, France, Austria, Switzerland, Liechtenstein, Italy, Germany, Slovenia, Romania, Slovakia, Ukraine, Hungary, Serbia and Montenegro, Scotland), North America (Canada, USA), Asia (Himalayas in China, India, Nepal, Bhutan), a part of South America and non-Himalayan parts of China.

The Chinese Wind Energy Association has estimated that about 40% of the 253-GW onshore exploitable power will be located in cold desert areas. The target by 2020 is for 30 GW in total, 70% of which will be located in cold climates. Canada has a target of more than 10 GW before 2020, 90% of them being designated as cold climates.

In Table 14.3 and Table 14.4, the existing wind farms operating in European and non-European cold climates, respectively, are listed. The data have been collected by the work of the XIX annex 'Wind energy in cold climates' of IEA, updated at the end of 2006. It represents a global total of slightly more than 600 MW installed.

14.2 Effect of ice on wind turbines

Wind turbine performance changes in response to ice accretion on the moving and stationary parts (Battisti, 2007). Turbines of different sizes and operating parameters (e.g. rotational speed) will have different behaviour on the same site depending on the combination of environmental conditions and type of wind turbine. Non-dimensional analysis (Battisti, 2008) based on the Langmuir parameter that describes the inertia effects of the water droplets indicates that for relatively small droplets $(d/D)^2 << 1$, that is for large body size, the icing will be not an important issue, while for small bodies or for smaller parts of larger bodies, icing will be important. Small wind turbines, due to the large rotational velocities and smaller chords (and profile thickness), are more prone to icing than larger turbines.

14.2.1 General icing characteristics

There are two requisites for the appearance of icing on an object (e.g. the rotor blade):

1. The surface temperature must be below 0 °C.
2. The surface must be exposed to impacts of supercooled water droplets (i.e. liquid water at temperature below 0 °C).

Recurrent conditions for the observed onset of icing are in-cloud icing, fog, sprays, snow and freezing rain. In clouds, operation of wind turbine is a common

Table 14.3 Data of installed wind farms in EU cold climates

Country	Site	Turbine manufacturer	Number of turbines	Total MW	Status	Site elevation m a.s.l.	Site icing	Site low temp.	Modifications icing	Modifications low temp.
FI	Paljasselkä	NORDTANK	1	0.065	Active	400	Heavy	–30°C	Yes	Yes
FI	Korsnäs	NORDTANK	4	0.8	Active	0	Slight	–30°C	No	Yes
FI	Sottunga	VESTAS	1	0.225	Active	0	Slight	–30°C	No	Yes
FI	Siikajoki	NORDTANK	2	0.6	Active	0	Slight	–30°C	No	Yes
FI	Kalajoki	NORDTANK	2	0.6	Active	0	Slight	–30°C	No	Yes
FI	Kemi	NORDTANK	3	0.9	Active	0	Slight	–30°C	No	Yes
FI	Pori	NORDTANK	1	0.3	Active	0	Slight	–30°C	No	Yes
FI	Hailuoto	NORDTANK	2	0.6	Active	0	Slight	–30°C	No	Yes
FI	Lammasoaivi	BONUS	3	1.5	Active	710	Heavy	–30°C	Yes	Yes
FI	Hailuoto	NORDTANK	2	1	Active	0	Slight	–30°C	No	Yes
FI	Ii	NORDTANK	1	0.5	Active	0	Slight	–30°C	No	Yes
FI	Eckerö	VESTAS	1	0.5	Active	0	Slight	–30°C	No	Yes
FI	Kökar	ENERCON	1	0.5	Active	0	Slight	–30°C	Yes	Yes
FI	Vårdö	ENERCON	1	0.5	Active	0	Slight	–30°C	Yes	Yes
FI	Finström	ENERCON	2	1.6	Active	0	Slight	–30°C	Yes	Yes
FI	Siikajoki	NORDTANK	2	1.2	Active	0	Slight	–30°C	No	Yes
FI	Lemland	VESTAS	4	2.4	Active	0	Slight	–30°C	No	Yes
FI	Olos	BONUS	5	3	Active	520	Heavy	–30°C	Yes	Yes
FI	Föglö	ENERCON	1	0.6	Active	0	Slight	–30°C	No	Yes
FI	Lumijoki	VESTAS	1	0.66	Active	0	Slight	–30°C	No	Yes
FI	Kuivaniemi	NEGMICON	6	5	Active	0	Slight	–30°C	No	Yes
FI	Meri-Pori	BONUS	8	8	Active	0	Slight	–30°C	Yes	Yes
FI	Kotka	BONUS	2	2	Active	0	Slight	–30°C	No	Yes
FI	Oulu	WINWIND	1	1	Active	0	Slight	–30°C	No	Yes
FI	Oulunsalo	NORDEX	1	1.3	Active	0	Slight	–30°C	Yes	Yes
SE	Suorva	BONUS	1	0.6	Active		Slight		Yes	
SE	Rodovålen	BONUS	1	0.6	Active		Heavy		Yes	
SE	Rodovålen	NORDEX	1	0.6	Active		Heavy		Yes	

SE	Rodovålen	NEGMICON	1	0.6	Active		Heavy		No	
SE	Kall	VESTAS	1	1.7	Active		Heavy		Yes	
SE	Kvarkenvind, Umeå	BONUS	1	0.6	Active		Slight		No	
SE	Äppelbo	NEGMICON	1	0.9	Active				No	
SE	Klimpfjäll	NEGMICON	3	2.7	Active				No	
SE	Kiruna	NEGMICON	6	5.4	Active				No	
SE	Aapua	VESTAS	7	10.5	Active					
SE	Seskarö	WinWinD	7	7	Active					
SE	Bondön									
CH	Grenchenberg	BONUS	1	0.15	Active	1300	Slight	–20°C	No	No
CH	Simplon pass	Husumer Schiffswerft	1	0.03	Active	2000	Heavy	–20°C	No	No
CH	Gäbris	LAGERWEY	1	0.08	Active	1100	Slight	–15°C	No	No
CH	Mt Crosin	VESTAS	6	4.16	Active	1200	Slight	–20°C	No	No
CH	Titlis	Husumer Schiffswerft	1	0.03	Active	3000	Heavy	–25°C	No	No
CH	Guetsch, Andermatt	LAGERWEY	1	0.75	Dismantled	2300	Heavy	–25°C	Yes	Yes
CH	StMoritz	Aventa	1	0.006	Active	2200	Heavy	–25C	No	No
CH	Guetsch, Andermatt	Enercon E-40	1	0.6	Active	2300	Heavy	–25°C	Yes	Yes
CH	Feldmoos Entlebuch	NEC-Micon	1	0.9	Active	1020	Slight	–15°C	No	Yes
CH	Crêt Meuron		7		Project	1300	Slight	–20°C		
CH	Gotthard		6		Project	2100	Heavy	–25°C		
CH	Grimsel		3		Project	2150	Heavy	–25°C		
CH	St. Brais		2		Project	1200	Slight	–15°C		
CH	Chaumont		2		Project	1200	Slight	–15°C		
CH	St.Croix		7		Project	1200	Slight	–15°C		
UK	Windy Standard	NEGMICON	36	21.6	Active	600	Slight			
UK	Hagshaw Hill, 50 km South of Glasgow	BONUS	26	15.6	Active		Slight			
IT	Acqua Spruzza		1	0.3	Active		Heavy			
IT	Malles venosta	LEITWIND	2	2.53	Active	1250				
NO	Sandhaugen	GE	1	1.5	Active	430				

(*continued*)

Table 14.3 Continued

Country	Site	Turbine manufacturer	Number of turbines	Total MW	Status	Site elevation m a.s.l.	Site icing	Site low temp.	Modifications icing	Modifications low temp.
NO	Nygaardsfjellet	Siemens	3	6.9	Active					
AT	Oberzeiring	Vestas	13	22.75	Active		Slight			
AT	Herschgi					154				
AT	Leitzersdorf					230				
AT	Prellenkirchen					170				
AT	Schenkenfelden									
AT	Zistersdorf					300				
DE	Brandenkopf					911				
DE	Chemnitz									
DE	Esens					1				
DE	Eulenberg					715				
DE	Ibbenbüren					170				
DE	Kirchdorf					8				
DE	Langeln					185				
DE	Lüppath auf Rügen						10			
DE	Radauanger					205				
DE	Rebgeshain					630				
DE	Sadisdorf									
DE	Sandbostel					13				
DE	Seitenroda					110				
DE	Steinbeck					42				
DE	Stübbeberg					190				
DE	Wattenbach Söhrewald					500				
DE	Zug					460				
Total				144.44						

IEA, Annex XIX inventory, update end 2006.

Table 14.4 Data of installed wind farms in non-European Union cold climates

Country	Site	Turbine manufacturer	Number of turbines	Total MW	Status	Site elevation m a.s.l.	Site icing	Site low temp.	Modifications icing	Modifications low temp.
Canada	North Cape (Prince Edward Island)	Vestas	8	5.28	Active		Slight	–25°C	No	Yes
Canada	Metane (Québec)	NEG-Micon	3	2.25	Active		Slight	–30°C	No	Yes
Canada	Le Nordais, phase 1 (Québec)	NEG-Micon	76	57	Active		Slight	–30°C	No	Yes
Canada	Le Nordais, phase 2 (Québec)	NEG-Micon	57	42.75	Active		Slight	–30°C	No	Yes
Canada	Tiverton (Ontario)	Tacke	1	0.6	Active		Slight	–30°C	No	Yes
Canada	Pickering (Ontario)	Vestas	1	1.8	Active		Slight	–25°C	No	Yes
Canada	Gull Lake (Saskatchewan)	Vestas	1	3.96	Active		Almost none	–30°C	No	Yes
Canada	Pincher Creek (Alberta)	Danish Windmatic	3	0.195	Active		Almost none	–30°C	No	Yes
Canada	Pincher Creek (Alberta)	Danish design	1	0.15	Active		Almost none	–30°C	No	Yes
Canada	Cowley (Alberta)	US Windpower (Kenetech), Nordex	72	40.095	Active		Almost none	–30°C	No	Yes
Canada	Pincher Creek, Castle River (Alberta)	Vestas	60	39.54	Active		Almost none	–30°C	No	Yes
Canada	Hill Spring (Alberta)	Vestas	4	2.46	Active		Almost none	–30°C	No	Yes
Canada	Peigan Nation Reserve	NEG-Micon	1	0.9	Active		Almost none	–30°C	No	Yes
Canada	Heackel Hill, White Horse (Yukon)	Bonus, Vestas	2	0.81	Active		Heavy	–40°C	Yes	Yes
China	Urumqi, Xinjiang	BONUS	13	1.95	Active			–40°C	No	Yes
China	XWPGP, Xinjiang Province	BONUS	4	1.2						
China	XWPGP, Xinjiang Province	BONUS	4	2						

(*continued*)

Table 14.4 Continued

Country	Site	Turbine manufacturer	Number of turbines	Total MW	Status	Site elevation m a.s.l.	Site icing	Site low temp.	Modifications icing	Modifications low temp.
China	XWEC, Xinjiang Province, (AN)	ANBONUS	10	1.2						
China	Buerjin Hydro Power, Xinjiang Province (AN)	ANBONUS	3	1.35						
China	IMEPA, Inner Mongolia	BONUS	12	7.2						
Russia	Murmansk	NEG-Micon	1	0.2	Active		Slight		No	
Japan	Tomamae Windfarm, Hokkaido	BONUS	20	20	Active	70				
Japan	Tomamae Town, Fuuraibo	BONUS	1	1	Active					
Japan	Hamatonbetsu, Hokkaido	BONUS	3	3	Active					
Japan	Enbetsu, Hokkaido	BONUS	3	3	Active					
Japan	Hamatonbetsu Green Fund, Hokkaido	BONUS	1	1	Active					
Japan	Iwaya Wind Farm, Tohoku district, Honshu	BONUS	25	32.5	Active					
US	Lake Benton, Minnesota			200	Active					
US	Searsburg, Vermont			6	Active		Slight			
US	Nine Canyon, Washington									
Total				479.39						

situation. Due to the relative velocity of the blades, condition 2 is also satisfied for very low wind speeds.

14.2.2 Icing parameters

The meteorological and climatic quantities related to icing are:

- the liquid water content of air (LWC);
- the air temperature (T);
- the droplet size (d or MVD);
- the atmospheric pressure (p).

For a complete evaluation of the probability of encountering an icing situation of a given severity, all these variables should be considered simultaneously, in relation as well with:

- the relative wind speed (W) of the blade;
- the transverse size of the blade (thickness or nose diameter).

The availability of information for these parameters is common in aeronautic fields and routinely measured, while for the wind energy field, LWC and MWD are not available or are measured at site, prejudicing the application of existing ice accretion codes.

14.2.3 Icing events

The icing day is a critical variable for defining the economic relevance of icing on WECS production and the convenience of installing turbines in icing-relevant sites. The icing day is a probabilistic concept (Battisti, Brighenti, *et al.*, 2005) arising from the subset of conditions defined by the shared area shown in Fig. 14.8. Aeronautical models consider the atmospheric states defined by the variables W, T, LWC and MVD as icing events, characterised in that their range is LWC > 0 (g/m^3), T < 0 (°C) and $W > 0$ (m/s). When such limits are simultaneously exceeded, ice will form. The direct icing duration (icing time) is defined as the minimum duration of the single event with a contemporary occurrence of such conditions and is expressed as:

$$t_i = t_{LWC>0} \cap t_{V>0} \cap t_{T<0} \qquad [14.1]$$

The intensity of the phenomenon can only be determined if the wind turbine's geometrical features and operating conditions are given. The condition expressed by Fig. 14.8 actually defines a necessary but not sufficient condition for icing. A range of simultaneous combinations of meteorological variables, each of them having the same probability of being exceeded, define the probability of icing.

Operationally, the icing day is considered as the sum of the number of hours during which the turbine is not free of ice. This depends not only on the incipient ice accretion duration time (turbine in-cloud operation – icing formation or direct

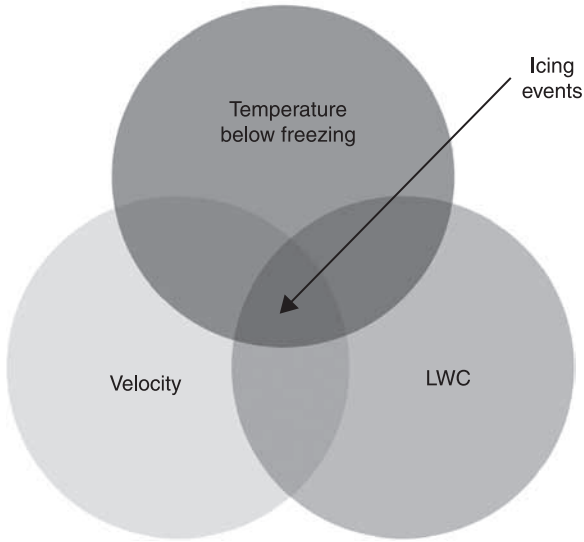

14.8 Definition of icing day.

icing) but also on the time duration during which the turbine cannot produce because of the persistence of ice on structures (extra time of ice or indirect icing). Usually, extra ice is not recorded by some ice detection devices, but observations (Durstewitz, 2003) indicate that it can be as high as 100% of the direct icing time and results in up to 50% of the increased system unavailability. But there is no clear consensus on this point.

14.2.4 Icing type

The type of ice that will be formed is dependent on the atmospheric and meteorological conditions, as well as on the thermal conditions prevailing during ice formation at the surface. Predicting the type and shape of the ice accretion for a specified set of icing conditions is difficult because of the complex interactions between the meteorological and turbine operating parameters. For the purpose of studying the ice formation, it is convenient to divide the ice into two classes: glaze and rime. In Fig. 14.9, the mechanism of ice formation is illustrated.

A mixture of these two types of icing is not uncommon because the atmospheric conditions change during an icing period, and it is called mixed ice.

Glaze ice is usually associated with large values of LWC of the air and with droplet size of 0–500 μm and temperatures between 0 and –5°C. It forms a transparent icecap with a glassy surface. The icecap adapts itself to the form of the enclosed object and can hardly be removed from it. It is compact, usually transparent,

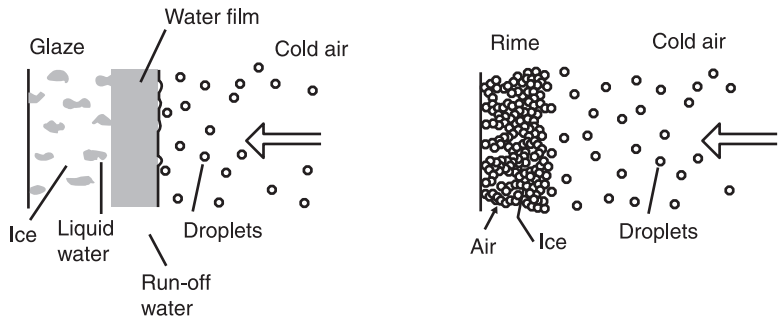

14.9 Glaze and rime ice: mechanism of formation.

almost bubble free, with strong adhesion and density close to 900 kg/m^3. Glaze ice is generally clear and is characterised by the presence of larger protuberances, commonly known as glaze horns, as shown in Fig. 14.10(a).

Rime is usually associated with freezing fog with a droplet size of 0–10 μm. When the air temperature is well below 0 °C (less than –5 °C), the super-cooled droplets freeze almost instantaneously on contact. Two types of rime ice are identified: hard rime, which is granular, white or translucent, density 600–900 kg/m^3, and soft rime, which is white or opaque, density 100–600 kg/m^3.

A mixed ice accretion will have some of the characteristics of both glaze and rime ice accretions. As shown in Fig. 14.10(b), the centre portion of a mixed ice accretion will have the characteristics of glaze ice accretion. This glaze centre will

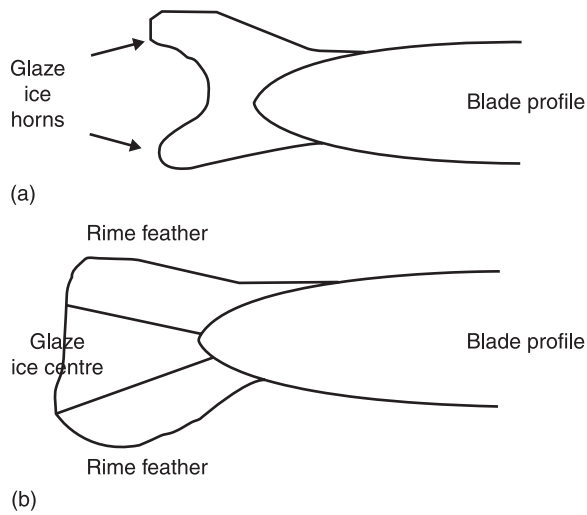

14.10 (a) Example of a glaze ice shape. (b) Example of mixed ice accretion.

be surrounded by rime ice accretions, commonly called rime feathers because of their thin, feather-like shape and delicate structure.

Atmospheric icing related to wind turbines operating in clouds and fog that have smaller droplet sizes than raindrops is able to supercool more and will therefore tend to accrete rime, whereas larger supercooled drops are associated with glaze accretion (Ackley and Templeton, 1979).

A correlation between droplet size and LWC with the temperature influence shown is presented in Fig. 14.11. The majority of these show the tendency that LWC decreases for increasing droplet size. This is reported by the experimental findings of Cober *et al.* (2001) as well. The solid curves represent the potential accumulations of ice on a cylinder (diameter 3 in.) in g/cm^2/h.

14.2.5 Offshore icing

Icing has been recognised as a serious long-lasting problem for ships and sea structures. There are substantial differences between offshore and continental regions, essentially due to the presence of the water and the boundary layer structures over sea and land, respectively.

Icing on the sea is caused, in order of importance, by:

- sea sprays originating from seawater;
- atmospheric icing originating from atmospheric freshwater.

Both phenomena can occur simultaneously and the relative prevalence is essentially linked to the height above the sea surface. Sea sprays do not usually reach higher than 15–30 m, depending on the relative velocity of the wind. The LWC drops with height, and at 4 m above the sea level and at wind speeds less

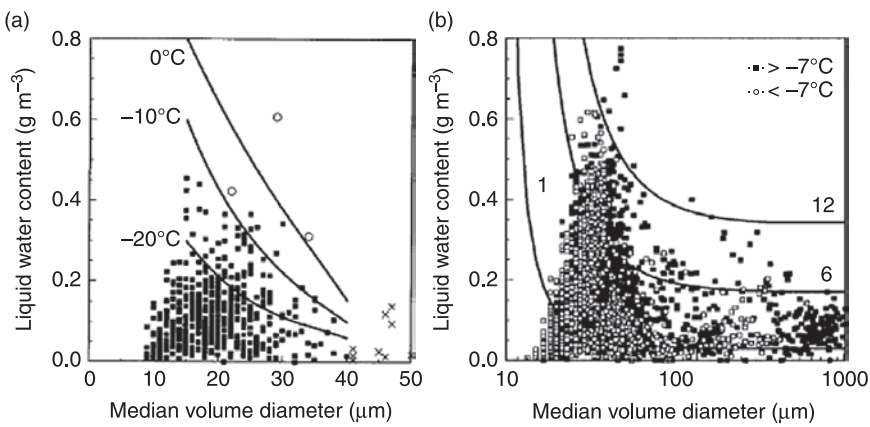

14.11 Relation between droplet size, liquid water content and air temperature. (Measured data from Cober *et al.*, 2001.)

than 25 m/s (Makkonen, 1984), it is one or two orders of magnitude smaller than the typical maximum values of LWC during atmospheric icing.

In offshore conditions, icepack or floating blocks (flows, driving ice, land-fast ice) on the sea surface cause additional static and dynamic forces on the turbine structure. The effects of sea ice occur as mechanical shocks and increased vibrations that may result in additional operational loads.

It is well recognised from field experiences that offshore wind turbines suffer from sea ice actions much less at the areas where sea ice is mostly land-fast ice compared with that of the drifting ice. For land-fast ice, the structure is typically surrounded by more or less uniform ice. The ice sheet interacting with the turbine structure produces a wide range of deformation states, each generating different reactions on the structure (Mróz *et al*., 2005). Static loads are induced by a stationary contact of the ice with the turbine tower, and the surface forces arise from loads applied by a combination of winds, currents drags and thermal expansion, which slowly push the ice cover against the structure. The tower behaves as a single, isolated pinning point resisting the applied driving force, which can be more or less distributed over the tower surface. Weather conditions, applied force level and icing–de-icing cycles of the interface determine the uniformity of the mutual ice–structure contact. Thick ice in cold seawaters may sometimes induce the pile-up phenomenon as a result of an irreversible damage of the offshore cantilever structure systems. A certain amount of this 'pack ice' occurs every winter, typically towards springtime, when sea ice starts to move. Dynamic loadings arise from pieces of floating ice or even ice fields that can cover several square kilometres, hitting against the structure with appreciable velocity (even higher than 1 m/s). The duration and the forces exchanged with the tower depend on the kinetic energy of the ice and on its features. Floating and pack ice on the water surface and atmospheric icing induce the wind turbine to excessive vibrations. Ice drift and hitting against the foundation might trigger structural vibrations, or even damage it by exciting the tower, while the structure's icing will flapwise excite the blades, but the main effect is felt on the tower (Battisti, Hansen, *et al*., 2005).

The turbine components need to be resistant to vibration under time-varying environmental or operational loads. Especially for cold climates, the wind turbine should incorporate sensors that monitor the environmental loads, including both those due to icing and to the sea ice, and the state of the structure. This concept needs more advanced diagnostic tools to be developed compared to current state-of-the-art ones. On the basis of this information, semi-active countermeasures are activated automatically to prevent excessive vibrations. One possible method of mitigating the vibrations is to embed damping and smart elements in the supporting structure of the wind turbine. These would be used to reduce the dynamic response and to increase the fatigue life of the structure. Structural damping is almost always an effective solution against excessive vibrations. The foundations of the wind turbines also have an effect on preventing ice-induced movements. In appropriate sites, the natural land-fast ice zone can be extended in the wind park

such that the static and dynamic ice forces on individual foundations remain small.

Sea ice accumulation on the tower could possibly modify the tower weight and aerodynamics, thus modifying the loads on foundations. Moreover, as different researchers showed in the study by Morcillo *et al*. (2004), the ice accumulation could accelerate the corrosion speed process of the tower and support structure, if appropriate offshore corrosion protection systems are not adopted.

14.2.6 Ice detection

Ice detection is a challenging task in wind energy. The analysis of the number of icing days during the wind resource evaluation phase often uses the combination of heated and unheated anemometers. For wind turbine operations, various sensor systems have been tested over the years, but none of them has yet proved sufficiently reliable and efficient. Ice detectors used in stationary conditions (meteorology applications) for aeronautics are heavy and installable only on the fixed parts of wind turbines such as the nacelle. Unfortunately, the relative velocities at the blade tip are much higher than those occurring at the nacelle (e.g. a 12 m/s wind speed at the nacelle corresponds to about 70 m/s relative velocity at the blade tip), and the local heat transfer is much enhanced at the blade tip, causing the icing process to be dissimilar between the nacelle and the blade. Most frequently, when the icing process is recorded as being incipient at the nacelle, the blade is in full icing and the maximum vibration sensors of the wind turbine have already intervened. There are direct and indirect icing-based detection concepts. The direct ones are based on reading of various physical parameters. From aeronautical applications, there are piezoelectric transducers, depolarising infrared laser light transducers and impedance-change transducers based on the change of dielectric constant of water ice. Common problems of such devices are the weights, which are excessive for applications on moving parts such as blades. Most applications are only indicative for wind turbines and need the contemporary measurement of indirect parameters, such as the power curve, the ambient temperature reading and accelerations. Also, the measurement of the increased weight of the blade due to ice through the blade root bending moments has been proposed. A variant is the measure of the gyroscopic moment of the hub. These methods rely on the fact that ice accretion is naturally uneven, so a mass imbalance always occurs. The methods must determine whether the monitored meteorological conditions and operational conditions are consistent with blade icing. Thus, in configurations in which blade mass imbalance is checked, both latter methods also need to measure the ambient temperature, the humidity and the yaw because blade imbalance can also result from yaw angle, and a near-zero yaw condition is necessary to avoid incorrect detection. The status of current ice detection technology for wind turbines is not reliable at the moment, as often the wrong variables are detected, with the consequence of waste of monitoring costs, uncertain monitoring and, where present, additional costs of energy for anti-

icing systems (waste of energy for anti-icing purposes). On the basis of the personal experience of the author, the only way for the early and accurate detection of ice onset is the contemporary measurement at the same location of the external surface temperature and the external surface wetness of the rotating frame (blade) at the correct position (both spanwise and chordwise).

14.2.7 Ice growth on wind turbines

Generally, there are three situations in which icing on WT can occur: standstill (the rotor is at rest), idling (the blades are rotating, but the wind turbine is not connected with the grid) and operation. Ice growth is also related to the wind turbine control strategy: pitch-controlled or stall-controlled wind turbines. In a pitch-controlled WT, blade leading edge (LE) ice accretion of up to 100% (of the chord length) could be observed (Seifert and Richert, 1997, 1998) during idling in icing conditions, as the pitch angle is reduced and the rotor speed is low. The angle of attack (AOA) at the sections produces negligible lift, and thus, neither centrifugal loads nor relevant lift forces are acting on the ice growing at the LE region, resulting in a much bigger growth rate. During power production, the relatively high rotor speed causes the onset of centrifugal forces on the ice at the LE, and the lift forces cause shear forces on the accreted surface and bending moment between the ice and the blade, resulting in the early break-off of the ice and the formation of erratic shapes. For this reason, the quantification of the ice mass distribution and the total ice mass is only possible on a statistical base and deduced from on-site observations. Figure 14.12 shows the turbine in different working conditions. Qualitative ice accretions are depicted on the blades.

Small ice accretions are evident during power production under icing conditions. Standstill causes a more serious problem because, depending on the wind direction, large areas of the blade can be exposed to icing, also in moderate winds. As a consequence, de-icing applied to a small blade region can be totally ineffective. Also, trailing edge ice accretion is possible.

Due to the increasing spanwise relative air velocity along the radius and the progressively reducing width of the blade, the ice accretion builds up more on the outer part of the blade with an approximately linear increase. In general, observations (take for all the one in Fig. 14.13) confirm that ice build-up is almost linear from the blade root to the tip with a maximum depth of ice accretion at the outer part. The growth is insignificant until the mid radius for large wind turbines. Due to the mass and surface forces and the superimposed vibration phenomena, the ice at the outer part of the blade breaks off and grows again during operation forming a typical saw tooth distribution. For this reason, Germanisher Lloyd (GL Wind, 2005) prescribes that 'the mass distribution (mass/unit length) shall be assumed at the LE. It increases linearly from zero in the rotor axis to the value m at half of the radius, and thus remains constant up to the outermost radius'. The following empirical rule is given:

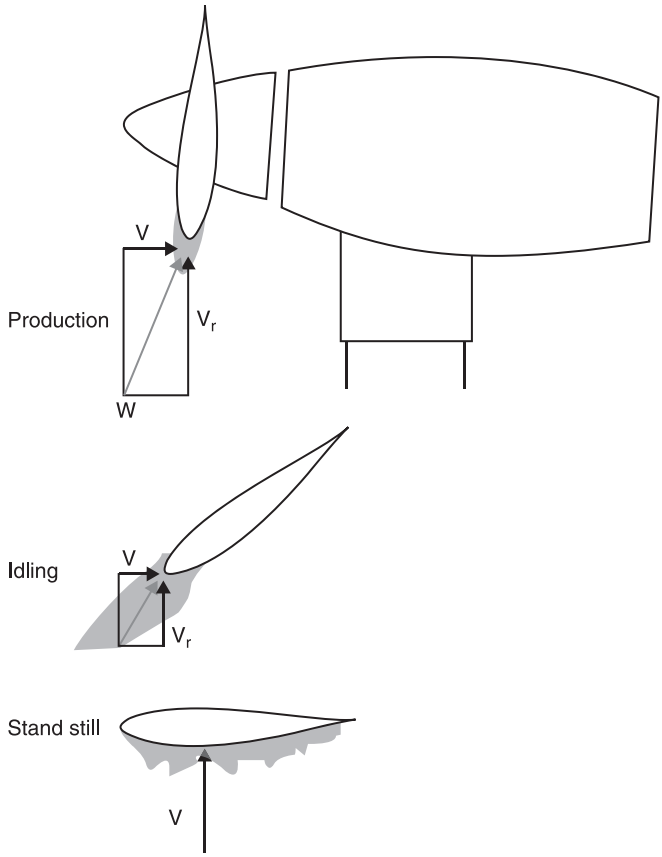

14.12 Qualitative example of lift forces caused by ice on the pitch-controlled blade in different working conditions.

$$
\begin{aligned}
m &= \rho_{ice} \times k \times c_{min}(c_{min} + c_{max})\ [kg/m] \\
\rho_{ice} &= 700\ kg/m^3 \\
k &= 0.00675 + 0.3 \times e^{\left(-0.32\frac{r}{r_l}\right)} \\
r_l &= 1\ m \\
c_{max} &= \text{maximum chord length} \\
c_{min} &= \text{chord length at the blade tip, linearly extrapolated} \\
&\quad \text{from the blade contour}
\end{aligned}
\qquad [14.2]
$$

This approach produces the mass distribution shown in Fig. 14.14 where the ice distribution for the three rotors of different size is simulated.

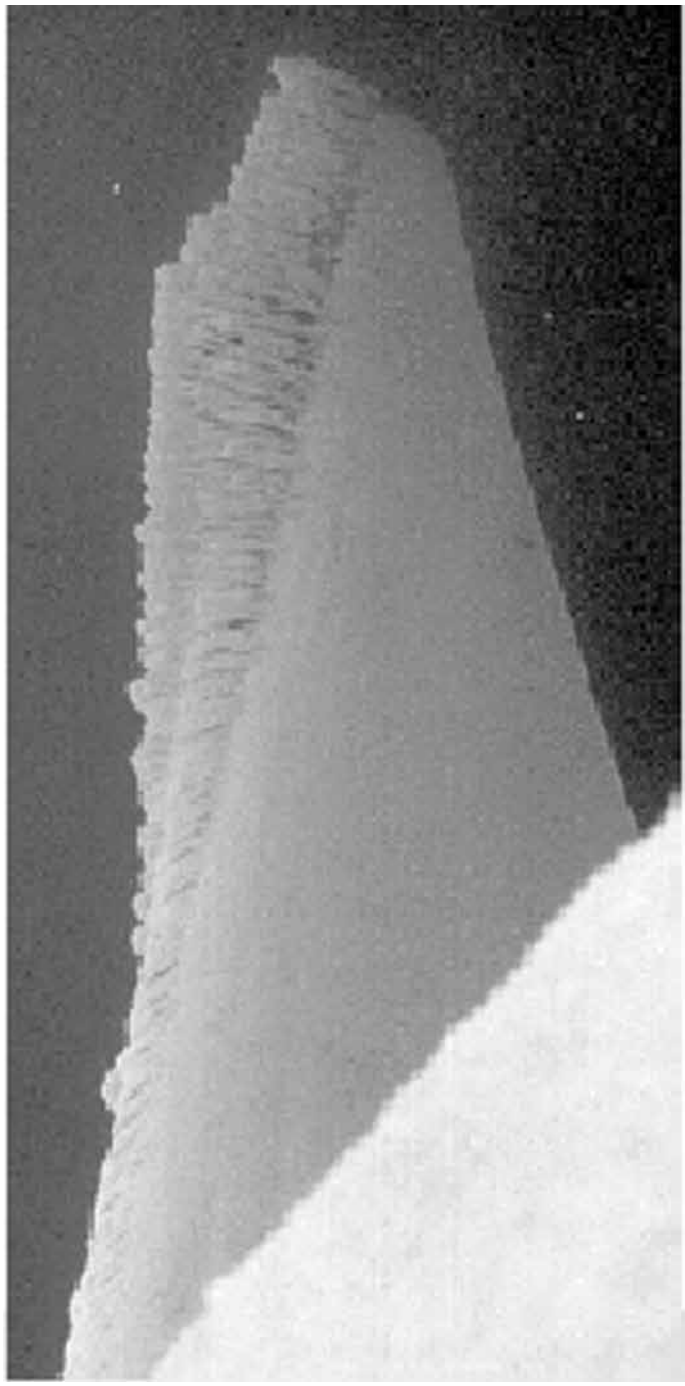

14.13 Picture of the distribution of a typical ice accretion.

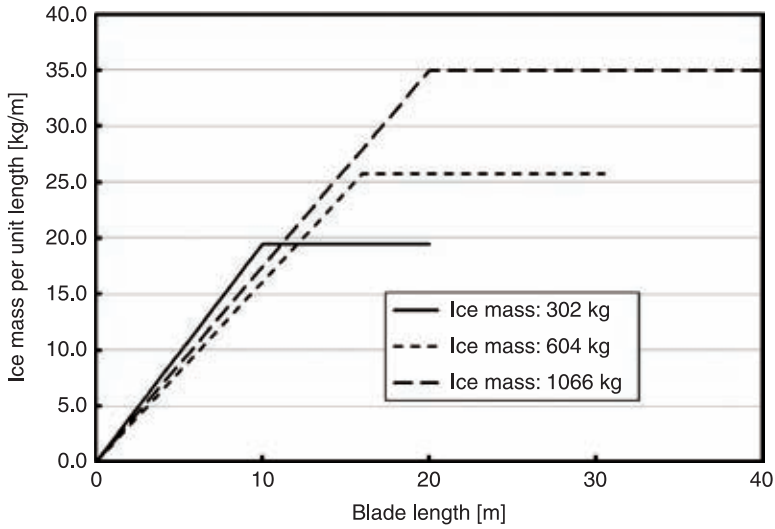

14.14 Mass distribution for three rotors of different sizes.

The mass inventory gives about 1066 kg of additional mass for each blade of 40 m span, 604 kg for the 30 m span and 302 kg for the 20 m span. These additional masses are in the order of 10–15% of the blade mass and become relevant for static and dynamic load analysis.

The ice affects the aerodynamic and aeroelastic behaviour of the rotor due to:

- the change of the mass per unit metre of the blades;
- the change of the aerodynamic performances (and forces) of the aerofoils;
- the change of the material mechanical properties with temperature;
- the effect on the control system (inhibition of the actuators and/or sensors, etc.).

The presence of ice on the rotor determines additional loads that can reduce the lifetime of some components. It should be safe to integrate such information with other measurements (temperature, wind velocity) and database retrievals (standard power curves, standard frequency spectra of the vibrations) to set up new strategies for rotor design.

Further information on the aeroelastic behaviour of the iced rotor can be found in part of work package 3 (WP3) of the EC project NNE5 2001-00259 (2001) and New Icetools (NICE), aimed at improved recommendations for load and design related to wind turbine in ice condition. WP3 deals with structural dynamics and turbine safety due to ice load conditions.

14.3 Effects of ice on aerodynamics and loads

The effects of ice on aerodynamic profiles include decreased lift, increased drag and instability caused by adverse moments. Ice accretion on aircraft has been

investigated for the past 50 years (see Al-Khalil *et al*., 1993; Gelder and Lewis, 1951; Neel *et al*., 1947; Thomas *et al*., 1996) but because of the detrimental effects on aircraft performance, only a few observations and tests are so far available for wind turbines (Bose and Rong, 1990; Makkonen and Autti, 1991; Makkonen *et al*., 2001a, 2001b; Seifert and Richert, 1998).

Furthermore, the following relevant differences arise between the two application fields:

- It is difficult to carry out tests on wind turbines in climatic tunnels.
- Among the few correlations recognised as valid in the aeronautical field, only a few data are usable for wind turbines, also because of the limited angles of attack ranges that have been investigated.
- Some physical parameter ranges (LWD, MVD) can only be estimated.
- Until now, the understanding of the aerodynamic behaviour has been undertaken by:
  - taking field measurements from an instrumented turbine during icing;
  - set up of semi-empirical aerodynamic models;
  - comparison with measurements and trying to tune the semi-empirical model in order to capture the real behaviour;
  - CFD approach.

The performance degradation caused by glaze and rime ice accretion can differ significantly due to the observable differences in form and texture. Glaze ice, which in severe cases is characterised by large ice horn formations near the LE, causes a large increase of drag and decreases the maximum lift coefficient because of flow separation behind these formations. A shift of the zero-lift AOA is observed, but it is not as severe as in the case of rime ice accretions. This is caused by the rougher surface of the rime accretion near the stagnation point that results in a thicker upper surface boundary layer near the LE than on glaze ice accretion. Although glaze ice accretions increase the surface roughness over the clean aerofoil, the shape has a much more significant effect on performance degradation. For this reason, a simplified performance degradation model of glaze ice horns is usually employed in tests without consideration of surface roughness effects with nearly the same accuracy, especially for maximum lift and drag. In some cases, the ice growth is sufficient to change the body shape and thereby affect the amount of collected water as the ice grows in size.

Rime ice, which is characterised by a rougher surface near the stagnation point and more streamlined appearance, generally causes a smaller increase in drag compared to glaze ice horns. Since rime ice accretions tend to retain the streamlined shape of the aerofoil, the surface roughness that causes premature transition is the primary cause of the increased drag. The LE surface roughness also causes a decrease in the maximum lift coefficient and a shift in the zero AOA as discussed earlier.

Formation of ice masses increases at approximately constant rates with increasing time in a rime icing condition and at a progressively increasing rate in glaze icing conditions.

The aerodynamic penalties depend on the aerofoil shape, which means the thickness of the aerofoil, the pointed LE and the flow separation from the suction side at high angles of attack.

Thicker aerofoils with blunt LE would be less prone to drag reduction with ice, and any correlation among ice shape, AOA and change in drag is more progressive. With respect to the two main modalities of ice accretion, the following general considerations can be drawn.

14.3.1 Smooth ice (glaze)

1. With growing ice accretion, the drag of the aerofoil increases due to the profile shape alteration, even if the profile shape tends to be replicated, and due to the attack angle variation, diminishing the power output of the turbine.
2. At the iced cross-section of the blade, the augmented chord length at the LE can lead to:
   (a) an increase of the bending moment at the blade root;
   (b) an increase of the pitching moment that is very important for the pitch control mechanism;
   (c) an increase of the lift coefficient (overpower).

14.3.2 Rough ice (rime)

1. With growing ice accretion, the drag of the airfoil increases due to the profile shape alteration, diminishing the power output of the turbine.
2. At the iced cross-section of the blade, the augmented chord length at the LE can lead to:
   (a) an increase of the bending moment at the blade root;
   (b) an increase of the pitching moment, which is very important for the pitch control mechanism.

Until now, the most systematic work has been undertaken experimentally in the WECO project (Tammelin *et al*., 2000), where the problem has been approached by an evaluation of the effect of simulated ice accretion on the aerodynamic performance of an artificially reshaped aerofoil. The shape of ice of the LE to be investigated in the wind tunnel was taken from plaster pieces modelled from ice fragments found close to a real iced WT (Fig. 14.15). LE ice accretion was investigated in a wind tunnel for a range of values of the ratio of ice length to chord (2% up to 44%). Stationary and non-stationary 2-D data of lift, drag and aerodynamic moment coefficients have been extracted in an open jet wind tunnel for AOA in the range of –10° to 30°. In Fig. 14.15, the results are shown. Compared to the clean profile, the A (2.2%) and B (22%) contamination levels

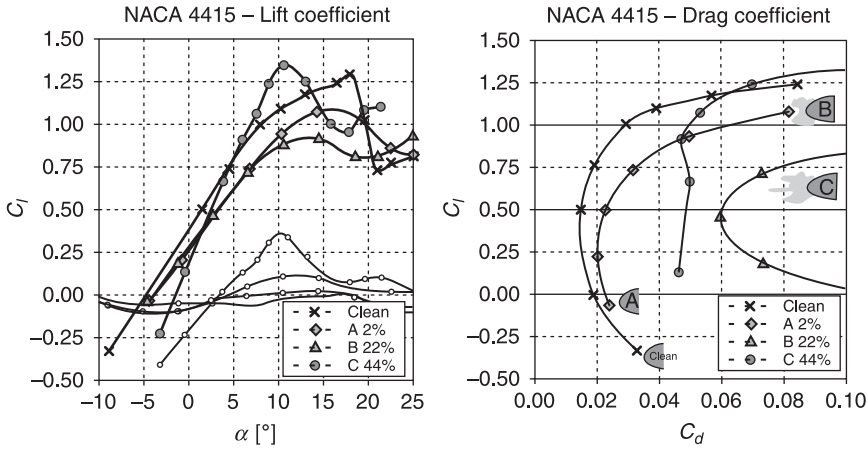

14.15 C_l, C_d performances of NACA 4415. (Readapted from Seifert and Richert, 1998.)

reduce the performances of the profile, while the effect of the large chord encountered in case C (44%) tends to anticipate the stall condition and leads to a comparable maximum lift.

Instationary measurements were performed for the iced and non-iced cross-sections in order to investigate the influence of icing on the dynamic stall behaviour. The results have shown no significant change of the behaviour of iced and non-iced C_l (α) curves. A shift of the zero-lift AOA of the iced airfoil compared to the clean one also resulted in a lower amplitude of the maximum and minimum lift coefficient in the stall region for the iced section. In particular, these results suggested that an influence on the dynamic behaviour in the post-stall region could be expected.

14.3.3 Procedure for assessing the performance of iced rotors

In the absence of any standard, and by considering the difficulty in predicting shape and dimension of the accreted ice on the blade, we arbitrarily introduce a procedure to help in obtaining icing scenarios and associated performance degradation. The steps are:

- Start from the performance of profiles contaminated by different ice thicknesses, for instance on the basis of the WECO results, and define the standards (ratios ice length to chord of A = 2%, B = 22% and C = 44%).
- Construct the performance of a similar clean airfoil (i.e. from NACA 4415 to NACA 4421).
- Define the performances of the similar iced aerofoil and introduce the Viterna method (Viterna and Corrigan, 1981) to obtain the contaminated profile performance above stall conditions.

Table 14.5 Definition of the contamination levels

Contamination level	Ratio of ice to chord
CL0	GL • 0.275
CL1	GL • 0.5
CL2	GL • Base mass distribution
CL3	GL • 2

- Build up scenarios of ice mass distribution on the blade (contamination levels).
- Determine, with some physically sound rule or with the aid of observation, the extent of the ice accretion along the blade.
- Interpolate between cases A, B and C to get the performance of arbitrarily contaminated sections of the blade and construct a look-up table for each section.
- Run the BEM code to get the iced power curve.

The level of contamination of the surface is defined in Table 14.5. The Germanischer Lloyd trapezoidal rule (GL Wind, 2005) is taken as the basis and denoted as CL2. Very light (CL0), light (CL1) and heavy (CL3) mass distributions are defined.

In Fig. 14.16, the mass distribution due to these contamination levels is given for the 32 m blade of the Tjaereborg wind turbine data. In Fig. 14.17, the resulting ice thickness is obtained by considering a suitable hypothesis on the local ice accretions.

14.4 Icing effect on power production

Two methods to study icing effects on power production have been historically used:

- direct power measurement, experimental, based on continuous data from WT test sites;
- calculation, based on the method explained in the preceding paragraphs.

According to the latter method, the resulting power curves, obtained for the four contamination levels, are shown in Fig. 14.18 for a 2 MW wind turbine.

The power curves are observed to show little change in shape for the first three contamination levels. Rather, they are simply offset to higher velocities with higher ice accretion. However, the fourth level, CL3, shows a marked change in the power curve. While this curve never reaches rated power, it does recover a lot of energy from the wind speeds below the rated wind speed. Thus, if the site has more frequent winds in this range, an increase of energy could be possible for CL3 compared to CL2.

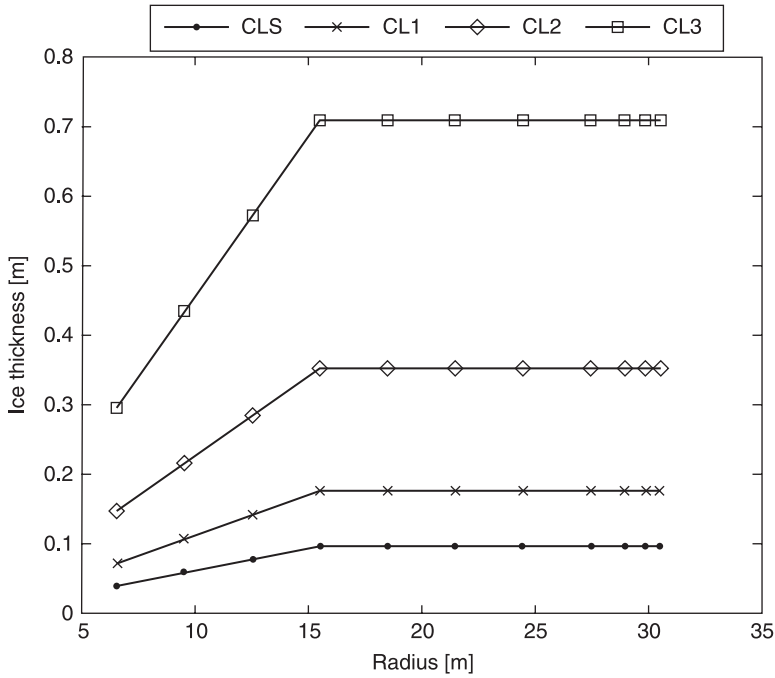

14.16 Ice mass distribution according to Table 14.5 contamination levels.

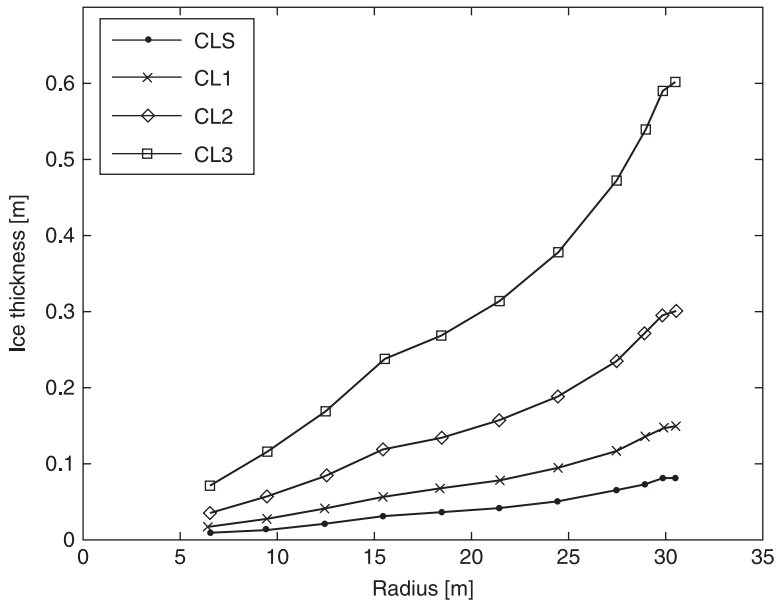

14.17 Ice maximum thicknesses according to Table 14.5 contamination levels.

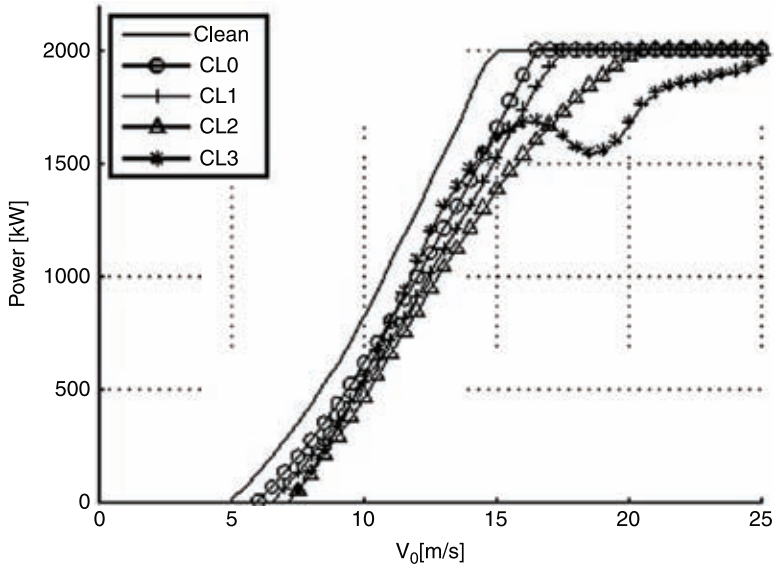

14.18 Calculated power curves for a 2 MW pitch control wind turbine in different blade ice accretion conditions.

As a consequence, the losses associated with aerodynamic degradation claim for a corresponding reduction in annual energy production (AEP).

14.5 Anti-icing and de-icing systems, design and performance

14.5.1 System assessment

The selection and design of anti-icing systems for wind turbines has to be based on the reliable evaluation of the heat fluxes that the blades exchange with the environment during icing conditions. The problem increases in complexity due to the dependency of the heat fluxes on a large number of variables that are both climate and turbine dependent.

As icing is a common occurrence in aviation, the wind energy research field can profit from the experience and adapt some solutions to their special needs, although basic differences do not make technology transfer obvious. Quite a number of aeronautical ice accretion-prediction codes have been developed to aid in the design of ice protection systems and in the certification of aircraft for flight in icing conditions: the LEWICE code from NASA (Wright, 1995, 2002), the CANICE code from École Polytechnique (Morency *et al*., 1999, 2000; Tran *et al*., 1996), the CAPTA code from ONERA (Guffond and Brunet, 1985), the ICE code from CIRA (Mingione and Brandi, 1998) and the 2DFOIL-ICE code from the University of Twente (Dillingh and Hoeijmakers, 2003). These codes adopt similar methodologies

for heat modules and they can predict water catch rates, water droplet impingement limits, ice accretion shapes and overall thermal ice protection system requirements. The use of these codes for the wind energy field is not straightforward. Important differences arise between aeronautical and wind applications. These are due to the climatic conditions at which they are calibrated, the adopted ice prevention strategy, the operating angles of attack of the profiles, the wall materials employed and the effect of rotation.

Only a few dedicated codes exist for analysis of ice accretion and ice prevention system design of wind turbines: the LEWICE 2.0 ANTICE code (Al-Khalil *et al*., 2001), adapted to predict anti-icing power requirements for wind turbines, and the TURBICE code (Makkonen *et al*., 2001a) that simulates ice accretion on wind turbine blades developed by the Technical Research Centre of Finland (VTT). Recently, the TREWICE code (Battisti, Fedrizzi, Rialti and Dal Savio, 2005) developed by the University of Trento has been made available either for thermal anti-icing or de-icing purposes. TREWICE can also model hot air anti-icing systems in both continuous and intermittent heating mode.

Safety insights and fatigue load considerations strive for no-ice-tolerant or for quasi-no-ice-tolerant strategies. IPS installed power and energy consumption depend on the amount of the heat fluxes required per unit surface and on the extent of the blade thermal protected area. The former depends in turn on the prescribed surface temperature (running wet or evaporative surface conditions), and the latter on both climatic conditions and blade geometry characteristics. These arguments will have basic implications for the WT selection process of site developers and break-even analysis of IPS in cold climates.

The selection, analysis and design of anti-ice thermal IPS for wind turbines involve an iterative procedure.

The first design stage is to assess the need of the ice prevention system. This step requires reliable information on icing severity of the site and the effect of ice on turbine dynamics. An aeroelastic code should assess whether the ice prevention system is actually required and whether its economic profitability is sustainable. IPSs affect both investment and operating costs in different ways depending upon site and selected IPS typology.

The type of IPS has to be selected and then designed. Usually the system has to be integrated into an existing design philosophy rather than being part of a dedicated machine for cold climates. Field tests should complete the procedure and dictate the operating rules of turbine and IPS.

This step is challenging because of:

- the lack of meteorological and site parameters;
- the lack of data (both thermal and mechanical) on blade material behaviour at very low (–20–0°C) and very high (70–110°C) temperatures for continuous service;
- the lack of available tools for design of IPSs. Some numerical tools developed for aeronautical fields are not very suited for use in wind turbines, because of

very different climatic conditions encountered (LWC, MVD, etc.), availability of such data, presence and control of ice detection systems, relative wind speed of moving parts, on-board available power for anti-icing, maximum demand during specific operations, materials used, effect on performance, rotating parts, typical icing time, need of certifications. Reliable numerical tools are quite difficult to build up and validate. They require very structured and heavy computational modules, some of which are not readily available for private companies or research centres;

- the need for additional efforts (both for design and certification) to integrate the IPS into current wind turbine design.

The suggested requirement in designing blade IPS is that the blade must be maintained sufficiently free of ice accretion to enable continued, safe and economic operation in icing conditions. While in the aeronautical field the recommended procedure is to design for the partial or complete evaporation of all impinging water in the most severe conditions (likely to be encountered in a condition of continuous icing), some tolerance for ice formation could be admitted under certain conditions in wind turbines. A heated blade designed on this basis will remain clear of ice under most situations with only a relatively small amount of runback forming.

A standard ice accretion code alone is not sufficient for designing a thermal anti-ice IPS. Usually the goal of ice accretions codes is to predict the local ice mass growing on the surface, while anti-ice prediction codes are designed to assess the heat flows to be provided at the surface to ensure a given temperature to be maintained at the surface. Ice accretion codes can be modified by adding an external heat source in the energy balance, which can possibly keep the blade's external temperature above freezing. Adding external heat means introducing a conjugate heat transfer analysis step. Usually the conjugate heat transfer analysis encompasses the external flow field, the blade wall conduction process and the inner flow field computation (when blade warm induct air circulation is employed).

The steady state conditions required from anti-icing computation introduces some simplification in the calculation path compared to unsteady processes involved in ice accretion. The simplified path of the ice prevention system assessment is depicted in Fig. 14.19.

14.5.2 Design procedure

Since IPSs on wind turbines cause additional investment and operational costs, some criteria are needed for the assessment of the benefits of such systems. Although in general, searching for appropriate structural solutions for IPSs should take into account actions exerted by both the sea ice and icing, in the following only an example of an integrated procedure for atmospheric icing is presented. The extension to include sea ice effect is straightforward and does not modify the underlying logic.

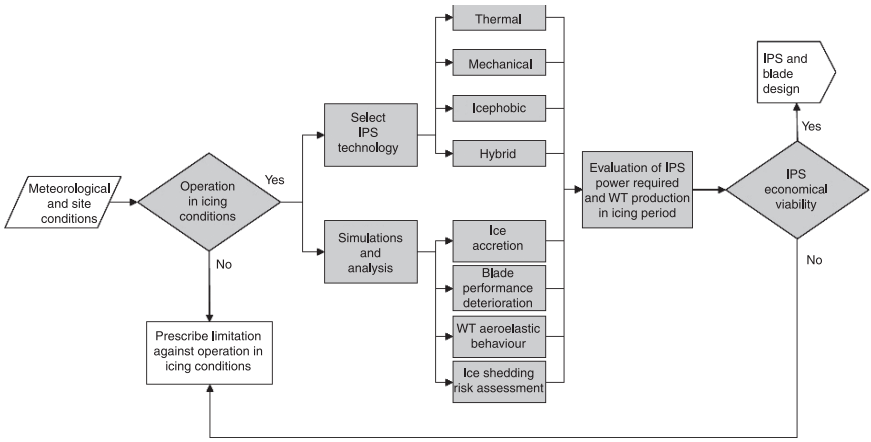

14.19 Simplified path for the ice prevention system (IPS) assessment procedure.

Figure 14.19 depicts a possible integrated design path for IPSs applied to the rotor as an explanatory situation.

On the basis of environmental data and technical guidance issues, manufacturer design requirements and objective, the procedure first assigns the boundary conditions for a series of numerical simulations and experimental campaigns. Ice accretion analysis is necessary to provide the new contaminated blade profile shape and the induced performance and loads. In this step the aeroelastic code simulations evaluate the ice accretion on the blades and consequent surface and mass loads. A performance deterioration analysis allows the energy output to be evaluated. Shed-ice trajectory and structural damage tolerance analysis is also an output of the integrated procedure. A technical level decision is now made on the need for an IPS. For light icing, where negligible structural and performance penalties exist and an acceptable risk for people and goods is evident, no IPS is required and only limitations can be prescribed for in icing operations. If the use of an IPS is found to be necessary instead, a preliminary selection of the technology is made on the basis of engineering experience.

Four types of systems are indicated in Fig. 14.19: thermal, mechanical, icephobic and hybrid surfaces. According to the choice, simplified methods are used to evaluate the anti-icing installed power and its energy consumption, and a break-even analysis is carried out to assess the economic viability of the system. In the case of the system ending as uneconomical, only limitations are prescribed for operation in icing conditions. However, if the selection of continuous anti-ice technology is confirmed as preliminarily viable, Fig. 14.20 indicates the full calculation path for system executive design, verification and certification. Numerical and in-field tests on models are necessary to assess the technical availability and reliability of the IPS. This step ends with the analysis of the

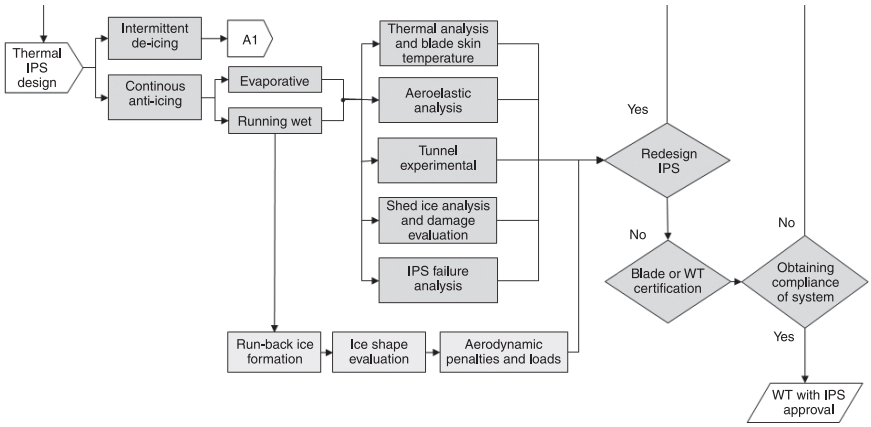

14.20 Ice prevention system design, verification and certification.

components' redesign. If a major redesign is needed, a new economic break-even point is required, otherwise only the technical approval path is followed.

14.5.3 Integration of the aeroelastic analysis in the anti-icing design procedure

A consistent step of temporal quantities that characterise the persistence of the icing on a given site is defined here as an event frequency level (EFL). The temporal quantities can be, for example, the number of hours of operation with ice on one, two and three blades and the number of sudden shedding events from one or two blades.

The following procedure is proposed to integrate the aeroelastic analysis into the de-icing design:

- A set of arbitrary contamination levels (CL) and EFL has to be defined.
- The CL–EFL couples determine a matrix of arbitrary load history cases where the 20-lifetime assessment can be carried out.
- A damage level can be defined for every CL–EFL couple as the increase in the 20-year equivalent load with respect to those of the standard case. The damage level matrix can be realised for a set of components of the WT.

Any given site can then be fitted into one of the CL–EFL matrices based on its meteorological characteristics.

In case the damage level exceeded a critical value D_{critical}, the data from the CL–EFL couple are fed as input to the anti-icing design procedure. The previous procedure relies on the basic hypothesis that there is sufficient information about temporal and physical characteristics of icing of a given site macro/micro

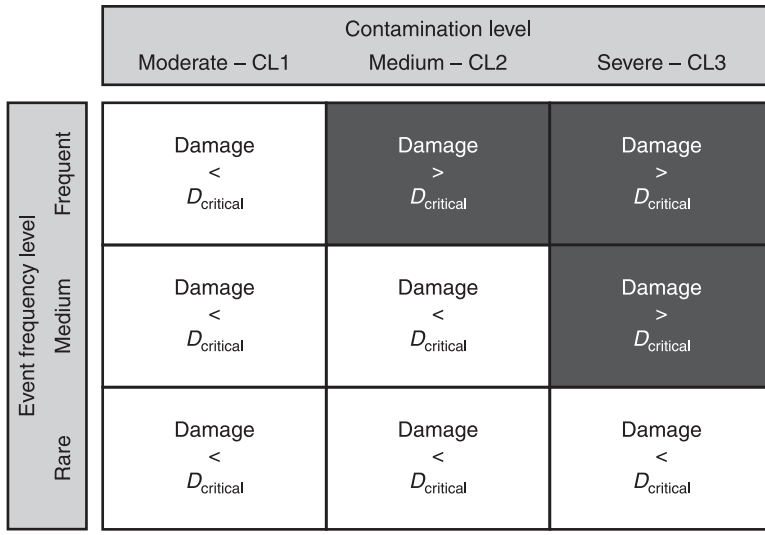

14.21 Scheme of the damage level matrix.

area. They can be originated from direct measurements or meteorological extrapolations.

Figure 14.21 presents a scheme for the damage level matrix.

14.6 Ice prevention systems, concepts, comparison and discussion

Three types of classification can be used for IPS: the first is very intuitive and is based on the principle of operation adopted – thermal, mechanical or other – the second is based on the energy requirement and the third is based on the duration of the applied means and is analysed by an intermittency factor.

By focusing on the principle of operation used, IPSs can be classified on mechanical, thermal or others, the latter grouping of all systems is not included in the first two.

In IPS mechanical methods, mechanical shocks are induced to break the ice cap. The main methods are: forced vibration, electromagnetic impulses, ultrasounds, electro- and magneto-strained envelopes, and changes in the alloy memory phase.

In IPS thermal methods, heat is applied to a selected wide area encompassing the water impingement region. Generally speaking, the heat needed to prevent ice in thermal-based anti-ice systems can be provided using two heating strategies, that is a distributed heat source generation (electrical pads) or a concentrated heat source generation (hot air). In the former case, the heat is generated at the desired location by means of the Joule effect, while in the latter the heat is produced in

one location and then distributed by means of a suitable carrier (generally air, but other intermediate heat carriers can also be used). Heat can be used to prevent impinging cloud droplets to freeze, either by evaporating or by maintaining them in liquid state (running wet option). In this case, we refer to the anti-icing system. In evaporative practice, sufficient heat is supplied to evaporate all water droplets impinging upon the heated surface, while in running wet only enough heat is provided to prevent freezing on the heated surface. Beyond the heated surface of a running-wet system, the water can freeze, resulting in run-back ice. For this reason, running-wet systems must be used carefully so as not to permit build-up of run-back ice in critical locations. When heat is used to dislodge or melt an existing ice cap, we refer to it as a de-icing system.

In a thermal IPS the heat source can be supplied either by extraction from the plant's own electrical system, or by a separate on-board generator with its own source of power. An interesting opportunity in wind turbines is to seek for regenerative energy sources as the heat released from electrical devices or heat exchangers, and the option will be analysed in the following sections.

Other IPSs include solar-radiation-absorbent coating, hydrophobic and ice-phobic coating, viscous products and greases.

Generally speaking, passive techniques do not always hinder ice formation, but help to limit its problematic effects. Special coatings result in no energy consumption, no moving mechanical parts and are typically easy to be fit. As drawbacks they do not remove ice, do not sufficiently prevent ice build-up, are not active during the night and are less efficient on cloudy days. Some possible aerodynamic performance issues and the risk of wear can both be of concern. Moreover, some coatings can be toxic or corrosive.

For energy analysis purposes, the most interesting way to classify thermal IPSs is through the time duration of the applied heat. For this aim we use an intermittency factor defined as the ratio of the duration of the heat application to the surface to the total time of the icing event, which will be the sum of the time duration of heat supply and the time duration where no heat is used. Equation [14.3] shows this ratio:

$$\tau = \frac{T_{\text{heat-on}}}{T_{\text{heat-on}} + T_{\text{heat-off}}} = \frac{T_{\text{heat-on}}}{T} \qquad [14.3]$$

On this basis, de-icing systems are characterised by an intermittency factor less than unity, which indicates cyclic operation, while anti-icing systems operate at an intermittency factor equal to unity, indicating continuous operation. In de-icing practice (which is widely used in the aeronautic field), sufficient heat is rapidly applied to the ice-surface interface in order to melt the bonding layer of ice; aerodynamic or centrifugal forces then remove the bulk of the ice. These two operating options determine quite different power and energy requirements, and different loads on the blades, thus leaving a different cost impact on the whole system.

14.6.1 Wind turbine IPSs in use

To the author's knowledge, among active systems, only rotor blade electric heating and hot air blade circulation systems are currently in use and commercially available for wind energy. Microwave and inflatable rubber boots on the LE of the blade are mechanical technologies still in progress and under development. Passive systems include some black painting treatment on the blade surface or Teflon coating to help in reducing surface wettability.

Rotor blade electric heating

Electrothermal heating and de-icing/anti-icing of wind energy turbine blades can be accomplished by electrical heating elements manufactured from various types of wire and foils.

Electrically heated foils at the LE (heating wires or carbon fibres) were initially developed at VTT (Technical Research Centre of Finland) in 1992 (Peltola *et al.*, 1999). The system supplies enough heat at the blade's external surface to keep the surface at a prescribed temperature. Ideally if any panel could be singularly heated, this strategy would lead to an isothermal surface and hence to the minimum heating supply. Some unavoidable heat walls' back side losses have to be considered, however. The system is quite effective for harsh conditions and works well as a de-icing system. After the original concept, different regions of the blade can be separately heated to gain maximum efficiency of the system, but electronic problems and difficulties in monitoring the temperature for each heated panel suggested switching to a simpler control system. There are two unsolved problems related to such a system: the first is related to the material of the heating elements, made of metal or carbon fibre, which can attract lightning strokes. The second is related to the structural problems caused to the position of the heating elements at the LE. The gravity forces acting as the rotor turns cause high deterministic loads on the blade's structure. Aerodynamic driving forces and superposed so-called edgewise vibration, caused by low damping of the natural frequency in this direction, are added to the gravity loads.

High strains in the GRP (glass fibre reinforced plastic) load carrying girder will cause even higher strain in the wires or fibres, respectively, of the heating elements. This is especially true if the heating elements are made of carbon fibre. Their Young's modulus is much higher compared to glass fibres and the consequence is that more load is carried by the heating fibres.

This method of heating the turbine blades has proved to be thermally effective but difficult to manage, suffering from thermal and mechanical fatigue, and thereby limiting their life span. Conductive fabrics have been used in de-icing and anti-icing aerospace structures as integrally bonded laminate that is used to thermally control a surface of an aircraft to which the laminate is bonded. The conductive fibres are of low weight, with no intrusion in terms of aerodynamics;

they are easy to handle compared to wire and foil, and most notably, they allow the even distribution of heat. The fibres may be arranged in woven, non-woven or braided forms of various styles and may be electrically conductive natural fibres, electrically conductive man-made fibres, semi-conductive natural fibres, semi-conductive man-made fibres, non-conductive natural fibres or non-conductive man-made fibres. Any of the fibres may be coated with conductive, semi-conductive or non-conductive materials. These factors contribute to a more efficient use of energy. Because wind turbines operate on very limited electrical resources and extreme atmospheric conditions, the system must be efficient as well as robust to provide protection. A variety of heater elements exists in the prior art. Although several patents have resulted in products for aeronautic applications, none of these heater elements have yet been commercially applied to heat and de-ice the surface of wind energy turbine blades. A recent trial (Pederson, 2008) involves a Vestas V90 turbine, utilising 93 heaters, 31 per blade, each zone containing 8–10 heaters, 7 zones per blade. A power pulse of 23 kW is sent to each zone to raise its temperature and de-ice the blades.

Hot air blade circulation systems

In-duct circulating air systems for the anti-icing and de-icing of aircraft components, especially airfoils, were originally developed in the 1950s and now represent the most often adopted systems for aircrafts wings. They were soon thought of for use in wind turbines, too: in fact, the first description of such an application for wind turbine rotors dates back to 1949 (Woigt, 1949). Here an in-duct circulating air system in the blade was described, wherein the air was heated by way of the waste heat from the electrical generator. The system did not come into commercial use until the 1980s, by which time more rational concepts had been developed for blades equipped with both de-icing and anti-icing systems (Enercon, 2003). The use of hot air in wind turbines comes from the great simplicity and reliability of the system, and from an efficient use of the heat released by dedicated electrical devices that can easily be carried by the air to the required locations.

There are basically two possible configurations for in-duct circulating air anti-ice systems, that is, the open-circuit and the closed-circuit systems, both obtained by arranging suitable partitioning walls inside the blade shell. Those configurations are schematically illustrated in Fig. 14.22. In the open-circuit system, the hot air enters at the blade root and flows towards the tip through a channel built in the LE area, where the anti-ice heat demand is greatest. The partitioning wall may possibly coincide with the blade spar. The air is expelled at the blade tip.

The static air pressure changes along the channel and is locally determined by a balance among the centrifugal forces, pressure losses and heat losses through the blade wall. A naturally aspirated flow can thus be established in the channel, depending on the inlet air pressure and temperature, the rotor turning speed and the

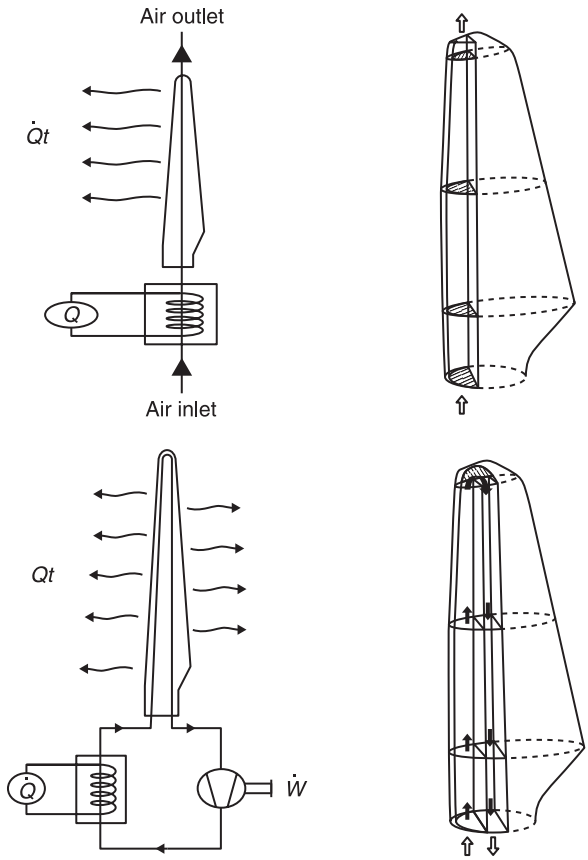

14.22 Schematic of the open-circuit and closed-circuit systems.

shape of the channel (channel section, aspect ratio and blade length). For given ambient and operating conditions, the thermal performance of the system is thus determined by the air mass flow and the inlet air pressure and temperature (Battisti and Dal Savio, 2003). In the closed-circuit system, two (or more) channels are created within the blade shell to enable the air to flow back from the tip towards the blade flange through a return channel. The exhausted air, back from the tip, is then reheated and cyclically routed into the rotor blade. This solution needs a fan to establish the flow within the channel, but it also provides ice protection on the blade aft portion (Battisti and Dal Savio, 2003; Battisti and Soraperra, 2003). Where glaze icing is a concern, this system prevents run-back freezing. Its thermal performance is better than that of the open channel version, despite its greater complexity and the need for mechanical power to promote the air circulation. Only a few works are available in the published literature on this topic, and they almost always refer to aeronautical systems (see e.g. Thomas, *et al*., 1996), which have important differences compared to wind turbines due to different materials and

solutions adopted. Even fewer papers are available on the related experimental issues, and they refer only to the use of electrical pads for anti-icing instead of internal air circulation (Battisti, 2006). The distribution of the air within the blade shell makes the control of the surface temperature a challenging task. The requirement of a minimum temperature at the LE leads to large gradients in the aft part, moving the design goal away from the isothermal wall, with the consequence of much higher heat fluxes compared to electric heated foils.

Although most of the anti-icing systems for aeronautic use are designed to evaporate a large part of the water caught by wings, such a strategy is not suitable for wind turbines due to the prohibitive amount of required heat.

Advantages of this solution are that the LE surface and thus the blade's aerodynamics are not affected and there are no negative effects on the lightning protection system. Disadvantages are due to the fact that GRP material is a good insulator and therefore during high wind speeds or during rotation of the rotor at low temperatures the heat losses due to forced convection will require very large heating power.

The rotor blade heating is usually activated at a given (recorded) external temperature (i.e. equal to or less than +2°C), provided the control system is informed that ice has formed on the rotor blades.

Despite its simplicity, any system employing in-duct hot gas has the following weaknesses:

- high heat flux needed due the high wall thermal resistance (unlike in the aeronautic field);
- air circulation systems required (closed circuit).

Due to the low thermal conductivity of the material used for blade shells ($\lambda_m < 1$ W/mK), and the thick walls adopted (10–70 mm), the thermal problem is dominated by the heat resistance through the wall. Only a marginal benefit is therefore obtained (a part of the very tip regions) through enhanced internal air circulation (as used in aircraft wings). As a consequence, very high temperatures are required at the blade's inner wall, which results in unacceptable working conditions for common GRP, stopping the system from being very efficient at low external temperature. A detailed analysis of the system is given in Battisti, Fedrizzi, Rialti and Dal Savio (2005). The use of more thermally conductive blade walls should reduce the problem. This goal could be accomplished by means of one or more of the following:

- drastic reduction of thickness;
- use of polymeric matrix charge variation;
- use of thermal bridges.

As a conclusion, thermal based anti-icing, as will become evident in the simulation presented below, shows the following characteristics:

- very high power density for anti-icing (1–10 kW/m^2);
- very high installed power for safe operation even in moderate icing conditions;

- applicable only for a small portion of blade surface to prevent excessive power requirement;
- when ice detection systems fail, or some delay in icing onset occurs, the available power for de-icing becomes inadequate to remove the ice formed.

Passive systems

Passive systems adopt black painting and special coatings, though the latter are still in the development phase. Black painting means that, in daylight, the blade heats up and the ice melts earlier than with white painted blades. However, in summertime the temperature of the blade's surface may affect the material properties of the GRP which is sensitive to high temperatures. Black blades appear to add minimal solar gain in windy areas, in summer or winter.

Special coatings of hydrophobic and ice-phobic material can reduce the shear forces between the ice and the blade's surface. Advantages of coating the whole surface of a rotor blade are relatively low cost, that no special lightning protection is required, that the blades are easy to maintain and that the whole surface is protected. New coating formulas are under development and will be discussed in the following sections.

Disadvantages of both systems are the ice throw during operation and possible asymmetrical ice accretion that leads to imbalance.

The energetic efficiency of an IPS

The presence of an ancillary system such as the IPS introduces an energy penalty in AEP. During IPS operations, the energy harvest is:

$$E_{\text{ice, ave}} = \int_{T_{\text{HEAT, ON}}} PA\,\mathrm{d}t = \int_{T_{\text{HEAT, ON}}} \frac{1}{2}\rho V^3 A\, Cp(V)\,\eta_{\text{m}}\,\eta_{\text{el}}\,\eta_{\text{aux}}\,\eta_{\text{IPS}}\,\mathrm{d}t \qquad [14.4]$$

Where $E_{\text{ice,ave}}$ is the average energy harvest during the icing period and operation of the IPS, η_{m} is the mechanical efficiency, η_{el} is the electrical efficiency, η_{aux} is the efficiency of the ancillary equipment and η_{IPS} is the efficiency of the IPS system, defined in Equation [14.5]. The IPS, $T_{\text{HEAT,ON}}$, is the period of operation. This duration may or may not coincide with the icing duration. This depends upon the anti-icing strategy adopted, and the efficacy of the ice detection systems to correctly switch on and off the IPS. The efficiency of an IPS can be defined as the following:

$$\eta_{\text{IPS}} = 1 - \frac{\dot{Q}_{\text{IPS, ave}}}{P_{\text{ice, ave}}} \qquad [14.5]$$

$\dot{Q}_{\text{IPS,ave}}$ is the average power used by the IPS, and $P_{\text{ice,ave}}$ the electrical power delivered during icing periods.

For an electrothermal system, the actual average heating power of the IPS-adopting electrical systems is given by the ratio of the ideal average heating power

(as required to keep the surface at the prescribed temperature) and the heating efficiency, which takes into consideration the heat losses in the wires and through the blade back wall, and can be synthetically expressed by an system efficiency factor ε depending on the kind of system adopted:

$$\dot{Q}_{\text{IPS, ave}} = \frac{\dot{Q}_{\text{IPS}}}{\varepsilon} \qquad [14.6]$$

where $\dot{Q}_{\text{IPS}}$ is the thermal power ideally required at the surface to prevent ice or carry out a given ice mitigation strategy.

As hot air systems are of concern, the IPS heating efficiency $\varepsilon_{\text{h.a.s}}$ is computed by taking into consideration that the surface temperatures differ from the (minimum) required. The efficiency also includes the mechanical power needed to promote the hot air flow within the system ($\overline{P}_{\text{m}}$) and the actual average heating power of the IPS is written as:

$$\dot{Q}_{\text{IPS, ave}} = \frac{\dot{Q}_{\text{IPS}}}{\varepsilon_{\text{h.a.s.}}} + \overline{P}_{\text{m}} \qquad [14.7]$$

As Table 14.6 states, computed on the basis of simulations carried out with TREWICE, depending on the adopted IPS principle, the maximum efficiency is achieved using heating foils, while for a hot air IPS, a considerable amount of heat is wasted because of the practical inability to obtain the theoretical minimum surface temperature for an optimum heat distribution.

Estimating the anti-icing power and energy requirement

The anti-icing thermal power requirement depends on several variables, which can be conveniently grouped as: meteorological, wind turbine characteristics and operation, and ice prevention system characteristics. The following functional relationship can be written:

$$\dot{Q}_{\text{IPS, ave}} = f\left(\underbrace{W, T, LWC, MVD,}_{\textit{meteorological}} \underbrace{Z,\ \textit{blade planform},\ \text{WT}\ \textit{control}, \lambda_{\text{mat}},}_{\textit{turbine}} \underbrace{T_{\text{s, min}}, A_{\text{heat}}, \varepsilon}_{\textit{ice prevention system}} \right) \qquad [14.8]$$

$T_{\text{s,min}}$ is the minimum allowable temperature of the external surface and A_{heat} is the heated area.

Table 14.6 Summary of the average system efficiency factor ε for different thermal IPSs

IPS principle	ε (average)
Heating foils	0.9
Hot air, closed channel	0.6
Hot air, open channel	0.3

For any set of values of the variables expressed by Eq. [14.8] conductive to actual icing events, the anti-ice thermal power can be calculated by means of suitable models (Makkonen, *et al*., 2001a; Battisti, Fedrizzi, Rialti and Dal Savio, 2005). With reference to the blade discretisation scheme of Fig. 14.23 and quantities of Table 14.7, the thermal power required for the protected area of the rotor to be kept free of ice is expressed as:

$$\dot{Q}_{\text{IPS, ave}} = \frac{Z}{\varepsilon}\sum_{j=1}^{N}\dot{q}_j^m L_j H_j \qquad [14.9]$$

Z being the number of blades and

$$\dot{q}_j^m = \frac{\sum_{k=M'}^{M''}\dot{q}_{\text{ICE},k}}{\sum_{k=M'}^{M''}h_k} \qquad [14.10]$$

where h_k is the width of the k-th panel (Fig. 14.23).

The anti-ice power requirement is proportional to the heated area. The extension of the heated part either in spanwise or in chordwise direction should be set by consideration of both the length of the impingement and the safety coefficient (k_j) based on engineering experience (e.e.). The heated chordwise ($S_{\text{s.s.}}$ stands for blade section suction surface wetted length and $S_{\text{p.s.}}$ stands for pressure surface wetted length) extension is therefore given by:

$$\mathrm{H}_j = \underbrace{k_j}_{\text{e.e.}} \times \underbrace{\left(s_{\text{s.s}} + s_{\text{p.s.}}\right)_j}_{\text{droplet traj. calc.}} \qquad [14.11]$$

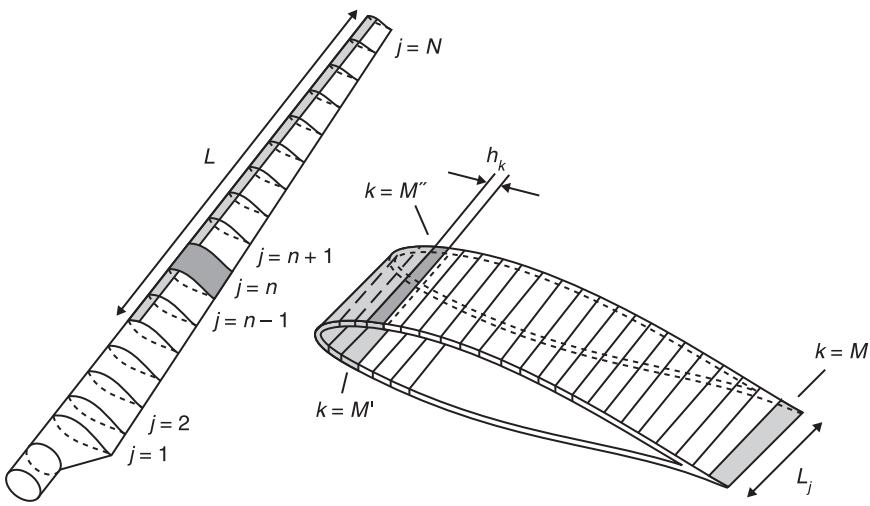

14.23 Blade discretisation scheme.

Table 14.7 Specifications of the variables appearing in equations [14.9] to [14.18]

A	Area	**Greek**	
c_p	Specific heat at constant pressure	β	Collection efficiency
c_w	Specific heat of liquid water	ε	Efficiency factor
H	Latent heat	ρ	Density
h_c	Convective heat transfer coefficient		
L	Blade length	**Subscripts and superscripts**	
LWC	Air liquid water content	∞	Undisturbed
K	Wetness fraction	*aero*	Aerodynamic
$\dot{m}$	Mass flow	*air*	Air
mm	Molecular mass	*ave*	Averaged
MVD	Mean volume of droplets	*conv*	Convective
p	Static pressure	*e*	Edge of boundary layer
Q	Heat	*ext*	External surface
$\dot{q}$	Specific heat flux	*ev*	Evaporative
$\dot{Q}$	Thermal power	*g*	Flowing into duct
r	Radius	*in*	Incoming
R	Wall thermal resistance	*imp*	Impingement
$\tilde{R}$	Universal gas constant	*int*	Internal surface
T	Temperature	*ke*	Kinetic
Z	Blade number	*m*	Mean
w	Relative speed	*out*	Exit
		ref	Reference
		sens	Sensible
		s	Surface
		out	Outgoing
		w	Water

The spanwise length also takes into account the risk connected with icing of the root section.

In Eq. 14.10 the term $\dot{q}_{\mathrm{ICE,k}}$ is the chordwise specific heat flux exchanged by the k-panel of the j-station of the blade, while the summation gives the spanwise heat flux of the N stations. $\dot{q}_{\mathrm{ICE,k}}$ is obtained by solving for each k-panel the mass and energy balance given by:

$$\dot{m}_{\mathrm{w,\,in}}\, c_{\mathrm{w}} \left(T_{\mathrm{w,in}} - T_{\mathrm{ref}}\right) - \dot{m}_{\mathrm{w,\,out}}\, c_{\mathrm{w}} \left(T_{\mathrm{w,\,out}} - T_{\mathrm{ref}}\right) + \beta\, LWC\, w_{\mathrm{w,\,imp}} \left[c_{\mathrm{w}} \left(T_{\mathrm{w,\,imp}} - T_{\mathrm{ref}}\right) + \frac{w^2_{\mathrm{w,\,imp}}}{2} \right]$$
$$- K \left[\frac{h_{\mathrm{c}}}{\rho_{\mathrm{air}} c_{\mathrm{p,\,air}} L^{(2/3)}} \frac{mm_{\mathrm{w}}}{\tilde{R}} \left(\frac{e^{\mathrm{sat}}_{\mathrm{v,\,s}}}{T_{\mathrm{s,\,ext}}} - \frac{r_{\mathrm{h}}\, e^{\mathrm{sat}}_{\mathrm{v,\infty}}\, p_{\mathrm{e}}}{T_{\mathrm{e}} p_{\infty}} \right) \right] \Delta H^{\mathrm{T=T_s}}_{\mathrm{ev}} - h_{\mathrm{c}} \left(T_{\mathrm{s,ext}} - T_{\infty}\right) - h_{\mathrm{c}} \left(T_{\mathrm{e}} + \frac{r w^2_{\mathrm{e}}}{2 c_{\mathrm{p,\,air}}} - T_{\infty} \right) + \dot{q}_{\mathrm{ice}} = 0 \qquad [14.12]$$

with the auxiliary equation:

$$\dot{m}_{\mathrm{imp}} + \dot{m}_{\mathrm{w,\,in}} - \dot{m}_{\mathrm{w,\,out}} - \dot{m}_{\mathrm{ev}} = 0 \qquad [14.13]$$

For the sake of simplicity, a 1-D heat transfer problem can be set (the accuracy of this hypothesis is satisfactory and will be discussed later). By discharging the first

two contributions in Eq. 14.12, being negligible, the various contributions in the energy balance have been renamed as follows:

$$\dot{q}_{\text{conv}} = h_{\text{c}}\left(T_{\text{s}} - T_{\infty}\right),\ \dot{q}_{\text{ev}} = \dot{m}_{\text{ev}}\ \Delta H_{\text{ev}},\ \dot{q}_{\text{sens}} = \dot{m}_{\text{imp}}\ c_{\text{w}}\left(T_{\text{s}} - T_{\infty}\right)$$
$$\dot{q}_{\text{aero}} = h_{\text{c}}\left(T_{\text{e}} + \frac{r\,w_{\text{e}}^2}{2\,c_{\text{p, air}}} - T_{\infty}\right),\ \dot{q}_{\text{ke}} = \dot{m}_{\text{imp}}\ \frac{w_{\text{w,imp}}^2}{2} \qquad [14.14]$$

and Eq. 14.12 can be written as:

$$\dot{q}_{\text{ICE},\,k} = \dot{q}_{\text{conv},\,k} + \dot{q}_{\text{ev},\,k} + \dot{q}_{\text{sens},\,k} + \dot{q}_{\text{aero},\,k} + \dot{q}_{\text{ke},\,k} \qquad [14.15]$$

Now, for heated foils IPS:

$$\dot{q}_{\text{ICE},\,k} = f(T_{\text{s, ext}}, \varepsilon) \qquad [14.16]$$

While in hot gas IPS, the conjugate heat transfer problem implies that:

$$\dot{q}_{\text{ICE},\,k} = \frac{1}{R_{\text{wall},\,k}} \cdot (T_{\text{s,int}} - T_{\text{s,ext}})_k \cdot A_{\text{m},k} = h_{\text{c,int},k} \cdot (T_{\text{g},\infty} - T_{\text{s,int}})_k \cdot A_{\text{int},k} \qquad [14.17]$$

A polytropic process can be used to obtain the air flow thermodynamic state at each *j*-station of the inner channel along the blade radial direction. The internal local temperature and heat transfer conditions of the *j*-section can therefore be only iteratively evaluated, since the *j*-thermodynamic state depends upon the *j*–1 state, and is constrained by the condition:

$$T_{\text{s, ext}} \geq T_{\text{s, min}} \qquad [14.18]$$

set by the design choice.

Determining $\dot{Q}_{\text{IPS,ave}}$ from $\dot{q}_{\text{j}}^{\text{m}}$ is rather complex and tedious, since each contribution has to be computed and integrated over the surface.

A comparison of the expected anti-icing power and its magnitude compared to the rated power of the turbine as the size varies is shown in Fig. 14.24.

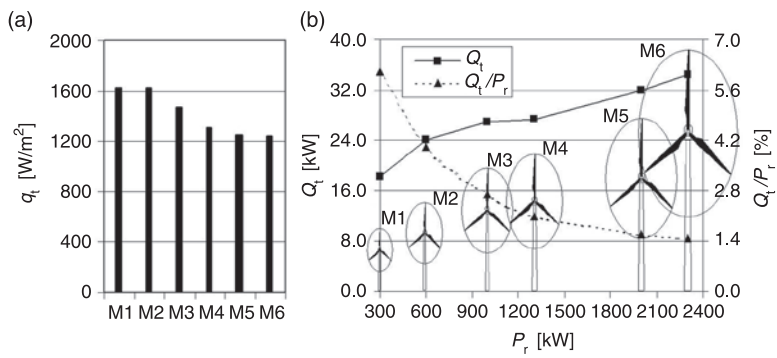

14.24 Comparison of the total expected electrical anti-icing specific power, q_t [kW/m^2], power Q_t [kW] and its magnitude compared to the rated power of the turbine as the size varies.

Final considerations are:

- When turbines with the same rated power are considered, the reduction of the number of blades leads to a decrease of the ratio of rotor anti-icing thermal power to rated turbine power.
- If a different rated power for the same number of blade is considered, the larger turbines are less penalised in terms of total anti-icing requirement compared to smaller ones.
- As for anti-icing power, the power produced increases with increasing machine sizes, but so does the length of the blade and consequently also the surface heat.

14.7 Emerging solutions for ice prevention systems

14.7.1 Inflatable rubber boots on the LE of the wing and control surfaces (pneumatic de-icing system)

Small aeroplanes often use mechanical de-icing systems consisting of a so-called inflatable rubber boot on the LE of the wings and control surfaces. The system tends to cause aerodynamic disturbance and causes additional noise, and it has to be divided into short sections to prevent it self-inflating because of the air being subject to the centrifugal effect. Originally the system was developed by Goodrich. In the normal non-inflated state the tubes lie flat and conform to the airfoil surface to which the de-icer is bonded. After the build-up (typically 6–13 mm of ice on the surface), the de-icers are inflated with compressed air. The inflation cycle lasts for a few seconds to achieve optimal ice shed and prevent additional ice formation on the inflated surface.

After the ice has cracked, its bond to the surface is broken and the ice is removed through centrifugal and aerodynamic forces. The de-icer is then allowed to deflate as the air is evacuated to atmosphere. Vacuum is then applied to ensure that there is no lifting of the surface on the low-pressure side of the airfoil. A part of the high risk of additional unavailability due to the increased complexity of such IPS, the effect of the roughness of the boots over the aerodynamic performance and noise emission is not clear yet. Also the wear and repair issues seem to pose serious limitations to the system used in field. Of unquestionable interest is the very low expected energy consumption.

14.7.2 Microwave

The use of microwaves is under investigation by LM Glasfibers (Mansson, 2004). A test rig for an LM 19, 1 blade has been set up. A microwave generator of 6 kW at 2.54 GHz and a power emission of less than 10 mW/m^2 has been used for preliminary tests. The power unit has a low impact on blade costs, and has no lightning issues, but the limited energy absorption in glaze ice obtained needs further tests to be carried out with higher power.

14.7.3 Low surface adhesion materials

Low adhesion of ice on blade surface can be accomplished by means of:

- hydrophobic surfaces (low wettability surfaces);
- ice-phobic surfaces.

There are two primary benefits of reducing ice adhesion:

- IPS requiring lower energy could be used;
- the removal of ice is cleaner.

Early studies in the aeronautic field on static ice adhesion to surfaces ended up with the following conclusions:

- adhesive shear stress increases linearly with decreasing surface temperature;
- silicones reduce the adhesion of the ice, but if provided as a coating layer, are stripped away with each ice removal, thus not providing a permanent coating;
- a poor correlation seems to exist between low ice adhesion and water repellence. It is uncertain if surfaces with hydrophobic properties will also have ice-phobic capability. Hydrophobicity does not necessarily produce ice-phobicity;
- ice-phobic characteristics of a material can change with time and repeated removal.

A given coating will behave differently in different icing conditions, rime or glaze (in dry or wet ice growth), because the hydrophobicity also plays a role.

In ice accretion processes, the water coalesces into beads during glaze ice accretion. Aerodynamic and mass forces (a part of surface non-homogeneities) will deform the beads, and alter the wetting process from place to place. In these regions the shape of ice could be altered, compared to regions where, once a thin layer of ice has formed over the surface, the surface or coating behaviour is totally masked, since the ice will grow over ice only.

Ice-phobic coatings may reduce or eliminate the need for traditional anti-icing systems. However, many existing ice-phobic coatings are based on a thermoplastic or thermosetting resin that may contain solid or liquid fillers. Due to the composition of these ice-phobic coatings the solid or liquid fillers settle upon the coated material's surface. The fluid interfaces or weak boundary layers on the surface of the materials provide ice adhesion strengths of no more than 300 kPa. However, unprotected thermoset or thermoplastic materials typically have poor erosion resistance, and adding solid or liquid fillers further decreases their erosion resistance. This is undesirable because the engine and aircraft components that most need ice build-up protection are positioned in severely erosive environments.

Therefore, there are ice-phobic coatings under development that have better erosion resistance than existing ice-phobic coatings with low ice shear strength in the range of 20 kPA to about 50 kPa.

Let us consider a typical wind turbine characterised by the data listed in Table 14.8. The centrifugal force of the mass of ice accreted at the tip and the superficial adhesion strength is:

$$\begin{aligned} F_c &= \omega^2 \cdot r \cdot m_{ice} \\ m_{ice} &= \rho_{ice} \cdot A \cdot t_{ice} \\ \left.\frac{F_c}{A}\right|_{tip} &= \rho_{ice} \cdot t_{ice} \cdot r \cdot \omega^2 \simeq 18 \text{ kPa} \end{aligned} \qquad [14.19]$$

For ice to shed spontaneously, the adhesion strength should be less than 18 kPa.

In Table 14.9 the ice adhesion value made with the static ice shear test methods for several commercially available products is reported merging data from

Table 14.8 Typical data of a MW-size wind turbine used for computing the superficial adhesion force required to shed the ice

Rated power	P_r = 1 MW
Rated speed	ω_r = 2 rad/s
Thickness of the ice cap at the tip	t_{tip} = 0.2 m
Ice density	ρ_{ice} = 700 kg/m^3

Table 14.9 Ice adhesion value of several commercially available products

Coatings	Shear stress (kPa)		
	Mean	Range	STD
PUR	411	328–541	88
SWR-1	372	304–508	82
SWR-2	485	308–576	108
WR	198	177–216	18
Al	461	314–550	94
Teflon	40–238	–	–
Epoxy paint (generic)	400	–	–
Polyurethane resin (urethane)	411	–	–
Acrylic silicone resin (generic)	198	–	–
PVC	90	–	–
Microphase Phasebreak B2	117	–	–
Microphase ESL	295	–	–
Twenty-first Century 51PC951	637	–	–
S&A of Fernandia RIP-4004	374	–	–
Kiss Cote® MegaGuard® LiquidCote	898	–	–
NuSil® R-2180	37	–	–

Merging data from Kimura *et al.*, 2004 and US2007/0254170, 2007.

Kimura, *et al*. (2004) and US2007/0254170 (2007). The tests have been carried at 0 °C and –10 °C. Note that the adhesion strength tends to increase as the temperature decreases.

With current materials, centrifugal forces are generally insufficient to cause ice shedding from any surface, even at the tip of the blade. Nevertheless some materials seem to be promising.

The performance in time (durability) depends dramatically on the degradation of the original surface bonding (i.e. on site conditions), thus while very low adhesion is possible, durability must be demonstrated both for repeated ice removals and for rain impingement at blade speed. Consequently the following conclusions can be drawn:

- icing prevention on wind turbine blades by coatings alone is, at the moment, in the incubation stage;
- the adhesion strength of an ice accretion could, however, be reduced when blades are treated with an appropriate coating;
- combinations of coatings with de-icing or anti-icing devices should be taken into consideration since a reduced adhesion might be helpful in improving the performance of ice protection systems.

14.7.4 Intermittent (cyclic) hot gas heating

The energy penalties for a turbine using continuous heating for icing protection are extremely large and in some cases may be prohibitive. An advantageous method (Battisti *et al*., 2006; Battisti and Fedrizzi, 2007) for icing protection in wind turbines can be accomplished by cyclical de-icing. Some ice is permitted to form on the surfaces but then is removed periodically during relatively short, intensive applications of heat.

A water film between the surface and the ice is caused by the application of heat, and permits the removal of the ice by aerodynamic forces. Because the heating is intermittent, heat is supplied successively to relatively small surfaces areas, and a constant load on a heat source is thus maintained. The total heat input for cyclical de-icing, therefore, can be greatly reduced from that required for continuous heating. If the large heating requirement associated with continuous hot gas heating can be reduced by the use of a cyclical hot gas de-icing system, the wind turbine performance penalties could be decreased from those incurred with the continuous heating system.

Even though the average thermal power level required for the two cases is comparable, the heating period ($t_{\text{Heat ON}}$) for the de-icing practice is much shorter than for the anti-icing system ($t_{\text{Heat ON}} + t_{\text{Heat OFF}}$). Contrary to aeronautical de-icing systems that employ ratios up to 10 (Yasilik, *et al*., 1992; Gray *et al*., 1952), low values of this ratio, that is 0.5:1.5, can be typical for WT. This is caused by the different thermal conductivities of the materials used to manufacture

the blade wall. The effect relates to the Fourier number which expresses the ratio between the thermal conduction and the thermal inertia of a body. Bodies with large Fourier numbers, that is, with high conductivity λ_{mat} and small thermal inertia ρc_{th} (such as aircraft wings made of aluminium alloy), allow large heat fluxes to readily diffuse through the volume. On the other hand, large heat fluxes cannot diffuse quickly through thick walls made of composites (low Fourier number), resulting in a large increase of the 'warm surface' (inner-side) temperature, without any significant heat diffusion at the 'cold surface' (outer-side) in short times. Therefore, in the latter case, low thermal power densities should be preferred for long warming periods. Numerical simulations (Battisti and Fedrizzi, 2007) have confirmed the validity of this approach. Figure 14.25 shows the intermittency factor variation versus the warm air temperature and LWC, for cold air temperature equal to –3 °C. The intermittency factor drops as the hot air temperature is increased, due to the reduction of the time required for the ice to melt. The chart shows an asymptotic trend as the temperature increases. Figure 14.25 also shows that, during de-icing operation and for warm-air temperatures more than about 140 °C, the maximum inner surface temperature rises above 100 °C. This figure could affect the structural integrity of the blade, and has been used as a maximum working temperature. A minimum warm-air temperature between 70 and 80 °C is required for the de-icing practice; at lower temperatures, the intermittency factor rapidly approaches the limit of 1. Figure 14.26 compares the anti-icing and de-icing systems in terms of energy consumption ratio for operation at an ambient temperature of –3 °C. The energy consumption ratio is defined in Eq. 14.20:

$$E_\tau = \frac{\dot{q}_{ave,de-icing} \cdot T_{heat-on}}{\dot{q}_{anti-icing} \cdot \left(T_{heat-on} + T_{heat-off}\right)} = \frac{\dot{q}_{ave,de-icing}}{\dot{q}_{anti-icing}} \cdot \tau = \dot{q}_{anti-icing} \cdot \xi \cdot \tau \qquad [14.20]$$

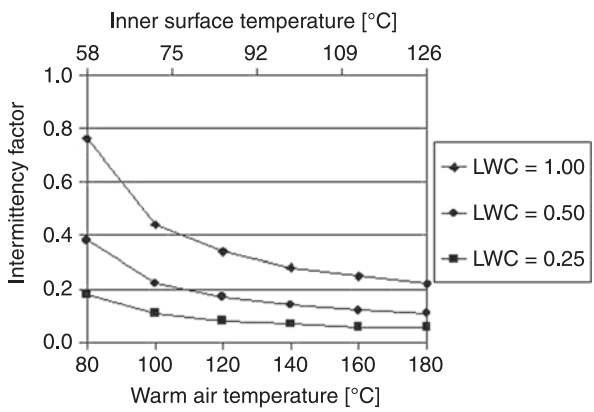

14.25 Intermittency factor vs warm air temperature at $T_{a,\infty}$ = –3°C.

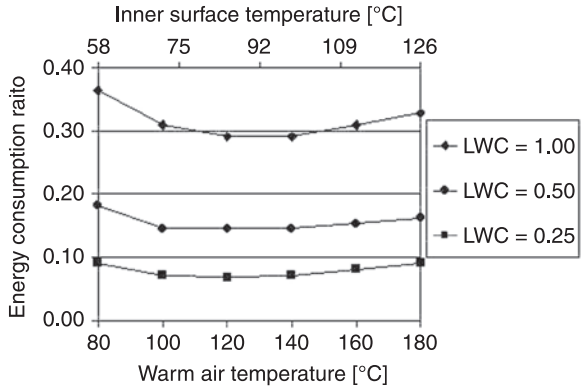

14.26 Energy consumption ratio vs warm air temperature at $T_{a,\infty} = -3°C$.

where ξ is a magnification factor representing the fraction of extra power required for de-icing, and τ is the intermittency factor given in equation [14.3]. The graphs show that this ratio is less than 40% in all the cases considered, when de-icing is adopted instead of anti-icing. All the three curves present a minimum at about 120 °C, meaning that the best compromise between employed heating power and de-icing heat-on time is obtained in this condition. Thus, this operational condition is preferred, if it is compatible with the air heater power installed and with the blade at safe-working temperature.

14.7.5 The regenerative ice prevention system

The regenerative option is concerned with the opportunity to use an available on-board heating source to provide energy for anti-icing/de-icing operations. Some dissipated energy could be collected from electrical devices, such as the electrical generator and the converter. In Fig. 14.27 the conceptual scheme is depicted.

With reference to Fig. 14.27, if we consider the electrical generator as a heat exchanger, the overall thermal efficiency is given by:

$$\varepsilon_g = \frac{T_{a,\,el,\,out} - T_{a,\,in}}{T_{w,\,gen} - T_{a,\,in}} \qquad [14.21]$$

where $T_{a,el,out}$ is the temperature of the air at the exit of the electrical generator, $T_{a,in}$ is the temperature of the air drawn from the environment and $T_{w,gen}$ is the working temperature of the generator wall.

The regeneration factor is given by:

$$R = \frac{T_{g,\,el,\,out} - T_{a,in}}{T_{a,b,in} - T_{a,in}} \qquad [14.22]$$

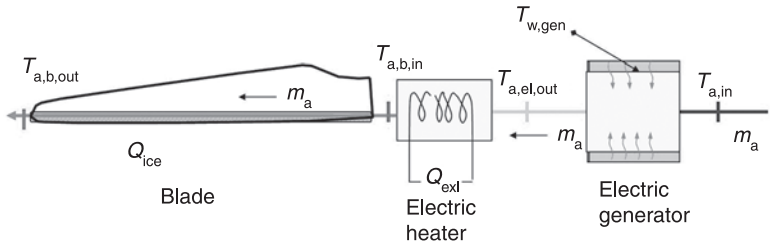

14.27 Conceptual scheme of the regenerative ice prevention system.

where $T_{a,b,in}$ is the temperature of the air entering the blade. The thermal power to be provided to the blade is:

$$\dot{Q}_{ext} = \dot{Q}_{IPS} = \dot{m}_a c_{p,air} \left(T_{a,b,in} - T_{a,in}\right) \cdot (1 - R) \quad [14.23]$$

and the thermal power released by the electrical generator is:

$$P_{g,el} (1 - \eta_{g,el}) = \dot{m}_a c_{p,air} (T_{a,b,in} - T_{a,in}) \quad [14.24]$$

The electrical power available will be:

$$P_{el,av} = P_{el}^{'} (1 - \eta_{g,el}) S_g \quad [14.25]$$

where $\eta_{g,el}$ is the electric efficiency of the electrical generator, S_g is the electrical active area of the generator and $P_{el}^{'}$ is the specific electrical power.

We now consider the following input data of Table 14.10, in which the graph of Fig. 14.28 is obtained.

The graph in Fig. 14.28 shows the regeneration factor R, and the ratio of the external, supplied thermal power to that available from internal sources $\dot{Q}_{ext}/P_{el,av}$ as function of the required blade air inlet temperature $T_{a,b,in}$. The simulations are made for two different mass flows of air: 1 and 2 kg/s. The graph clearly shows that with an air-sucked mass flow of 1 kg/s the regenerative effect is approaching 100%, as a relatively low air temperature is required at the blade root. The external power drops accordingly and can even become less than that available, thus leading anti-icing to be integrally fulfilled only from internal sources. As the mass flow increases, the benefit decreases, because the heat extraction process through the electrical generator is less efficient.

Table 14.10 Data for evaluation of the heat flux demand ratio of regenerating systems

$T_{w,gen}$	Working temperature of the generator	100°C
$T_{a,in}$	Ambient temperature, sucked	–3°C
P_{el}	Specific power of the generator	125 kW/m^2
$\eta_{g,el}$	Efficiency of the generator	0.95

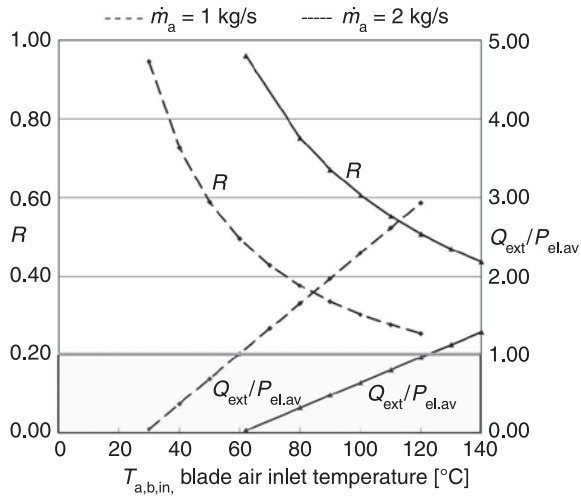

14.28 Regeneration factor and heat flux demand ratio for different air mass flows versus air inlet blade temperature.

Intermittent heating realised without using intermittent electric heaters but through a continuous heating source (the electrical generator) allows a decisive gain in availability.

The supplied power for anti-icing can also be obtained from other ancillary heat generating systems (e.g. the converter into the tower).

The electrical generator can use an independent cooling system thus optimising both the cooling process and the anti-icing process.

RIME-Tech regenerative ice mitigation effusive technology

RIME-Tech (US2005/0242233, 2005) is a technology based on the known concept of the film heating, for both anti-icing and de-icing purposes. It is based on the generation of a spatially continuous film of air partially or totally enveloping the external blade surface. The film is created by ejection of air from the inside to the outside of the blades through slots or arrays of holes made in the wall, as schematically shown in Fig. 14.29.

The air forming the film is first aspirated through the rear part of the nacelle or the tower bottom and is warmed up by flushing the electric devices, such as the trafo/inverter within the tower or the electric generator in the nacelle. The warm air is thus supplied to the blade through the root of each blade and then rooted to the portions of the wall equipped with the holes. The ejection process can either be continuous or cyclic in time by setting an appropriate intermittency factor. Preliminary computations show that the anti-ice heat flux requirement at the blade

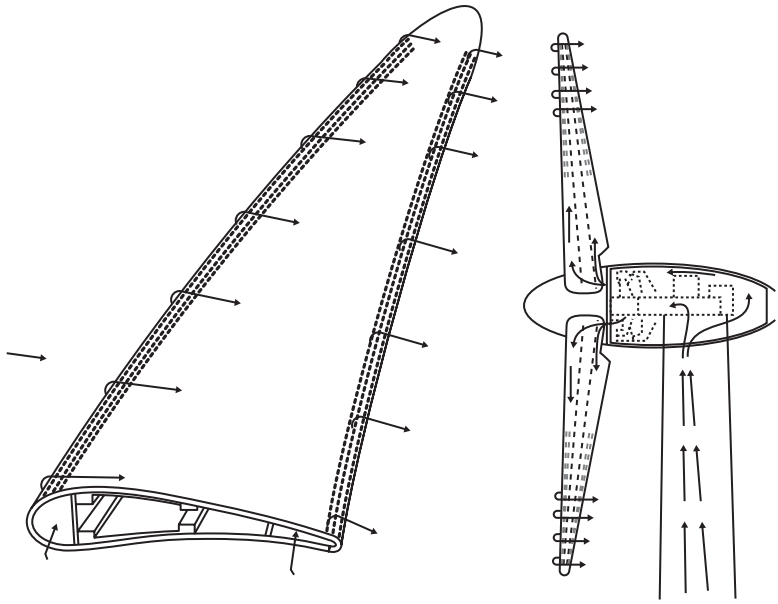

14.29 Air heating scheme and RIME-tech IPS general concept.

surface is reduced by up to 50–70%, therefore only warm air is needed for anti-ice purposes and the regenerative scheme takes full advantage of this solution.

The heat transfer mechanism is shown in Fig. 14.30. The film heating combines two heat exchange effects: the convective one at the surface and through the holes in the wall, and the 'film' one at the external surface where warm and cold air mix. The mixing produces both an increase of the heat exchange coefficient by convection, dependent on the fluids' flow features, and an increase of the air temperature at the surface. The net effect is, however, a decrease of the heat fluxes from the surface to the cold stream. This effect is shown in Fig. 14.31 where a comparison of the external wall temperatures distribution at the LE region among impermeable wall (current technology) and the permeable wall (RIME-Tech) is presented. The simulations have been made with TREWICE (Battisti, Fedrizzi, Rialti and Dal Savio, 2005). Film heating can achieve very smooth and isothermal blade skin temperatures, compared to traditional hot gas systems. The injection temperature of the air is about +10°C. The air ejection also reduces the collection efficiency of the blade profile, thus decreasing the quantity of water impinging on the surface. From an economic point of view, the operating costs are virtually zero, since air heating can be obtained by a regenerative effect. Educated shaping of the inner channels could ideally lead to natural aspirated flow, due to a pure centrifugal effect or to a very light air pumping requirement. In this configuration, the system does not need an icing detection system to establish icing onset, since

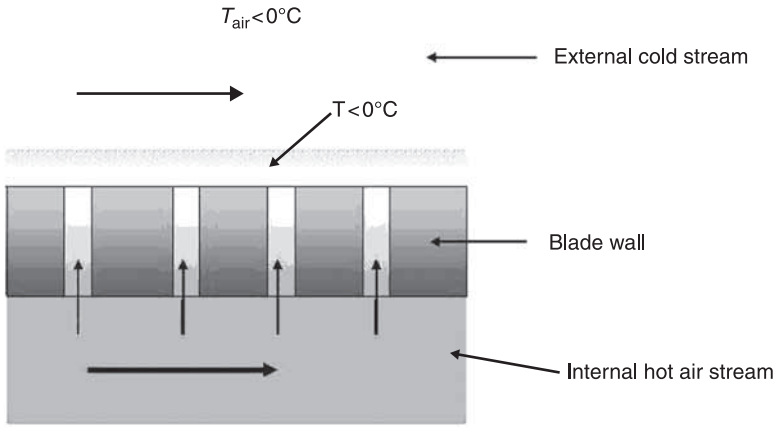

14.30 Heat transfer mechanism for film heating.

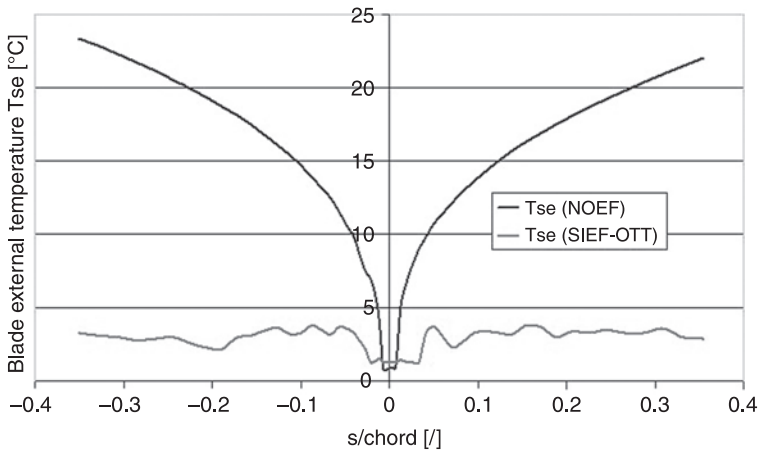

14.31 Comparison of the external wall temperatures distribution at the LE region for the impermeable wall (current technology) and the permeable wall (RIME-Tech).

as the wind turbine rotates the flow is automatically established and the anti-icing effect performed.

14.8 Ice throw and icing risk

Construction and operation of a wind energy facility in cold climates would create some increased health and safety hazards due to ice throw and ice damage on the mechanical structure of the wind turbine and this is well documented

in the literature (Frank and Seifert, 1997; Morgan, *et al*., 1998; Seifert, *et al*., 2004).

Persons, animals and facilities within the ice throw hazard zone could theoretically be at risk of being struck by falling ice fragments, which could result in damage, injury or death.

Sudden detachment of ice pieces having different weights and shapes can occur from the tower, nacelle and rotor blade surfaces during standstill, idling and operation. During the turbine operation, the accreted ice can be periodically removed through intensive warming or mechanical actions. Gravitational, aerodynamic and centrifugal forces eject the detached ice fragments. The area on the ground around the wind turbine that is covered by the ice fall is dependent, among other parameters, on the mass and the size of the ejected ice. A recent map of the ice pieces collected at the ground of the alpine test site of Gütsch in Switzerland (Cattinis, 2008) is shown in Fig. 14.32.

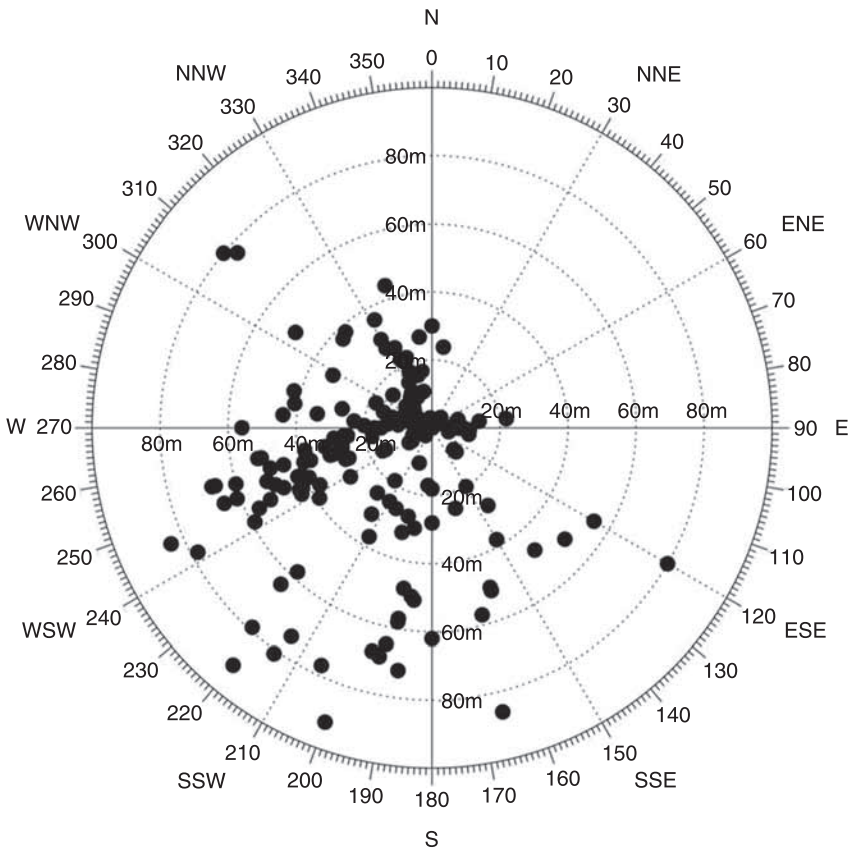

14.32 Collected ice fragments at the alpine test site of Gütsch in Switzerland.

More than 200 fragments with mass up to 8 kg and travelling distances up to 92 m have been collected on the ground around an Enercon E-40 equipped with hot air IPSs. It has been recognised that the risk from ice throw is very high during and immediately after each blade heating cycle, and since the area is a ski resort, special precautions have been adopted to avoid accidents (the winter walking trails were placed further away and warning signs were installed).

In general the ice trajectory is dependent upon the loading and stress state at the time of failure, and on the type and progression of failure before separation. An extensive literature search on this potential hazard indicated that no advanced analytical modelling has been accomplished; this is probably due to the complexity of the analysis, coupled with the extremely low incidence of ice throw reports. Under certain conditions ice can form on wind turbine towers and rotor blades in a variety of ways, but many of these do not lead to an ice throw hazard; an example of this would be normal light frosting of a stopped blade. The study of ice throw and its related risks is one of three areas of work originated in the WECO project (Tammelin, *et al*., 2000). As part of this work, analytical modelling techniques have been developed to determine the probabilistic ice throw hazard in the vicinity of a turbine using variables for turbine and tower geometry, rotor speed, gravity, fragment dimensions and aerodynamic lift and drag. Risk is expressed in terms of the number of expected strikes per square metre per year. Observations and measurements on ice fragments found on the ground around wind turbines were collected and experimental tests were conducted to investigate the aerodynamic forces on iced airfoils and the ice fragments themselves. Significant findings included that (1) ice fragments ranged from 0.1 to 1.0 kg in size and (2) no ice throw distances over 100 m had been reported (Morgan *et al*., 1998; Tammelin and Seifert, 2001).

Coupled with the analytical conclusions described above, this suggests that the risk of being struck by ice diminishes at distances greater than 100 m from each tower at the proposed facility.

Experience with wind turbines in North America (noted for its cold climate and harsh winters) has not identified ice throw as a problem. With newer turbine designs, control sensors typically detect the additional weight and slower movement of the blades with ice build-up and stop the rotors; the rotors are usually restarted after the ice has been shed. Known incidents involving ice are limited to ice shed onto a project vehicle parked underneath a turbine.

Given the stochastic nature of the ice shed, the risk assessment relative to the ice shedding from wind turbines can be carried out by applying statistical methods such as the Monte Carlo Method to the ballistic model, which solves the ice pieces' trajectory. Suitable density functions can be set for each of the input parameters to the trajectory equation. The output fragment distribution on the ground is possibly presented in terms of strike probability and recurrence period as a function of input parameters such as varying ice pieces' mass and shape.

Battisti (Battisti *et al*., 2005d) performed numerical simulations to predict the ice fragment distribution on the ground around a MW-size three-bladed wind

Table 14.11 Turbine geometrical and operating conditions

R_b [m]	H_{tower} [m]	ω_R [RPM]	λ [–]	ρ_{ice} [kg/m^3]	ρ_{air} [kg/m^3]
25	60	25	5.45	750	1.3

turbine. In addition to the above mentioned input density functions, the operational data of Table 14.11 were used for the simulations.

The ice fragments' thickness varied between 1 and 9 cm, while tests were performed with ice pieces of mass 0.18–0.36 kg. Finally the annual number of ice strikes was evaluated. The number of icing days per year adopted (5 days/year) N, was multiplied by the average ice accretion mass per day, computed on the basis of accretion models on the rotor (75 kg/day), and divided by the average mass of the cast ice pieces (0.18 or 0.36 kg):

$$N = \frac{n_{idy} \cdot m_{id,\,avg}}{m_{avg}} \qquad [14.26]$$

From this value, the strike probability per year per square metre P_y is computed from the ice fragment distribution on the ground. The strike probability is also evaluated in terms of recurrence period, as:

$$T = \left(P_y \cdot S_{cov}\right)^{-1} \qquad [14.27]$$

where S_{cov} represents the surface on the ground covered by the object for which the risk analysis is carried out; in this study, the area covered by a person was considered, i.e. about 1 m^2.

The ice fragment distribution on the ground, computed by considering the standstill condition, is taken as a reference. In fact, it is representative of the current recommended control strategy to stop the rotor in case of blades icing. Ice fragments with average mass of 0.36 kg and 5 cm thick are considered for the simulations.

Figure 14.33 and Fig. 14.34 show the product of the computation with 10^4 shedding events. Figure 14.33 shows that the majority of the ice fragments fall below the turbine blades, as they follow the wind direction. The turbine tower position is represented by means of a black dot. Ice fall on the nacelle cannot be avoided with the potential of damage to the nacelle anemometers.

Due to the wind action, a few pieces fall outside the area swept on the ground by the rotor yawing, in the prevailing wind direction. The same result is proposed in Fig. 14.34 in terms of P_y.

Apart for an area very close to the turbine tower, the strike probability is anywhere lower than 2 strikes/m^2/year. The white contour presents a recurrence period of ten years, meaning that a person or an object that lies on the contour has the average probability of being struck once in ten years. As can be seen, a distance greater than 25 m (0.5 D_r) from the turbine tower is satisfactory to reduce the probability of ice accidents below one in ten years. The above results are in

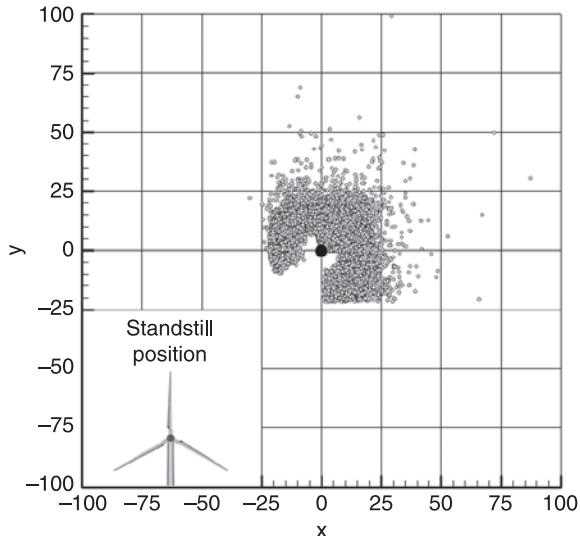

14.33 Ground ice cover in standstill conditions for ice fragments with average mass of 0.36 kg and thickness of 5 cm.

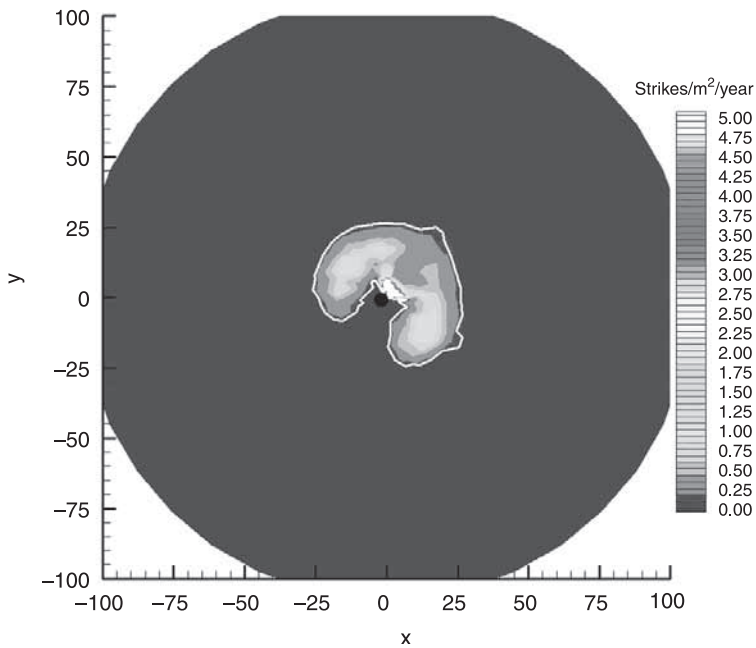

14.34 Strike probability in standstill conditions for ice fragments with average mass of 0.36 kg and thickness of 5 cm.

agreement with the experimental data collected by Seifert *et al*. (2004) about the safety distance from wind turbines. They proposed a simplified empirical equation developed for a still standing WT:

$$d = V\left(\frac{D/2 + H}{15}\right) \qquad [14.28]$$

where d (m) is the maximum falling distance, V (m/s) is the wind speed at hub height, H (m) is the hub height and D (m) the rotor diameter.

Ice debound and throw during turbine operation was then analysed as a consequence of sudden removal of the ice fragments of a given thickness and average mass.

Figures 14.35 and 14.36 show the strike probability in strikes/m^2/year for ice fragments with 0.36 kg average mass, being 1 and 5 cm thick respectively. Once again, the white contours represent the recurrence period: ten years recurrence period is represented with the continuous lines, while the dash-dotted lines stay for a period of 50 years.

The comparison of the two figures shows the different ice pieces' distribution on the ground. In Fig. 14.34 the strike probability is anywhere lower than 0.6 strikes/m^2/year, while in Fig. 14.35 strike probability higher than 1.3 strikes/m^2/year is revealed in the area very close to the turbine. Since 10^4 ice shedding events

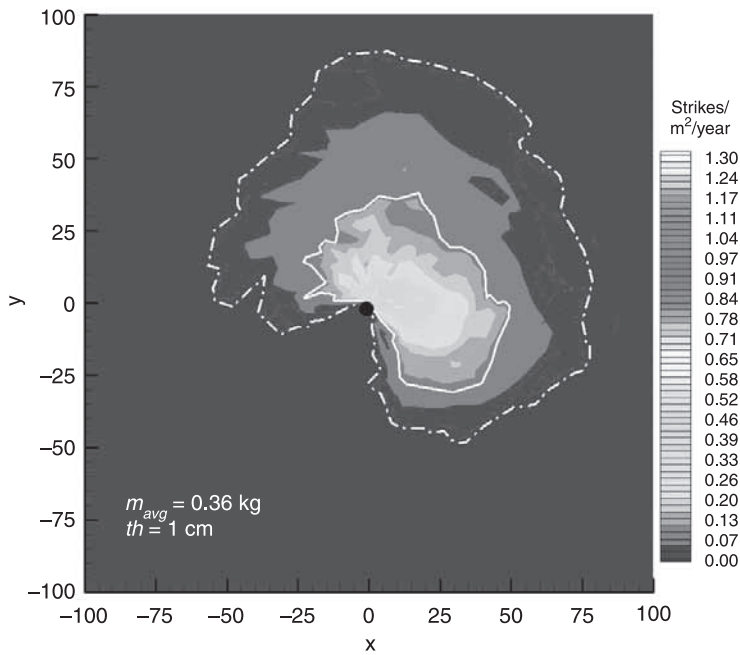

14.35 Strike probability in strikes/m^2/year for ice fragments with 0.36 kg average mass and 1 cm thickness during WT operations.

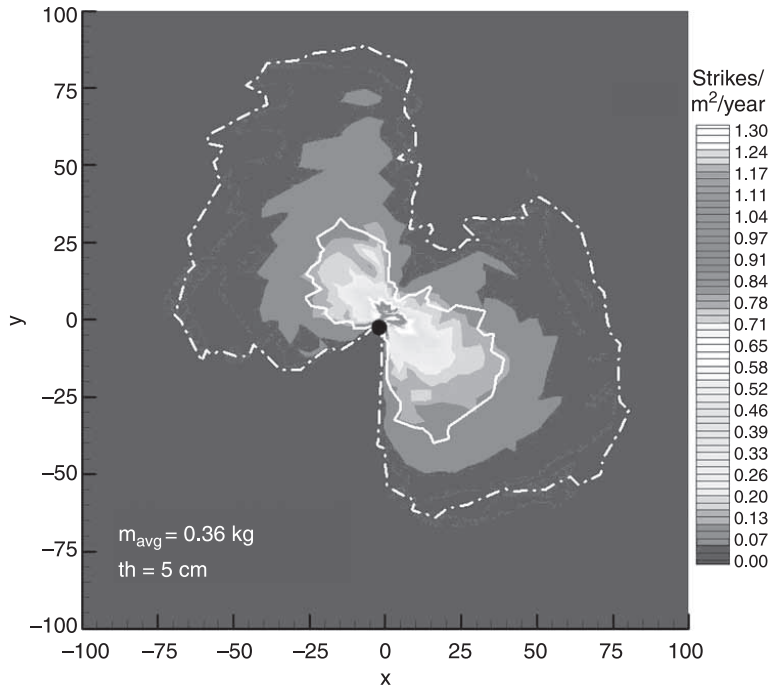

14.36 Strike probability in strikes/m^2/year for ice fragments with 0.36 kg average mass and 5 cm thickness, during WT operations.

were considered for both simulations, in the first case the fragments have a more scattered distribution on the ground than in the latter case. This is due to the marked wind transport of the thinner fragments compared to the larger ice pieces. In both simulations the 10 year recurrence period enclosure is slightly higher than the one in Fig. 14.34 (with still rotor) due to the initial imposed acceleration and again to the wind action on the thinner pieces; the ten year contours have a maximum extension of about 30–40 m (0.6–0.8 D_r), and the 50 year areas have an extension of about 80–90m (1.6–1.8D_r). Comparison of the recurrence period enclosures shows that the contour areas for the 1 cm thick fragments are slightly larger than the ones for the 5 cm thick pieces. However, the important difference is in the shape of the areas: the ones for the 1 cm thick fragments (Fig. 14.35) are extended in the prevailing wind direction. The ones for the 5 cm thick fragments (Fig. 14.36) are extended in the prevailing initial direction at the time of their removal from the blades; shapes with two lobes are in fact obtained in the latter case.

The maximum throwing distance for each computed case was compared to the one calculated by means of the relationship proposed by Seifert *et al*. (2004), who introduced a simplified empirical equation representing such a 'risk circle' without the need for detailed calculations:

$$d = (D + H) \times 1.5 \qquad [14.29]$$

using the same variables as equation [14.28].

For the cases presented in Figs 14.35 and 14.36, a maximum distance of about 200 m was computed. This has to be compared with the solution of the empirical equation [14.29], which furnishes a value of 165 m. For the considered wind and site and ice piece features, the solutions presented in this numerical model result in more conservative values.

A far more important safety problem arises for the maintenance operators, who need to approach the tower closely. A risk assessment can be performed assuming a possible intervention scenario. Equation [14.30] allows the calculation of the strike probability, expressed in strikes per hour, suffered by a worker walking towards the wind turbine, downwind of the turbine along a straight path, as indicated in Fig. 14.37 during WT operation.

$$P_{\mathrm{h}} = \frac{L_{\mathrm{path}} \times W_{\mathrm{path}} \times \overline{P}_{\mathrm{y,\,path}}}{24 \times n_{\mathrm{idy}}} \qquad [14.30]$$

Putting figures into the calculation gives:

$$P_{\mathrm{h}} = \frac{75\ \mathrm{m} \times 1\ \mathrm{m} \times 0.2 \dfrac{\mathrm{strikes}}{\mathrm{m}^2\,\mathrm{year}}}{24 \times 5 \dfrac{\mathrm{days}}{\mathrm{year}}} = 0.13\ \mathrm{strikes/hour} \qquad [14.31]$$

Since the ice fragments are spread over a larger terrain, when the WT is operating, a lower risk is encountered by operators working in the vicinity of the turbine. During standstill, a higher risk is possible close to the wind turbine. With the same data, a P_h of 1.25 strikes/hour is possible approaching the wind turbine.

To summarise:

- Wind turbine operation under icing conditions increases the probability of being struck at a given distance from the turbine, compared to the probability that results from stopping the rotor. This is due to the initial acceleration of the fragments that are about to detach, and to the significant wind transport of light and thin ice pieces that are produced by means of the de-icing practice. However, even in the worst case, the contours corresponding to a recurrence period of 50 years restrict an area that is not exceeding the safety distances of usual applications. In the same manner, minimum distances between wind turbines in wind farms are not influenced.
- The ice fragment thickness has a minor effect on the assessment of the recurrence period contours, but the removal of light and thin pieces at sites with high average wind velocities (where the wind transport effect becomes predominant) produces wider areas covered by ice fall.

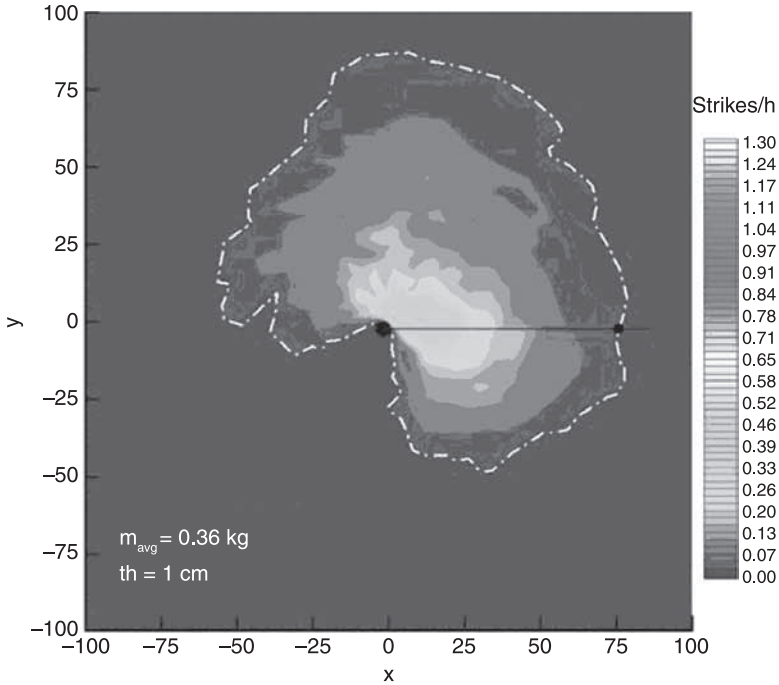

14.37 Strike risk probability suffered by a worker walking towards the WT, downwind of the WT along a straight path of 75 m (operation with de-icing in progress, P_h = 0.13 strikes/hour).

- De-icing practice potentially determines a smaller thickness of ice fragments and higher frequency of detachments. If one only considers the effect on the rotor aerodynamics and loading, frequent detachment of thin ice pieces is desirable. However, if energy savings connected to the de-icing practice and the risk reduction for people and objects are taken into account, less frequent removals of thicker ice fragments might be wanted.
- If recurrence period enclosures might suggest safety distances for the general public from objects from the wind turbine, the safety problem for operators, who need to approach the tower closely, is still unresolved; the probability of being struck is much higher as the distance from the turbine decreases. For the considered environmental conditions, the simulations carried out show that a person walking to and from the tower for 10 hours (during an icing day) has between 1 and 10 odds on average of being struck. The number and duration of the maintenance tasks have to be stated to evaluate the risk for the operators. Further investigation has to be carried out in this area.
- A result of the wind resource assessment during the icing period would give the correct orientation of the tower maintenance door to allow the safest access to the WT for the maintenance people (who drive and walk in the direction of the wind).

- The impact speed of the ice fragments on the ground is also critical in ice risk assessment: the kinetic energy of lighter ice pieces means that they will impact a person or an object with negligible effect, even though carried farther from the turbine. In the future, this analysis should be integrated into the ice risk assessment.

14.9 Energy loss in cold climates and economic risk

On cold climate sites, the potential energy production losses due to ice accretions on blades and the downtime for excessively low temperatures have to be taken into account in the economic feasibility study. If we confine the analysis to the icing accretions periods (usually the temperature does not fall below the standstill threshold), the AEP can be obtained from:

$$\text{AEP} = P_{\text{clean blade}} \times \left(8760 - t_{\text{iced blade}}\right) + \sum_{i=1}^{n} P_{\text{iced blade},\, i} \times t_{\text{iced blade},\, i} \qquad [14.32]$$

where $P_{\text{clean blade}}$ is the average wind turbine power output when the aerofoil is not contaminated by ice accretion, and $P_{\text{iced blade},i}$ is the average power output during the i-th icing event.

As previously stated, the break-even cost of an ice prevention system depends on many parameters. They include:

- ice prevention device typology and operation efficiency,
- site specific parameters: the probability or the time of icing, the wind resource, the air temperature and the adopted operating strategy in icing conditions,
- turbine specific parameters: the effect of the icing on the turbine power curve and production.

A simple approach to estimate the break-even conditions is presented in the following.

As the costs of the ice prevention system (installation, operation and maintenance) are less than the costs of the energy production losses suffered because of icing, the IPS will improve the project economics. The latter represents the IPS benefits that are the revenues that the extra AEP during the icing periods would provide. At the break-even point, where the minimum benefits necessary to cover all expenditures are reached, the following condition is achieved:

$$\text{Annual IPS costs} = \text{annual IPS benefits} \qquad [14.33]$$

This condition is translated into the following:

$$\frac{I_{\text{IPS}}}{a} + \text{O\&M}_{\text{IPS}} = c \times \text{AEP}_{\text{loss}} \qquad [14.34]$$

where I_{IPS} is the cost of the de-ice/anti-ice device, a is the annuity factor and c is the selling price of energy. $\frac{I_{IPS}}{a}$ therefore represents the IPS capital to be paid annually. The O&M costs include both maintenance (M_{IPS}) and electric consumption (E_{IPS}) costs during the whole year, that is:

$$\text{O\&M}_{IPS} = c' \times E_{IPS} + M_{IPS} \quad [14.35]$$

where c' is the cost of energy (supposed for the sake of generality to be different from c).

The IPS electric consumption depends on icing period duration, weather conditions (especially on air temperature and wind speed distributions), wind turbine characteristics (rotor tip speed, heating surface of blades and number of blades) and type of anti-ice/de-ice device. The O&M can be written as:

$$\text{O\&M}_{IPS} = c' \times \sum_{i=1}^{n} \dot{Q}_{IPS,\,ext,\,i} \times t_{\text{iced blade},\,i} + M_{IPS} = c' \times \frac{\sum_{i=1}^{n} \dot{Q}_{IPS,\,i} \times t_{\text{iced blade},\,i}}{\varepsilon_{IPS}} + M_{IPS} \quad [14.36]$$

where $\dot{Q}_{IPS,i}$ is the power required at the external surface of the blade to maintain it at temperatures above 0 °C (for instance +2 °C) in the i-th icing event, and obtained, for instance, through the method outlined in the previous paragraphs, while $\dot{Q}_{IPS,ext,i}$ is the installed IPS power and ε_{IPS} is its overall efficiency. Assuming that the IPS electric need is provided directly by the WT (and not from the electric grid), or c = c' and after substituting, the break-even condition is given by:

$$\frac{I_{IPS}}{a} + c \times \frac{\sum_{i=1}^{n} \dot{Q}_{IPS,\,i} \times t_{\text{iced blade},\,i}}{\varepsilon_{IPS}} + M_{IPS} = c \times \text{AEP}_{loss} \quad [14.37]$$

Equation [14.36] can be used to carry out a break-even simulation for preliminary design purposes.

Let us consider operating a 1300 kW three-bladed wind turbine, located at 1900 m a.s.l. in a mountainous site. The turbine is equipped with an IPS which heats the blade surface up to 2 °C when icing conditions are detected. Only the outer half of each blade is heated. The IPS characteristics and costs are illustrated in Table 14.12. The modified blade is manufactured with special features dedicated to IPS performance gain (e.g. high conductivity materials). The weather conditions are obtained using the method based on Battisti, Brighenti *et al.* (2005).

Figure 14.38 shows the minimum icing days period to achieve economic use of IPS, as a function of wind resource (expressed as mean wind speed at the hub height of 50 m) and AEP during the icing period when an electric IPS is employed. Figures 14.39 and 14.40 show the same when a hot gas IPS is used instead. The energy yield during the icing period is here parametrically expressed as a percentage of the AEP in the absence of ice accretion, but it can be computed with the method outlined in the previous paragraphs. The electric anti-icing system needs higher investment cost compared to hot air systems, while its higher system efficiency

Table 14.12 Site weather conditions and IPS data used for break-even simulation of Figs 14.38, 14.39 and 14.40

Weather conditions during icing period	
Mean temperature	−4.89 °C
Temperature Gauss parameters	$m = 2$, $s = 7$
Wind scale Weibull parameter	$k = 1.5$
Mean LWC	0.8 g/m^3
LWC Weibull parameters	$k = 2$, $A = 0.9$
IPS characteristics	
Electric IPS	Efficiency = 0.9
	Cost = 13% of WT cost
Hot air IPS	Efficiency = 0.3 (for standard blade)
	0.6 (for modified blade)
	Cost = 2 % of WT cost (for standard blade)
	7 % of WT cost (for modified blade)

(supposed at 0.9) allows the annual operating costs (that is, the electricity feed costs to be contained). The break-even analysis illustrated in Figs 14.38, 14.39 and 14.40 indicates that the critical duration of icing depends on the wind resource and on the IPS investment costs. Light icing conditions suggest that the IPS is not generally convenient for low wind speed sites. In harsher environments, leading to more relevant AEP losses, hot air IPS break-even is achieved for fewer icing days at the same site compared to the electric one. This profitability is higher for

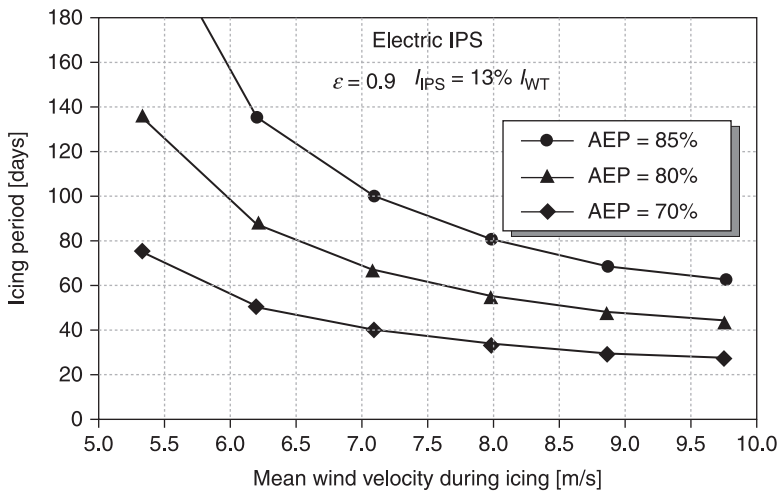

14.38 Minimum icing period required to achieve economics of IPS, as a function of wind resource (expressed as mean wind speed at the hub height of 50 m) and annual energy production during the icing period for electric IPS.

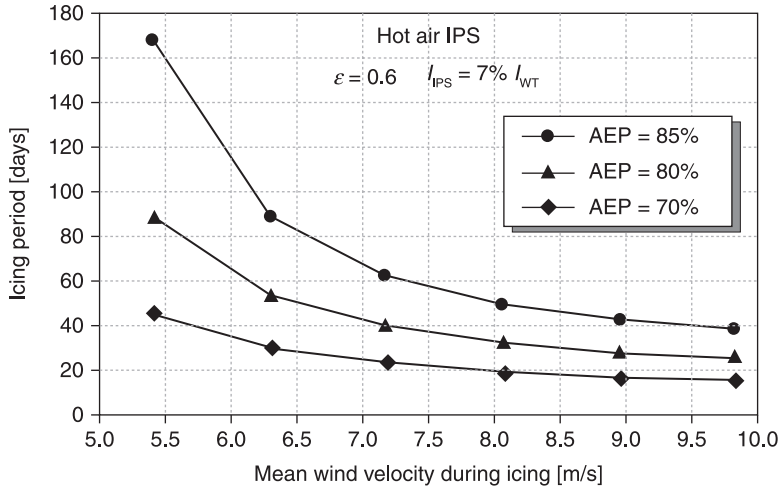

14.39 Minimum icing period required to achieve economics of IPS, as a function of wind resource (expressed as mean wind speed at the hub height of 50 m) and annual energy production during the icing period for hot gas IPS (closed circuit, Fig. 14.22).

the simplest execution of the hot air IPS (single channel, see Fig. 14.22), but such a system becomes unprofitable for low or medium winds because of the very high energy consumption due to the low thermal efficiency of the IPS (Brighenti, 2006).

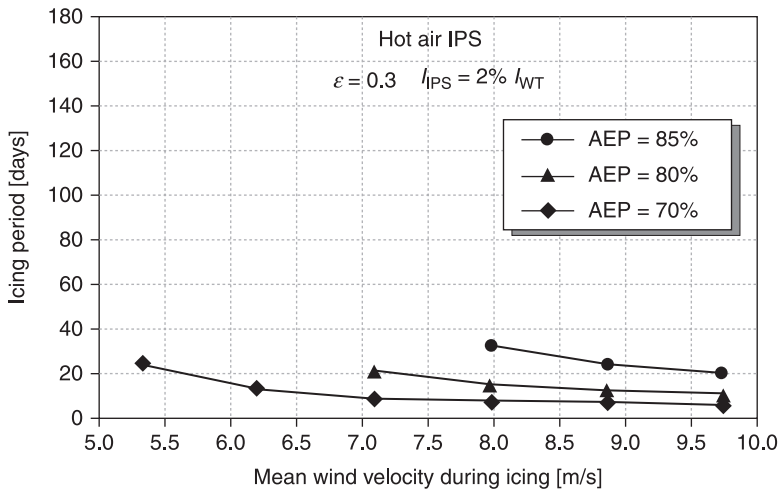

14.40 Minimum icing period required to achieve economics of IPS, as a function of wind resource (expressed as mean wind speed at the hub height of 50 m) and annual energy production during the icing period for hot gas IPS (closed circuit, Fig. 14.22).

14.10 References

Ackley, S F, Templeton, M K, 1979. *Computer Modeling of Atmospheric Ice Accretion*, CRREL REPORT 1979, 79.

Al-Khalil, K M, Keith, T G, De Witt, K J, 1993. New concept in runback water modeling for anti-iced aircraft surfaces, *Journal of Aircraft*, 1993, 30(1), pp.41–9.

Al-Khalil, K M, Miller, D R, Wright, W B, 2001. *Validation of NASA thermal ice protection computer codes: Part 3 – The validation of Antice*, NASA/TM-2001-210907, 2001.

Battisti, L, 2006. *Ice prevention systems selection and design*, Special course, Master of Science in Wind Energy, DTU, June 2006.

Battisti, L, 2007. *Wind Turbine Aerodynamics*, Lecture Seres 2007-05 Von Karman Institute for Fluid Dynamics, ISBN-13-978-2-930398-75-3.

Battisti, L, 2008. *Ice prevention systems design*, Classes notes, Special Course, 41820 Master on Wind energy DTU Copenhagen.

Battisti, L, Dal Savio, S, 2003. *Sistema antighiaccio per pale di turbine eoliche. Parte I: valutazione del fabbisogno energetico*, 58° Congresso ATI, Padova, Italy, 8–12 September 2003.

Battisti, L, Soraperra, G, 2003. *Sistema antighiaccio per pale di turbine eoliche. Parte II: sistemi a circolazione di aria*, 58° Congresso ATI, Padova, Italy, 8–12 September 2003.

Battisti, L, Brighenti, A, Dal Savio, S, Dell'Anna, S, 2005. *Evaluation of anti-icing energy and power requirement for wind turbine rotors in cold climates*, Proceedings of the VII BOREAS Conference, 7–8 March 2005, Finnish Meteorological Institute, Saarisalka, Finland.

Battisti, L, Hansen, M O L, Soraperra, G, 2005. *Aeroelastic simulations of an iced MW-Class wind turbine rotor*, Proceedings of the VII BOREAS Conference, Finnish Meteorological Institute, Saarisalka, Finland, 7–8 March 2005.

Battisti, L, Fedrizzi, R, Rialti, M, Dal Savio, S, 2005. *A model for the design of hot-air based wind turbine ice prevention system*, Proceedings of World Renewable Energy Congress (WREC05), Aberdeen, UK, 22–27 May 2005.

Battisti, L, Fedrizzi, R, Rialti, M, Dell'Anna, S, 2005d. *Ice risk assessment for wind turbine rotors equipped with de-icing systems*, Proceedings of the VII BOREAS Conference, Finnish Meteorological Institute, Saarisalka, Finland, 7–8 March 2005.

Battisti, L, Giovannelli, A, 2006. 'Wind Turbine Installations for high Elevations', 8th Biennial ASME Conference on Engineering Systems Design and Analysis, Torino, Italy, 4–7 June 2006.

Battisti, L, Baggio, P, Fedrizzi, R, 2006. Warm-Air Intermittent De-Icing System for Wind Turbines, *Wind Engineering*, 2006, 30, no. 5.

Battisti, L, Fedrizzi, R, 2007. 2D Numerical Simulation of a Wind Turbine De-Icing System Using Cycled Heating, *Wind Engineering*, 2007, 31, no. 1.

Bose, N, Rong, J Q, 1990. *Power reduction from ice accretion on a horizontal axis wind turbine*, Proceedings of 12th British Wind Energy Association, Wind Energy Conference, Norwich, UK, 27–30 March 1990.

Brighenti, A, 2006. *Wind turbine installations in cold climates*, PhD thesis, Universty of Trento, 2006.

Cattinis, R, 2008. *Alpine Test Site Gütsch*, Proceedings of Winterwind 2008, Norrköping, Sweden, 9–10 December 2008.

Cober, S G, Isaaq, G A, Strapp, J W, 2001. *Characterization of Aircraft Icing Environments that Include Supercooled Large Droplets*, Journal of Applied Meteorology, *American Meteorological Society*, 2001, 40, pp.165–78.

Dillingh, J E, Hoeijmakers, H W M, 2003. *Simulation of ice accretion on airfoils during flight*, University of Twente, Faculty of Mechanical Engineering, Section Engineering Fluid Dynamics, 2003.

Durstewitz, M, 2003. Windenergie in kalten Klimaregionen, *Erneuerbare Energien*, 2003, 12, pp. 34–5.

EC project, 2001. *New Icetools*, NNE5 2001-00259, NICE.

Enercon, 2003. *E-66 20.70 Technical Description*, Enercon International GmbH, 04 April 2003.

Frank, R, Seifert, H, 1997. Ice im Kanal, *DEWI Magazine*, 1997, 10.

Gelder, F T, Lewis, J P, 1951. *Comparison of heat transfer from airfoil in natural and icing conditions*, NACA TN 2480, 1951.

GL Wind, 2005. *Guideline for the Certification of Wind Turbines*, Part 1, par. 4.4.5, pp. 4–26.

Gray, V H, Bowden, D T, von Glahn U, 1952. *Preliminary results of cyclical de-icing of a gas-heated airfoil*, NACA-RM-E51J29.

Guffond, D, Brunet, L, 1985. *Validation du programme bidimensional de captation*, ONERA, RT n°20/5146 SY, 1985.

Kimura, S, Sato, T, Kosugi, K, 2004. *The effect of anti-icing paint on the adhesion force of ice accretion on a wind turbine blade*, Proceedings of BOREAS VI International Conference, Finnish Meteorological Institute, Pyhätunturi, Finland, 9–11 April 2003.

Laakso, T, Holttinen, H, Ronsten, G, Horbaty, R, Lacroix, A, Peltola, E, Tammelin, B, 2003. *State-of-the-art of wind energy in cold climates*, internet. Available at *http://arcticwind.vtt.fi*.

Maissan, J F, 2001. *Wind Power Development in Sub-Arctic Conditions with Severe Rime Icing*, TSYE Corporation – Circumpolar Climate Change Summit and Exposition, ed. by The Northern Review Whitehorse, Yukon, Canada, 19–21 March 2001.

Makkonen, L, 1984. *Atmospheric icing on sea structures*, CRREL Monograph 84-2, U.S. Army Cold Regions Research & Engineering Laboratory.

Makkonen, L, Autti, M, 1991. *The effects of icing on wind turbines*, Wind Energy: Technology and Implementation, EWEC 91, 575–80.

Makkonen, L, Laakso, T, Marjaniemi, M, Finstad, K J, 2001a. Modeling and prevention of ice accretion on wind turbines, *Wind Engineering*, 2001, 25(1), pp.3–21.

Makkonen, L, Laakso, T, Marjaniemi, M, Wright, J, 2001b. *Results of Pori wind farm measurements*, VTT Energy Reports 42/2001.

Mansson, J, 2004. *Why de-icing of wind turbine blades?*, Global Windpower 2004 Conference and Exhibition, Chicago, 18–21 March 2004.

Mingione, G, Brandi, V, 1998. Ice accretion prediction on multielement airfoils, *Journal of Aircraft*, 1998, 35(2), pp.240–46.

Morcillo, M, Chico, B, de la Fuente, D, Almeida, E, Joseph, G, Rivero, S, Rosales, B, 2004. *Atmospheric corrosion of reference metals in Antarctic sites*, Cold Regions Science and Technology, 40, pp.165–78.

Morency, F, Tezok, F, Paraschivoiu, I, 1999. Anti-icing system simulation using CANICE, *Journal of Aircraft*, 1999, 36(6), pp.999–1006.

Morency, F, Tezok, F, Paraschivoiu, I, 2000. Heat and mass transfer in the case of anti-icing system simulation, *Journal of Aircraft*, 2000, 37(2), pp.245–52.

Morgan, C, Bossanyi, E, Seifert, H, 1998. *Assessment of Safety Risks Arising from Wind Turbine Icing*, Proceedings of BOREAS IV International Conference, Finnish Meteorological Institute, Hetta, Finland, 31 March–2 April 1998.

Mróz, A, Holnicki-Szulc, J, Kärnä, T, 2005. *Mitigation of ice loading on off-shore wind turbines*, feasibility study of a semi-active solution, 2nd ECCOMAS Thematic Conference on Smart Structures and Materials, Lisbon, Portugal, 18–21 July 2005.

Neel, C B, Bergrun, N R, Jukoff, D, Schlaff, B A, 1947. *The calculation of the heat required for wing thermal ice prevention in specified icing conditions*, NACA TN 1472, 1947.

Peltola, E, Marjaniemi, M, Stiesdal, H, 1999. *An ice prevention system for the wind turbine blades*, Proceedings of the European Wind Energy Conference, Nice, France, 1–5 March 1999, pp.1034–37.

Pederson, E, 2008. *Wind turbine ice protection system (WTIPS)*, Kelly Aerospace Thermal Systems, Winterwind, Norrköping, Sweden, 09–10 December 2008.

Seifert, H, Richert, F, 1997. *Aerodynamics of iced airfoils and their influence on loads and power production*, European Wind Energy Conference, Proceedings of the international conference, Dublin, Ireland, 6–9 October 1997, pp. 458–63.

Seifert, H and Richert, F, 1998. *A Recipe to Estimate Aerodynamics and Loads on Iced Rotor Blades*, Proceedings of Boreas IV International Conference, Enontekiö, Hetta, Finland, 31 March–2 April 1998.

Seifert, H, 2003. *Technical requirements for rotor blades operating in cold climate*, DEWI, Deutsches Windenergie-Institut GmbH.

Seifert, H, Westerhellweg, A, Kröning, J, 2003. *Risk Analysis of Ice Throw from Wind Turbines*, Proceedings of BOREAS VI International Conference, Finnish Meteorological Institure, Pyhatunturi, Finland, 9–11 April 2004.

Sheldahl, R E, Klimas, P C, 1980. *Aerodynamic characteristics of 7 symmetrical airfoil sections through 180-degree angle of attack for use in aerodynamics analysis of vertical axis wind turbine*, Sandia National Laboratories: SAND80-2114, 1980.

Tammelin, B, Seifert, H, 2001. *Large wind turbines go into cold climate regions*, Proceedings of European Wind Energy Conference (EWEC 2001) International Conference, Copenhagen, DK, 2–6 July 2001.

Tammelin, B, Cavaliere, M, Holtinnen, H, Morgan, C, Seifert, H, 2000. *Wind Energy in Cold Climate*, WECO Final Report (JOR3-CT95-0014) ISBN 951-679-518-6, Finnish Meteorological Institute, Helsinki, Finland.

Thomas, S K, Cassoni, R P, MacArthur, C D, 1996. *Aircraft anti-icing and deicing techniques and modeling, Journal of Aircraft*, 1996, 33(5), pp.841–53.

Tran, P, Brahimi, M T, Pueyo, A, Tezok, F, Paraschivoiu, I, 1996. Ice accretion on aircraft wings with thermodynamic effects, *Journal of Aircraft*, 1996, 32(2), pp.444–46.

US2005/0242233, 2005. Patent Application. *Anti-icing system for wind turbines*, 2005.

US2007/0254170, 2007. Patent Application. *Erosion resistant anti-icing coatings*, November 2007.

Viterna, L A, Corrigan, R D, 1981. *Fixed pitch rotor performance of large horizontal axis wind turbines*, NASA CP-2230, USA, 1981.

Woigt, H, 1949. German Patent Application. *Deutsche Patentschrift n.842330*, 1949.

Wright, W B, 1995. *Users manual for the improved NASA Lewis ice accretion code LEWICE 1.6*, NASA Contractor Report, 1995.

Wright, W B, 2002. *User manual for the NASA gleen ice accretion code LEWICE-Version 2.2.2*, NASA/CR-2002-211793, 2002.

Yasilik, A D, De Witt, K J, Keith, T G, 1992. Three-dimensional simulation of electrothermal deicing systems, *Journal of Aircraft*, 1992, 29–6, pp.1035–42.

15

Offshore environmental loads and wind turbine design: impact of wind, wave, currents and ice

J. VAN DER TEMPEL, N. F. B. DIEPEVEEN,
W. E. DE VRIES and D. CERDA SALZMANN,
Delft University of Technology, The Netherlands

Abstract: In order to design offshore wind turbines, an engineer must understand the environmental loads that are imposed on the structure. This chapter describes the wind, wave, current and ice loading phenomena and how to translate the environmental characteristics to design loads against which the structure must be designed.

Key words: environmental loads, load cases, offshore, wind turbines, gravitational loads.

15.1 Introduction

For the design of offshore wind turbines, the assessment of environmental parameters is a little bit more extensive than for turbines on land. Onshore, turbines can be designed following a class prescribing the wind regime and the required resilience of the turbine design. Offshore, the wind climate presents itself in a slightly different form: winds are less turbulent but stronger and wind shear is less pronounced. But, more importantly, the design of the offshore wind turbine is governed by environmental loads such as waves, current and, in some areas, ice.

This chapter focuses on the offshore environment loads such as wind, waves, currents and ice. It describes the phenomena driving them and the way to convert environmental forces into loads on the offshore wind turbine. From the general load determination, the design loads can be defined.

15.2 Overview of environmental loads

For calculating the loads on the offshore wind turbine a mechanical model of the structure is introduced. Figure 15.1 shows the offshore wind turbine in its environment,[7] including the external loads by wind, waves and current, respectively V_{wind}, U_{wave} and U_{current}. These environmental conditions lead to the environmental loads on the support structure, while the weight of the wind turbine and the weight of the support structure lead to gravitational loads. In Fig. 15.2, the offshore wind turbine support structure is modeled as a stick, with the environmental loads and gravitational loads projected on it. Here, the support structure is limited to a two-dimensional model, so no consideration will be given to the loads and dynamics in

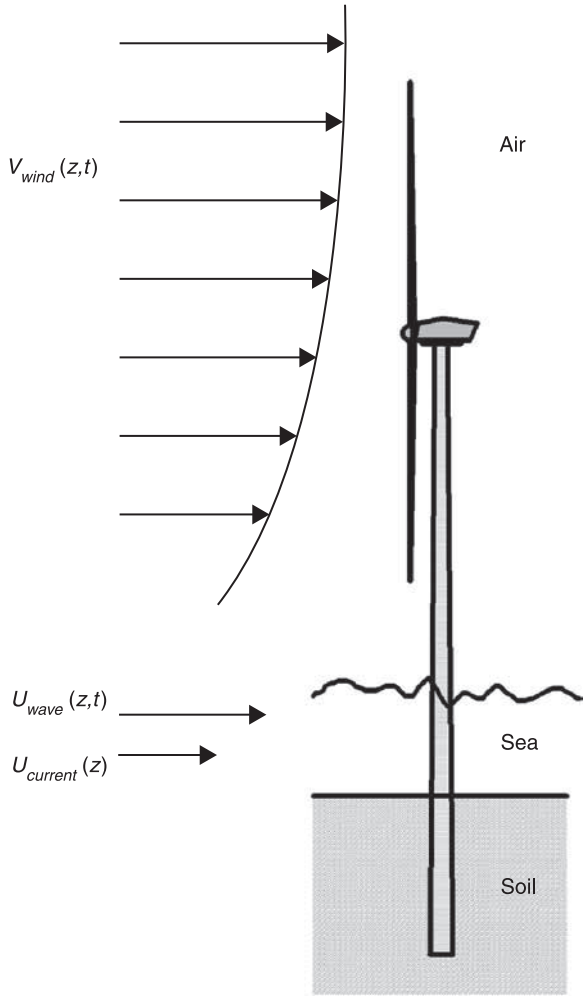

15.1 Offshore wind turbine environmental conditions.

the y-direction perpendicular to the x-z plane. Also, all environmental loads are assumed to be acting in the x-direction.

15.3 Wind

15.3.1 Description of wind field

From field experiments, it is known that the undisturbed wind velocity is variable in space, time and direction.[1]

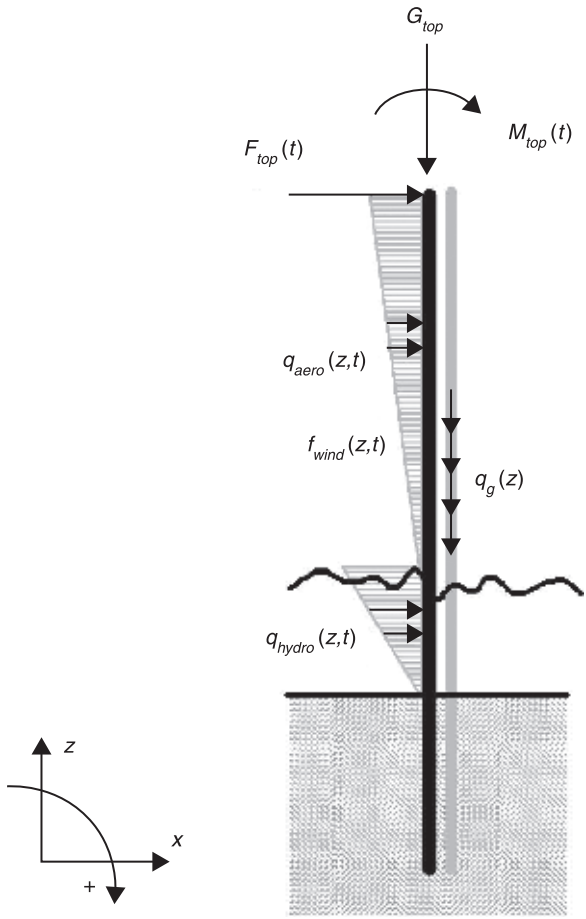

15.2 Loads on stick model of support structure.

Since merely a two-dimensional model is considered here, the variations in direction will be neglected; the wind speed will be considered to be acting in the *x*-direction only. Given this limitation, the wind velocity still varies both in height and in time. An example of an actual wind speed profile at a frozen time moment is given in Fig. 15.3. The following sections will cover the descriptions of the variations of the wind speed in height and in time, as well as the effect that these variations cause on the rotating blades.

15.3.2 Wind speed variations with height

Due to friction between the moving air and the earth's surface, wind gets decelerated at low heights, giving the mean wind speed a variation with height.

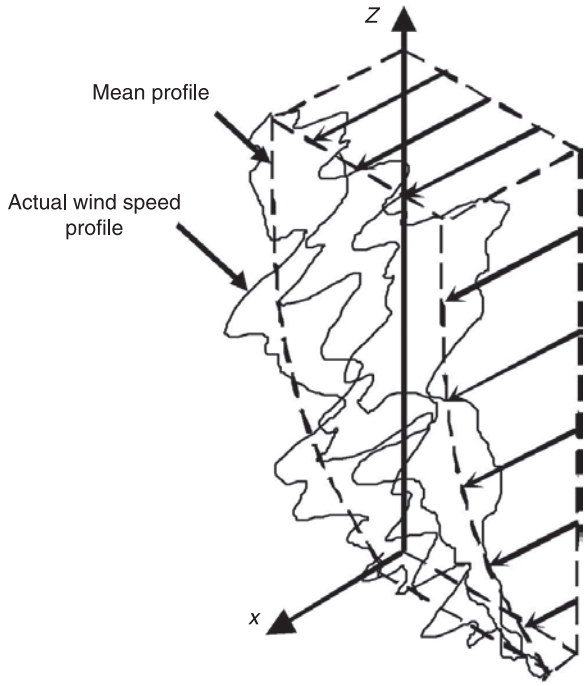

15.3 Actual wind speed profile.[6]

The mean wind speed decreases from heights about 2 km above the ground, where the effects of the friction are negligible, down to the surface, where its value becomes (practically) zero. This layer is called the atmospheric boundary layer. The vertical variation of the mean wind speed, the mean wind speed profile, can be expressed by different functions. One of the most commonly used functions to describe such a profile is the logarithmic profile:[2]

$$V(z) = V_{\text{ref}} \cdot \frac{\ln\left(\frac{z}{z_0}\right)}{\ln\left(\frac{z_{\text{ref}}}{z_0}\right)} \qquad [15.1]$$

where:

$V(z)$ = mean wind speed at height z (m/s)
V_{ref} = mean wind speed at the reference height z_{ref} (m/s)
z_{ref} = reference height (m)
z_0 = surface roughness length (m)

An example of a mean wind speed profile is shown in Fig. 15.4. The surface roughness length z_0 is a parameter that depends on the type of surface. Values for this parameter are 0.20 mm for a calm open sea and 0.50 mm for a rough sea.[3]

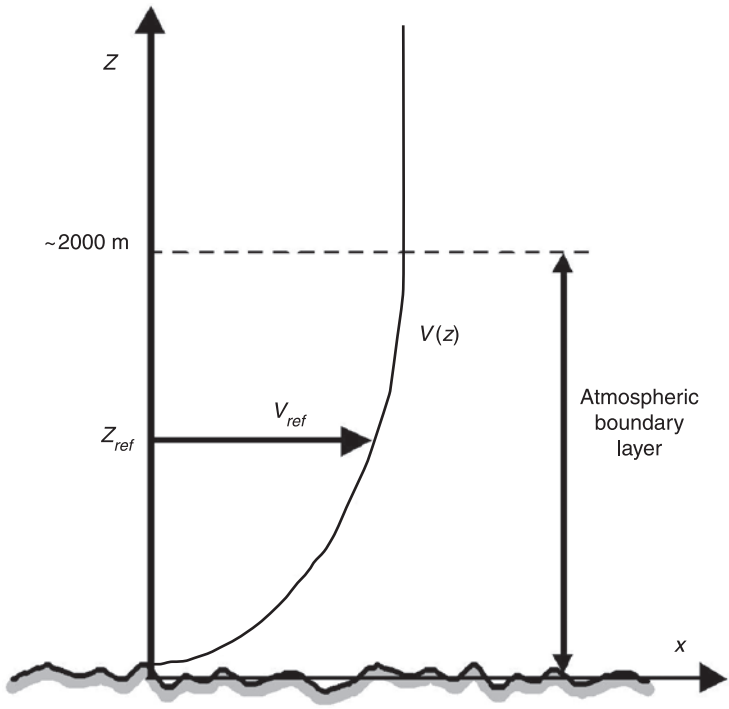

15.4 Mean wind speed profile.

These values are significantly lower than for onshore wind due to the absence of buildings, trees, etc.

It is noted that a measured mean wind speed can only be used in combination with a given reference height. A common choice for the reference height is z_{ref} = 10 m.[4] However, in the context of wind turbines, the hub height can be a natural choice for z_{ref}, provided that measurements at that height are available.

Next to the logarithmic profile description, the power-law description is also commonly used (equation [15.2]). The shear coefficient α_{shear} for offshore conditions is 0.12.

$$V_w(z) = V_{w,r}\left(\frac{z}{z_r}\right)^{\alpha_{\text{shear}}} \qquad [15.2]$$

Both profiles are used in the industry and do not give significant differences.

15.3.3 Turbulence

When wind is measured in the field, a time-varying wind speed can be found as shown in Fig. 15.5. From this time series the statistical parameters can be calculated: the mean wind speed and the standard deviation.

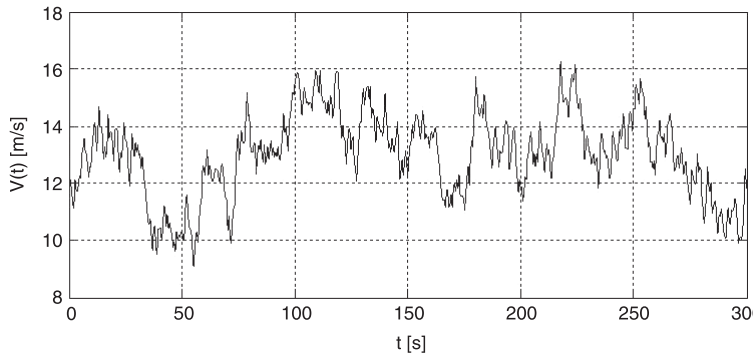

15.5 Time-varying wind speed measurement.

The turbulence intensity is defined as the standard deviation of the time-varying wind speed divided by the mean wind speed, in percentage:

$$I_t = \frac{\sigma}{V_w}\% \qquad [15.3]$$

The turbulence intensity is dependent on height and on the roughness of the terrain. Rougher terrain and lower altitude give higher turbulence intensities. Design standards give descriptions of the turbulence intensity based on these roughness and altitude parameters. For design cases, fixed turbulence levels can be selected for specific sites. Figure 15.6 shows the recommended turbulence intensities as a function of wind speed for different standards. For offshore wind conditions, the turbulence intensity is significantly lower than onshore: 11% offshore and 20% onshore. The reader is, however, reminded that this is true only for the turbulence of undisturbed wind. Turbines that operate in the wake of another turbine will experience more turbulence. As a rule of thumb, the spacing between offshore turbines is therefore at least seven times the rotor diameter. This distance helps reduce the amount of additional turbulence, and gives the wind flow time to regain speed from the undisturbed wind above and below the rotor area.

Next to the longitudinal turbulence (in the direction of the wind), the lateral and vertical turbulence intensities are also defined by the standards. Different descriptions are available ranging from isotropic turbulence ($I_u = I_v = I_w$) to height-dependent correlations.

Turbulence can also be represented in a spectral form. Several models have been fitted to the turbulence spectrum. The von Kármán and Kaimal spectra are the most commonly used models (equations [15.4] and [15.5]), although turbulence spectra over sea generally contain even greater low-frequency content. These models are based on the mean wind speed, the turbulence intensity and a length scale:

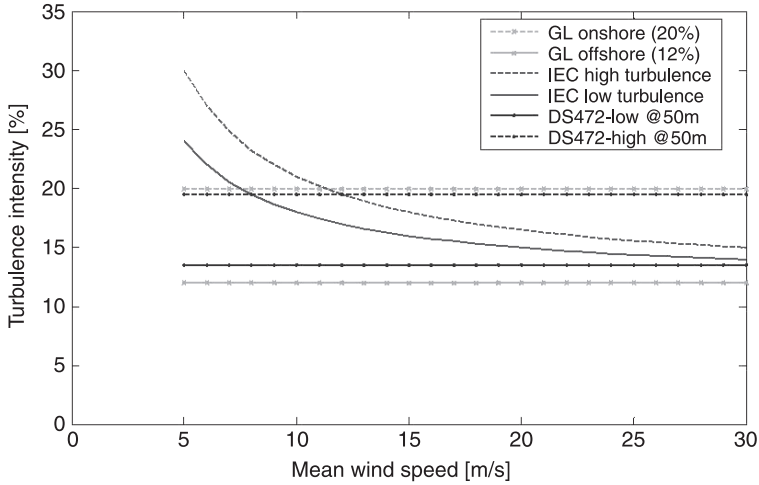

15.6 Turbulence intensity as a function of wind speed from different standards.[3]

$$S_{\text{Karman}}(f) = \frac{\sigma_v^2 4L_v / V_w}{\left(1 + 70.8\left(fL_v / V_w\right)^2\right)^{5/6}} \quad [15.4]$$

$$S_{\text{Kaimal}}(f) = \frac{\sigma_v^2 4L_v / V_w}{\left(1 + 6fL_v / V_w\right)^{5/3}} \quad [15.5]$$

where:

σ_v = standard deviation of the wind speed (m/s)
L_v = integral length scale (model dependent) (m)
V_w = mean wind speed (m/s)
f = frequency (Hz)

The precise definition of the length scales is again prescribed in the literature or in design standards. When these spectra are applied in calculation tools, these prescribed values can be selected generally. The underlying relationships between parameters are then fixed. No preference exists for either method.

15.3.4 Extreme wind speeds and gusts

Two basic extreme wind load cases can be defined: the extreme hourly mean wind speed with given return period (1, 50, 100 years) and the extreme incident wind speed within a given short time interval.

The extreme hourly mean wind speed is found by taking a large number of measured means and selecting the extremes above a chosen threshold. These extremes are then plotted on a log-linear scale over the number of occurrences per

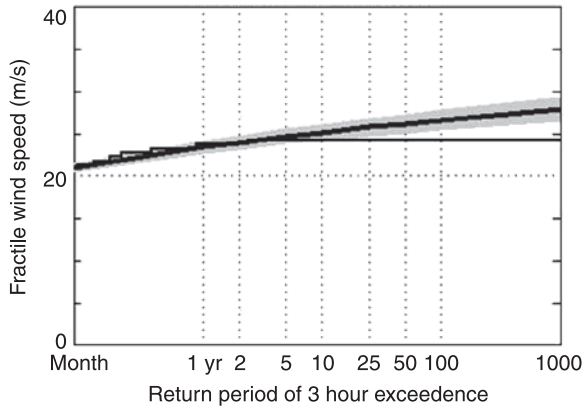

15.7 Gumbel fit (higher line with gray 95% confidence interval) for data recordings of mean wind speed (stepped lower line).

time interval (month, year). By fitting a distribution curve through these measured values, an extrapolation can be made of the expected maximum in periods beyond the measurement period. One of the most commonly used is the Gumbel distribution, as shown in Fig. 15.7.

In onshore wind turbine design, the design standards give a prescribed extreme wind speed for different classes. Table 15.1 shows the values given by the IEC. The classes are used as reference for the design of the turbine; they are not directly linked to specific sites. Offshore sites are classed as 'S' (special), which are not defined and require site-specific analysis.

15.4 Waves

15.4.1 Waves, the surface of the sea

Waves at sea occur when wind is blowing across the water surface. They occur from small ripples up to house-high giants.

Table 15.1 Location classes according to IEC with yearly hourly mean wind speed ($V_{w,\ ext\ 1h}$) and extreme 10 min mean wind speed ($V_{w,\ ext\ 10min}$) in (m/s) at hub height

	Class			
	I	II	III	IV
$V_{w,\ ext\ 1h}$	10	8.5	7.5	6.0
$V_{w,\ ext\ 10min}$	50	42.5	37.5	30

For the purpose of describing the wave climate at a specific location, a climate is usually considered to be stationary within periods of three hours. This means that within such periods of time, the statistical properties of the wave climate are assumed to be constant. The wave characteristics within such durations are called sea states and can be described statistically by a variance density spectrum, commonly referred to as a wave spectrum. A wave spectrum is typically obtained by performing a fast Fourier transform (FFT) on the wave time series of a sea state. Standard wave spectra have been developed which can describe a wave climate using a limited number of parameters (a method similar to the wind spectra described in the previous section). Two often-used standard wave spectra are:

- the Pierson–Moskowitz wave spectrum, for fully developed seas
- the JONSWAP wave spectrum, for fetch-limited wind-generated seas

Figure 15.8 shows a plot of these standard wave spectra. Both these spectra can be derived from the parameters H_s and T_z, the significant wave height and the mean zero-crossing wave period. The Pierson–Moskowitz spectrum can be expressed as follows:

$$S_{\mathrm{PM}}(\omega) = \frac{A}{\omega^5}\exp\left(-\frac{B}{\omega^4}\right) \qquad [15.6]$$

with:

$$A = \frac{4\pi^3 H_s^2}{T_z^4} \qquad [15.7]$$

$$B = \frac{16\pi^3}{T_z^4} \qquad [15.8]$$

where:

$S_{\mathrm{PM}}(\omega)$ = Pierson–Moskowitz variance density spectrum (m^2s)
ω = angular frequency (rad/s)
H_s = significant wave height (m)
T_z = mean zero-crossing wave period (s).

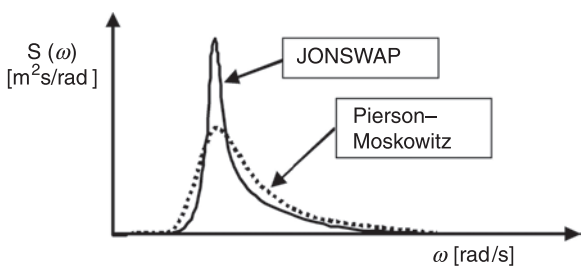

15.8 JONSWAP and Pierson–Moskowitz wave spectra.

The JONSWAP spectrum is based on wave measurements carried out in 1968 and 1969 during the Joint North Sea Wave Project (JONSWAP) in the North Sea. This spectrum has the shape of the Pierson–Moskowitz spectrum, but is modified by a peak enhancement. The JONSWAP spectrum follows from the formulas below:

$$S_{\mathrm{JS}}(\omega) = nf \cdot \frac{A}{\omega^5} \exp\left(-\frac{B}{\omega^4}\right) \cdot \left(\gamma^{\exp\left\{-\frac{1}{2}\left(\frac{\omega-\omega_m}{\sigma\omega_m}\right)^2\right\}}\right) \quad [15.9]$$

$$\omega_m = \left(\frac{4}{5}B\right)^{1/4} \quad [15.10]$$

where:

$S_{\mathrm{JS}}(\omega)$ = JONSWAP variance density spectrum (m^2s)
n_f = normalizing factor between JONSWAP and Pierson–Moskowitz spectrum
γ = peak shape parameter
ω_m = modal angular frequency (rad/s)
σ = numerical parameter
= σ_a for $\omega < \omega_m$
= σ_b for $\omega \geq \omega_m$

The average values for the spectrum's peak shape parameter and numerical parameters were taken from the measurements of the JONSWAP. They are:

$$\gamma = 3.3 \quad [15.11]$$

$$\sigma_a = 0.07 \quad [15.12]$$

$$\sigma_b = 0.09 \quad [15.13]$$

For the value of the peak shape parameter given in equation [15.11], the offshore section at the Delft University of Technology found a normalizing factor for equation [15.9] of Ref. 5:

$$nf = 0.625 \quad [15.14]$$

With the formulae and values given above, the JONSWAP variance density spectrum can now be expressed with the spectral parameters H_s and T_z:

$$S_{\mathrm{JS}}(\omega) = 2.5\pi^3 \cdot \frac{H_s^2}{T_z^4\omega^5} \exp\left(-\frac{16\pi^3}{T_z^4\omega^4}\right) \cdot \left(3.3^{\exp\left\{-\frac{1}{2}\left(\frac{\omega-\omega_m}{\sigma\omega_m}\right)^2\right\}}\right) \quad [15.15]$$

with:

$$\omega_m = \left(12.8 \times \frac{\pi^3}{T_z^4}\right)^{1/4}$$

$$\sigma = \sigma_a = 0.07 \text{ for } \omega < \omega_m \quad [15.16]$$

$$\sigma = \sigma_b = 0.09 \text{ for } \omega \geq \omega_m \quad [15.17]$$

15.5 Current

In principle, current velocities vary in space and time as wind velocities do. However, both the length and the timescales of the variations in the current velocity are much larger than those for wind. They are also large compared to the horizontal dimensions of a monopile and the range of periods of interest for determining the pile's dynamic behavior. Currents may therefore be considered as a horizontally uniform flow field of constant velocity, which is only a function of the vertical z-coordinate.

Because of the lack of more specific information for a particular site, current models for structural design will usually define a simple current profile over depth, using the known current velocity at the water surface as an input parameter. A commonly used method – the power law profile (similar to the wind shear profile in section 15.3) taken from Ref. 5 – will be used for the current:

$$U_{\text{current}}(z) = U_{c0}\left(\frac{z+d}{d}\right)^{1/7} \quad [15.18]$$

where:

$U_{\text{current}}(z)$ = current velocity at elevation z for $-d \leq z \leq 0$ (m/s)
U_{c0} = current velocity at MSL (m/s)
z = vertical coordinate, measured positively upwards from MSL (m)
d = water depth (m).

15.6 Hydrodynamic loads

Both the water particle velocities and the accelerations cause hydrodynamic loads on the support structure of an offshore wind turbine. For the calculation of the hydrodynamic loads on slender piles, the basic model is the Morison equation, named after J R Morison who derived it in 1950.[5] This equation covers the total hydrodynamic loads, and will therefore be used to calculate q_{hydro}. The Morison equation for a motionless slender pile in water reads:

$$q_{\text{hydro}} = f_i + f_d = \frac{\pi}{4}\rho_w C_M D^2 \dot{U}_w + \frac{1}{2}C_D \left|U_w\right| \cdot U_w \quad [15.19]$$

where:

q_{hydro} = $\mathrm{d}F/\mathrm{d}z$ = total hydrodynamic load per unit length (N/m)
f_i = $\mathrm{d}F_i/\mathrm{d}z$ = hydrodynamic inertia load per unit length (N/m)
f_d = $\mathrm{d}F_d/\mathrm{d}z$ = hydrodynamic drag load per unit length (N/m)
C_M = inertia coefficient

C_D = drag coefficient
D = monopile outer diameter (m)
ρ_w = mass density of water (kg/m^3)
$\dot{U}_w$ = horizontal water particle acceleration (m/s^2)
U_w = horizontal water particle velocity (m/s)

Since the Morison equation is essentially an empirical equation, the values of its drag and inertia coefficients have been determined experimentally in a variety of ways. For the inertia coefficient C_M, a value of 2 is widely accepted for objects with a circular cross-section. For the drag coefficient C_D, Det Norske Veritas uses a value of 0.7 for a circular cylinder in the deterministic fatigue analysis.[4]

For the calculation of the drag load, the horizontal water particle velocity is needed, which depends on both the current and the wave velocity. If the structure itself is also moving (for instance a floating turbine), its velocity should be taken into account as well. The equation for the velocity of a water particle relative to a node on the monopile then reads:

$$U_{\text{rel}}(z,t) = U_{\text{current}}(z) + U_{\text{wave}}(z,t) - U_s(z,t) \quad [15.20]$$

where:

U_{rel} = relative velocity of water to structure (m/s)
U_{current} = current velocity (m/s)
U_{wave} = horizontal water particle velocity due to waves (m/s)
U_s = horizontal velocity of the structure (m/s)

When a structure is moving, according to Ref. 1, Morison's equation becomes:

$$q_{\text{hydro}} = \frac{\pi}{4}\rho_w C_M D^2 \cdot \dot{U}_{\text{wave}} - \frac{\pi}{4}\rho_w \left(C_M - 1\right) D^2 \cdot \dot{U}_s + \frac{1}{2}\rho_w C_D D \cdot \left|U_{\text{rel}}\right| \cdot U_{\text{rel}} \quad [15.21]$$

where:

$\dot{U}_{\text{wave}}$ = horizontal water particle acceleration due to waves (m/s^2)
$\dot{U}_s$ = horizontal acceleration of the structure (m/s^2)

Finally, the diameter of the structure can also vary in height, meaning that its magnitude is a function of z. Thus, equation [15.21] can de rewritten as:

$$\begin{aligned} q_{\text{hydro}}(z,t) = {} & \frac{\pi}{4}\rho_w C_M \left[D(z)\right]^2 \dot{U}_{\text{wave}}(z,t) - \frac{\pi}{4}\rho_w \left(C_M - 1\right)\left[D(z)\right]^2 \dot{U}_s(z,t) \\ & + \frac{1}{2}\rho_w C_D D(z) \cdot \left|U_{\text{rel}}(z,t)\right| \cdot U_{\text{rel}}(z,t) \end{aligned} \quad [15.22]$$

15.6.1 Diffraction

The basic assumption of the Morison equation is that the submerged members on which the wave loads are calculated do not affect the waves. As long as the

cylinder diameter is relatively small compared to the wavelength this assumption is valid. For large-diameter structures, like the monopile support structures for offshore wind turbines placed in relatively shallow water with consequently reduced wavelength, the validity of the Morison equation can be compromised.

The effect that a structure has on the wave field is called diffraction. To incorporate this effect in the Morison equation, the MacCamy–Fuchs correction is introduced in Fig. 15.9. This correction reduces the magnitude of the inertia coefficient. The correction factor is dependent on the ratio of diameter over wavelength: D/λ_{wave}. Figure 15.9 shows the reduction of C_M for increasing ratio.

15.7 Long-term wave description

All wave events discussed in the previous sections dealt with sea conditions that are assumed stationary for a certain period of time. The wave conditions during these periods are called sea states and they typically last three hours. When long-term effects of the wave climate at a certain site are studied to find the probability of extremes or to calculate the lifetime fatigue damage, a large amount of data is required. These data can be taken by measurements from buoys, platforms or satellites, or can be estimated from large meteorological and oceanographic models fed and calibrated with measurements from a large number of stations. The resulting sea states are binned into a scatter diagram. This diagram gives the probability of the occurrence of each combination of H_s and T_z for that location. Every bin represents the probability of occurrence of wave conditions having that specific combination of parameter values, with which the wave spectrum according to a selected spectral model can be determined. The size of the bins can

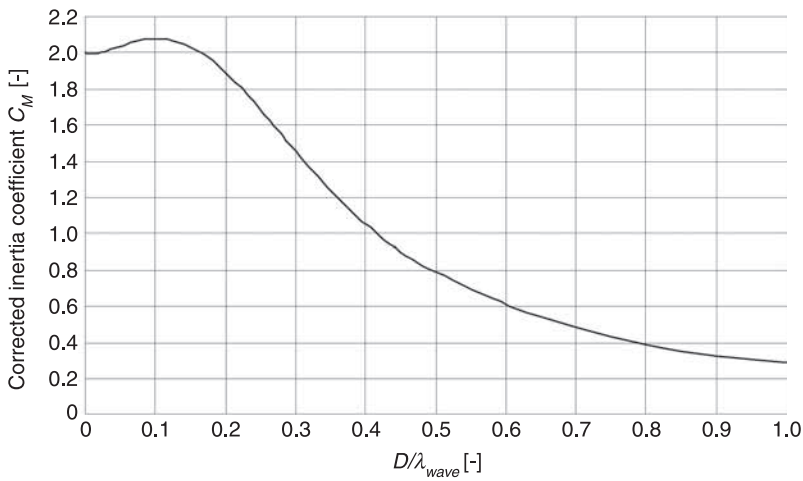

15.9 MacCamy–Fuchs diffraction correction of the inertia coefficient C_M in the Morison equation for cylinder diameter over wavelength.

be selected arbitrarily, i.e. larger bins will remove a lot of detail but reduce the total number of sea states. A typical bin size for H_s is steps of 0.5 m and for T_z steps of 2 s.

On looking at the cloud of occurrences in a wave scatter diagram, we find that there is some linear relationship hidden in the cloud of occurrences, i.e. the cloud runs from bottom-left to top-right. The general direction of this cloud is of course trivial, i.e. large waves have large periods (or they become too steep and break) and small waves have smaller periods. But to fix a linear relationship would considerably reduce the variability reflected in the diagram and discard valuable information. Because scatter diagrams are very site-specific, the assumed linear relationships of one location should not be superimposed onto the next. Table 15.2 shows the scatter diagram for the OWEZ or 'NL1' location

15.8 Ice loads

Not all offshore wind turbines will be subjected to ice. The North Sea does not freeze in winter, even when temperatures are below zero for a long period. In the design, items like ice coverage on blades (icing) can be an issue, but this is treated in the turbine design. For offshore wind turbines in the Baltic area, ice loads are an item of design. Here, the sea freezes for longer periods of time. The ice coverage floats with wind and tides and thus exerts loads on the structure.

For the design of offshore wind turbines, two main phenomena need attention in design:

Table 15.2 Wave scatter diagram for H_s and T_z with occurrence in parts per thousand for the OWEZ

	T_z (s)								
H_s (m)	0–1	1–2	2–3	3–4	4–5	5–6	6–7	7–8	Sum:
6.5–7.0									0.0
6.0–6.5								0.1	0.1
5.5–6.0							0.1	0.1	0.2
5.0–5.5							0.1	0.1	0.2
4.5–5.0							1		1.0
4.0–4.5							4		4.0
3.5–4.0						4	5		9.0
3.0–3.5						19	0.1		19.1
2.5–3.0					0.1	38			38.1
2.0–2.5					27	43			70.0
1.5–2.0				0.1	115	5			120.1
1.0–1.5				6	220	1			227.0
0.5–1.0				236	145	1			382.0
0.0–0.5	1		1	113	14	0.1			129.2
Sum:	1.0	0.0	1.0	355.1	521.1	111.1	10.4	0.3	1000

- maximum ice load
- dynamic ice load

The maximum ice load on the structure is found by estimating the most probable maximum thickness of the ice on the location of the offshore wind farm. This information is typically available from national weather and/or shipping institutes that have these data in records for several decades, giving a good maximum design estimate. The maximum stress can then be defined with an empirical formula for the crushing strength of ice:[8]

$$\sigma = 9.4 \times 10^5 (d^{-1/2} + 3|\theta|^{0.78}) \quad [15.23]$$

where:

σ = crushing strength (Pa)
d = crystal size (cm)
θ = temperature (°C)

When an ice floe drifts on the current through an offshore wind farm, the floe will break at more or less constant intervals: ice accumulates, pressure builds up against the structure until the crushing strength is reached (equation [15.22]). As the ice breaks, the structure will move in its natural frequency. When the breaking of ice occurs at the natural frequency or a multiple of the natural frequency, the structure will resonate significantly, causing increased bending stress.

The characteristic length of a floating ice sheet affected by the breaking process can be calculated as:

$$L_c = \left[\frac{Eh^3}{12\gamma(1-\nu^2)} \right]^{1/4} \quad [15.24]$$

where:

L_c = characteristic length (m)
γ = specific weight of water
ν = poisson's ratio of ice, typically 0.3

To reduce the ice loads on structures, ice cones are used. These are triangular-shaped steel or concrete rings that lift the ice up to help it break more easily, reducing direct vertical load on the structure.

15.9 References

1. Molenaar, D-P. Cost-effective design and operation of variable speed wind turbines. PhD thesis, Delft University of Technology. 2003.
2. Walker, J F and Jenkins, N. *Wind energy technology*. England: John Wiley & Sons Ltd. 1997.
3. Manwell, J F, *et al*. *Wind energy explained – Theory, design and application*. England: John Wiley & Sons Ltd. 2002.
4. Det Norske Veritas (DNV). *Design of offshore wind turbine structures*. DNV-OS-J101. 2004.

5. Vugts, J H. *Handbook of bottom founded offshore structures*. Lecture notes, Delft University of Technology. 2001.
6. van der Tempel, J. *Design of support structures for offshore wind turbines*. PhD thesis, Delft University of Technology, Section Offshore Engineering. 2006.
7. Cerda Salzmann, D J. *Dynamic response calculations of offshore wind turbine monopile support structures*. MSc thesis, Delft University of Technology, Section Offshore Engineering. 2004.
8. Michel, B. *Ice mechanics*. Québec, Canada: Les Presses de l'Université Laval. 1978.

16

Design, construction and installation of support structures for offshore wind energy systems

K. LESNY and W. RICHWIEN, University of Duisburg-Essen, Germany

Abstract: This chapter discusses design, construction and installation of support structures for offshore wind turbines. Structures fixed to the seabed are an appropriate choice for moderate water depths. However, with offshore wind energy expecting to move further offshore, flexible or floating structures will be more feasible than fixed ones. The design of the support structures is particularly influenced by the load characteristics resulting from the environmental impact, the variation of the site conditions within the wind farm and the available construction and installation facilities. The support structure is to be designed to withstand not only the controlling extreme event, but also the effect of continuous cyclic loading on its operating behaviour.

Key words: fixed support structures, flexible or floating structures, foundation design, cyclic loading, installation.

16.1 Introduction

Design and structural layout of support structures for offshore wind turbines is primarily influenced by their specific load characteristics and the available construction and installation facilities. In contrast to land-based turbines, the additional loading caused by waves and currents, ice and, if required, ship collisions must be taken into consideration. However, the dead weight of the slender turbines is extremely small compared to the horizontal loads and, if required, bending moments from the environmental impact, leading to very unfavourable load conditions.

The large number of offshore wind turbines planned per wind farm requires a high degree of prefabrication, but this is limited by the variation of the subsoil conditions within a wind farm. Construction and installation of the foundations further depend on the availability of the necessary facilities on land, and the offshore installation equipment. Installation work offshore is extremely weather-dependent which may lead to large costs when keeping the equipment available during downtime.

Against this background the basic concepts of design and construction of support structures for offshore wind turbines are presented in this chapter. In the first part, various support structures including their structural layout and bearing behaviour are introduced. The general design methodology and appropriate design concepts are outlined and the possibilities of foundation optimization are discussed

in the second part of this chapter. After that, installation techniques for the different foundation types are presented. The chapter ends with an outline of future trends and an overview of sources of further information.

16.2 Types of support structure

16.2.1 Classification

The support structure of an offshore wind turbine is commonly referred to as the foundation body embedded in or placed on the seabed, including the part of the structure that reaches above the waterline up to the level where the tower is connected. Support structures for offshore wind turbines can be classified into two groups:

1. structures fixed at the seabed
2. flexible or floating structures.

Fixed support structures are foundation concepts that have been adopted from the classical oil and gas industries (see Fig. 16.1), such as steel framework structures (e.g. jackets or tripods), gravity based foundations or suction buckets. Monopiles were also used for special structures in offshore engineering, and meanwhile they are the most frequently used foundation concept in the offshore wind industry.

The following discussion focuses on fixed support structures that are suitable for small to moderate water depths. With greater water depths the loading on the support structure increases and consequently its mass increases as well, which may result in an uneconomic design. Under such conditions the use of flexible or floating support structures may be more feasible. However, such structures are still in the prototype phase and therefore comprise future trends to be outlined in section 16.6.

16.2.2 Fixed support structures

The basic concepts, the fundamental bearing behaviour and some structural details of monopiles, gravity based foundations, steel framework structures and suction buckets are presented in the following.

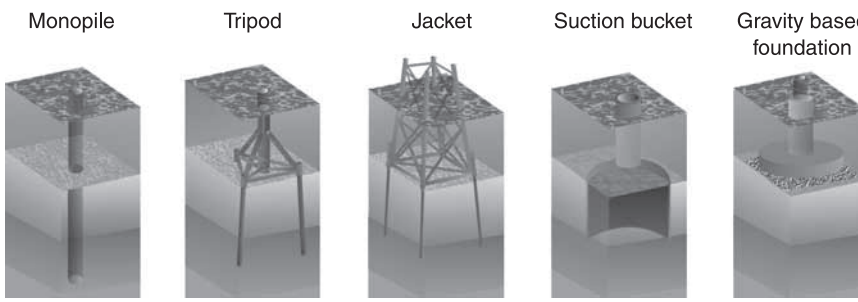

16.1 Fixed support structures for offshore wind turbines (Lesny, 2010).

16.2 Monopiles for the North Hoyle wind farm (© RWE Innogy GmbH).

Monopiles

Monopiles are usually steel pipe piles (see Fig. 16.2). They extend above the water level where the tower is connected with a so-called transition piece (see section 16.5.1).

Acting as an extension of the tower into the subsoil, the monopile is the simplest foundation solution, but at the same time it shows a very complex load transfer behaviour as it has to carry the whole environmental and operational loading. The loading is predominantly transferred into the subsoil by lateral bedding as the amount of vertical loading and torsional moments in contrast to horizontal loading and bending moments is very small. The pile head is freely supported and the pile is flexible with a full or partial restraint in the soil. This concept is depicted in Fig. 16.3. Near-surface soil layers with a sufficient bearing capacity are therefore of vital importance for the lateral load transfer.

Up to now monopiles have only been installed in water depths up to about 25 m with correspondingly moderate wave loading. Deeper water and the accompanying increase in loading, as well as higher performance wind turbines, directly result in greater diameters and embedment lengths of a monopile and may lead to uneconomic and technically unfavourable design solutions.

Gravity based foundations

The classical form of a gravity based foundation is the caisson of reinforced concrete, steel or a composite. Caissons have a cellular design (see Fig. 16.4) and

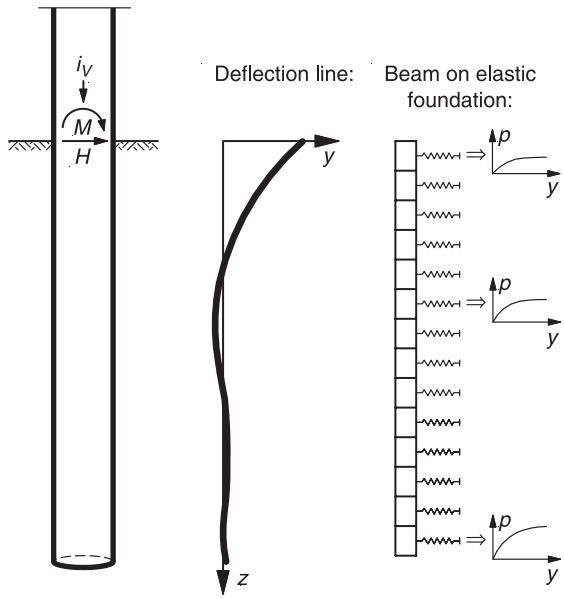

16.3 Load transfer behaviour of monopile foundations.

are, due to their compact structure, exposed to high hydrodynamic loading. Therefore they must have on the one hand a high volume to ensure the necessary floating stability, but on the other hand a large bulk. This means that a sufficient ballasting either with sand, gravel, concrete, ore or water is required for the later sinking and the load transfer during operation. The first tower segment is usually installed with a ring flange connection (see Fig. 16.4).

As with a monopile, a gravity based foundation transfers the whole structural loading into the subsoil. The loads are transferred by normal and shear stresses in the foundation base down to a depth that reaches between once and twice the diameter of the foundation (see Fig. 16.5). Soil layers with a sufficient bearing capacity from the surface down to great depths are therefore required when choosing a gravity based foundation.

In order to avoid erosion in the base area, gapping is not permitted if the caisson is placed directly on the soil surface (e.g. GL, 2005). In this case only compressive stresses can be transferred in the base area. To guarantee this, the contact area must be uniform and even, to ensure a close contact between the base of the foundation and the ground. Steel or concrete skirts, which are installed along the edge of the foundation base and penetrate into the soil during placement (see Fig. 16.5), prevent erosion in the foundation base and also improve the bearing capacity if they are sufficiently long.

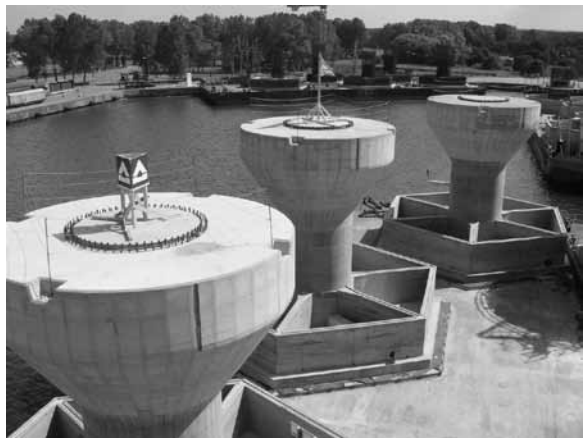

16.4 Fabrication of concrete gravity based foundations, for the Lillgrund wind farm, on special barges (© HOCHTIEF Construction AG, Civil Engineering and Marine Works, Hamburg, Germany).

Steel framework structures

Steel framework structures for offshore wind turbines are, for example, jackets or tripods. These structures are usually anchored in the seabed with piles, but in principle shallow foundations or suction buckets may also be used. A jacket

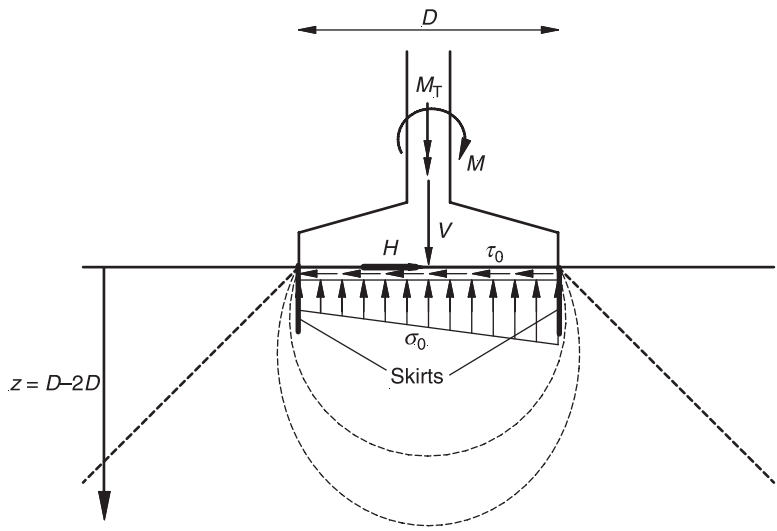

16.5 Load transfer behaviour and depth of influence for gravity based foundations.

usually has four supporting legs (Fig. 16.6) which are inclined to reduce the reaction forces and improve their dynamic behaviour.

A tripod structure (Fig. 16.7) comprises a main pipe and three legs. For a statically expedient layout of the nodes the water depth should be large enough so that the main nodes are below the wave influence zone (Dörfeldt and Bicker, 2004). Figure 16.8 shows a tripile which is a new type of structure developed specifically for offshore wind turbines. Here, the main node is located above the water level. The three foundation legs are welded to the tower structure with a supporting cross-piece of flat steel elements.

Due to the spread-out character of a steel frame the loads applied on the single foundation elements (e.g. the piles) are reduced, and the structure itself often has less bulk than a compact foundation. As a result, the foundation dimensions remain within feasible limits which makes them especially suitable for greater water depths or in cases of thick soft layers near the surface where other foundation concepts are not appropriate.

The single foundation elements are subjected to alternating tensile and compression loads and the bending moments applied to the structure. In the case of piles the compression piles transfer the loading by shaft friction and base resistance whereas the tension piles transfer the loading by shaft friction only (see Fig. 16.9). Horizontal loads are transferred by inclining the piles or by lateral bedding in the

16.6 Jackets for the test field Alpha Ventus (© DOTI 2009, Photographer: Mathias Ibeler).

16.7 Tripods for the test field Alpha Ventus (© C. Pohl).

case of vertical piles. However, due to the continuous change between tension and compression a loss of soil stiffness can occur, which impairs the dynamics of the whole structure (see Byrne and Houlsby, 2002). It is therefore often recommended to suppress the tensile forces by appropriate additional ballasting of the structure.

16.8 BARD Tripile foundation for the Hooksiel demonstration plant (© BARD Engineering GmbH).

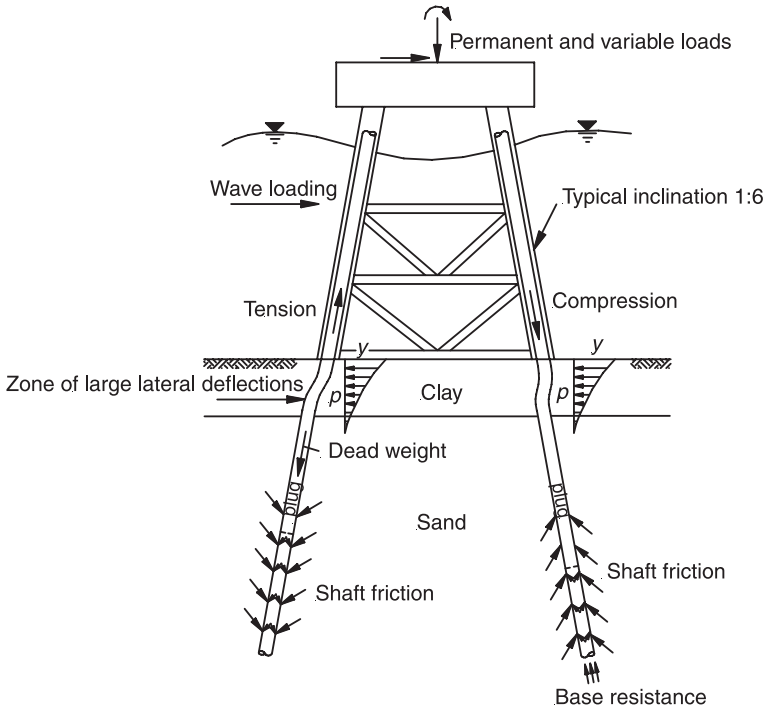

16.9 Load-bearing behaviour of a jacket foundation (Lesny, 2010).

Suction buckets

A suction bucket foundation is a steel cylinder which is closed at the top. It differs from the classical foundation concepts only in its unique method of installation as it is embedded into the soil by the creation of a vacuum inside the cylinder. Other than a suction bucket which corresponds to a shallow foundation, suction piles or suction anchors are also possible depending on the type of load transfer and the geometric dimensions (see Fig. 16.10).

In contrast to classical gravity based foundations the embedment zone of a suction bucket contributes to the load transfer as well. This prevents erosion in the base area and increases the safety, in particular against bearing resistance failure and sliding. However, a full contact between the suction bucket and the soil in the inside of the bucket is required. The contact area must therefore be grouted if necessary.

In principle, two variations of a suction bucket foundation are possible for offshore wind turbines: a single suction bucket foundation and a spread-out structure such as a jacket or tripod, which is founded on a number of suction buckets.

The capacity for tension loads, which is important in case of spread-out structures, primarily depends on the shear resistance in the embedment zone. Additionally, the tension loads create a negative pressure depending on the load

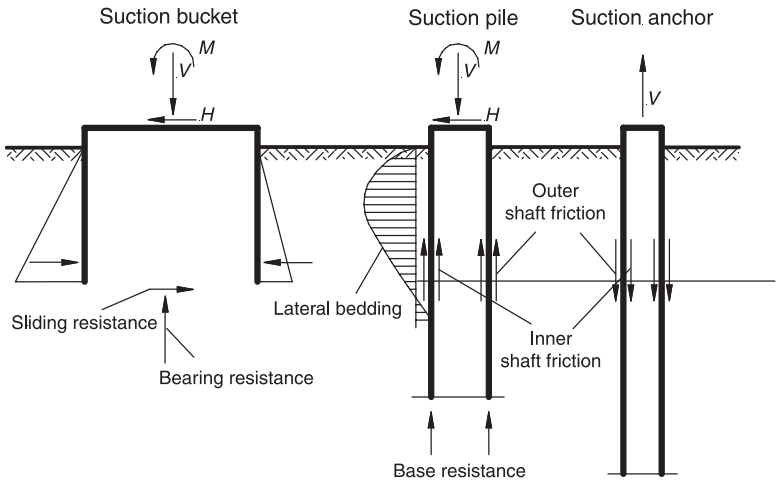

16.10 Load-transfer behaviour of suction buckets, suction piles and suction anchors.

frequency and the drainage conditions, which is limited by the cavitation of the pore water (see Tjelta, 1994; Bye *et al*., 1995; Kelly *et al*., 2003; Houlsby *et al*., 2005). This passive suction pressure has a decisive influence on the maximum tension resistance of cohesive soils in undrained conditions. However, vertical tension cracks and the simultaneous occurrence of horizontal and moment loading can impair the tension capacity (Andersen *et al*., 1993; Dyvik *et al*., 1993). In non-cohesive soils the passive suction pressure is induced by dilation depending on the initial density of the soil. As a result only a temporary increase in the tension capacity occurs as it vanishes due to drainage (Tjelta, 1995; Byrne, 2000).

A suction bucket foundation is a relatively new concept for offshore wind turbines. Up to now, it has been used only in Frederikshavn (Denmark) as a prototype for a Vestas V90 3.0 MW (see Fig. 16.11).

16.3 Design methods and techniques

16.3.1 Design concept

According to the relevant guidelines available for the design of offshore wind turbines (e.g. DNV, 2004; GL, 2005 with reference to API, 2000; BSH, 2007) the foundation has to be designed so that, under the influence of the environmental and operational loading, its stability over the operational life is guaranteed and the occurring deformations do not impair the serviceability of the turbine. As the design cannot be performed in a closed form usually a two-stage procedure such as the one presented in Fig. 16.12 is adopted (for details see Lesny, 2010).

In the first design stage the main dimensions of the foundation for the quasi-static loading resulting from an extreme event with a defined recurrence frequency

16.11 Prototype of a suction bucket foundation for a 3 MW offshore wind turbine in Frederikshavn (DK) (Ibsen, 2008).

are determined. For that, two limit states have to be verified. In the ultimate limit state an appropriate safety against the consequences of the extreme event has to be maintained, whereas in the serviceability limit state the allowable deformations of the structure, e.g. a maximum nacelle rotation, must not be exceeded.

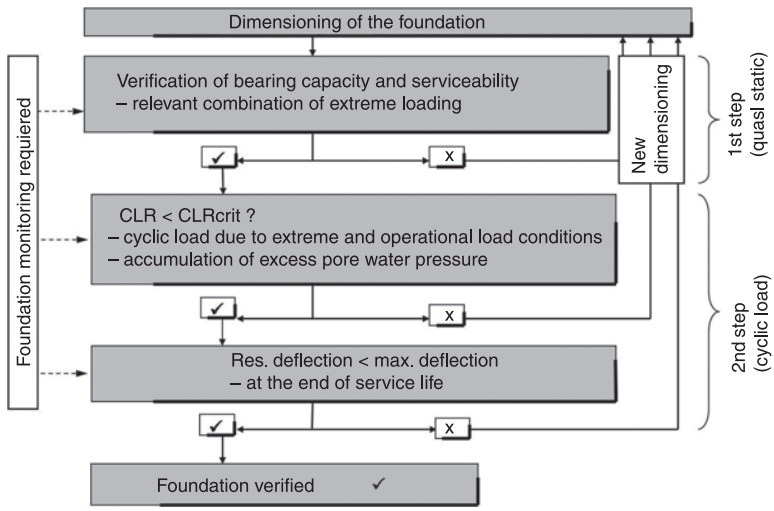

16.12 Two-stage design concept for the foundation of an offshore wind turbine.

In the ultimate limit state for each failure mode to be investigated, a limit state equation

$$E_d \leq R_d \qquad [16.1]$$

compares the design values of the effect of actions E_d with the design resistance R_d.

The design values of the effects of actions and the resistances are obtained from their characteristic values E_k and R_k by the application of partial factors which introduce the required safety level. Various procedures are possible to apply partial factors (for details see Eurocode 7, 2005, and a discussion in Lesny, 2009). A very straightforward approach is the application of partial factors (here: γ_F and γ_R) directly on the resultant effects of actions and resultant resistances:

$$E_d = E_k \cdot \gamma_F \qquad [16.2a]$$

$$R_d = \frac{R_k}{\gamma_R} \qquad [16.2b]$$

The safety factors are specified in the relevant design guidelines (e.g. GL, 2005; DNV, 2004).

The limit state equation for the serviceability limit state includes the comparison of the existing deformations with the allowable deformations without application of safety factors.

In the second stage, the operating behaviour of the foundation under continuous cyclic loading resulting from the environmental impact including intermittent extreme events is analysed. It is important to ensured that the allowable deformations of the structure are not exceeded over its expected lifetime.

Within this stage the extent to which the cyclic loading causes an accumulation of excess pore water pressure first has to be evaluated, since needs to be considered within the further design. It then has to be ensured that a progressive failure of the foundation under operating conditions does not occur. This is the case if a critical cyclic load ratio, which has to be defined for the foundation, is exceeded and the deformations no longer stabilize. If a progressive failure can be excluded, the accumulated deformations from the cyclic loading are calculated and compared with the limit value derived from the serviceability of the wind turbine.

16.3.2 Dimensioning the foundation

Monopiles

With a monopile foundation the design parameters are the diameter, the embedment length and the wall thickness. The standard design method is the *p-y* method which is based on the model of the beam on elastic foundation, idealizing the soil as a series of independent springs (see Fig. 16.3). In this model the nonlinear soil behaviour is considered by a nonlinear spring stiffness defined by the so-called

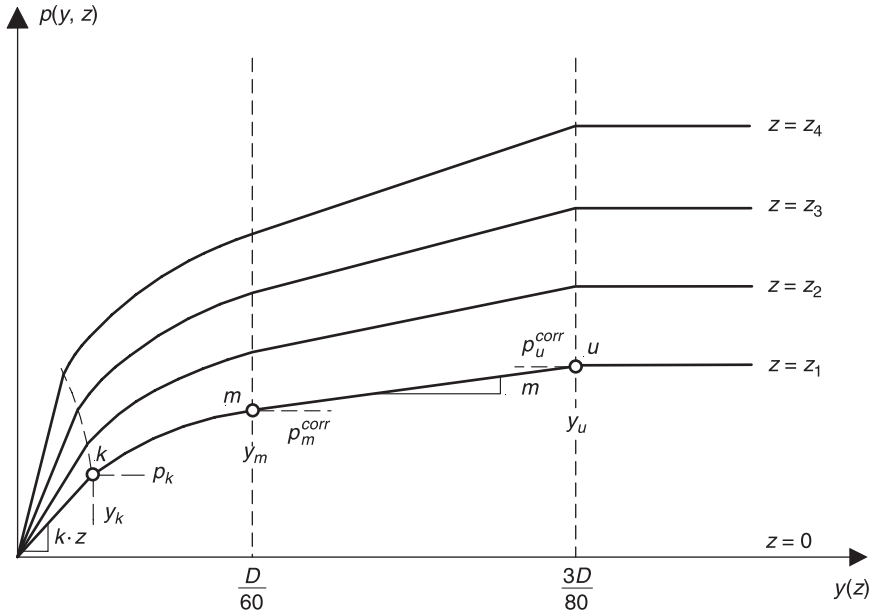

16.13 Qualitative progression of *p-y* curves for sand in various depths *z* according to Reese *et al.* (1974) (Lesny, 2010)

p-y curve which relates the subgrade reaction *p* to the horizontal displacement *y* in a certain depth *z* along the pile.

The *p-y* curves have been developed for various types of soil usually from a small number of field tests on piles with diameters of less than 1 m. Fig. 16.13 shows exemplarily the *p-y* curves developed by Reese *et al.* (1974) for sand.

The initial gradient $k \cdot z$ shown in Fig. 16.13 is related to the stiffness of the soil by the relationship $k = E_S/D$ where E_S is the oedometer modulus of the soil and D the pile diameter (Terzaghi, 1955). As the initial gradient increases linearly with depth z, a linear increasing soil stiffness is therefore assumed as well. The factor k is given, for example, in DNV (1992) as a function of the relative density of the soil and the corresponding angle of internal friction (see Fig. 16.14).

The corrected maximum subgrade reaction $p_u^{corr}(z)$ of the *p-y* curves shown in Fig. 16.13 is derived from the theoretical maximum subgrade reaction $p_u(z)$ which itself is based on two failure modes depending on the depth z along the pile (Parker and Reese, 1971; Reese *et al.*, 1974). In the near-surface area a three-dimensional earth pressure model, as shown in Fig. 16.15, is used.

In greater depths a two-dimensional failure model was used, in which the subsoil in the area of the pile is idealized by cubic elements (Fig. 16.16). This model is based on the assumption that only horizontal yielding occurs, but no vertical displacements. More details of the *p-y* method and an overview of various *p-y* curves are presented, for example, in Reese and van Impe (2001) and Lesny (2010).

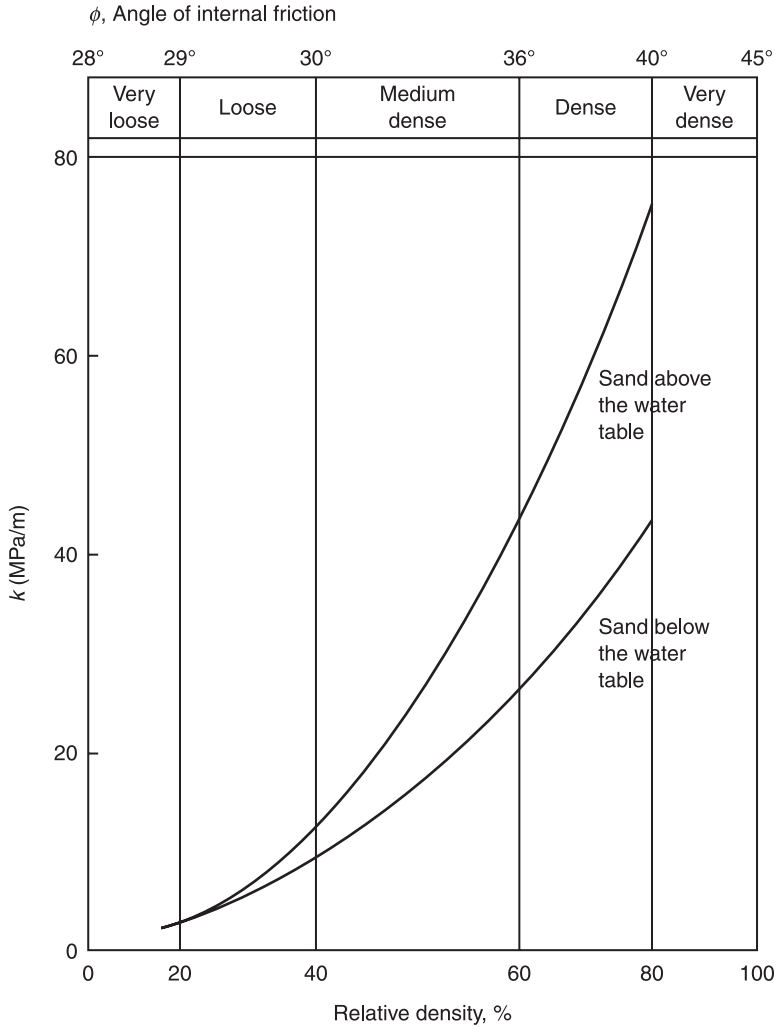

16.14 Factor k of the initial increase of the p-y curve for sand as a function of the angle of internal friction and the relative density (DNV, 1992).

The general applicability of this method for monopile diameters up to 6 m or even more in sandy subsoil as often encountered in the southern North Sea has been verified in a comprehensive finite-element analysis conducted by Wiemann (2007). However, it has also been shown in this study that the assumption of a linearly increasing soil stiffness with depth significantly overestimates the actual stiffness conditions around the tip of the monopile. As a consequence the pile length determined with the p-y method does not provide a sufficient restraint of

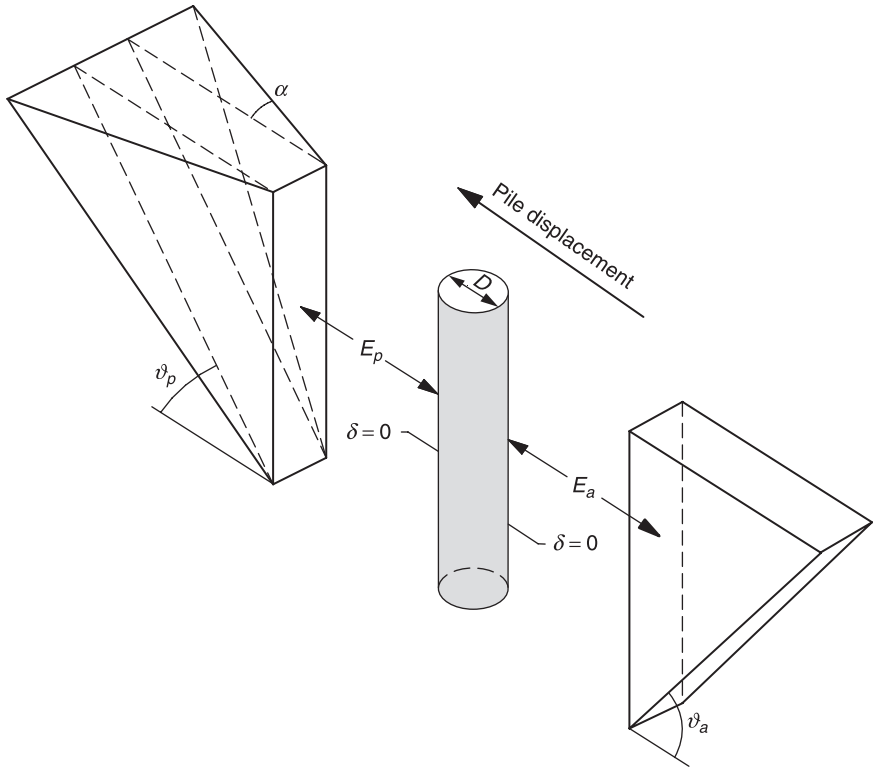

16.15 Failure model for calculating the maximum subgrade reaction for sand in the near-surface area according to Reese *et al.* (1974) (Lesny, 2010).

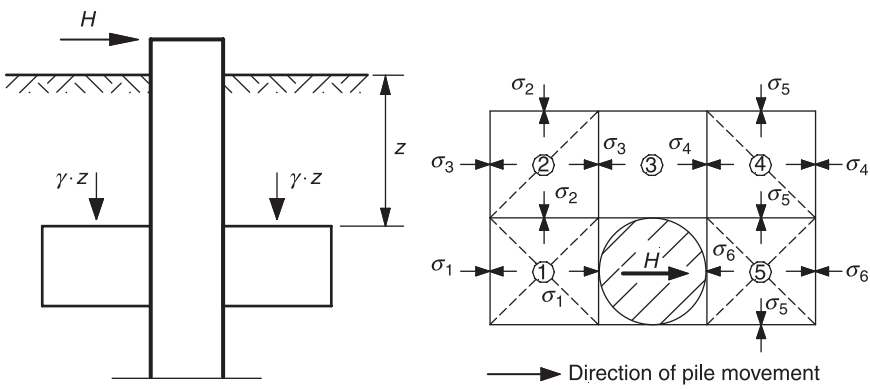

16.16 Failure model for calculating the maximum subgrade reaction for sand in greater depths according to Reese *et al.* (1974) (Lesny, 2010).

the pile in the soil. Wiemann showed that with a simple modification of the factor k a full restraint can be achieved:

$$k^*(D) = k_{ref} \cdot \left(\frac{D_{ref}}{D} \right)^{\frac{4(1-a)}{4+a}} \quad [16.3]$$

Empirical values for the exponent a are $a \approx 0.6$ for medium dense natural sands and $a \approx 0.5$ for dense natural sands. As a reference pile (with the parameters D_{ref} and k_{ref}) the pile tested by Reese *et al*. (1974) with a diameter of $D_{ref} = 0.61$ m was adopted.

However, the pile head displacements are not necessarily reduced by this modification and are still underestimated using the *p-y* method compared to the finite-element results (see Wiemann, 2007). Therefore, this method should be used with great care until further validation, especially by prototype measurements, is achieved.

Gravity-based foundations

The standard design methods for gravity based foundations comprise the classical bearing capacity formulae for shallow foundations and the approaches for calculating the foundation displacements and rotations. Design parameters are the base area $A = a \cdot b$ and, if the bearing capacity of skirts is to be taken into account, also the embedment depth of the skirts in the soil.

The characteristic bearing resistance $R_{n,k}$ of a gravity based foundation under drained conditions is defined as (Buisman, 1940; Terzaghi, 1954):

$$R_{n,k} = a \cdot b \cdot \left(\underbrace{\gamma_{2,k} \cdot b \cdot N_b}_{\text{self weight of soil}} + \underbrace{\gamma_{1,k} \cdot d \cdot N_d}_{\text{embedment depth}} + \underbrace{c'_k \cdot N_c}_{\text{cohesion}} \right) \quad [16.4]$$

The bearing resistance is a vertical resistance and is compared to the resultant vertical load in the base area in the framework of equation [16.1]. In equation [16.4] a and b are the length and the width of the foundation, d is its embedment depth, c'_k is the characteristic value of the effective cohesion and $\gamma_{1,k}$, $\gamma_{2,k}$ are the characteristic unit weights of the soil above and below the foundation base. N_b, N_d and N_c are dimensionless factors describing the contributions from the self weight of the soil, the foundation depth and the cohesion to the bearing resistance. These factors are themselves combinations of factors considering effects such as the shear strength of the soil beneath the foundation as a function of the angle of internal friction, the foundation shape, the presence of horizontal loading, and also the shear resistance in the embedment zone of the foundation, if applicable. The factors are tabulated, for example in DNV (1992, 2004), API (2000), Eurocode 7 (2005).

A bending moment loading is taken into account by the concept of the effective foundation area (Meyerhof, 1953; de Beer, 1963). In this concept the combination of bending moment and vertical load is replaced by an eccentric vertical load, and

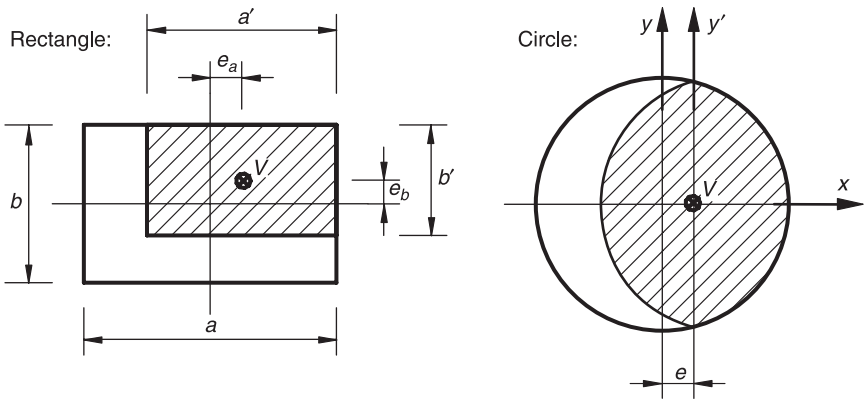

16.17 Concept of the effective foundation area (Lesny, 2010).

the area of the foundation is reduced until the vertical load acts centrically again (see Fig. 16.17). For a rectangular foundation the effective foundation area is:

$$A' = a' \cdot b' = \left(a - 2 \cdot e_a\right) \cdot \left(b - 2 \cdot e_b\right). \qquad [16.5]$$

In this case the real dimensions of the base area must be replaced by the effective ones within the bearing resistance calculation.

For undrained conditions the bearing resistance is:

$$R_{n,k} = a \cdot b \cdot \left(\gamma_{1,k} \cdot d + c_{u,k} \cdot N_c\right) \qquad [16.6]$$

In equation [16.6] it is assumed that the undrained shear strength $c_{u,k}$ is constant over the depth. However, with normally consolidated or only slightly over-consolidated soils the undrained shear strength increases with increasing depth which may affect the bearing resistance if the zone of influence reaches great depths (see section 16.2.2). This problem is discussed, for example, by Houlsby and Wroth (1983), Kusakabe *et al*. (1986), Tani and Craig (1995), Ukritchon *et al*. (1998) and Liyanapathirana and Carter (2005).

Under horizontal loading, sliding can further occur along the foundation base or along the tip of the skirts. Failure along the boundary of soft and firm soil layers is also possible. For drained conditions the characteristic horizontal sliding resistance $R_{t,k}$ is defined as:

shear plane in the soil: $$R_{t,k} = A \cdot c'_k + V_k \cdot \tan \varphi'_k \qquad [16.7a]$$

shear plane in the footing base: $$R_{t,\,k} = V_k \cdot \tan \delta_{S,k} \qquad [16.7b]$$

In equation [16.7] V_k is the characteristic vertical loading, c'_k and φ'_k, the characteristic values of effective cohesion and effective angle of internal friction, respectively. A is either the full or the effective foundation area in the case of moment loading. The parameter tan $\delta_{S,k}$ describes the roughness of the footing base and is usually assumed to be tan $\delta_{S,k}$ = tan φ'_k for foundations cast in-situ and

$\tan \delta_{S,k} = 2/3 \cdot \tan \varphi'_k$ for precast foundations. For undrained conditions the sliding resistance is:

$$R_{t,k} = A \cdot c_{u,k}. \quad [16.8]$$

In equation [16.8] $c_{u,k}$ is the characteristic value of the undrained shear strength of the soil. DNV (2004) limits the load inclination in this case to $H_k/V_k = 0.4$.

Bending moments may also cause an overturning of the foundation if the ground is sufficiently firm. However, as the point of rotation is difficult to calculate, the proof against overturning is often replaced by limiting the maximum load eccentricity (but see also DNV, 2004). The safety against uplift is, with offshore gravity based foundations, inevitably complied with – as a secondary condition – otherwise this type of foundation would not be practicable.

Vertical displacements and rotations are of particular interest for gravity based foundations. They are controlled primarily by the stress and deformation history, the actual stress level, the over-consolidation ratio of cohesive soils or the initial density of non-cohesive soils. Due to the resulting complex load–deformation behaviour of the foundation, most procedures are based on the isotropic elastic half-space theory, although the behaviour of the soil is known to be non-linear and the deformations are predominantly plastic. However, the assumption of linear-elastic behaviour is justified if the loading is small and far away from the failure state.

For homogeneous subsoil conditions, vertical displacements and rotations can be calculated, for example by closed form solutions available in the literature (see Poulos, 2001; Brown, 1969; Poulos and Davies, 1974).

However, the aforementioned approaches do not sufficiently describe the complex system behaviour of a gravity based foundation for an offshore wind turbine. More appropriate for this kind of problems are so-called system laws which have been developed in recent years (e.g. see Nova and Montrasio, 1991; Gottardi and Butterfield, 1995; Martin, 1994; Cassidy, 1999; Lesny, 2001; Kisse, 2008). System laws are based on a consistent description of the system behaviour of a shallow foundation under complex loading up to failure integrating both, the ultimate limit state and the serviceability limit state. Kisse and Lesny (2008) presented the general application of a system law to an offshore wind turbine.

For the proof of the penetration resistance of structural skirts and dowels, reference is made to, for example, DNV (1992) or Tjelta *et al*. (1986).

Steel framework structures

The design parameters of the axially loaded piles used to fix steel framework structures to the seabed are the pile diameter, the embedment length in the soil and the wall thickness.

The characteristic resistance of a compression pile in the ultimate limit state is calculated with the characteristic values of base resistance and shaft friction:

$$R_{1,k} = q_{b1,k} \cdot A_b + \int_z \left(q_{s1,k}(z) \cdot A_s(z) \right) dz \quad [16.9]$$

where $q_{b1,k}$ is the characteristic value of the pile base resistance, $q_{s1,k}(z)$ the characteristic value of the local pile shaft friction in depth z, A_b is the base area and A_s the shaft area of the pile referred to the relevant diameter. With tension piles only the pile shaft resistance is considered.

The characteristic value of the base resistance of cohesive soils in the defined contact area depends on the undrained shear strength $c_{u,k}$ of the soil:

$$q_{b1,\,k} = N_{c0} \cdot c_{u,\,k} \qquad [16.10]$$

The bearing capacity coefficient N_{c0} is usually assumed to be $N_{c0} = 9$. The base resistance of non-cohesive soil is:

$$q_{b1,\,k} = \sigma'_v \cdot N_{d0} \le q_{b1,\,k,\,\max} \qquad [16.11]$$

with the effective vertical stress σ'_v and the bearing capacity factor N_{d0}. Table 16.1 includes the bearing capacity factor N_{d0} and limit values of the base resistance $q_{b1,k,\max}$ for various types of soil.

The inner and outer shaft friction of the pile is determined either on the basis of total stresses (α-method), effective stresses (β-method) or as a combination of both (λ-method).

For cohesive soils the α-method is often used which is based on the undrained shear strength of the soil $c_{u,k}(z)$:

$$q_{s1,k}(z) = \alpha \cdot c_{u,k}(z) \qquad [16.12]$$

The parameter α is defined according to DNV (1992) and API (2000) as:

$$\alpha = 0.5 \cdot \left(\frac{c_{u,\,k}}{\sigma'_v} \right)^{-\psi} \le 1.0 \text{ with: } \Psi = \begin{cases} 0.5 & \text{for } c_{u,\,k} / \sigma'_v \le 1.0 \\ 0.25 & \text{for } c_{u,\,k} / \sigma'_v > 1.0 \end{cases} \qquad [16.13]$$

Table 16.1 Interface friction angle δ_k, bearing capacity factor N_{d0}, and maximum values of base resistance $q_{b1,k,max}$ and shaft friction $q_{s1,k,\max}$ in non-cohesive soils according to DNV (1992) and API (2000)

Soil	δ_k [°]	$q_{s1,k,max}$ [kN/m²]	N_{d0} [–]	$q_{b1,k,max}$ [MN/m²]
Very loose sand, loose sand-silt, medium dense silt	15	47.8	8	1.9
Loose sand, medium dense sand-silt, dense silt	20	67.0	12	2.9
Medium dense sand, dense sand-silt	25	81.3	20	4.8
Dense sand, very dense sand-silt	30	95.7	40	9.6
Dense gravel, very dense sand	35	114.8	50	12.0

In the β-method, which is used for non-cohesive soils but is assumed to be more suitable for cohesive soils as well (see Burland, 1973; Meyerhof, 1976), the shaft friction is derived from the effective overburden pressure σ'_v:

$$q_{s1,k}(z) = K \cdot \tan\delta_k \cdot \sigma'_v(z) = \beta \cdot \sigma'_v(z) \quad [16.14]$$

where K is the earth pressure coefficient and tan δ_k the interface friction angle which is usually $\delta_k \approx \varphi'_k$. For larger displacements, however, the residual shear strength of the soil is more appropriate, i.e. $\delta_k = \varphi_{res,k}$ (see Randolph, 1983). For normally consolidated soils K is derived from an increased earth pressure at rest K_0 (Meyerhof, 1976):

$$K = 1.5 \cdot K_0 \quad [16.15]$$

For over-consolidated cohesive soils Mayne and Kulhawy (in Randolph and Murphy, 1985) relate K to the overconsolidation ratio OCR:

$$K = 1.5 \cdot K_0 \cdot OCR^{\sin\varphi'_k} \quad [16.16]$$

For non-cohesive soils a simple definition of K is given in DNV (1992) and API (2000) with an upper limit of the shaft friction according to Table 16.1:

$$K = \begin{cases} 0.8 & \text{open pipe piles without soil plug} \\ 1.0 & \text{open pipe piles with soil plug or closed-ended pile} \end{cases} \quad [16.17]$$

In the λ-method (Vijayvergiya and Focht, 1972) the average shaft friction is a function of the average values of the effective vertical stress $\bar{\sigma}'_v$ and the undrained shear strength $\bar{c}_{u,k}$:

$$\bar{q}_{s1,k} = \lambda \cdot \left(\bar{\sigma}'_v + 2 \cdot \bar{c}_{u,k}\right) \quad [16.18]$$

The parameter λ is defined, for example, by Kraft *et al*. (1981), as a function of the pile-soil stiffness K_s:

$$\text{for NC clays: } \lambda = 0.178 - 0.016 \ln K_s \quad [16.19a]$$

$$\text{for OC clays: } \lambda = 0.232 - 0.032 \ln K_s \quad [16.19b]$$

$$\text{with: } K_s = \frac{\pi \cdot D \cdot q_{1s,k,\max} \cdot L^2}{(EA)_{pile} \cdot t_{\max}} \quad [16.19c]$$

where D and L are the pile diameter and embedment length, respectively, EA the axial stiffness of the pile, $q_{1s,k,\max}$ the maximum shaft friction and $t_{\max}$ the displacement necessary to mobilize it.

Beside these methods, procedures have been developed in recent years in which the pile bearing capacity is derived from site investigations. The best known procedures are based on the cone tip resistance $q_{c,k}$ measured in a cone penetration test (CPT).

With the CPT-based procedures it is assumed that the cone penetrometer corresponds to a model pile. The following values for base resistance and

shaft friction are recommended by, for example, Toolan & Fox (1977), Young (1991) and DNV (1992):

$$q_{b1,\,k} = \begin{cases} 0.7 \cdot q_{c,k} & OCR = 2-4 \\ 0.5 \cdot q_{c,k} & OCR = 6-10 \end{cases} \leq 15\,\mathrm{MN/m^2} \qquad [16.20a]$$

$$q_{s1,\,k} \approx \begin{cases} q_{c,k}/300 \leq 120\,\mathrm{kN/m^2} & \text{compression} \\ q_{c,k}/400 & \text{tension} \end{cases} \qquad [16.20b]$$

More detailed procedures for determining the pile bearing capacity are described in Jardine *et al*. (2005), Lehane *et al*. (2005), Clausen *et al*. (2005) and Kolk *et al*. (2005).

The CPT-based procedures are a clear improvement compared to the aforementioned standard design procedures. However, comparisons with the results of static pile load tests show that, especially with pipe piles, the results are influenced by the way that a possible plugging of the soil inside the pile is considered (see discussion in Jardine *et al*., 2005; Clausen *et al*., 2005; Lehane *et al*., 2005; Xu *et al*., 2005). As a result, it is currently difficult to reliably predict the pile bearing capacity with any of the procedures presented here.

For the consideration of possible pile group effects reference is made to, for example, Poulos and Davis (1980) for axially loaded piles and Brown *et al*. (1988), Remaud *et al*. (1998), McVay *et al*. (1998) amongst others for laterally loaded piles.

Suction bucket foundations

The design of suction bucket foundations under operating conditions is performed according to the design procedures either for gravity based foundations or for steel framework structures as introduced before, depending on the structural layout and the geometric dimensions of the suction buckets. The evaluation of the penetration resistance during installation is discussed by Houlsby and Byrne (2005a, 2005b) for non-cohesive and cohesive soils and by Feld (2001) for non-cohesive soils.

16.3.3 Analyzing foundation operating behaviour under cyclic loading

An operational life of 50 years is usually assumed for the foundation of an offshore wind turbine. Thus, the analysis of the operating behavior must consider the cyclic load effects during this time period including the occurrence of intermittent extreme events. All relevant guidelines require such an analysis, but do not specify how this evaluation may be performed. This is related to the fact that the foundation behaviour under cyclic loading is very complex and up to now no specific design procedure has established itself as an accepted method.

Cyclic loading causes an accumulation of plastic strains in the vicinity of the foundation (cyclic creep) which is often accompanied by hardening (in normally

consolidated clays or loose sands) or softening of the soil (in over-consolidated clays or dense sands). Additionally, excess pore water pressure may be accumulated, depending on the drainage conditions (system geometry, permeability of the soil and load frequency). Cyclic creep especially depends on the cyclic stress ratio, *CSR*, of the soil which is defined as:

$$CSR = \frac{\left(\sigma_1 - \sigma_3\right)_{cyc}}{\left(\sigma_1 - \sigma_3\right)_{max,\ stat}} \qquad [16.21]$$

where $(\sigma_1 - \sigma_3)_{cyc}$ is the cyclic deviator stress and $(\sigma_1 - \sigma_3)_{max,stat}$ is the deviator stress at failure under static conditions. Other influence parameters include the cyclic load amplitude, number of load cycles, load frequency and stress history.

For high *CSR*, the deformation increments increase and lead to a progressive failure of a soil element after very few cycles. If the *CSR* can be maintained sufficiently small, decreasing deformation increments with increasing number of cycles lead to a stabilization of the deformations and failure can only occur after a large number of cycles. Especially in cohesive soils, shakedown has been observed for very small *CSR* where the plastic increments reach zero after a certain number of cycles (see Fig. 16.18).

For laterally loaded piles *p-y* curves have also been established for cyclic loading, for example by Matlock (1970) and Reese *et al*. (1974), but these methods include only a flat deterioration of the curves. Dunnavant and O'Neill (1989) as well as Long and Vanneste (1994) suggested methods in which the *p-y* curves deteriorate depending on the number of cycles. However, these methods are based on tests with only a few load cycles, and effects such as soil hardening or softening are not (explicitly) considered. Especially for the large number of cycles to be considered for a monopile foundation an extremely unfavourable foundation performance is the consequence (see discussion in Lesny, 2010).

The influence of cyclic loading on the axial pile bearing capacity is often only roughly taken into consideration, for example by limiting the proportion of cyclic loads on the total loading or by a global reduction of the static pile bearing capacity

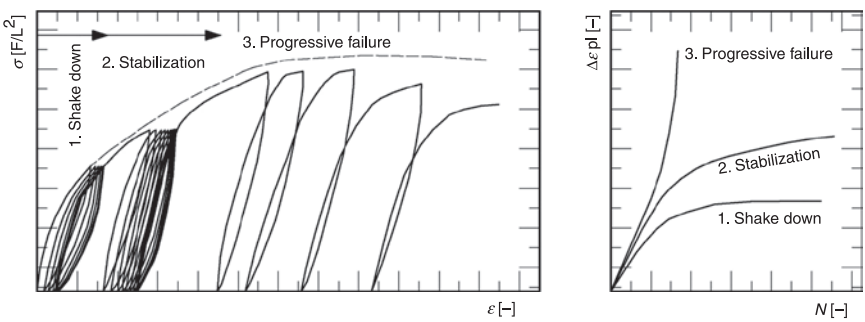

16.18 Soil behaviour under cyclic loading (Lesny and Hinz, 2009).

(e.g. Schwarz, 2002). Various authors use a rheological spring model similar to the one depicted in Fig. 16.3 by modifying the stiffness of the springs depending on the cyclic loading (e.g. Karlsrud *et al*., 1987; Karlsrud and Nadim, 1990; Swinianski and Sawicki, 1991). Poulos (1981, 1983) has developed a procedure for analyzing the pile bearing capacity on the basis of the boundary element method. In this method the influence of cyclic loading is taken into consideration by the degradation concept according to Idriss *et al*. (1978) which describes the changing shape of the hysteresis loop in a cyclic element test (see Fig. 16.19):

$$\delta = \frac{E_{SN}}{E_{S1}} = \frac{\varepsilon_{c1}}{\varepsilon_{cN}} = N^{-a} \qquad [16.22]$$

The behaviour of suction bucket foundations under cyclic loading has been analysed for example by Kelly *et al*. (2003), Houlsby *et al*. (2005), Jostad *et al*. (1997) and Clukey *et al*. (1995). An extended system law concept as mentioned in section 16.3.2 has been introduced by Byrne and Houlsby (2000) to numerically model the suction bucket behaviour under cyclic loading.

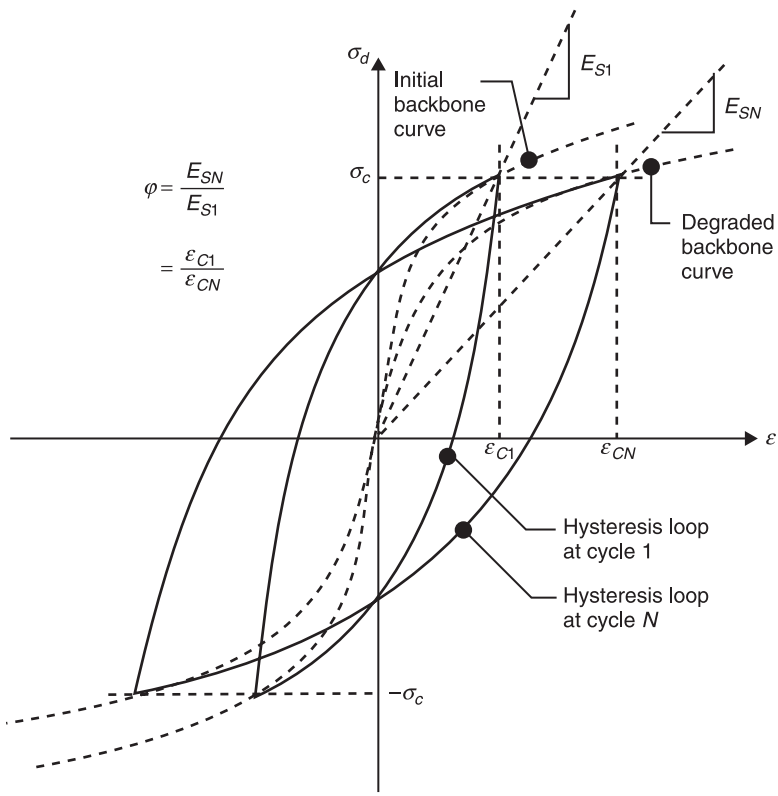

16.19 Hysteresis loop of the first and the *N*th cycle in a stress-controlled cyclic undrained triaxial test (Moses and Narasimha Rao, 2003).

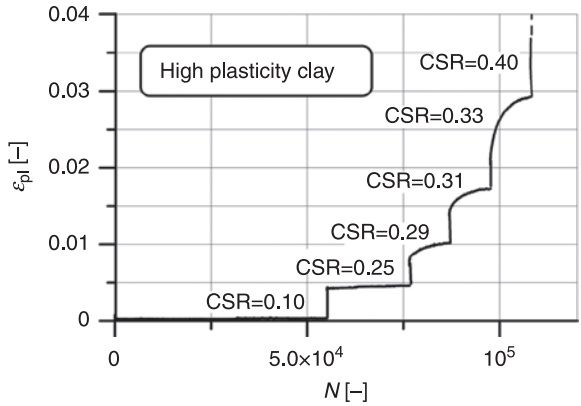

16.20 Results from a multistage triaxial test on high plasticity clay (Lesny and Hinz, 2009).

The operating behaviour of gravity based foundations has been investigated by, for example, England *et al*. (1997), Sawicki *et al*. (1998) and Craig (2004). The Norwegian Geotechnical Institute developed a design concept for gravity based foundations in cohesive soils which is based on a combination of soil mechanical element tests and standard design procedures to evaluate the foundation stability (see e.g. Andersen, 1976; Andersen and Lauritzsen, 1988; Andersen, 1992).

Hinz (2009) adopted this concept in a design procedure developed for monopile foundations. In this concept, cyclic multistage triaxial tests are used to investigate the soil behaviour under cyclic loading with varying load intensity. The results of such tests are exemplarily depicted in Fig. 16.20.

In Fig. 16.20 a stabilization of the plastic deformations can be observed at each CSR below the one which induces progressive failure. The accumulated plastic deformations can therefore be approximated for each CSR by a power law using the degradation concept in equation [16.22]. Stress levels with different cyclic stress ratios can be considered by the well-known Miner's rule (see Hinz, 2009).

The test results are implemented either in a finite-element routine or in a standard design method such as the strain wedge method developed by Ashour and Norris (1998) (see Hinz, 2009; Lesny and Hinz, 2009). With that, the accumulated plastic deformations of the soil can be calculated for an arbitrary number of cycles and for different stress levels.

16.4 Site-specific design optimization

16.4.1 Design criteria

The design of foundations for offshore wind turbines depends on various factors resulting either from the site-specific conditions at the wind farm or from the available construction and installation technology.

Foundation design is primarily affected by the subsoil conditions in the area of the wind farm. The subsoil conditions determine the general foundation concept, that is, if a shallow (e.g. a gravity based foundation) or a deep foundation (e.g. a jacket) is appropriate, and if a preparation of the seabed or further soil improvement measures is necessary. The available bearing capacity of the subsoil then determines the dimensions of the foundation depending on the actual loading.

However, an optimization of the foundation design is primarily limited to the spatial variability of the subsoil conditions in the wind farm. Homogenous subsoil characteristics, at least in parts of the wind farm, allow for a standardized design and a high degree of prefabrication and series production. Extensive site investigations are therefore fundamental to reliably identify the local subsoil conditions at each turbine location. From the results of the site investigations typical soil profiles may be determined which are the basis for developing suitable foundation concepts at an early stage of the design.

Besides the subsoil the water depth is a decisive criterion for the choice of an appropriate foundation type because an increase of the water depth directly leads to an increase of the resultant moments and uplift forces. Especially compact structures such as gravity based foundations or monopiles become uneconomic whereas spread-out structures, flexible or floating structures may become more feasible.

The available construction technology also affects the foundation optimization. This includes the method of construction and installation as well as the use of existing or new technologies. The prefabrication on land of the foundations for a large number of wind turbines requires sufficient construction facilities and storage areas in harbours or plants as close as possible to the wind farm location to minimize the costs for transportation across the sea.

Design and construction further depend on the available installation equipment. For example, the maximum monopile diameter which can be installed by pile driving to-date is limited to about six metres regardless of the soil conditions. The use of jack-up units is further limited to water depths of about 40 to 50 m maximum depending on the length of their legs and the bearing capacity of the subsoil.

In the design optimization, monitoring and repair during operation under offshore conditions also need to be considered as well as the later removal of the structure after the end of its operation which is usually a mandatory requirement for the approval of a wind farm.

16.4.2 Structural layout

An optimization of the structural layout of the foundation is primarily aimed to reduce the loading. For example, the wave load on a cylindrical structure increases disproportionately with its diameter (see e.g. Mittendorf *et al*., 2004). This is of special importance for monopile foundations due to their large diameter and their sensitivity to horizontal and bending moment loading. The wave load can be

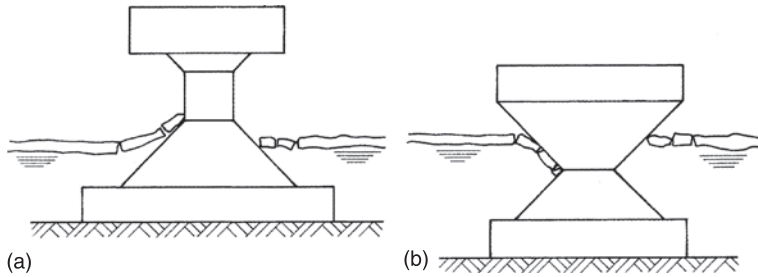

16.21 Conical structures: (a) upwards breaking cone, (b) downwards breaking cone (Wagner, 1990).

easily reduced by conically tapering the pile diameter from the seabed level up to above the wave zone.

The ice loading of an offshore wind turbine can be reduced by forming an ice cone at still water level. Figure 16.21 shows the two possible layouts, either forcing the ice breaking upwards or breaking it downwards. Usually a downward breaking ice cone is chosen, such as the one shown in Fig. 16.4 for the gravity-based foundations in the Lillgrund wind farm.

Scouring around the foundation, which particularly occurs in loose non-cohesive sediments, has an impact on the foundation bearing behaviour and therefore has to be considered within the optimization of the structural layout as well. As the prediction of the scour depth to be expected is very difficult (see discussion in Lesny, 2010) a scour protection is usually installed.

The simplest form of scour protection is the placement of a stone filling or of geotextile containers filled with sand or gravel (see Fig. 16.22). However, these measures have no filter effect, so colmation and suffusion can occur as well as contact erosion and secondary scouring at the edges of the scour protection. Washing away of individual stones or sacks by strong currents is also possible.

More suitable, therefore, are mineral or geotextile filters. Mineral filters comprise several fill layers with defined grading. Geotextile filters are flexible mats either of fabric or non-woven or a combination of both. They are covered by a protective layer of sand or gravel and weighted down by a stone filling. A filter must be mechanically and hydraulically stable and therefore follows certain filter rules as defined, for example, in Stein (1981), where other types of scour protection are discussed as well.

16.5 Foundation installation techniques

16.5.1 Installation of monopiles

Monopiles are prefabricated on land, loaded onto transport barges and towed to the location. It is also possible to seal the open piles and float them either

16.22 Geotextile containers as scour protection around a monopile (© Forschungszentrum Küste).

individually or together to the wind farm location. At the site, the piles are lifted out of the water or from the barge by a floating crane or from a jack-up unit and brought into position.

Monopiles are usually installed by above-water or underwater driving (see Fig. 16.23) where diameters of up to 4,5 m have been realized to date. Driving of larger diameter piles is possible provided there are suitable subsoil conditions (see also section 16.4.1). The pile is either driven with a guide or free-standing if the ground is stable enough. However, the pile can also be installed by a drive-drill combination with flushing or vibration support if the design embedment depth cannot be reached with pile driving alone. In very firm soils or rock, the placement of piles in predrilled boreholes and grouting of the space between pile and ground is another option.

Fig. 16.24 shows the installation of the transition piece on the monopile. The transition piece provides an access platform with ladders, a boat landing and the cable ducts for the underwater cables and allows for self-aligning between monopile and tower to ensure its verticality. The connection between monopile and transition piece is usually grouted.

16.23 Driving of a monopile with a jack-up unit (© RWE Innogy GmbH).

16.5.2 Installation of steel framework structures

Steel framework structures are prefabricated in a dry dock on land. Jackets are either placed on a barge and brought to the location or they are self-floated and towed in a horizontal position to the location. Tripods are usually towed in an upright position, so the floatability must be ensured by appropriately designed base pipes or buoyancy aids.

Floating cranes are used in shallow water to lift and position smaller steel frames from the barge (see Fig. 16.25). If necessary the steel frame is brought into an upright position by controlled flooding of its legs and the floatation aids with the support of the floating crane. It is then guided by the crane and placed on the seabed. Larger steel frames are launched from the barge into the water (for this procedure see e.g. Hsu, 1991). By controlled flooding and deballasting of individual pipe sections the steel frame is erected with a 90° turn and sunk by further flooding.

Especially in soft soils a steel frame is often placed on so-called mudmats which ensure a temporary seabed stability before the piles are installed. Mudmats are skirted steel sections, which penetrate the soil by the self-weight of the structure. The piles are then usually installed by pile driving (see section 16.5.1).

16.24 Transition piece installed by Van Oord at Q7, Prinses Amalia WP (© Van Oord Dredging & Marine Contractors).

16.5.3 Installation of gravity based foundations

Most gravity based foundations are constructed either fully or partly in a dry dock, a lock or a floating dock (see Fig. 16.26). For the transport of floatable structures the dock is flooded and the structure is then towed to the planned

16.25 Positioning and sinking of a jacket using a floating crane (© F + Z Baugesellschaft mbH, Hamburg).

16.26 Construction of gravity based foundations for the offshore wind farm Middelgrunden in a dry dock (© Middelgrunden Wind Turbine Cooperative).

16.27 Transport of a gravity based foundation to the location of the offshore wind farm Middelgrunden (© Middelgrunden Wind Turbine Cooperative).

location. The stability of the structure during transport must be verified (see Wagner, 1990; Clauss *et al*., 1988). Non-floatable structures are usually transported on barges (see Fig. 16.27).

Before installation, the seabed must be prepared. This includes the removal of soft top layers, the levelling and alignment of the seabed surface, the placement of a base layer or, if necessary, preloading or compaction of the ground. A coarse base layer or an additionally placed geotextile filter serves as a drainage to accelerate consolidation, especially in cohesive soils.

After positioning of the structure at the location the sinking process starts. Sinking is usually carried out by ballasting with water, and the controlled flooding of the caisson cells. The sinking of massive gravity based foundations is carried out by floating cranes.

The sinking of the structure is a critical process as an uncontrolled placement of the foundation on the seabed may lead to local stress peaks in the base that may cause damage to the foundation. Therefore, sinking requires calm weather, and the speed must be adjusted to the local conditions so that the foundation touches the seabed impact free. Additionally installed dowels serve as positioning aids and prevent the foundation from moving sideways (e.g. Eide and Larsen, 1976). After sinking, the space between the base plate and the seabed is, if necessary, grouted with underwater concrete or cement mortar and the caisson cells are ballasted with soil or other suitable material.

16.5.4 Installation of suction buckets

A suction bucket foundation is fabricated on land and towed to the location. For this purpose the suction buckets are either sealed and act as floats by themselves, or floatation aids are attached to the structure. In either case, barges and floating cranes are not necessary.

At the location the structure is placed on the seabed where the suction bucket first sinks by its self-weight to a certain depth into the soil. Because this process is to a large extent uncontrolled the structure must be placed as perpendicular as possible to avoid local stress peaks in the skirts when they touch the seabed.

After that, the water inside the bucket is pumped out creating a negative pore water pressure (suction). However, this is only possible if, during penetration under self-weight, a full contact is established between soil and skirts to avoid the forming of flow channels along the skirts and the subsequent erosion.

In non-cohesive soil the suction causes a flow from the outside to the inside which reduces the effective stresses inside the suction bucket to almost nill. Thus the resistance in the base area of the bucket and the shaft friction on the inner wall are reduced, and the soil is loosened up. At the same time a hydrostatic pressure difference inside/outside is created. All these effects induce further penetration of the suction bucket into the seabed (see Fig. 16.28).

In cohesive soils, where almost no flow develops, the hydrostatic pressure difference is the decisive factor besides self-weight and ballast. Much greater suction stresses are thus needed for the suction bucket to penetrate the soil.

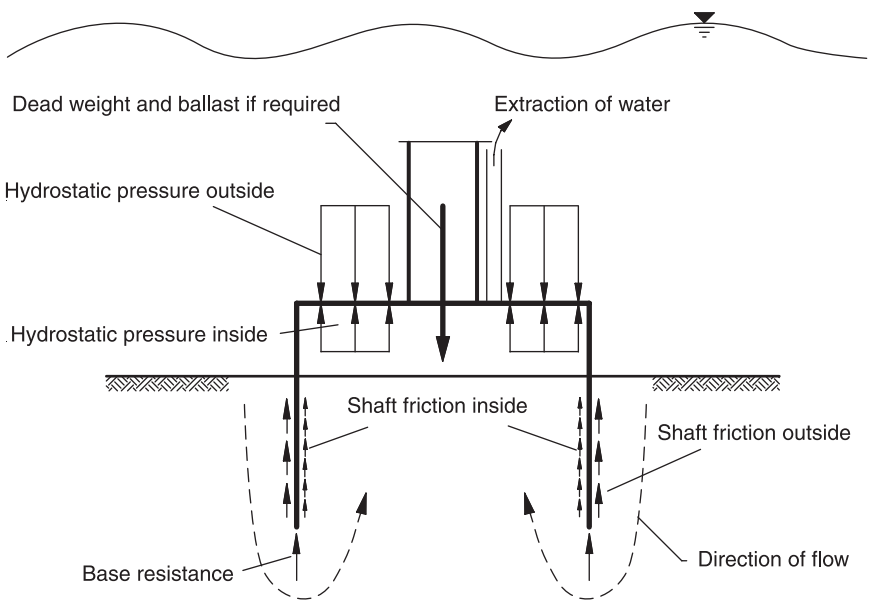

16.28 Installation of a suction bucket foundation (Lesny, 2010).

Ring stiffeners are attached to the inside of the suction bucket in order to avoid buckling of the skirts. Buckling may result from manufacturing imperfections or by elastic deformations when placing the suction bucket on the seabed and is enforced by the changed stress state around the bucket due to the induced flow (see Tjelta, 1995).

The maximum achievable penetration depth of a suction bucket in non-cohesive soil is limited to ca. $H \approx D$ to avoid a global piping failure inside the suction bucket which occurs when the hydraulic gradient created by the suction exceeds a critical value (see Tjelta, 1995; Houlsby and Byrne, 2005b). In cohesive soil, failure can occur when the suction pressure applied is greater than the undrained shear strength of the soil and a soil plug is detached in the base area. Later on, cracks may impair the penetration process in firm cohesive soils (Houlsby and Byrne, 2005a).

16.6 Future trends

The foundation concepts introduced here are suitable for shallow to moderate water depths up to approximately 40–50 m (with steel framework structures). However, with the further exploitation of offshore wind energy, there will be the need to move further offshore where greater water depths are encountered. Fixed foundation concepts are no longer suitable here because with increasing water depth the loading also increases and as a consequence the structural dimensions and the installed masses may become too large. In this situation flexible or floating support structures may be a better choice. However, up to now only conceptual studies and a very few prototypes exist.

Flexible structures are, for example, guyed towers such as the one depicted in Fig. 16.29. Prestressed guy lead lines are connected at the level of the resultant external loading and anchored in the seabed with anchor piles, suction anchors or anchor plates. Between the guy lead lines fender lines are spanned, which would absorb the elastic energy in the case of a ship collision. Due to the flexibility of the structure, the loading – in particular the moment loading – is reduced (Clauss *et al*., 1988). Due to the guying, the maximum moment is located in the upper section of the tower. Down to this point the loads are statically determinate and are not influenced by water depth or wave load (Carey, 2002). The bending moment reduces to null at the foundation level, so that only the self-weight of the structure is transferred to the subsoil. This clearly reduces the dimensions of the foundation. Further on, the tower and the guying are only marginally influenced by the subsoil conditions allowing for a standardized design.

With floating support structures the floating body can be a semi-submersible, a buoy or a barge-type body (see Fig. 16.30). In the transport state semi-submersibles and buoys are at the height of the waterline. Before operation they are ballasted and sunk, so that only the superstructure is above water. With a tension leg platform, positioning and stabilization is reached with prestressed anchors (see

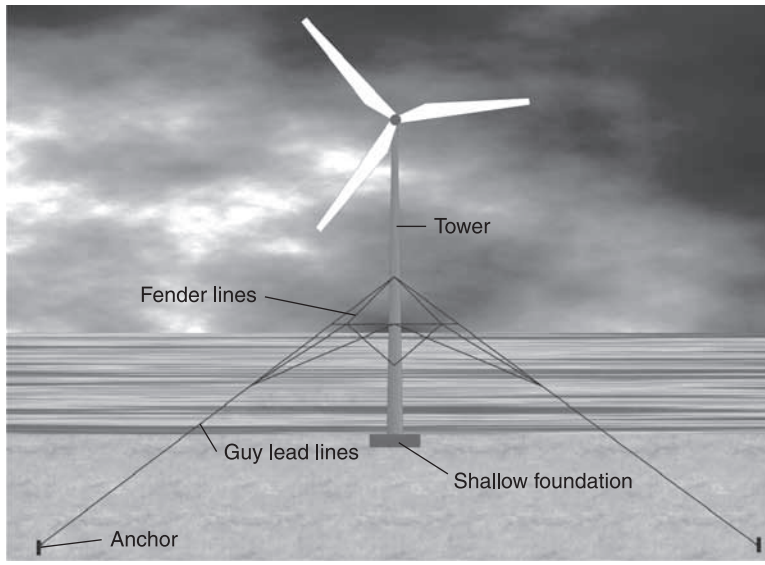

16.29 Concept of a guyed support structure according to Carey (2002) (Lesny, 2010).

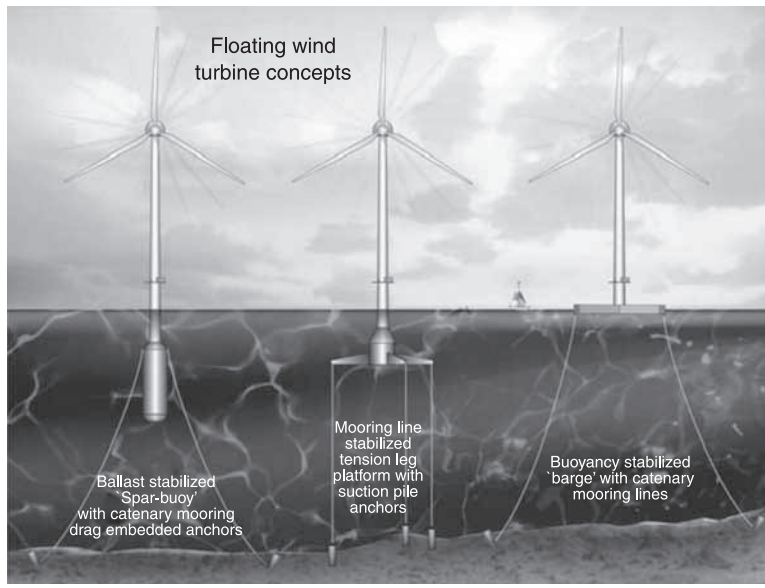

16.30 Concepts of floating support structures (Butterfield *et al.*, 2007).

16.31 Large-scale prototype tension leg platform (© Blue H Technologies BV).

Clauss *et al*., 1988). A prototype of a large-scale tension-leg platform was erected in 2007 in a water depth of more than 100 m in Italy (see Fig. 16.31).

Buoys are stabilized by ballast, whereas barge type structures are stabilized by buoyancy. These structures are positioned by flexible mooring. Anchoring in the seabed is done for all structures either with anchor piles or suction anchors.

In 2009, the first full-scale buoy type floating structure carrying a 2,3 MW wind turbine was installed north of Stavanger in Norway. The structure consists of a steel cylinder filled with a ballast of water and rock. It reaches 100 metres below the waterline and is moored to the seabed with three anchor piles. This concept is suitable for water depths of 120 to 700 metres (StatoilHydro, 2009).

16.7 Sources of further information and advice

A first evaluation of the available knowledge of foundation design for offshore wind turbines had been published by Wiemann *et al*. (2002). The current state of the art is presented in a handbook written by Lesny (2010) which provides further references to specific topics.

The design of laterally loaded piles is generally illustrated in Reese and van Impe (2001). The applicability of these methods to monopile foundations has been investigated by Wiemann (2007). Hinz (2009) evaluated the behaviour of monopiles under cyclic loading. CPT-based procedures for the design of axially loaded piles have been developed by Jardine *et al*. (2005), Lehane *et al*. (2005), Clausen *et al*. (2005) and Kolk *et al*. (2005). Suction buckets are the subject of various publications, for example by Byrne (2000), Houlsby *et al*. (2005) as well

as Houlsby and Byrne (e.g. 2005a and b). Regarding the design of gravity based foundations, reference is made to the numerous publications of the Norwegian Geotechnical Institute.

The certification societies such as the German Lloyd (see GL, 2005, and http://www.gl-group.com) or Det Norske Veritas (see DNV, 2004, and http://www.dnv.com/) have published guidelines which also address foundation design. Often reference is made to the recommendations published by the American Petroleum Institute (see API, 2000).

In Germany, the Federal Maritime and Hydrographic Agency has published standards for site investigations and design of offshore wind turbines (BSH 2007, 2008) which are mandatory for wind farms planned in the German Exclusive Economic Zone.

Various research groups or initiatives deal among others also with foundation design (e.g. GIGAWIND, ForWind, Fraunhofer-Institut fuer Windenergie und Energiesystemtechnik). Reference is also made to the following interest groups, associations and websites:

British Wind Energy Association (see http://www.bwea.com/)
Danish Wind Industry Association (see http://www.windpower.org/)
Deutsche Energieagentur (DENA) (see http://www.dena.de/)
Deutsches Windenergie Institut DEWI (see http://www.dewi.de),
European Wind Energy Association (see http://www.ewea.org/)
International Renewable Energy Agency (IRENA) (see http://www.irena.org/)
National Offshore Wind Association of Ireland (http://www.nowireland.ie/))
Netherlands Wind Association (see http://www.nwea.nl)
http://www.offshorewindenergy.org/
http://www.offshore-wind.de
http://offshorewind.net
http://www.offshorewindfarms.co.uk

The presented summary is not exhaustive.

16.8 References

Andersen, K H (1976), *Behaviour of Clay Subjected to Undrained Cyclic Loading*, Oslo, Norwegian Geotechnical Institute, Publication No. 114.

Andersen, K H (1992), *Foundation Design of Offshore Gravity Structures*, Oslo, Norwegian Geotechnical Institute, Publication No. 185.

Andersen, K H and Lauritzsen, R (1988), *Bearing Capacity for Foundations with Cyclic Loads*, Oslo, Norwegian Geotechnical Institute, Publication No. 175.

Andersen, K H, Dyvik, R and Schrøder, K (1993), *Pull-Out Capacity Analyses of Suction Anchors for Tension Leg Platforms*, Oslo, Norwegian Geotechnical Institute, NGI Publication No. 189.

API (2000), 'Recommended Practice for Planning, Designing and Constructing Fixed Offshore Platforms. Working Stress Design', *American Petroleum Institute*.

Ashour, M and Norris, G (1998), 'Undrained Laterally Loaded Pile Response in Sand', *Speciality Conference on Earthquake Engineering and Soil Dynamics*, Seattle, Paper No. 63, 1356–67.

Brown, P T (1969), 'Numerical Analyses of Uniformly Loaded Circular Rafts on Elastic Layers of Finite Depth', *Géotechnique*, Vol. 19, No. 2, 301–6.

Brown, D A, Morrison, C and Reese, L C (1988), 'Lateral Load Behavior of Pile Group in Sand', *Journal of Geotechnical Engineering*, Vol. 114, No. 11, 1261–76.

BSH (2007), 'Design of Offshore Wind Turbines', *BSH Nr. 7005*, Hamburg und Rostock, Bundesamt fuer Seeschifffahrt und Hydrographie.

BSH (2008), 'Ground Investigations for Offshore Wind Farms', *BSH Nr. 7004*, Hamburg und Rostock, Bundesamt fuer Seeschifffahrt und Hydrographie.

Buisman A S Keverling (1940), 'Grondmechanica', in: Klopper J, *Toegepaste Mechanica, Deel IV*, Delft.

Burland, J B (1973), 'Shaft Friction of Piles in Clay – A Simple Fundamental Approach', *Ground Engineering*, Vol. 6, No. 3, 30–42.

Butterfield, S, Musial, W, Jonkman, J and Sclavounos, P (2007), 'Engineering Challenges for Floating Offshore Wind Turbines', *Conference Paper NREL/CP-500-38776*, Golden, National Renewable Energy Laboratory.

Bye, A, Erbrich, C T, Rognlien, B and Tjelta, T I (1995), 'Geotechnical Design of Bucket Foundations'. *Proceedings of the 27th Offshore Technology Conference*, Houston, Texas, Paper No. OTC 7793, 869–83.

Byrne, B W (2000), *Investigations of Suction Caissons in Dense Sand*, Oxford, PhD Thesis, Magdalen College, University of Oxford.

Byrne, B W and Houlsby, G T (2000), 'Experimental Investigations of the Cyclic Response of Suction Caissons in Sand', *Proceedings of the Offshore Technology Conference*, Houston, Texas, Paper No. OTC 12194.

Byrne, B W and Houlsby, G T (2002), 'Investigating Novel Foundations for Offshore Windpower Generation', *Proceedings of the 21st International Conference on Offshore Mechanics and Arctic Engineering*, Oslo, Norway, Paper No. OMAE2002-28423.

Carey, J (2002), 'Guyed Support Structures for Offshore Wind Turbines', Hannover, *Tagungsunterlagen 2. Gigawind Symposium Offshore-Windenergie, Bau- und umwelttechnische Aspekte*.

Cassidy, M J (1999), *Nonlinear Analysis of Jack-Up Structures Subjected to Random Waves*, Oxford, PhD Thesis, University of Oxford.

Clausen, C J F, Aas, P M and Karlsrud, K (2005), 'Bearing Capacity of Driven Piles in Sand, the NGI Approach', in: Gourvenec S and Cassidy M, *Frontiers in Offshore Geotechnics*, London, Taylor & Francis Group, 677–81.

Clauss, G, Lehmann, E and Östergaard, C (1988), *Meerestechnische Konstruktionen*, Berlin, Springer.

Clukey, E C, Morrison, M J, Garnier, J and Corté, J.F (1995), 'The Response of Suction Caissons in Normally Consolidated Clays to Cyclic TLP Loading Conditions', *Proceedings of 27th Offshore Technology Conference*, Houston, Texas, Paper No. OTC 7796, 909–18.

Craig, W H (2004), 'Centrifuge Model Testing for Offshore Structure Research and Design', in: Triantafyllidis, T., *Cyclic Behaviour of Soils and Liquefaction Phenomena*, Leiden, A A Balkema, 355–62.

De Beer, E E (1963), Grundbruchberechnungen schraeg und ausmittig belasteter Flachgruendungen, VDI-Zeitschrift 105, part 1) Nichtbindiger Boden, No. 9, 372–80, part 2) Boden mit innerer Reibung und Kohaesion, No. 11, 453–60, part 3) Rein bindiger Boden, No. 15, 625–35.

DNV (1992), 'Foundations', *Classification Note 30.4*, Det Norske Veritas Classification A/S.
DNV (2004), 'Design of Offshore Wind Turbine Structures', *Offshore Standard DNV-OS-J101*, Det Norske Veritas Classification A/S.
Dörfeldt, S and Bicker, S (2004), 'Lastannahmen und Strukturanalyse eines Tripod Fundamentes', 3. Tagung Offshore Windenergie, Hamburg, Germanischer Lloyd, 51–67.
Dunnavant, T W and O'Neill, M W (1989), 'Experimental p-y Model for Submerged, Stiff Clay', *Journal of Geotechnical Engineering*, Vol. 115, No. 1, 95–114.
Dyvik, R, Andersen, K H, Hansen, S B and Christophersen, H P (1993), 'Field Tests of Anchors in Clay. I: Description', *Journal of Geotechnical Engineering*, Vol. 119, No. 10, 1515–49.
Eide, O T and Larsen, L G (1976), 'Installation of the Shell/Esso Brent B Condeep Production Platform', *Proceedings of the Offshore Technology Conference*, Houston, Texas, Paper No. OTC 2434.
England, G L, Dunstan, T and Wan, R G (1997), 'Drained Granular Material under Cyclic Loading with Temperature-Induced Soil/Structure Interaction', *Applied Mechanics Review*, Vol. 50, No. 10, 553–78.
Eurocode 7 (2005), DIN EN 1997-1: 'Entwurf, Berechnung und Bemessung in der Geotechnik – Teil 1: Allgemeine Regeln', Berlin, *Normenausschuss Bauwesen im Deutschen Institut für Normung e. V.* (German Version).
Feld, T (2001), '*Suction Buckets, a New Innovative Foundation Concept Applied to Offshore Wind Turbines*', Aalborg, PhD Thesis, Aalborg University.
GL (2005), Rules and Guidelines – Industrial Services, Hamburg, *Germanischer Lloyd Windenergie*, Edition 2005.
Gottardi, G and Butterfield, R (1995), 'The Displacement of a Model Rigid Surface Footing on Dense Sand under General Planar Loading', *Soils and Foundations*, Vol. 33, No. 3, 71–82.
Hinz, P (2009), 'Beurteilung des Langzeitverhaltens zyklisch horizontal belasteter Monopile-Gründungen', in: Richwien, W, *Mitteilungen aus dem Fachgebiet Grundbau und Bodenmechanik der Universitaet Duisburg-Essen*, Heft 37, Essen, VGE GmbH.
Houlsby, G T and Byrne, B W (2005a), 'Design Procedures for Installation of Suction Caissons in Clay and Other Materials', *Geotechnical Engineering*, Vol. 158, Issue GE2, 75–82.
Houlsby, G T and Byrne, B W (2005b), 'Design Procedures for Installation of Suction Caissons in Sand', *Geotechnical Engineering*, Vol. 158, Issue GE3, 135–44.
Houlsby, G T and Wroth, C P (1983), 'Calculation of Stresses on Shallow Penetrometers and Footings', *Proceedings of the IUTAM/IUGC Symposium of Seabed Mechanics*, 107–12.
Houlsby, G T, Kelly, R B, Huxtable, J and Byrne, B W (2005), 'Field Trials of Suction Caissons in Clay for Offshore Wind Turbine Foundations', *Géotechnique*, Vol. 55, No. 4, 287–96.
Hsu, T H (1991), 'Design and Dynamic Analysis of Offshore Platforms', in: Herbich, J., *Handbook of Coastal and Ocean Engineering*, Vol. 2, Oxford, Gulf Professional Publishing, Chapter 2, 55–144.
Ibsen, L B (2008), 'Keynote: NGM 2008: Implementation of a New Foundations Concept for Offshore Wind Farms', *15th NGM Sandefjord*, Norway, 19–33.
Idriss, I M, Dobry, R and Singh, R D (1978), 'Nonlinear Behavior of Soft Clays During Cyclic Loading', *Journal of the Geotechnical Engineering Division*, ASCE, Vol. 104, No. GT12, 1427–47.
Jardine, R J, Chow, F C, Overy, R and Standing, J (2005), *ICP Design Methods for Driven Piles in Sands and Clays*, London, Thomas Telford.

Jostad, H P, Andersen, K H and Tjelta, T I (1997), *Analysis of Skirted Foundations and Anchors in Sand Subjected to Cyclic Loading*, Oslo, Norwegian Geotechnical Institute, Publication No. 199.

Karlsrud, K and Nadim, F (1990), 'Axial Capacity of Offshore Piles in Clay', *Proceedings of the Offshore Technology Conference*, Houston, Texas, Paper No. OTC 6245, 405–16.

Karlsrud, K, Nadim, F and Haugen, T (1987), *Piles in Clay under Cyclic Axial Loading – Field Tests and Computational Modelling*, Oslo, Norwegian Geotechnical Institute, Publication No. 169.

Kelly, R B, Byrne, B W, Houlsby, G T and Martin, C M (2003), *Pressure Chamber Testing of Model Caisson Foundations in Sand*, Department of Engineering Science, University of Oxford, London, Thomas Telford.

Kisse, A (2008), 'Entwicklung eines Systemgesetzes zur Beschreibung der Boden-Bauwerkinteraktion flachgegruendeter Fundamente auf Sand – Darstellung des Single Surface Hardening Models', in: Richwien, W, *Mitteilungen aus dem Fachgebiet Grundbau und Bodenmechanik der Universitaet Duisburg-Essen*, Heft 34, Essen, VGE GmbH.

Kisse, A and Lesny, K (2008), 'Design of Offshore Structures Using the Single Surface Hardening Model', *Proceedings of the Second International British Geotechnical Association Conference on Foundations*, Dundee, 949ff.

Kolk, H J, Baaijens, A E and Vergobbi, P (2005), 'Results from Axial Load Tests on Pipe Piles in Very Dense Sands: The EURIPIDES JIP', in: Gourvenec, S and Cassidy, M, *Frontiers in Offshore Geotechnics*, London, Taylor & Francis Group, London, 661–67.

Kraft, L M, Focht, J A and Amerasinghe, S F (1981), 'Friction Capacity of Piles Driven into Clay', *Journal of the Geotechnical Engineering Division*, ASCE, Vol. 107, No. GT11, 1521–41.

Kusakabe, O, Suzuki, H and Nakase, A (1986), 'An Upper Bound Calculation on Bearing Capacity of a Circular Footing on a Non-Homogenous Clay', *Soils and Foundations*, Vol. 26, No. 3, 143–48.

Lehane, B M, Schneider, J A and Xu, X (2005), *A Review of Design Methods for Offshore Driven Piles in Siliceous Sand*, Perth, UWA Report GEO 05358.

Lesny, K (2001), 'Entwicklung eines konsistenten Versagensmodells zum Nachweis der Standsicherheit flachgegruendeter Fundamente', in: Richwien, W., *Mitteilungen aus dem Fachgebiet Grundbau und Bodenmechanik der Universitaet Essen*, Heft 27, Essen, Glueckauf.

Lesny, K (2009), 'Safety of Shallow Foundations – Limit State Design according to Eurocode 7 vs. Alternative Design Concepts', *Georisk*, Assessment and Management of Risk for Engineered Systems and Geohazards, Vol. 3, No. 2, 97–105.

Lesny, K (2010), *Foundations for Offshore Wind Turbines – Tools for Planning and Design*, Essen, VGE GmbH.

Lesny, K and Hinz, P (2009), 'Design of Monopile Foundations for Offshore Wind Energy Converters', in: Iskander, M, Laefer, D F, Hussein, M H, Contemporary Topics in Deep Foundations, Geotechnical Special Publication, No. 185, American Society of Civil Engineers, 512–519.

Liyanapathirana, D S and Carter, J P (2005), 'Undrained Bearing Capacity of Shallow Foundations on Structured Soils', in: Gourvenec, S and Cassidy, M, Frontiers in Offshore Geotechnics, London, Taylor & Francis Group, 451–57.

Long, J H and Vanneste, G (1994), 'Effects of Cyclic Lateral Loads on Piles in Sand', *Journal of Geotechnical Engineering*, Vol. 120, No. 1, 225–44.

Martin, C M (1994), *Physical and Numerical Modelling of Offshore Foundations under Combined Loads*, Oxford, Ph.D. Thesis, University of Oxford.

Matlock, H (1970), 'Correlations for Design of Laterally Loaded Piles in Soft Clay', *Proceedings of the Offshore Technology Conference*, Paper No. OTC 1204, Houston, Texas.

McVay, M, Zhang, L, Molnit, T and Lai, P (1998), 'Centrifuge Testing of Large Laterally Loaded Pile Groups in Sand', *Journal of Geotechnical and Geoenvironmental Engineering*, Vol. 124, No. 10, 1016–26.

Meyerhof, G G (1953), 'The Bearing Capacity of Footings under Eccentric and Inclined Load', *Proceedings of the 3rd International Conference on Soil Mechanics and Foundation Engineering*, Zuerich, Vol. 1, 440–45.

Meyerhof, G G (1976), 'Bearing Capacity and Settlement of Pile Foundations', *Journal of the Geotechnical Engineering Division*, ASCE, Vol. 102, No. GT3, 197–228.

Mittendorf, K, Nguyen, B and Zielke, W (2004), 'Seegang und Seegangsbelastung II', Hannover, *Tagungsunterlagen 3. Symposium Offshore-Windenergie, Bau- und umwelttechnische Aspekte*.

Moses, G G and Narasimha Rao, S (2003), 'Degradation in Cemented Marine Clay Subjected to Cyclic Compressive Loading', *Marine Georesources and Geotechnology*, Vol. 21, 37–62.

Nova, R and Montrasio, L (1991), 'Settlements of Shallow Foundations on Sand', *Géotechnique*, Vol. 41, No. 2, 243–56.

Parker, F and Reese, L C (1971), 'Lateral Pile-Soil Interaction Curves for Sand', *Proceedings of the International Symposium on the Engineering Properties of Sea-floor Soils and their Geophysical Identification*, University of Washington, Seattle, USA, 212–23.

Poulos, H G (1981), 'Cyclic Axial Response of Single Pile', *Journal of the Geotechnical Engineering Division*, ASCE, Vol. 107, No. GT1, 41–58.

Poulos, H G (1983), 'Cyclic Axial Pile Response – Alternative Analyses', *Proceedings of the Conference on Geotechnical Practice in Offshore Engineering*, ASCE, 403–21.

Poulos, H G (2001), 'Spannungen und Setzungen im Boden, in: Smoltczyk, U, *Grundbautaschenbuch, Band 1*, 6. Auflage, Berlin, Ernst & Sohn, Berlin, 255–305.

Poulos, H G and Davis, E H (1974), *Elastic Solutions for Soil and Rock Mechanics*, New York, John Wiley & Sons.

Poulos, H G and Davis, E H (1980), *Pile Foundation Analysis and Design*, New York, John Wiley & Sons.

Randolph, M F (1983), 'Design Considerations for Offshore Piles', *Proceedings of the Conference on Geotechnical Practice in Offshore Engineering*, ASCE, 422–39.

Randolph, M F and Murphy, B S (1985), 'Shaft Capacity of Driven Pipe Piles in Clay', *Proceedings of the 17th Offshore Technology Conference*, Houston, Texas, Paper No. OTC 4883, 371–78.

Reese, L C and van Impe, W F (2001), *Single Piles and Pile Groups under Lateral Loading*, Rotterdam, A A Balkema.

Reese, L C, Cox, W R and Koop, F D (1974), 'Analysis of Laterally Loaded Piles in Sand', *Proceedings of the Offshore Technology Conference*, Houston, Texas, Paper No. OTC 2080.

Remaud, D, Garnier, J and Frank, R (1998), Laterally Loaded Piles in Dense Sand: Group Effects, in: Kimura, Kusakabe and Takemura, *Centrifuge 98*, Rotterdam, A A Balkema, 533–38.

Sawicki, A, Swidzinski, W and Zadroga, B (1998), 'Settlement of Shallow Foundation due to Cyclic Vertical Force', *Soils and Foundations*, Vol. 38, No. 1, 35–43.

Schwarz, P (2002), 'Beitrag zum Tragverhalten von Verpresspfaehlen mit kleinem Durchmesser unter axialer zyklischer Belastung', in: Vogt, N and Floss, R, *Schriftenreihe des Lehrstuhls und Pruefamts fuer Grundbau, Bodenmechanik und Felsmechanik der Technischen Universitaet Muenchen*, Heft 33.

StatoilHydro (2009), Hywind – Factsheet. Available from: *http://www.statoil.com* [accessed 1 December 2009].

Stein, D (1981), *Kolkbildung und ihre Verhinderung an Offshore-Plattformen*, MRM Marine Rohstoffe und Meerestechnik, Band 5, Essen, Glueckauf.

Swinianski, J and Sawicki, A (1991), 'A Model of Soil-Pile Interaction owing to Cyclic Loading', *Canadian Geotechnical Journal*, Vol. 28, 11–19.

Tani, K and Craig, W H (1995), 'Bearing Capacity of Circular Foundations on Soft Clay of Strength Increasing with Depth', *Soils and Foundations*, Vol. 35, No. 4, 21–35.

Terzaghi, K (1954), *Theoretische Bodenmechanik*, 5. Auflage, Berlin, Springer.

Terzaghi, K (1955), 'Evaluation of Coefficients of Subgrade Reaction', *Géotechnique*, Vol. 5, No. 4, 297–326.

Tjelta, T I (1994), 'Geotechnical Aspects of Bucket Foundations Replacing Piles for the Europipe 16/11-E Jacket', *Proceedings of the 26th Offshore Technology Conference*, Houston, Texas, Paper No. OTC 7379, 73–82.

Tjelta, T I (1995), 'Geotechnical Experience from the Installation of the Europipe Jacket with Bucket Foundations', *Proceedings of the 27th Offshore Technology Conference*, Houston, Texas, Paper No. OTC 7795, 897–908.

Tjelta, T I, Guttormsen, T R and Hermstad, J (1986), 'Large-Scale Penetration Test at a Deepwater Site', *Proceedings of the 18th Offshore Technology Conference*, Houston, Texas, Paper No. OTC 5103.

Toolan, F E, Fox, D A (1977), 'Geotechnical Planning of Piled Foundations for Offshore Platforms', *Proceedings of the Institution of Civil Engineers*, Part 1, Vol. 62, 221–44.

Ukritchon, B, Whittle, A J and Sloan, S W (1998), 'Undrained Limit Analyses for Combined Loading of Strip Footings on Clay', *Journal of Geotechnical and Geoenvironmental Engineering*, Vol. 124, No. 3, 265–76.

Vijayvergiya, V N and Focht, J A (1972), 'A New Way to Predict Capacity of Piles in Clay', *Proceedings of the 4th Offshore Technology Conference*, Houston, Texas, Paper No. OTC 1718, 865–74.

Wagner, P (1990), *Meerestechnik*, Berlin, Ernst & Sohn.

Wiemann, J (2007), 'Bemessungsverfahren fuer horizontal belastete Pfaehle – Untersuchungen zur Anwendbarkeit der p-y Methode', in: Richwien, W, *Mitteilungen aus dem Fachgebiet Grundbau und Bodenmechanik der Universitaet Duisburg-Essen*, Heft 33, Essen, Glueckauf.

Wiemann, J, Lesny, K and Richwien, W (2002), 'Gruendung von Offshore-Windenergieanlagen – Gruendungskonzepte und geotechnische Grundlagen', in: Richwien, W, *Mitteilungen aus dem Fachgebiet Grundbau und Bodenmechanik der Universitaet Essen*, Heft 29, Essen, Glueckauf.

Xu, X, Lehane, B M and Schneider, J A (2005), 'Evaluation of End-Bearing Capacity of Open-Ended Piles Driven in Sand from CPT Data', in: Gourvenec, S. and Cassidy, M, Frontiers in Offshore Geotechnics, London, Taylor & Francis Group, 725–31.

Young, A G (1991), 'Marine Foundation Studies', in: Herbich, J, Handbook of Coastal and Ocean Engineering, Vol. 2, Chapter 7, 445–596.

17

Integrated offshore wind farm planning and design

M. B. ZAAIJER, Delft University of Technology, The Netherlands

Abstract: Designing for offshore wind energy is more challenging than for onshore wind energy, not least because it involves integration of several major elements from different suppliers. The chapter first describes the context in which the design activities take place and the context in which offshore wind farms have to operate. It then suggests several design tools and their use for site-specific offshore wind farm design and for the design of general-purpose elements that can be reused in various wind farms.

Key words: offshore wind farm design integration, systems engineering tools, offshore wind farm design context.

17.1 Introduction

In many ways, designing for offshore wind energy is more challenging than for onshore wind energy. For one, the harsh offshore environment raises demands on support structures, corrosion protection and climate control in the nacelle, while generally deteriorating working conditions. This generally doubles investment costs per kilowatt installed capacity compared to onshore wind farms, while higher wind speeds only compensate about half of that through increased electricity production. This increases the burden on designers to find optimal solutions, which is also more challenging than for onshore wind farms. The costs of an onshore wind farm are dominated by the wind turbine, so its optimisation can focus on that part of the system. Offshore, the wind turbines, support structures, electrical infrastructure, installation works and maintenance all provide significant contributions to the cost of energy. This means that optimisation involves many aspects, different design teams and tradeoffs involving different parts of the system. This emphasises the importance of integration for offshore wind farm design, which is the subject of this chapter.

Section 17.2 sketches the setting in which design and planning activities for offshore wind energy take place. It discusses the system elements and the involvement of people, and identifies various asynchronous processes and alternative forms of organisation that affect design integration. Section 17.3 provides the setting for design for offshore wind energy. Besides identification of the offshore conditions that dominate technology development for offshore wind energy, it discusses various non-technical issues that influence the design. The integration of design in a wind farm development project is treated in Section 17.4. Following the main steps in the design process, several methods are

suggested to support integration in these steps. Not all of the elements of an offshore wind farm are actually designed as part of a wind farm development project. For instance, the wind turbines are selected from a limited list of earlier designed and catalogued products. This complicates integration of the design activities of these elements, which precede the design of the wind farm. Nevertheless, Section 17.5 discusses possibilities for integration and makes observations of design in practice. Section 17.6 reflects on changes in the design context for offshore wind energy, developments in design organisation and methodologies and trends in design solutions. This chapter closes with sources of further information in Section 17.7.

17.2 Overview of the system, parties and processes

17.2.1 Components and procedures of an offshore wind farm

Figure 17.1 shows the elements of offshore wind farms as they are made to date. The level of detail chosen in the figure is such that it includes all current offshore wind farm designs, although some elements may be missing in particular farms.

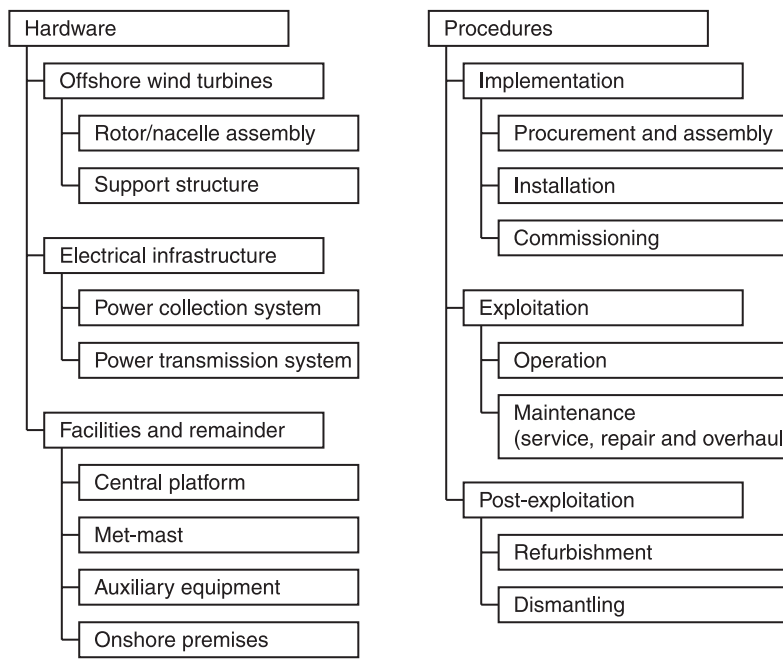

17.1 Generic breakdown of hardware and procedures of offshore wind farms treated in this chapter. Terminology based on van Rooij (2001).

This is not the only possible solution to contribute to fulfilling our energy needs using offshore wind energy resources. For instance, offshore production and transportation of hydrogen would also be a candidate solution. However, Fig. 17.1 defines the scope of interest for this chapter. Although many ideas presented in this chapter also apply to other possible solutions, the type of system given by Fig. 17.1 is used to provide examples and practical consequences of the abstract ideas.

17.2.2 People and communication

Parties involved

Parties that affect or are affected by the development of offshore wind farms are called the stakeholders. Although the stakeholders and their interrelationships can be different for different projects, Fig. 17.2 shows a typical diagram of the inner circle of stakeholders. The developer takes a central role in this diagram. The left-hand side of the diagram shows the parties that set the boundary conditions for the development; the right-hand side of the diagram shows the parties that are involved in realising the project and performing the procedures identified in the previous section. The latter stakeholders constitute the supply chain and perform the planning and design processes that precede the implementation.

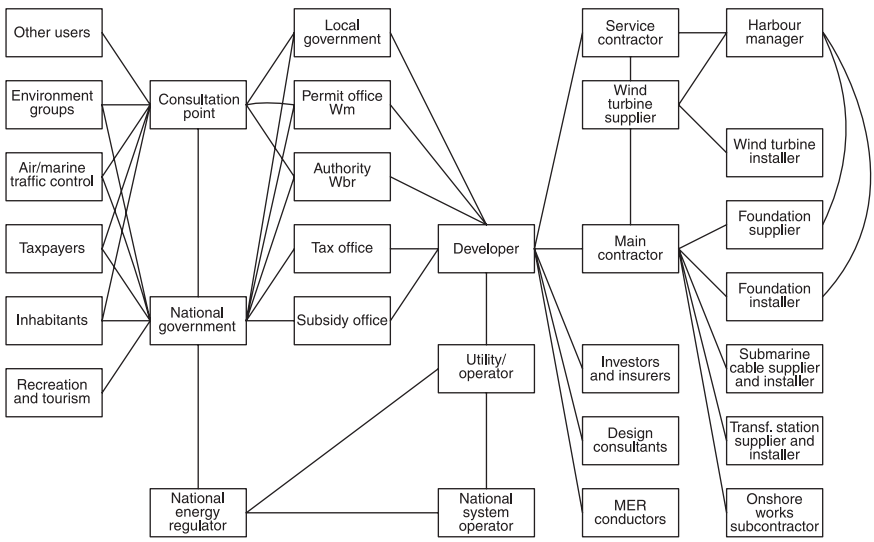

17.2 Stakeholders in the development of offshore wind farms in The Netherlands. Wm = Environmental Management Act, Wbr = Public Works and Water Management Act, MER = Environmental Impact Assessment (Dutch abbreviations). Adapted from unpublished material by E. H. M. Mast.

Communication, terminology, reference systems etc.

The people working in the supply chain have a wide range of different backgrounds and training. This means that they have a different frame of reference, which may lead to miscommunication. This applies to both informal and formal communication. In informal communication, terms such as foundation and turbine have multiple interpretations if the boundary of the subsystem is not specified. Terms such as hub height and water depth need a specification of the reference water level. Non-specialists may not be aware that wind directions express 'coming from', while wave directions express 'going to'. In formal communication, such as interfaces between software tools, coordinate systems need to correspond or proper transformations need to be applied. Turbine and offshore engineers consider the positive z-axis to point upward, while geotechnical engineers consider it pointing down. The origin of the coordinate system can be, for instance, at the seabed, lowest astronomical tide, mean sea level, the still water line or at the tower top. It can be fixed to the earth frame of reference or rotate with wind direction or nacelle direction. To avoid miscommunication and errors, it helps to set up clear definitions at the beginning of a project, such as is done by van Rooij (2001).

17.2.3 Design and planning processes in offshore wind energy development

Site-specific and general-purpose design

This chapter deals with integrated offshore wind farm planning and design. However, the development of an offshore wind farm is not a single process. The final stage in developing an offshore wind farm is the site-specific design initiated by the project developer. This design includes, for instance, selection of the site, definition of the farm layout, specification of support structures and formulation of installation procedures. These activities can be integrated. This stage also includes selection of, for instance, the rotor-nacelle assembly and installation equipment, which have been designed in preceding processes. Although it is theoretically possible to design these elements as part of a particular wind farm, this is not observed in practice. Turbines are designed as general-purpose components, which can be used in different wind farms. This is beneficial because the increased production volume reduces the costs and risks, while the disadvantage of not performing site-specific optimisation is small. Installation equipment is designed as a multi-purpose tool so that its costs do not have to be written off on just one project. The design processes of these elements cannot be synchronised with the site-specific design process. Because the design of these elements nevertheless has a large impact on the final performance of the wind farm, this chapter also discusses multi-purpose design in the context of the final application in an offshore wind farm.

Integration for different contractual structures

As mentioned in the previous section, the activities in site-specific design can be integrated. The possibilities of integration in practice are affected by the organisation of the project and in particular by the legal relations between the parties. Some types of relations stimulate cooperation and enable integration. This is, for instance, the case when two parties are divisions of the same company. Vertical supply chain integration, where parties that contribute to different parts of the implementation process merge in one company, is therefore positive for integration of planning and design. Close cooperation and integration usually implies sharing risks. At the other end of the spectrum, relations between parties in the supply chain can be arranged by contracts that apply to only one specific project. Contracts usually divide the risks and separate the planning and design processes of the involved parties.

Opportunities for integration of overall planning and design depend on the contractual arrangement implemented by the project developer. Table 17.1 shows three types of arrangements used in previous developments. A consortium enables a high level of integration when it contains the main suppliers. Since the members carry responsibility in the project together, they can share and divide the work and risks as the project moves along. However, the solutions are likely to be fixed by the standard technologies of the partners. In multi-contracting, the project developer takes the responsibility for the overall design. This provides the opportunity for design integration, while at the same time keeping all options open. Based on the overall design solution, the project developer contracts the suppliers that further detail the design based on the provided interface definitions. This approach requires a high level of knowledge about offshore wind farm design on the part of the developer. When the project developer hires a general contractor, who is responsible for the main aspects of implementation and perhaps operation, the general contractor becomes the central party for planning and design. The general contractor can be a consortium or arrange its contribution through multi-contracting, leading to similar opportunities for integration as mentioned previously, albeit within the restrictions set by the project developer.

Table 17.1 Contract arrangement for several realised offshore wind farms

Wind farm	Year of installation	Contract type
Nysted, DK	2003	General contractor
Kentish Flats, UK	2005	General contractor
Barrow, UK	2006	Consortium
Burbo Bank, UK	2007	Multi-contracting
Q7, NL	2007	Multi-contracting

Data taken from Kleineidam (2007).

Parallel process of strategic planning and design

Strategic planning and design are both processes that eventually lead to decisions about which actions to take. There is a great deal of interaction or overlap between these processes and they are not always clearly separated. Strategic planning deals with high level aspects such as needs and values in the context of the company's longer-term interests. Design deals with more practical and technical aspects such as form, properties and functions (Roozenburg and Eekels, 1995). Both processes can proceed along various lines, but some more or less generic steps can be observed. Figure 17.3 illustrates these steps and indicates which intermediate results of the design process are needed for strategic planning (for a multi-contracting approach). The figure also shows that the strategic planning process adjusts the requirements and targets for the design process. The overall project planning should identify and synchronise the milestones for both processes, specifying the needed information exchange.

17.3 Design and context of offshore wind farms

17.3.1 Fundamentals of the design process

Before going into details of design for offshore wind energy, this section discusses the fundamentals of design. This clarifies terminology used in the rest of this chapter and provides an appropriate mindset.

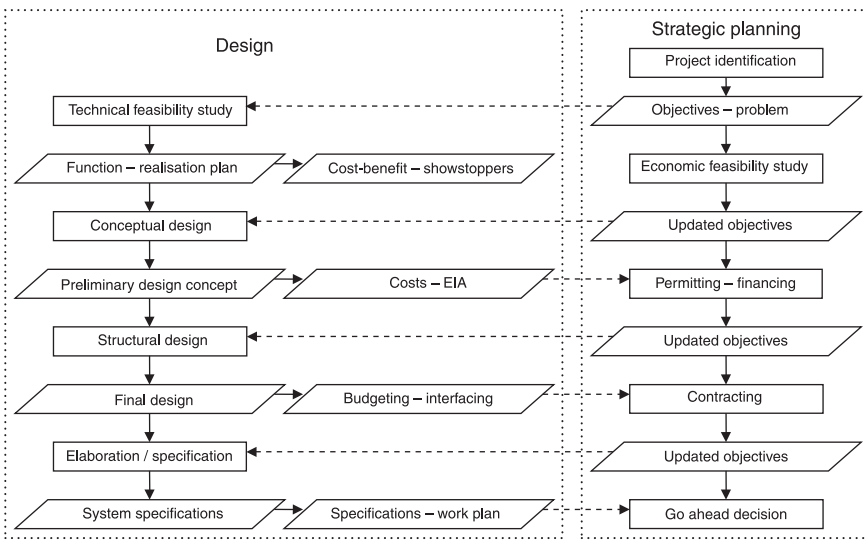

17.3 Generic steps in the design process and data needed for the strategic planning process. Left-most column adapted from Kühn *et al.* (1998a).

Design is a process to determine which actions to undertake to achieve a purpose. It starts with a desire to change what is happening in the world from its natural course and ends with a blueprint for action. The blueprint usually describes how to manufacture hardware and procedures for its use. The basic steps of this process are shown in Fig. 17.4.

Figure 17.4 indicates that design is not a sequential process from needs to blueprint, but includes iterations. Particularly, unsatisfactory designs may lead to synthesis of new solutions or even revisiting requirements that may appear unfeasible or undesirable. Furthermore, the iterations lead to inclusion of ever more detail. Most research, textbooks, design tools and other elements of the knowledge base for offshore wind energy focus on simulation and evaluation, which are closely related to the natural and behavioural sciences. In contrast, this chapter deals with all the steps in the design process and with the flow of the entire process.

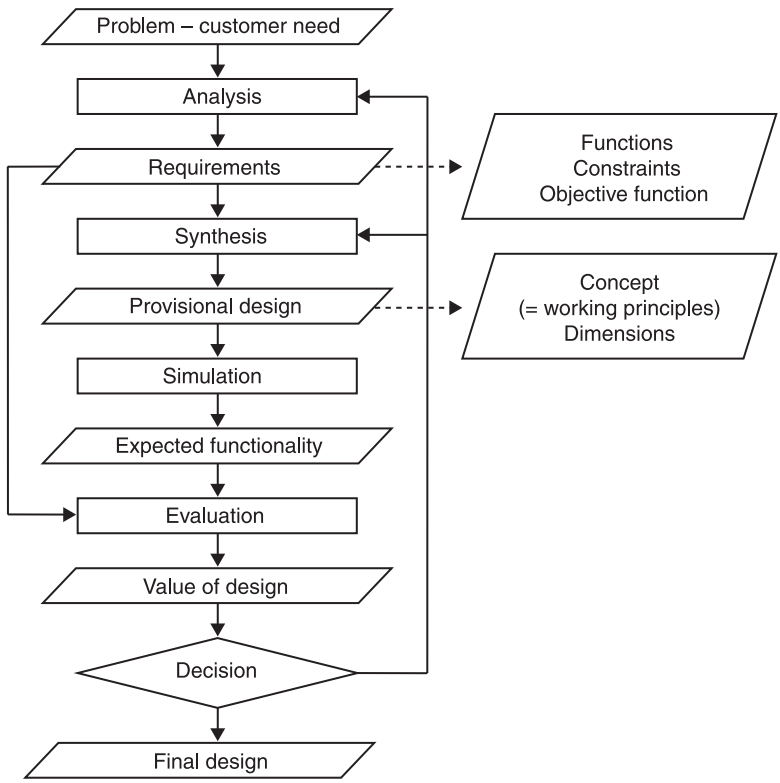

17.4 Basic steps and information in a design process. Adapted from Roozenburg and Eekels (1995).

As evidenced by the feedback and feed forward arrows, the requirements play a pivotal role in the process. They can be further divided into three categories: functions, constraints and the objective function. The first category specifies what type of behaviour is desired. The desired functions are related to the synthesised solutions through working principles. This chapter will use the term 'concept' to indicate the description of the solution that reveals these working principles. The second category specifies what is and what is not allowed. This may include a description of unacceptable behaviour, but most constraints are expressed as limits or ranges for certain properties of the solution. Constraints for parameter values are related to the design solution through dimensioning; any set of dimensions of the design solution for which the constraints are met represents and acceptable solution. Finally, the objective function expresses how acceptable solutions are ranked. The design process aims to optimise the objective function, subject to the constraints and the available design resources. How well a solution scores in terms of the objective function is often called its performance.

17.3.2 Differences between onshore and offshore wind energy

Different conditions

When going offshore, several conditions change from the onshore situation. The most significant changes to the environment in which the wind farm is applied are indicated in Table 17.2. To understand how these different conditions affect the design solutions their effect on the functions, constraints and objective function needs to be understood. The effect on each of these three categories of requirements is treated below.

Changed functions, working principles and concepts

The functions relating to the primary process, conversion and transportation of energy remain unchanged. The environment imposes no fundamental reasons to

Table 17.2 Different conditions for onshore and offshore wind farms

	Onshore	Offshore
Surface conditions	Land (with obstacles)	Water
Wind climate	'Low' wind speed/ 'high' turbulence	'High' wind speed/ 'low' turbulence
Air conditions	Mild/dry	Salty/moist/corrosive
Biological environment	Mainly birds	Birds/fish/mammals/ benthos
Societal environment	Inhabited areas/industrialised areas/landscapes	Shipping/exploitation/ nature reserves

use other working principles for these functions and therefore the concepts used in onshore wind farms can also be applied in offshore. In effect, offshore wind turbines and electrical infrastructure show great resemblance with their onshore equivalents.

The functions to support the energy converter and the electrical infrastructure also remain the same in offshore, but in this case new potential working principles emerge. As for onshore support structures, the loads can be transferred directly to the fixed earth, but the sea enables the ability to use buoyancy for a floating support structure concept. Although such concepts are new for wind energy, the working principle has previously been used for other offshore applications.

The offshore procedures are most affected by the environment. Logistic functions such as transport of people and hardware, and enabling access and installation are the same as onshore, but the sea surface demands totally different working principles. Because similar functions are required for other offshore applications, working principles and concepts can be copied to some extent.

Changed constraints and dimensions

The largest changes in the formulations and values for the constraints are seen in the following consequences of the offshore environment:

- no obstacles for logistics;
- hydrodynamic and ice loading;
- other wind loading (parametric change of wind speeds and turbulence);
- other material deterioration (more corrosion);
- less noise restriction;
- less and other visual impact restriction;
- less and other spatial restrictions;
- siting constraints to limit effects on nature.

Examples of clear responses to these changes are pre-assembly of large subsystems before offshore transport and installation, stronger support structures, sealing of the nacelle, increased tip speeds (better energy conversion but higher noise), array arrangements (instead of line arrangements) and more turbines per farm. Because the working principles and physics are known from onshore wind energy and other offshore applications, assessing whether a solution meets the constraints can be based on existing knowledge. Nevertheless, for proper dimensioning this knowledge and the simulation tools have to be adjusted for offshore wind energy.

Changed objective function

The performance of a wind farm can be measured against many criteria, such as its contribution to the electricity supply, its power quality and its impact on the

environment. Invariably most weight is attached to the cost of energy. This is not different offshore or onshore. However, the value of and contributions to this performance indicator differ significantly for the two situations. As a ballpark figure, the cost of energy from an offshore wind farm is about 1.5 times higher than that of a wind turbine at a good onshore location. This emphasises the need for proper optimisation. Figure 17.5 shows the difference in the cost distributions. Since costs of an offshore wind farm are evenly spread over several main contributions, optimisation of an offshore wind farm cannot focus on a singular aspect. Because of the interactions between the elements, optimisations cannot be performed per element, but have to be done from a systems perspective. This is the challenge of integrated design of offshore wind farms.

17.3.3 Non-technical issues

Characterisation

Although an offshore wind farm is in essence a technical system, its conception is certainly not driven by technical factors only. The processes that achieve conversion from wind energy to electricity and the effect that the environment has on the conversion system are dominated by technical considerations. The working principles that lead to the desired functionality and the constraints that avoid for instance premature collapse are based on the laws of physics. However, the

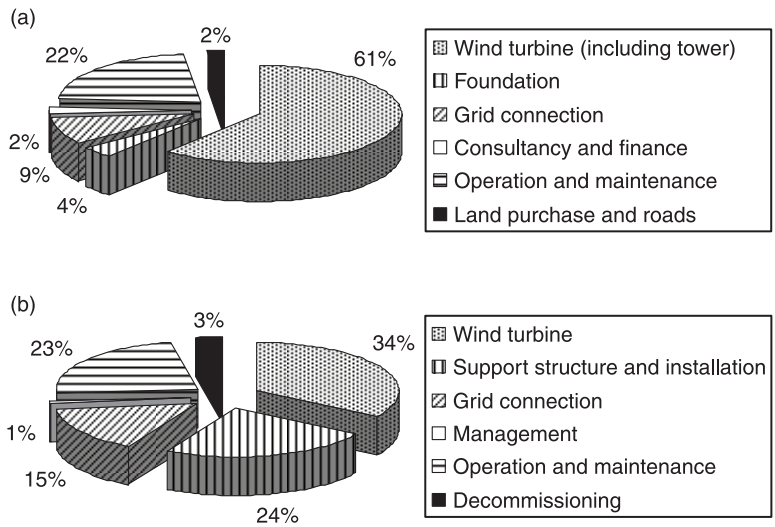

17.5 Typical distribution of levelised production costs for onshore (a) and offshore (b) wind farms. Onshore data based on typical ranges of contributions given by Morthorst (2004) and offshore data provided by Kühn *et al.* (1998b).

judgement of the system and its effect on the environment is subject to the value system of human society. Some values are expressed formally, for example in laws and regulations, and some values are informal, such as public opinion. The economic value is the result of a complex process of human interaction. The dynamics of this value system are governed by institutions, which are structures of cooperative behaviour in communities. Institutions can relate to informal groups, such as a community that shares a NIMBY feeling, and to formal organisations, such as a government. These are all non-technical issues that affect the design of a wind farm.

The influence of non-technical issues and their dynamics are less understood than those of the technical factors that follow the laws of physics. The better the effects are understood or written down in regulations, the better they can be incorporated in the design process as constraints or in the valuation of the system. This has already been indicated for some such effects in Section 17.3.2: the last four bullets in the list of changed constraints and the cost of energy as an indicator of the objective function are affected by non-technical issues. Some non-technical effects lead to such high uncertainties and risks, that they are not treated as part of the design process, but as part of the strategic considerations in the planning process. After making a balance with the company's interest, the planning process leads to internal constraints and criteria for the objective function. The following sections illustrate some of the important non-technical factors and how these affect design and strategy.

Legislation and regulation

Legislation and regulation reflect what authorities consider acceptable or not, and provide a means to stimulate developments that they find desirable. Authorities balance various interests in the formulation of legislation. Most legislation and regulation is enforced in the permitting process and can therefore be integrated in the planning phase of a project in a natural way. Some legislation is enforced during operation, such as some labour safety regulations, and need to be duly anticipated. Legislation differs per country and sometimes even per region. There is no prospect that legislation will be harmonised throughout Europe, as governments do not have the intention to do so (European Commission, 2005a). Requirements will therefore differ for different sites. Due to regular change of legislation in some countries, requirements may even change during the development phase of a project.

Legislation can affect strategy and design in various ways. Permitting procedures may set explicit constraints, such as restrictions on hub height or wind farm size. Such restrictions can easily be incorporated in the design process as part of the requirements. They only affect strategy if the design team cannot obtain an acceptable solution with these restrictions that meets the originally established strategic objectives. The tendering procedures may also set constraints and besides that they provide additional criteria for the objective function. The tender criteria used for ranking of bids have to be included in the design process next to the internal criteria and the weight of each is a strategic choice. The tender criteria are usually

more or less clear enough to use in the design process. Legislation may also prescribe certain procedures, of which the outcome is uncertain. For instance, it may prescribe consultation with external parties as part of the permitting process. Due to the uncertainties, such procedures usually require that people who make strategic decisions stay in close contact with designers of relevant aspects of the wind farm.

Stakeholders in society

Figure 17.2 gave an overview of the stakeholders in offshore wind farm development. Many stakeholders, such as suppliers, customers and the government, can exert influence through their economic or legal relation with the project developer. Several stakeholders in society do not have these means to directly influence the development. Important stakeholders in society are:

- other users of the sea and seabed;
- environmental interest groups;
- air and marine traffic control (radar);
- taxpayers (subsidy);
- coastal inhabitants;
- suppliers and consumers of coastal recreation and tourism.

Their interest affects wind farm design in various ways. As mentioned in the previous section, authorities balance their interests in legislation. To protect individuals and groups of people that are personally affected, they usually have the opportunity to ask for an evaluation of their individual interest in the permitting process. A more informal approach is also possible. Communication between developer and stakeholders can lead to mutual understanding and alternative solutions. Involving stakeholders has proven beneficial in the past by avoiding opposition of permits (Sorensen *et al*.., 2002). Solving conflicts of interest in this way may also avoid the formulation of stricter legislation. The decision to involve stakeholders as well as the balance between giving and taking is largely strategic.

Environmental impact

As for the interest of the stakeholders, the interest of the non-human environment is protected by legislation. An environmental impact assessment (EIA) is required as part of the permitting process. EIAs are performed on different scales and levels of detail according to the requirements at national level (European Commission, 2005b). Because not all potential impacts of offshore wind farms are well understood, the requirements for EIA are not always well defined and worst-case scenarios may need to be considered. As far as the environment is protected by legislation or defended by environmental interest groups, the previous sections apply. Developers may find it of strategic importance to be more careful about the environment than required, in order to maintain a positive image.

This is often done because they want to underline the positive environmental effects of offshore wind energy (European Commission, 2005b).

Economics

Since costs and value of energy are among the main criteria in the objective function, economics play a decisive role in the evaluation of design solutions. To some extent, the cost and value are determined by the technology of the design solution. For example a smaller pile will be less expensive than a larger pile and simple technology is likely less expensive than advanced technology. However, costs and value also strongly depend on market economics. Some of these economics can be influenced by negotiations, but other economic developments are outside the sphere of influence of the developer. For instance, steel prices doubled between summer 2006 and summer 2008 and dropped by about a third in spring 2009 (TTI, 2009). There is a negative economic value for the (perceived) risks of a design solution, which translates to insurance costs and financing costs. The latter is also influenced by the investment market. Economic developments may lead to considerable uncertainties, particularly for the long-term developments of the revenues if this is not mitigated by price agreements or feed-in tariffs. The influence of economics is not only a design issue, but also requires strategic decisions.

17.4 Wind farm design and integration (site specific)

17.4.1 Integrated design: what it is and what it is not

The term 'integrated design' can be interpreted in many ways. As a fashionable word, it is often used to create the impression that everything has been taken into account. Although this is commendable, taking everything into account does not necessarily lead to a better product. Integrated design approaches actually provide greatest value in their ability to separate the process, problem and solution into smaller, manageable and understandable parts. As one of the significant contributors to integrated design, systems engineering provides structure to make such separations, while at the same time attending to the interactions between the elements. Referring to Fig.17.4, this means that functions, constraints, objective function and provisional design are broken down into smaller parts than can be related to the system level. This section presents some tools that can be applied to offshore wind farm design. Most tools are selected from course material provided by Hamann and van Tooren (2003, 2004). The tools are presented as part of the design process, to give them context. It is not intended to describe the design process as seen in practice or to prescribe an approach. Rather, the tools are suggestions for approaches that can be helpful and that have proven themselves in various applications. It is up to the designer to select which tools are most appropriate at certain points in the design process. Some of the suggested

tools can also be applied in other situations, such as for subsystem or detailed design.

Wind farm design in practice may sometimes be observed to be intuitive and straightforward, not requiring elaborate tools. When many boundary conditions for siting and farm layout are set by regulation or when the conceptual design is largely copied from other wind farms, most attention can indeed be spent on detailing the design of the subsystems. At that point in the process, many issues relating to design integration are already fixed.

17.4.2 Preparations and site selection

Requirements specification and targets

Terms of reference describe the desired outcome, the participants, the resources and the overall planning of a project. They can be drafted at initiation of a wind farm development as the outcome of the first step of strategic planning. During the project, they are used to check progress and compliance with the original intentions. The first task in the design process is to expand and clarify the objectives and criteria used in the terms of reference to specify the outcome of the project. As discussed in Section 17.3.1, three types of requirements can be identified: functions, constraints and the objective function. Functional requirements and constraints together make up the list of requirements, which forms the definition of the design problem. Functional requirements become important in the conceptual design phase and are therefore treated in Section 17.4.3. Constraints can be set by various stakeholders, such as the authorities, the transmission system operator (TSO), the utility, the investors, the insurers and the company management. Constraints can apply to all aspects of the design and design process, such as prescribed or prohibited solutions and prescribed analysis methods, but mostly they provide limits to certain properties of the solution, such as noise levels. A requirements discovery tree can be used to identify requirements. This is an AND-tree, in which the sum of requirements at a lower level equals the requirement at a higher level. Different starting points can be applied in structuring the tree. An example of the top levels of a requirements discovery tree is shown in Fig. 17.6.

Site selection and multicriteria analysis

When the site is not specified externally, but there is freedom of selection for the developer, there are a number of things to consider. First of all, there are constraints, as discussed in the previous paragraph. Most common constraints are exclusions of areas used by others, such as for shipping, military exercise or extracting other natural resources. Secondly, there are properties of the site that relate to the objective function. In this early stage of the project, it is impossible to quantify the effects of the site on the objective function accurately. Therefore, performance indicators are used. A multicriteria analysis is needed to get an overall performance impression

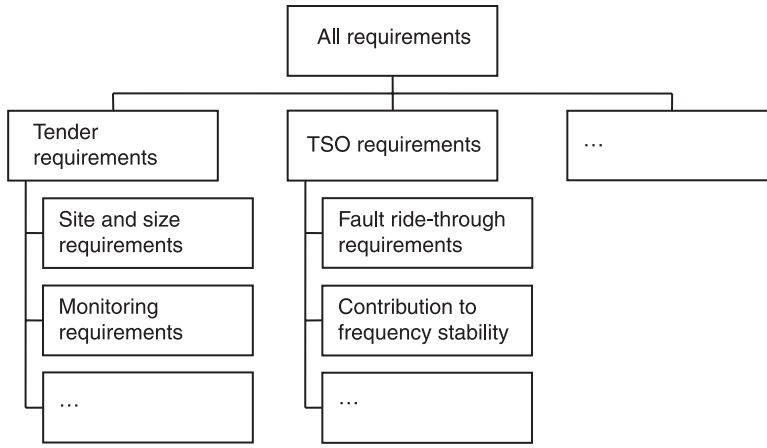

17.6 Example of the top levels of a requirements discovery tree, organised by source.

based on these indicators. One quantitative approach is given by the following steps.

- Define a list of system-level performance indicators that covers all properties of interest.
- Define metrics for each indicator. Preferably, these are computed values, such as electricity production. Otherwise, use a tabulated conversion such as: excellent = 10, good = 8, fair = 7, etc.
- Define weights for each of the indicators.
- Get agreement about the assessment process and fix it.
- Score all options, multiply metric and weight for each indicator and add up the results.
- Rank the options based on total score.
- Treat the ranking sensibly, acknowledging the simplifications in the process.

Figure 17.7 shows an example of a simpler multicriteria analysis without using metrics for the performance indicators. Hatching or colours can be used to get a quick visual impression of the scores. Some cost models have been developed for GIS applications that give the cost of energy as a function of location (Kooijman *et al*.., 2001; Cockerill *et al*.., 1998). These can be used to determine one of the important performance indicators.

17.4.3 Conceptual design

Functional breakdown tree, functional flow diagram and design option tree

The conceptual design fixes the working principles that are used to obtain the desired functions. Some examples for offshore wind farm design are given in

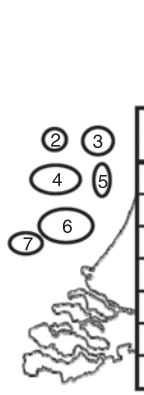

Criteria locations	Wind climate	Wave climate	Currents	Water depth	...
1	+	+	0	0	
2	0	0	0	0	
3	0	+	0	0	
4	0	0	0	0	
5	–	+	0	+	
6	0	+	–	+	
7	0	0	–	0	

Legend

+	Positive evaluation with respect to this criterion
0	Neutral evaluation with respect to this criterion
–	Negative evaluation with respect to this criterion

17.7 Example of multicriteria analysis for site selection in the Dutch sector of the North Sea (not shown are the criteria: soil conditions, other users, distance to grid and distance to ports). Adapted from Epema and Obdam (2006).

Table 17.3. Following the logical sequence of steps in Fig. 17.4, the definition of function precedes the synthesis of concepts. In reality, the definition of functions is rarely explicit in offshore wind farm design and designers tend to think in terms of conceptual solutions. This stimulates reproduction of earlier solutions. When the designer aims at innovation, it may be helpful to first express the functional requirements in a functional breakdown tree or functional flow diagram. Both diagrams display all desired functions, but the first one uses a hierarchical order in an AND-tree, while the second one expresses how the functions are invoked in time, giving their order in parallel, sequential, alternative or iterative processes. For each of the functions, an OR-tree of candidate solutions can be drafted. The highest level of this design option tree names the overall solution for that function,

Table 17.3 Examples of functions, working principles and concepts

Function	Working principle	Concept
Keep structure in position	Friction under vertical pressure	Gravity-base foundation
Provide installation platform	Vertical bearing of seabed	Jack-up vessel
Protect cable on seabed	Shield with top layer of seabed	Cable trenching
Avoid ship collision	Attract attention	Blinking lights

for example gravity-base foundation. At each node in the tree, a list of alternative solutions is formulated, e.g. solid or ballasted. The latter option in this example can branch into concrete and steel. There may be a need to move back and forth between solution and function. For instance, the function 'install foundation' splits differently for a floating foundation than for a monopile.

Component relations, the N2 diagram and system trade-offs

If an offshore wind farm were just a sum of its components, the best design option could simply be chosen for each function independently. However, the total system exists through and despite the interactions between its elements. An N2 diagram provides an overview of the relations between the elements. It shows the elements on the diagonal of a matrix and uses the cells to indicate the relations. Figure 17.8 shows the format of an N2 diagram using the high-level definition of the wind farm of Fig. 17.1 and an example of a particular relation. The relations between the elements affect the evaluation of constraints and the objective function. The example given in Fig. 17.8 shows that the installation loads affect the evaluation of constraints for strength and collapse of the offshore turbines.

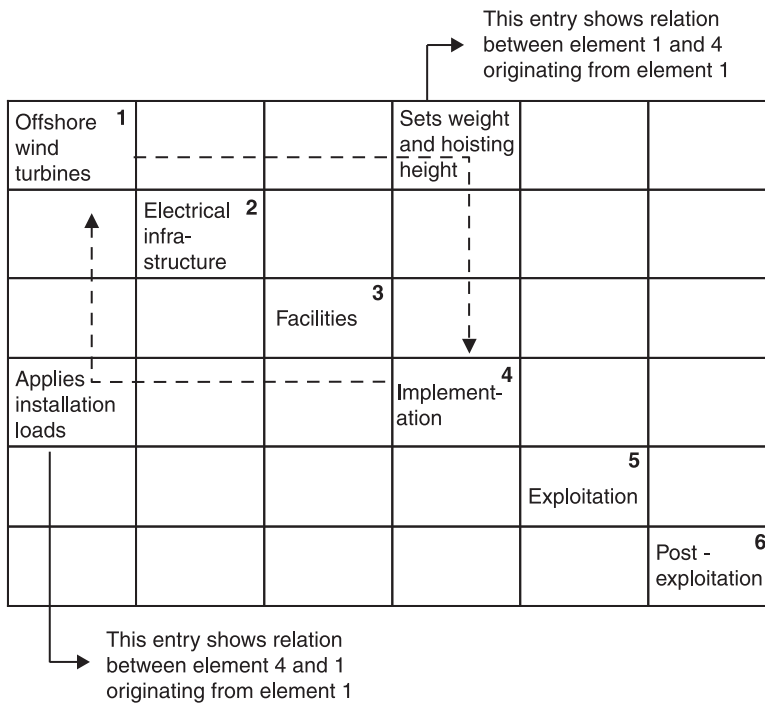

17.8 Format of the N2 diagram, which shows the relations between elements of the system.

This may consequentially affect the objective function through the need for strengthening. The objective function may also be directly affected through interactions. In the case of wake effects the interaction between different turbines in the farm reduces the electricity production. The interactions and their effect on the constraints and the objective function are indicators of the need for close cooperation between the designers of the respective elements. The example shows the need of cooperation between support structure and installation design.

In the conceptual design phase, the insight into the interactions and their direct or indirect effects on the objective function help to make trade-offs that relate to more than one element. The most discussed trade-off is between maintenance costs and availability on the one hand, and turbine costs and efficiency on the other. This involves the elements 'wind turbines' and 'exploitation'. In a trade-off, one sub-quality of the objective function is improved, at the cost of another sub-quality. Determining whether the overall effect on the objective function is positive or negative usually needs quantitative information and therefore parametric analysis of the relevant elements.

17.4.4 Preliminary design

Decomposition of the solution and technical budgeting

The early design steps can and need to be organised with much interaction between the designers of different elements. However, as the design becomes more detailed and time-consuming it is no longer possible to work together with the growing design team and to allow everything to keep changing in the design iterations. At this point, the structure of the design process should facilitate a more compartmentalised organisation of the work. Considering that the high-level conceptual design solution is fixed at this stage, a common approach is to divide the project team according to a division of the solution in several parts or clusters of elements. Knowledge of the relations between the elements, as collected in the N2 diagram, helps decomposition of the solution in clusters with weak relations. This is depicted in Fig. 17.9. The blocks indicate elements of the solution in a hierarchical AND-tree and the lines beneath them indicate strong and weak relations. Reorganising the hierarchy leads to clusters with only weak relations. Designers that work on one cluster need strong, daily, interactions but can work more or less autonomously from other clusters.

The systems engineers and project managers need to guard the overall system performance and the effects of the weak relations. To eliminate the weak relations from the daily design process, they can be replaced by interface definitions that fix the effect of the relation. Geometric specifications of the physical connections act as constraints for both clusters. Other specifications, such as interface loads, act as constraint for one of the clusters (the originating element in an N2 diagram) and as external condition for the other (the affected element). Technical budgeting can

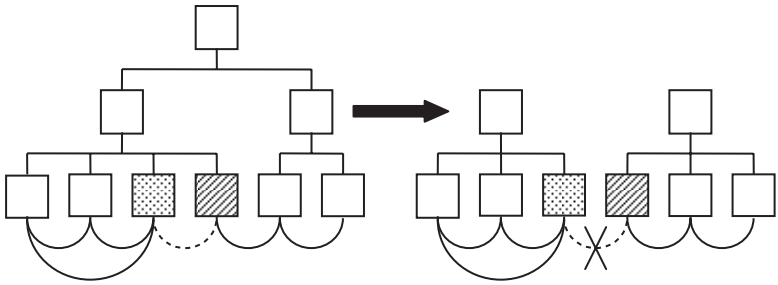

17.9 Decomposition of the solution with weak relations between the clusters (squares are elements of the solution and semicircles are relations).

be used to divide system targets into targets for the clusters, e.g. a division of total costs or of the electrical losses. The technical budgets and interface definitions are revisited at longer intervals and are only changed subject to strong arguments.

Cost modelling and numeric optimisation

Considering the dominance of the cost of energy in the objective function, cost modelling can be used to support the design process. Cost models use engineering design models, curve fits to cost data of existing components, quotations and guesses to express costs and energy production as a function of the main design or interface variables. For turbine design usually rotor diameter and rated power are used as independent variables, while for a wind farm for instance the location, farm power capacity and the number of turbines are variable. By coupling cost modules for different elements of the wind farm, the overall costs can be assessed, as done by Elkinton (2007). Numeric optimisation can be part of the engineering design model used to determine the design of a particular element and it can be used as a shell around the cost model to minimise wind farm costs.

Cost models help to set realistic targets for the overall cost performance and support technical budgeting. Engineering design models and numeric optimisation can be used to support dimensioning by the designer.

Integrated analysis

The N2 diagram helps identify which clusters of components have strong physical interactions. Although it may not always be practical to emphasise the integration of such clusters in the design process, it is important to realise the effect of these interactions on the properties of the (sub-) system. Probably the most researched interaction is between the rotor-nacelle assembly and the support structure. It is evident that these are not designed together in practice, as the rotor-nacelle

assembly is an off-the-shelf product for a wind farm designer. However, research shows the importance of using an integral model of support structure and rotor-nacelle dynamics to assess the effect of combined wind and wave loading. The better the design process facilitates integrated analysis of such clusters, the more accurate the assessment of the constraints and objective function will be.

17.5 Technology development for offshore wind farms (general purpose)

17.5.1 Differences with site-specific design integration

Section 17.4.1 stated that the value of design integration can be found in the ability to break the design down into smaller parts, while maintaining their relations to the system-level requirements and properties. Some of the important elements of an offshore wind farm, such as the rotor-nacelle assembly and the installation vessel, are designed prior to the planning and design of the wind farm. The designers of such elements have to anticipate how their product will be used by their customers in order to assess its ability to meet the requirements eventually set for the entire wind farm by the developer. The interaction with the design process of other elements of the wind farm is replaced by supplier/customer interactions. Setting the interface requirements and technical budgets therefore becomes the result of market analysis and the strategic planning process of the product. Nevertheless, some engineering tools and knowledge as discussed in the previous sections for site specific design are still useful for the design of products that will be used in various wind farms. This section treats this engineering contribution to general-purpose design and makes some observations from studies and design in practice.

17.5.2 Relevance of integration tools

As mentioned in the first paragraph of the section about site specific design (17.4.1), the value of integration tools is largely their ability to separate the process, problem and solution. Although this reduces the interactions in the design process, it is also a means to identify and control the interactions that are important. In general-purpose design, many design interactions are impossible altogether because the rest of the wind farm is designed at a later stage. Still, the integration tools can help to put the design in the context of the product's future use. Much information needed to use the aforementioned tools can be anticipated because the design solutions of offshore wind farms show much similarity. This is particularly the case when a specific market segment is selected, such as shallow water sites with high wind speeds. Zooming in on the design solutions of different wind farms will reveal more and more differences, showing that at some point a generic description in the engineering tools will no longer be sufficient. Table 17.4 gives an overview

Table 17.4 Application of tools for design integration in the design process for general purpose products

Tool	Use
List of requirements and requirements discovery tree	Collect the same set of requirements as a wind farm developer, assessing the informal requirements for instance by interviews. Identify the subset of relevant requirements.
Multicriteria analysis for site selection	Assess criteria and weights of a wind farm developer and base targets for the general-purpose design on these. Acknowledge how important the relevant criteria are to overall performance.
Function breakdown tree, function flow diagram and design option tree	Use function diagrams of general-purpose design to assess functional hierarchy and interfaces with the rest of the system and consistency with overall functionality. Use reverse engineering of functions and design options or previous wind farms.
N2 diagram	Use N2 diagram of entire wind farm to assess interactions that determine the relevance of requirements and functions in the aforementioned tools.
Decomposition of the solution	Identification of a cluster with strong interactions may lead to strategic partnership or extension of the product boundaries to enable more design coordination.
Technical budgeting	Perform technical budgeting of wind farm targets, based on, for instance, literature or interviews, to set realistic targets.
Cost modelling, engineering models and numerical optimisation	Use cost models for wind farms to set realistic targets and to get initial designs in the same way as for site specific design.
Integrated analysis	Use one or more reference designs for elements with which an integrated analysis is preferable.

of the tools that were presented in Section 17.4 and indicates how they can be useful for general-purpose design.

17.5.3 Case studies

The essence of what could be called integration for general-purpose design is the inclusion of its anticipated effects in the final application in an offshore wind farm. To enable this anticipation of effects, several design research projects have treated the design of a general-purpose element as if it were part of an offshore wind farm design project. In these projects, one or more cases were formulated to set conditions for the offshore wind farm design. This setup enables analysis of the general-purpose design in its future environment by design integration for the defined cases. Such case studies can fully use the integration tools discussed in

Section 17.4, rather than the reduced versions of the previous section. Examples of research projects in which this approach can be observed are Opti-OWECS, 'cost optimising of large-scale offshore wind farms' and DOWEC (Kühn *et al*.., 1998a; ELKRAFT, 1999; Hendriks and Zaaijer, 2004). These projects used a collaboration of different companies to create the proper setting for design integration. A company that designs a general-purpose product can consider hiring the services of designers from other companies to create a similar setting at critical points in their design process. However, it must be noted that the validity of this type of design integration is in principle restricted to the selected cases.

17.5.4 Technology development in practice

Section 17.5.1 indicated that the designers of general-purpose elements are faced with the burden of anticipating the value of their product in future offshore wind farms. What is evident is that any form of anticipation of the future use of the general-purpose element requires knowledge of areas outside the regular expertise and scope of the design team. Companies deal with this more and more by employing people with such complementary knowledge, by cooperating with other companies in research projects and by visiting each other's conferences. What is not evident, is how companies handle the integration issue in practice. Relative to making a truly integrated design of an offshore wind farm, the surrogate integration methods that are suggested in the previous two sections are less than optimal. Although companies might use similar or more advanced methods, there is no evidence of that in the public domain. Nevertheless, many aspects of the design process and solutions observed in practice can be explained using the insights presented in this chapter. Several examples are given in Table 17.5. Interestingly, the conceptual design of several site-specific elements is also performed ahead of wind farm design. Examples are the development of foundation concepts, floating concepts and maintenance strategies. Although the dimensions of these concepts will be finalised during site-specific design, the knowledge about such concepts is considered to be more generic. The generation of such knowledge requires many resources, which are normally not available in a wind farm development project. The knowledge needed for far-reaching innovations is therefore developed with the potential to be used in many future wind farms.

17.6 Future trends

17.6.1 Developments in context and requirements

Many new regulations have been formulated since the beginning of offshore wind energy, when the then existing regulations were not considered sufficiently adjusted to the new application. Ever since, there has been continuous development and, at the time of writing, the dust has not yet settled. Most countries are now

Table 17.5 Examples of observations about developments in practice explained using the mindset of this chapter

Observation	Origin
Climate control in nacelle	Anticipated constraint set by customers based on offshore (air) conditions
Increasing tip speeds of rotors	Reduced noise constraint enabling increased power performance and reduced costs
Upscaling	Trade-off between increased electricity production and less increased costs, due to high level of 'fixed' costs (scale independent)
Focus on reliability improvement	Trade-off between turbine performance and O&M costs and availability
Analysis tools for combined loading	Need for integrated analysis of rotor-nacelle and support structure
Access vessel concepts	New working principles compared with offshore access
Vessel type installation equipment	Trade-off between increased equipment costs and improved installation performance (faster and cheaper)
Installation vessel concepts	Extrapolation of current design solutions as indication of future designs

debating whether the offshore transmission system should be a responsibility of the TSO or of the wind farm developer. As a responsibility of TSOs, an offshore grid can be created, enabling both international exchange of electricity and connection of offshore wind farms. New knowledge about environmental impact and concern about cumulative impact affects regulation for EIAs. Developments are moving further offshore, away from harbour facilities and into deeper waters, leading to other conditions for the support structures and for logistics.

17.6.2 Developments in design objectives and organisation

The early offshore wind farms were small demonstration projects that received considerable support from all stakeholders. Designers could focus on technology and rely largely on solutions used for onshore wind energy and in the offshore industry. An increase in size and amount of offshore wind farms has raised targets for profit and put stricter constraints on risks and on the impact on society, on the environment and on the electricity system. To meet the objective and constraints, there is an increasing interest in moving from copied technology to innovative solutions, dedicated to this application. This implies an extension of the design domain, with many new options to be explored. This search for innovation will remain for some time to come.

Various legal structures of cooperation can be observed, affecting the possibilities for design integration as discussed in Section 17.2.3. The increasing

demands increase the need for design integration. Project developers will play an increasingly important role in design integration and it can already be observed that they are generating the necessary expertise.

17.6.3 Development of design methodologies

The methods sketched in this chapter are just an extract of the possibilities. Although these and other methods have been tested in various other applications, there is limited to no proof of their effectiveness for offshore wind farm design. The history of offshore wind farms is so young that many options to support design integration still need to be tested. The first development will be that companies will establish their common practices. In the longer term, more and newer methods that are developed for other applications will be made suitable and tested for this application. Examples are knowledge-based engineering and design engineering engines. The latter method facilitates multi-disciplinary design analysis and optimisation. Such methods are being developed and tested in the UpWind project (Anon., 2010). In addition, methods will be developed to support integration issues of general-purpose designs, in particular for the design of the rotor-nacelle assembly.

17.6.4 Trends in technology

As mentioned in Section 17.6.2, there is an increasing interest in dedicated innovations. Already many innovations can be observed that signify an evolution of the technology. Examples are the vessel type jack-up equipment, the 'bunny ear' installation method with two rotor blades assembled in the harbour and fully variable speed turbines with robust squirrel cage or permanent magnet generators. In response to moving farther offshore, tripods and lattice towers are developed and in the future this may lead to floating turbines, larger wind farms, accommodated maintenance vessels or even an offshore workspace. Various revolutionary conceptual changes are suggested, such as return to stall control, two-bladed rotors or vertical axis turbines. Climbing cranes, self-installing turbines or complete assembly in the harbour are suggested to avoid hoisting equipment. Various electrical farm layouts and control are being investigated, including speed control of clusters of wind turbines and DC connections. A candidate integral solution is proposed as the so-called 'energy islands' with multiple functions, including energy storage. Which of these suggestions will eventually become reality is for the time being an interesting point of debate.

Another point of debate is the optimum size of turbines for offshore wind farms. Already, the typical size of offshore wind turbines exceeds that of onshore wind turbines. This helps to mitigate the costs of offshore operations and structures, which are very high but scale up benignly with the increase of turbine size. Further potential for growth of turbines is assessed with models for

up-scaling, which relate properties such as loads, stress, mass, rotational speed, rated wind speed, energy yield and costs to the size of the turbine as indicated by its rated power and rotor diameter. Scaling models helps to identify design drivers and needs for technological change. When combined with cost models for other elements of an offshore wind farm, they can support the assessment of optimum scale although substantial uncertainty has to be considered.

17.7 Sources of further information and advice

For effective design of offshore wind farms, knowledge from various disciplines is needed, including at least the physics of the applied technology, engineering design methodology and management of technological developments. This section suggests various sources of further information that address any of these issues in the specific context of offshore wind energy and some sources that treat generic aspects of design methodology.

At the time of writing, the only comprehensive textbook about offshore wind energy technology is that by Twidell and Gaudiosi (2009). Some textbooks about wind energy have a separate section or chapter about offshore wind energy (Hau, 2005; Manwell *et al*.., 2002; Kühn, 2002). Various research projects have provided public reports. Besides the projects mentioned in Sections 17.5.3 and 17.6.3, of particular interest are CA-OWEE, Downvind, COD and WE@Sea. Links to websites of some of these projects can be found on the website by Zaaijer *et al*.. (2008). Articles relating to offshore wind energy can be found in various journals about wind energy, particularly Wind Energy, Wind Engineering and special issues of Solar Energy Engineering. The journal Wind Energy published two special issues on offshore wind energy in 2009 (Vol. 12, issues 2 and 5). There are proceedings of the conference series European Offshore Wind (EOW) and Offshore Wind Energy in Mediterranean and other European Seas (OWEMES), and various other conference series have sessions about offshore wind energy, such as the European Wind Energy Conference (EWEC), World Wind Energy Conference (WWEC), International Offshore (Ocean) and Polar Engineering Conference (ISOPE) and the International Conference on Ocean, Offshore and Arctic Engineering (OMAE). All these sources treat a variety of issues, such as resources, climatological conditions, environmental impact and specific technologies. However, other than optimisation algorithms, design methodologies are rarely addressed.

There are many textbooks about generic aspects of designing. Invariably, they bear most relevance to design problems of a specific nature, such as consumer product design, engineering design or systems engineering. Examples are the books of Cross (2000), Hubka and Eder (1988), Kroll *et al*.. (2001), Otto and Wood (2001), Pahl and Beitz (1996), Ullman (2003) and Ulrich and Eppinger (2000), but many other textbooks are equally useful. There are many conferences and journals about product design and engineering design, such as the Journal of

Engineering Design, Research in Engineering Design and Journal of Design Research. Designers and design researchers organise themselves into various associations, such as the Design Council and the Delft Center for Engineering Design (DCED). These sources are useful for a general overview and to get ideas about tools. However, so far there is no source that provides extensive and explicit information about the utility of design methods for the design of offshore wind farms.

17.8 References

Anon. (2010), *Upwind*. EWEA. Available from: *http://www.upwind.eu* [Accessed 28 January 2010].

Cockerill, T T, Harrison, R, Kühn, M and van Bussel, G J W (1998), *Opti-OWECS final report, volume 3: comparison of offshore wind energy at European sites*. Delft: Institute for Wind Energy.

Cross, N (2000), *Engineering design methods: strategies for product design*. Chichester: Wiley.

Elkinton, C N (2007), *Offshore wind farm layout optimization*. PhD dissertation. Amherst: University of Massachusetts.

ELKRAFT. (1999), *Cost optimizing of large-scale offshore wind farms, final report*. Haslev: SK Power Company.

Epema, T and Obdam, T (2006), *Offshore wind farm design: OE5662*. Student assignment report. Delft: Delft University of Technology

European Commission. (2005a), *Concerted action for offshore wind energy deployment (COD), work package 3: legal and administrative issues*. Utrecht: SenterNovem.

European Commission. (2005b), *Concerted action for offshore wind energy deployment (COD), work package 4: environmental issues*. Utrecht: SenterNovem.

Hamann, R J and van Tooren, M J L (2003), *Systems engineering and technical management techniques – part 1*. Delft: Delft University of Technology.

Hamann, R J and van Tooren, M J L (2004), *Systems engineering and technical management techniques – part 2*. Delft: Delft University of Technology.

Hau, E (2005), *Wind turbines: fundamentals, technologies, application, economics*. Berlin: Springer.

Hendriks, H B and Zaaijer, M B (2004), *DOWEC: executive summary of the public research activities*. Petten: ECN.

Hubka, V and Eder, W E (1988), *Theory of technical systems: a total concept theory for engineering design*. Heidelberg/New York: Springer.

Kleineidam, P (2007), *Multi-contracting: how to manage the supply limits*. Available from: *http://www.eow2007proceedings.info/allfiles/270_Eow2007presentation.ppt* [Accessed 6 March 2008].

Kooijman, H J T, de Noord, M, Volkers, C H, Machielse, L A H, Hagg, F, Eecen, P J, Pierik, J T G and Herman, S A (2001), 'Cost and potential of offshore wind energy on the Dutch part of the North Sea'. In P Helm and A Zervos (eds.), *European wind energy conference: wind energy for the new millennium* (pp. 218–221). München-Florence: WIP-Renewable Energies-ETA.

Kroll, E, Condoor, S S and Jansson, D G (2001), *Innovative conceptual design: theory and application of parameter design*. Cambridge: Cambridge University Press.

Kühn, M (2002), 'Offshore wind farms'. In R Gasch and J Twele (eds.), *Wind power plants: fundamentals, design, construction and operation*. Berlin: Solarpraxis.

Kühn, M, Bierbooms, W A A M, van Bussel, G J W, Ferguson, M C, Göransson, B, Cockerill, T T, Harland, L A and Vugts, J H (1998a), *Opti-OWECS final report, volume 1: integrated design methodology for offshore wind energy conversion systems*. Delft: Institute for Wind Energy.

Kühn, M, Bierbooms, W A A M, van Bussel, G J W, Ferguson, M C, Göransson, B, Cockerill, T T, Harrison, R, Harland, L A, Vugts, J H and Wiecherink, R (1998b) *Opti-OWECS final report, executive summary: structural and economic optimisation of bottom-mounted offshore wind energy converters*. Delft: Institute for Wind Energy.

Manwell, J F, McGowan, J G and Rogers, A L (2002), *Wind energy explained: theory, design and application*. Chichester: Wiley.

Morthorst, P E (2004), 'Costs and prices'. In H Chandler (ed.), *Wind energy – the facts: an analysis of wind energy in the EU-25*. Brussels: EWEA.

Otto, K N and Wood, K L (2001), *Product design: techniques in reverse engineering and new product development*. Upper Saddle River, NJ: Prentice-Hall.

Pahl, G and Beitz, W (1996) *Engineering design: a systematic approach*. Berlin/Heidelberg/New York: Springer.

Roozenburg, N F M and Eekels, J (1995), *Product design: fundamentals and methods*. Chichester: Wiley.

Sorensen, H C, Hansen, L K, Hammarlund, K and Larsen, J H (2002), 'Experience with and strategies for public involvement in offshore wind projects', *Int J Environ Sustainable Dev*, 1, 327–36.

TTI. (2009), *Steel price trend*. Fort Worth, TX: TTI. Available from: *http://www.ttiinc.com/object/ME_Materials_Steel* [Accessed 25 March 2009].

Twidell, J and Gaudiosi, G (2009), *Offshore wind power*. Brentwood: Multi-Science Publishing.

Ullman, D G (2003), *The mechanical design process*. New York: McGraw-Hill.

Ulrich, K T and Eppinger, S D (2000), *Product design and development*. New York: McGraw-Hill.

van Rooij, R P J O M (2001), *Terminology, reference systems and conventions*. Delft: DUWIND.

Zaaijer, M B *et al*.. (2008), *Offshore wind energy – information for professionals*. Delft: DUWIND. Available from: *http://www.offshorewindenergy.org* [Accessed 1 August 2008].

18

Operation and maintenance of offshore wind energy systems

L. W. M. M. (LUC) RADEMAKERS, H. (HENK) BRAAM and T. S. (TOM) OBDAM, Energy Research Centre of the Netherlands (ECN), The Netherlands

Abstract: Presently, ambitious plans exist to install large offshore wind farms in Europe and the USA. For offshore wind farms, the costs for operation and maintenance (O&M) contribute to the costs of energy substantially, approximately 30%. In this chapter, the issues relevant for O&M, such as turbine reliability, weather conditions, equipment for transfer of personnel, crane vessels for hoisting of parts and the use of condition monitoring systems are discussed. Since at present hardly any operational experiences are available from offshore wind farms, models are being used to estimate the costs and downtime. In this chapter, models used in the planning phase of a wind farm are described which are needed to assess the financial risks. Furthermore, a method is described to estimate the future O&M costs of an operating wind farm, making use of operational data. Key to this method is the structured approach to collecting and analysing operational data such as failure and maintenance data, SCADA data and results from condition monitoring programs.

Key words: operation and maintenance, offshore wind energy, cost estimation.

18.1 Introduction

18.1.1 Offshore wind farms and their operation and maintenance aspects

A typical layout of an offshore wind farm is sketched in Fig. 18.1. The wind farms consist of a number of turbines, switchgear and transformers (mostly located within the wind farm) and a substation onshore to feed the electrical power into the grid. The first wind farms have been located in shallow waters at short distances from the shore in order to gain experience with this new branch of industry. Presently, most offshore wind farms are located at distances typically 8 to 30 km from the shore in water depths of 8 to 20 m. Usually monopiles are being used as a sub-structure and the turbine towers are mounted on the monopiles by means of transition pieces. The size of an offshore wind farm is 50 to 200 MW and consists of turbines with a rated power of typically 1 to 3 MW. Future wind farms are planned further offshore and will consist of larger units, typically 5 MW, and the total installed capacity will be 200 to 500 MW. New and innovative substructures are presently being developed to enable wind turbines to be sited in deeper waters and to lower the installation costs.

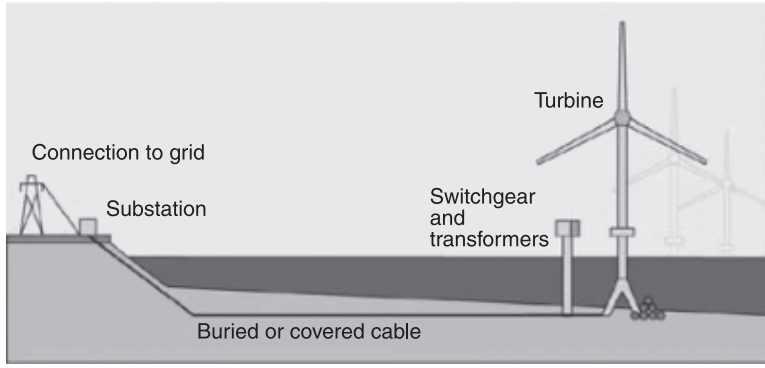

18.1 Typical layout of an offshore wind farm.[1]

All systems and components within the wind farm need to be maintained. Typically, turbines are being visited twice a year and each visit has a duration of 3 to 5 days. In the future, the aim is to improve turbine reliability and maintainability and reduce the frequency of preventive maintenance to no more than once a year. In addition to the turbine maintenance, also regular inspections and maintenance are carried out on the substructures, the scour protection, the cabling and the transformer station. During the first year(s) of operation, the inspection of substructures, scour protection and cabling is done typically once a year for almost all turbines. As soon as sufficient confidence has been obtained that these components do not degrade rapidly, operators may decide to choose longer inspection intervals or to inspect only a subset of the total population.

The maintenance aspects relevant for offshore wind farms are, among others:

- *Reliability of the turbines*. Turbine manufacturers design their offshore turbines, by contrast with onshore turbines, in such a way that the individual components are more reliable and are able to withstand the typical offshore conditions. This is being done by reducing the number of components, choosing components of better quality, applying climate control and using automatic lubrication systems for gearboxes bearings, etc. Often, the turbine control is modified in such a way that not every single failures lead to a standstill. Making better use of the diagnostics and using redundant sensors can assist in this.
- *Maintainability of the turbines*. If offshore turbines fail, maintenance technicians need to access the turbines and carry out maintenance. Especially in case of failures of large components, offshore turbines are being modified to make replacements of large components easy, by making modular designs or by building in an internal crane to hoist large components, see Fig. 18.2.
- *Weather conditions*. The offshore weather conditions, mainly wind speeds and wave heights, do have a large influence on the O&M procedures of offshore

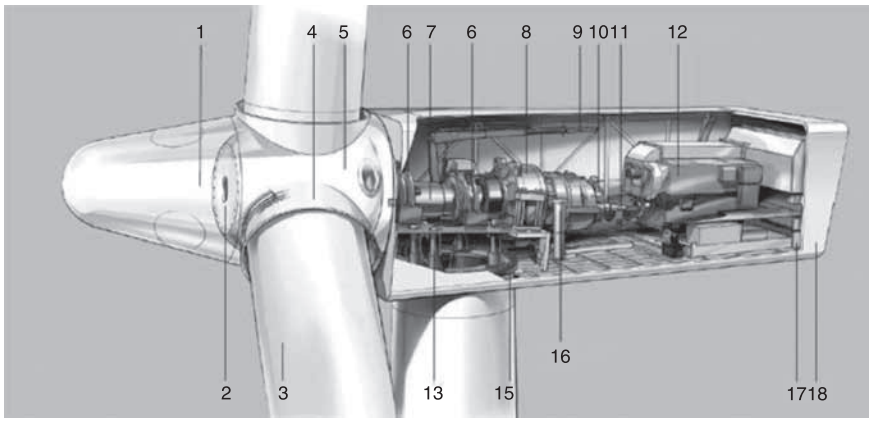

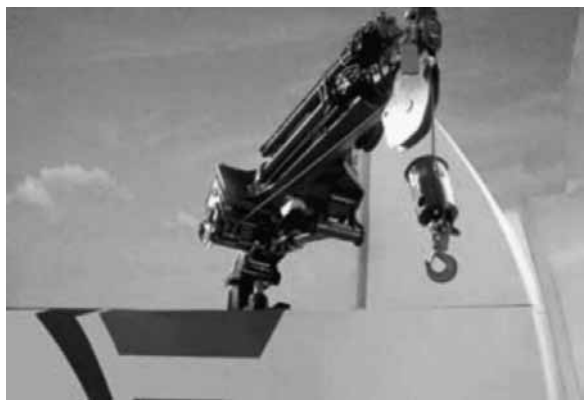

18.2 Examples of internal cranes in the Siemens 3.6 (top) and Repower 5 M (bottom) turbines.

wind farms. The maintenance activities and replacement of large components can only be carried out if the wind speed and wave heights are sufficiently low. Preventive maintenance actions are therefore usually planned in the summer period. If failures occur in the winter season, it is possible that technicians may not be able to access the turbines for repair actions due to bad weather and this may result in long downtimes with consequent revenue losses.

- *Transportation and access vessels*. For the current offshore wind farms, small boats like the Windcat, Fob Lady or SWATH boats are being used to transfer personnel from the harbour to the turbines. In bad weather, helicopters are also being used – see Fig. 18.3. Rigid inflatable boats (RIBs) are only used for short distances and during very good weather situations. The access means as shown in Fig. 18.3 can also transport small spare parts. For intermediate sized

18.3 Examples of transportation and access equipment for maintenance technicians. Windcat workboat (top), Fob Lady (middle), SWATH boat (bottom).

(*Continued*)

18.3 (Continued) Helicopter.

components such as a yaw drive, main bearing or pitch motor, it is often necessary to use a larger vessel for transportation, for example a supply vessel.

- *Crane ships and jack-up barges*. For replacing large components such as the rotor blades, the hub and the nacelle and in some cases also for components like the gearbox and the generator, it is necessary to hire large crane ships, see Fig. 18.4.

18.1.2 Operation and maintenance key figures

Wind energy has become a significant branch of industry. Since the mid 1990s, the annual turnover of many European manufacturers has increased by 30–40% per year. Now that wind turbines have gone beyond the experimental stage, designers, manufacturers, owners, project developers and suppliers are putting more emphasis on lowering the operational costs over the total lifetime in order to improve the economics of wind energy projects. Especially, the economics of offshore wind parks are strongly dependent on the failure behaviour of the turbines. Small failures, although frequently appearing, will have minor impact on the availability of *onshore* wind turbines. However, in *offshore* wind farms, these small failures can lead to high unavailability and high operational costs due to the difficult accessibility and expensive repair costs.

For onshore wind turbines, a lot of operating experience has been collected and analysed, among others as published in Ref. 2, Ref. 3, and Ref. 5; see also Table 18.1. For offshore wind farms, however, hardly any operating experience has been collected and analysed in a structured way and made public. Some data recently published are given in Table 18.2.

The figures collected in public databases and made publicly available should be interpreted with great care.

18.4 Examples of external cranes for replacement of large components; jack-up barge ODIN (top) and crane ship Sea Energy (bottom).

- In many cases, the owners of turbines are not obliged to submit data to the databases (with the exception of Ref. 2). Therefore, the number of failures and costs derived from these databases should be considered as minimum values.
- Often, costs for repairing failures are not paid by the turbine owner; the costs might be covered by warranty or service contracts. An example of how costs for corrective maintenance may develop over the lifetime of a wind turbine is given in Fig. 18.5. Clearly, it can be seen that, in the first years of operation, the costs for corrective maintenance are not paid directly by the owner.[2] Normally after year five, the warranty contracts come to an end and it is unclear how the O&M costs will develop over the remaining lifetime.
- The figures published by the turbine owners are often presented with some comments to mention that not all costs are included, see for instance Table 18.2.

Since hardly any public figures are available on O&M of offshore wind farms to assess the feasibility of new wind farms in the planning phase, ECN has developed

Table 18.1 Key figures for O&M onshore (investment costs ≈ €1000/kW)

Failure rate	1.5 to 4 failures per year
Availability	>98%
Service contract	0.5 to 0.8% of investment costs per year (5 to 8 €/kW)
Service contract incl. warranty	1.0 to 1.6% of investment costs per year (10 to 16 €/kW)
Costs for corrective maint: year 5	0.5 to 0.8% of investment costs per year (5 to 8 €/kW)
Costs for corrective maint: year 15	4 to 6% of invest. costs per year (40 to 60 €/kW)
Average O&M costs over lifetime	2 to 4% of invest. costs per year
Insurance costs	5 to 8 €/kW (machine damage, third parties, revenue losses)
Levelised production costs (O&M costs)	5 to 10% of kWh price (of which half due to maint.) 0.5 (year 1) to 1.5 (year 10) €cent/kWh

Table 18.2 Recently published key figures for O&M of existing offshore wind farms[6]

Wind farm	Country	Turbines	Distance from shore (km)	Water depth (m)	O&M costs (€/kWh)*
Middelgrunden	DK	20 × Bonus 2 MW	2–3	2–6	1.20–1.90
	The specified costs include the cost of O&M as well as administration, insurances, coordination and electricity consumption.				
North Hoyle	UK	30 × Vestas V80 2 MW	7–8	12	2.06–2.31
	The article mentions that since the wind farm is still under warranty the availability and non-routine maintenance cost risk is carried by the turbine manufacturer. It is unclear whether these maintenance costs are included in the listed figure.				
Scroby Sands	UK	30 × Vestas V80 2 MW	2–3	13–20	1.45–1.46
	According to the documents, the turbine maintenance costs have been included in these figures.				
Kentish Flats	UK	30 × Vestas V90 3 MW	8–10	5	1.55
	The figure includes cost of turbine O&M (estimated value from O&M contract with turbine manufacturer), insurance, lease and rent, surveys, import power and administration.				

* The O&M costs for the UK wind farms were expressed in UK pounds. For comparison purposes these figures have been converted using 1 pound = 1.5 Euro. This rate was valid at the date the figures were published.

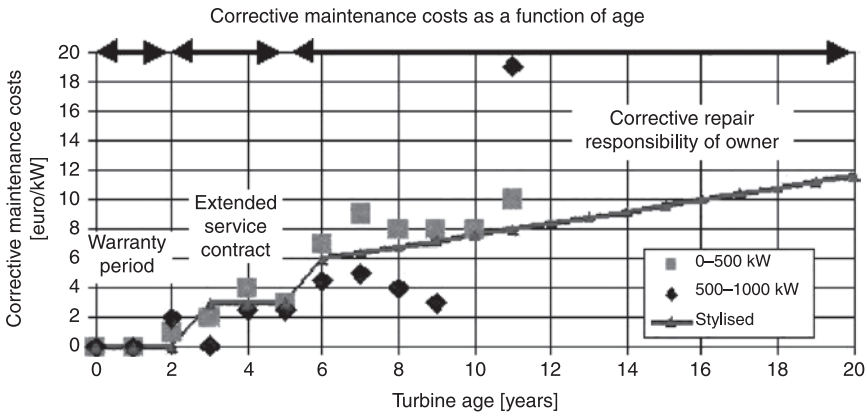

18.5 Development of the costs for corrective maintenance in the different stages of the lifetime, seen from the perspective of the turbine owner.[2] The figure shows a large variation of the costs after the end of warranty period in year five, and it shows that the costs are dependent on the size of the turbines.

a software package called the 'ECN O&M Tool'.[10–12] This tool is now being used worldwide and also ECN uses the tool to assist developers of offshore wind farms in analysing the O&M aspects during the planning phase. From the various analyses that have been carried out during the last few years with this tool, it is concluded that, for a typical offshore wind farm in the North Sea, the costs O&M are estimated in the range of 1.8 to 3.1 €ct/kWh, taking into account preventive and corrective maintenance for the turbines, the substructures, and the electrical infrastructure.

18.2 Operation and maintenance issues

18.2.1 Types of maintenance

At a general level, maintenance can be subdivided into preventive and corrective maintenance. Corrective maintenance is performed after a breakdown or an obvious fault has occurred. Preventive maintenance is intended to prevent equipment breakdown, and consists of repair, service or component exchange. According to textbooks and publications on O&M (e.g. Ref. 7 and Ref. 8), preventive maintenance and corrective maintenance can again be split up into different categories – see Fig. 18.6.

- Preventive maintenance:
  - calendar-based maintenance, based on fixed time intervals or on fixed numbers of operating hours

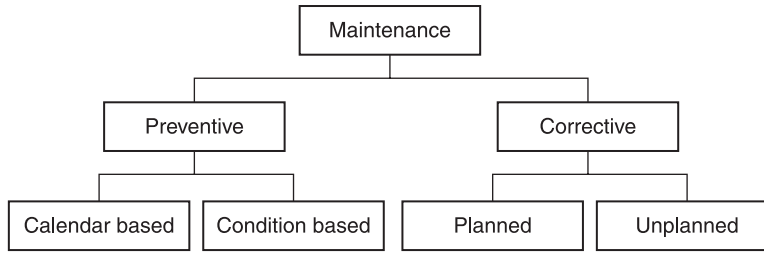

18.6 Schematic overview of different maintenance types.

  - condition-based maintenance, based on the actual health of the system
- Corrective maintenance:
  - planned maintenance, based on the observed degradation of a system or component (a component failure is expected in due time and should be maintained before it occurs)
  - unplanned maintenance, necessary after an unexpected failure of a system or component

Both condition-based preventive maintenance and planned corrective maintenance are initiated based on the observed status or degradation of a system. The main difference between these two categories is that condition-based preventive maintenance is foreseen in the design, but it is not known in advance when the maintenance will have to be carried out, while the occurrence of planned corrective maintenance is not foreseen at all. For wind energy applications, the practical meaning of this distinction is not relevant and further on only three types of maintenance will be considered:

- calendar-based maintenance
- condition-based maintenance
- unplanned corrective maintenance

18.2.2 Development of an operation and maintenance plan

Generally, the costs for maintaining an offshore wind farm will be determined by estimating the costs for corrective, preventive and condition-based maintenance. If during the planning phase of a wind farm an O&M plan needs to be developed, the approach is usually that cost models are being used to analyse the costs and downtimes of different O&M scenarios. Usually, a 'normal' baseline is selected first, meaning that personnel are being transferred to the wind farm by small boats, and crane vessels are being used to replace large components. If the estimated costs and downtime are considered to be high, the analysts may choose other means for access of personnel (e.g. a helicopter) and choose a jack-up barge

instead of a crane ship. Different scenario studies can be carried out and the most cost effective one can be considered for more detailed investigations and technical assessment.

In Fig. 18.7, the different cost components are drawn schematically. The O&M costs consist of preventive maintenance costs that are usually determined by one or two visits per year. After three or four years the preventive maintenance costs can be somewhat higher due to oil changes in gearboxes. On top of that there are corrective maintenance costs that are more difficult to predict. At the beginning of the wind farm operation, the corrective maintenance costs can be somewhat higher than expected due to teething troubles. Finally, it might be that major overhauls (e.g. replacement of gearboxes or pitch drives) are foreseen once or twice per turbine lifetime. The actual replacement will be dependent on the observed condition.

The costs for preventive maintenance can be modelled straightforwardly by multiplying the number of visits per year with the costs. Downtime is equal to the time technicians are actually visiting the turbines.

For corrective maintenance and condition-based maintenance, the approach for cost modelling is somewhat more complex and some considerations are given in the following sections.

18.2.3 Corrective maintenance

For many technical systems, three phases can be identified over the lifetime and this is also schematically drawn in Fig. 18.7.

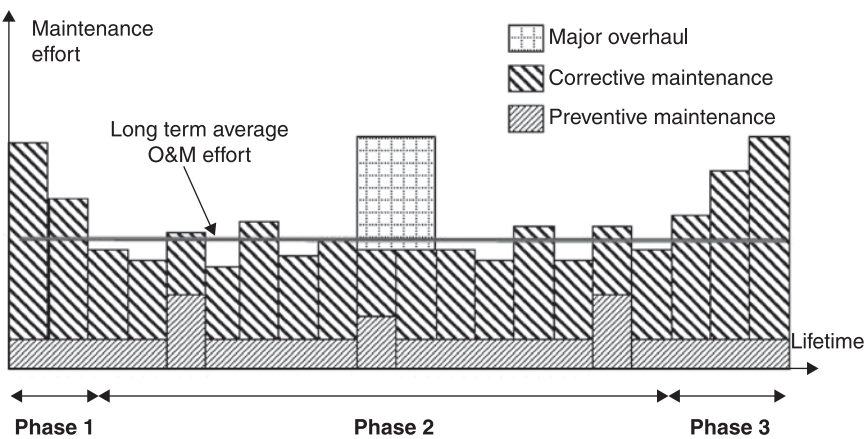

18.7 Schematic overview of the maintenance effort over the lifetime of a turbine. In reality, none of the lines is constant; the actual maintenance effort will vary from year to year.

Phase 1: During the commissioning period, the burn-in problems usually require additional maintenance effort (and thus cost). Time should be spent on finding the right settings of software, changing minor production errors, etc. During this period, the maintenance effort usually decreases with time. The turbine manufacturer usually provides a contract to the customer with a fixed price for the first five years of operation. The contract includes commissioning, preventive and corrective maintenance, warranties and machine damage.

Phase 2: During this phase, random failures might be expected, and the failure rate is more or less constant over this period. However, in reality the actual maintenance effort will vary from year to year and will fluctuate around the long-term average value, which is displayed by the gray line marked as "long term average 08 m effort". After about 10 years of operation, it is very likely that some of the main systems of the turbines should be revised, for example pitch motors, hydraulic pumps, lubrication systems, etc. With the offshore turbines, hardly any experience is available up to now on how often a major overhaul should be carried out. The exact point in time at which the overhaul(s) should take place is presently not known, perhaps after 7 years, 15 years, or not at all. The major overhaul in fact is to be considered as 'condition-based maintenance'.

Phase 3: At the end of the lifetime, it is likely that more corrective maintenance is required than in the beginning of the lifetime. It is presently unclear how much more this is likely to be.

Determining the corrective maintenance costs of an offshore wind farm is similar to the approach for asset management and risk analyses being used in many branches of industry. The risk is defined as *Risk = Probability of failure × Consequences*. For offshore wind farms, the risk is expressed in terms of (annual) costs, the probability of failure is changed into the (annual) failure frequency of components, and the consequences are being determined by the repair costs. The repair costs consist among others of labour costs, material costs, costs for access vessels and/or crane ships and revenue losses. So:

Expected annual O&M costs
= Expected annual failure frequency × Repair costs.

When determining the annual O&M costs, in fact most effort is being put into (1) determining the annual failure frequencies of components (see also Section 18.4) and (2) the repair costs that consist of labour costs, costs for equipment, spare parts costs and revenue losses. As compared to onshore maintenance, the weather conditions play an important role in the determination of especially the downtime and the associated revenue losses (see also Section 18.3.2).

18.2.4 Condition-based maintenance

Condition-based maintenance requires a proper determination and prognosis of the 'health' of the system, so-called condition monitoring. Depending on the type of

system and component, a wide variety of condition monitoring methods and techniques is available. For instance *offline*, one can perform periodic visual inspections, analyse oil samples, or carry out vibration measurements periodically. Another option is to permanently install systems that are dedicated to performing certain measurement and analysis tasks and that automatically report analysis results and events (alarms, warnings) to operators. Such systems are referred to as *online* condition monitoring systems. Another source of information for health determination is operational data from SCADA systems, for example the number of starts and stops, changes of temperatures over time, or occurrence of alarms. It should be noted that condition-based maintenance mainly makes sense if:

1 the design life of the component is shorter than that of the entire turbine – meaning that repair or replacement of the component is foreseen, but it is not clear when;
2 cost savings are expected compared to scheduled and corrective maintenance only; and
3 it is clear that the dominant cause of failure is indeed wear – meaning gradual degradation towards the end of the design lifetime; this in contrast to abrupt damage due to extreme events, design or manufacturing errors and the like.

Gearbox oil, as an example of the first point, will be replaced several times during the turbine lifetime. Condition-based maintenance can be applied to determine if the oil needs to be changed after four years (calendar-based) or maybe after seven years (condition-based). This could save one oil change within the turbine lifetime.

So-called 'safe life components', such as rotor blades, main bearing, or gearbox, usually have a design lifetime that is at least the same as for the turbine, which is typically 20–25 years. If such components fail during the lifetime of the turbine, the failure cause is usually extreme loading, poor installation or manufacturing, or other unforeseen conditions, such as lightning or accidents. Large repairs or replacements of safe life components are not foreseen within the turbine lifetime and therefore monitoring the health and degradation is difficult to justify. One reason, however, for using condition monitoring systems in the case of safe life components is minimising consequential damage. In case unexpected failures show up, they can be detected at an early stage and catastrophic failures can be avoided.

An example of what a successful application of offline condition-based maintenance should look like is schematised in Fig. 18.8 with the solid curve: at $t = 5$ a significant change in the condition is observed, at the next inspection at $t = 6$ a critical level ('yellow light') is exceeded and action should be taken, and repair is carried out during the next preventive maintenance at $t = 7$. Offline inspection is sufficient since (a) the failure progresses slowly and (b) the speed of progress is known from early experiences.

Online condition monitoring would make sense if the fault progresses faster than the time between two inspections, as illustrated by the dashed curved line. In this

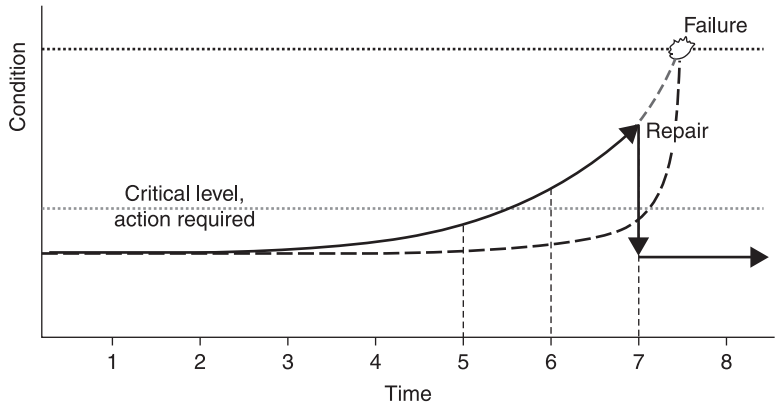

18.8 Condition-based maintenance based on inspections at regular inspection intervals (solid line) or on online monitoring (dashed line).

case, it is possible to prevent component failure and possible consequence damage, by shutting down the system. Since the fault progresses so fast, there is no opportunity to better plan the preventive maintenance actions. Online monitoring becomes more and more important if inspection intervals become larger as is the case for offshore wind farms. The inspection intervals for offshore wind farms are larger than for onshore turbines, typically once per year instead of twice a year. So-called 'sudden failures' are difficult to detect at all at an early stage with condition monitoring, either online or offline. Therefore condition-based maintenance should not be applied for sudden failures. More information on condition monitoring and the suitability for wind turbine applications can be found in Ref. 14 and Ref. 15.

Data from condition monitoring systems (but also from offline inspections and oil samples) in fact provide information on the remaining lifetime of the components, for example a gearbox. In an ideal situation, condition monitoring data from an offshore wind farm should provide information such as which turbines need maintenance in the short term, say within a few months from now, and which turbines require replacement of, for example, gearboxes in the longer term. If the results of condition monitoring measurements are combined with the repair or replacement costs, an estimate is obtained of the (annual) costs for condition-based maintenance.

18.3 Operation and maintenance models and strategies

18.3.1 Modelling approaches

As already mentioned in Section 18.1.2, hardly any figures are publicly available about O&M costs and downtime of offshore wind farms. Such figures are helpful

in the planning phase of a wind farm, among others, to assess the feasibility of the wind farm. Since these figures are not available and probably not applicable to the specific wind farm under consideration, it is recommended to make a detailed analysis of the O&M aspects and make use of O&M modelling tools. Such tools can be for instance time simulation models like 'CONTOFAX' from the Delft University of Technology, Ref. 13, 'O2M' from GarradHassan,[10] and 'BMT SLOOP' from BMT.[9] The approach is based on Monte Carlo analysis with turbine failures occurring on a stochastic basis. Delays associated with poor weather are simulated using a statistical wave module based on spectral analysis. Wave heights are correlated with wind speeds such that the effect of poor accessibility during periods of high wind is captured in the calculation of lost production revenue.

The ECN O&M Tool[11,12] works differently. It is intended to be used in the planning phase of an offshore wind farm and should be used to determine the long-term average annual costs (indicated by the horizontal line in Fig. 18.7), downtime and revenue losses. The ECN O&M Tool is in fact the only tool that has received a validation statement from the certifying body Germanischer Lloyd (see Ref. 12) and this tool will be discussed in more detail in the following sections.

The output of the models is usually the average annual downtime, annual costs for O&M, and the uncertainty bounds. Depending on the capabilities of the different tools, more detailed information can be obtained for O&M optimisation, for example downtime and costs per season, cost drivers or downtime caused by limitations in logistic aspects.

18.3.2 ECN operation and maintenance tool

The ECN O&M tool focuses on determining the costs and downtime resulting from unplanned corrective maintenance. The process of cost modelling is illustrated in Fig. 18.9. First, a baseline O&M strategy is determined to maintain the intended wind farm. For the baseline strategy, best guesses are made by the project team for the different input parameters (failure rates, characteristic values of vessels and equipment, and weather conditions). The model results in costs and downtime, and the project team can start analysing the results. Cost drivers can be identified and based on these possible areas for improvement (e.g. using more reliable components or vessels with improved accessibilities) can be identified. If the project team has selected an optimal maintenance strategy, it is recommended to analyse the uncertainties with the probabilistic part of the model. By doing so, insight is gained into how the different uncertainties in the input parameters contribute to the uncertainties in the outcome of the model.

The model to determine the long-term yearly average costs and downtime due to unplanned corrective maintenance is based on the repair process as depicted in Fig. 18.10. In general, it can be stated that the central operation office will be

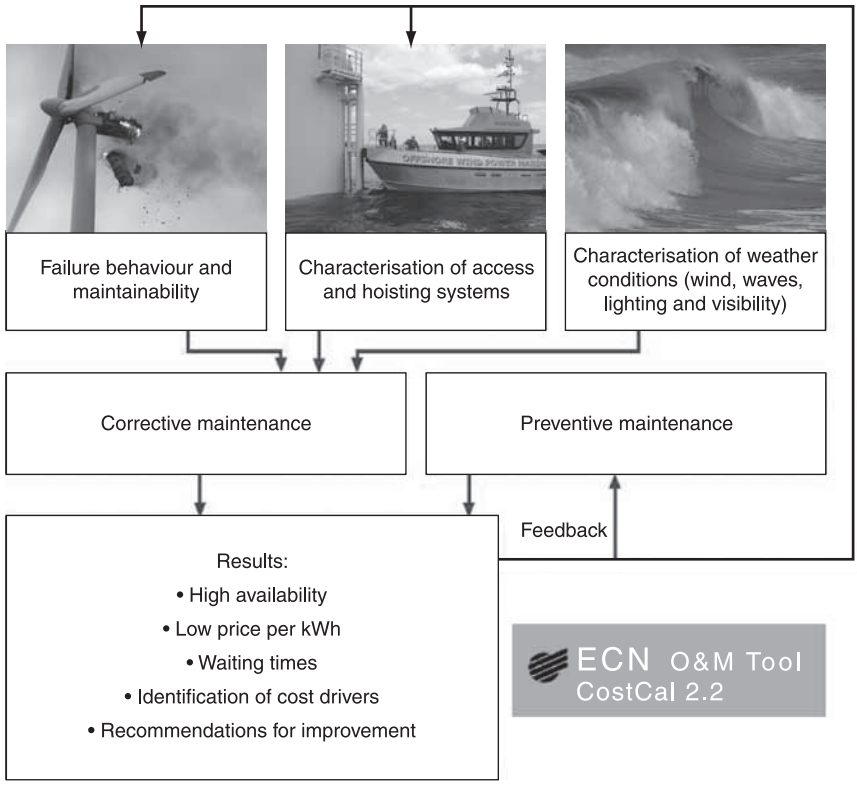

18.9 Schematic representation of the ECN O&M Tool for determining the O&M costs and downtime of an offshore wind farm.

informed that an alarm has been triggered. Once the operator has notified the alarm, he has to decide whether the turbine can be restarted remotely or whether visit is necessary to determine whether the wind turbine can be restarted without maintenance or if maintenance is required first. If repair is necessary, the operator needs to organise the repair action, mobilise the crew, a ship and if necessary spare parts and large hoisting equipment.

The time to repair (TTR) can be split up into four time intervals.

1 The interval *T_logistics* denotes the period of time between when the wind turbine was shut down and the repair crew is organised and ready to travel to the turbine for repair. In this period, also the time needed to organise equipment and spare parts is considered. So the length of this interval depends on the availability of an inspection team, the availability of materials and the availability of equipment for travelling and hoisting. The availability of personnel or equipment strongly depends on the company policy. Own personnel or third parties can do the maintenance, and equipment can be owned or hired, etc.

2 Once the repair crew and the equipment for travelling are, in principle, ready for take off, it might happen that the weather forecast during the period that the mission has to be carried out (*T_mission*) is such that it is not allowed or would be irresponsible to take off. This interval is denoted as *T_wait*. The length of this interval is dependent on the duration of the mission and the device planned (see also Fig. 18.10). Due to its dependency on weather conditions (wind speed and/or wave height) the duration of this interval shows large scatter and should be treated as a stochastic quantity. As the ECN O&M Tool determines long-term yearly average quantities the average value of the waiting time is used in this model.
3 The interval *T_travel* denotes the time needed to travel to the wind turbine that has to be inspected or repaired.
4 The interval *T_repair* is the time needed to carry out the repair.

The ECN O&M Tool has been implemented in two MS-Excel sheets:

WaitingTime.xls to determine the annual (or seasonal) average waiting time (*T_wait*) as a function of the mission time (*T_mission*);
CostCal.xls to determine the annual (or seasonal) average downtime and costs.

WaitingTime.xls

Offshore equipment can be used or repair actions can be carried out if the wind and wave conditions are below certain values. Based on wind and wave data for a selected location, the program *WaitingTime.xls* determines when the weather conditions are suitable for carrying out certain repair actions and calculates the

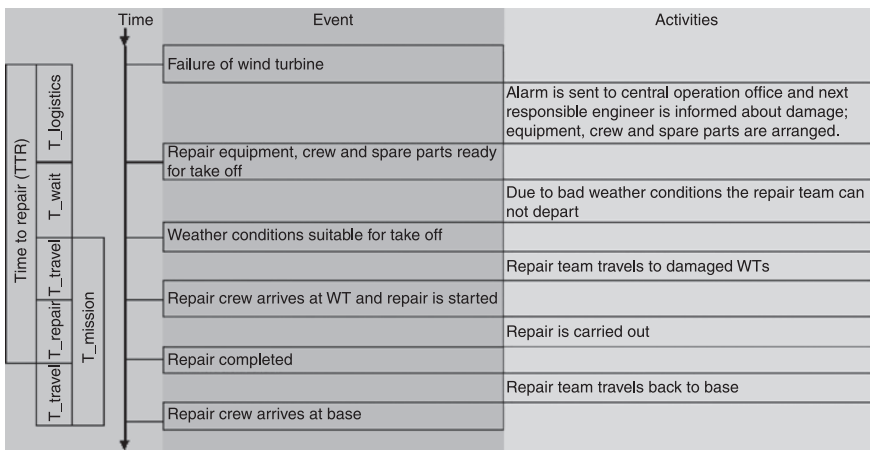

18.10 Repair process.

average time one has to wait before a suitable weather window will occur after a failure. The program uses time series with three-hourly wind and wave data as input. It results in second- or third-order polynomials for the mean value and the standard deviation of the waiting time as a function of the duration of the maintenance activity. In Fig. 18.11an example is given of such a polynomial.

The example represents the annual average waiting time as a function of the mission time at the location 'IJmuiden Munitiestortplaats' and is based on 11 years of measured data. The mission can be carried out up to a significant wave height of H_s = 1.5 m and a wind speed of V_w = 12 m/s. Similar polynomials can also be generated per season and for different weather limits H_s and V_w.

CostCal_xls

The program *CostCal_xls* is being used to determine the long-term annual (or seasonal) costs for O&M and the associated downtime. The program focuses on *unplanned_corrective maintenance*. The program uses among others the following input:

1 weather windows and waiting time polynomials as generated by *WaitingTime_xls*;
2 wind turbine and wind farm information such as number of wind turbines, capacity factor of the wind farm, investment costs of turbines, costs of technicians, length of working day, etc.;
3 failure behaviour of the turbines and the repair actions that are foreseen;
4 characteristic values of access systems (weather limits, costs, mobilisation time, etc.).

During the modelling process, users spend more time on generating input parameters for item 3, which is discussed here in more detail. First of all, the ECN

Processing of data		
Date	H_s [m]	V_w [m/s]
Max values:	1,5	12
01-01-1990 1:00	0,35	2,7
01-01-1990 4:00	0,4	2,8
01-01-1990 7:00	0,41	1,9
01-01-1990 10:00	0,37	2,3
30-12-2001 22:00	1,39	3,6
31-12-2001 1:00	1,29	1,8
31-12-2001 4:00	1,31	3,5
31-12-2001 7:00	1,11	7
31-12-2001 10:00	1,38	7,9
31-12-2001 13:00	1,53	7
31-12-2001 16:00	1,44	6,1
31-12-2001 19:00	1,69	6,1
31-12-2001 22:00	1,41	8,7

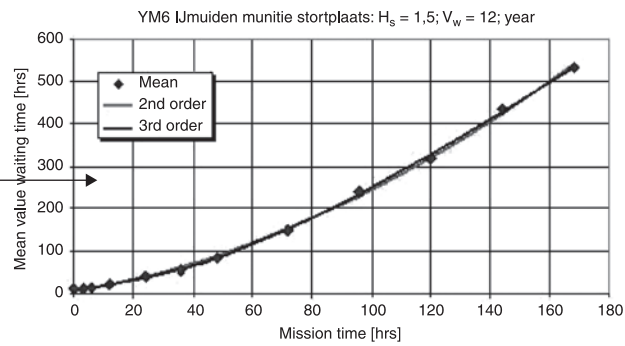

18.11 Example of determining relationship between average waiting time and mission time.

O&M Tool requires the occurrence frequencies of failures and associated repair actions as input. Unfortunately, such data are hard to obtain. Often data should be derived from generic databases (e.g. Ref. 2. and Ref. 3), or (more preferred) from similar turbines. (Approaches to collecting and feeding back operational experiences from other wind farms will be discussed in more detail in Section 18.4.) If such data can be obtained, mostly only overall annual failure frequencies of the main components are available. Engineering judgement is required to determine the different failure modes of these components. A certain percentage of the component failures comprise failure modes that are small and easy to repair, whereas another percentage comprises failure modes that are more severe and require, for instance, large crane ships during the repair action. In order to avoid that, the model needs to analyse each individual failure mode and its associated repair actions, and all maintenance actions are categorised into a different maintenance categories (MCs). An example of the categorisation of maintenance actions with associated equipment is given in Table 18.3.

In addition to the categorisation of maintenance classes, it is also necessary to exactly describe how the repair is going to be carried out and how the equipment is going to be used. An example of a detailed description is given in Table 18.4. This step-by-step description is considered by all users as very relevant; often it is concluded afterwards that repair actions are more complex than originally foreseen.

The information per maintenance class is limited to the use of equipment (vessels and crane ships). Subsequently, each maintenance class is again split up into a limited number of fault type classes (FTCs). An FTC determines the average costs per repair action taking into account labour costs, costs of spare parts and consumables, costs of equipment and revenue losses caused by downtime. An FTC also determines the mission time per repair action and thus the associated waiting time due to bad weather conditions (see also Fig. 18.11). The total downtime consists

Table 18.3 Example of possible subdivision in maintenance categories (MCs)

MC 1:	Remote reset, no personnel and equipment, no repair time
MC 2:	Small repair inside, only personnel and tools, repair time less than 1 day (e.g. replacement of carbon brushes)
MC 3:	Small repair outside, only personnel and tools, repair time less than 1 day (e.g. cleaning of blades)
MC 4:	Replacement of small parts, small internal crane hoisting outside, repair time around 1 day (e.g. replacement of pitch motor)
MC 5:	Replacement of large parts, large internal crane needed (e.g. replacement of gearbox, generator etc.); repair time typically 1 to 2 days
MC 6:	Replacement of large parts, large external crane needed (e.g. replacement of hub, nacelle, yaw system); repair time typically 2 to 3 days

Table 18.4 Example of description (MC 4: Replacement of small parts)

Smaller spare parts such as a pitch motor, a yaw motor or parts of a hydraulic system need to be transported to the turbine, put on the platform and hoisted into the nacelle with the help of the internal crane. A typical maintenance action looks as follows:
1 an access vessel with two to four technicians and the spare part travels to the failed turbine
2 the technicians are transferred from the access vessel
3 technicians inspect failed component and decide whether replacement is needed
4 the failed component needs to be replaced, the spare component is hoisted to the platform with the small crane on the lower turbine platform
5 the failed component is dismantled and lowered outside the tower to the platform using the internal crane
6 the spare component is hoisted from the platform using the internal crane and mounted
7 the failed component is hoisted to the access vessel using the small crane on platform (depending on the capabilities of the platform and the crane, this step can be done later; the failed part can be stored for some time on the platform)
8 personnel return to the access vessel and it travel back to the harbour.

of the four intervals given above: logistic time to organise equipment and spare parts, waiting time due to bad weather, travel time and repair time (see also Fig. 18.10). The model *CostCal.xls* is equipped with input sheets to define the above-mentioned costs, mission times and capabilities of vessels and crane ships.

The process of 'grouping' the different failure modes into a manageable set of FTCs with identical costs and downtime, and the determination of the average annual occurrence frequencies of each FTC is given in Fig. 18.12. The ECN O&M Tool typically deals with 10 to 15 FTCs. If for the baseline O&M scenario all input parameters have been defined, the program immediately shows the output, as presented in Table 18.5. The program also generates plots and pie charts to determine cost drivers or aspects that dominate downtime (see Fig. 18.13). The results may be a reason to optimise the O&M strategy, by selecting different vessels, changing the turbine design, improving component reliability or using a hotel boat.

The ECN O&M Tool model will in most cases be used as a deterministic model in which only mean values or the maximum likelihood are considered. The model can also be used as a probabilistic model to take into account the uncertainties in the parameters, for example failure frequencies and costs. To do this, the add-in module @Risk[18] should be used. The model can generate, for instance, the cumulative density function of the O&M costs per kWh, or determine which uncertain input parameter influences the uncertainty of the results the most by means of a tornado diagram (see Fig. 18.14 a and b).

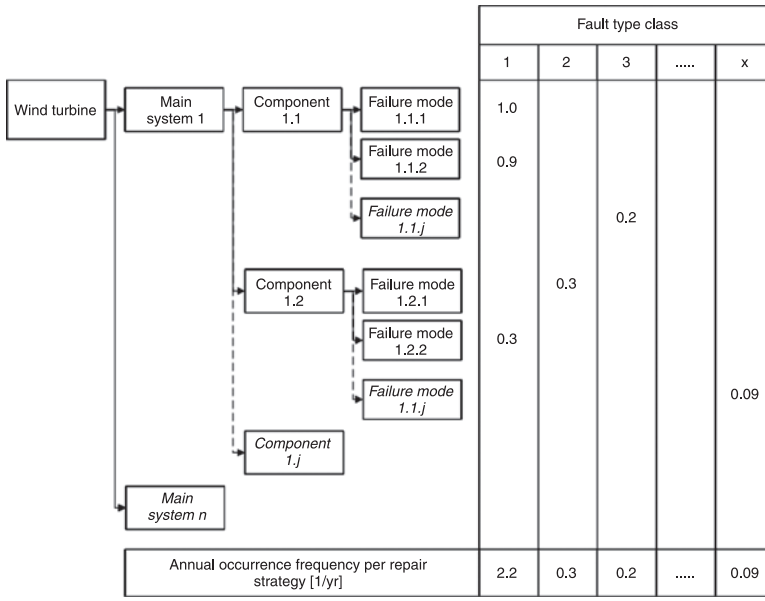

18.12 Process of grouping small and severe failures into manageable sets of FTCs.

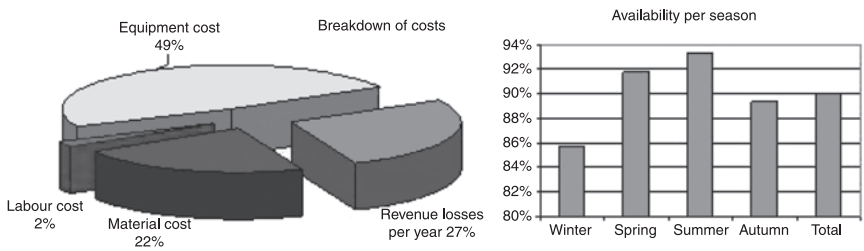

18.13 Example of model output (graphs and pie charts).

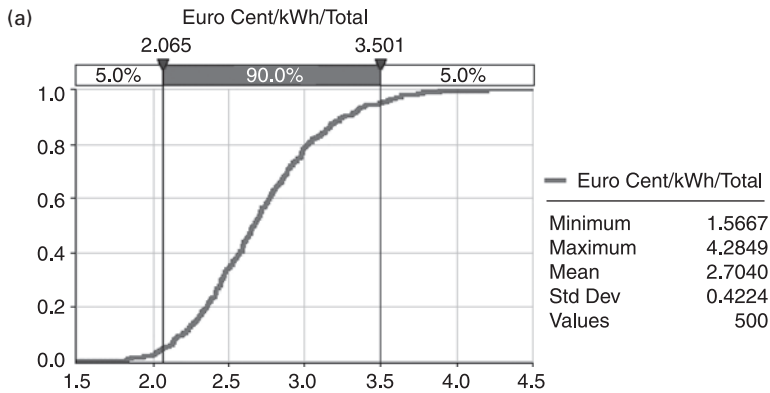

18.14 (a) Example of CDF and tornado diagram.

(*Continued*)

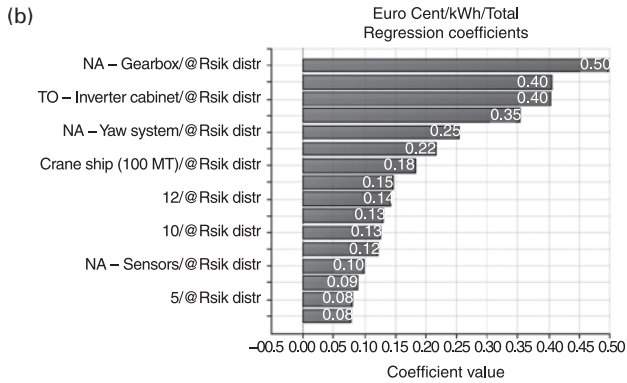

18.14 (Continued) (b) Example of CDF and tornado diagram.

Table 18.5 Example of model output.

Results for single wind turbine			Winter	Spring	Summer	Autumn	Total
Downtime per year							
Corrective	Logistics	hr	85	85	85	85	340
	Waiting	hr	72	22	17	61	171
	Travel	hr	1.88	1.88	1.88	1.88	7.53
	Repair	hr	11	9	9	11	41
	TOTAL corrective	hr	170	118	113	159	560
Preventive	TOTAL preventive	hr	1	9	20	2	32
	TOTAL	hr	**171**	**127**	**133**	**162**	**592**
Availability		%	**92.2%**	**94.2%**	**93.9%**	**92.6%**	**93.2%**
Loss of production per year		MWh	277	164	122	237	801
Energy production per year		MWh	3.279	2.674	1.897	2.980	10.831
Revenue losses per year		k€	**36.0**	**21.3**	**15.8**	**30.9**	**104.2**
Costs of repair per year							
Material costs							
Corrective	TOTAL corrective	€	23.049	23.049	23.049	23.049	92.195
Preventive	TOTAL preventive	€	350	3.400	6.550	700	11.000
	TOTAL	€	**23.399**	**26.449**	**29.599**	**23.749**	**103.195**
Labour costs							
Corrective	Wages	€	2.589	2.536	2.536	2.589	10.251
	Daily allowance	€	0	0	0	0	0
	TOTAL corrective	€	2.589	2.536	2.536	2.589	10.251
Preventive	TOTAL preventive	€	300	3.920	6.440	600	11.260
	TOTAL	€	**2.889**	**6.456**	**8.976**	**3.189**	**21.511**
Equipment costs							
Corrective	MOB/DEMOB	€	18.137	18.137	18.137	18.137	72.548
	Waiting	€	12.623	5.052	4.023	9.848	31.546
	Repair	€	12.011	11.991	11.991	12.011	48.005
	TOTAL corrective	€	42.772	35.180	34.151	39.996	152.099
Preventive	TOTAL preventive	€	450	5.680	9.460	900	16.490
	TOTAL	€	**43.222**	**40.860**	**43.611**	**40.896**	**168.589**
Total costs of repair per WT		k€	**69.8**	**74.1**	**82.5**	**68.2**	**294.8**
Total cost per kWh		€ Ct/kWh	**2.13**	**2.77**	**4.35**	**2.29**	**2.72**

18.4 Collecting operational experiences

18.4.1 Why use operational experiences for operation and maintenance optimisation?

When collecting data it is recommended to clearly define the objectives of the data collection process. If the data are going to be used for reliability engineering, asset management and optimisation of O&M procedures clear procedures should be developed and implemented for the day-to-day tasks of technicians, operators and other people involved. Once the objectives are clear (e.g. deriving failure rates from O&M data, determining the degradation of a component or quantifying a certain repair action for a failed component) it almost automatically specifies what kind of data needs to be stored and how it should be analysed to obtain the required information.

Recently, ECN has developed a concept for collecting and analysing operational data of an offshore wind farm and to use the data for estimating future O&M costs. The concept is called the O&M Cost Estimator (OMCE) and the structure is presented in Fig. 18.15. The structure shows that:

- first *data* has to be collected
- next the data has to be processed to derive relevant *information* (within the OMCE structure, these data processing tools are called 'building blocks')
- then some of the results of the data processing need to be combined and parameters can be derived for Cost Modelling and optimisation
- finally new cost estimates can be made with a cost modelling tool (in this case the 'OMCE Calculator', which is a more advanced tool than the models discussed in Section 18.3.2).

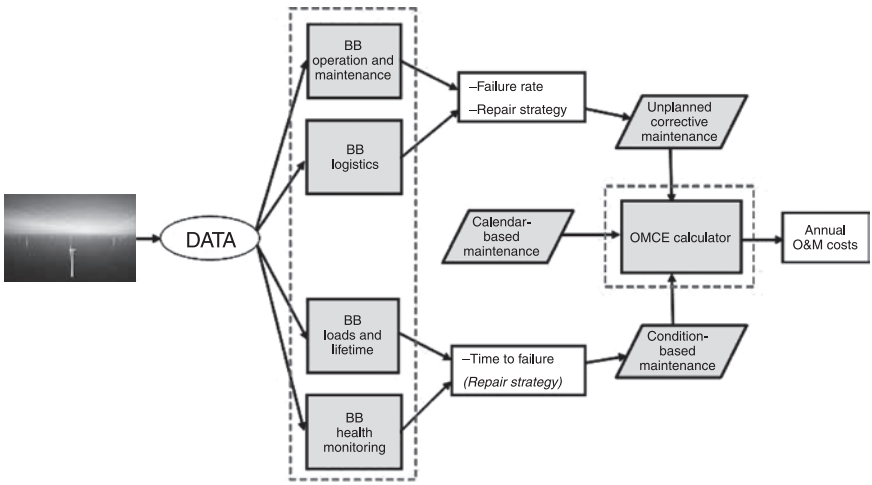

18.15 Structure of the O&M cost estimator.

Offshore wind farms generate among others the following types of data.

Operation and maintenance data

- lists with alarms and failures
- handwritten or digital reports from technicians with the work carried out and findings from inspections
- (monthly) reports with preventive maintenance actions carried out
- (annual) reports with maintenance actions on the substructure and electrical grid

Condition monitoring data

- wind farm system control and data acquisition (SCADA) systems comprising, among others, 10-minute statistical data on temperatures, pitch and yaw angles, wind speed and direction, power output and rotational speed
- results from dedicated measurement systems, such as drive-train condition monitoring systems or load measurement campaigns (see also Ref. 16 and Ref. 17)
- inspection reports (e.g. visual inspections, endoscopies, oil sample analysis results)
- end-of-guarantee inspections (due diligence)

Logistic data

- use of spare parts and stock control
- use of equipment (vessels, crane ships etc.), including their response time and maximum weather limits during operation
- use of crews
- lists with weather conditions at the site

Presently, the data originate from various sources and are collected as different datasets, in different formats, at different locations. In most cases, operators collect the data but are not aware of the information that is 'hidden' in the large amounts of data. Usually the data are being used to investigate certain events (e.g. time series may explain the reason for an unexpected shut down, or SCADA data may explain why a bearing is overheating and when the temperature started to increase). In addition, the data are being used to assess the performances of the wind farms periodically, but at a more general level: downtime, power output, operational costs, top 10 alarms etc. As long as the turbines are running well, operators store the data but they hardly ever process it to determine reliability figures or long-term trends and component degradation in a systematic manner. In the following sections, the building blocks dealing with 'O&M data', 'condition monitoring data' and 'logistics data' will be discussed in more detail to propose methods for collecting and analysing offshore wind farm data in a more

structured way. The BB 'loads & lifetime' is designed to take into account the fact that each individual turbine observes a different loading pattern that may thus require a different O&M strategy. The results of this BB should be combined with the BB 'health monitoring' when developing an optimal strategy for condition-based maintenance. The contents of the BB 'loads & lifetime' will not be discussed here; more information about this subject can be found in Ref. 17.

18.4.2 Operation and maintenance data

The objective of collecting and analysing operation and maintenance data is mainly to determine failure rates of components, which can be used to determine the need for unplanned corrective maintenance. Within the Maintenance Manager project,[4] a database structure has been developed, implemented and tested to collect the maintenance information from wind turbines in a more systematic manner. At present, maintenance technicians use a free format to describe the failure or the work carried out (e.g. '*failure of the hydraulic pitch system*' might be the same as '*leakage in the pitch cylinder*'). For O&M modelling purposes, it is difficult to analyse such data sheets statistically and to derive failure rates of components. A prerequisite for further analysis is that the information stored is unambiguous, and to avoid the free format and options for various interpretations as much as possible. To facilitate this, the data collection system should be such that the technicians can report the failures and repair actions preferably by means of pull-down menus. Free formatted input should be allowed, but only for supplementary information. These pull-down menus should contain relevant options only. For instance, once a component is chosen, the failure modes applicable for that component only should be accessible. The specifications of a database for collecting failures and O&M data of wind turbines are discussed below.

The database should consist of three main parts: a definition part, a registration part and a data analysis and reporting part.

Definition part

In the definition part, the wind farm, the wind turbines and the possible failure modes and repair actions have to be specified. For this a breakdown of the turbine into main systems and subsequently into components has to be made:

- Wind farm
  - Wind turbine
    - Main systems
      - Components
        - Failure modes
          - Repair actions

For each separate component the possible failure modes and repair actions have to be specified beforehand. This can be done by means of a failure mode and effect analysis (FMEA). In order to perform the analyses, which have been described in the previous section, it is essential that for each maintenance action at least the following parameters should be registered:

- report ID
- wind farm ID and/or name
- turbine ID and/or name
- date and time that the turbine stopped
- date and time that the turbine was restarted after the failure
- the system and component that the maintenance action is performed on
- the failure mode that the failure can be categorised in
- the type of repair carried out

Registration part

After the definition, part of the database has been completed; technicians have access to this database system and can fill out the maintenance sheets in a more systematic manner by making use of pull-down menus with predefined answers. An example of a registration form is shown in Fig. 18.16. Filling in the required fields is less time-consuming than filling in handwritten (or typed) sheets and converting them later on for further processing.

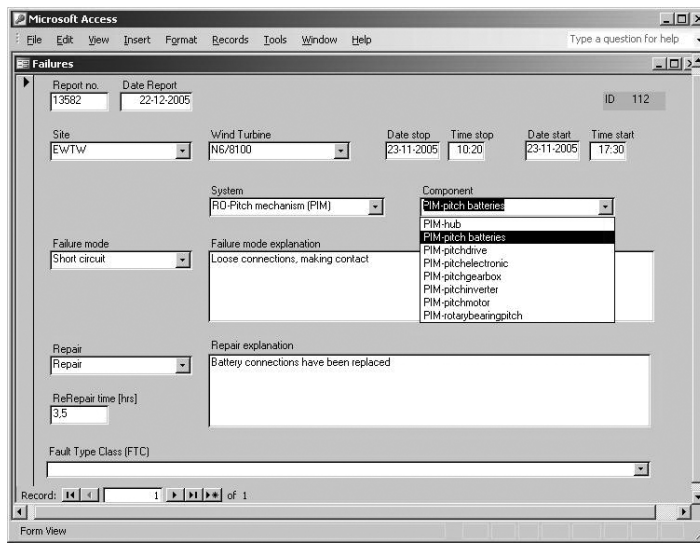

18.16 Example of a database for failure collection; using predefined answers enables systematic collection of wind turbine failures.

Analysis and reporting part

In Fig. 18.17 an example is presented from the analysis of maintenance reports. At the top of the figure, the distribution of the failures over the main systems of the turbine under consideration is shown. In the right-hand part of the figure, the largest contribution to the failures is analysed using a CUSUM-plot, which represents the cumulative number of failures as a function of the cumulative operational time. The derivative of this curve is by definition the failure frequency. By assessing yearly derivatives of this curve, it is easy to see the variation in failure rates over the three years. However, the yearly averages of the failure frequency neglect trends in the failure behaviour and are not always suitable as a future estimate of the failure frequency. In order to make an accurate estimation of the failure frequency for the coming years, the failure frequency should be calculated over a user-defined period, based on the observed trend in the failure behaviour in the CUSUM-plots.

In the example shown in Fig. 18.17, the failure frequency after about 15 years of cumulative operational time is fairly constant. Engineering judgement is necessary to decide which part of the curve is representative of the future failure behaviour. In this case, it was concluded that the future estimate of the failure frequency is best based on the period after 15 years of cumulative operational time. If in a certain period of elapsed time T an x amount of failures is observed, the estimated failure frequency λ is calculated using:

$$\hat{\lambda} = \frac{x}{T}$$

When performing reliability analyses, it is common practice to specify a confidence limit on the estimate of, in this case, the failure frequency. For a certain

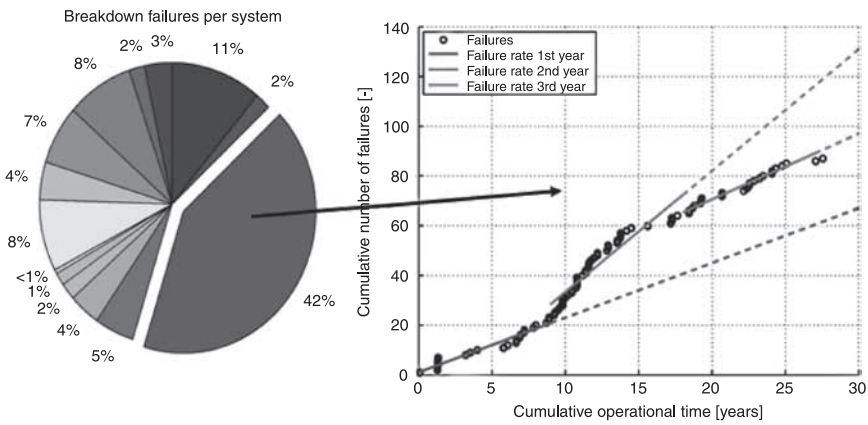

18.17 In the left-hand part of the figure, the percentage of failures per system is presented. For the largest contribution, the cumulative number of failures as a function of cumulative operational time is presented in the right-hand figure.

Table 18.6 Future estimate of failure frequency for the example shown in Fig.18.17

	Failure frequency
Upper confidence limit	2.79/year
Estimated mean	2.23/year
Lower confidence limit	1.71/year

confidence level $(1-\alpha)$ the upper λ_U and lower λ_L confidence limits of the estimated failure frequency can be calculated using:

$$\lambda_U = \frac{\chi^2_{\alpha,2x}}{2T} \text{ and } \lambda_L = \frac{\chi^2_{(1-\alpha),2x}}{2T},$$

where x represents the cumulative number of failures, T the cumulative operational time, and the $\chi^2_{(1-\alpha)}$ symbol a chi-square distribution with a $(1-\alpha)$ confidence. For the example shown in Fig. 18.17, the values given in Table 18.6 can be calculated based on a confidence level of 90% using data from year 18 onwards (slope of the red line in the graph). Including the trend in the middle part of the graph would lead to too high a failure rate for the near future.

18.4.3 Condition monitoring data

Condition monitoring data should be used to estimate the remaining lifetime of components and to estimate which group of failures is expected to fail say within 1, 2 or 5 years from now on. With this information, an estimate can be made of the amount of condition-based maintenance. Before specifying how condition monitoring measurements (both online and offline) can be implemented for O&M modelling and optimisation, some conclusions are given which are typical for condition monitoring systems in wind turbines. The conclusions are based mainly on the results of the CONMOW project, Ref. 14 and Ref. 15.

1 Vibration monitoring systems especially are able to accurately determine which component in a drive train is failing. Such measurements are suitable for organising additional inspections and limiting consequential damage.
2 Offline and online monitoring of gearbox oil by particle counters do indicate degradation of gearboxes at an early stage.
3 For all techniques tested in the CONMOW project – analysis of time series, SCADA data – and vibration measurements there was not sufficient knowledge in order to assess if critical limits were exceeded and how fast failures would develop. The latter two are minimum requirements to be fulfilled in order to change from calendar-based maintenance to condition-based maintenance.

4 It was concluded (and also confirmed by experiences outside the project) that at present there is insufficient knowledge available on criteria to assess the *green, yellow* and *red* status of a failure and to make prognoses of how the failures will develop over time. Such knowledge should be obtained from a larger population of identical wind turbines and longer measurement periods during which faults occur. It is therefore recommended to store data centrally so that cross analyses and comparisons between turbines and sites can be made.
5 Drive-train vibration monitoring should be permanent and online since failures may develop within a period of time that is shorter than the regular maintenance interval. If failures are detected at an early stage, consequential damage can be avoided. Further, vibrations often show up under specific operating conditions.
6 The systems produce large amounts of data that are difficult and time-consuming to interpret by wind turbine owners. The first analyses of raw data should be done by a dedicated expert team in order to derive information relevant for maintenance planning and feedback. Only this information should be provided to operators and design teams. An example of a parameter changing over time is the bearing temperature, see Fig. 18.18. De-trending, using the rotational speed and nacelle temperature, has drastically reduced the signal variability. The effect is that the resulting plots show only little variability as long as the component is not degrading.
7 The analyses of SCADA data showed that it is possible to determine not only trends but also other phenomena that may influence the optimal operation of the wind turbine, for example detecting changes of the controller settings that have an influence on the power curve, or detecting failures of the measurements or diagnostics by comparing signals of redundant sensors or combining different signals.

A step-by-step procedure for setting up a meaningful condition monitoring programme of which the results can be used for O&M modelling is given below.

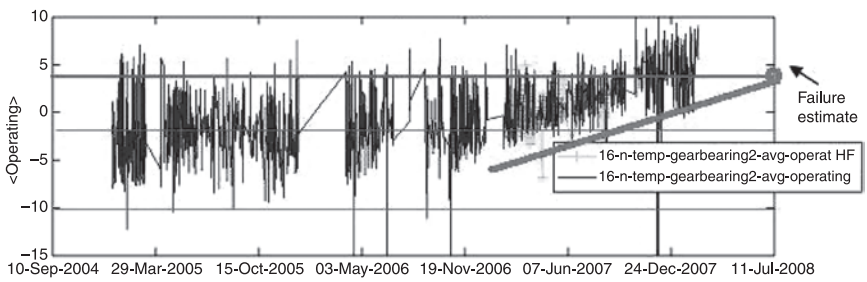

18.18 Example of a visualisation from de-trended SCADA statistical data; slow increase of the bearing temperature indicating wear.

Identification of vulnerable components and failure modes

Prior to the installation of all kinds of sensors and methods it is necessary to identify which kind of components fail gradually and which components fail suddenly. Furthermore, an assessment should be made of whether the component failure is critical, and if so if measurement systems are available that are able to measure the failures (see also Section 18.2.4 for an overview of possible options). As indicated in the CONMOW project, Ref. 14 and Ref. 15, a failure mode effects and criticality analysis could assist in selecting the most appropriate condition monitoring system.

Definition of measurement system and instrumentation

Once the most suitable systems and methods are identified and installed, it is necessary to describe in detail which kind of sensors are being used (or need to be added). The same holds for those sensors that are already installed for other purposes, e.g. for control and safety, including all SCADA data. At least the following should be specified.

- sensor location
- sensor type and specifications
- measured quantity (temperatures, pressures, mechanical, electrical, status etc.)
- logging frequency
- measurement range and resolution
- accuracy and long-term stability
- filtering, averaging or other processing steps
- validation and signal quality.

In addition to these specifications, it is also necessary to define in what way the measured data can be used to determine degradation of a specific component, for example:

- Are there any known functional relationships with other operational signals (e.g. rotational speed or power) and environmental conditions (e.g. temperatures), or is it possible to group signals (e.g. pitch angles for three blades or similar signals of other turbines)? Combining and/or grouping signals can be done to (1) verify if the signals are still functioning and (2) de-trend the signal and determine the actual degradation.
- Are the limits to indicate the 'green', 'yellow' and 'red' light available?
- Are the signals only being used for condition monitoring purposes or also for other purposes, i.e. part of the control loop or of the safety system?

Definition and implementation of algorithms

Once the instrumentation and possibilities for early failure detection are described in detail, the algorithms for data analysis should be developed. Some algorithms

need to be implemented in the different measurement systems, to give real-time warnings or to reduce large amounts of data to some key figures.

Data storage

A database should be developed to store the data that are generated by the measurement systems together with the results of the real-time analyses. Some of the algorithms specified under Step 3 may require signals from various measurement systems and data sources. If so, such algorithms can be implemented in the database, and queries can be executed to obtain the required information. The results, however, are not real-time, but it is foreseen that the majority of the analyses will be carried out by executing database queries; only urgent alarms need to be dealt with online.

Reporting and presentation of results

The results of measurements and data analyses in real time should be presented to the operator of a wind farm, but only in case real errors occur. The in-formation should be as accurate as possible and false alarms should be avoided:

- Is the error correct or is it a false alarm due to a failed sensor?
- If the error is correct, should it lead to an immediate shut down, does it require an on-site inspection or can the repair action be postponed until the next preventive maintenance action?
- Is the error caused by degradation of the component (e.g. wear of the bearing) or is it an off-design condition (e.g. misalignment of a high speed shaft).

The data can be presented as graphs, to show the degradation over time as is done in Fig. 18.18, or as values in a tabular format in case the remaining lifetime of components can be determined accurately.

18.4.4 Logistics data

When modelling the O&M aspects of an offshore wind farm, the BB 'Operation and Maintenance' and 'Health Monitoring' will provide 'failure rates' and 'times to failure' respectively of wind turbine components. The costs to repair such (expected) failures depend on the required crew size, the types of transportation and crane vessels used, the costs of spare parts and the revenue losses due to downtime. To determine these costs it is necessary to investigate the logistic data in more detail and to determine, per maintenance or repair class, how many visits are necessary, if weather conditions are indeed as restrictive as expected, what kind of vessels are being used during repair actions, etc. The logistic data are available for most of the offshore wind farms but in most cases not in a format that can be processed straightforwardly. Types of data that can be thought of are:

- periodic (usually monthly and yearly) overviews with the performances of individual turbines and of the total wind farm (e.g. energy production, downtime, availability, comparison with the contractual availability)
- alarm lists and SCADA data per turbine and the entire wind farm (time, cause, duration), often processed automatically to determine the top ten of failures and downtime
- results of online condition monitoring systems and of offline oil samples
- overview of retrofit actions planned (*condition based maintenance*)
- information about weather and the number of workable days
- use of spare parts
- scheduled maintenance actions (*preventive maintenance*) of turbines and balance of plant (BOP)
- vessel transfer plans.

The above types of data are usually collected from different sources. What is missing in most cases is a clear overview of how, for instance, the alarms as listed in the alarm lists are related to the vessel transfers, or which kind of visits are related to the failure of certain components. Detailed investigations, and combining all sources of information with explanations from plant operators, are needed to derive the relevant information. Such a process is very labour intensive and in practice never gets done.

Below a procedure is proposed to collect the same data but in a more structured way to enable automated data processing and to reduce the amount of labour for data analysis drastically. Three aspects are crucial for this.

1 Instead of collecting the different sources of information on a periodic (monthly) basis and grouping them according to the types of data for all wind turbines (e.g. alarms, vessels transfer, losses, scheduled maintenance), it is necessary to make a chronological list of events per turbine in which all relevant types of data are stored. By doing so, analyses can be performed per turbine (e.g. statistical analyses, trend analyses) and later on, the results of the individual turbines can be aggregated to the wind farm level.
2 For each turbine an event list needs to be defined in which all events are listed in chronological order. This means that, most likely manually, it should be assessed if alarms or visits are independent of each other and can be treated as individual events or if they should be grouped and combined with vessel transfers and repair actions.
3 After the events are identified, each event should be classified as a 'repair class' ranging from automatic and remote resets (with limited repair effort) to replacement of large parts and making use of a large crane.

An example of an event list for one turbine with a repair classification is given in Fig. 18.19. If the data is collected in this manner, statistical data can be derived and presented in tables (see Table 18.7), graphs like a CUSUM plot or as CDFs

of the downtime. If case event lists are available for all turbines, the data of one single turbine can be compared with the average data of all turbines, as for instance in Fig. 18.20.

Event nr.	3			
Start event [date] [time]	21-4-2008 19:36			
Event type	Shutdown with visit (personnel only, small boat)			
Turbine ID or system ID	Turbine 1			
Nr. maintenance action	3.1	3.2	3.3	3.4
Start [date] [time]	23-4-2008 9:00	27-4-2008 7:00	5-5-2008 7:00	6-5-2008 13:30
End [date] [time]	23-4-2008 16:40	27-4-2008 19:00	5-5-2008 18:20	6-5-2008 15:12
Duration [hr]	7,7	12,0	11,3	1,7
Downtime [hr]				
Type of maintenance action	Remote reset	Inspections	Finalisation (or repair)	Finalisation (or repair)
Weather condition	1 = bad	0 = good	0 = good	0 = good
Scada information	Code/text n	Code/text n	Code/text n	Code/text n
Crew size		2	4	2
Vessel personnel		Windcat 2	Windcat 2	Windcat 1
Travel time (one way)		0,75	0,75	0,75
Mobilisation time [hr]		0	0	0
Supply vessel	n.a.	n.a.	n.a.	n.a.
Mobilisation time [hr]				
Crane vessel	n.a.	n.a.	n.a.	n.a.
Mobilisation time [hr]				
Explanations	Again yaw system??	Inspection: failed yaw motor, new one ordered	Replacement almost ready	System works OK
Main system ID				Yaw system
Component ID				Yaw motor
Work carried out				Replacement
Spare part in stock?				Yes
Logistic time spare part [hr]				24
Consumables				Consumable n
End event				6-5-2008 15:12
Duration event [hr]				355,6
Downtime event [hr]				355,6

18.19 Example of an event: 'Shut down with visit' which requires a remote reset and three visits to fix it.

Table 18.7 Example of a format to report results of statistical analyses of logistic data (fictitious data)

Turbine ID	#		**Total downtime**		Reporting period from . . .	to . . .
Total number of alarms reported	1000	[–]	10000	[hr]		
Number of relevant events	**650**	**[–]**	**11000**	**[hr]**		

							Downtime per event			
1. Resets (auto or remote)	**500**	**[–]**	**1500**	**[hr]**			**Min**	**Average**	**Max**	
1.1 Errors	280	[–]	1000	[hr]			0,1	3,6	25,7	[hr]
1.2 Control, ambient	220	[–]	**500**	[hr]			0,1	2,3	5,3	[hr]
	#		**Total downtime**		**# of visits**		**Downtime per event**			
2. Visit required	**150**	**[–]**	**9500**	**[hr]**	**264**	**[–]**	**Min**	**Average**	**Max**	
2.1 Preventive	40	[–]	250	[hr]	40	[–]	5	6	8	[hr]
2.2 Planned corrective (cond. based)	40	[–]	250	[hr]	40	[–]	5	6	8	[hr]
2.3 Paint	4	[–]	140	[hr]	8	[–]	20	35	60	[hr]
2.4 Corrective small	50	[–]	2000	[hr]	100	[–]	20	40	80	[hr]
2.5 Corrective crane ship	16	[–]	6860	[hr]	76	[–]	200	429	1000	[hr]

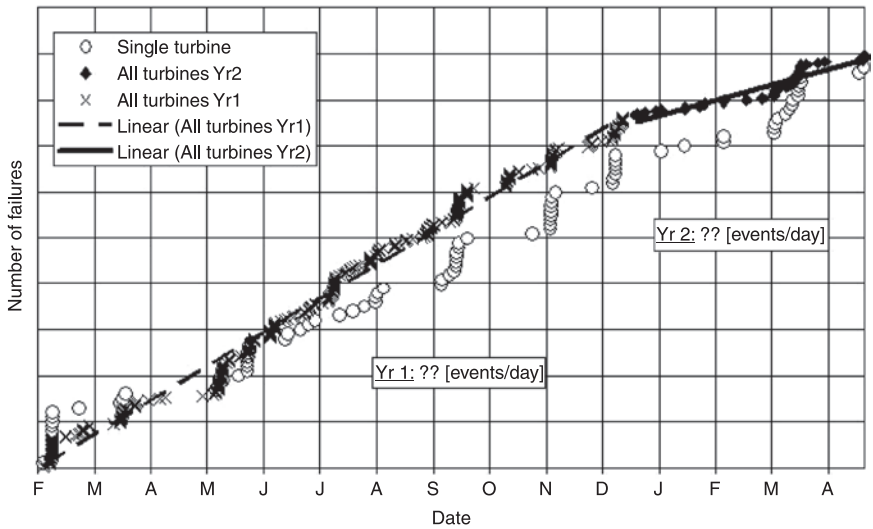

18.20 Example of a CUSUM plot, showing the performance of a single turbine in comparison with the performances of the entire wind farm. The failure rate of the entire wind farm is decreasing in year 2, whereas the failure rate of the single turbine is lower, but remains constant in year 2.

18.5 Site-specific operation and management optimisation and future trends

As indicated in Section 18.3.2, most of the currently available cost models are being used in the planning phase of an offshore wind farm to make an estimate of the O&M aspects such as costs and downtime, to make an assessment of the uncertainties of these aspects due to uncertainties in the input parameters, and to assess the impact of using different access vessels or crane ships on the O&M aspects. At present, procedures to use cost models during the operational phase of a wind farm such as the O&M Cost Estimator described in Section 18.4.1 are not common practice. The reasons for that are that (1) approaches to collect and analyse operational data as described in Section 18.4 are not yet implemented in the daily practices of wind farm operation and (2) the exchange of data and information between the wind farm owner and the parties doing O&M (often the turbine manufacturer) are not well organised. In this section, examples will be given of how O&M models can be used to optimise a wind farm located close to the shore (near shore) and a wind farm far offshore in deeper waters (far offshore).

18.5.1 Near-shore wind farm

A fictitious baseline wind farm is considered which consists of 100 turbines of 2.8 MW each planned at approximately 25 km from the harbour from which all

vessels (transportation of personnel, transportation of spare parts, and large crane ships) can depart. The travel time from the harbour to the turbine and vice versa with small vessels is assumed to be approximately 45 minutes to 1 hour. Personnel travel to the wind farm in the morning and return in the evening to carry out maintenance. The wind farm is connected to the grid via two transformer stations. In case of a transformer station failure, 50 turbines will be shut down. The water depth is between 10 and 20 m. The weather conditions at the North Sea, (IJmuiden Munitietstortplaats YM6, 52°33'00" north and 4°03'30" east) are assumed.

For the baseline configuration it is assumed that the following methods and equipment will be used for transfer of personnel and spare parts and for hoisting of larger components.

- The turbines are equipped with an internal crane that can hoist up to 30 tonnes, and a platform at the tower base for intermediate storage of parts during the replacement actions. Hoisting can only be done in average wind speeds of $V_w \leq 6$ m/s.
- Access vessels such as the boats shown in Fig. 18.3 will be used for transporting and transferring personnel and for transporting spare parts up to say 250 kg. These vessels are equipped with a small crane to put spare parts from the deck onto the wind turbine platform. Transportation of personnel and access to turbine can be done at $V_w \leq 12$ m/s and $H_s \leq 1.5$ m. For larger components, above 250 kg, a supply vessel is needed to transport the spare part to the turbine. Putting spare parts from the access vessel (or supply vessel in the case of larger parts) on the platform and vice versa can be done at $V_w \leq 12$ m/s and $H_s \leq 1.5$ m. Hoisting of parts from the platform into the nacelle is done by the internal crane at $V_w \leq 6$ m/s and $H_s \leq 1.5$ m.
- Larger components such as a generator or gearbox (with a weight of up to 30 tonnes) will be transported to the turbine by a repair vessel, put on the platform and hoisted into the nacelle with the help of a large internal crane. The same maximum weather conditions apply as under the previous bullet.
- To hoist the complete rotor, nacelle or other large part, a crane ship with a 100 tonnes crane is needed. The replacement of the failed component will take about 1–2 days. Prior to the actual replacement, inspections will be carried out and visits are needed to dismount the component. After the replacement, several visits are necessary for commissioning. Transportation of personnel and access to the turbine can be done up to $V_w = 12$ m/s and $H_s = 1.5$ m. During the hoisting activities, the weather conditions should be good, i.e. wind speed less than 6 m/s (hoisting) and 10 m/s (working in open nacelle). During positioning of the crane ship, the wind speed should be less than 12 m/s and the wave height less than 2.0 m.

For modelling purposes, it is assumed that preventive maintenance will be carried out once a year and will last three working days. Every five years a large

preventive maintenance action is foreseen, among other things to change the gearbox oil. The failure rate is assumed to be 4.5 failures per year per turbine for those failures that require a visit of technicians. In addition, five remote resets are assumed per turbine per year. Finally, it is assumed that the transformers will fail 0.3 times per year. The cost model revealed that the availability of the baseline scenario would be 93.7% and the O&M will cost 2.6 €ct/kWh. In order to reduce the downtime, it is necessary to determine what causes the downtime. The ECN O&M Tool provides detailed information for determining drivers of costs and downtime, among others the graph as shown in Fig. 18.21. As can be seen, most of the downtime is caused by repair actions related to the generator, the gearbox and the transformer. The white part of the bars indicates that the time waiting for good weather is dominant.

To investigate the sensitivity of the O&M costs of baseline results as a function of variations of the input parameters and to determine upper and lower values for O&M costs, the following alternatives have been analysed.

Alternative 1: Increasing the size of the turbine; using 56 turbines of 5.0 MW each, instead of 100 turbines of 2.8 MW each. If the O&M strategy is kept constant and it is assumed that the reliability of the turbines is similar to that of the 2.8 MW turbines, the number of accesses and repairs will reduce. Also the overall BOP costs will reduce due to the lower number of foundations. Since the 5.0 MW turbines are not as mature as the 2.8 MW turbines, a 20% lower reliability has been assumed.

Alternative 2: The distance to the shore will be 40 km instead of 25, meaning a longer travel time of the vessels.

Alternative 3: Similar to Alternative 2 but making use of a hotel boat to stay overnight and to store intermediate spare parts. The hotel boat will require

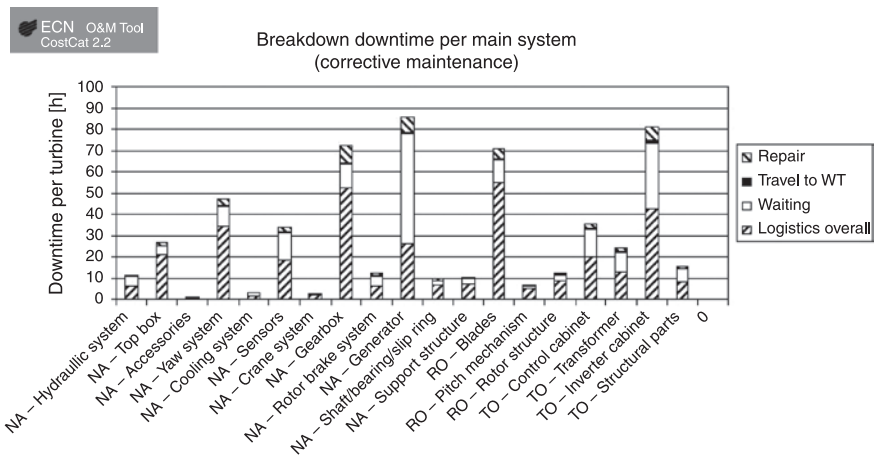

18.21 Breakdown of downtime per main system. NA = nacelle; RO = rotor; TO = tower.

Table 18.8 Summary of cost and downtime

Scenario	No. of turbines	Distance (km)	Reliability	Hotel boat	Availability [%]	O & M costs [ct/kWh]
Baseline	100	25	–	No	93.7%	2.60
Alternative 1	56	25	80%	No	92.1%	2.38
Alternative 2	100	40	–	No	93.4%	2.63
Alternative 3	100	40	–	Yes	94.0%	2.79
Alternative 4	100	25	120%	No	94.9%	2.17
Alternative 5	100	25	–	No	94.9%	2.24

high investment costs and annual costs for operations, but it should lead to shorter travel times and longer working days of technicians. The rates of technicians have been increased since they are employed offshore 24/7. Instead of large access vessels, cheaper RIB boats will be used.

Alternative 4: Baseline with improved reliability (20%).

Alternative 5: Improved O&M baseline scenario, which means that the access vessel is capable of transporting spare parts for of up to 2000 kg to the turbine and avoiding the use of a supply vessel.

The results are summarised in Table 18.8. *(Please note that these results are only relevant for this fictitious wind farm and should not be considered as generally applicable; they are only meant to demonstrate the capabilities of cost modelling.)*

18.5.2 Far-offshore wind farm

For future large offshore wind farms at distances of more than typically 50 km from the harbour, different maintenance strategies need to be developed. The travelling times from the harbour to the turbines becoming more than 1 hour strongly reduces the net working time. It is likely that hotel boats or living quarters will be used for technicians to stay overnight. It is likely that the wind farms will become larger and will consist of turbines larger than, say, 3 MW. For such large applications, it is likely that wind farm operators will hire large equipment for a longer period of time instead of hiring the equipment per event as is the case for smaller wind farms. Or such vessels can be shared by more than one wind farm. Hiring such equipment for a longer period of time will strongly reduce the mobilisation/demobilisation costs and the logistic time for ordering such a vessel.

With the ECN O&M Tool a far-offshore wind farm, consisting of 120 turbines of 5 MW each, has been modelled at 50 km offshore. A hotel boat will be used for personnel to stay overnight and for the storage of spare parts. An improved access vessel will be used, which can be operated up to 2.5 m significant wave heights. The cost model revealed an availability of 94.8% and kWh costs of 2.33 €ct. The

O&M costs of large offshore wind farms seem to be in the same range as for the near-shore wind farms.

From this it can be concluded that large offshore wind farms at far-offshore sites are feasible, but only if larger turbines can be used with a reliability similar to the presently used onshore Multi MegaWatt class, and if hotel boats in combination with improved access vessels can be used, and if the costs and logistic times of large crane barges can be reduced.

18.5.3 Operation and maintenance modelling versus the real world

As indicated in Section 18.1.2 hardly any operational experiences of offshore wind farms are made public. It is the authors' experience that the effort for preventive maintenance can be estimated rather accurately. Furthermore, the failure rates of components to determine the effort for corrective maintenance can also be determined accurately from generic databases or (more preferably) from operational experiences. However, the amount of so-called 'unplanned corrective maintenance' caused by serial problems, design and development errors and leading to retrofits for the entire population, are likely to be underestimated in an O&M modelling process. The same holds for the number of visits and repair actions needed to replace large components. Estimates made initially by O&M experts mostly show an optimistic value for the number of visits needed.

18.6 References

1. *http://www.offshore-sea.org.uk/site/*5.
2. Durstewitz, M *et al*.. (2002), *Wind Energy Report Germany 2001; Annual Evaluation of WMEP*, ISET, Germany 2002 (and subsequent years).
3. Windstats Newsletter, Quarterly International Publication, 1994–2003, *www.windstats.com*.
4. Braam, H and Rademakers, L W M M (2001), *The MAINTENANCE MANAGER Collecting and Analysing Maintenance Data of Wind Turbines*, ECN-C-01-012.
5. BTM Consult. (2002), *World Market Update 2001*, Chapter 6. Denmark, March 2002.
6. *http://www.berr.gov.uk/files/file42918.pdf; /file41542.pdf; /file34791.pdf; /file41543.pdf*; and */file41600.pdf, 2008*
7. Bengtsson, M (Mälardalen University, Sweden) (2004), 'Condition based maintenance system technology – Where is development heading?', *Euromaintenance 2004, Proceedings of the 17*th *European Maintenance Congress*, 11–13 May 2004, Barcelona, Spain.
8. Davies, A, editor (1998), *Handbook of Condition Monitoring; Techniques and Methodology*. Chapman & Hall, ISBN 0 412 61320 4.
9. Stratford, P (2007), 'Assessing the financial viability of offshore wind farms', *Proceedings EWEC 2007*, Milan, Italy, 7–10 May 2007.
10. Philips, J L, Morgan, C A and Jacquimin, J (2006), 'Evaluating O&M Strategies for offshore wind farms through simulation – the impact of wave climatology', *OWEMES 2006, Civitavecchia*, Italy, 20–22 April.

11. Rademakers, L W M M, Braam, H, Obdam, T S (ECN Wind Energy), Frohböse, P (Germanischer Lloyd) and Kruse, N (HAW Hamburg). (2007), 'Tools for estimating operation and maintenance costs for offshore wind farms: State of the Art', *Presented at the Hamburg Offshore Wind Conference 2007*, Hamburg.
12. Rademakers, L W M M, Braam, H and Obdam, T S (2008), 'Estimating costs of operation and maintenance for offshore wind farms', *Presented at the European Wind Energy Conference 2008*, Brussels, ECN-M-08-027.
13. Rademakers, L W M M, Braam, H, Zaaijer, M B and van Bussel, G J W (2003), 'Assessment and optimisation of operation and maintenance of offshore wind turbines', *Proceedings EWEC 2003*, Madrid, 16–19 June 2003.
14. Wiggelinkhuizen, E J, Rademakers, L W M M, Verbruggen, T W, Watson, S J, Xiang, J, Giebel, G, Norton, E J, Tipluica, M C, Christensen, A J Becker, E (2007), CONMOW (CONdition Monitoring Offshore Wind turbines) Final Report, ECN-E-07-044, July 2007.
15. Wiggelinkhuizen, E J, Verbruggen, T, Braam, H, Rademakers, L, Xiang, J Watson, S (2008), 'Assessment of condition monitoring techniques for offshore wind farms', *Paper Presented in the Journal of Solar Engineering*, August 2008, Volume 130, Issue 3, 031004.
16. Verbruggen, T W and van der Werffl, P A (2007), *Conditiebewaking rotor bladen; Belastingsmetingen m*et *optische sensoren*, ECN-E–07-025, April 2007.
17. Obdam, T S, Rademakers, L W M M and Braam, H (2009), 'Flight leader concept for wind farm load counting and performance assessment', *Proceedings EWEC 2009*, Marseille, 15–19 March, 2009.
18. D Vose. (2000), *Risk Analysis: A Quantitative Guide*, second edition, John Wiley & Sons, Ltd; ISBN 0-471-99765-X

Index

Large-scale wind power generation is one of the fastest developing sources of renewable energy and already makes substantial contributions to power grids in many countries worldwide. With technology maturing, the challenge is now to increase penetration, and optimise the design, construction and performance of wind energy systems. Fundamental issues of safety and reliability are paramount in this drive to increase capacity and efficiency.

Wind energy systems: Optimising design and construction for safe and reliable operation provides a comprehensive review of the latest developments in the design, construction and operation of large-scale wind energy systems, including in offshore and other problematic environments.

Part I provides detailed coverage of wind resource assessment and siting methods relevant to wind turbine and wind farm planning, as well as aeroelastics, aerodynamics and fatigue loading that affect the safety and reliability of wind energy systems. This coverage is extended in Part II, where the design and development of individual components is considered in depth, from wind turbine rotors to drive train and control systems, and finally tower design and construction.

Part III explores operation and maintenance issues, such as reliability and maintainability strategies and condition monitoring systems, before discussing performance assessment and optimisation routes for wind energy systems in low wind speed environments and cold climates. Part IV reviews offshore wind energy system development, from the impact of environmental loads such as wind, waves and ice, to site-specific construction and integrated wind farm planning, and of course the critical issues and strategies for offshore operation and maintenance.

With its distinguished editors and international teams of contributors, *Wind energy systems* will be a standard reference source for wind power engineers, technicians and manufacturers, as well as researchers and academics involved in this expanding field.

Professor John Dalsgaard Sørensen is Head of Wind Energy Systems and Technologies (WEST) at Aalborg University (AAU), Denmark and is noted for his research on wind energy structures and wind turbines. **Professor Jens Nørkær Sørensen** is Head of Fluid Mechanics at the Department of Mechanical Engineering, Technical University of Denmark (DTU) and is noted for his research in fluid dynamics and the aerodynamics and aero-acoustics of wind turbines.

Woodhead Publishing Limited
80 High Street, Sawston
Cambridge CB22 3HJ
UK

ISBN 978-1-84569-580-4

Woodhead Publishing
1518 Walnut Street 1100
Philadelphia, PA 19102
USA

www.woodheadpublishing.com
www.woodheadpublishingonline.com

WP
WOODHEAD
PUBLISHING